PMEL Tsunami Forecast Volume for the Northern California, Vol #3

Contents

Foreword

Tsunamis have been recognized as a potential hazard to United States coastal communities since the mid-twentieth century, when multiple destructive tsunamis caused damage to the states of Hawaii, Alaska, California, Oregon, and Washington. In response to these events, the United States, under the auspices of the National Oceanic and Atmospheric Administration (NOAA), established the Pacific and Alaska Tsunami Warning Centers, dedicated to protecting United States interests from the threat posed by tsunamis. NOAA also created a tsunami research program at the Pacific Marine Environmental Laboratory (PMEL) to develop improved warning products. The scale of destruction and unprecedented loss of life following the December 2004 Sumatra tsunami served as the catalyst to refocus efforts in the United States on reducing tsunami vulnerability of coastal communities, and on 20 December 2006, the United States Congress passed the "Tsunami Warning and Education Act", under which education and warning activities were thereafter specified and mandated. A "tsunami forecasting capability based on models and measurements, including tsunami inundation models and maps. . . " is a central component for the protection of United States coastlines from the threat posed by tsunamis. The forecasting capability for each community described in the PMEL Tsunami Forecast Series is the result of collaboration between the National Oceanic and Atmospheric Administration office of Oceanic and Atmospheric Research; National Weather Service; National Ocean Service; National Environmental Satellite, Data, and Information Service; the University of Washington's Joint Institute for the Study of the Atmosphere and Ocean; and United States Geological Survey.

NOAA Center for Tsunami Research

Abstract

The National Oceanic and Atmospheric Administration has an established priority to provide timely and accurate forecasts of tsunami arrival and impact along Pacific and Atlantic Ocean coastlines and along coasts of the Caribbean Sea. As part of this ongoing effort, tsunami forecast models have been developed for six Northern California communities. Each forecast model is composed of a set of three nested grids and a set of parameters that contain variables necessary for numerical simulation. Construction of the nested set of grids starts with a baseline grid set derived from a high-resolution Digital Elevation Model. The baseline grid set is developed to cover an extensive area around each community and provides the basis for construction of an operational forecast model. This high-resolution grid set undergoes a process of subsampling and coverage reduction to reduce computational time while ensuring that topographic and bathymetric features, critical to accurately resolve wave dynamics, are preserved. During the development process, forecast model results are monitored for deviations from those computed with the computationally expensive, but more accurate, baseline model grid set. Development and subsequent validation and stability testing of the resultant tsunami forecast model is conducted to ensure model performance and robustness across a suite of scenarios. Specifically, historical tsunami events and synthetically generated mega Mw=9.3 events around the Pacific Basin were used for validation and stability testing of the six Northern California forecast models. Validation results show that model output consistently tracks observed data within an expected accuracy tolerance, thus lending confidence in the quantitative estimate of the tsunami time series, inundation, and runup provided by these models. In addition to robustness, reproducibility of results was verified by comparing development results with those attained during end-to-end operational system testing. Any differences noted in this report may well be attributed to updates to one or more of the forecast system components after completion of model development. Overall, validation results combined with benchmarking show that the Northern California forecast models developed for operational use by NOAA's two Tsunami Warning Centers consistently generate 4 hours of tsunami simulation in 10 minutes of CPU time without compromising forecast results.

Introduction and Objective

The NOAA Center for Tsunami Research (NCTR) at the NOAA Pacific Marine Environmental Laboratory (PMEL) has developed a tsunami forecasting capability for operational use by NOAA's two Tsunami Warning Centers located in Hawaii and Alaska (Titov *et al*., 2005). The capability is contained within an application suite designed to quickly and efficiently provide accurate basin-wide warning of approaching tsunami waves. Termed Short-term Inundation Forecast of Tsunamis (SIFT), the application combines a graphical user interface with data ingestion and numerical models to produce estimates of tsunami wave arrival times, amplitudes, currents, and flooding at each of 75 coastal communities. The selected communities were prioritized by National Weather Service Tsunami Warning Centers in partnership with state emergency managers. Each location has potentially vulnerable populations and/or economic or logistic assets located

along the Pacific and Atlantic Ocean coasts and along coasts of the Atlantic Ocean's Caribbean Sea. In order to maximize time available for response, the SIFT system integrates several key components: deep-ocean observations of tsunamis in real-time; a basin-wide, deep-ocean, pre-computed propagation database of water level and flow velocities based on potential pre-defined seismic unit sources; an inversion or fitting algorithm to refine the tsunami source based on the observations during an event; and tsunami inundation forecast models, alternatively referred to in literature and communication as Standby Inundation Models (SIMs).

The objective of this volume is to detail the process of developing tsunami forecast models for six communities along the Northern California coast. The models are used in real-time by operational centers to provide guidance to communities so that they may take action in advance of potential flooding and/or high current velocities induced by a tsunami, if one is generated. The system also offers assurance if there is no tsunami, alleviating fears preventing false alarms.

Forecast Methodology

The general methodology followed by NCTR for modeling tsunami impact along coastal areas is to reconstruct tsunami events using a linear combination of unit source propagation solutions in deep water. This reconstruction, in turn, provides boundary and initial conditions to computationally propagate tsunami waves across a set of three coastal, nested grids (A, B, and C), each of which is successively finer in resolution but reduced in coverage area, moving from offshore to onshore. Within the finest resolution and smallest grid in the set of three (C-grid), the near-shore details are resolved to the point that model output can be directly compared with observations at the tide gauge location within the same grid domain, also referred to in later chapters, as warning point or reference point comparisons. The C-grid, then, serves as the basis for the National Weather Service to operationally provide an estimate of wave arrival times, wave amplitude, currents, and simulation of wave inundation or flooding before tsunami waves reach a coastline.

Development of the operational tsunami forecast grid set starts with construction of one relatively high resolution, typically 1/3 arc sec [~10-meter], digital elevation model (DEM) by either the National Center for Environmental Information (formerly National Geophysical Data Center) or NOAA Center for Tsunami Research. Relative resolution is noted, since all bathymetry and topography data used represent the best available at the time of construction. Data from federal and state government, university, and private sources are incorporated into a large spatial extent area in order to reproduce wave dynamics along the coastline for which inundation is to be computed. A high-resolution baseline set of grids is then developed from the DEM. Due to the time constraints associated with real-time tsunami forecasting and the lengthy execution time associated with computation, this high-resolution grid set can not be used operationally. Rather, once developed, the high-resolution grid set, or model, is used as reference for development of the more computationally efficient tsunami forecast model set of grids. Hereafter referred to as the 'reference forecast model,' the high-resolution model is iteratively reduced in size. At the same time, resolution is coarsened by subsampling in

order to decrease numerical run time, while preserving the model's relevant topographic and bathymetric features. The trade-off between high resolution and computation time presents a significant challenge during tsunami forecast model development, but it is necessary in order to produce a set of grids that will meet operational requirements to provide 4-hours of tsunami simulation within 10-minutes of wall-clock time. For this reason, tsunami forecast models are often referred to as 'optimized' models. The overarching goal is to maximize the amount of time that a community has to react to a possible tsunami threat by providing accurate information quickly.

Each of the seventy-five community-specific tsunami forecast models, developed and reported in this set of technical volumes, collectively represent one element of the NOAA operational forecast capability. The complete forecast methodology incorporates additional elements in order to operationally track the propagation of tsunami waves across the forecast grids and provide both rapid and accurate estimates of wave arrival times, wave height, currents, and flooding soon after a tsunami has been generated. Combined, these elements form the Short-term Inundation Forecasting of Tsunamis (SIFT) application developed jointly by NOAA Center for Tsunami Research and National Weather Service. Specifically, a pre-computed tsunami propagation database, deep-ocean observations, a numerical model for computation, and a graphical user interface are the remaining elements that round out the forecast methodology.

The propagation database element consists of deep-water wave elevations and flow velocities pre-computed for a continuous series of 50 x 100 [km] unit sources along all known subduction zones within each ocean basin. Gica *et al.*, (2008) provide details of database generation, including design and seismic considerations. A detailed presentation of unit sources and characteristics of each are provided in **Appendix A**. Complimentary to the database, the observation methodology element serves to constrain numerical computation to the actual tsunami rather than to the earthquake mechanism. As tsunami waves propagate across the ocean, observations at Deep-ocean Assessment and Reporting of Tsunamis (DART®) stations and equivalent international deep-ocean platforms are automatically ingested into the SIFT application in real-time. (High quality, deep-ocean observations from other technologies may at some future time provide additional constraints.) The actual tsunami observed in the deep ocean provides a measure of the energy imparted to the ocean for wave generation as compared with sea surface elevation computed solely from earthquake source parameters through an inversion, or fitting, algorithm. The result is an observation-constrained estimate of the tsunami source in terms of the propagation database unit sources that best reproduce observed tsunami waves. These database unit sources are then linearly combined to produce synthetic boundary and initial conditions of water elevation and flow velocities to initiate tsunami forecast computations. A propagation solution for a specific event can, therefore, be expressed as a linear combination of unit sources. The multiplicative factors present in a linear combination of unit sources are referred to as scaling factors, slip amounts or alphas in later chapters.

The Method of Splitting Tsunami (MOST) numerical model is currently used in the SIFT application as the numerical computation element. MOST is a suite of numerical

simulation codes that solve the Non-linear Shallow Water equations (NSW). MOST is capable of simulating three processes of tsunami evolution: generation, transoceanic propagation, and inundation (flooding)

The MOST model has been verified for applicability to tsunami modeling with extensive testing against a number of laboratory experiments and benchmarks (Synolakis *et al.*, 2008; National Tsunami Hazard Mitigation Program, 2012). Community tsunami forecast models developed for use with MOST have been successfully used for simulations of many historical tsunami events for which data are available. In particular, events impacting the Pacific Ocean Basin after individual tsunami forecast models have been developed have been used to show individual and collective model accuracy and efficiency (Titov and González, 1997; Titov *et al.*, 2005; Titov, 2009; Tang *et al.*, 2008; Wei *et al.*, 2008). Comparison of model forecasts with observations at deep-ocean and coastal tide gauge locations, and with inundation (flooding) survey results after each successive tsunami event, continue to show the robustness of each methodology element as well as that of the collective application.

Design Considerations

Design of the geographical extent of forecast model grids takes into account the onset of nonlinear effects in shallow water and the reduction in wavelength that tsunami waves undergo as they propagate from deep into shallow waters. The onset of non-linear effects in wave evolution, as water depth decreases and wave amplitude grows, is the limiting factor in the use of the linearly combined solution that serves as the basis for the basin-wide propagation forecast. Before non-linear effects appear, the linear, deep-ocean solution is used to provide boundary and initial conditions for the forecast models. The linear solution enters the model through the boundary of the outermost grid and is then allowed to evolve in a non-linear way as it propagates into shallower waters. Thus, the offshore extent of the outermost forecast model grid is designed to overlap the deep-water, linear, solution prior to the onset of non-linear effects.

A second factor in determining the offshore extent of the exterior forecast model A-grid is dictated by the numerical constraint to maintain a minimum number of grid nodes per wavelength. The reduction in phase speed and wavelength experienced by tsunami waves when they travel from deep to shallow waters translates into a need to increase grid resolution in order to satisfy this requirement and ensure all relevant wave numbers are resolved.

Of the two grid design factors that control the offshore extent of the forecast model, the second one - the need for a minimum number of grid nodes per wavelength - is, in most cases, the overriding consideration, since significant non-linear effects usually appear in very shallow coastal waters.

In addition to the above-mentioned two factors, inclusion of local bathymetric and topographic features must also be considered when determining the geographical coverage of the forecast model grids. Such features may play a significant role in wave

propagation and may not have been appropriately captured in the coarse, basin-wide grid used to compute the propagation database.

Numerical stability of the MOST model's time-marching, explicit numerical scheme is controlled by the Courant-Friedrichs-Levy (CFL) condition. The CFL condition sets an upper limit on the maximum allowable time step in order to guarantee numerical stability. Model grid spacing, time step and wave speed determine the value of the CFL number for each grid node. Finer-scale spatial grids or greater water depths require shorter time steps to ensure CFL values remain in the stable range, which, in turn, increase the amount of computation required to simulate a specific real-time interval.

Post development testing

The development of a tsunami forecast model is intended to provide several hours of reliable and stable simulations of tsunami impact at specific communities within 10 minutes of wall clock time. Confirmation of performance during development is accomplished by testing the forecast model with historical event observations and with a set of synthetic tsunami events covering a range of source locations and magnitudes. The forecast model development environment involves the use of local hardware and software applications to pre-process data, compute simulations, and post-process results. Once model development is completed, additional testing is conducted to ensure that the same measure of performance is achieved in operations. This testing is intended to lend confidence that each forecast model performs as developed, to produce results consistent with those attained during development, and to assure those who rely on the tsunami forecast models that consistent results are produced, irrespective of hardware platform.

Overall, the purpose of this standardized testing can be summarized as three-fold: first, to ensure and document that results of runs through the operational SIFT tsunami forecast application are consistent with those obtained by the modeler during forecast model development; second, to test the forecast model for consistency and accuracy, and to document forecast efficiency over a representative range of generation locations and magnitudes; and third, to identify bugs, logic flow shortcomings, or other issues in need of resolution by either the SIFT software development and integration team or by an individual forecast model developer. Once identified, all issues are given priority to be resolved for timely update and release to the two NOAA Tsunami Warning Centers.

Considerations specific to each model and testing results are presented by the modeler in the distinct community sections within each of the volumes in the tsunami forecast model development series. Results of post-development testing, as independently conducted, are presented in each section as supplemental material.

Testing Procedure

The general procedure followed to test each tsunami forecast model is to initiate the model with historical tsunami event(s) and with a standard set of synthetic tsunami scenarios through the SIFT forecast system. Results are compared with those obtained during development, documented, and reported to the model developer. Specific testing steps include:

1. Identification of site appropriate testing scenarios contained within a standard set of synthetic events, historical events, and customized synthetic scenarios that may have been used during forecast model development.
2. Selection of unit sources and parameters necessary to generate the suite of initial conditions for each selected synthetic scenario and historical event.
3. Submission of test model runs through the SIFT forecast system, and export of all results from within the A, B, and C-grids. Forecasts at Tsunami Warning Centers warning points, flooding along the C-grid coast, and time series at the validation location (typically a tide gauge) are all exported.
4. Documentation of metadata, including specifics related to testing hardware and the SIFT forecast system version used in testing.
5. Examination of forecast model results for instabilities in any grid. Time series and results plots, especially coastal flooding areas at all locations within the C-grid, are examined.
6. Comparison of forecast model results obtained through the SIFT forecast system with those obtained during forecast model development. Tsunami maximum and minimum amplitudes and wave arrival times are compared, as are characteristics of later waves in time series.
7. Summarization of results with specific mention of consistency and time efficiency.
8. Notification to forecast model developer and/or to forecast software development team of inconsistencies or issues for evaluation and remediation.
9. Retesting of those forecast models identified as having inconsistencies in the forecast system when reported issues have been addressed or explained.

Synthetic simulations were run on a DELL PowerEdge R510 computer equipped with two Xeon E5670 processors at 2.93 GHz, each with 12 MB of cache and 32GB of memory. System processors were hex core and supported hyper-threading, resulting in the computer performing as a 24-processor core machine. Additionally, the testing computer supported 10 Gigabit Ethernet for fast network connections. This computer configuration is similar or the same as the configurations of the computers installed at the Tsunami Warning Centers, so the variance in compute times should be slight.

Volume Overview

Volume number three in the 14-volume tsunami forecast model development series documents the construction and testing of tsunami forecast models for six communities along the U.S. Northern California coast. Bathymetric inputs to the model, model validation using historical tsunami event data, model stability and robustness, and sensitivity testing using synthetic tsunami events are presented and discussed in chapter format for: Crescent City, Eureka, Arena Cove, Point Reyes, San Francisco, and Monterey. Results that include coarse identification of potential tsunami sources of greatest concern to each community highlight the model's use in applications other than forecasting but should be considered only in the context of this report volume and should not be used as a proxy for a complete hazard assessment that is more appropriately conducted systematically using the respective reference models. Reproducibility of development results and overall model performance through the operational SIFT application are provided in a supplement that serves to complete each of the six Northern California volume chapters.

1. PMEL Tsunami Forecast Model for Crescent City, California

Diego Arcas
Burak Uslu

Table of Contents

LIST OF FIGURES

LIST OF TABLES

1.   Crescent City, CA

Crescent City, California, is a coastal community on the Pacific Ocean in Northern California. The city lies atop the seismically active Cascadia subduction zone. Offshore bathymetric features, including the Emperor Seamounts, the Hess Rise, the Mendocino Escarpment, and the eroded Koko Seamount serve to channel energy toward Crescent City from a tsunami originating in the northern Pacific Ocean. **Figure 1** shows the northern California coast including Crescent City, California, in relation to the Mendocino Escarpment, identifiable as an abrupt change of ocean depth offshore of the community forecast site. **Figure 2** shows an aerial view of the Crescent City Harbor along with local topography and population concentration. The characteristic crescent shape sandy beach for which the city is named is evident. A map of the forecast area is provided in **Figure 3** to identify transit routes both along and away from the coast. **Figure 4** shows an aerial close-up of the Crescent City Bay and Harbor with the location of the tide gauge warning point shown in relation to the harbor breakwaters.

Crescent City is presumed to be more vulnerable to tsunamis than any other city along the West Coast of the United States, based on frequency of impact from past events. Tsunami waves tend to get amplified in the area around Crescent City, and the observed wave heights in Crescent City Harbor are typically an order of magnitude greater than those measured in other locations along the West Coast. The reasons for amplification of tsunami waves have not been clearly identified, though most evidence points to the combined effect of two factors:

> 1. The presence of the Mendocino Escarpment, an abrupt 1000-m seafloor depth discontinuity immediately offshore of the Northern California coast, with the potential for channeling tsunami energy toward Crescent City.
>
> 2. The tendency of the Crescent City Harbor to amplify wave frequencies around the 20-min period, perhaps being the most likely cause of elevated tsunami wave heights observed in the area. A substantial amount of tsunami energy can be found in the 20-min frequency band, which undoubtedly contributes to the amplification of the tsunami within the harbor boundaries.

These reasons make Crescent City one of the highest priority sites along the United States west coast for a tsunami inundation study and the development of a forecast model for operational inclusion. The objective of the present work is to develop an operational forecast model for the community of Crescent City, the second most populous coastal community in California north of San Francisco, with a population of approximately 7500 (http://www.crescentcity.org), second only to Eureka in population and economic relevance. It is noted, however, that the overall importance of providing an accurate tsunami forecast for Crescent City stems from the wave amplification effects experienced by tsunamis when they reach Crescent City. As discussed earlier, due to local and far-field bathymetric effects in conjunction with local harbor resonance, far-field tsunami waves in Crescent City tend to peak significantly higher than anywhere else along the United States west coast. Consequently, estimated tsunami wave heights at Crescent City are likely to provide tsunami forecasters and emergency managers with probable maximum tsunami wave

heights to be expected along the United States west coast. This report describes the development and testing of the Crescent City, California, tsunami forecast model, including bathymetric grid development, model verification, and sensitivity testing using synthetic tsunami events.

1.1. Model development

Modeling of Crescent City is accomplished by development of a set of three nested grids that telescope down from a large spatial extent to a grid that finely defines the localized community. The basis for these grids is a high-resolution digital elevation model constructed by NCTR or, more commonly, by the National Geophysical Data Center using best available bathymetric, topographic, and coastal shoreline data for an at-risk community. For each community, data are compiled from a variety of sources to produce a digital elevation model referenced to Mean High Water in the vertical and to the World Geodetic System 1984 in the horizontal (http://ngdc.noaa.gov/mgg/inundation/tsunami/inundation.html). From these digital elevation models, a set of three high resolution, "reference" models are constructed which are then "optimized" to run in an operationally specified period of time.

1.1.1. Historical events and tide gauge

Crescent City has a long history of being impacted by tsunamis. The tsunami generated by the moment magnitude 9.2 Great Alaska Earthquake of March 1964 in Prince William Sound a profound effect on the community. Twelve people in Crescent City lost their lives and the city sustained more than $15 million in tsunami-related losses (http://www.humboldt.edu/~geology/earthquakes/tsunami!/n_coast_tsunamis.html). Tide gauge data recorded inside Crescent City harbor during this event confirmed tsunami impact. Subsequent tsunamis have been generated and recorded at the Crescent City tide gauge. However, only four ve potential records are of high enough quality for use in the validation of the Crescent City forecast model. These are records obtained during the 1996 Andreanof Island, 2007 Peru, 2006 Kuril, and 2006 Tonga events.

1.1.2. Bathymetry and topography

1.1.2.1. Reference grids

Three bathymetric/topographic source grids developed by NCTR with different extension and resolutions were used to create reference and forecast grids for Crescent City. Color-filled contour plots of each source grid are shown in **Figures 5–7**. Specific digital elevation model metadata for each reference grid is provided in **Table 1**. The reference outer A grid was constructed by cropping the original digital elevation model constructed by NCTR to cover an area extending North to South from the southern half of Vancouver Island to northern California, approximately 100 miles South of the Mendocino Escarpment (**Figure 8**). The reference grid retained the resolution of the original 36-arc-sec data. The offshore grid boundary extends into 3000-m-deep water, which was deemed more than sufficient for use in conjunction with the NCTR-maintained propagation database. It has been estimated based on experience with the development of previous forecast models that, at 1000-m depth, the tsunami wavelength should still be long enough to be accurately resolved by the NCTR constructed 4-arc-min propagation grid.

Table 1. Digital elevation model metadata for the source grid A, B, and C.

	Grid A	Grid B	Grid C
ncols	1400	1200	240
nrows	1000	480	330
Lat (°)	39.0–53.0N	41.5–43.4983N	41.7165–41.7829N
Lon (°)	132.0–122.01W	124.8–125.0017W	124.2345–124.1431W
Zmin (m)	−5419.6	−980.99	−43.79
Zmax (m)	0.0	1387.5	174.9
Cellsize (arc sec)	36	6	1
average zonal cell size (m)	773.36	136.79	23.0698
meridional cell size (m)	1113.2	185.53	30.9221
east-west dimension (km)	772.58	65.52	7.5899
north-south dimension (km)	1557.4	222.45	7.3904
number of nodes in grid	1400000	576000	79200

For reference grid B, a smaller area extending offshore into 600-m-deep waters and located in the southern half of reference grid A was selected (**Figure 9** and **Table 2**). Once again, the original digital elevation model data resolution of 6 arc sec was preserved in the reference B grid, as was the total covered area in the original raw data grid.

For reference grid C, the full resolution, 1 arc sec, and extent of the original digital elevation model data were again preserved. **Figure 10** shows a contour plot of the bathymetry within reference grid C. Differences between the initial digital elevation model C grid and the stabilized reference C grid are shown in **Figure 11**. Final grid parameters for the reference model and for the forecast model are presented in **Table 2**.

Several instabilities developed inside reference grid C, mainly due to the presence of offshore surface single-node islands and to the poor resolution of very fine structures like the breakwaters that embay the harbor. Minor modifications were introduced to the bathymetry in order to stabilize the model. In the case of features that may play a relevant role in the determination of the wave dynamics, the elevation values of some grid nodes were modified to enhance the presence of the feature, as was the case with the breakwaters. It can be seen in **Table 2** that reference grid C has a spatial resolution of 23 and 31 m in the zonal and meridional directions. This level of resolution is barely adequate to resolve the 30-m-wide breakwaters in Crescent City harbor. In order to enhance the presence of the breakwaters, they had to be widened in some parts.

Other unstable features, like shallow areas surrounding small sea surface piercing rocks, were made deeper, since they do not have any major effect on the overall wave dynamics, but have the potential for generating instabilities.

Table 2. MOST setup and input parameters for reference and forecast models for Crescent City, CA.

Grid	Region	Reference Model Coverage Lat. [°N] Lon. [°W]	Cell Size ["]	nx × ny	Time Step [sec]	Forecast Model Coverage Lat. [°N] Lon. [°W]	Cell Size ["]	nx × ny	Time Step [sec]
A	Northern California/ Southern Oregon	48.98–39.01 128.5–123.52	36 × 36	449 × 998	3.3	44.495–40.515 126.995–123.535	72 × 72	174 × 200	6.45
B	Crescent City	43.498–41.5 124.8–124.007	6 × 6	1200 × 480	1.1	41.9983–41.5016 124.6–124.05	12 × 12	166 × 150	2.15
C	Crescent City	41.7829–41.7165 124.2345–124.1431	1 × 1	330 × 240	1.1	41.7829–41.7168 124.2345–124.1434	2 × 2	165 × 120	2.15

	Reference	Forecast
Minimum amplitude of input offshore wave [m]	0.001	0.001
Minimum offshore depth [m]	10	5
Water depth for dry land [m]	0.1	0.1
Friction coefficient (n^2)	0.0009	0.0009
CPU time for a 4-hr simulation	33 min	<10 min

Computations were performed on a single Intel Xeon processor at 3.6 GHz, Dell PowerEdge 1850.

1.1.2.2. Optimized grids

The final set of optimized or forecast model grids providing a run time of 4 hr of tsunami simulation in less than 10 min of CPU time is shown in **Figures 12–14**. Extents for reference and optimized grids are compared in **Table 2**. Even though forecast model grid A still extends into waters deeper than 2000 m, it has undergone a substantial reduction in coverage with respect to reference grid A. In addition, the grid has been sub-sampled to one half the resolution of the reference A grid. Forecast model grid B also provides reduced coverage in area and resolution (12 arc sec) with respect to its companion reference grid (6 arc sec). Forecast model grid C has been sub-sampled from the 1-arc-sec reference grid C to a 2-arc-sec forecast model grid C. The overall area of coverage, however, has been preserved.

1.1.3. Model setup

The area of extent for each of the three nested grids is shown in **Table 2**. Grid A has latitudinal and longitudinal coverage of approximately 10 degrees and 5 degrees, respectively. The coverage within grid B is approximately 2° latitudinal and .7° longitudinal. Coverage within grid C is approximately .07° latitudinal and .14° longitudinal, reflecting the fine scale community focus. The MOST model reference and forecast setup parameters for Crescent City are compared in **Table 3**. Input friction coefficient, input depths, and minimum offshore wave amplitude remain unchanged for both reference and forecast models. Input number of steps is decreased from approximately 39,000 for the reference model to approximately 20,000 for the forecast model.

Table 3. MOST model setup parameters for Crescent City, California (reference model and forecast model)

	Reference model	Forecast model
Minimum amplitude of input offshore wave (m)	0.001	0.001
Input minimum depth for offshore (m)	10	5
Input "dry land" depth for inundation (m)	0.1	0.1
Input friction coefficient (n**2)	0.0009	0.0009
let a and b runup	1	1
max eta before blow up (m)	100.0	30.0
Input time step (sec)	1.1	2.15
Input amount of steps	20000	20093
Compute "A" arrays every n-th time step, n=	3	3
Compute "B" arrays every n-th time step, n=	1	1
Input number of steps between snapshots	60	12
...Starting from	1	0
...Saving grid every n-th node, n=	1	1

1.2. Results and Discussions

1.2.1. Model validation

Four available time series of recorded tsunamis (2007 Peru, 2006 Tonga, 2006 Kuril, and 1996 Andreanof) at the Crescent City tide gauge were used for model validation. These records were the only ones available from NCTR's database exhibiting a signal-to-noise ratio sufficiently large to be used in the validation.

Historical events for which reference and optimized runs were made are listed in **Table 4**, as are simulated mega tsunamis for which only optimized runs were tested for the Crescent City forecast model (**Table 5**).

Simulated mega tsunamis tested are shown in **Table 5**. Stability testing was conducted using the standard suite of simulated 9.3 Mw events with an $\alpha = 29$ m as discussed in Tang *et al*. (2009). **Table 5** lists each event, including unit source pairs used for each simulation.

1.2.2. Detiding

The detiding procedure applied to the four historical events with available tide gauge data is illustrated here using the Kuril November 2006 event as a case study. In order to isolate the tsunami signal from the non-tsunami sea level changes a high-pass filter is applied to the tide gauge data. **Figure 15** shows the original time history for the Kuril, November 2006, event with time origin at the time of the earthquake. Interpolation of the available data was used to fill in the gaps of missing data points in the gauge signal before filtering. In order to isolate the tsunami signal, the data were processed to:

1. Demean the signal.

2. Fit a spline using the Matlab function *csaps*(*ts*, *csig*, *p*), where *t s* is the vector of time values, *csig* is the vector containing the sea surface elevation signal, and *p* is the smoothing parameter. The *p* values vary between 0 and 1, with *p* = 0 corresponding to a least-squares straight line fit to the data, while, at the other extreme, i.e., for *p* = 1, is the variational, or "natural" cubic spline interpolant. For this time history a value of *p* = 0.999999999 was used.

3. Subtract the series obtained by the spline fit from the demeaned original signal.

Figure 16 is an expanded view of the tsunami on the original tide gauge signal (blue) with gaps of missing data superimposed on the interpolated signal (red). **Figure 17** shows the original tide gauge time series (blue). The spline fitted signal (red) that will subsequently be removed from the original data appears superimposed on the raw data. **Figure 18** shows the result of removing the spline fit from the raw data, effectively removing the low frequencies associated with tidal variations from the signal and exposing the isolated tsunami signal.

Table 4. Historical events used for model validation for Crescent City, California.

Event	Earthquake Date Time (UTC)	Lat. (°)	Lon. (°)	Subduction Zone	Seismic Moment Magnitude (Mw)	Tsunami Magnitude[1]	Model Tsunami Source
1946 Unimak	1946-04-01 12:28:56	53.32N	163.19W	Aleutian-Alaska-Cascadia (ACSZ)	[2]8.5	8.5	7.5 × b23 + 19.7 × b24 + 3.7 × b25
1994 East Kuril	1994-10-04 13:23:28.5	43.60N	147.63E	Kamchatka-Kuril-Japan-Izu-Mariana-Yap (KISZ)	[3]8.3	8.1	9.0 × a20
1996 Andreanov	1996-06-10 04:04:03.4	51.10N	177.410W	Aleutian-Alaska-Cascadia (ACSZ)	[3]7.9	7.8	2.40 × a15 + 0.80 × b16
2001 Peru	2001-06-23 20:34:23.3	17.28S	72.71W	South America (SASZ)	[3]8.4	8.2	5.70 × a15 + 2.90 × b16 + 1.98 × a16
2003 Rat Island	2003-11-17 06:43:31.0	51.14N	177.86E	Aleutian-Alaska-Cascadia (ACSZ)	[3]7.7	7.8	[4]2.81 × b11
2006 Tonga	2006-05-03 15:27:03.7	20.39S	173.47W	New Zealand-Kermadec-Tonga (NTSZ)	[3]8.0	8.0	8.44 × b29
2006 Kuril	2006-11-15 11:15:08.0	46.71N	154.33E	Kamchatka-Kuril-Japan-Izu-Mariana-Yap (KISZ)	[3]8.3	8.1	[4]4.0 × a12 + 0.5 × b12 + 2.0 × a13 + 1.5 × b13
2007 Kuril	2007-01-13 04:23:48.1	46.17N	154.80E	Kamchatka-Kuril-Japan-Izu-Mariana-Yap (KISZ)	[3]8.1	7.9	−3.82 × b13
2007 Solomon	2007-04-01 20:40:38.9	7.79S	156.34E	New Britain-Solomons-Vanuatu (NVSZ)	8.1	8.2	12.0 × b10
2007 Peru	2007-08-15 23:41:57.9	13.73S	77.04W	South America (SASZ)	[3]8.0	8.1	4.3 × a9 + 4.1 × b9
2007 Chile	2007-11-14 15:41:11.2	22.64S	70.62W	South America (SASZ)	[3]7.7	7.6	0.81 × a22 + 0.33 × a23 + 0.11 × b23

[1]Equivalent tsunami source moment magnitude from model source constrained by tsunami observations.
[2]López and Okal (2006)
[3]Centroid Moment Tensor
[4]The tsunami source was obtained during real time and applied to the forecast

Table 5. Synthetic megatsunamis tested (subset of 16 of the 18 commonly used, Tang et al., 2009)

Scenario	Subduction Zone	Unit Source Combination
KISZ 22–31	Kamchatka-Kuril-Japan-Izu-Mariana-Yap	A22–A31, B22–B31
KISZ 1–10	Kamchatka-Kuril-Japan-Izu-Mariana-Yap	A1–A10, B1–B10
ACSZ 12–21	Aleutian-Alaska-Cascadia	A12–A21, B12–B21
ACSZ 22–31	Aleutian-Alaska-Cascadia	A22–A31, B22–B31
ACSZ 38–47	Aleutian-Alaska-Cascadia	A38–A47, B38–B47
ACSZ 56–65	Aleutian-Alaska-Cascadia	A56–A65, B56–B65
CASZ 1–10	Central America	A1–A10, B1–B10
SASZ 40–49	South America	A40–A49, B40–B49
NTSZ 20–29	New Zealand-Kermadec-Tonga	A20–A29, B20–B29
NTSZ 30–39	New Zealand-Kermadec-Tonga	A30–A39, B30–B39
NVSZ 28–37	New Britain-Solomons-Vanuatu	A28–A37, B28–B37
MOSZ 1–10	Manus-Oceanic Convergent Boundary	A1–A10, B1–B10
NGSZ 3–12	North New Guinea	A3–A12, B3–B12
EPSZ 6–15	East Philippines	A6–A15, B6–B15
RNSZ 12–21	Ryukus-Kyushu-Nankai	A12–A21, B12–B21
KISZ 32–41	Kamchatka-Kuril-Japan-Izu-Mariana-Yap	A32–A41, B32–B41

1.2.3. Model stability and reliability

In order to test the stability and reliability of the model before it is used in operations, a series of tests have been designed to ensure the performance of the model even in those scenarios where its stability may be compromised by the size of the event.

With this idea in mind a set of 16 megatsunamis originating from different regions of the Pacific Ocean and with a magnitude Mw = 9.3 have been designed in order to put the forecast model to the test with very large events arriving at Crescent City from all possible directions. The model is then run to ensure stability during 24 hr of tsunami simulation.

The definition of the 16 simulated tsunamis used to test the stability and reliability of the Crescent City forecast model is based on a unit source approach to partition worldwide subduction zones into manageable blocks for tsunami source isolation and modeling. Subduction zones have been broken up into fault segments, or unit sources, each measuring 100-km long by 50-km wide. A pre-computed propagation database has been created from each of these discrete earthquake rupture segments by computing wave propagation throughout the entire Pacific Ocean Basin (Gica *et al.*, 2008). Water level and flow velocities over all basin grid points are contained in the database from a total of 403 unit sources from earthquakes of 100 km $\times$ 100 km and 1-m rupture. Each simulated event used for Crescent City testing involves 20 unit sources with a scaling coefficient of 29 muniformly distributed along the rupture area. A more precise definition of these 16 synthetically generated events can be found in **Table 5**. Details of Pacific Basin unit sources are provided in **Appendix A**.

In order to stabilize the forecast model in any of the cases where it may have gone unstable, a limited number of modifications had to be introduced into grid C. A visual image of the differences between the final forecast model grid and the reference grid is shown in **Figure 19**.

1.2.4. Results of tested events

Figures 20 through 30 show plots of the time series comparison between high resolution reference and tsunami forecast models for each of the events listed in **Table 4**. In addition, the time series of the tsunami signal recorded at the Crescent City tide gauge during the 1996 Andreanof, 2006 Tonga, 2006 Kuril, 2007 Kuril, and 2007 Peru events are included in the plots as well. Results show that the optimized forecast model reproduces the high-resolution results at the time of tsunami arrival. Result comparisons later in the time series where later waves dominate, are, however, inconsistent. Wave interaction due to reflection and refraction factor into these later waves and require non-linear investigations to model accurately. Comparison of model results with Crescent City tid egauge observations during specific historical events for which data are available, show that the model well establishes arrival time, amplitude, and rate of decay.

Figures 31 through 41 compare the maximum sea surface elevations for each high-resolution reference and tsunami forecast model for the historical events used in testing the Crescent City model. In all cases, forecast model results are consistent with those obtained from counterpart high-resolution reference models.

1.2.5. Inundation results

Figures 42 to 57 show the maximum sea surface elevations irrespective of time for each one of the simulated tsunamis given in **Table 5**. The resulting time series plot in the bottom left hand panel of the figure displays the estimated time of first wave arrival to the tide gauge (located in the left hand panel of the figure) and the maximum wave height for each event. In all, 16 far-field and near-field scenarios were tested.

1.2.6. Discussion

As expected, comparison of the reference inundation model results with observed values at the tide gauge yields a better correlation than when observed values are compared against the forecast model results. While, in general, during the first couple of hours of simulation reference and forecast model results do not differ greatly, the errors associated with the use of the coarser forecast model grid seem to have a cumulative effect over time, consequently there is a much larger discrepancy in the later waves of the time series of **Figures 20 through 30** than in the waves occurring in the first few hours.

The difference in the results of the reference and forecast model grids is undoubtedly associated with the lower resolution and smaller coverage of the optimized grids in relation to the reference grids. Necessary modifications of the forecast model grids to pass the robustness and stability tests, while they minimize the possibility of the model becoming unstable in an operational setting, introduce additional differences between the reference and forecast model grids which result in discrepancies in the model results.

An extended optimized forecast model grid A large enough to include the Mendocino escarpment was also tested to investigate inclusion of this bathymetric feature in the grid resulted in better correlation in the later waves of the reference vs. forecast model comparison. The time series obtained with this extended grid is shown in **Figure 58** in comparison with that obtained with the original forecast model grid. It can be seen that even though there are differences in the later waves, the new time series does not really introduce an improvement when compared with the observations. Consequently, the regular optimized grid A was retained.

1.3.   Summary and Conclusions

A set of reference inundation models and optimized forecast models was prepared for Crescent City, California. Instabilities were encountered in the preparation of reference grid C, mainly associated with the breakwaters and with single node islands. The instabilities were manually corrected or addressed by smoothing a cluster of nodes, when the origin of the instability could not be traced back to a single node.

After the first few hours of tsunami simulation, discrepancies between the reference and optimized forecast models become more prominent. This is probably associated with a cumulative error when the lower resolution forecast model grids are used in the simulation.

Comparison of available tide gauge data observed during the Peru 2007, Tonga 2006, Kuril 2006, and Andreanof 1996 events shows better correlation with the high-resolution reference grids than with the optimized grids. Comparison with both the reference and forecast model grids seems to improve for larger events; such is the case in the Kuril 2006 event. It is important from an operational standpoint to notice that even if the forecast model does not provide a good comparison between the observations and the forecast model, the order of magnitude of the tsunami is generally correctly captured in optimized model results.

The optimized forecast model developed for Crescent City, California, provides a 4-hr forecast of first wave arrival, amplitudes, and inundation tide gauge warning point within 10 min, based on testing with available historical data and simulated events as presented in this report.

Acknowledgments

FIGURES

Figure 1. Aerial image of northern California showing the Crescent City forecast area in relation to offshore bathymetry.

Figure 2. Aerial overview image of Crescent City showing the harbor area, local topography, and population concentration (courtesy of Google Earth).
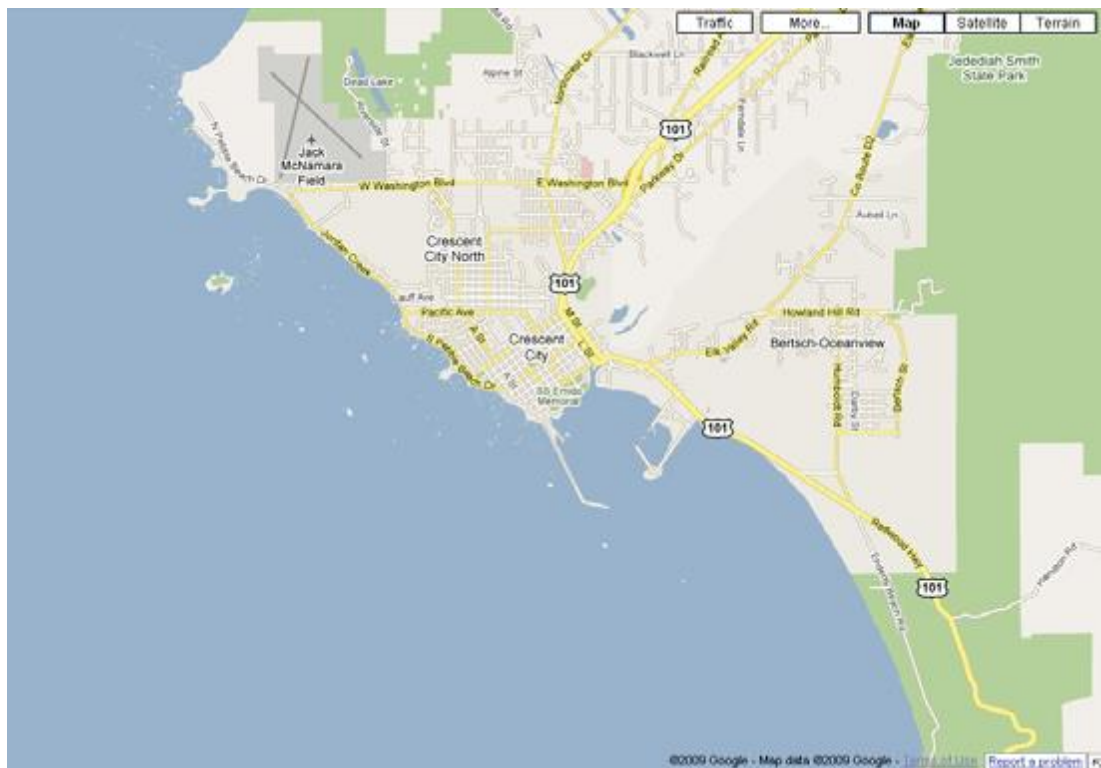
Figure 3. Map of Crescent City, California showing regional infrastructure. Transit routes along and away from the coast are identified in yellow (courtesy of Google Earth).

Figure 4. Aerial view of Crescent City, California, showing closeup of harbor and breakwaters. The location of the tide gauge is identified by a marker "A" in relation to the main dock area denoted by the green marker (courtesy of Google Earth).
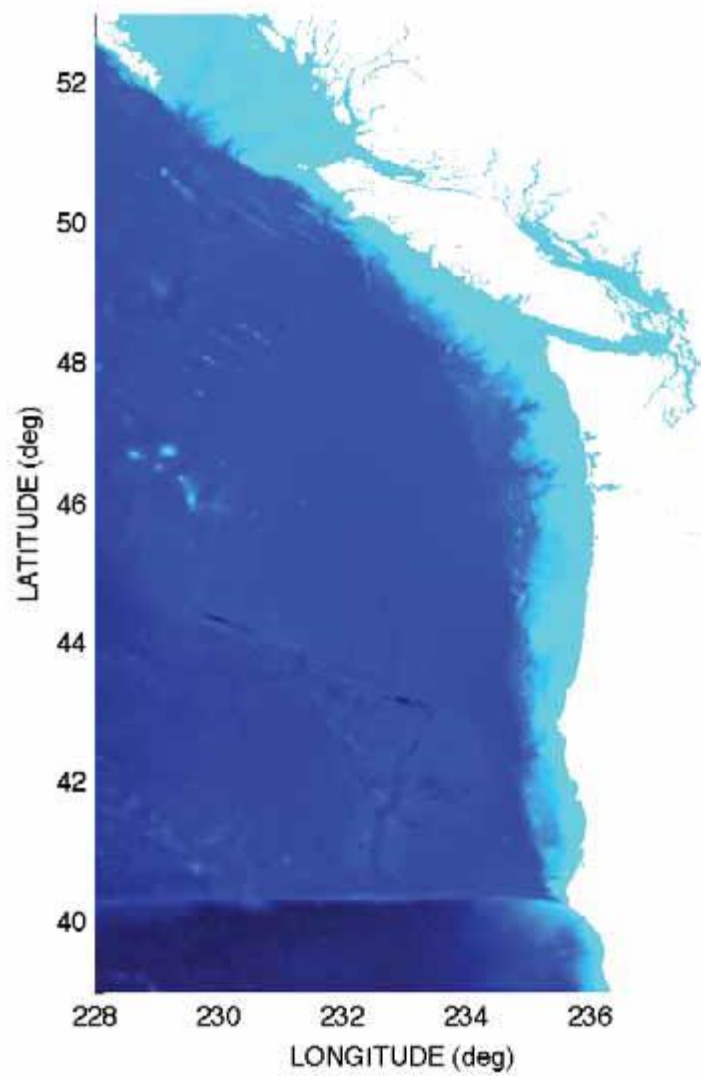
Figure 5. Color-filled surface plot o initial digital elevation model for grid A of the Crescent City forecast model.
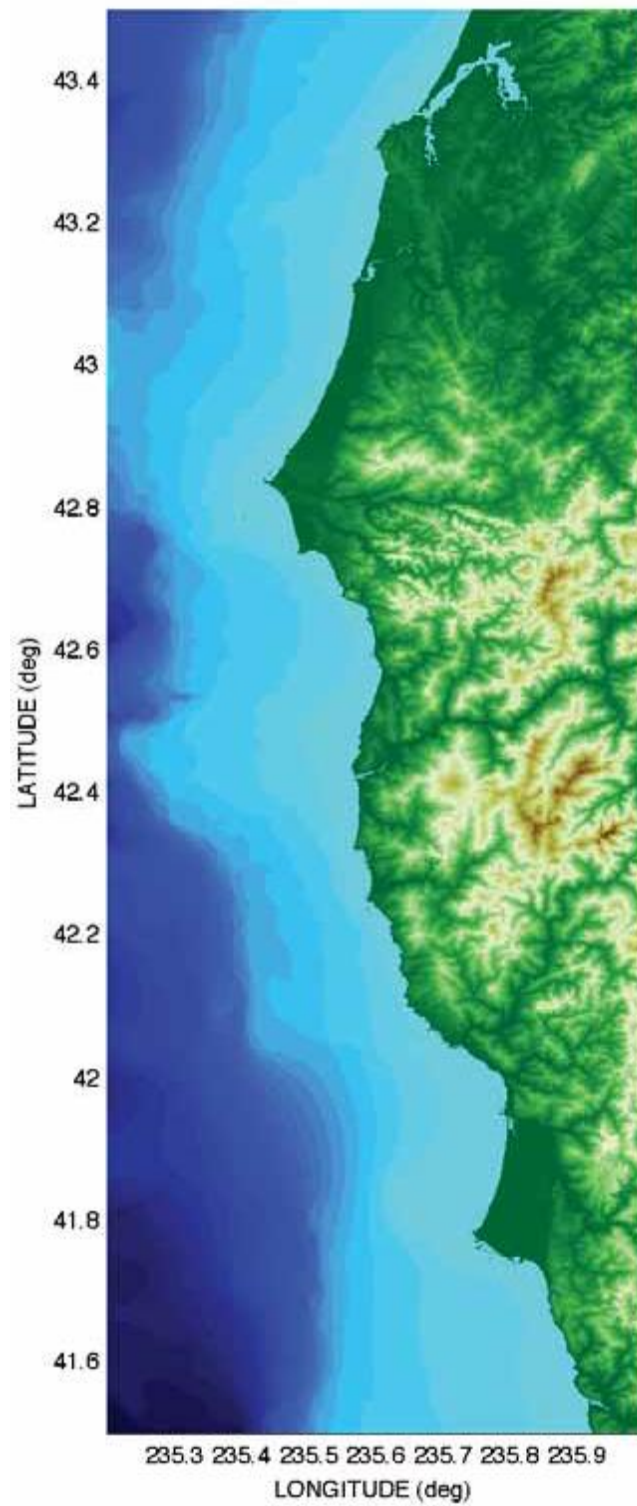
Figure 6. Color-filled surface plot of digital elevation model for grid B of the Crescent City forecast model.
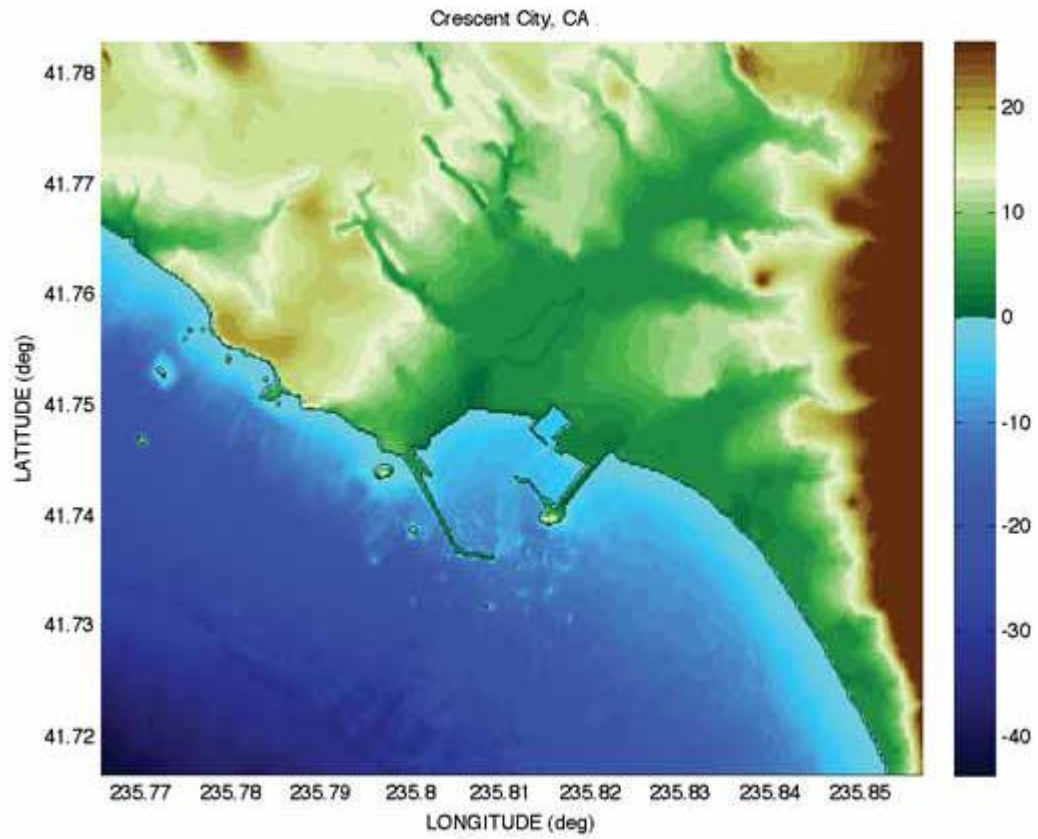
Figure 7. Color-filled surface plot of digital elevation model for grid B of the Crescent City forecast model.
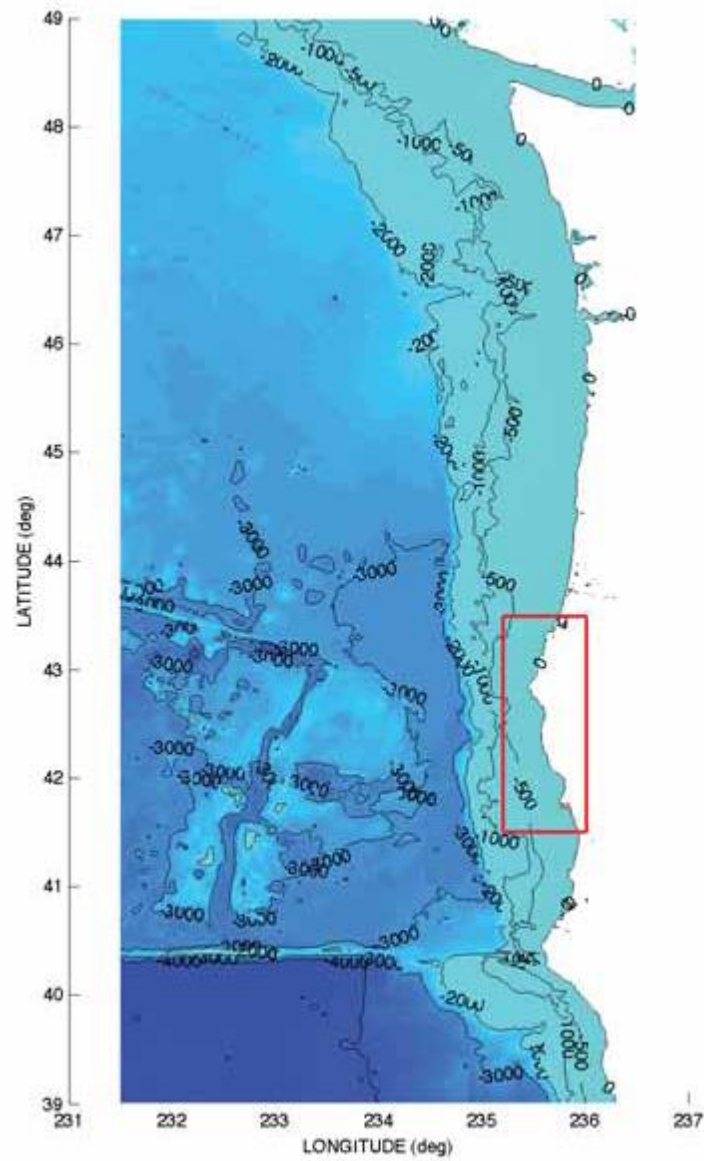
Figure 8. Contour plot of reference A grid. The outline of the adopted reference B grid is shown as a boxed overlay. Bathymetric contour units are in meters.
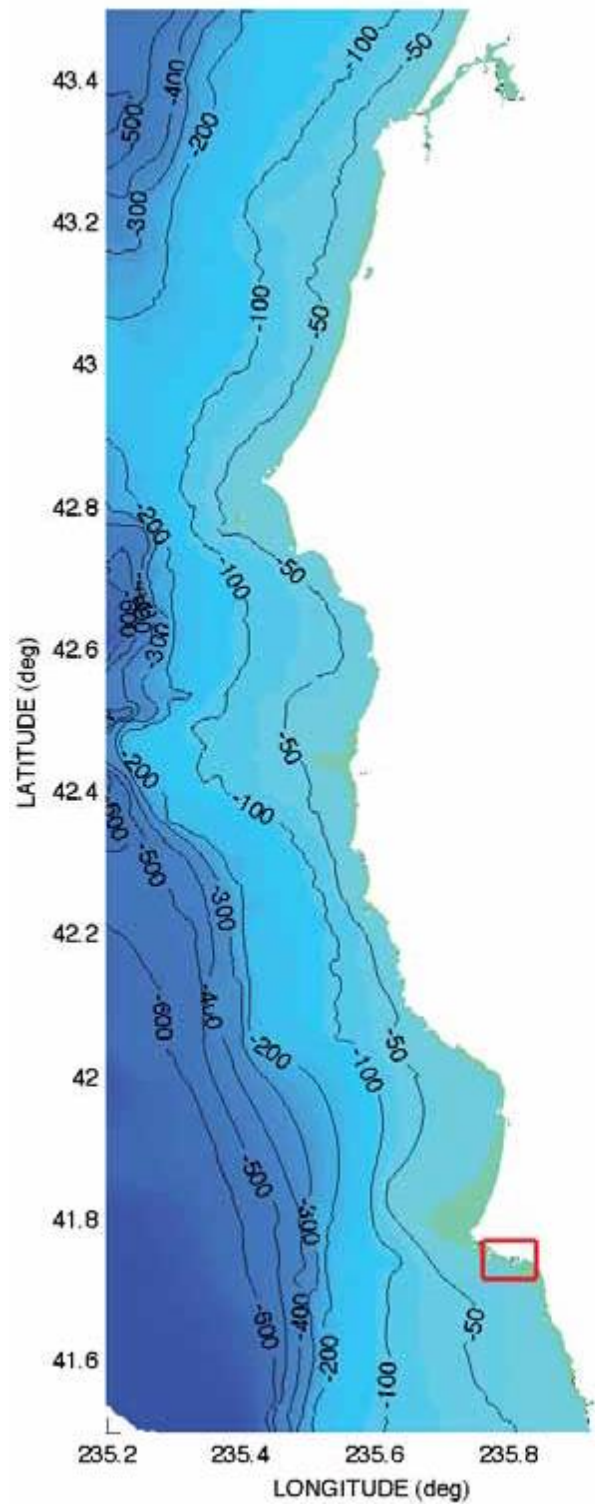
Figure 9. Contour plot of reference grid B. The outline of the adopted reference grid C is shown as a boxed overlay. Bathymetric contour units are in meters.
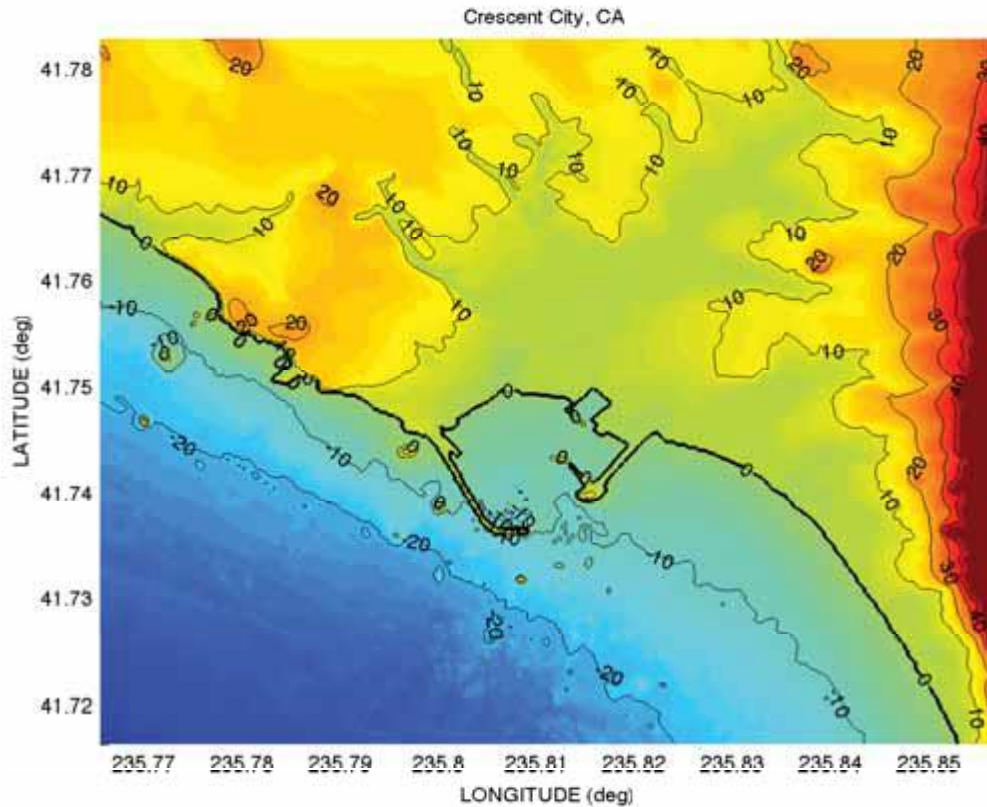
Figure 10. Contour plot of reference grid C. Bathymetric contour units are in meters.
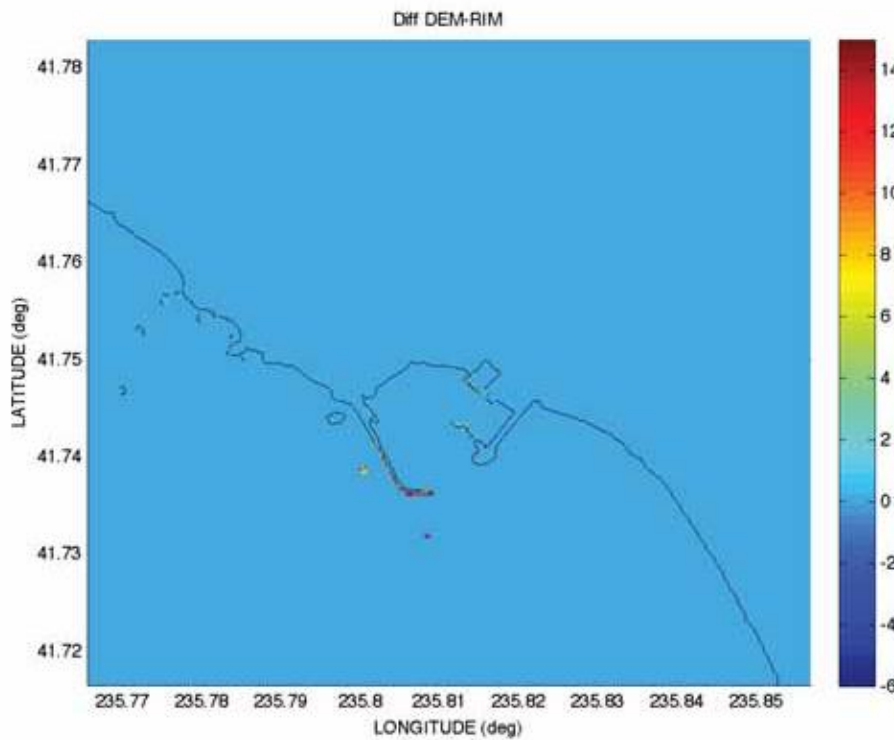
Figure 11. Differences in meters between the initial digital elevation model C grid and the stabilized reference grid C.
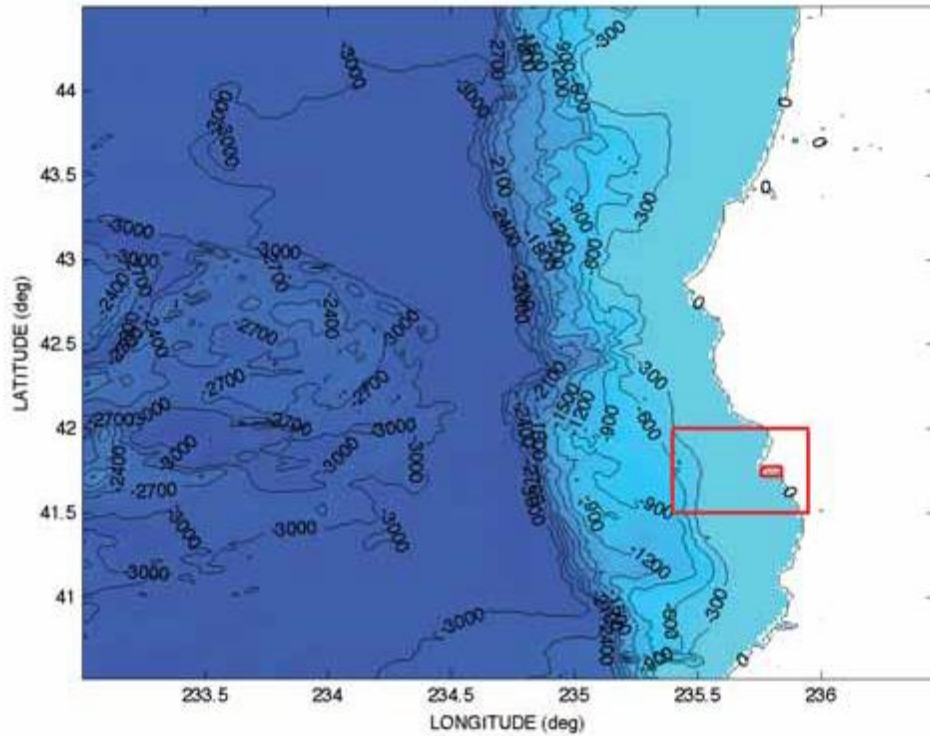
Figure 12. Coverage of the optimized A grid. The relative position of the optimized B and C grids are shown as boxed red overlays. Bathymetric contour units are in meters.
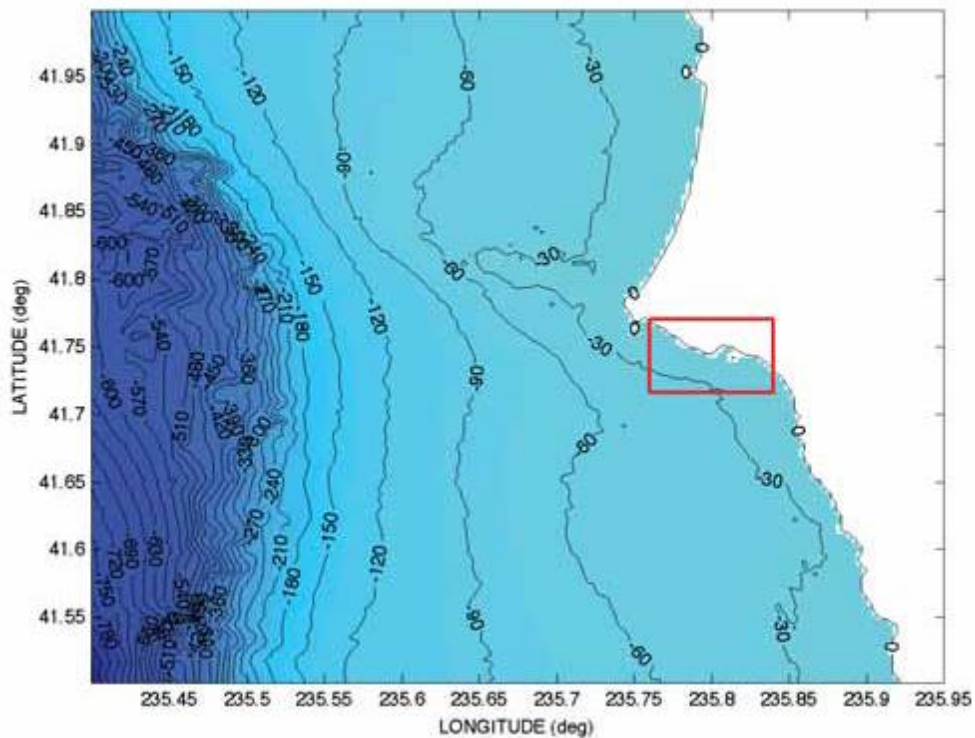
Figure 13. Coverage of the optimized B grid. The relative position of the optimized C grid is shown as a boxed red overlay. Bathymetric contour units are in meters.
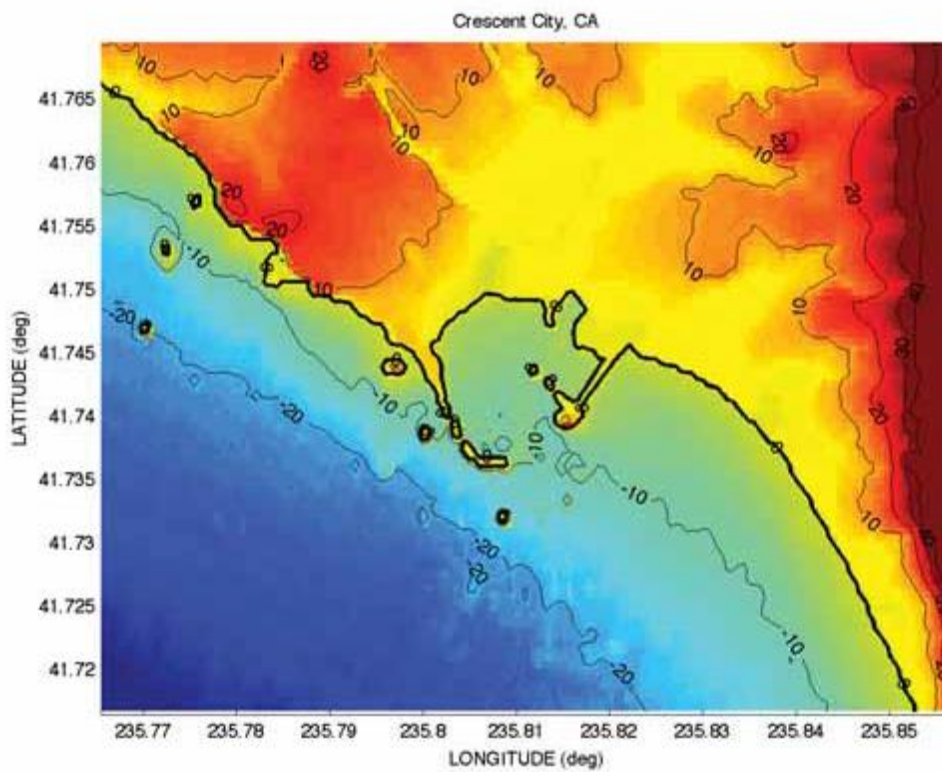
Figure 14. Contour plot of reference C grid. Bathymetric contour units are in meters.
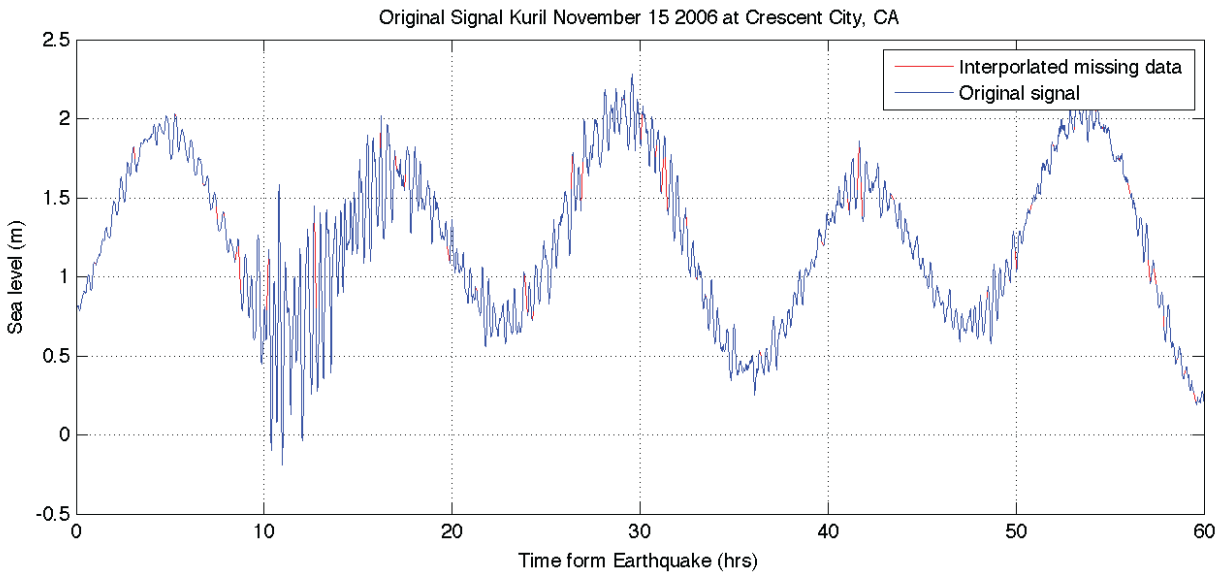
Figure 15. Original observed time series for 2006 Kuril event.
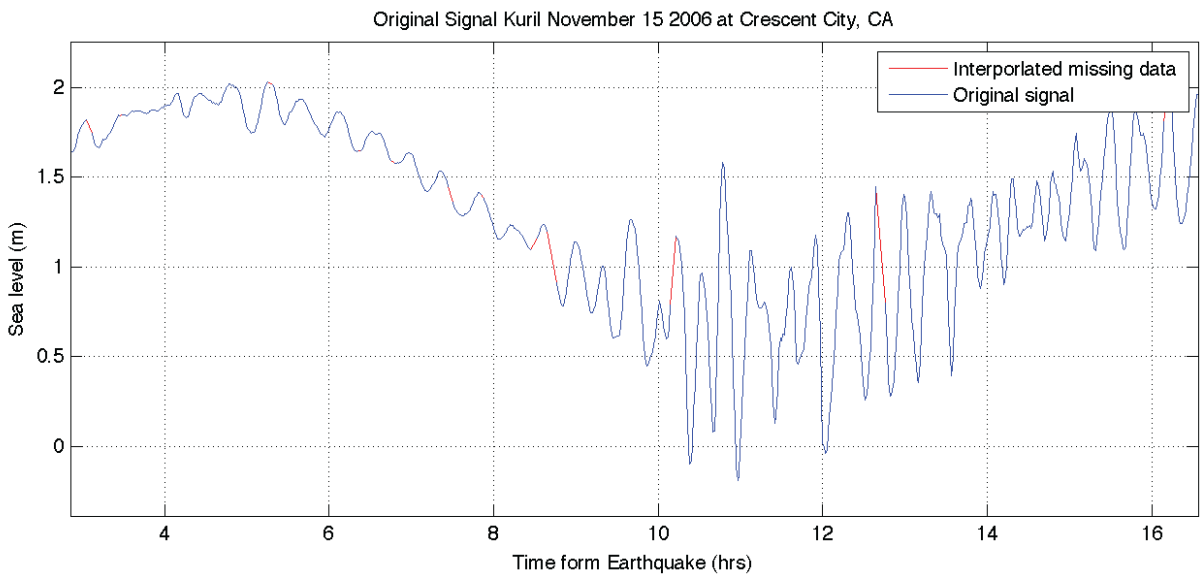
Figure 16. Detailed view of the 2006 Kuril tsunami signal as observed in the tidal record at the Crescent City tide gauge.
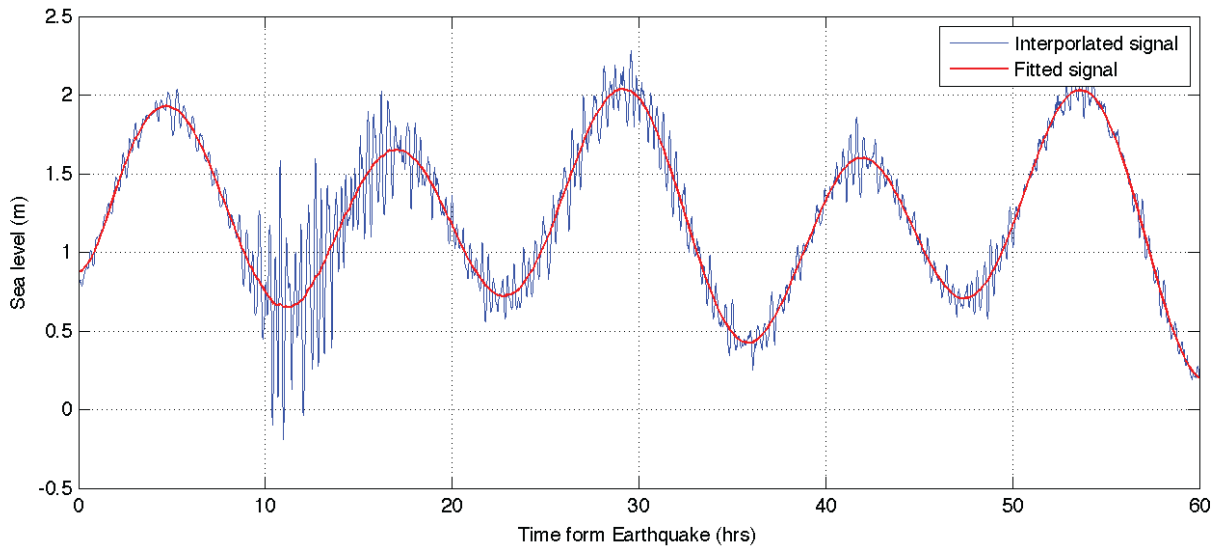
Figure 17. Original series, spline fit, and tsunami signal, Kuril 2006.
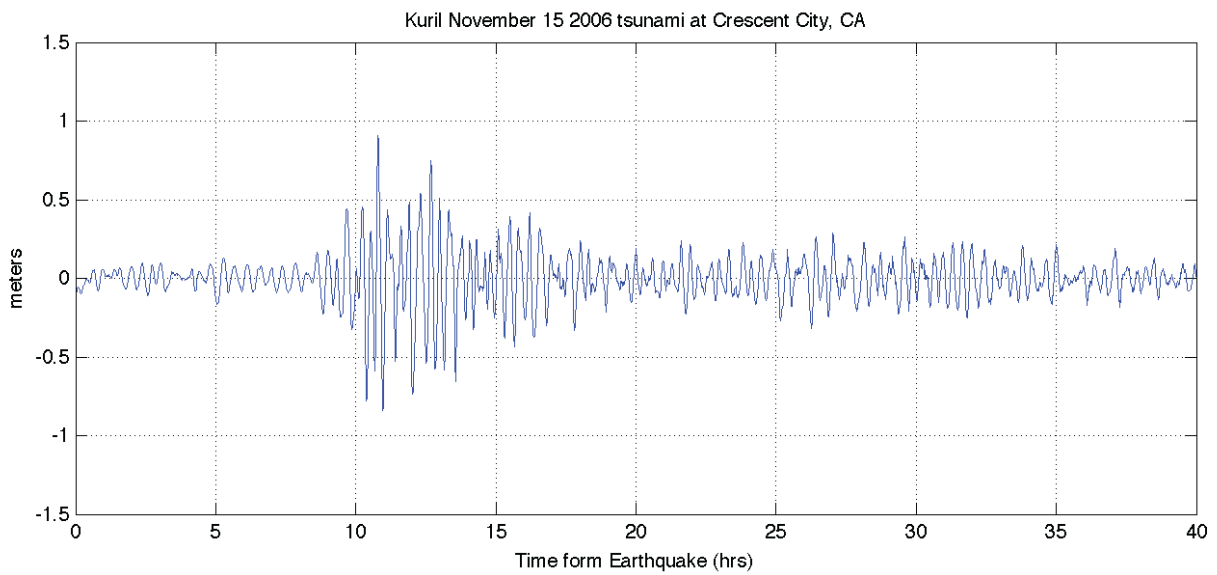
Figure 18. Original observed time series, spline fit, and tsunami signal, Kuril 2006.
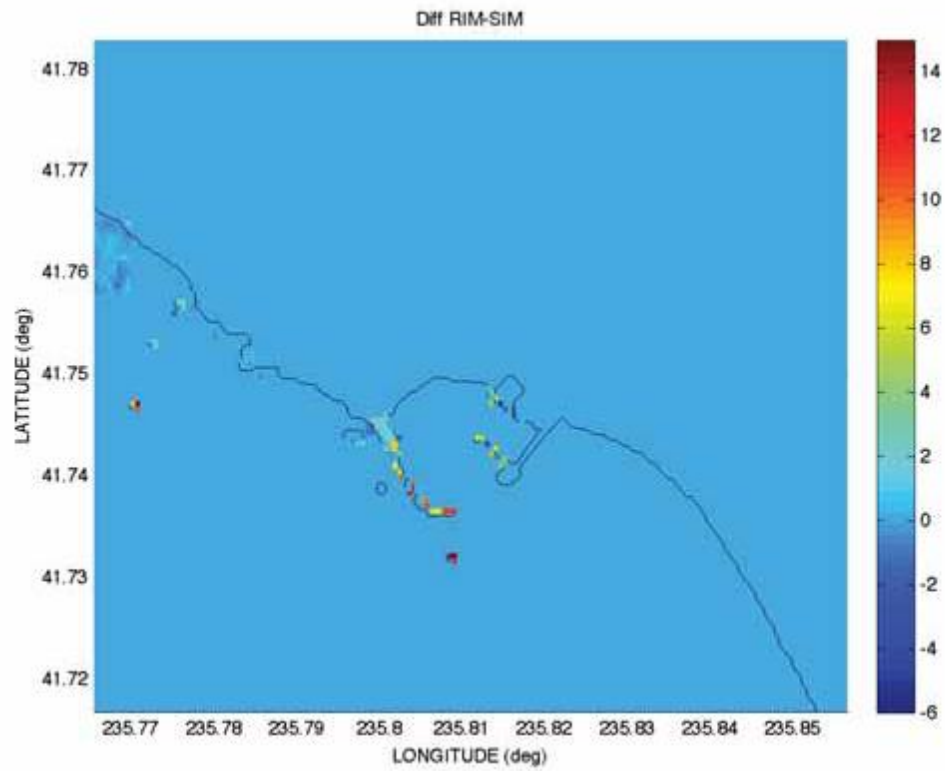
Figure 19. Differences in meters between the initial digital elevation model C grid and the stabilized reference C grid.
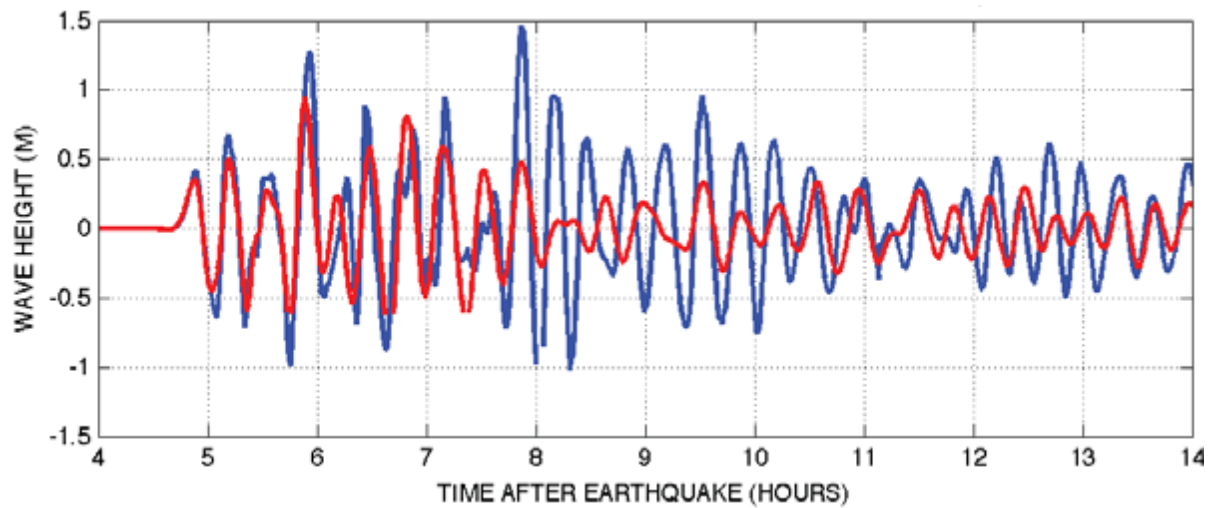
Figure 20. Time series comparison of reference vs. forecast model for the 1946 Unimak event, blue — reference model, red — optimized forecast model.
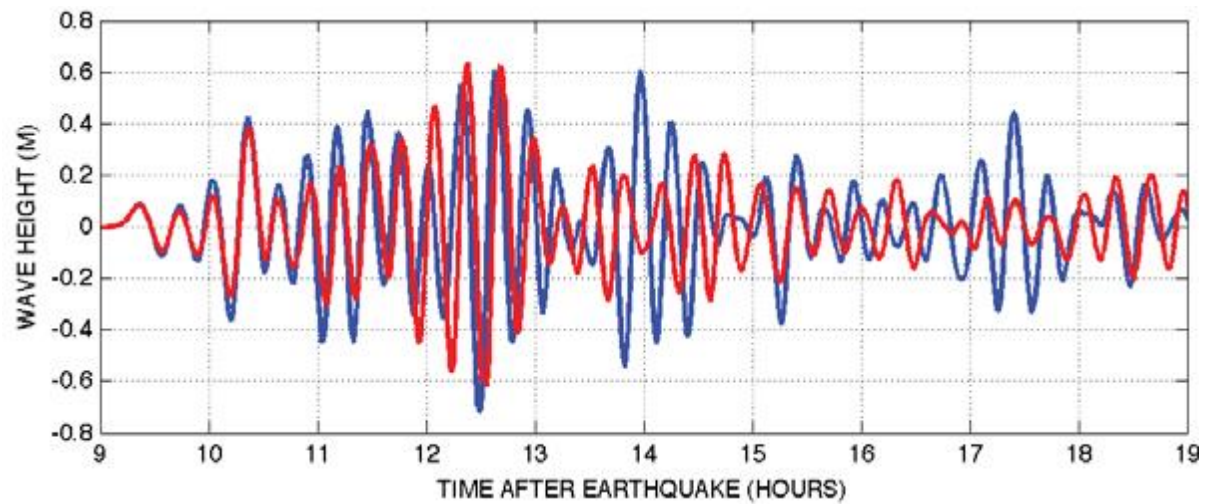
Figure 21. Times series comparison of reference vs. forecast model for the 1994 Kuril event, blue —reference model, red —optimized forecast model.
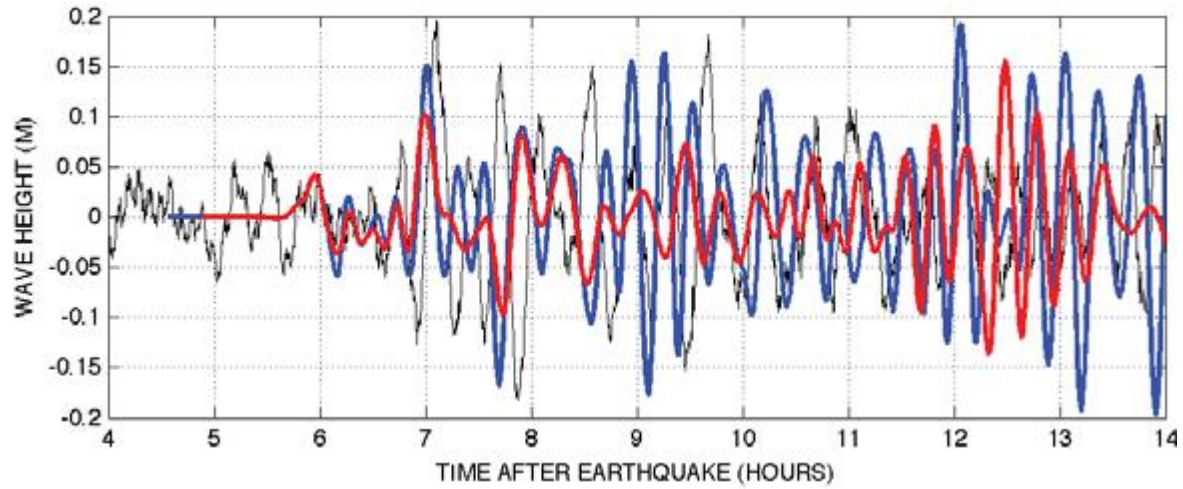
Figure 22. Time series comparison of tide gauge, reference model, and forecast model for the 1996 Andreanof event, black—tide gauge data, blue—reference model, red—optimized forecast model.
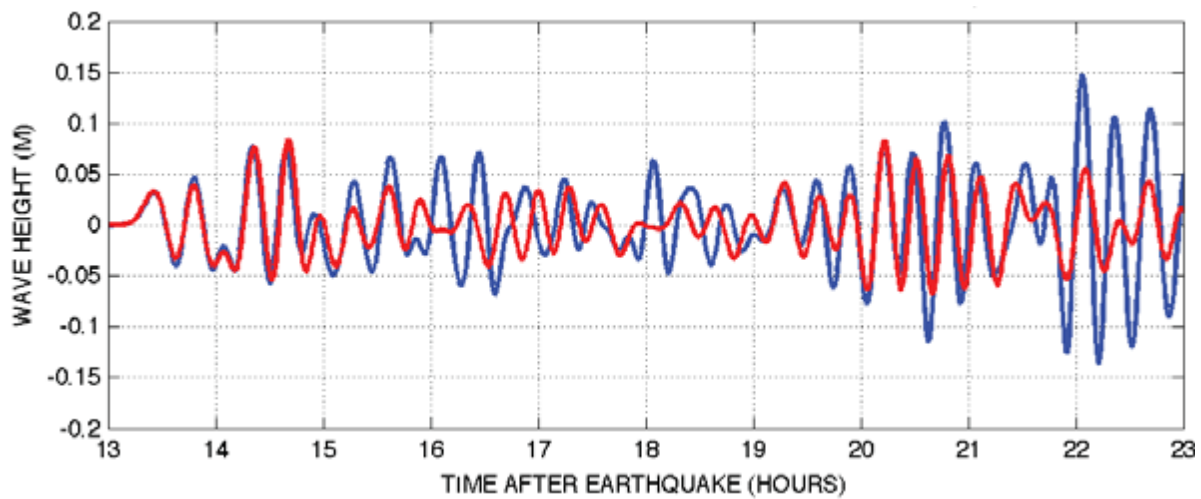
Figure 23. Time series comparison of reference vs. forecast model for the 2001 Peru event, blue—reference model, red—optimized forecast model.

28
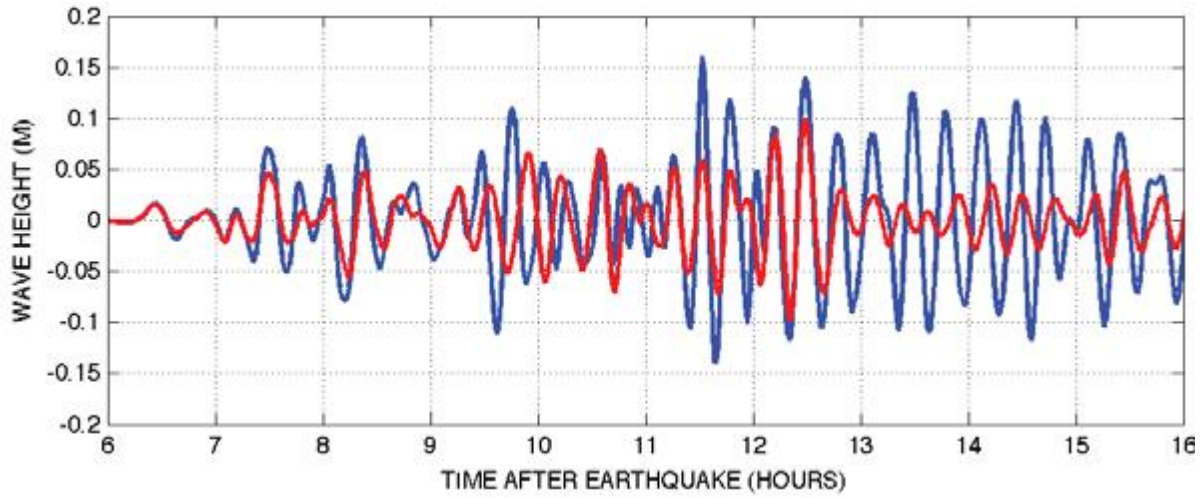
Figure 24. Time series comparison of reference vs. forecast model for the 2003 Rat Island event, blue—reference model, red—optimized forecast model.
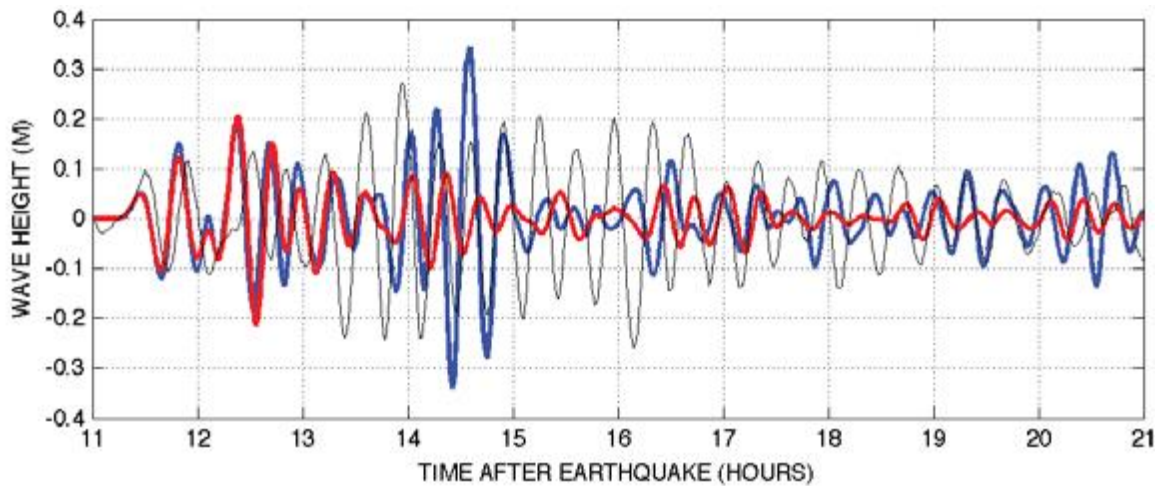
Figure 25. Time series comparison of tide gauge, reference model, and forecast model for the 2006 Tonga event, black—tide gauge data, blue—reference model, red—optimized forecast model.
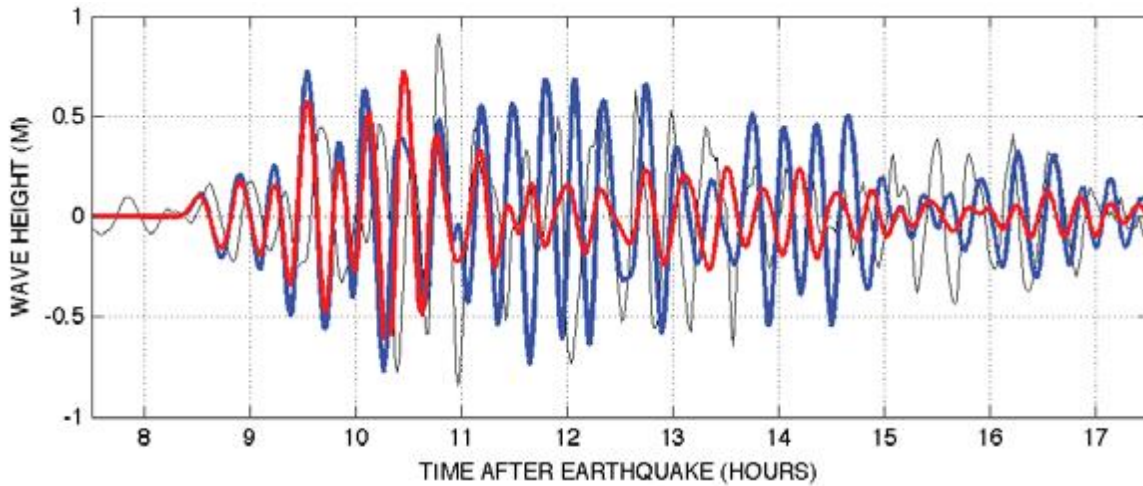
Figure 26. Time series comparison of tide gauge, reference model, and forecast model for the 2006 Kuril event, black—tide gauge data, blue—reference model, red—optimized forecast model.
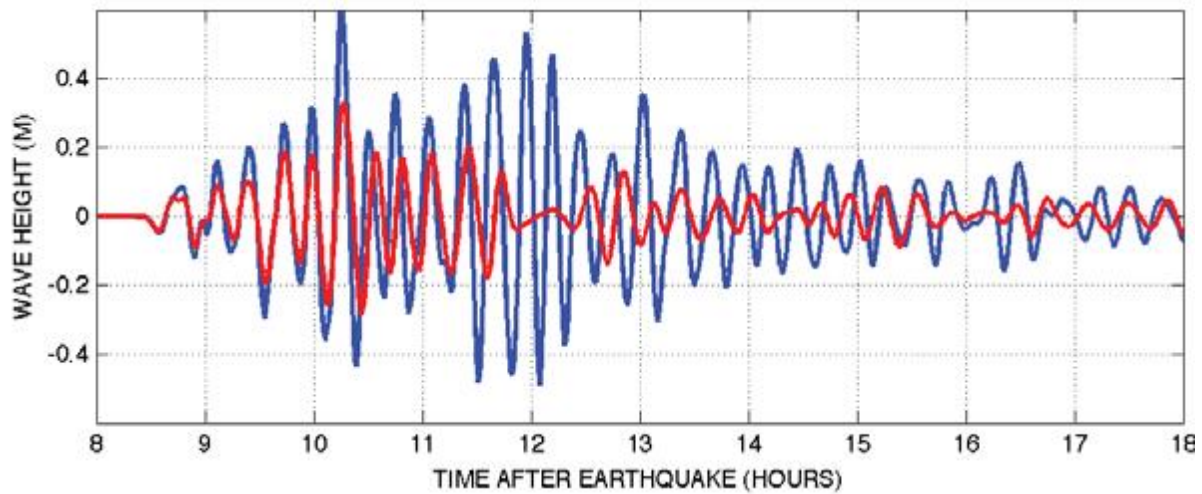
Figure 27. Time series comparison of reference vs. forecast model for the 2007 Kuril event, blue—reference model, red—optimized forecast model.
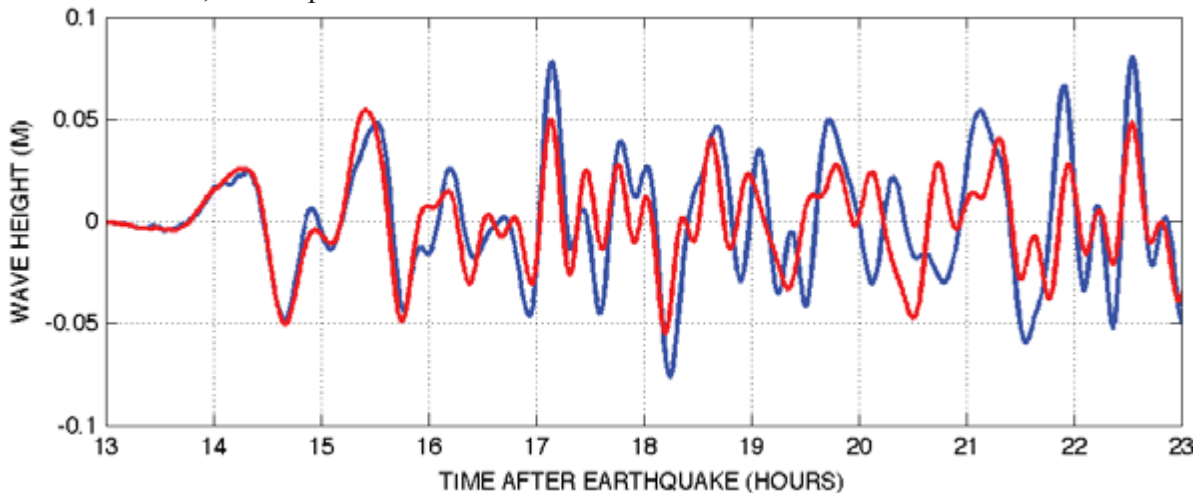
Figure 28. Time series comparison of reference vs. forecast model for the 2007 Solomon event, blue—reference model, red—optimized forecast model.
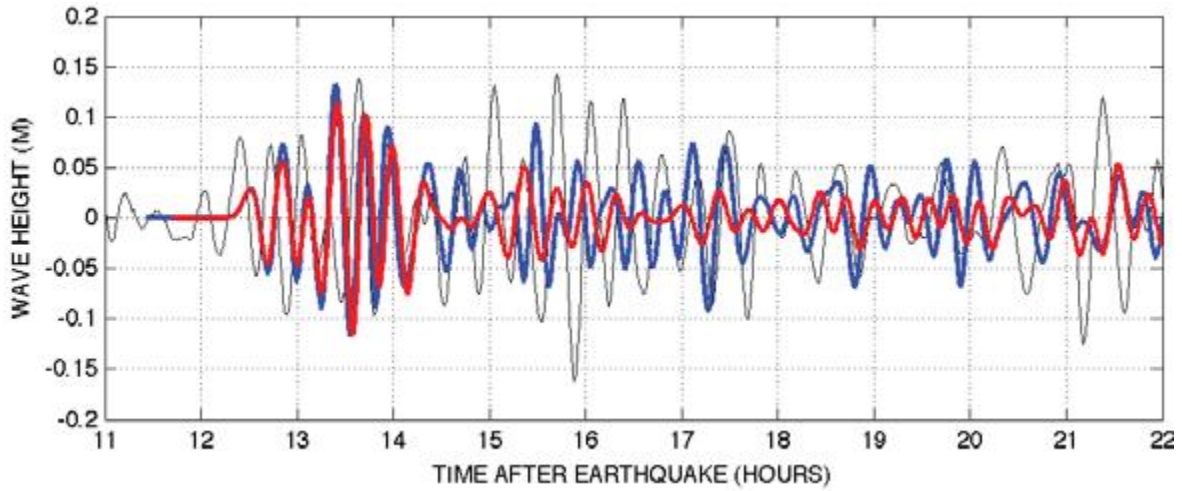
Figure 29. Time series comparison of reference vs. forecast model for the 2007 Peru event, blue—reference model, red—optimized forecast model.
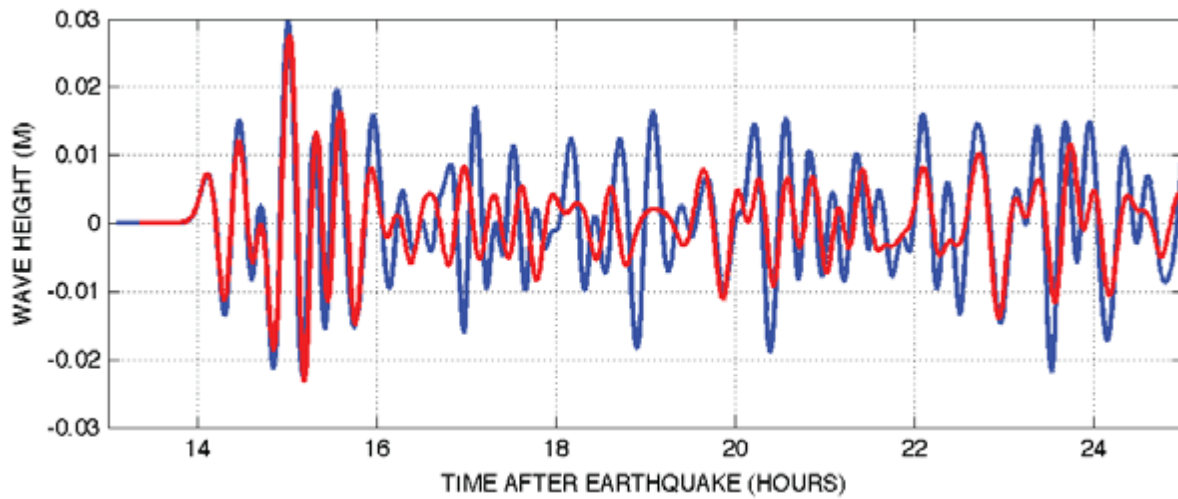
Figure 30. Time series comparison of reference vs. forecast model for the 2007 Chile event, blue—reference model, red—optimized forecast model.
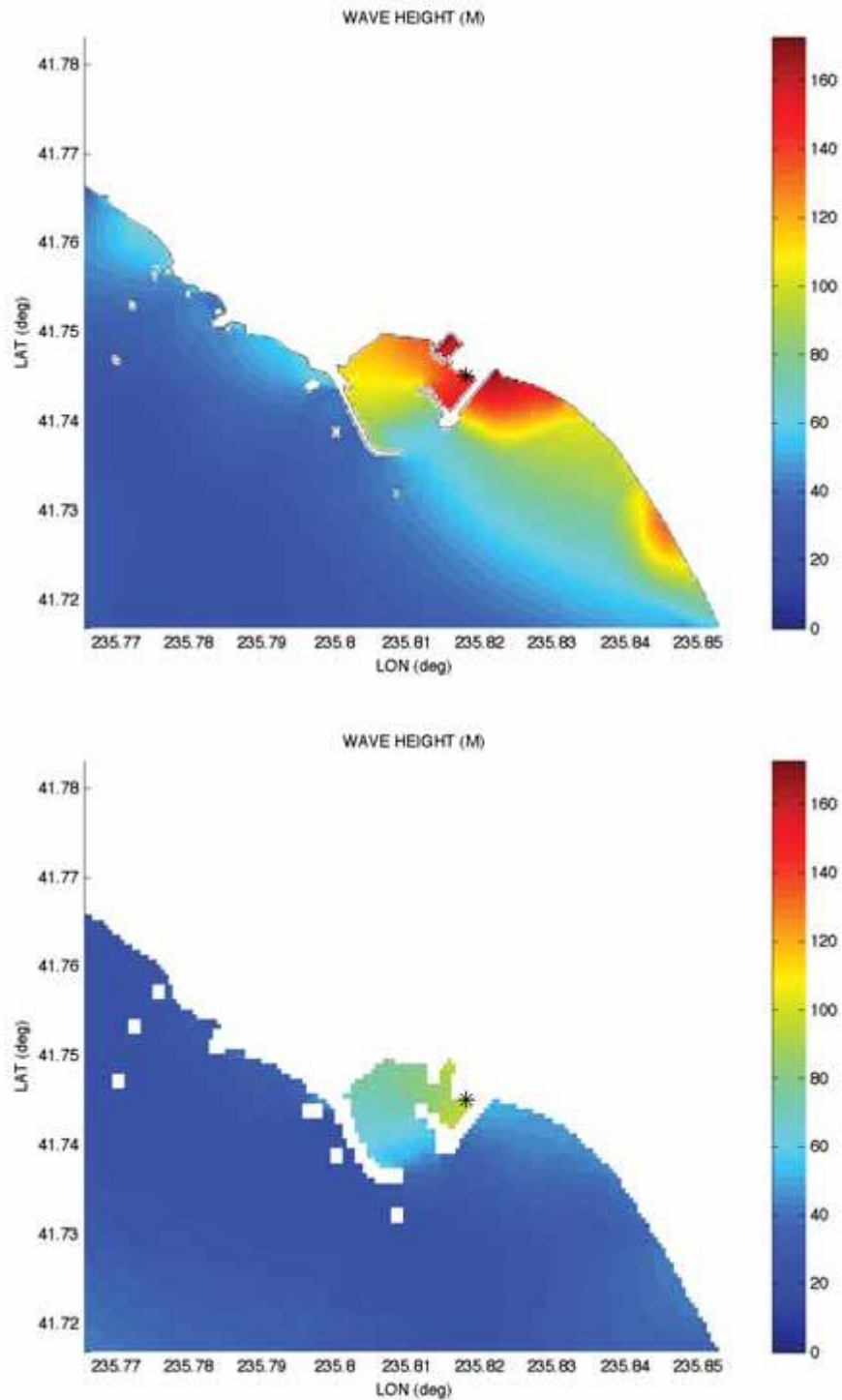
Figure 31. Maximum wave heights (cm) computed with forecast model grids. Asterisk indicates location of the tide gauge (reference model—upper, forecast model—lower) for the 1946 Unimak event.
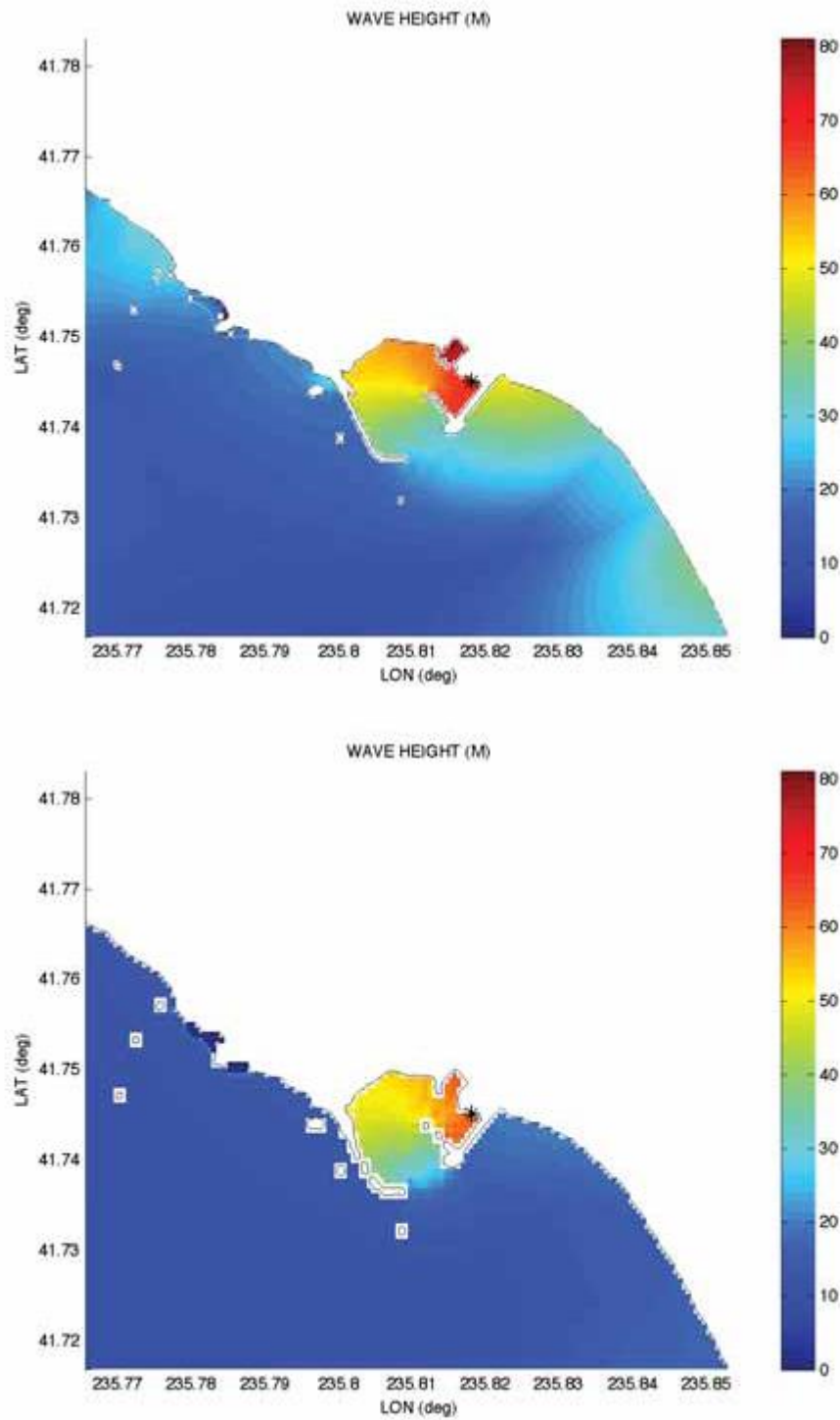
Figure 32. Maximum wave heights (cm) computed with forecast model grids. Asterisk indicates location of the tide gauge (reference model—upper, forecast model—lower) for the 1994 Kuril event.
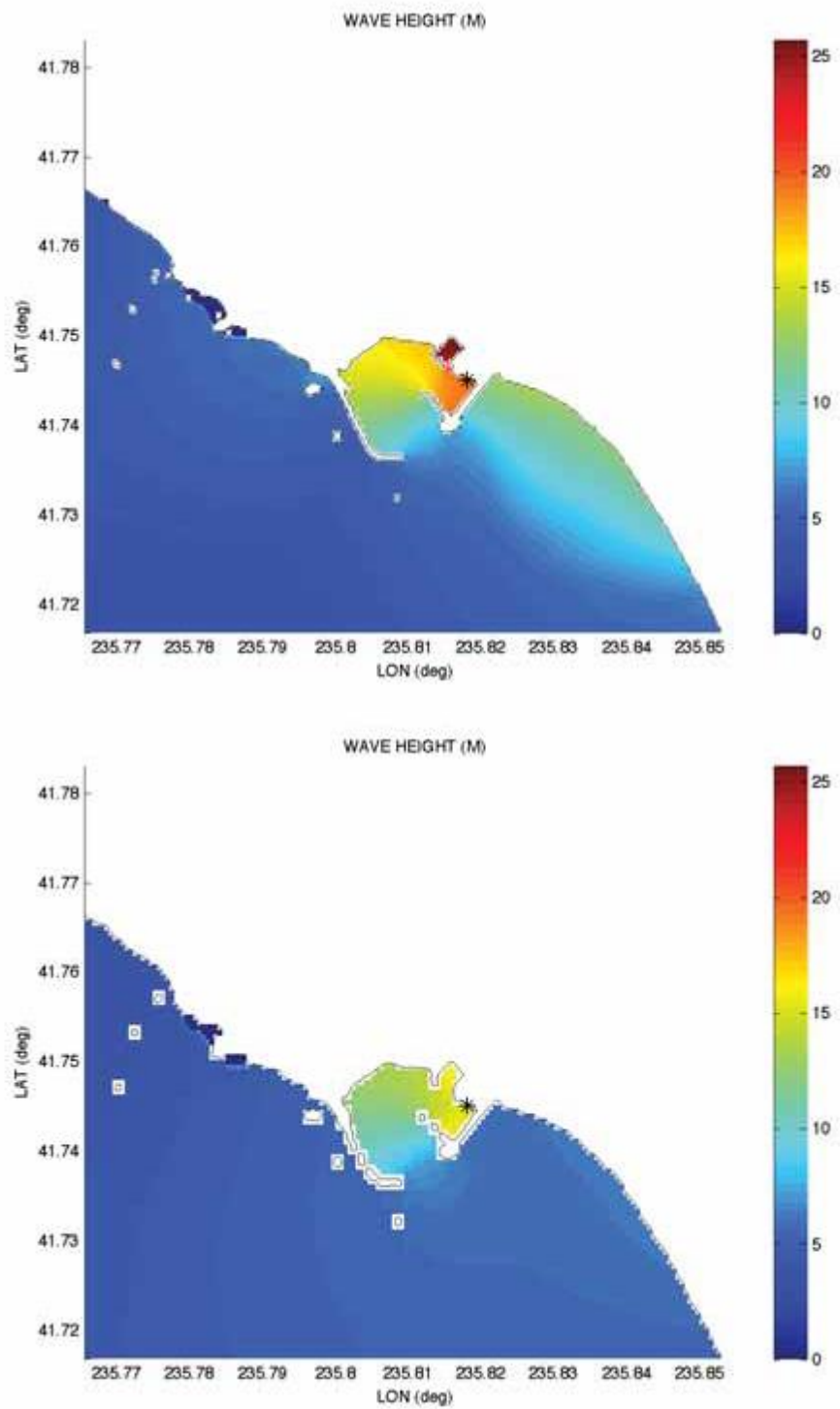
Figure 33. Maximum wave heights (cm) computed with forecast model grids. Asterisk indicates location of the tide gauge (reference model—upper, forecast model—lower) for the 1996 Andreanof event.
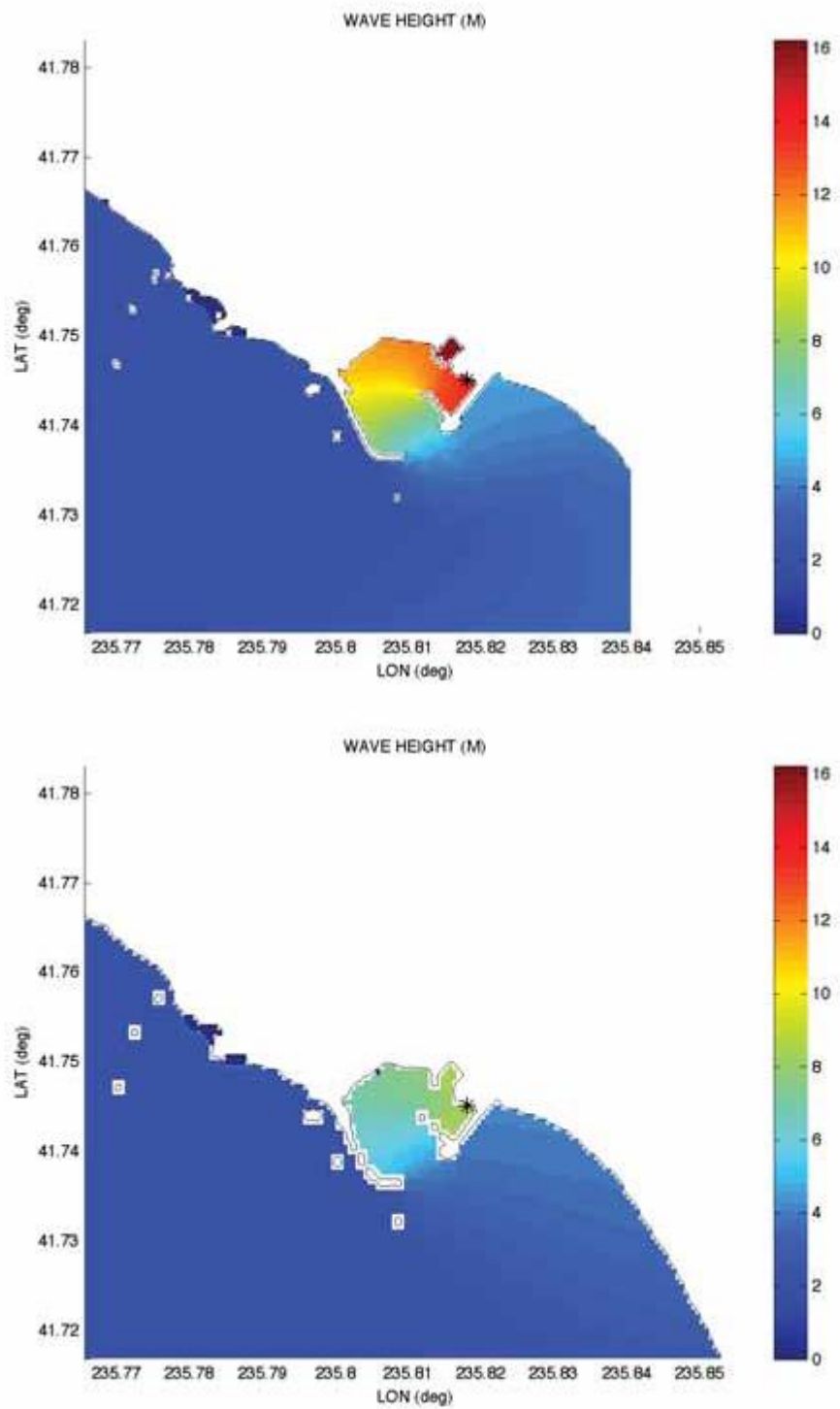
Figure 34. Maximum wave heights (cm) computed with forecast model grids. Asterisk indicates location of the tide gauge (reference model—upper, forecast model—lower) for the 2001 Peru event.
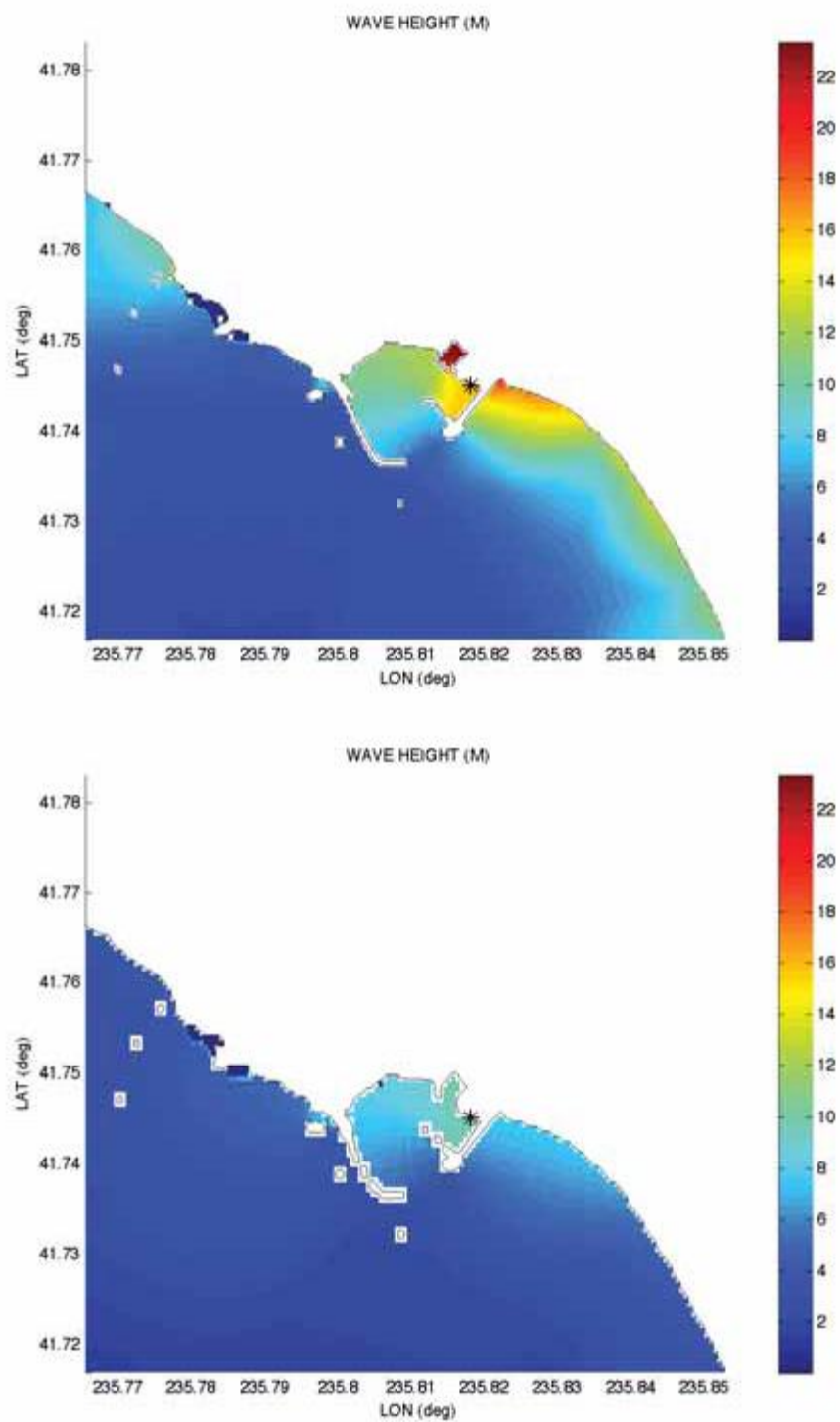
Figure 35. Maximum wave heights (cm) computed with forecast model grids. Asterisk indicates location of the tide gauge (reference model—upper, forecast model—lower) for the 2003 Rat Island event.
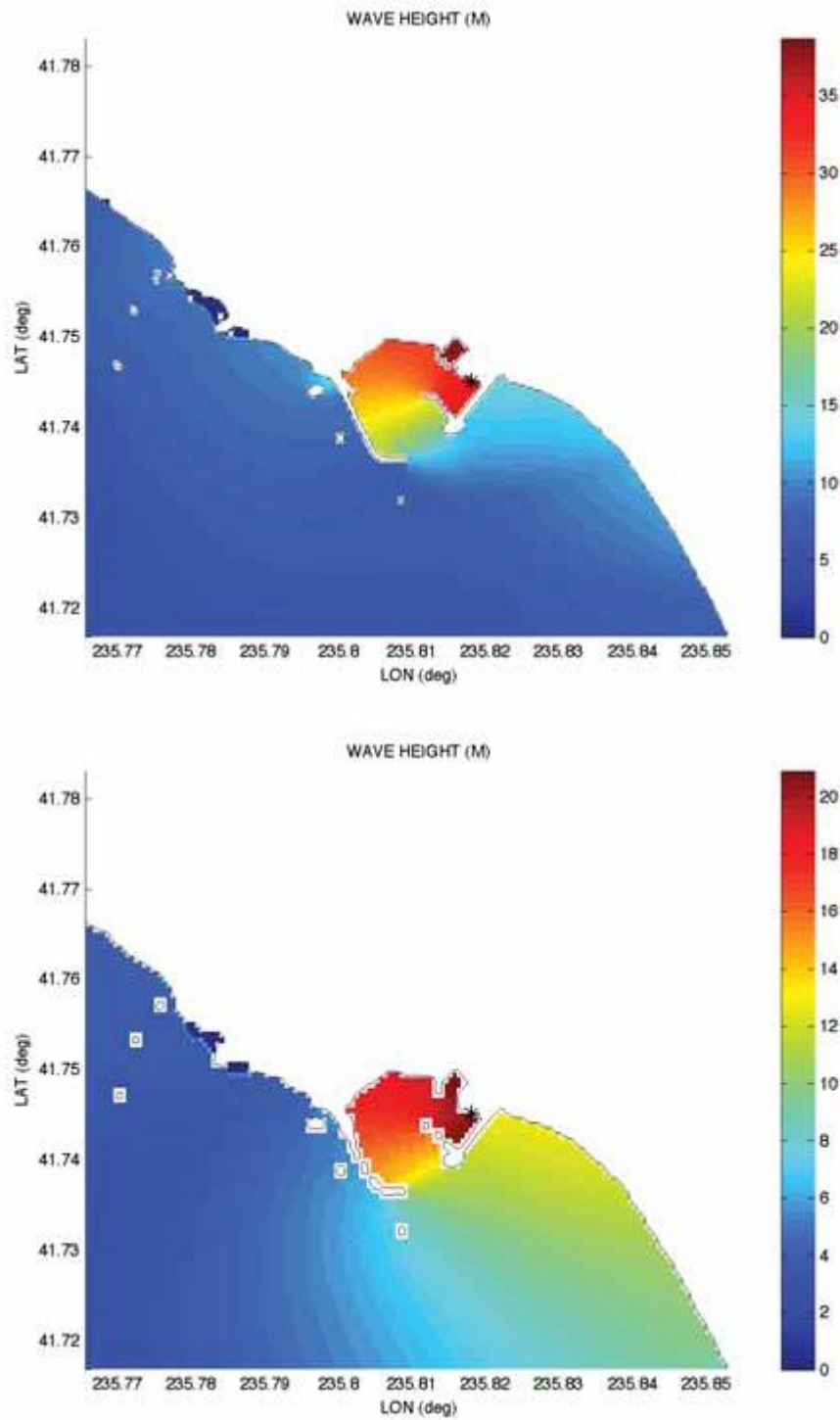
Figure 36. Maximum wave heights (cm) computed with forecast model grids. Asterisk indicates location of the tide gauge (reference model—upper, forecast model—lower) for the 2006 Tonga event.
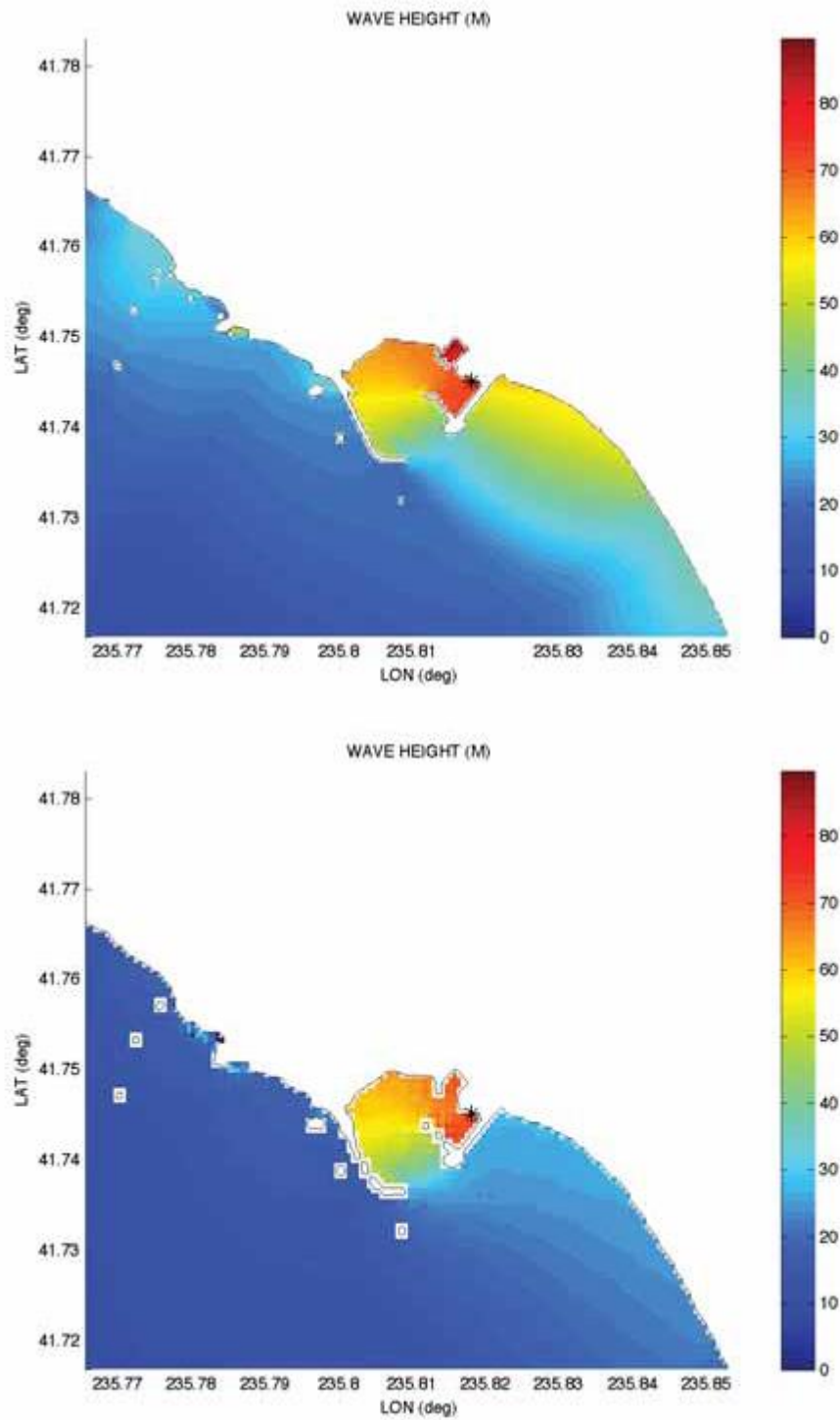
Figure 37. Maximum wave heights (cm) computed with forecast model grids. Asterisk indicates location of the tide gauge (reference model—upper, forecast model—lower) for the 2006 Kuril event.
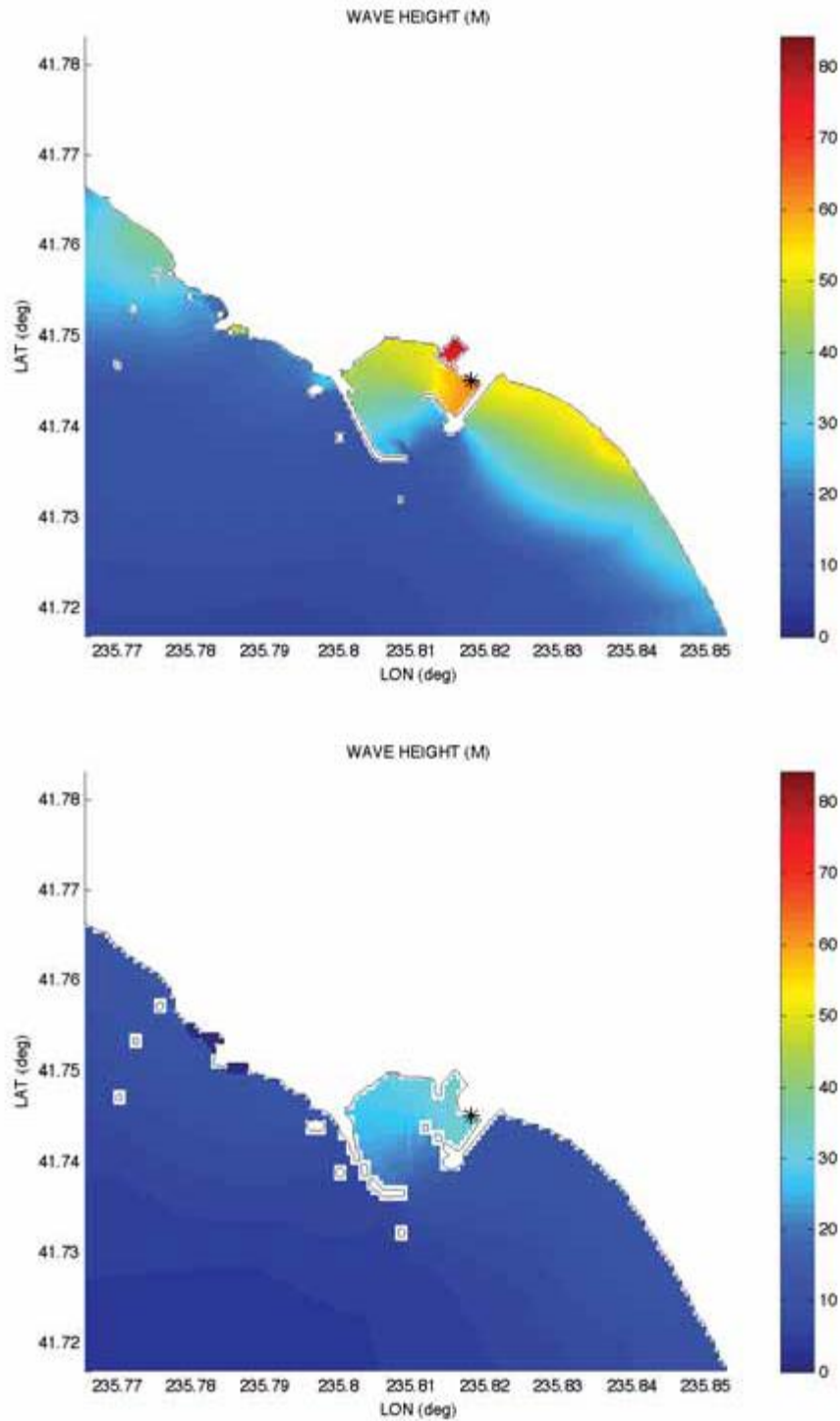
Figure 38. Maximum wave heights (cm) computed with forecast model grids. Asterisk indicates location of the tide gauge (reference model—upper, forecast model—lower) for the 2007 Kuril event.
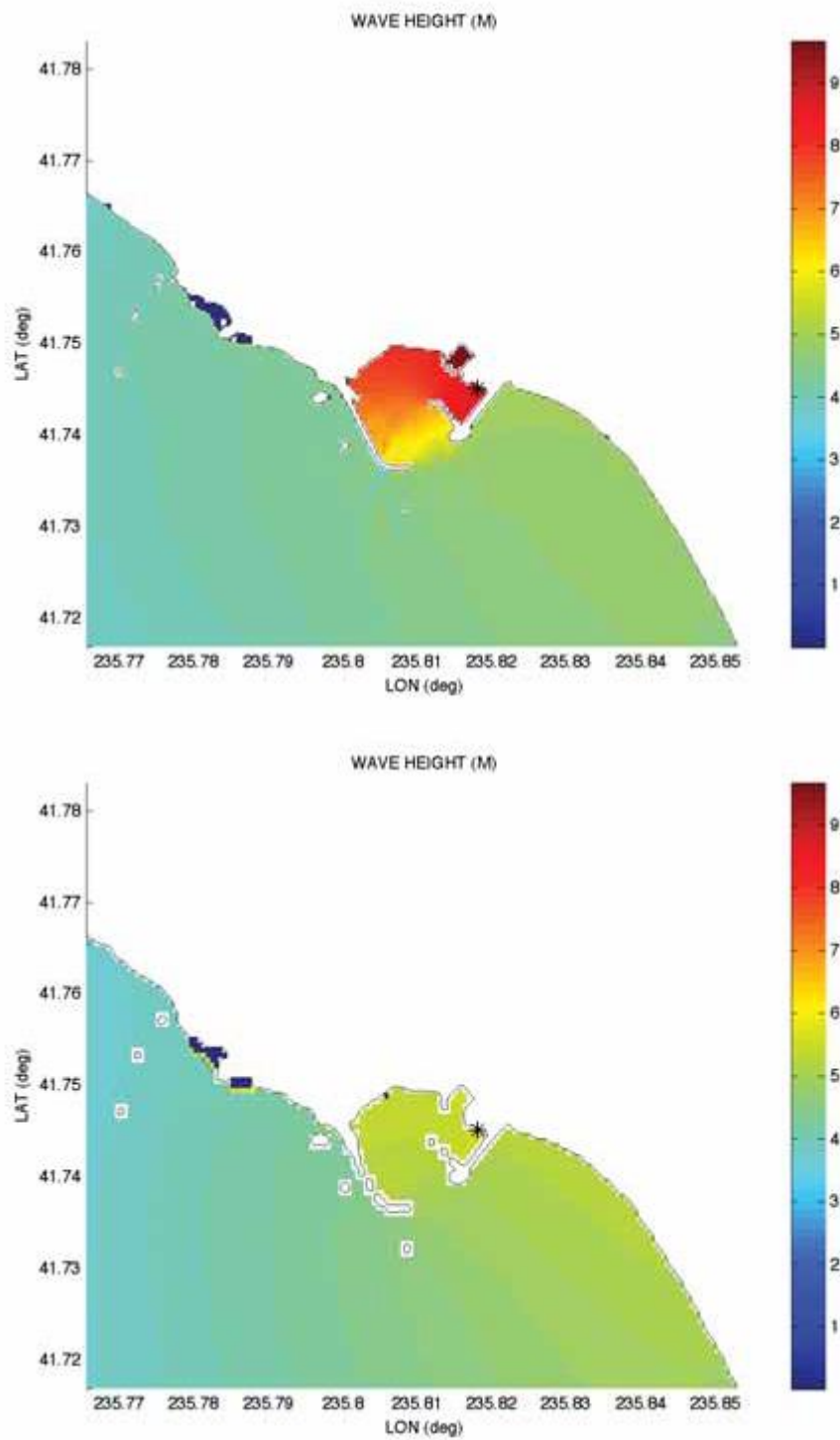
Figure 39. Maximum wave heights (cm) computed with forecast model grids. Asterisk indicates location of the tide gauge (reference model—upper, forecast model—lower) for the 2007 Solomon event.
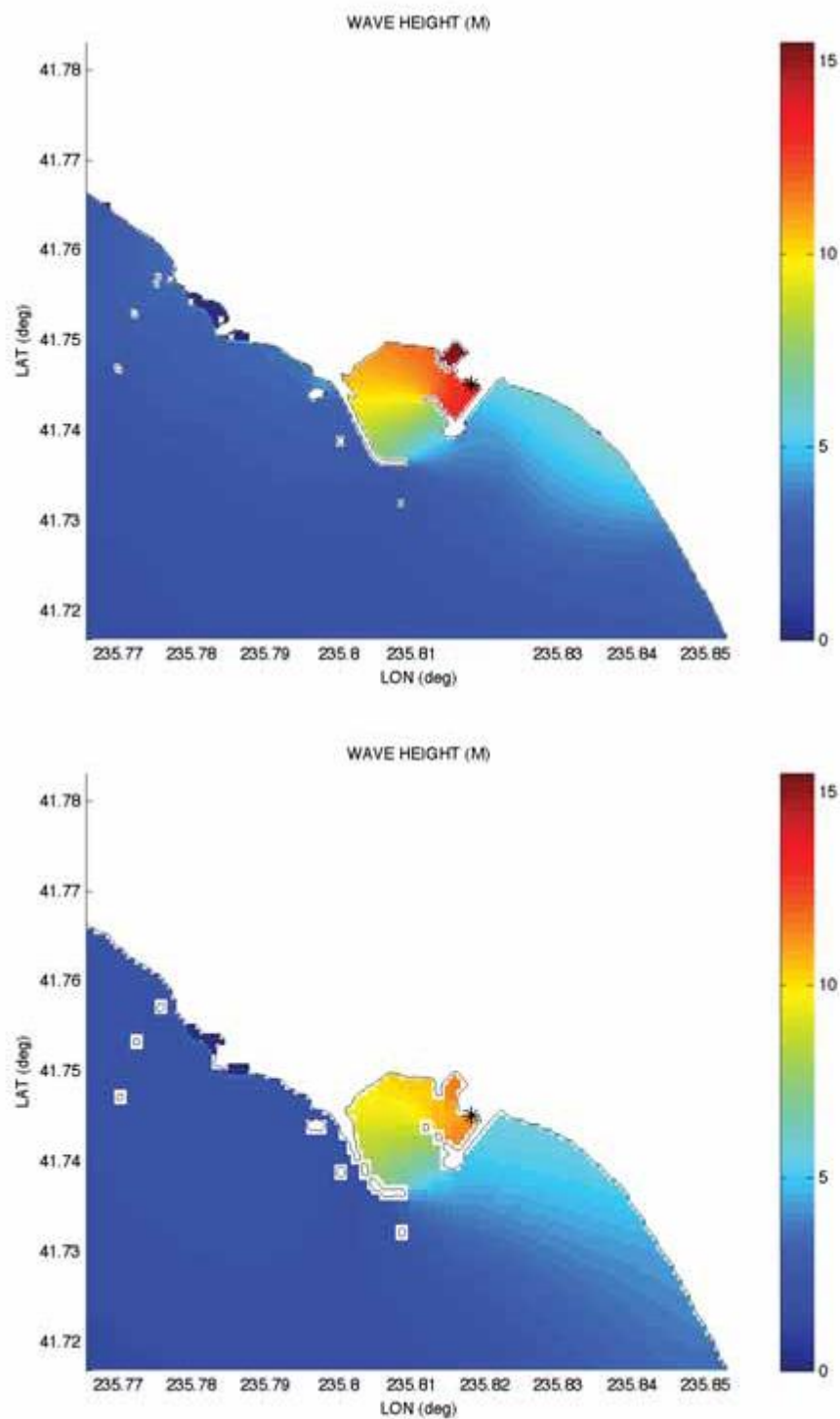
Figure 40. Maximum wave heights (cm) computed with forecast model grids. Asterisk indicates location of the tide gauge (reference model—upper, forecast model—lower) for the 2007 Peru event.
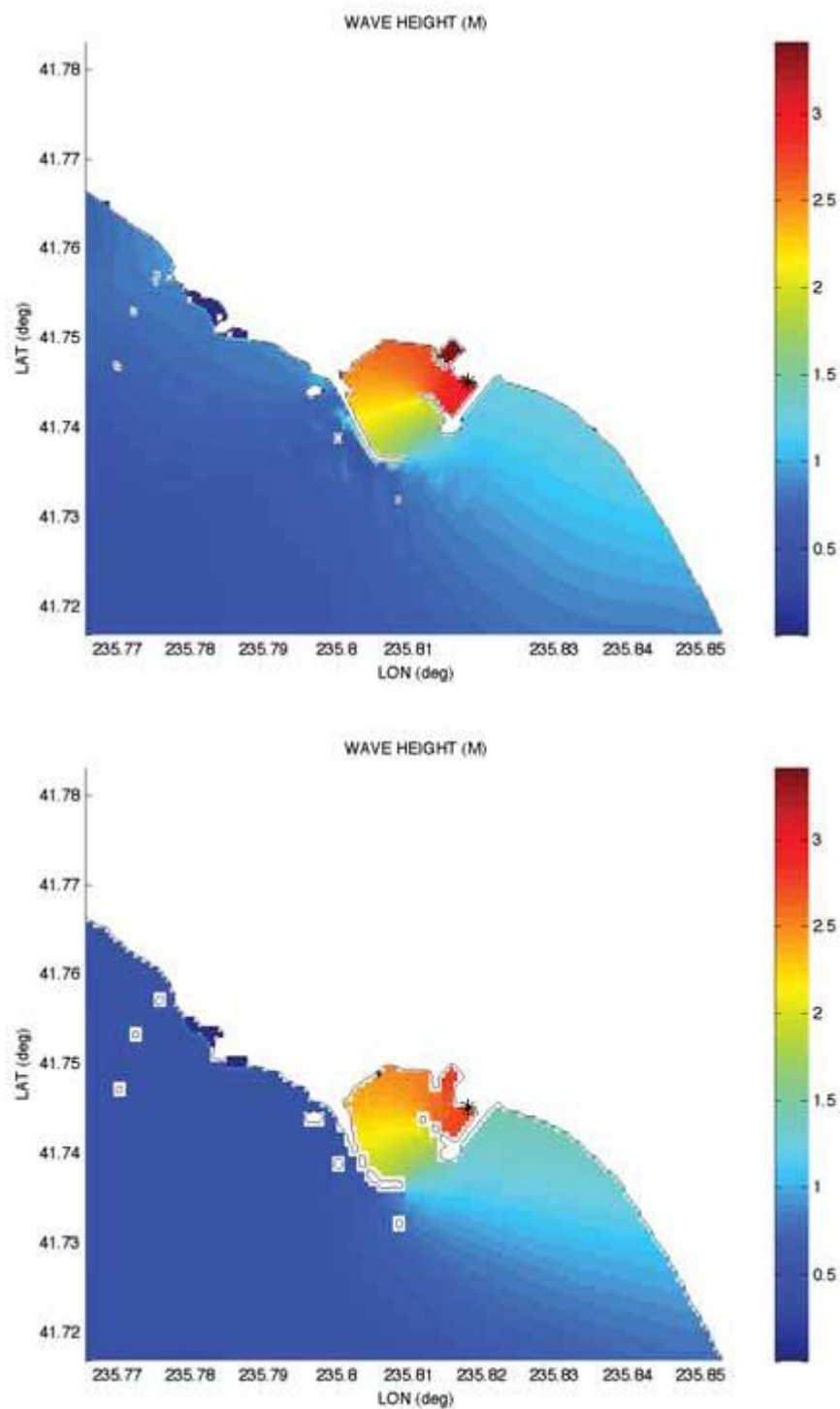
Figure 41. Maximum wave heights (cm) computed with forecast model grids. Asterisk indicates location of the tide gauge (reference model—upper, forecast model—lower) for the 2007 Chile event.
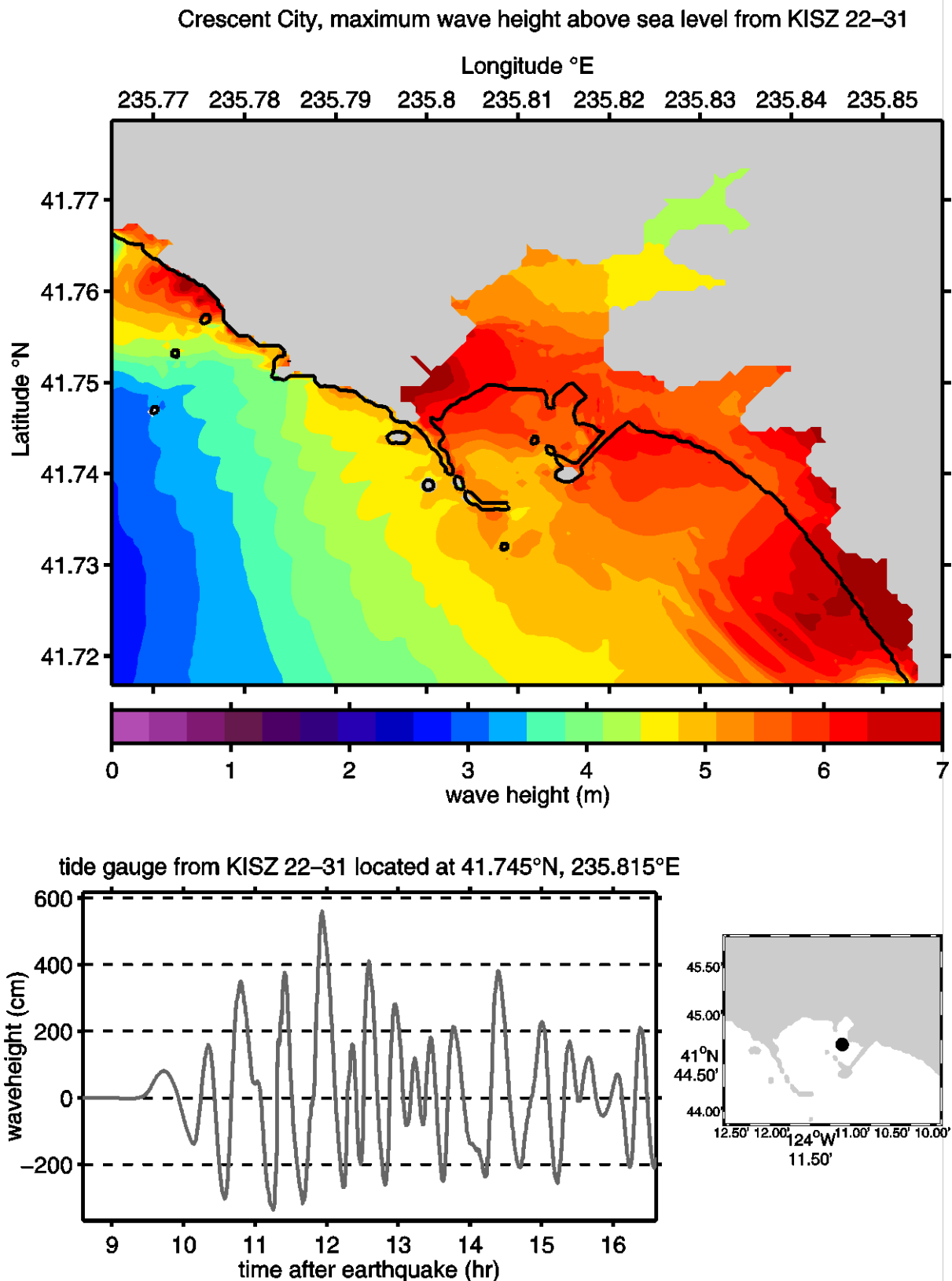
Figure 42. Maximum wave height plot and time series results for the forecast model using synthetic megatsunami Event KISZ 22–31 for Crescent City, California.
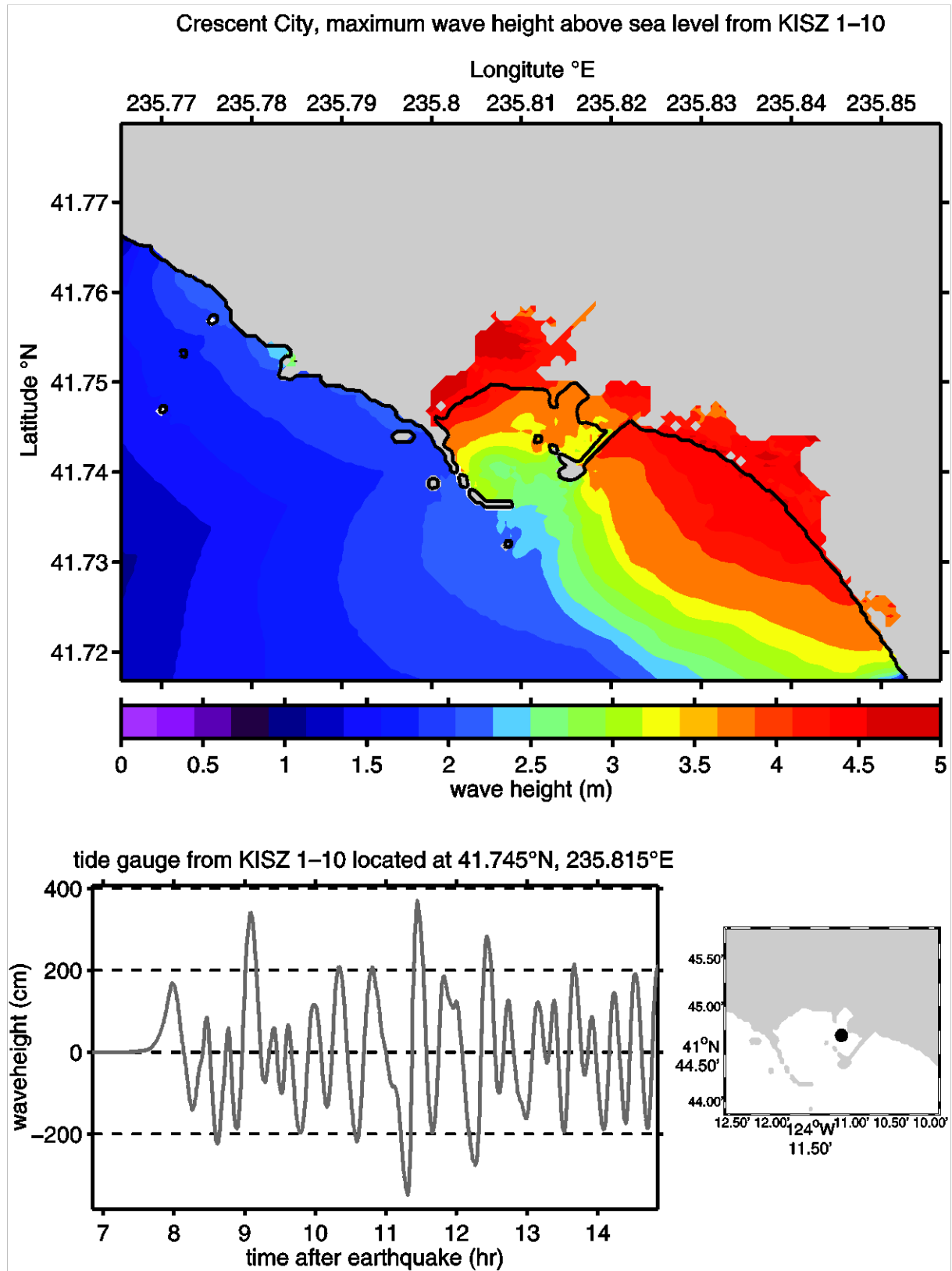
Figure 43. Maximum wave height plot and time series results for the forecast model using synthetic megatsunami Event KISZ 1–10 for Crescent City, California.
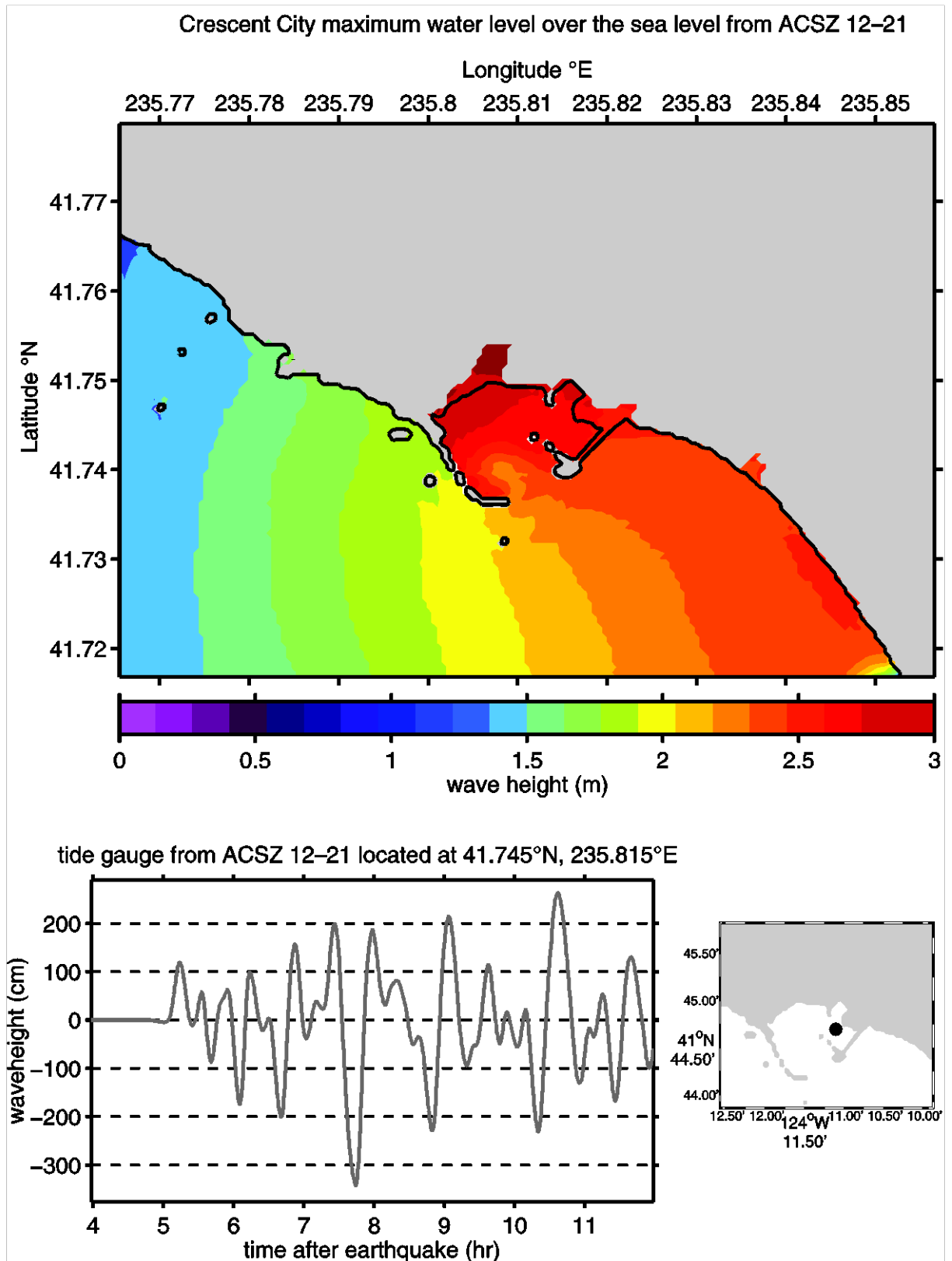
Figure 44. Maximum wave height plot and time series results for the forecast model using synthetic megatsunami Event ACSZ 12–21 for Crescent City, California.
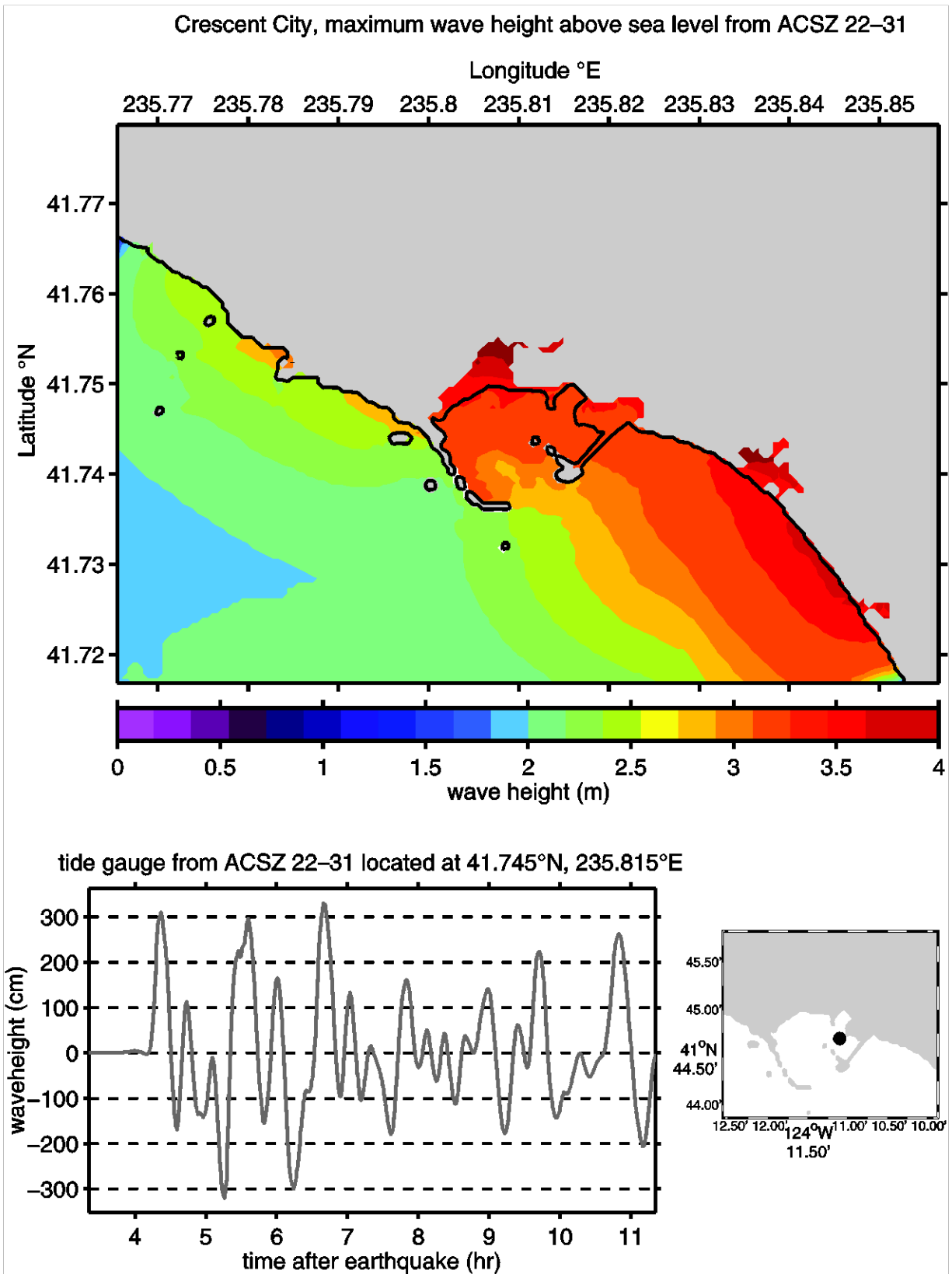
Figure 45. Maximum wave height plot and time series results for the forecast model using synthetic megatsunami Event ACSZ 22–31 for Crescent City, California.
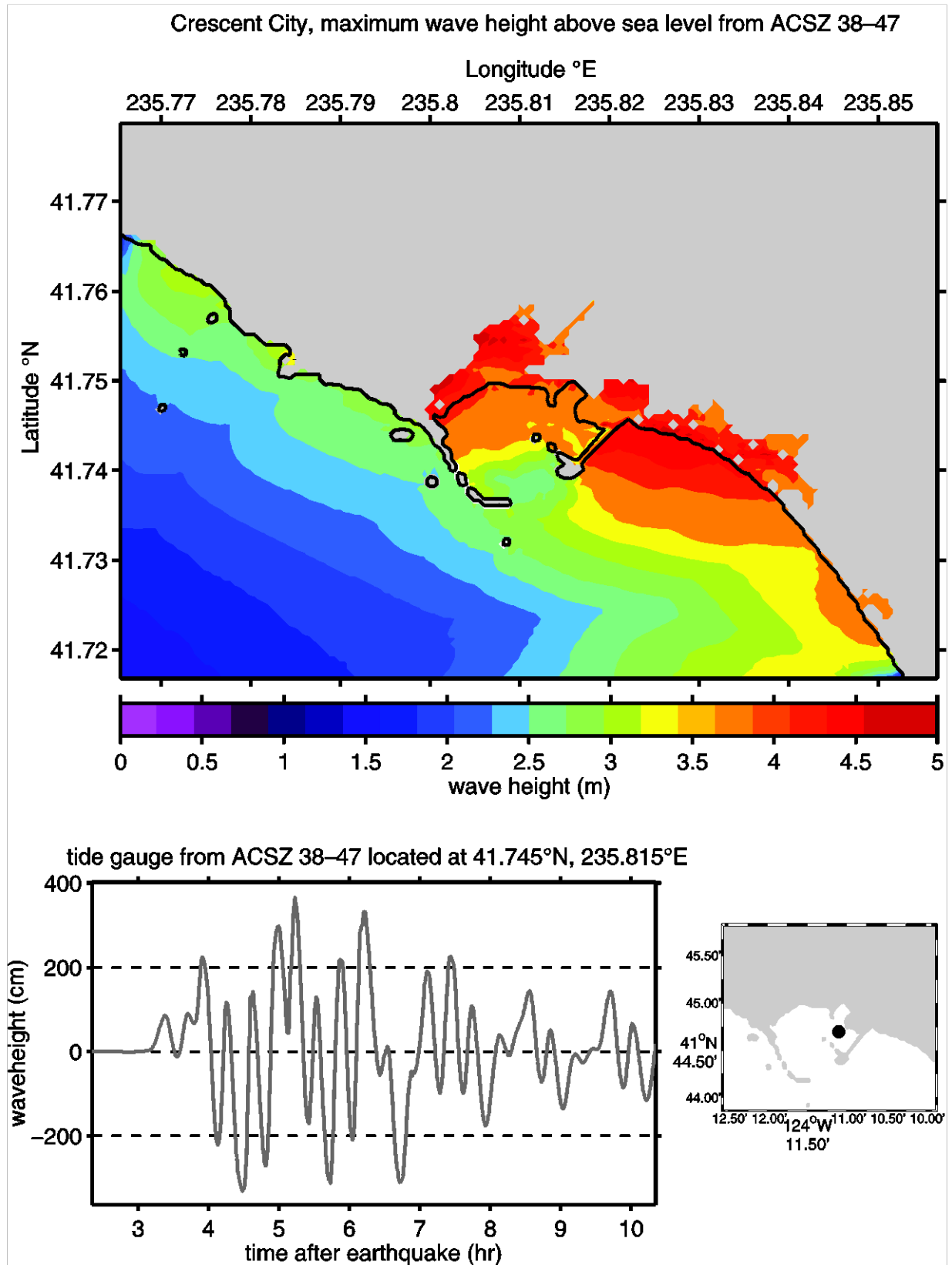
Figure 46. Maximum wave height plot and time series results for the forecast model using synthetic megatsunami Event ACSZ 38–47 for Crescent City, California.
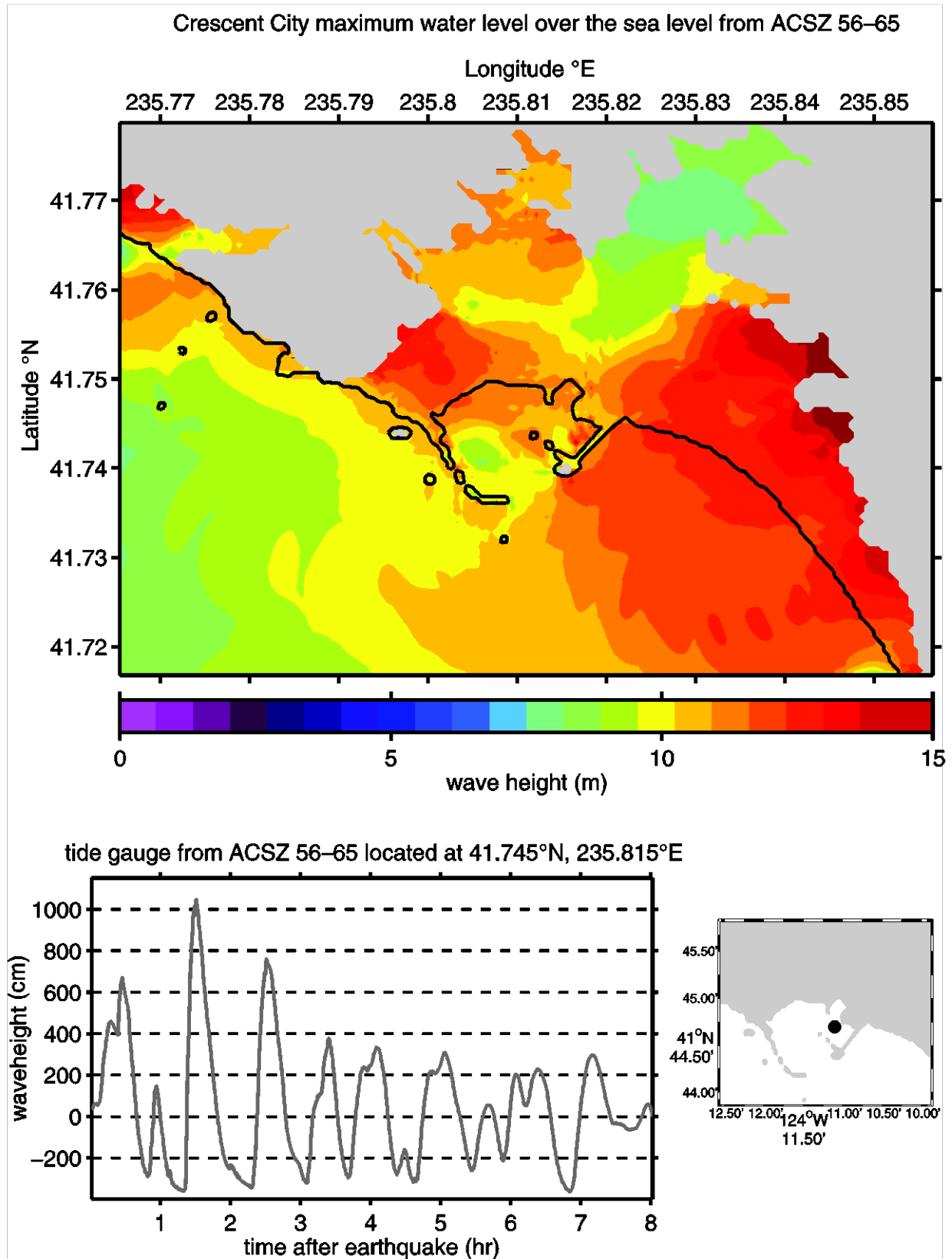
Figure 47. Maximum wave height plot and time series results for the forecast model using synthetic megatsunami Event ACSZ 56–65 for Crescent City, California.
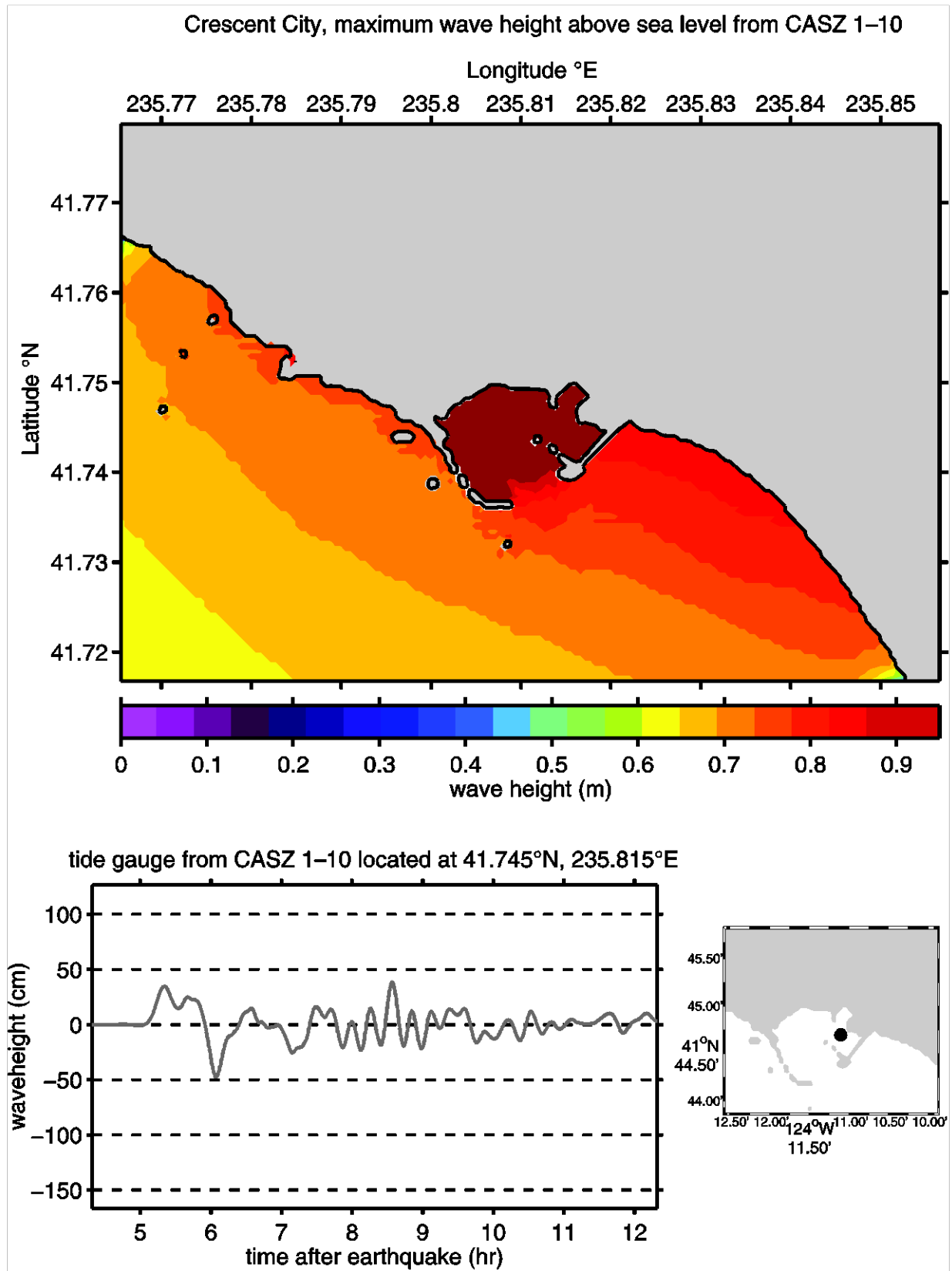
Figure 48. Maximum wave height plot and time series results for the forecast model using synthetic megatsunami Event CSSZ 1–10 for Crescent City, California.

Figure 49. Maximum wave height plot and time series results for the forecast model using synthetic megatsunami Event SASZ 40–49 for Crescent City, California.
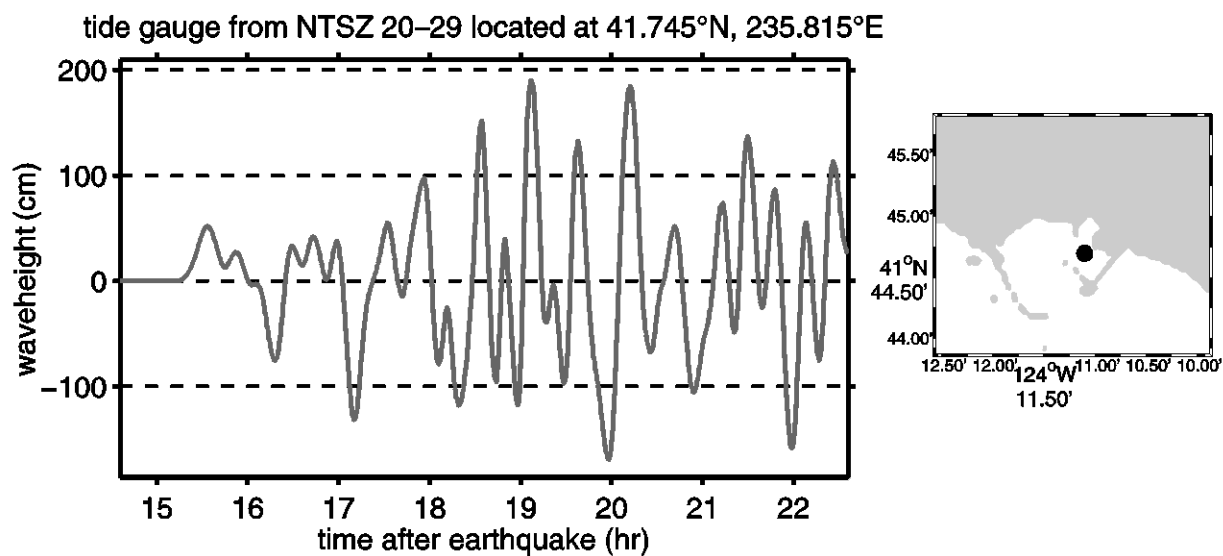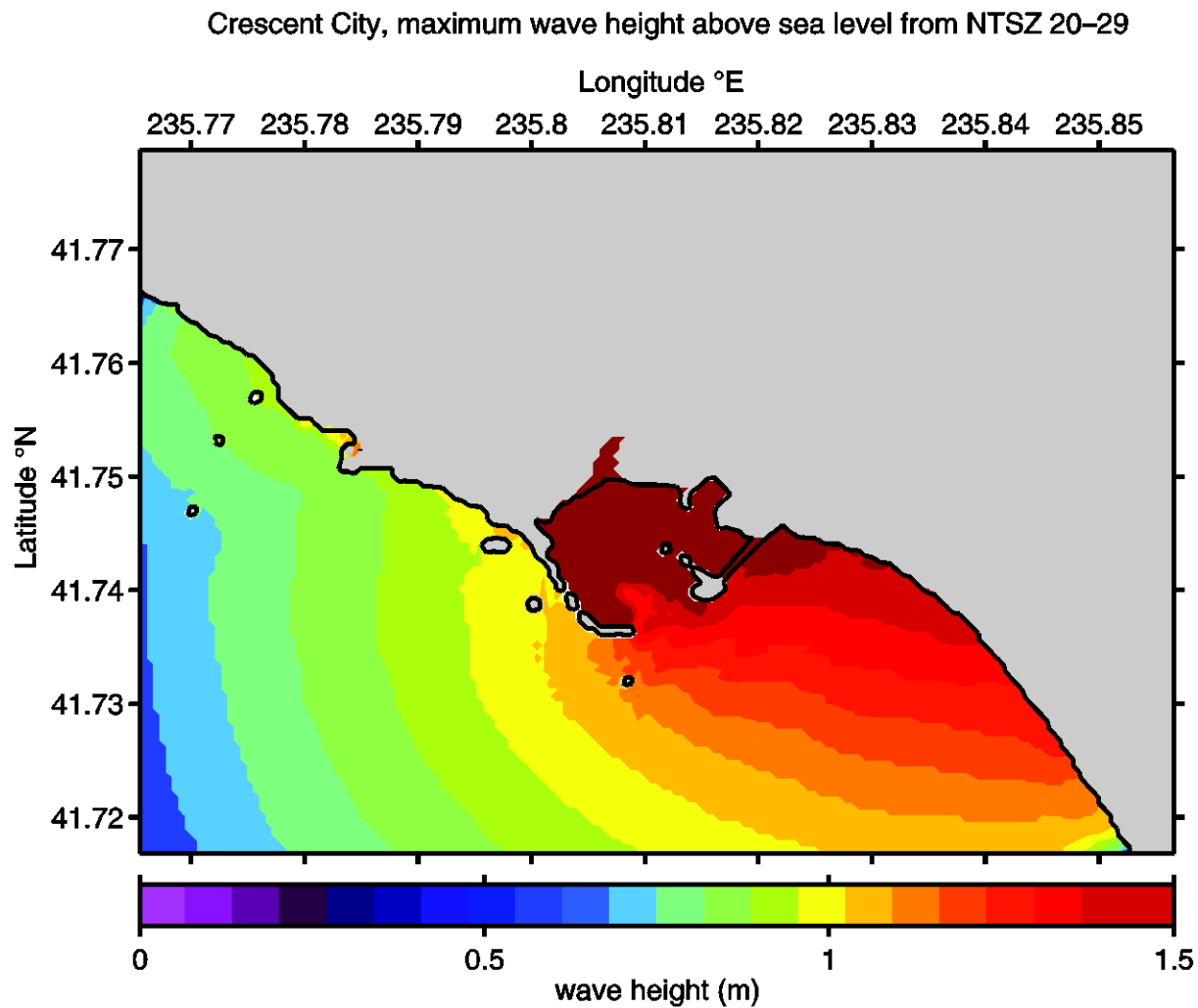
Figure 50. Maximum wave height plot and time series results for the forecast model using synthetic megatsunami Event NTSZ 20–29 for Crescent City, California.
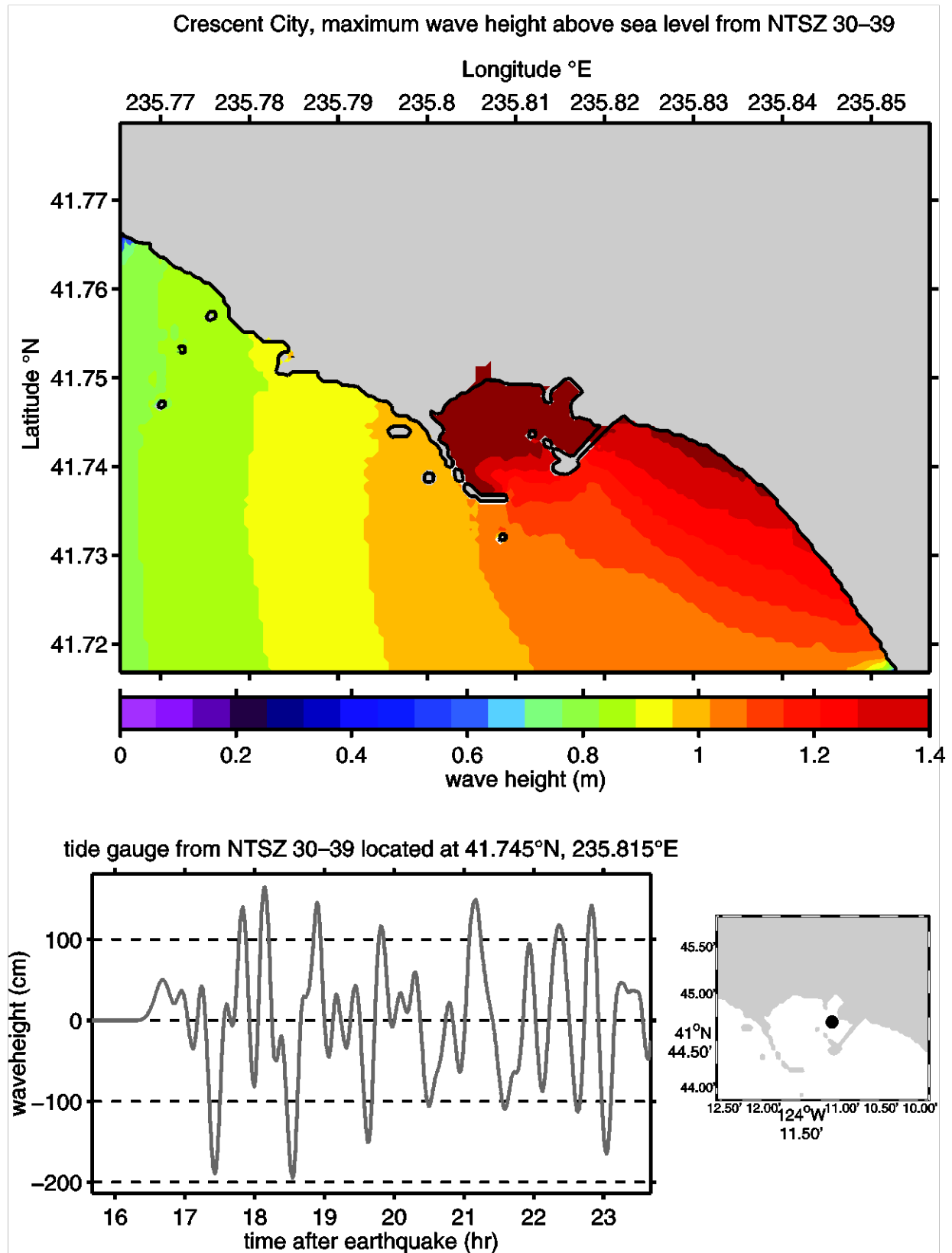
Figure 51. Maximum wave height plot and time series results for the forecast model using synthetic megatsunami Event NTSZ 30–39 for Crescent City, California.
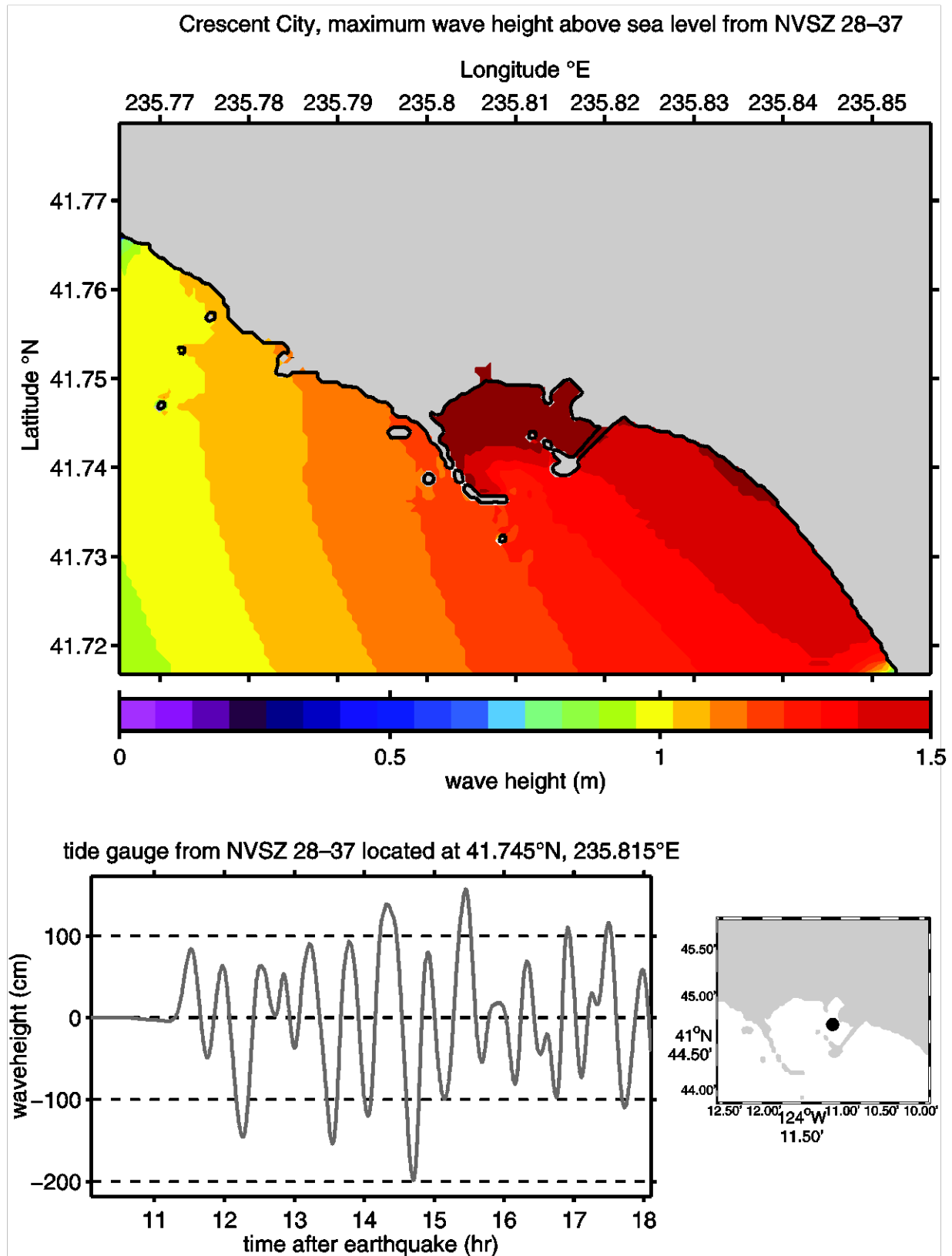
Figure 52. Maximum wave height plot and time series results for the forecast model using synthetic megatsunami Event NVSZ 28–37 for Crescent City, California.
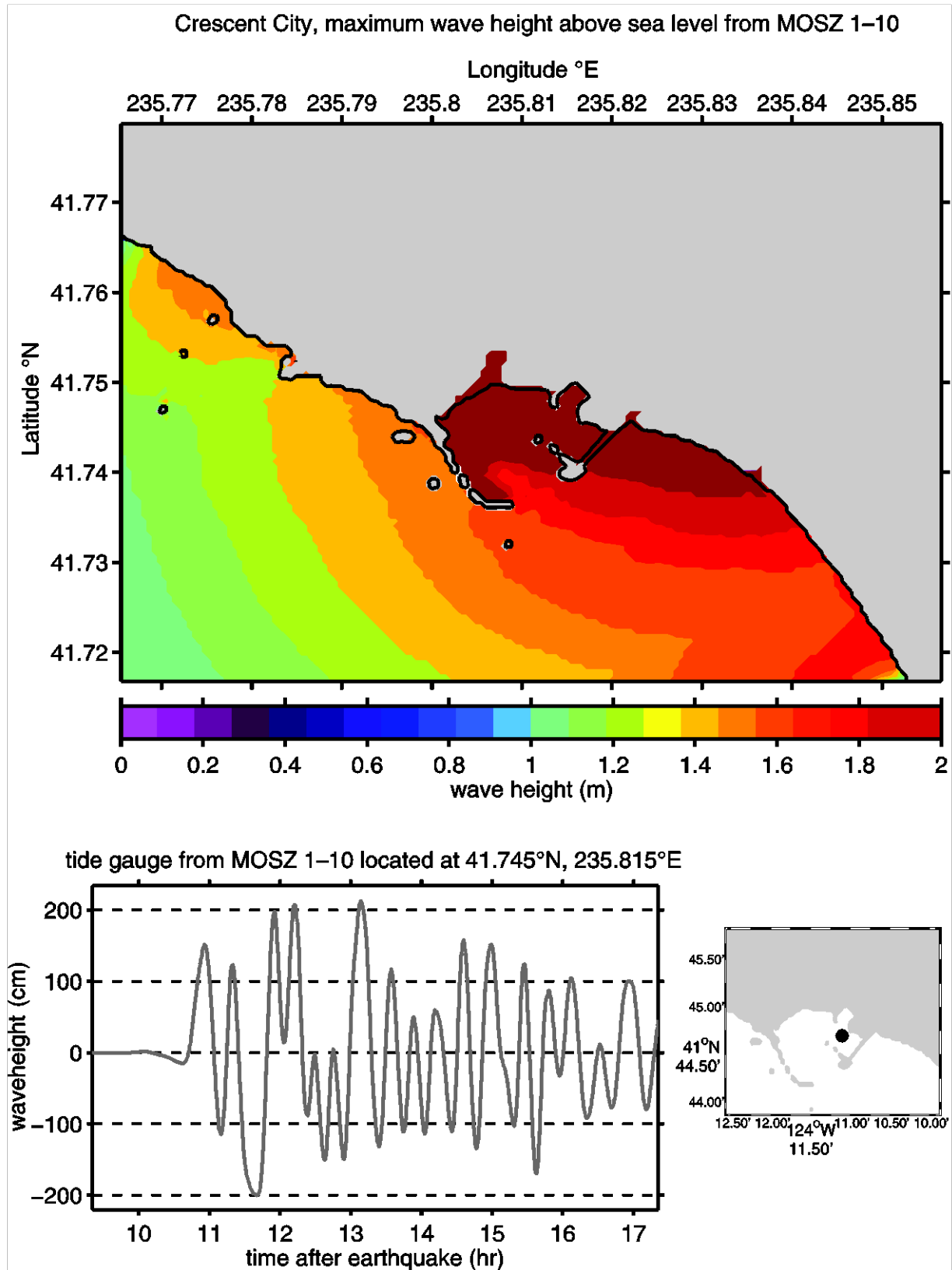
Figure 53. Maximum wave height plot and time series results for the forecast model using synthetic megatsunami Event MOSZ 1–10 for Crescent City, California.
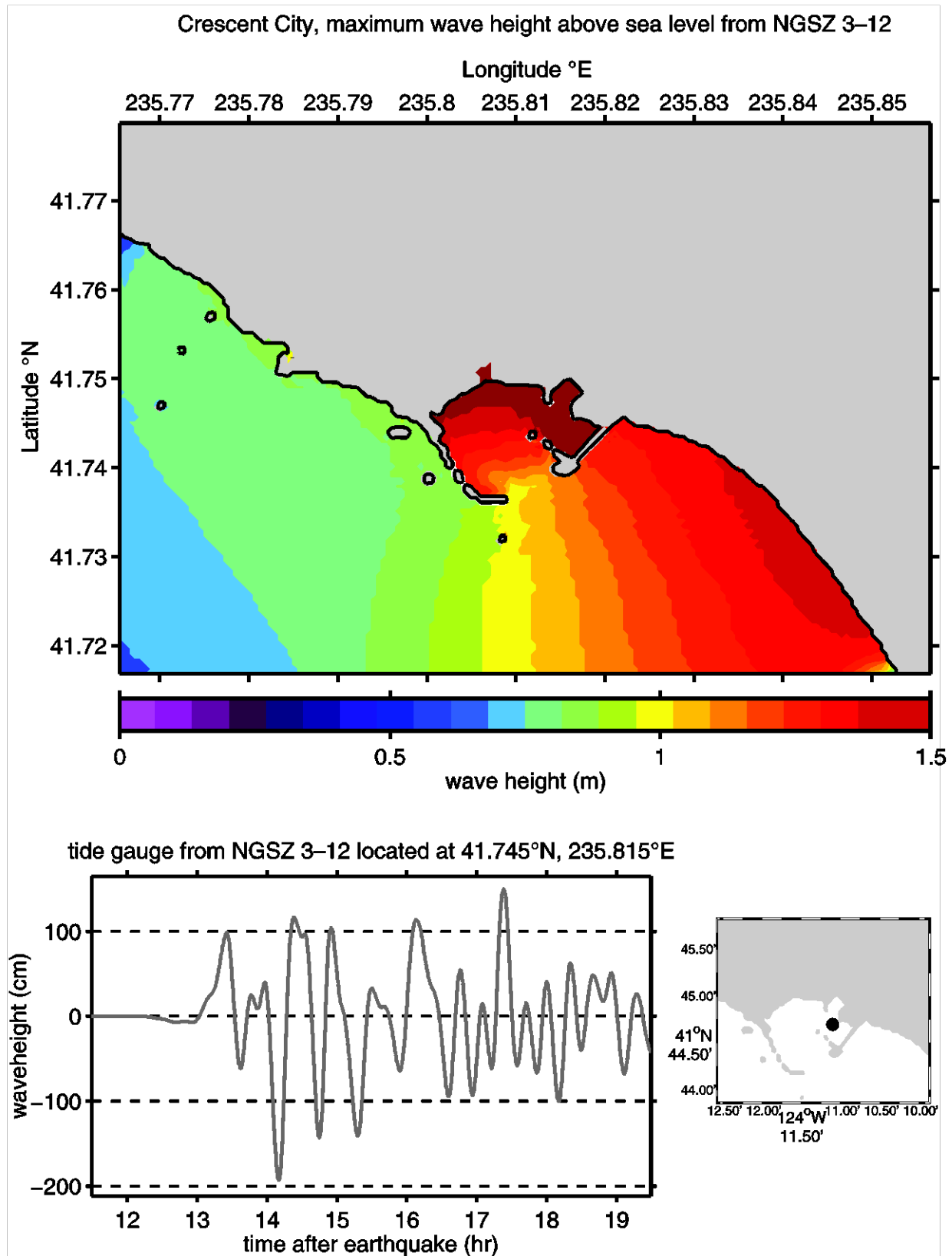
Figure 54. Maximum wave height plot and time series results for the forecast model using synthetic megatsunami Event NGSZ 3–12 for Crescent City, California.
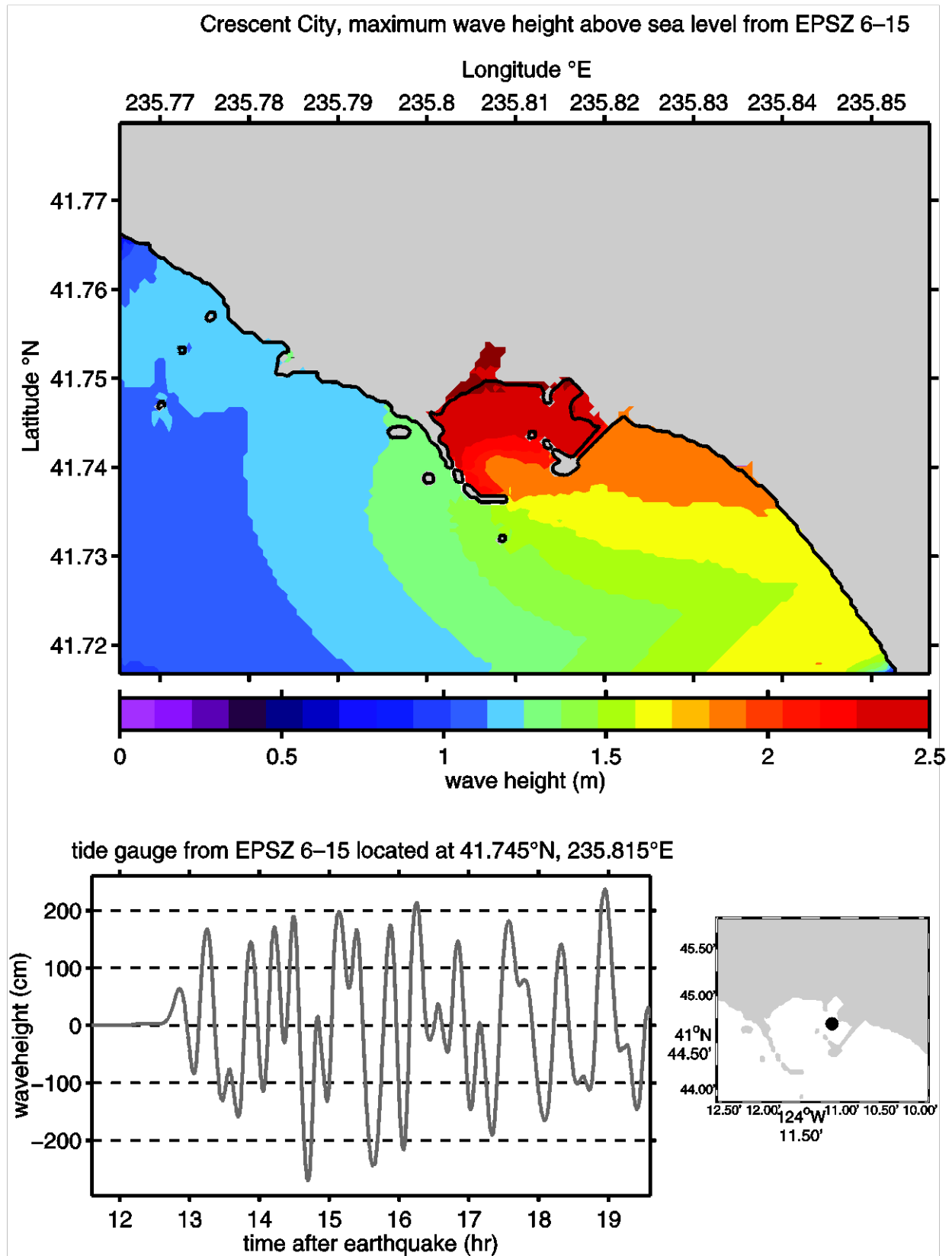
Figure 55. Maximum wave height plot and time series results for the forecast model using synthetic megatsunami Event EPSZ 6–15 for Crescent City, California.
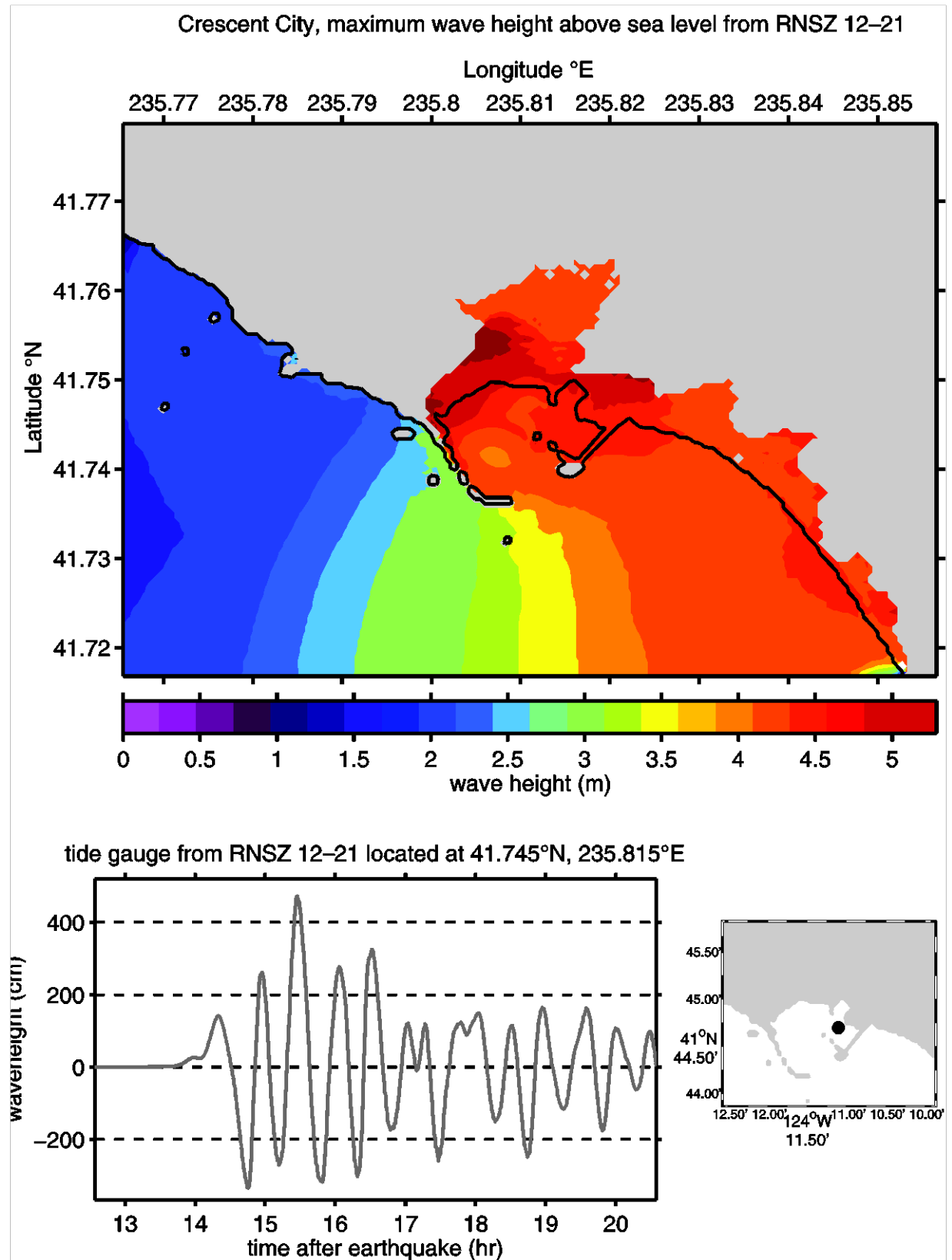
Figure 56. Maximum wave height plot and time series results for the forecast model using synthetic megatsunami Event RNSZ 12–21 for Crescent City, California.
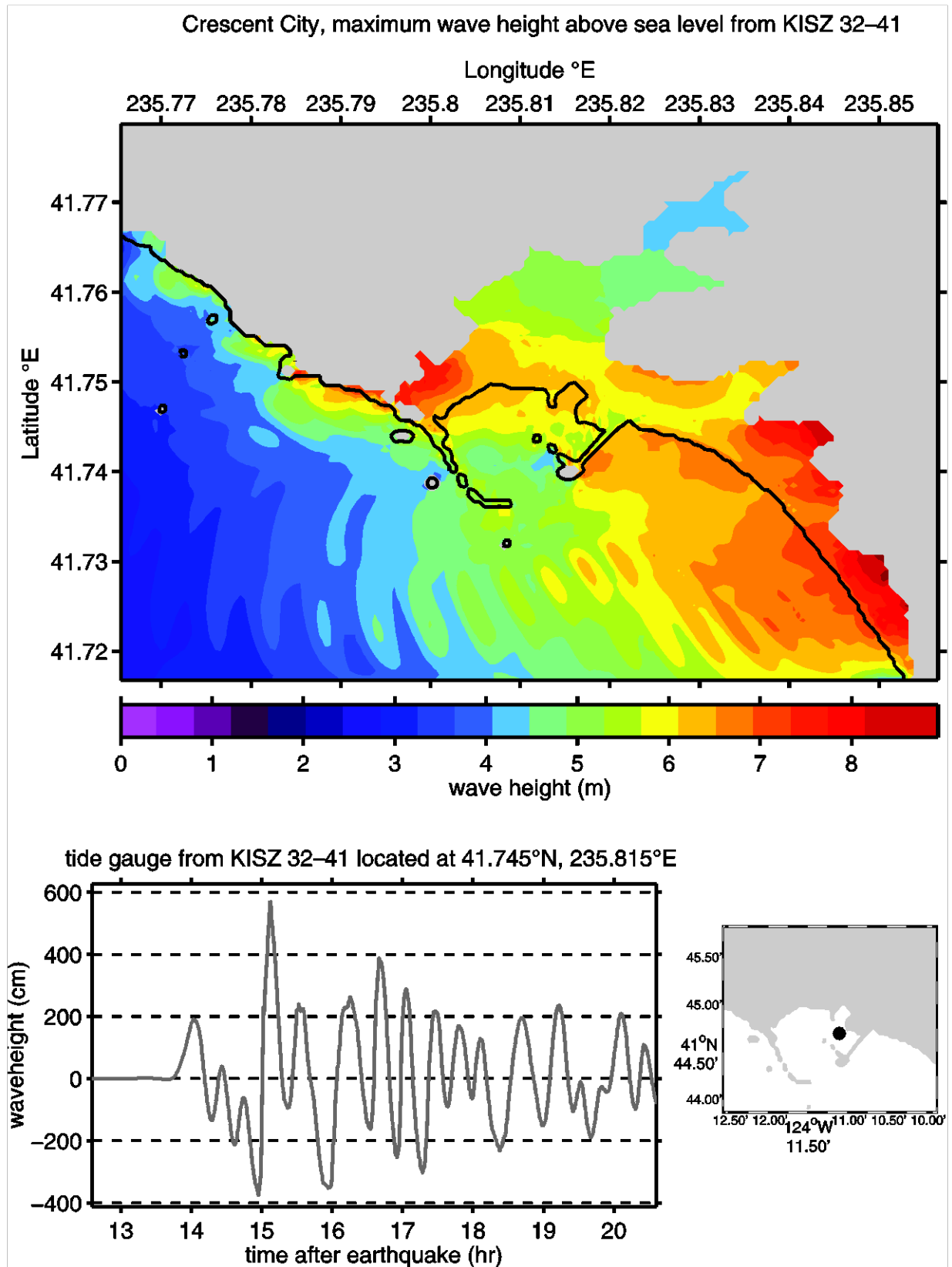
Figure 57. Maximum wave height plot and time series results for the forecast model using synthetic megatsunami Event KISZ 32–41 for Crescent City, California.
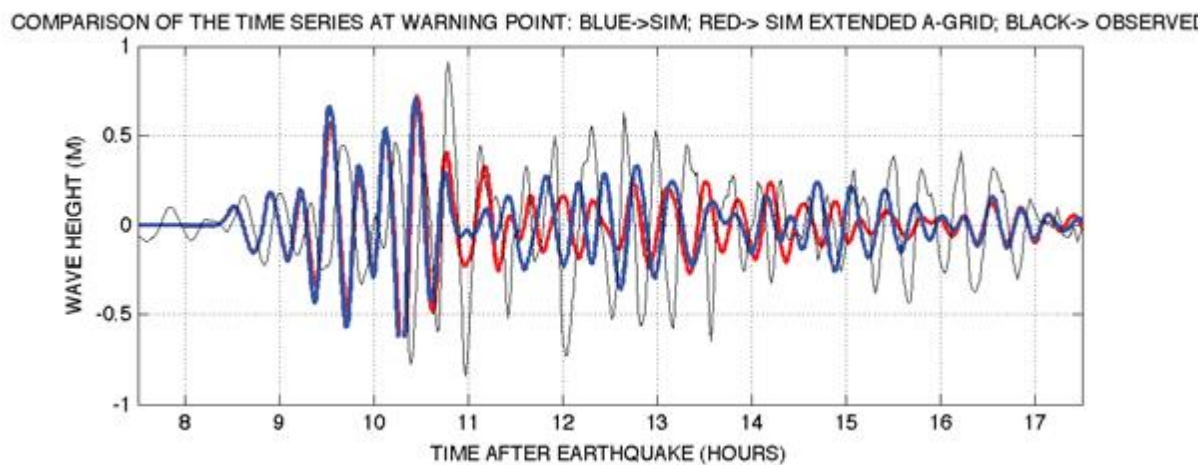
Figure 58. Time series at the tide gauge with extended forecast model grid A (blue) and with regular forecast model grid A (red). The black line is observed values for the Kuril 2006 event.

SUPPLEMENT: Synthetic testing — Crescent City, California

The Crescent City forecast model was tested with NOAA's tsunami forecast system version 3.2. The Crescent City forecast model was tested with four synthetic scenarios and one historical tsunami event. Test results from the forecast system and comparisons with the results obtained during the forecast model development are shown numerically in **Table S1** and graphically in **Figures S1 to S4**. The results show that the forecast model is stable and robust, with consistent and high quality results across geographically distributed tsunami sources and mega-event tsunami magnitudes. The model run time (wall clock time) was 2 min for a 4 hr simulation. This run time is within the 10 min run time for 4 hr of simulation time and satisfies time efficiency requirements.

Four synthetic events were run on the Crescent City forecast model. The modeled scenarios were stable for all cases tested, with no instabilities or ringing. Results show that the largest modeled height was 541.8 cm and originated in the Kamchatka-Kuril-Japan-Izu-Mariana-Yap (KISZ 22-31) source. Amplitudes greater than 175.5 cm were recorded for all of the test sources. The smallest signal of 175.5 cm was recorded at the far field Central and South America (CSSZ 91-100) source. Direct comparisons of output from the forecast tool with results of both the Tohoku 2011 historical event and available development synthetic events demonstrated that the wave patterns were similar in shape, pattern, and amplitude.

Table S1. Maximum and minimum amplitudes (cm) at the Crescent City warning point for synthetic and historical events tested using SIFT 3.2 and obtained during development.

Scenario Name	Source Zone	Tsunami Source	α [m]	SIFT Max (cm)	Development Max (cm)	SIFT Min (cm)	Development Min (cm)
Mega-tsunami Scenarios							
KISZ 22-31	Kamchatka-Yap-Mariana-Izu-Bonin	A22-A31, B22-B31	29	541.8	542.8	-331.6	-331.8
ACSZ 50-59	Aleutian-Alaska-Cascadia	A50-A59, B50-B59	29	404.1	403.2	-310.4	-312.8
CSSZ 91-100	Central and South America	A91-A100, B91-B100	29	175.5	175.5	-153.8	-153.7
Historical Events							
2011 Tohoku	New Zealand-Kermadec-Tonga	4.66 b24 + 12.23 b25 + 26.31 a26 + 21.27 b26 +22.75 a27 + 4.98 b27		244.8	244.8	-279.9	-279.9

(a)

(c)

(b)

(d)
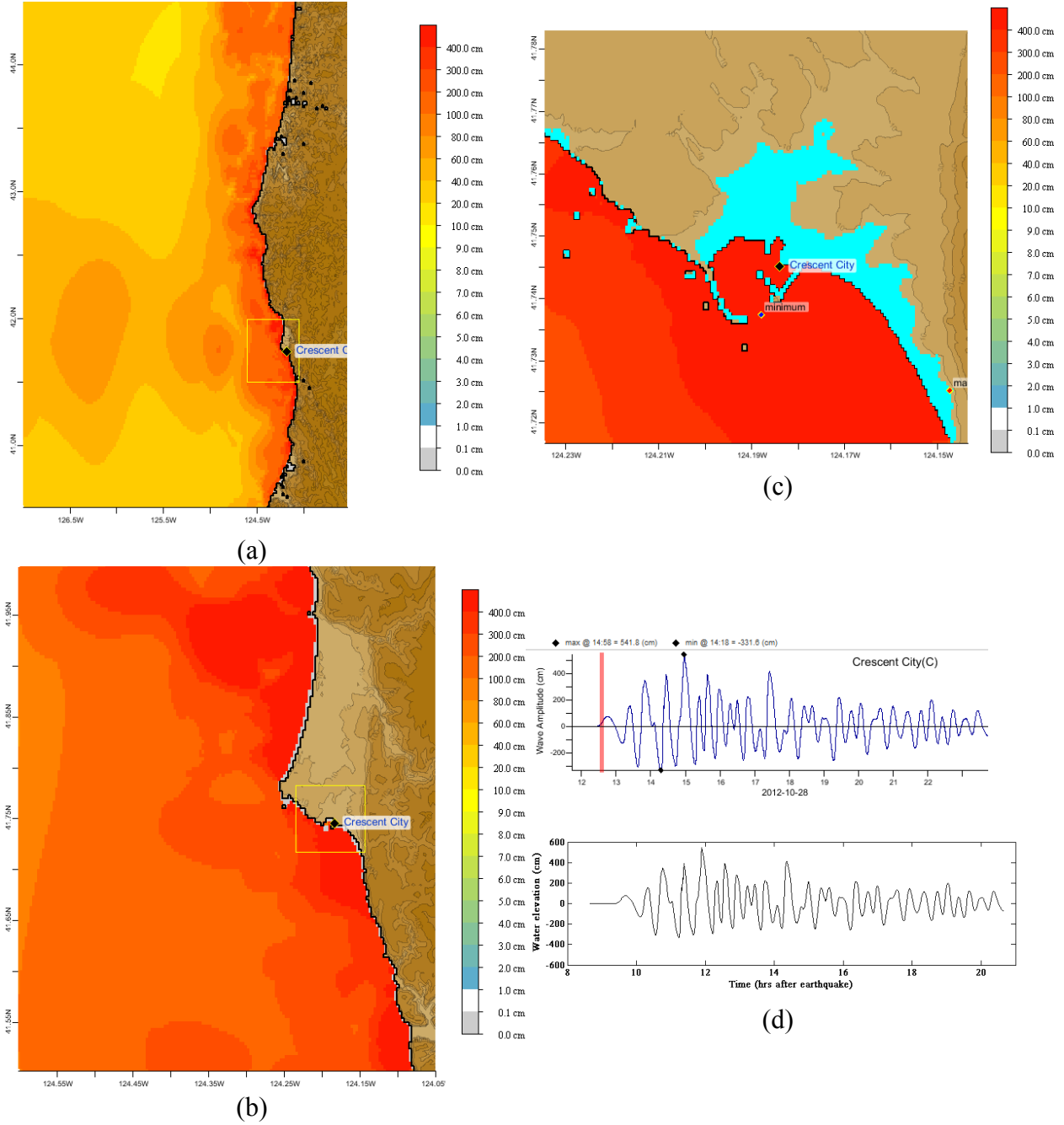
Figure S1. Response of the Crescent City forecast model to synthetic scenario KISZ 22-31 (α=29). Maximum sea surface elevation for (a) A grid, (b) B grid, and (c) C grid. Sea surface elevation time series at the C-grid warning point (d). The lower time series plot displays the result obtained during model development, shown for comparison with test results.

(a)

(b)

(c)

(d)

Figure S2. Response of the Crescent City forecast model to synthetic scenario ACSZ 50-59 (α=29). Maximum sea surface elevation for (a) A grid, (b) B grid, and (c) C grid. Sea surface elevation time series at the C-grid warning point (d). The lower time series plot displays the result obtained during model development, shown for comparison with test results.

(a)

(b)

(c)

(d)

Figure S3. Response of the Crescent City forecast model to synthetic scenario CSSZ 91-100 (α=29). Maximum sea surface elevation for (a) A grid, (b) B grid, and (c) C grid. Sea surface elevation time series at the C-grid warning point (d). The lower time series plot displays the result obtained during model development, shown for comparison with test results.

Figure S4. Response of the Crescent City forecast model to 2011 Tohoku tsunami. Maximum sea surface elevation for (a) A grid, (b) B grid, and (c) C grid. Sea surface elevation time series at the C-grid warning point (d). The lower time series plot displays the result obtained during model development, shown for comparison with test results.

2. PMEL Tsunami Forecast Model for Eureka, California

Hongqiang Zhou and NCTR Staff

Contents

2.1   Model Development

The objective of this work is to provide a high quality forecast model for Eureka, California, and surrounding communities on Humboldt Bay. The model will enable emergency planners at the local, state, and national levels to protect the people and resources of this region from the dangers of tsunami events.

2.1.1   Forecast area

Eureka is in Humboldt County of Northern California, 270 miles north of San Francisco. The city is located on Humboldt Bay–a large, deep-water bay which is home to both large industrial docks and numerous marinas serving fishing and recreational boats. A map of the area is shown in Figure 2.1. The population of Eureka is 27,191 (U.S. Census Bureau, 2010). Neighboring Arcata, located on the northern edge of Humboldt Bay, has a population of 17,231 (U.S. Census Bureau, 2010b).

Humboldt Bay is about 13 miles long and consists of Arcata Bay to the north of Eureka, the South Bay, and the central Bay area. The bay entrance is south of Eureka and is protected by jetties, making the entrance easier for boats. Eureka is situated at the center of Humboldt Bay, on the hill overlooking the thinnest part of the bay's channels. Arcata is to the north, and other smaller unincorporated communities, such as Fairhaven, Manila, Indianola, and King Salmon surround the bay. A channel from the bay entrance to north of Eureka is dredged to a depth of 35–40 feet to accommodate larger vessels docking at a number of shipping facilities on the central bay in and around Eureka. The aerial image in Figure 2.2 shows the bay entrance and looks north to Eureka and Arcata Bay beyond. There are three islands in the Bay, all just north of Eureka: Indian Island is the largest, Woodley Island is the second and the site for a marina, and Daby Island is the smallest.

There are a number of sites in the area to consider when assessing tsunami threats. There are two small air-fields in the region: the Eureka Municipal Airport is located south of Fairhaven on the spit across from Eureka, and Murray Field is just to the northeast of Eureka in the Fay Slough area. A natural gas and electric power plant is sited opposite the bay's entrance and north of King Salmon. The main transportation artery in the region, Highway 101, borders Humboldt Bay from north to south, connecting Eureka and Arcata and the rest of California.

The Humboldt Bay National Wildlife Refuge is an important natural and tourist component of the Bay. The Refuge is mainly in the shallow and marshy South Bay but also rings Arcata Bay. The mudflats and eelgrass beds here provide habitat for local and migratory birds, with estimates as high as 100,000 birds being present. The Bay is also important for spawning and feeding fish.

2.1.2   Historical events and data

NOAA's National Ocean Service (NOS) operates a tide gauge sensor at North Spit in Humboldt Bay. The gauge is located on the dock at the Humboldt Bay Coast Guard Station, at 40.76633° N and 124.21725° W. The dock is near the bay entrance on the inshore side of spit, across the bay and south of Eureka. The tide gauge was established in August of

1977. The mean tidal range at the gauge location is 1.5 m. An image of the tide gauge shack on the Coast Guard pier is shown in Figure 2.3. There are historical accounts of tsunami runup heights available from the National Geophysical Data Center (NGDC) tsunami runup database (`http://www.ngdc.noaa.gov/nndc/struts/form?t=101650&s=167&d=166`), and we will use the available data for comparison with the model predictions.

The tide gauge data must be de-tided and smoothed before comparing it to the model predicted wave heights. First, a running mean filter with a width of 1 hr is constructed and used to eliminate outlier points with greater than 6 standard deviations difference between the smoothed and original time series. Then the tidal and instrument noise are eliminated using a band-pass digital Fourier filter with cutoffs at the high and low frequency ends of 8 min and 3 hr. The resulting observed sea surface height changes due to historical tsunamis are used to compare and validate our modeled time series predictions of those events.

2.1.3   Model setup

The grids developed for the reference and forecast models were derived from the Pacific basin-wide 30 arc-second grid developed at NCTR and the 1/3 arc-second digital elevation model (DEM) developed by NGDC (Carignan et al., 2010). This DEM is shown in Figure 2.4. The extents and parameters of the forecast and reference model grids are detailed in Table 2.1. The forecast and reference grids were set up using matching boundaries. The A-grid covers the United States coast from central California in the south to central Oregon in the north, and out to the deep ocean to the west. The B-grid focuses on the region surrounding Humboldt Bay. It was designed to cover the bathymetry and topography of Point Mendocino to the south of Humboldt and Patrick's Point to the north. The highest resolution C-grid zooms in on Humboldt Bay itself, with its goal to describe the waves and water levels of the Bay and along the coastal spits. The developed reference and forecast model grids are shown in Figures 2.5 and 2.6, respectively. A significant portion of the modeled tsunami waves, typically 4 to 10 hr of modeled tsunami time, pass through the model domain without appreciable signal degradation. Input parameters of both models are also presented in Table 2.1. Time series of simulated water surface elevations are output at a reference grid node in the C-grid of each model that is the closest to the actual tide gauge location. These reference grid nodes are denoted by a red star in Figures 2.5 and 2.6, respectively. The water depth in the forecast model grid at the reference node is 5.7 m.

2.2   Results and Discussion

2.2.1   Model validation

We use thirteen historical tsunamis to validate and test the Eureka forecast and reference models. The locations, magnitudes, and unit source combinations used to describe these events are presented in Table 2.2. The selected events range from smaller to larger originating earthquakes (7.7 to 9.2 Mw) and are from various locations around the Pacific Rim. The majority of these events are more recent, since we have higher quality descriptions of the earthquakes and can describe the tsunamigenic responses more accurately. The locations and magnitudes of the thirteen historical events are plotted in Figure 2.7.

Results and comparisons from the forecast and reference models for the historical events are shown in Figures 2.8-2.20. In each figure, the top two axes show the maximum amplitude for the forecast and reference models, respectively, and the lower axis shows the time series of wave amplitude from both models at the reference grid nodes. Measurement data of the tide gauge is also plotted on this axis when available for an event. Note that the color scale and axes limits change from figure to figure.

The first tsunami event used for validation is due to the 1946 Unimak 8.5 Mw earthquake. The forecast and reference model results are shown in Figure 2.8. Both models show similar wave heights offshore, with the main difference being the location of the wave cusps. Heights inside the harbor are also well matched except for the bay opposite the jetty entrance. The time series of wave amplitude at the tide gauge shows that the forecast model predictions match the reference model well at that location.

The model responses to the 1960 Chilean tsunami are shown in Figure 2.9. Wave heights of almost a meter are predicted on the ocean side of the Humboldt Bay spits, while in the Bay the maximum height is less, i.e., about 0.75 m. Both the forecast and reference models predict inundation in the South Bay and along the slough north of Eureka. The tide gauge time series shows that the forecast model is doing a good job of resolving the tsunami response.

The 1964 Alaskan earthquake, with a magnitude of 9.3 Mw, caused damage and deaths in Alaska, Oregon, and California. In Figure 2.10, the predicted wave heights are shown to agree well between the two models (note that the color scale has been allowed to wash out the ocean maxima so that the details inside the Bay are apparent). Inside the Bay, maxima are 2.6 and 2.7 m for the forecast and reference models, respectively. Observations from the event of waterlines on docks and structures estimated maximum runup of 2.1 m (`http://www.ngdc.noaa.gov/nndc/struts/form?t=101650&s=167&d=166`). Both models predict inundation at many locations around the bay, including Eureka itself. The time series at the tide gauge shows the models predict similar waves with magnitudes of 1.3 m.

The next four events used for validation are all moderate events that have not caused much impact on Eureka. The 1994 Kuril earthquake is predicted to cause offshore waves on the order of 20 cm (Figure 2.11), while inside the bay the highest values are approximately 14 cm. Both the maximum height maps and the tide-gauge time series match well between the two models. For both the 1996 Andreanof (Figure 2.12) and 2003 Rat Island (Figure 2.13) earthquakes, we have real tide-gauge data, but the resulting waves at Eureka are so small that the tsunami signals are uneasy to be separated from the background noises. For the 1996 Andreanof event, the predicted wave heights are less than 10 cm at all points in the C-grid, while for the 2003 Rat Island event, there are no values greater than 7 cm. Figure 2.14 shows the predictions for the 2006 Tonga event, and the forecast and reference models agree well, showing maxima of approximately 20 cm south of the jetty on the ocean side and no significant waves inside the harbor.

The Kuril events of 2006 and 2007 are shown in Figures 2.15 and 2.16, respectively. The 2006 tsunami led to stronger waves at Eureka, and this is reflected in the plots. The tide gauge data for the 2006 event is plotted in the lower panel of Figure 2.15, and the models predict values that are comparable in magnitude, if not exact wave timing. For both events, the forecast model works well in reproducing the wave heights predicted by the reference model.

The Solomon tsunami of 2007 (Figure 2.17) is interesting because, although it results in a small tsunami with maximum wave heights of less than 10 cm, the wave heights inside the harbor are comparable to the ocean values. Both the forecast and reference models show ~ 8 cm wave elevations in the Bay north of the entrance and east of Eureka itself.

The Chilean earthquake of 2010, which caused major destruction and over 500 deaths in Chile, is shown in Figure 2.19. The forecast and reference models predict similar patterns of distributed maximum wave elevations, with waves of over 30 cm on the ocean side of the spits. Inside the harbor, the reference model shows higher wave heights opposite the channel entrance. The tide gauge at Eureka measured wave peaks between 10 and 20 cm. The forecast and reference models reproduce the time series at the tide gauge very well, predicting quality estimates of both amplitude and phase. It should be noted, though, that the modeled time series are delayed by 11 min to give a better correlation. This temporal offset for this 2010 Chile event has been observed at other sites and the cause is under investigation. Note that there is no significant inundation for this strong event.

The last event presented here for model validation is the 2011 Tohoku tsunami. In Figure 2.20, the comparison between the forecast and reference model for maximum wave elevations shows very good agreement inside Humboldt Bay (the color scale has been pushed to highlight the variation inside the bay). Minimal inundation is seen in South Bay and the northeast corner of Arcata, which are both low marshy areas. The time series in the lower panel shows high correlation between the model predictions and the tide gauge data. The highest wave is seen to be the second one, arriving almost an hour after the first and peaking near 0.9 m. For this event, we have once again delayed the model predictions, here by 12 min, to provide a better timing match.

2.2.2 Test of model stability using synthetic scenarios

To further test the stability and robustness of the forecast model, we use a set of 21 synthetic tsunamis. These events are "synthetic" in the sense that they do not represent actual historical earthquakes, but allow us the flexibility to stress-test our model using large forcing inputs from many different directions. Among them, 19 are Mw 9.3 events that each uses a set of 20 unit sources, corresponding to a rupture area of 1000 km by 100 km, and are located all around the Pacific Basin and in each subduction zone. For comparison, the 2004 Indian Ocean tsunami that resulted in hundreds of thousands of deaths in Indonesia and was detectable globally was the result of a Mw 9.1 earthquake. We also run tests using a moderate Mw 7.5 earthquake and a micro-event, to ensure that the model triggers correctly for low energy events. Table 2.3 describes the synthetic events and their unit source combinations. Figure 2.21 shows the locations of these events and their positions relative to Eureka. The distributed maximum wave elevations in the C-grid and time series of wave amplitudes at the Eureka tide gauge location, as predicted by the forecast model, are shown in Figures 2.22-2.42. Once again, note that the color table mapping and plot limits vary from figure to figure.

The events originating from the Kamchatka-Yap-Mariana-Izu-Bonin (KISZ) sources (Figures 2.22-2.25) are predicted to force waves ranging from 1.2 to 1.9 m in height at the Eureka tide gauge location. The largest of these originates from the KISZ32-41 (Figure 2.24) source set and is seen to cause flooding on the North Spit, on the northern edges of Arcata Bay, in

South Bay, and in the low farmland opposite the bay mouth. Inundation is also seen in the other KISZ events presented, but to lesser extents.

The Aleutian-Alaska-Cascadia subduction zone (ACSZ) events are shown in Figures 2.26-2.30. The largest response of all the synthetic events presented, as would be expected, is from the near-field ACSZ56-65 event (Figure 2.36) whose source is on the Juan de Fuca fault and is the closest event used for testing. The model predicts 10 m waves on the beach and extensive inundation. Inundation is predicted to overwash both spits and flood all the lower marsh and farmland areas, and more significantly, some of the inhabited regions of Eureka and Arcata. At the tide gauge inside the bay, the waves peak near 5 m. The other ACSZ events lead to 1-1.5 m waves at the tide gauge and moderate flooding.

The Central and South America (CSZZ) events are seen in Figures 2.31-2.34, and all force waves of less than a meter, with minimal inundation observed. The CSSZ01-10 event (Figure 2.31) shows an interesting effect: the initial waves arrive 5 hr after the event and are less than 0.2 m. But waves three times as large arrive from 16 to 24 hr after the event, suggesting the larger wave energy arriving at Eureka does not travel directly there, but is reflected from the south Pacific.

The remaining source zones events, originating in the southern and southwest Pacific Ocean, are predicted to cause minimal to moderate waves at Eureka. The strongest of these is the North New Guinea event (NGSZ03-12) shown in Figure 38, where 3 m wave heights are seen at the coast and a maximum wave of almost 1.6 m at the tide gauge location. Moderate inundation is predicted from this event in most of the lower, marshy areas.

Both the medium and micro synthetic events (Figures 2.41 and 2.42) show minimal and negligible response at Eureka. This result is still important, in that it shows that the forecast model will correctly trigger and predict events with very low energy. Finally, and most importantly, note that, for all the synthetic events tested, the forecast model developed here for Eureka is stable under extreme forcing.

2.3   Summary and Conclusions

We have developed a set of optimized and reference tsunami forecast models for Eureka and Humboldt Bay. The models have been validated using historical tsunami events and stress-tested with synthetic mega-tsunami scenarios. For historical events where tide gauge data are available, the model predictions were compared with the actual measurements and reasonable agreement was observed. The C-grid developed for the forecast model has resolutions in longitude and latitude of 2.0 and 1.6 arc-sec, corresponding to a grid spacing of ~ 47 m. The model can complete a 4-hr simulation in under 10 min of CPU time, providing fast wave height estimates. From the synthetic model testing, it is seen that the tsunami event most threatening the region would be a near-field earthquake on the Jan de Fuca fault, possibly leading to maximum waves of 10 m in C-grid, 5–6 m on the bay, and major inundation. Far-field events from the Kamchatka-Yap-Mariana-Izu-Bonin source zone and, to a lesser extent, the Southern Pacific zones can also lead to large waves and inundation at Eureka.

The models developed here are capable of giving quality predictions of wave heights in response to tsunamis. These models are part of NOAA's tsunami forecast and warning

system and will be used to predict, in real-time, the potential threat of tsunami waves for the people and resources of the communities on Humboldt Bay.

Acknowledgments

Supplement: Test of the Eureka, California, Forecast Model

The Eureka forecast model was tested with NOAA's tsunami forecast system version 3.2. The Eureka forecast model was tested with four synthetic scenarios and one historical tsunami event. Test results from the forecast system and comparisons with the results obtained during the forecast model development are shown numerically in Table S2.1 and graphically in Figures S2.1 to S2.5. The results show that the forecast model is stable and robust, with consistent and high quality results across geographically distributed tsunami sources and mega-event tsunami magnitudes. The model run time (wall clock time) was under 16.3 minutes for 10 hours of simulation time, and under 6.5 minutes for 4 hours. This run time is within the 10 minute run time for 4 hours of simulation time and satisfies time efficiency requirements.

Four synthetic events were run on the Eureka forecast model. The modeled scenarios were stable for all cases tested, with no instabilities or ringing. Results show that the largest modeled height was 476 cm and originated in the Aleutian-California-Cascadia (ACSZ 56-65) source. Amplitudes greater than 75 cm were recorded for all of the test sources. The smallest signal of 83 cm was recorded at the far field Central and South America (CSSZ 89-98) source. Direct comparisons of output from the forecast tool with results of both the Tohoku 2011 historical event and available development synthetic events demonstrated that the wave patterns were similar in shape, pattern, and amplitude.

Figures

Figure 2.1: Map of the Eureka area. (Courtesy of the North Coast Sea Kayakers Assoc.)

Figure 2.2: An aerial photo of Eureka and Humboldt Bay. Arcata Bay is in the upper left corner and the north part of South Bay is to the right. Eureka is in the upper left quadrant of the photo. The smaller community of King Salmon is in the center-right, opposite of the bay entrance.

Figure 2.3: Image of the Eureka tide gauge shack, on the pier at the Humboldt Bay Coast Guard Station.
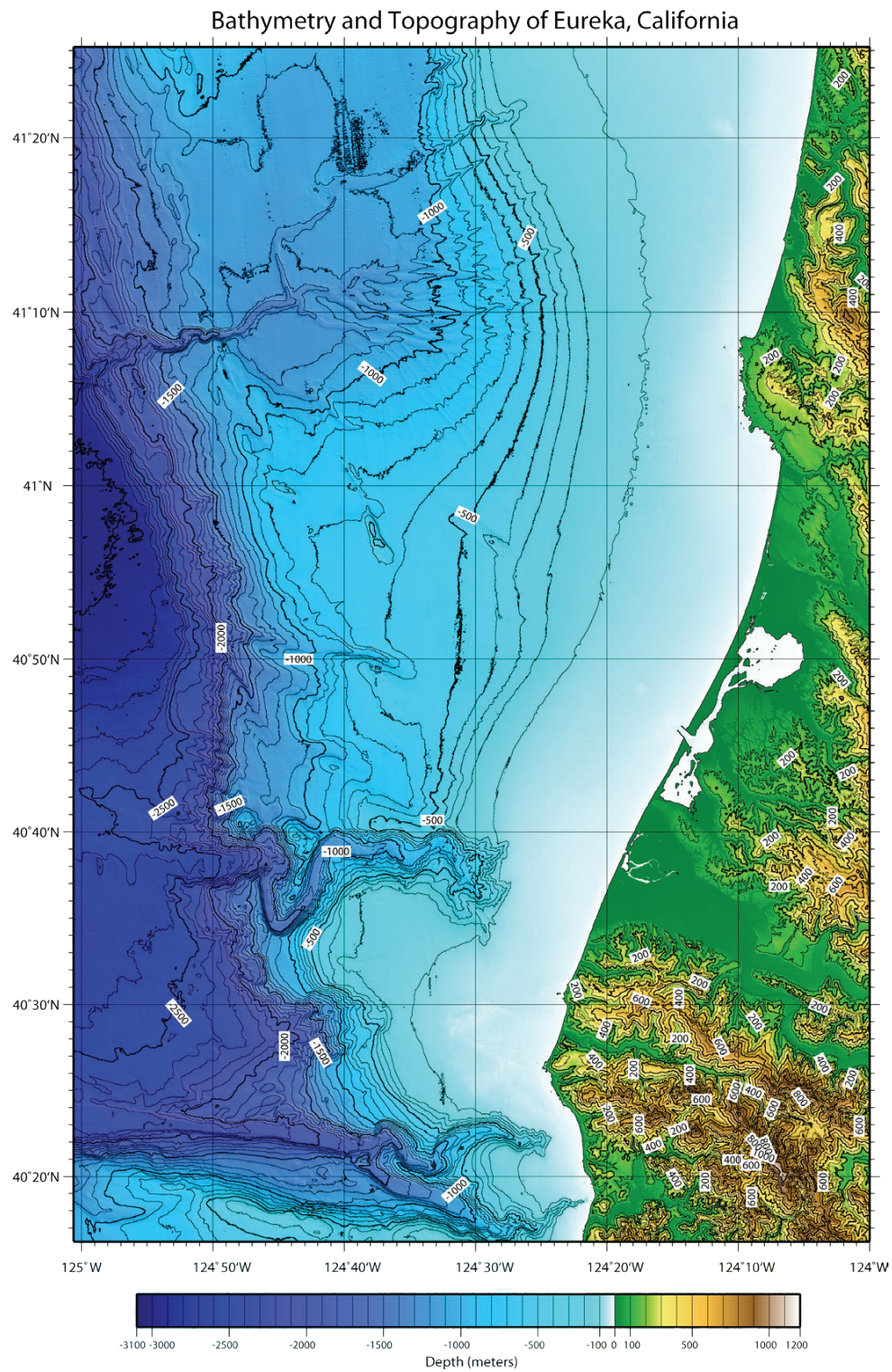
Figure 2.4: Shaded-relief image of the Eureka DEM. Bathymetric and topographic contour intervals are 100 meters. (Courtesy of NGDC)
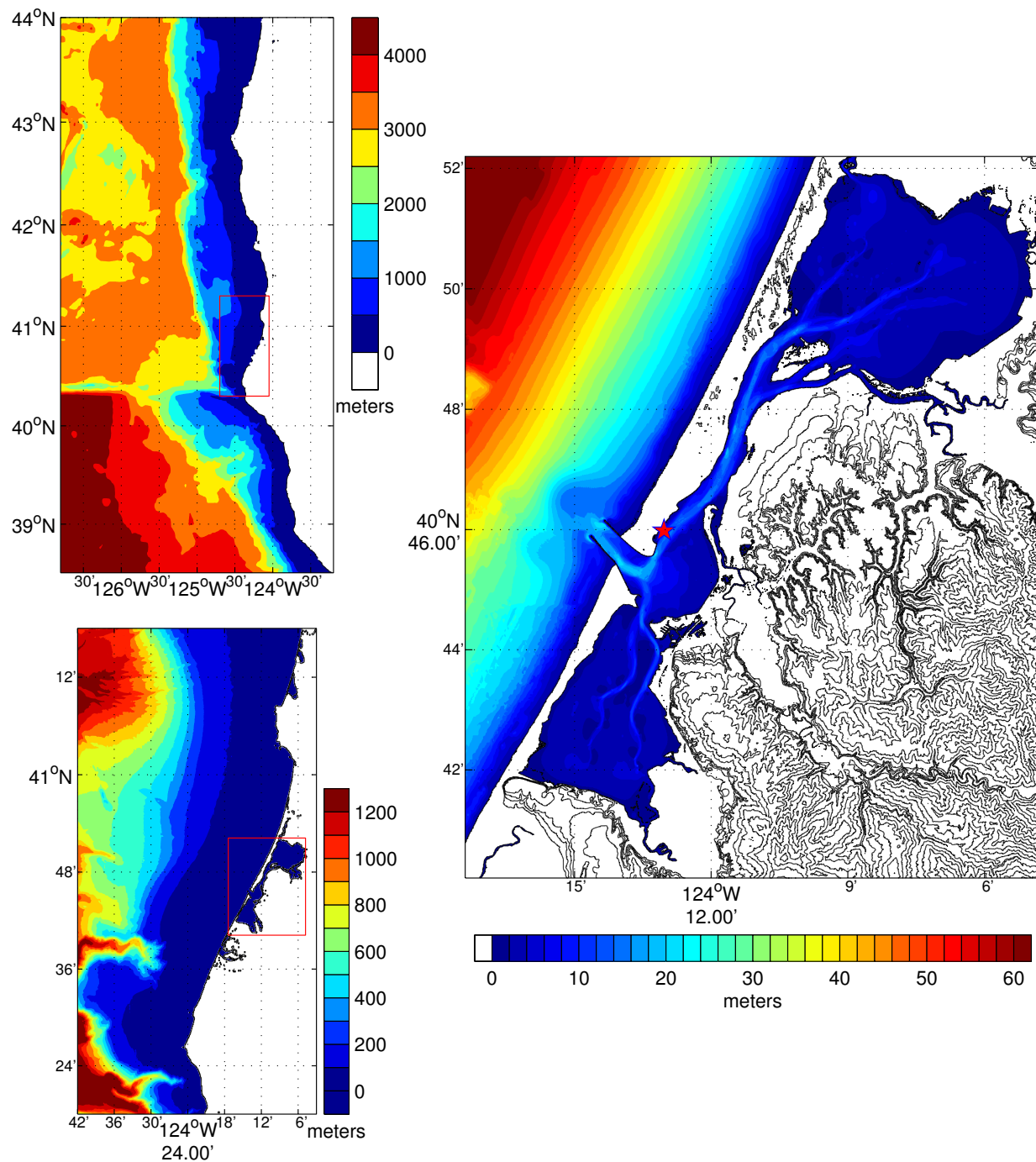
Figure 2.5: Bathymetry (meters) for the reference inundation model grids. The A-grid is shown in the top left panel, the B-grid in the bottom left panel, and the C-grid in the right panel. The topography of the C-grid is shown using contours with 10 m intervals from 0 to 40 and then 40 m intervals for higher values. The red boxes in the A and B plots show the position of the nested B and C-grids, respectively. The red star shows the location of the Eureka tide gauge installation.
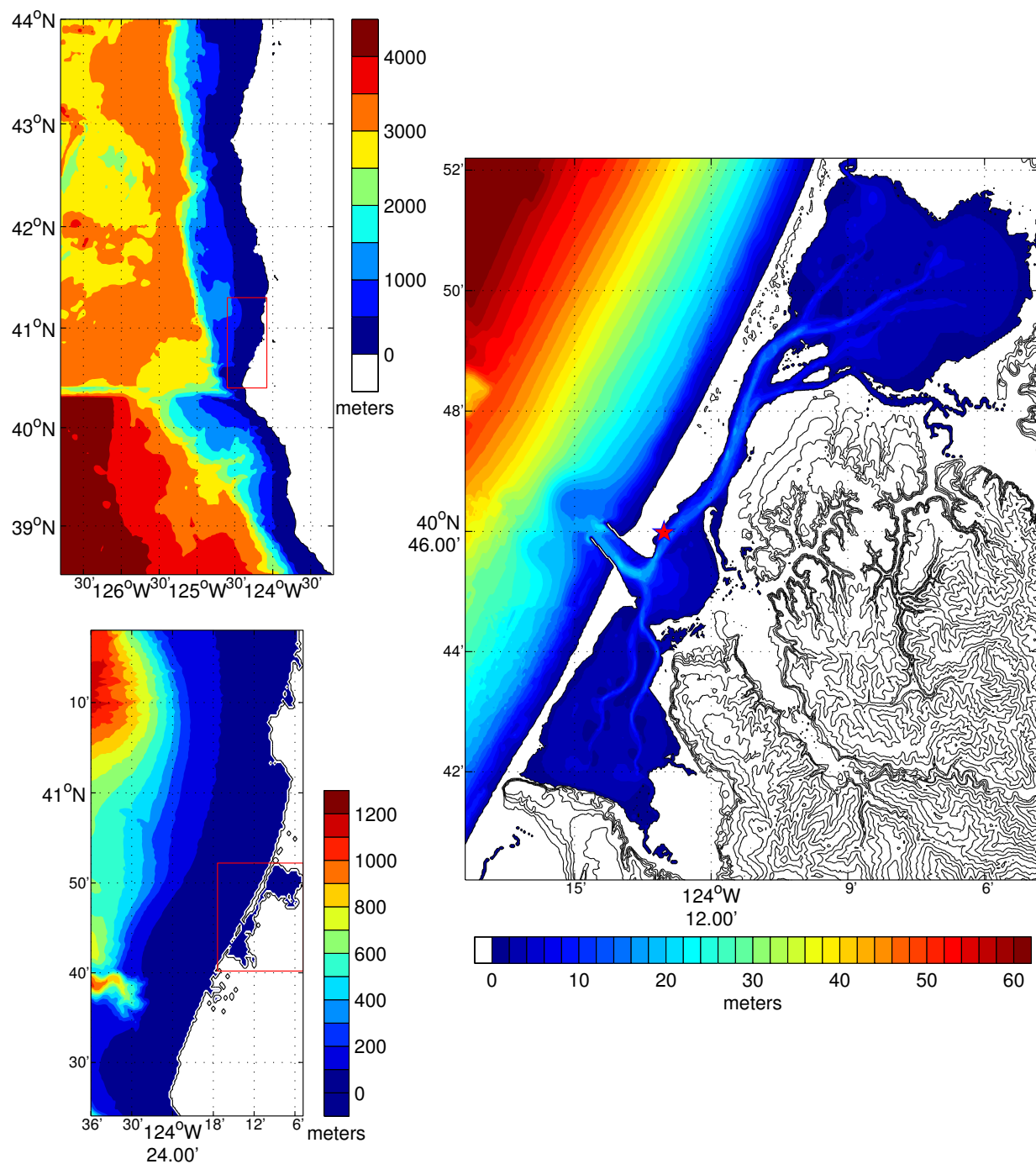
Figure 2.6: Bathymetry (meters) for the forecast inundation model grids. The A-grid is shown in the top left panel, the B-grid in the bottom left panel, and the C-grid in the right panel. The topography of the C-grid is shown using contours with 10 m intervals from 0 to 40 and then 40 m intervals for higher values. The red boxes in the A and B plots show the position of the nested B and C-grids, respectively. The red star shows the location of the Eureka tide gauge installation.
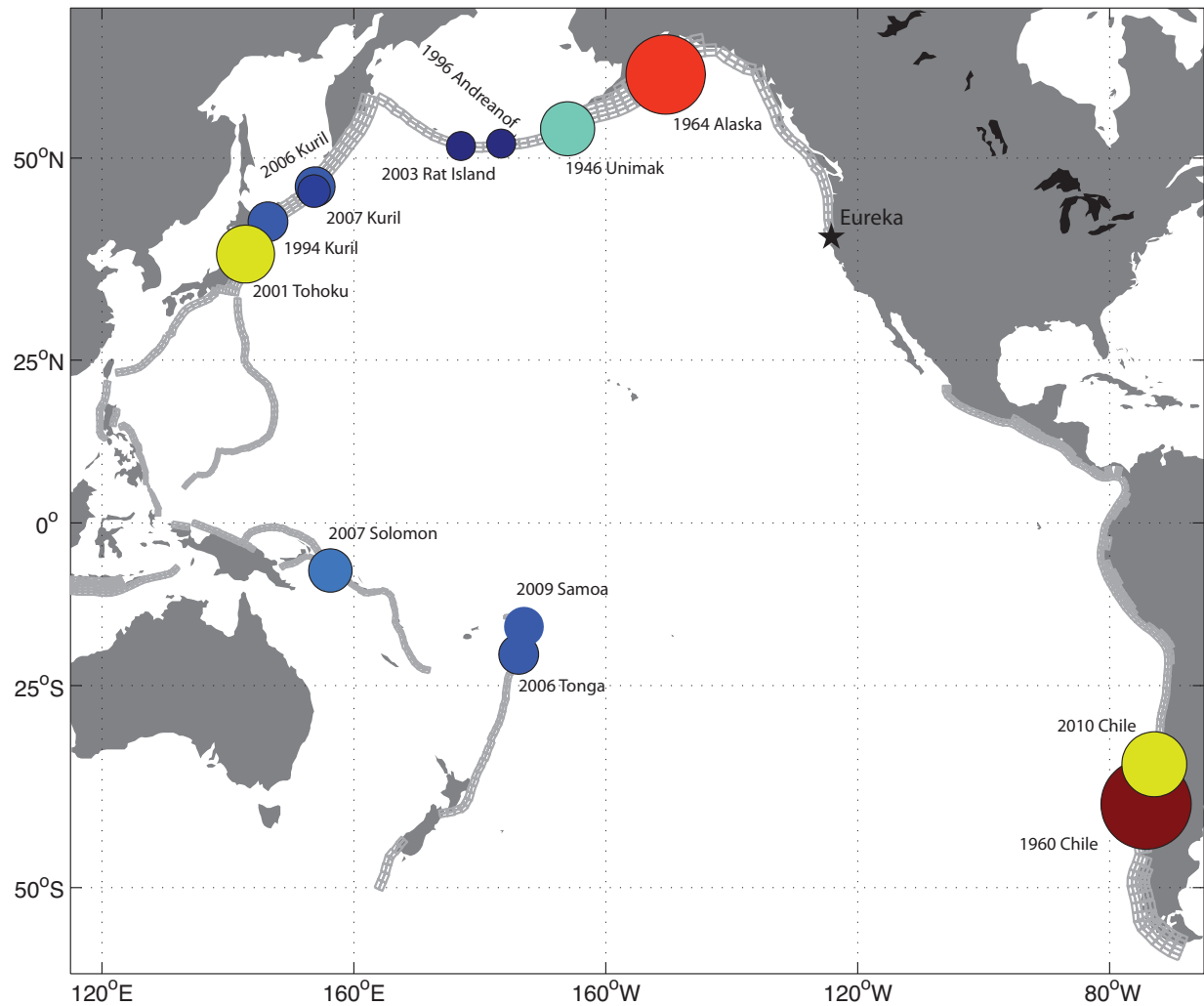
Figure 2.7: Map of the Pacific Ocean Basin showing the locations and magnitudes of the 12 historical events used to test and validate the Eureka model. Relative earthquake magnitude is shown by the varying sizes and colors of the filled circles. The largest magnitude earthquake used in model validation was the 1964 Alaska Mw 9.2 earthquake. The star denotes Eurekas location.
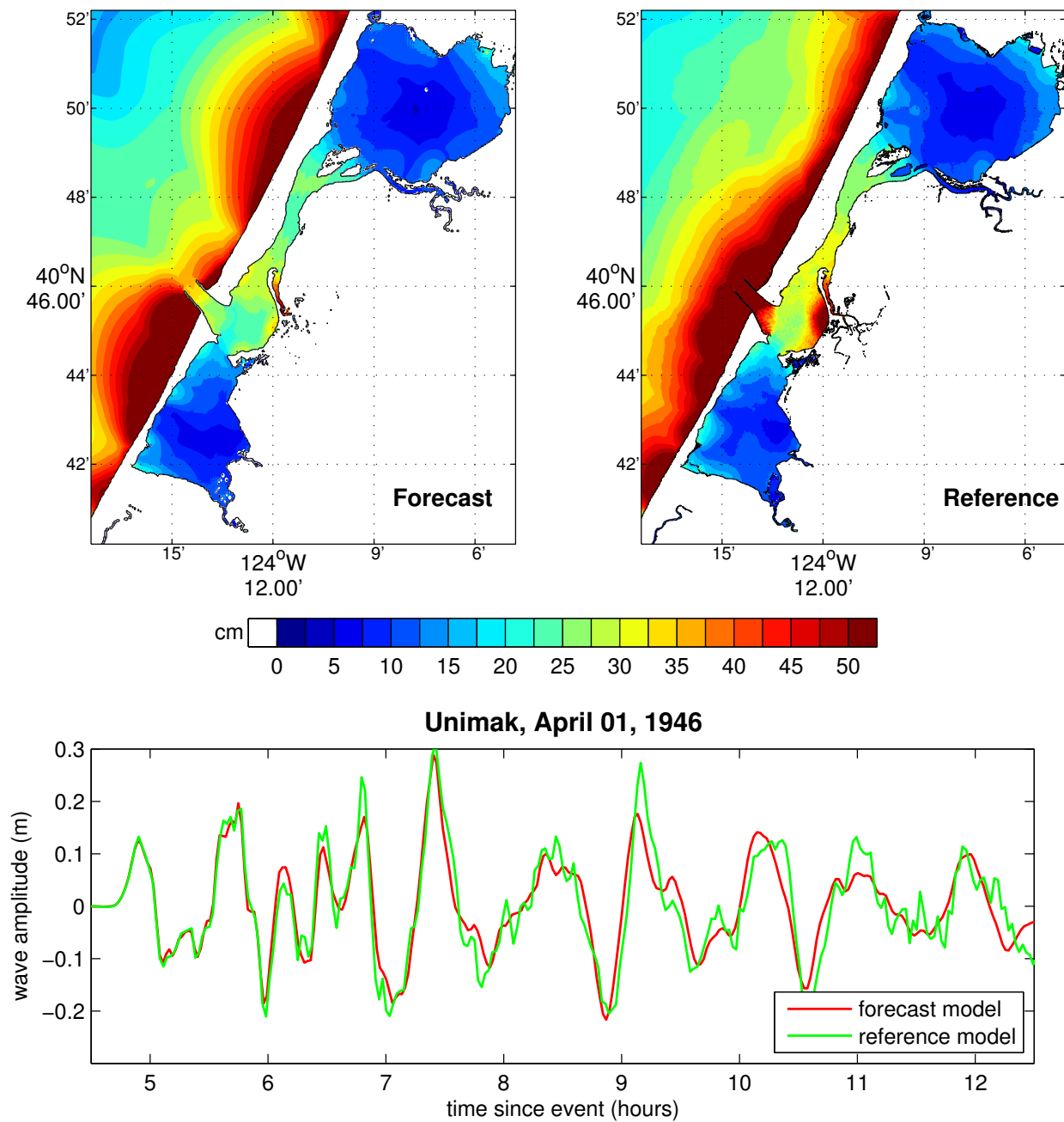
Figure 2.8: Model results for the 1946 Unimak Mw 8.5 event. The upper two panels show, respectively, the forecast and reference model maximum wave height predictions. The lower panel shows the forecast model (red) and reference model (green) wave amplitudes at the Eureka tide gauge.
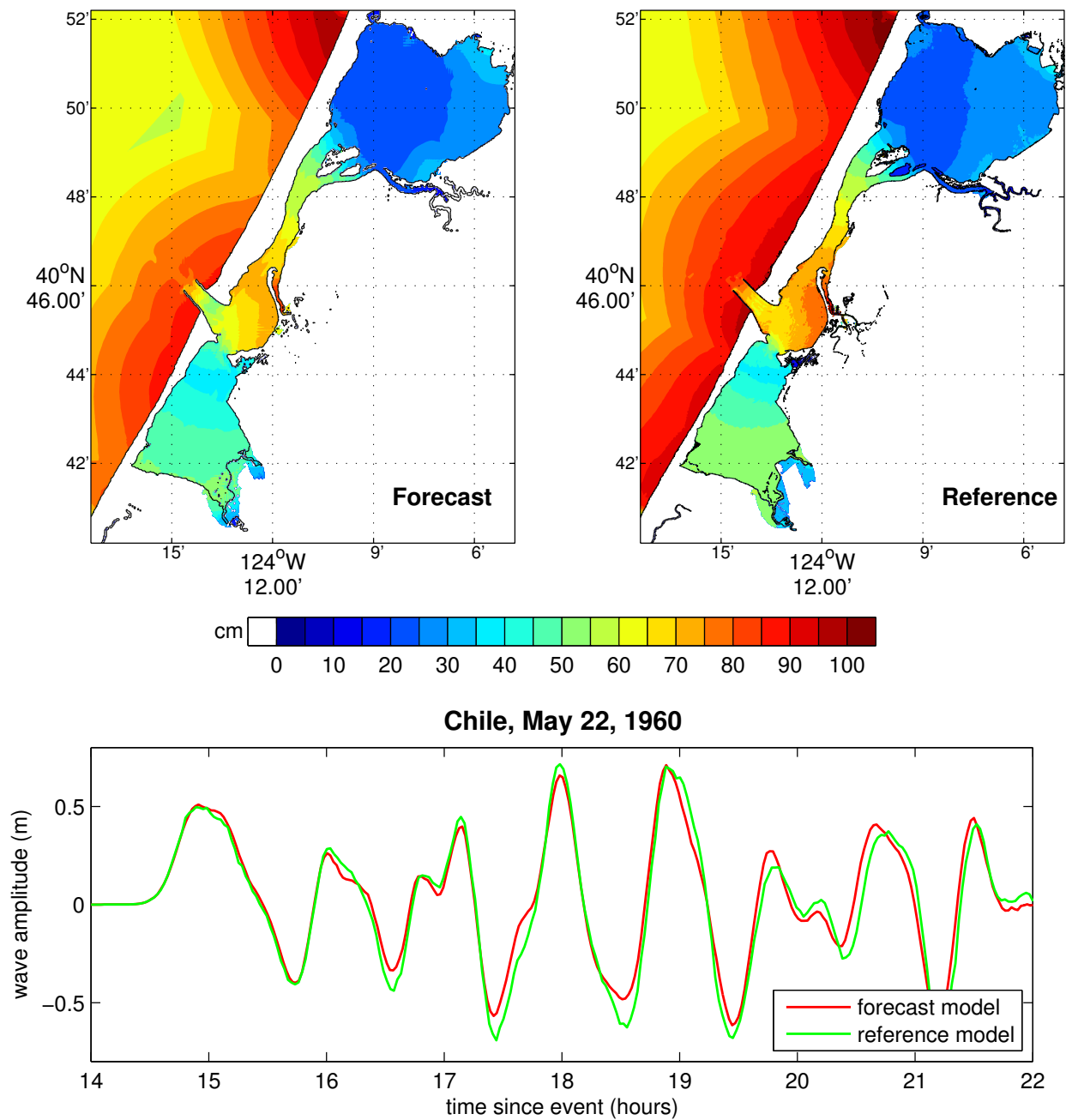
Figure 2.9: Model results for the 1960 Chile Mw 9.2 event. The upper two panels show, respectively, the forecast and reference model maximum wave height predictions. The lower panel shows the forecast model (red) and reference model (green) wave amplitudes at the Shemya tide gauge.
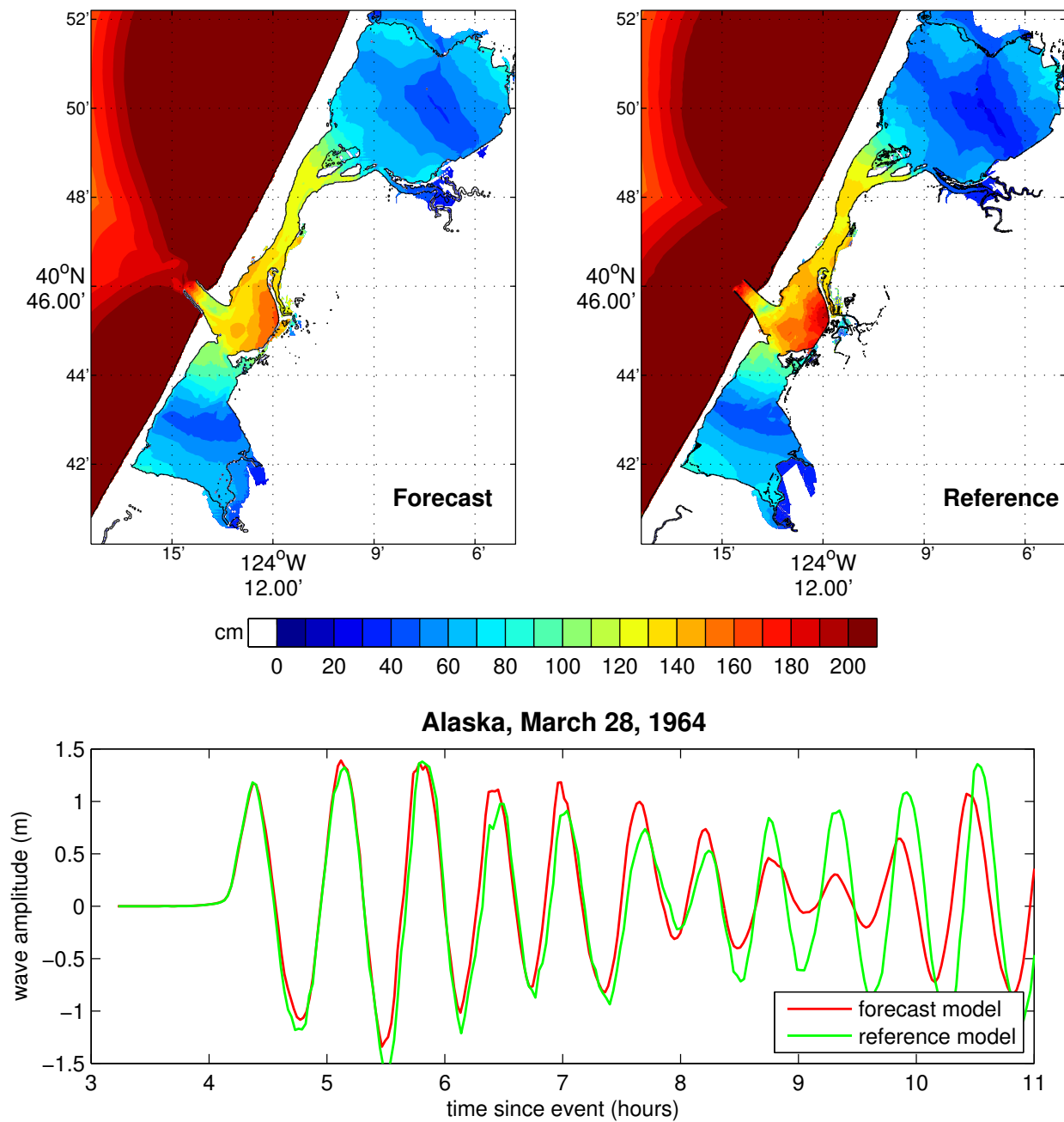
Figure 2.10: Model results for the 1964 Alaska Mw 9.2 event. The upper two panels show, respectively, the forecast and reference model maximum wave height predictions. The lower panel shows the forecast model (red) and reference model (green) wave amplitudes at the Shemya tide gauge.
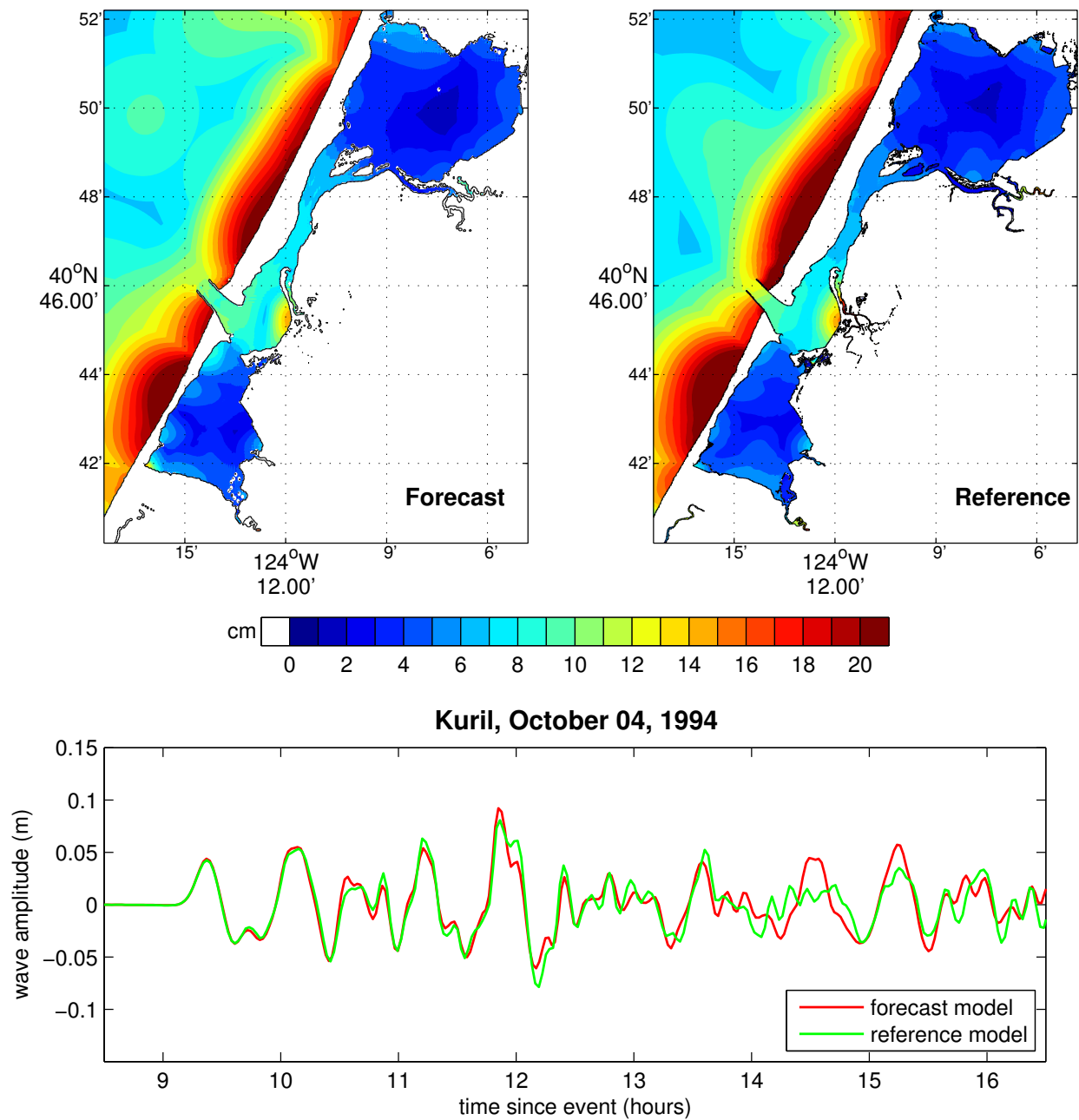
Figure 2.11: Model results for the 1994 Kuril Mw 8.3 event. The upper two panels show, respectively, the forecast and reference model maximum wave height predictions. The lower panel shows the forecast model (red) and reference model (green) wave amplitudes at the Shemya tide gauge.
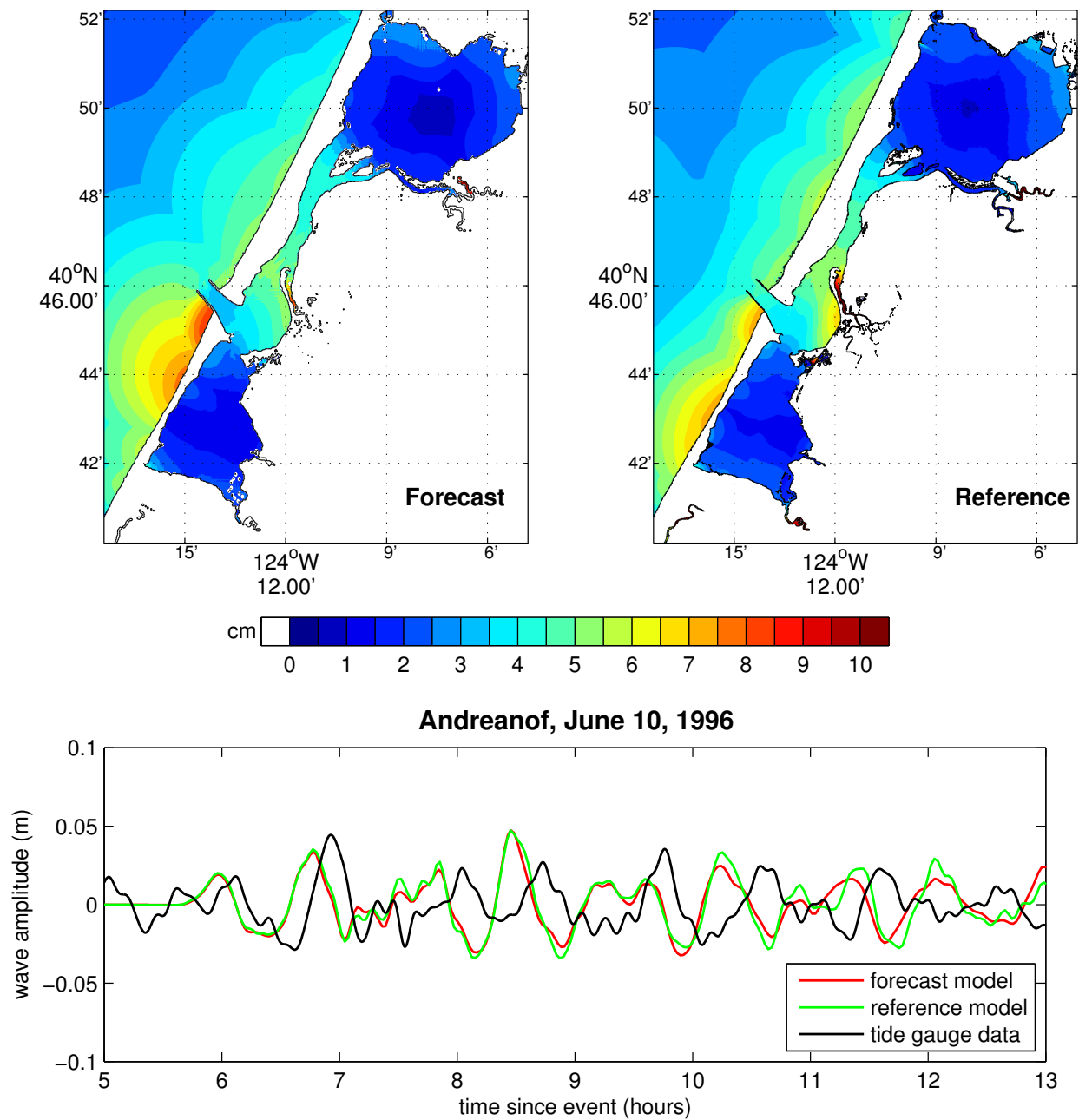
Figure 2.12: Model results for the 1996 Andreanof Mw 7.9 event. The upper two panels show, respectively, the forecast and reference model maximum wave height predictions. The lower panel shows the forecast model (red) and reference model (green) wave amplitudes at the Shemya tide gauge.
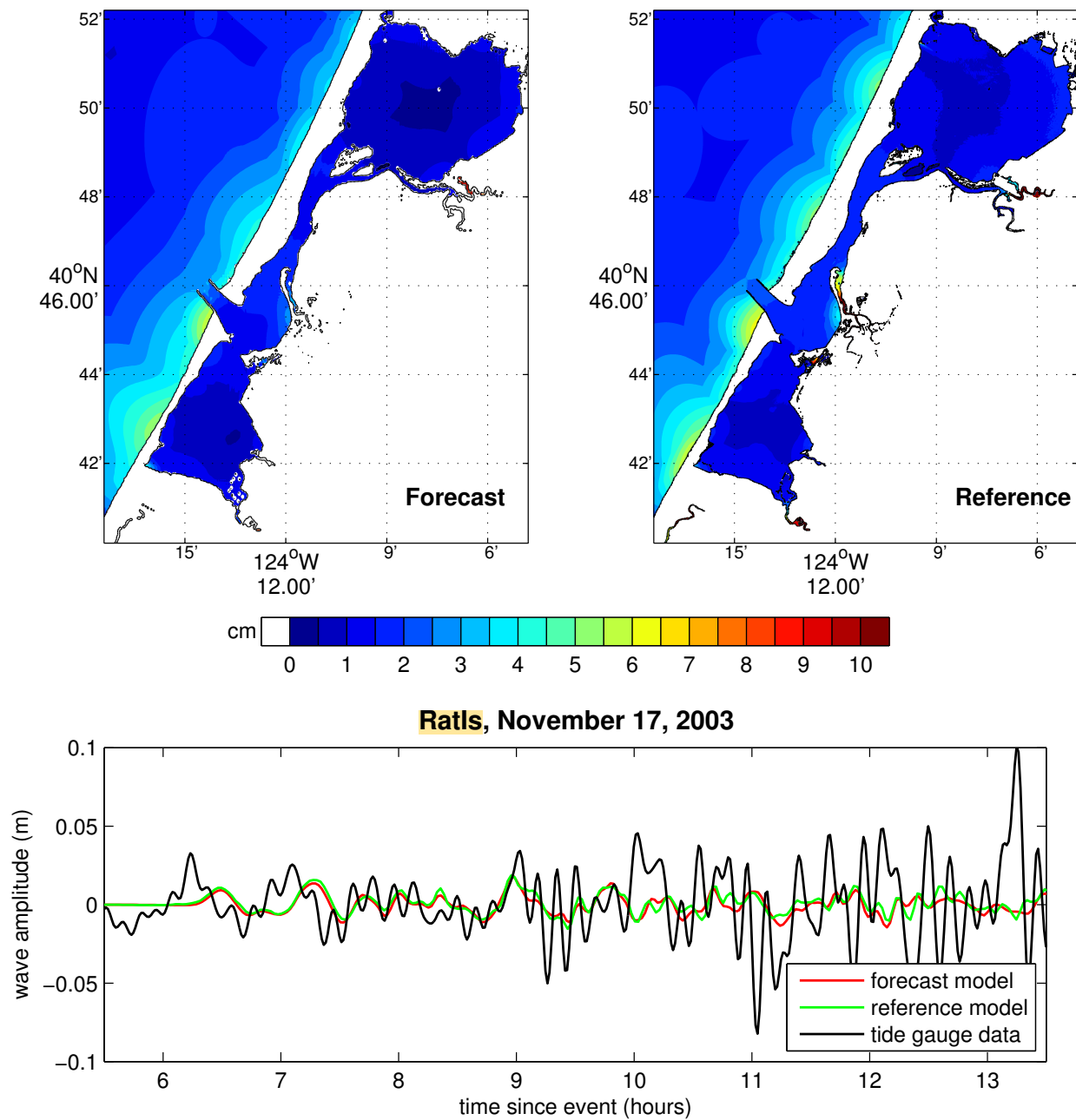
Figure 2.13: Model results for the 2003 Rat Island M_w 7.7 event. The upper two panels show, respectively, the forecast and reference model maximum wave height predictions. The lower panel shows the forecast model (red) and reference model (green) wave amplitudes at the Shemya tide gauge.
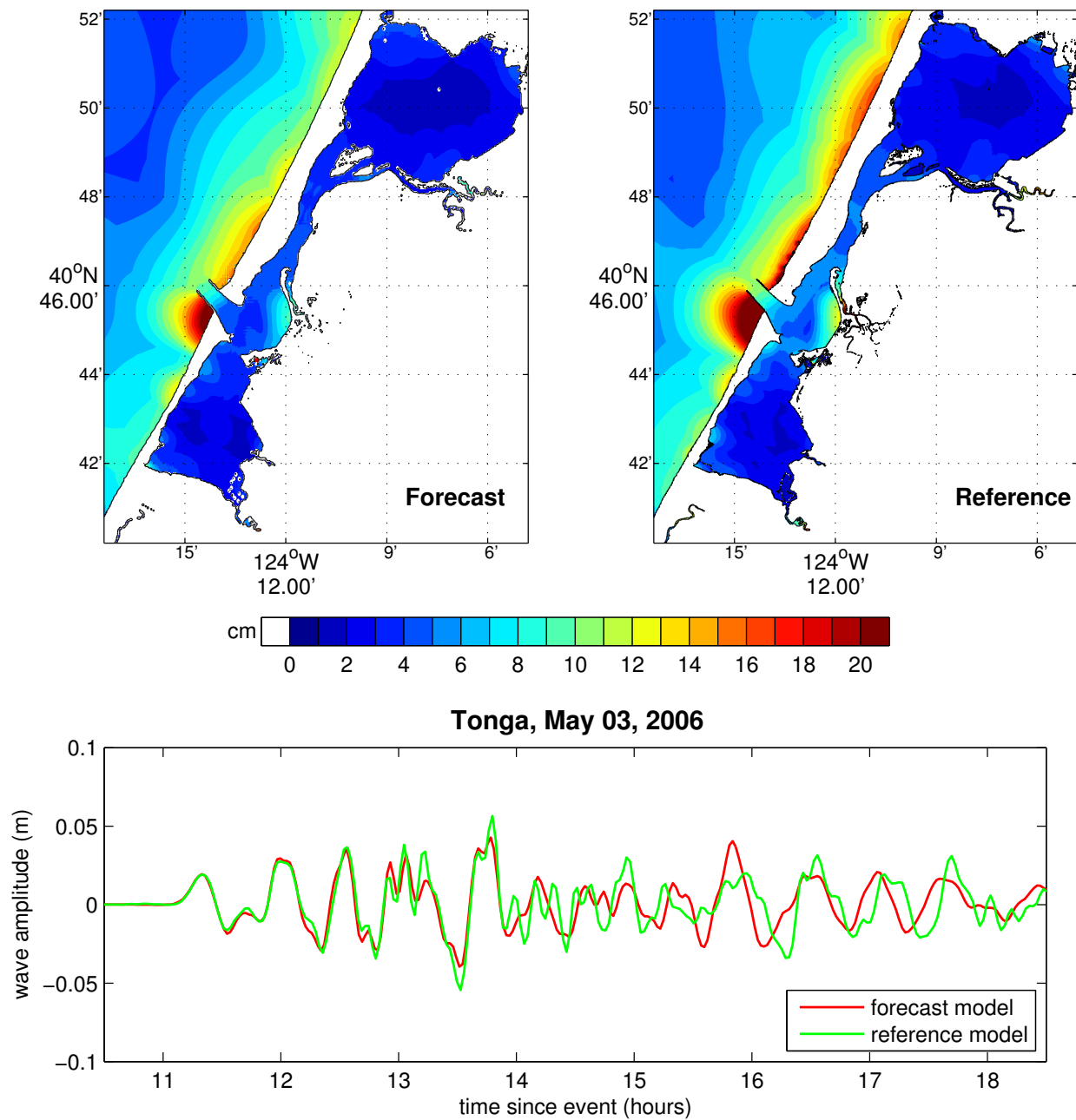
Figure 2.14: Model results for the 2006 Tonga Mw 8.0 event. The upper two panels show, respectively, the forecast and reference model maximum wave height predictions. The lower panel shows the forecast model (red) and reference model (green) wave amplitudes at the Shemya tide gauge.
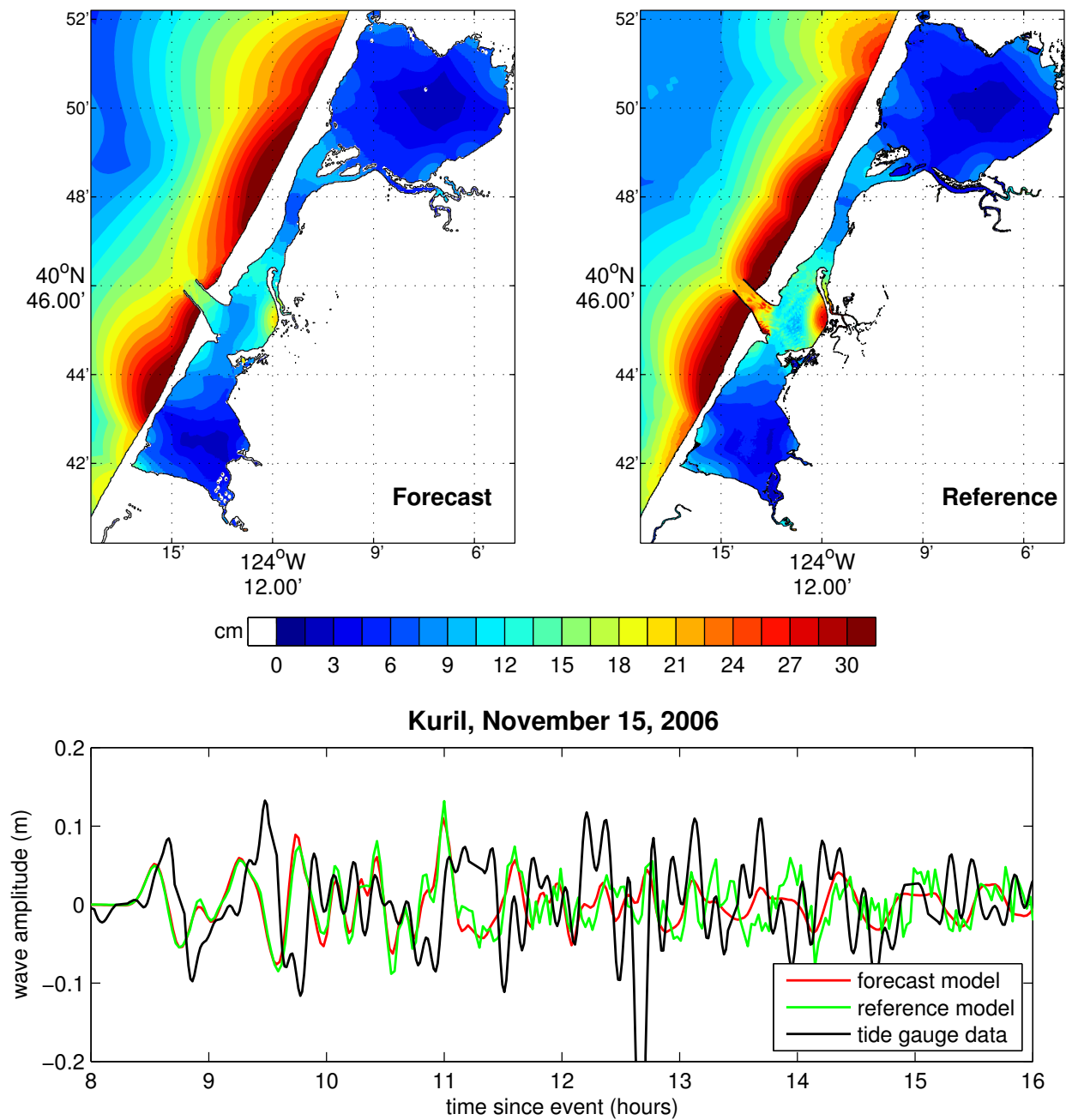
Figure 2.15: Model results for the 2006 Kuril Mw 8.3 event. The upper two panels show, respectively, the forecast and reference model maximum wave height predictions. The lower panel shows the forecast model (red) and reference model (green) wave amplitudes at the Eureka tide gauge.
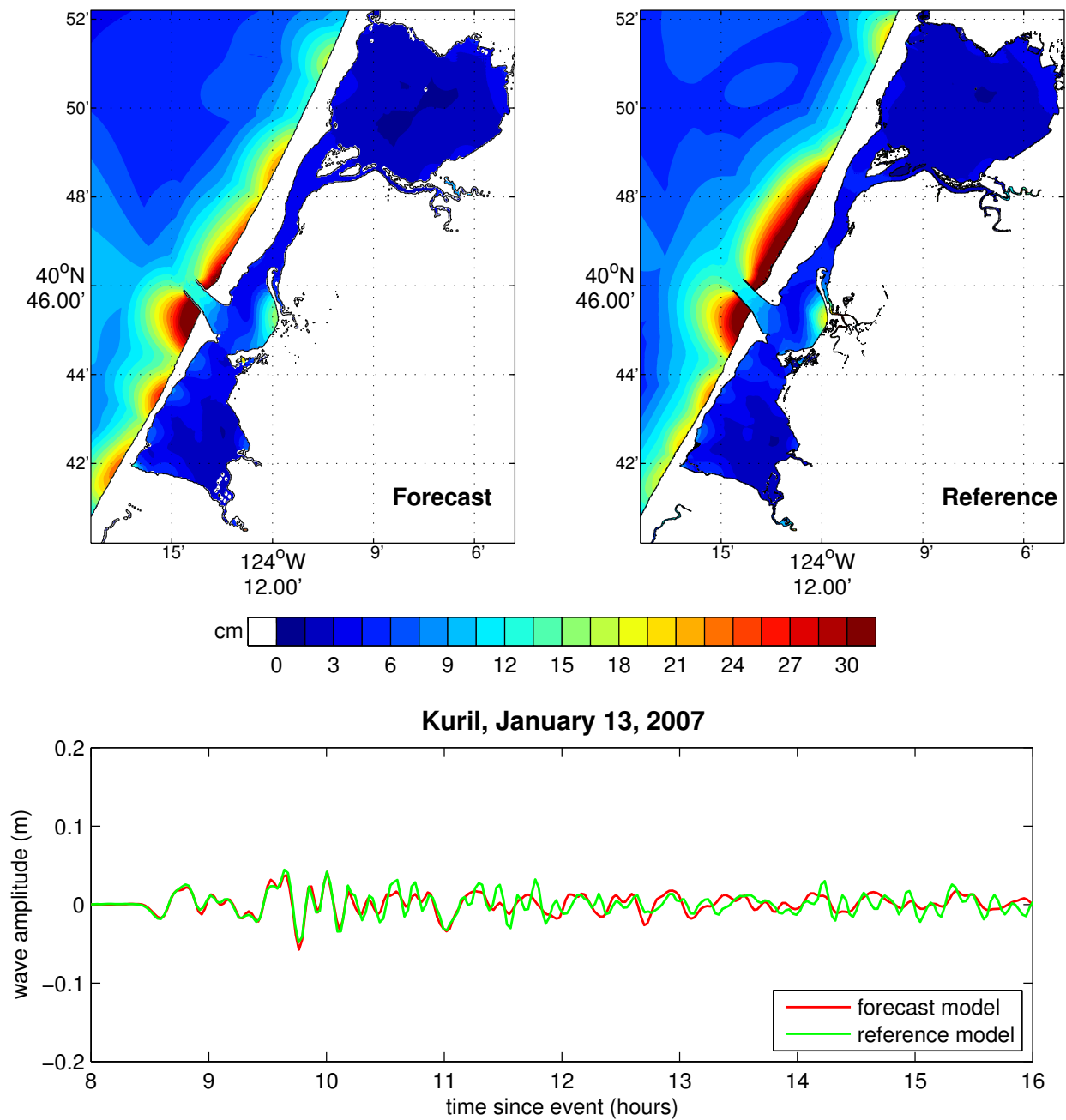
Figure 2.16: Model results for the 2007 Kuril Mw 8.1 event. The upper two panels show, respectively, the forecast and reference model maximum wave height predictions. The lower panel shows the forecast model (red) and reference model (green) wave amplitudes at the Eureka tide gauge.
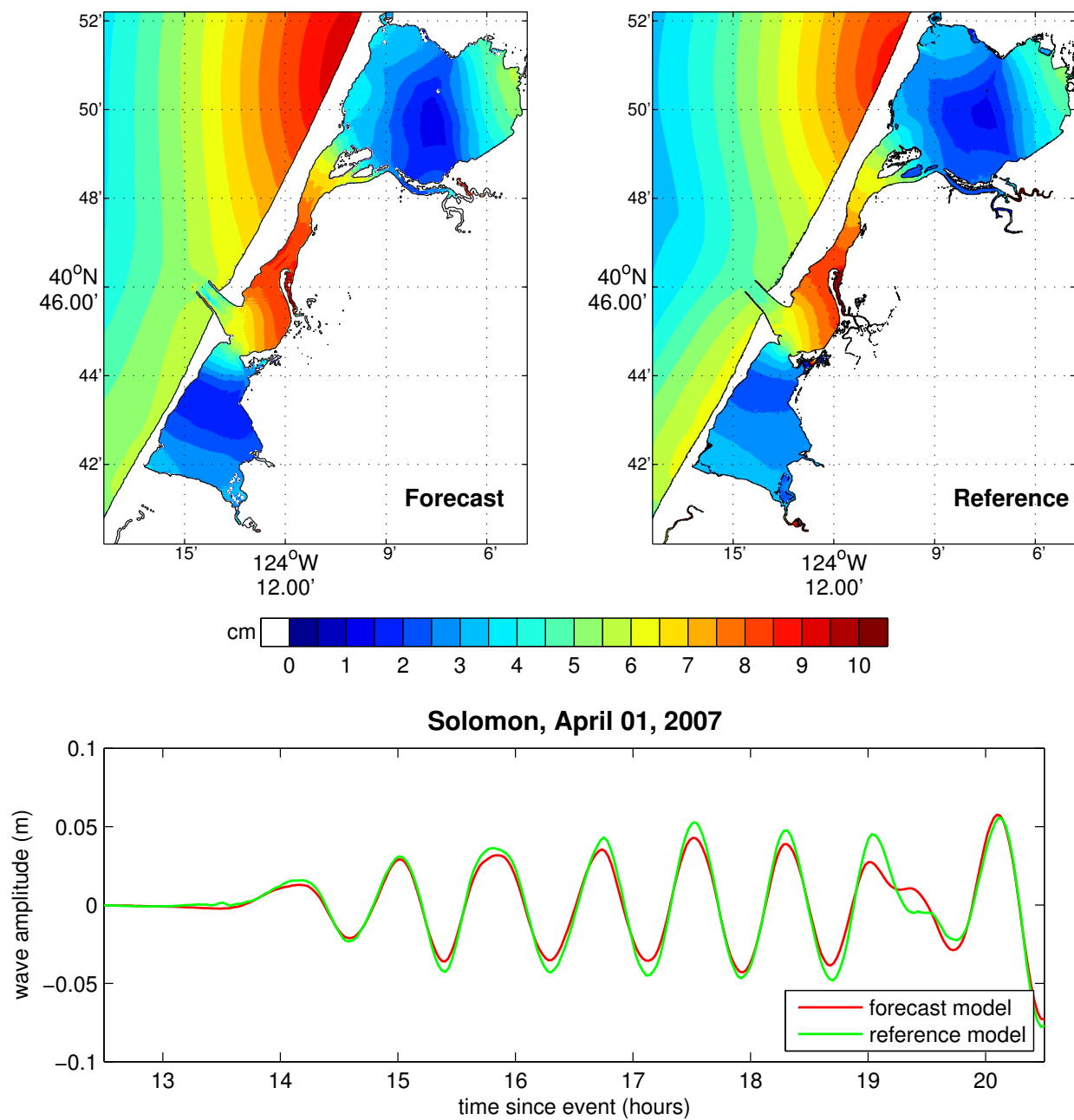
Figure 2.17: Model results for the 2007 Solomon Mw 8.1 event. The upper two panels show, respectively, the forecast and reference model maximum wave height predictions. The lower panel shows the forecast model (red) and reference model (green) wave amplitudes at the Eureka tide gauge.
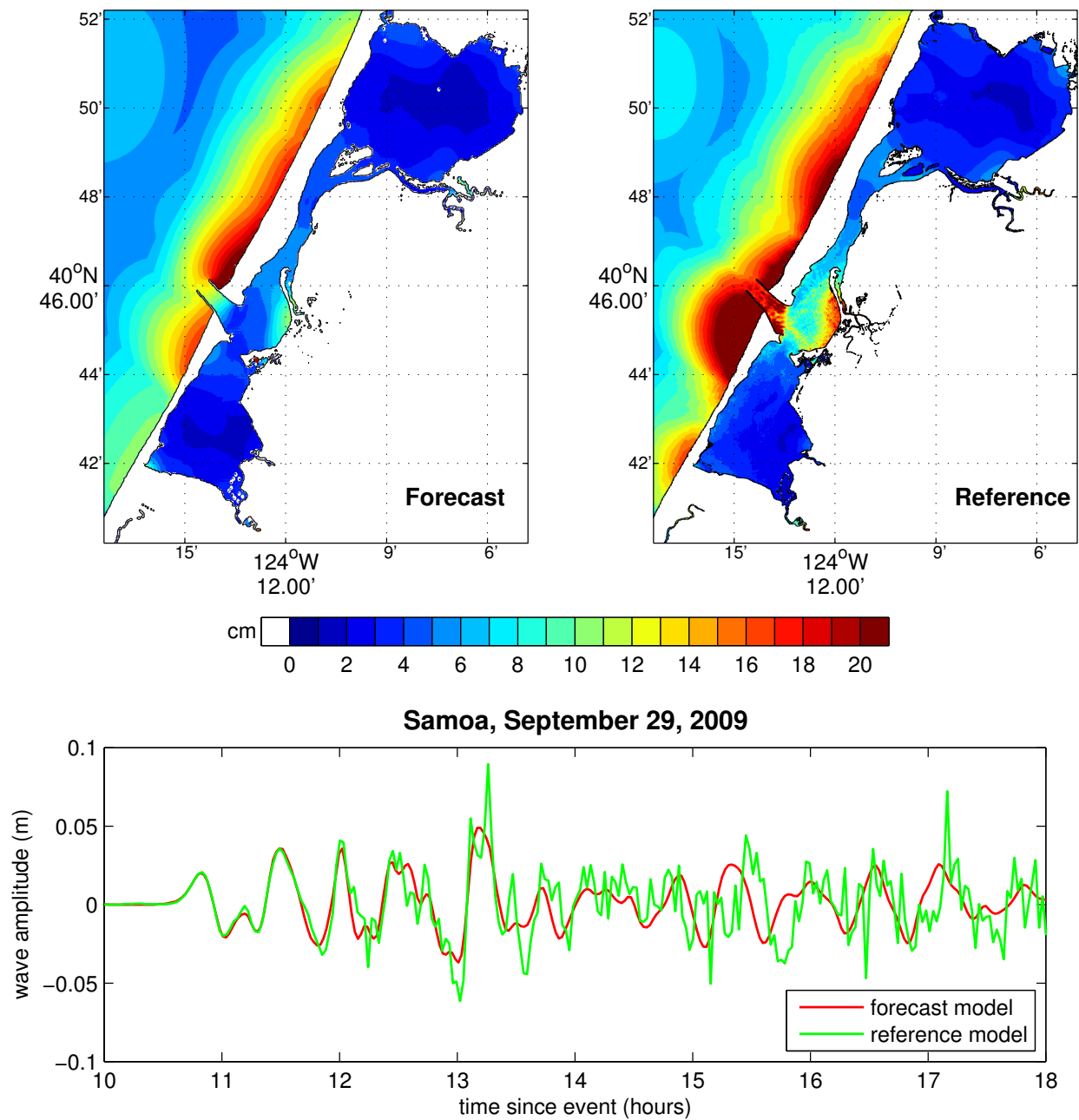
Figure 2.18: Model results for the 2009 Samoa Mw 8.0 event. The upper two panels show, respectively, the forecast and reference model maximum wave height predictions. The lower panel shows the forecast model (red) and reference model (green) wave amplitudes at the Eureka tide gauge.
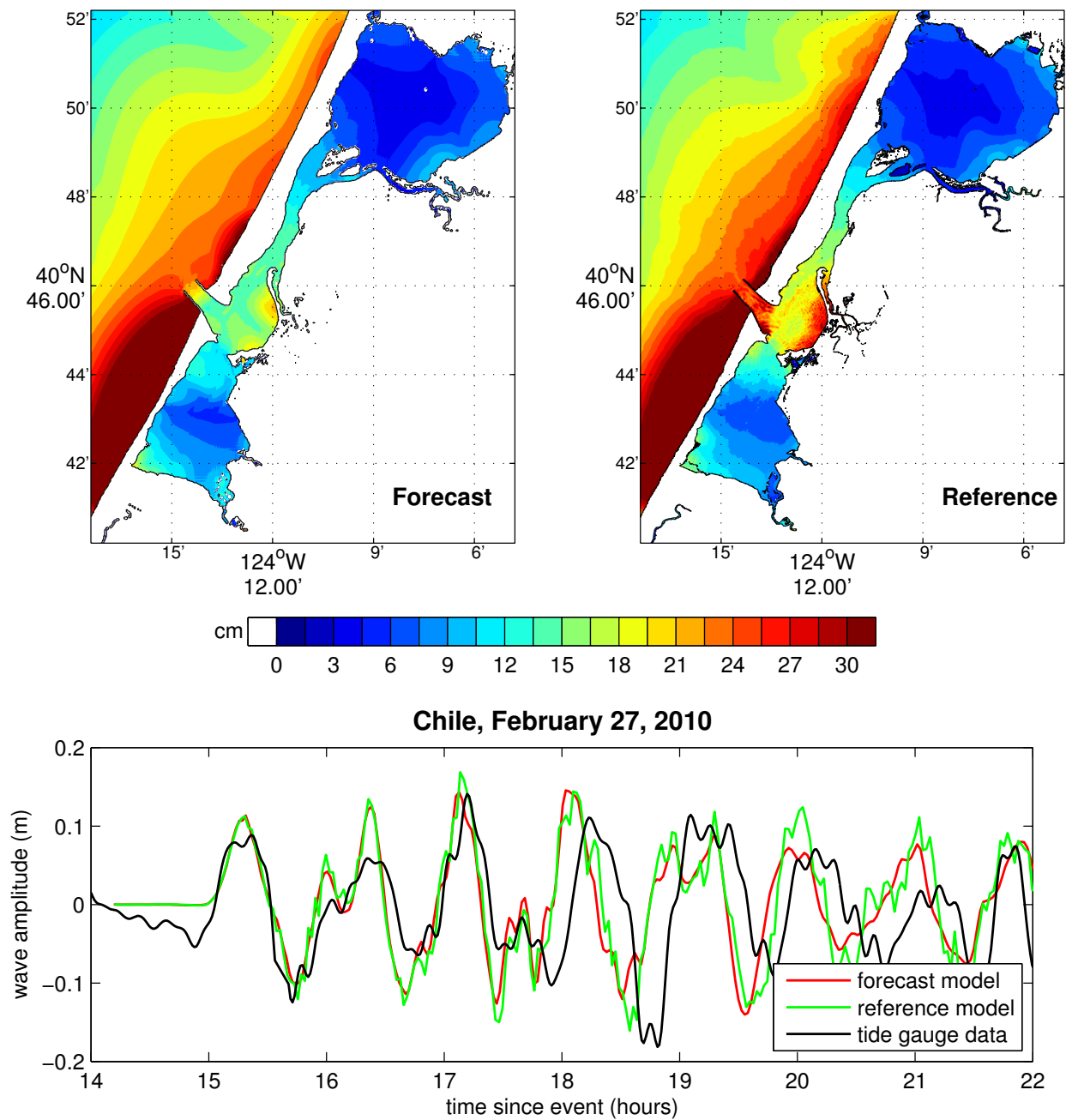
Figure 2.19: Model results for the 2010 Chile Mw 8.8 event. The upper two panels show, respectively, the forecast and reference model maximum wave height predictions. The lower panel shows the forecast model (red), reference model (green) and observed (black) wave amplitudes at the Eureka tide gauge.
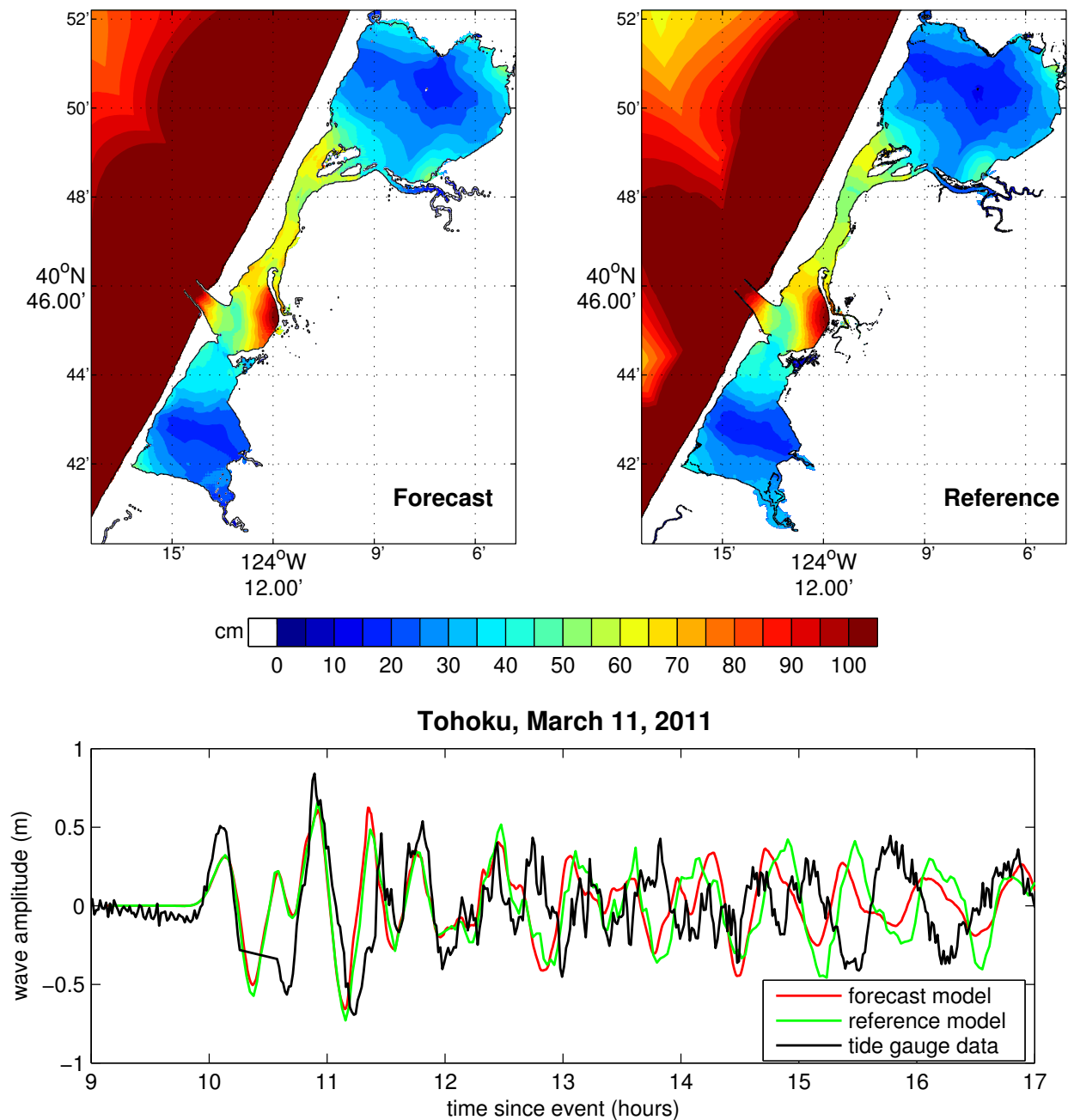
Figure 2.20: Model results for the 2011 Tohoku Mw 9.0 event. The upper two panels show, respectively, the forecast and reference model maximum wave height predictions. The lower panel shows the forecast model (red), reference model (green) and observed (black) wave amplitudes at the Eureka tide gauge.
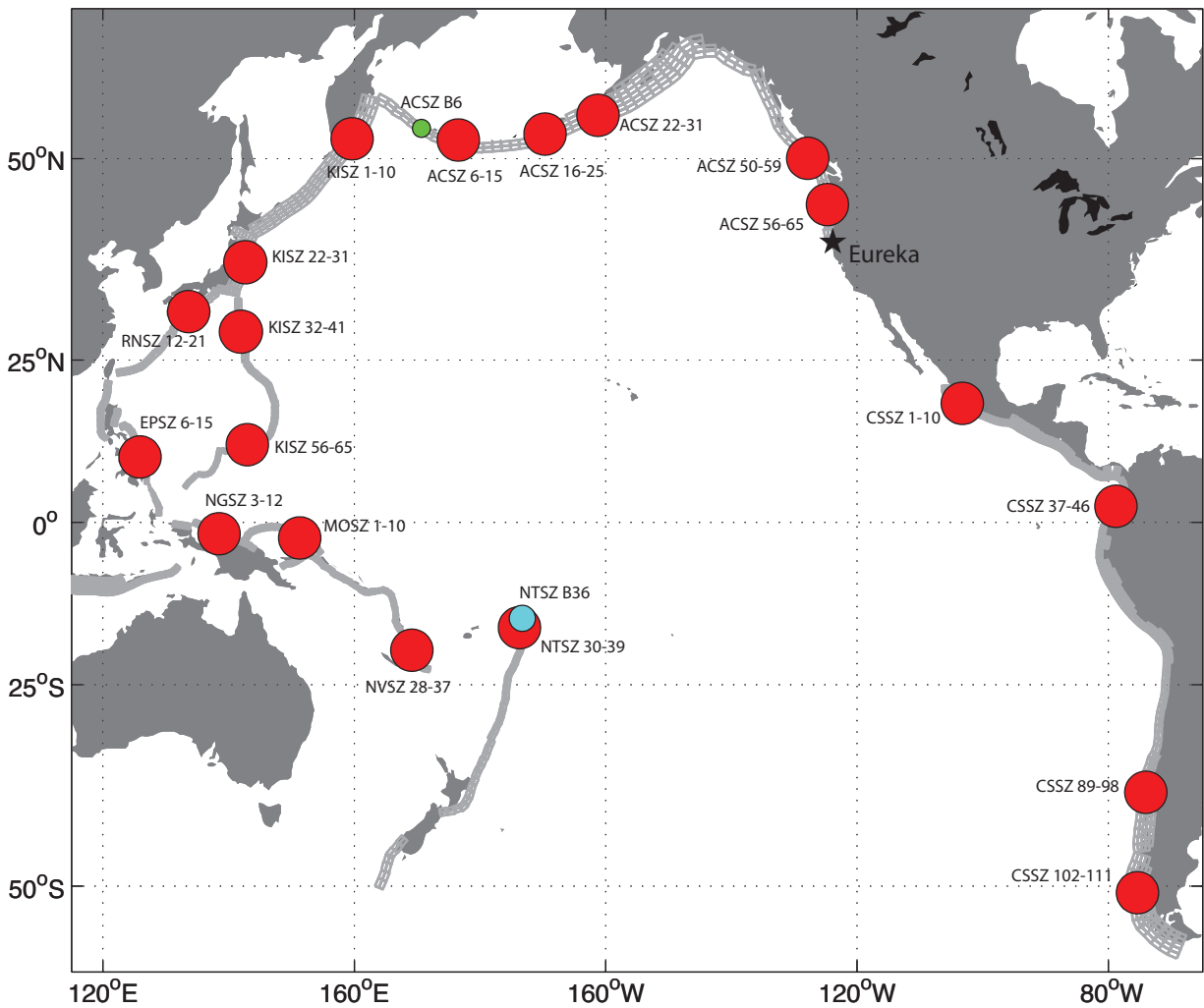
Figure 2.21: Map of the Pacific Ocean Basin showing the locations of the 19 simulated Mw 9.3 events (red circles) and the medium (Mw 7.5, blue circle) and micro event (Mw 9.3, green circle) used to test and validate the Eureka model. The solid star denotes the location of Eureka.
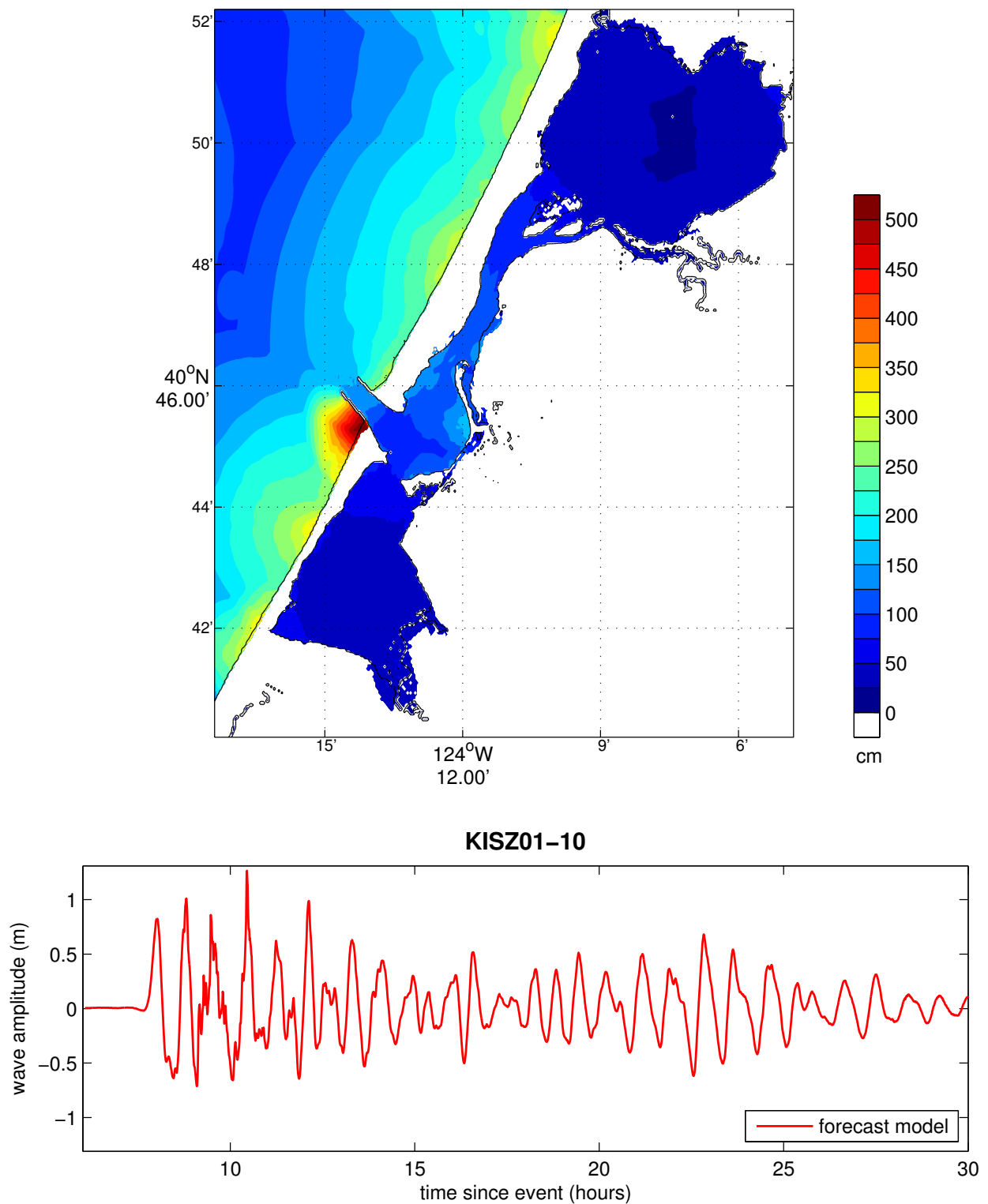
Figure 2.22: Results from the forecast model for the KISZ 1-10 synthetic event. The upper panel shows the map of predicted maximum wave height in the Eureka C-grid and the lower panel shows the time series of wave amplitude at the tide gauge location.
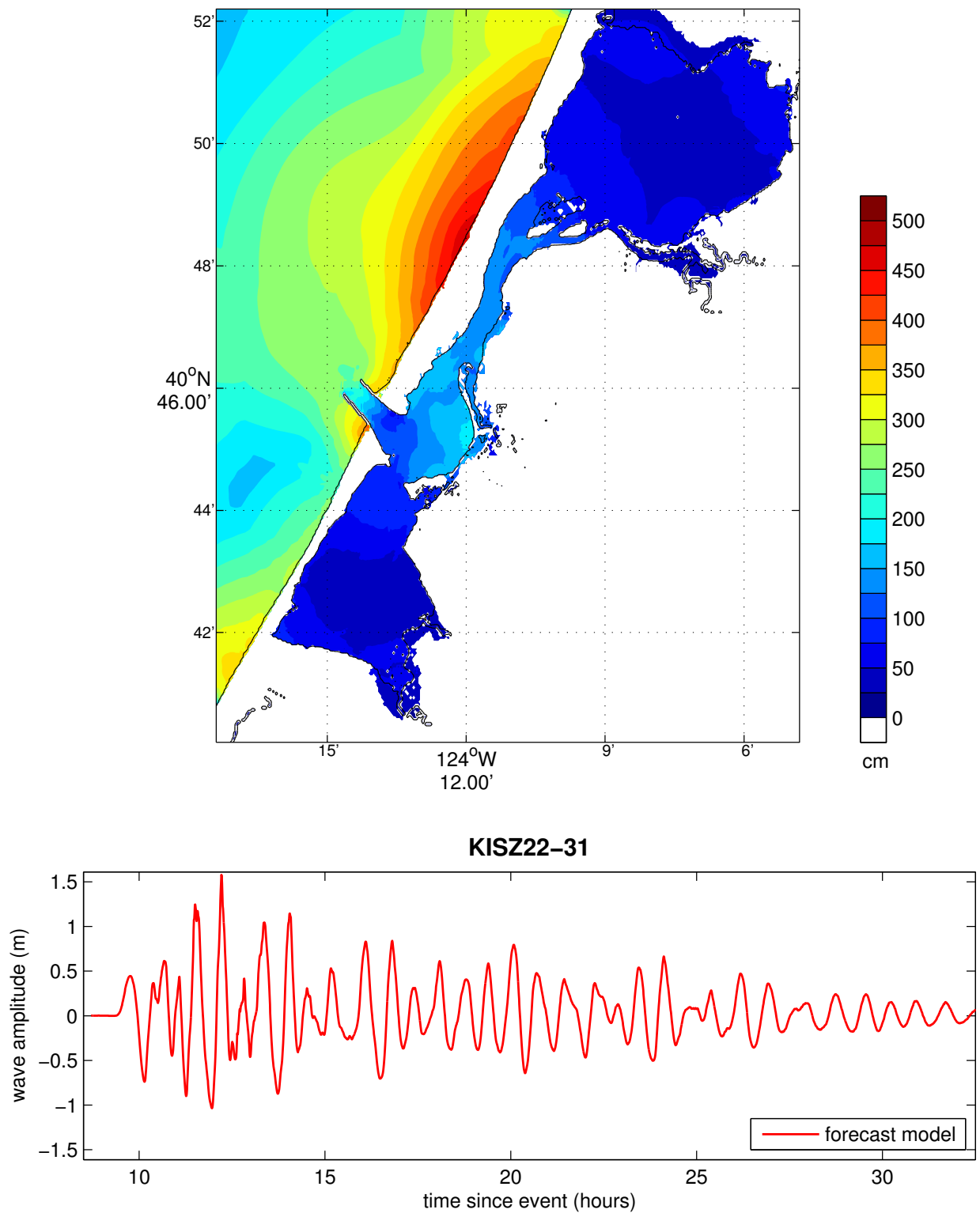
Figure 2.23: Results from the forecast model for the KISZ 22-31 synthetic event. The upper panel shows the map of predicted maximum wave height in the Eureka C-grid and the lower panel shows the time series of wave amplitude at the tide gauge location.
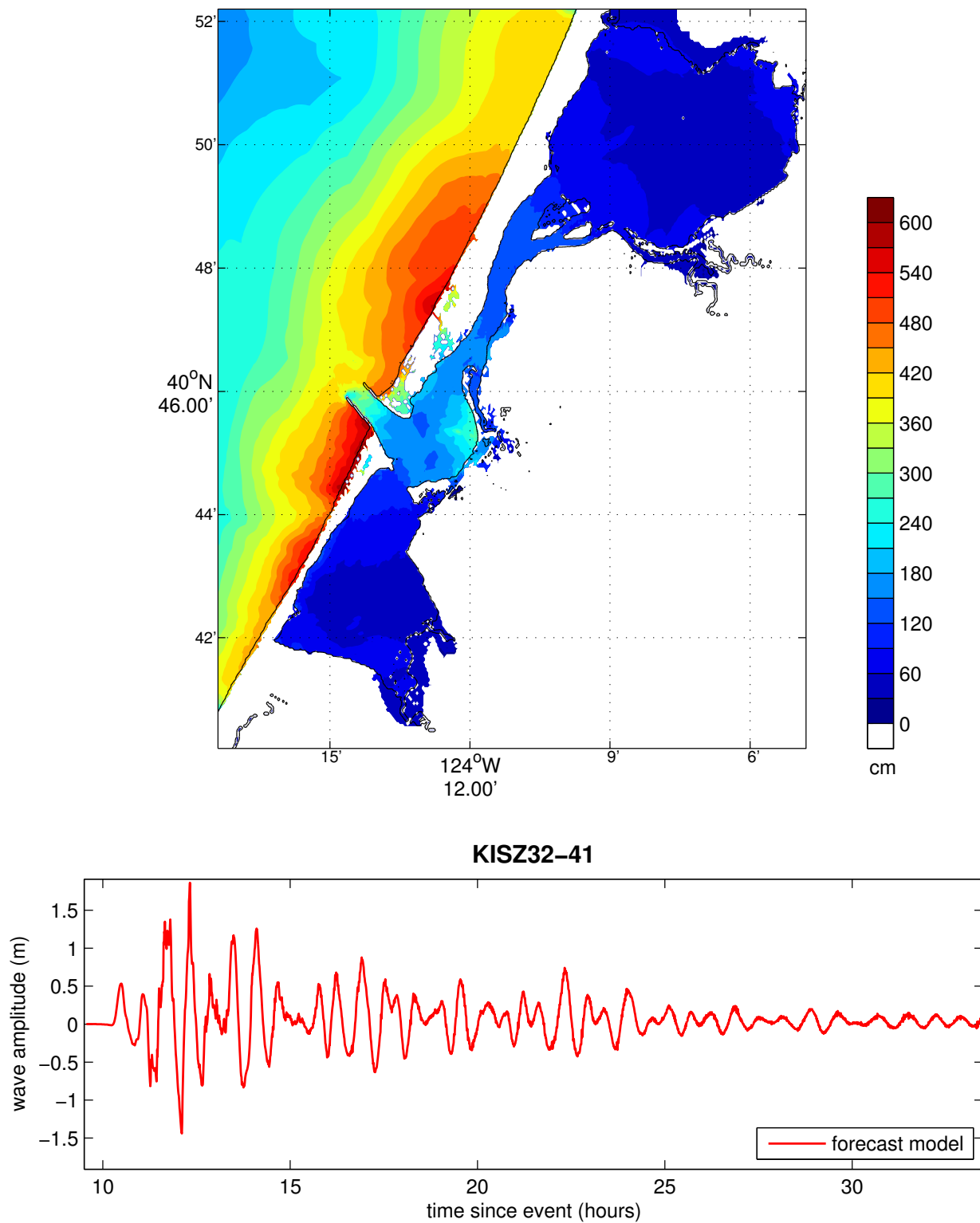
Figure 2.24: Results from the forecast model for the KISZ 32-41 synthetic event. The upper panel shows the map of predicted maximum wave height in the Eureka C-grid and the lower panel shows the time series of wave amplitude at the tide gauge location.
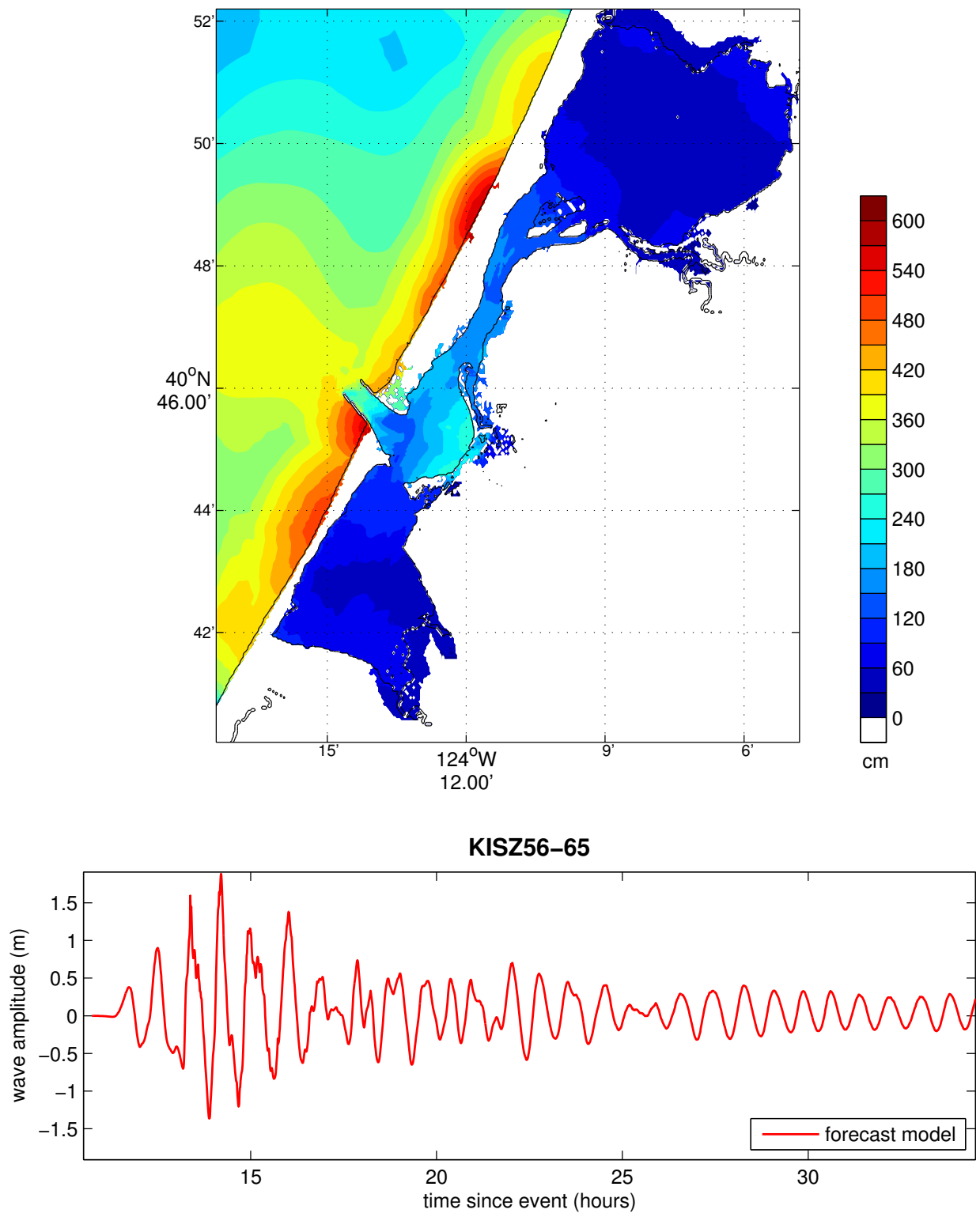
Figure 2.25: Results from the forecast model for the KISZ 56-65 synthetic event. The upper panel shows the map of predicted maximum wave height in the Eureka C-grid and the lower panel shows the time series of wave amplitude at the tide gauge location.
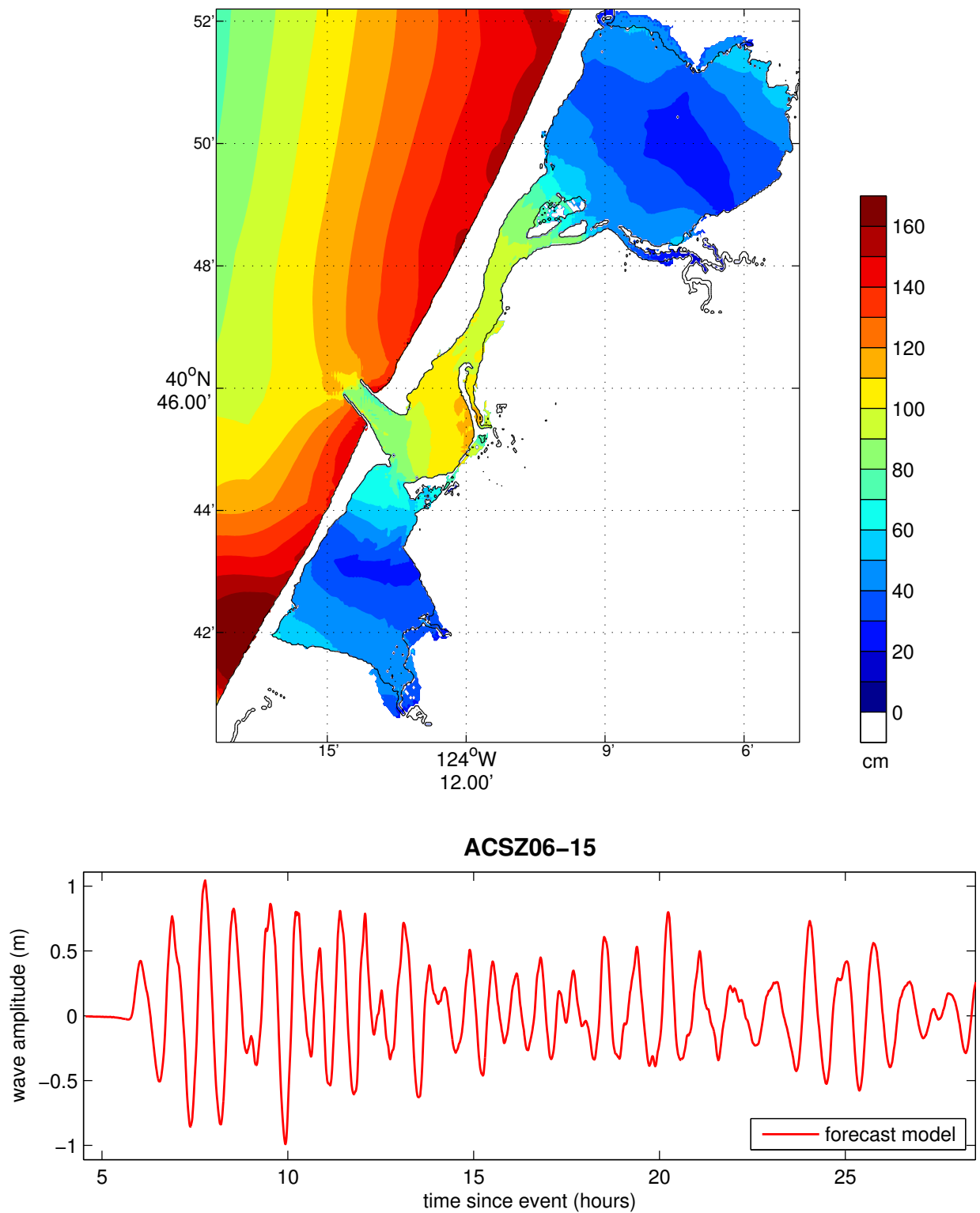
Figure 2.26: Results from the forecast model for the ACSZ 6-15 synthetic event. The upper panel shows the map of predicted maximum wave height in the Eureka C-grid and the lower panel shows the time series of wave amplitude at the tide gauge location.
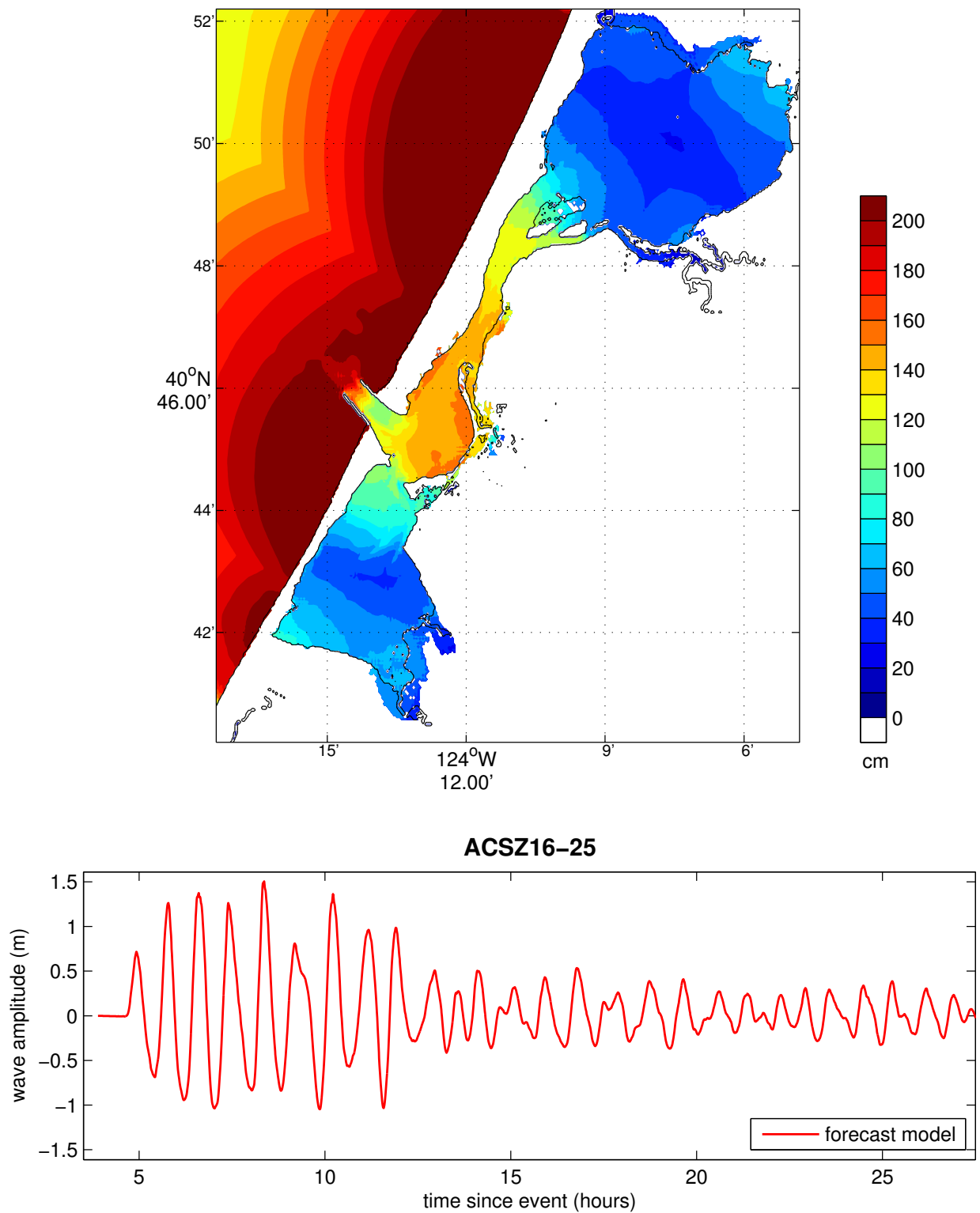
Figure 2.27: Results from the forecast model for the ACSZ 16-25 synthetic event. The upper panel shows the map of predicted maximum wave height in the Eureka C-grid and the lower panel shows the time series of wave amplitude at the tide gauge location.
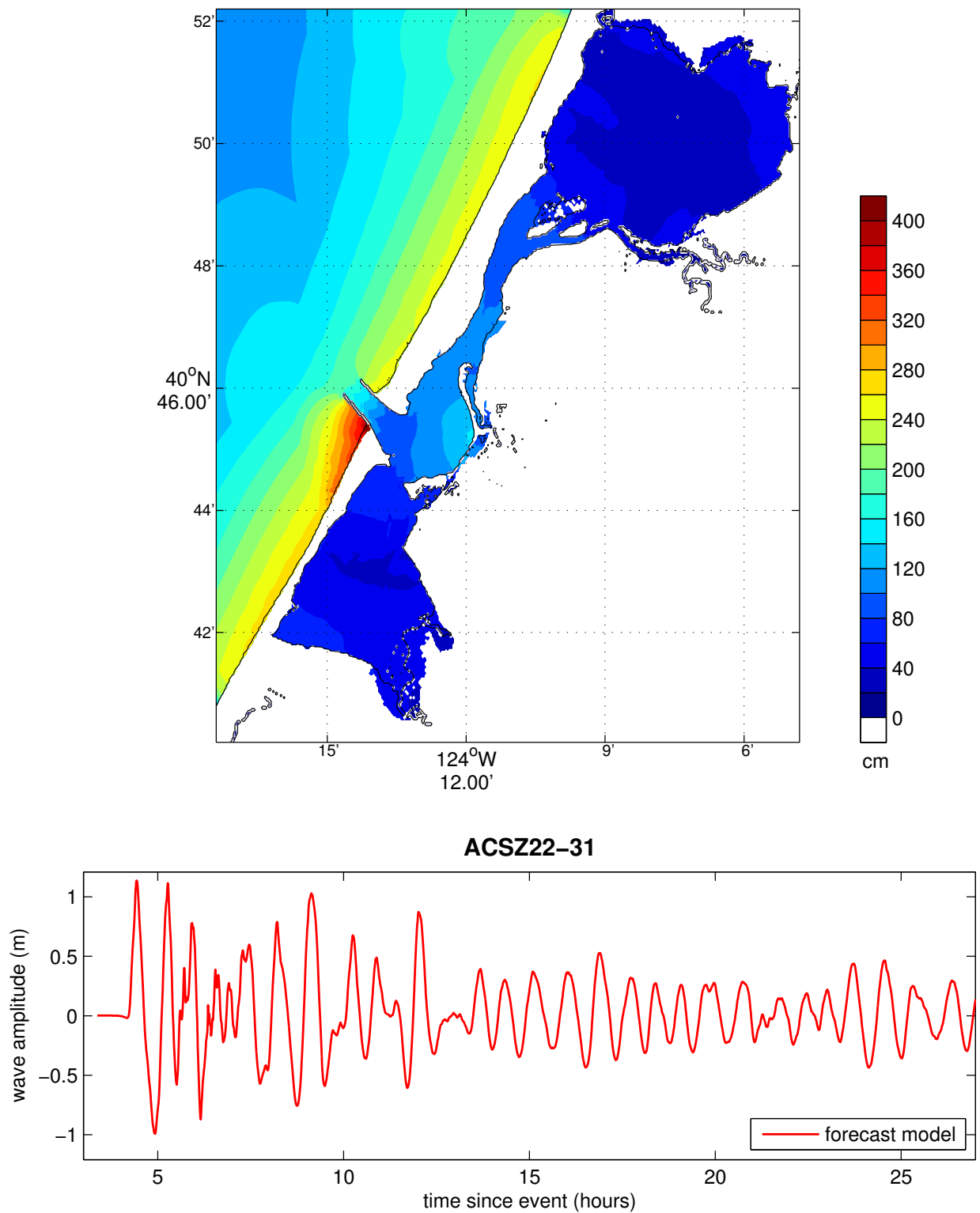
Figure 2.28: Results from the forecast model for the ACSZ 22-31 synthetic event. The upper panel shows the map of predicted maximum wave height in the Eureka C-grid and the lower panel shows the time series of wave amplitude at the tide gauge location.
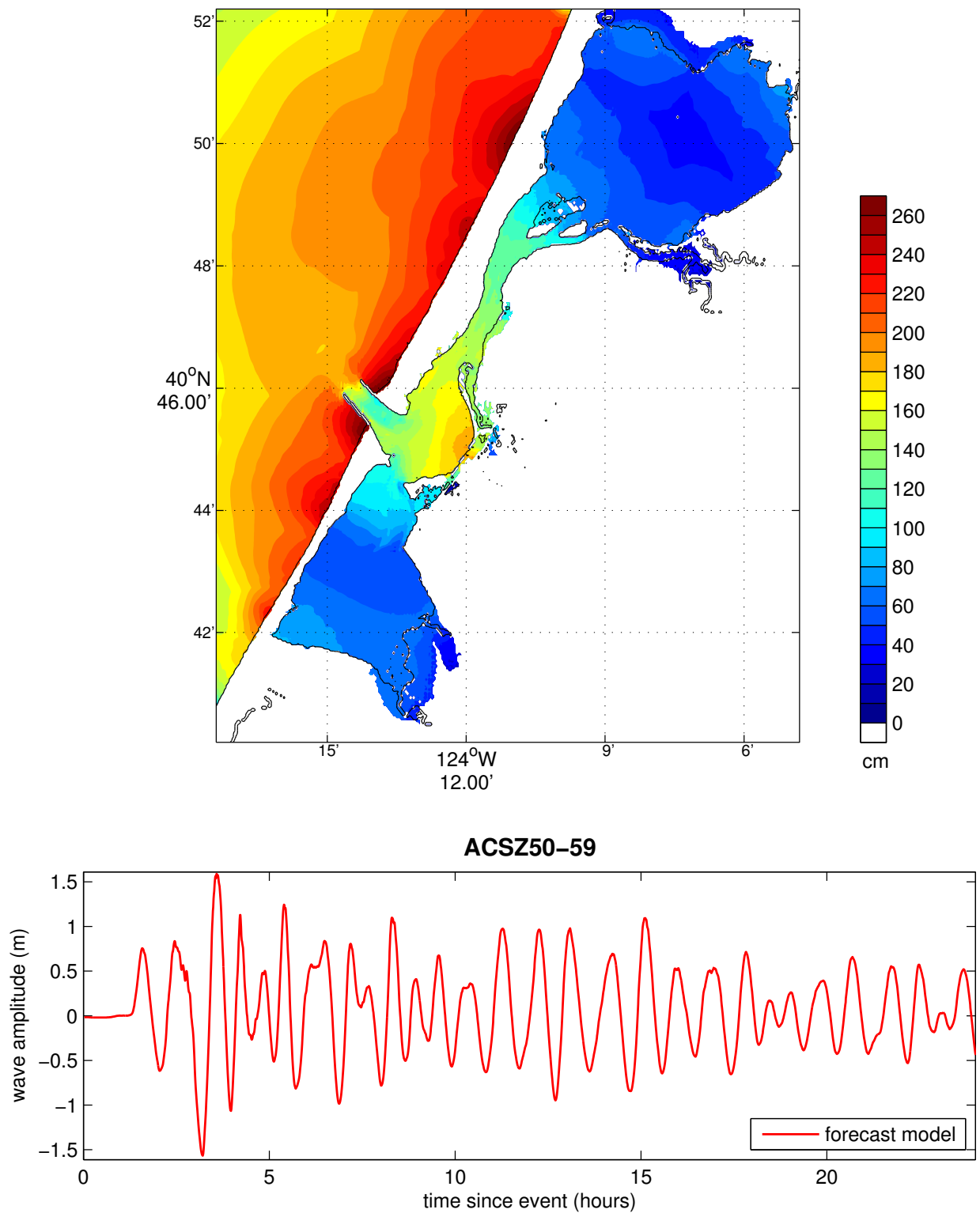
Figure 2.29: Results from the forecast model for the ACSZ 50-59 synthetic event. The upper panel shows the map of predicted maximum wave height in the Eureka C-grid and the lower panel shows the time series of wave amplitude at the tide gauge location.
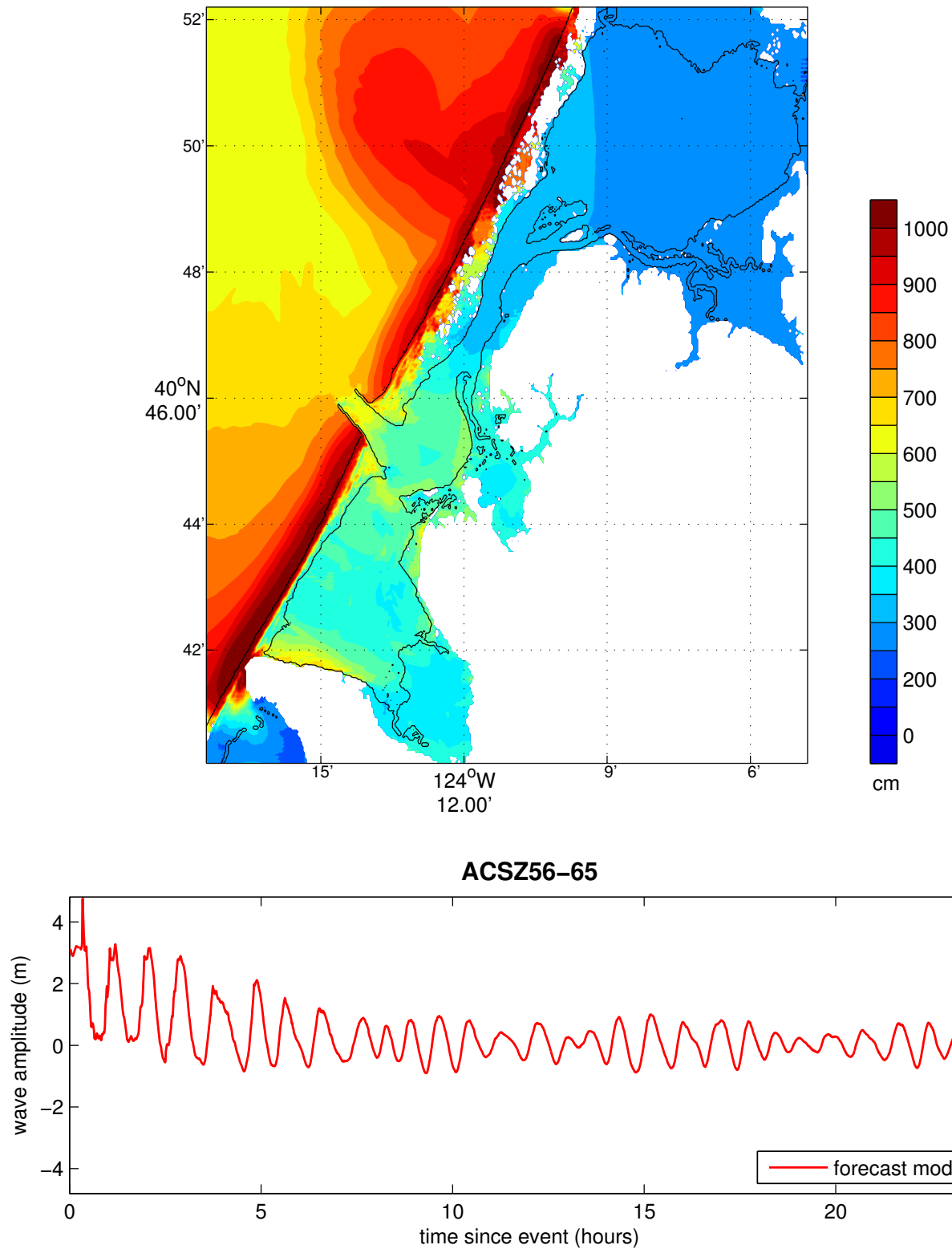
Figure 2.30: Results from the forecast model for the ACSZ 56-65 synthetic event. The upper panel shows the map of predicted maximum wave height in the Eureka C-grid and the lower panel shows the time series of wave amplitude at the tide gauge location.
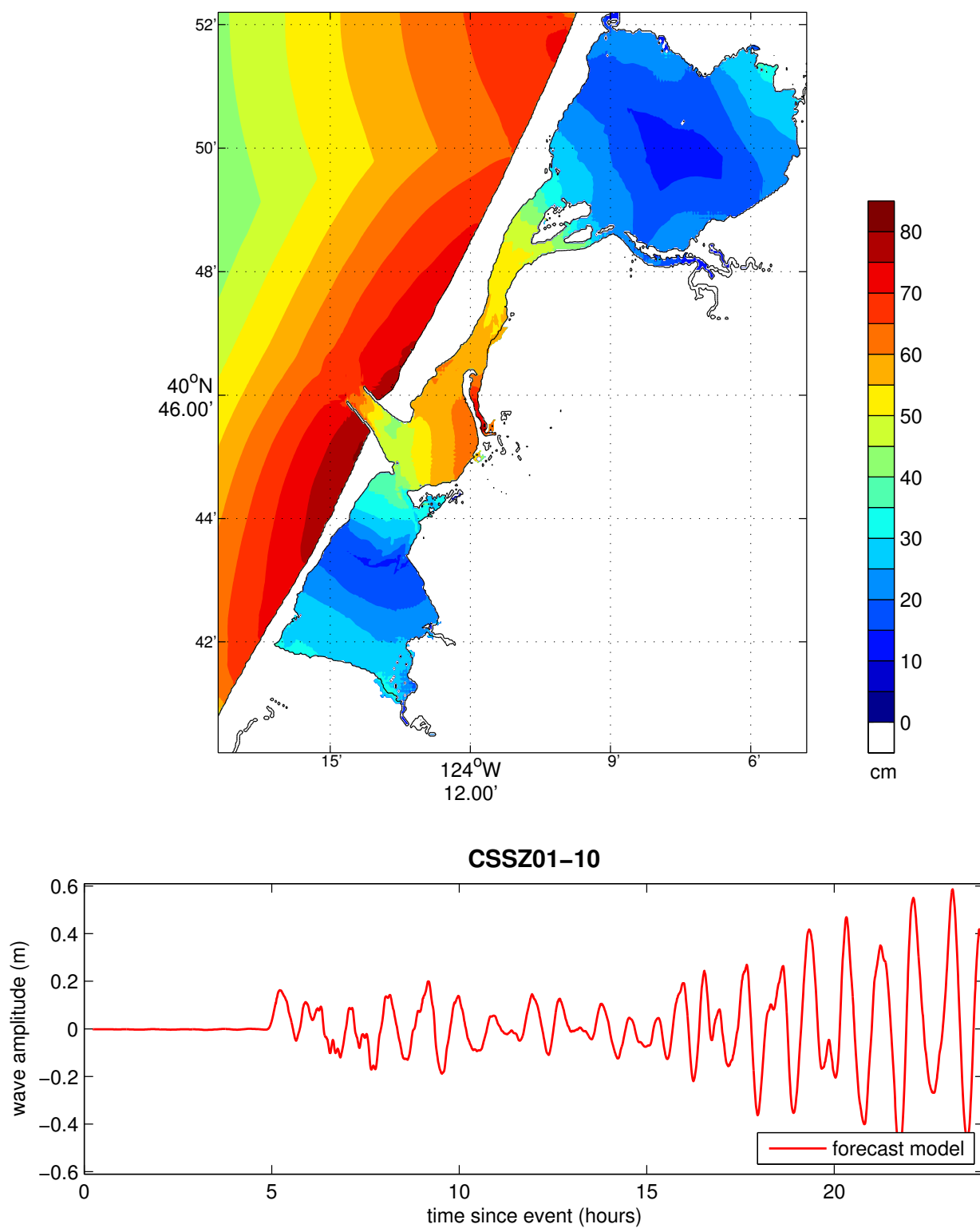
Figure 2.31: Results from the forecast model for the CSSZ 1-10 synthetic event. The upper panel shows the map of predicted maximum wave height in the Eureka C-grid and the lower panel shows the time series of wave amplitude at the tide gauge location.
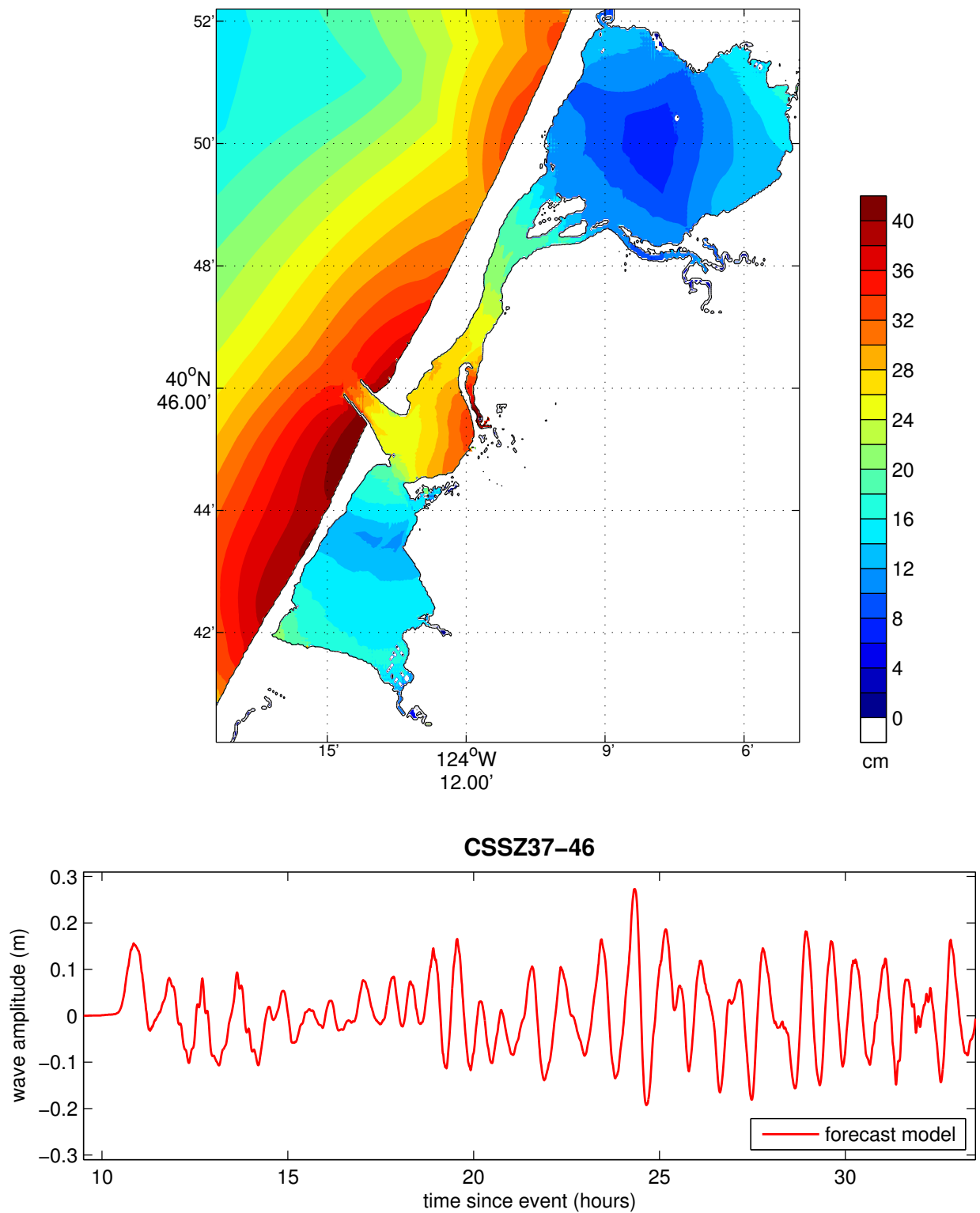
Figure 2.32: Results from the forecast model for the CSSZ 37-46 synthetic event. The upper panel shows the map of predicted maximum wave height in the Eureka C-grid and the lower panel shows the time series of wave amplitude at the tide gauge location.
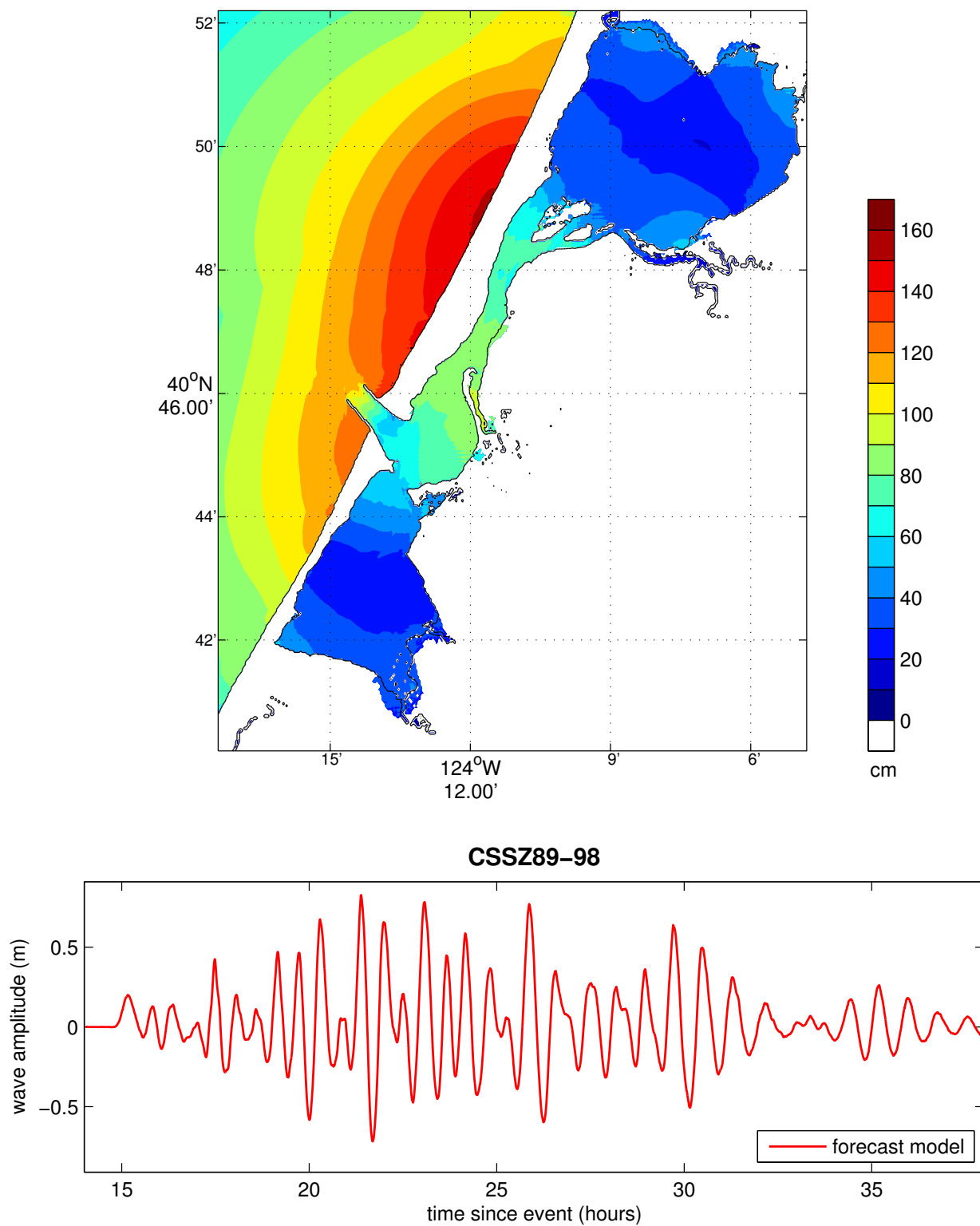
Figure 2.33: Results from the forecast model for the CSSZ 89-98 synthetic event. The upper panel shows the map of predicted maximum wave height in the Eureka C-grid and the lower panel shows the time series of wave amplitude at the tide gauge location.
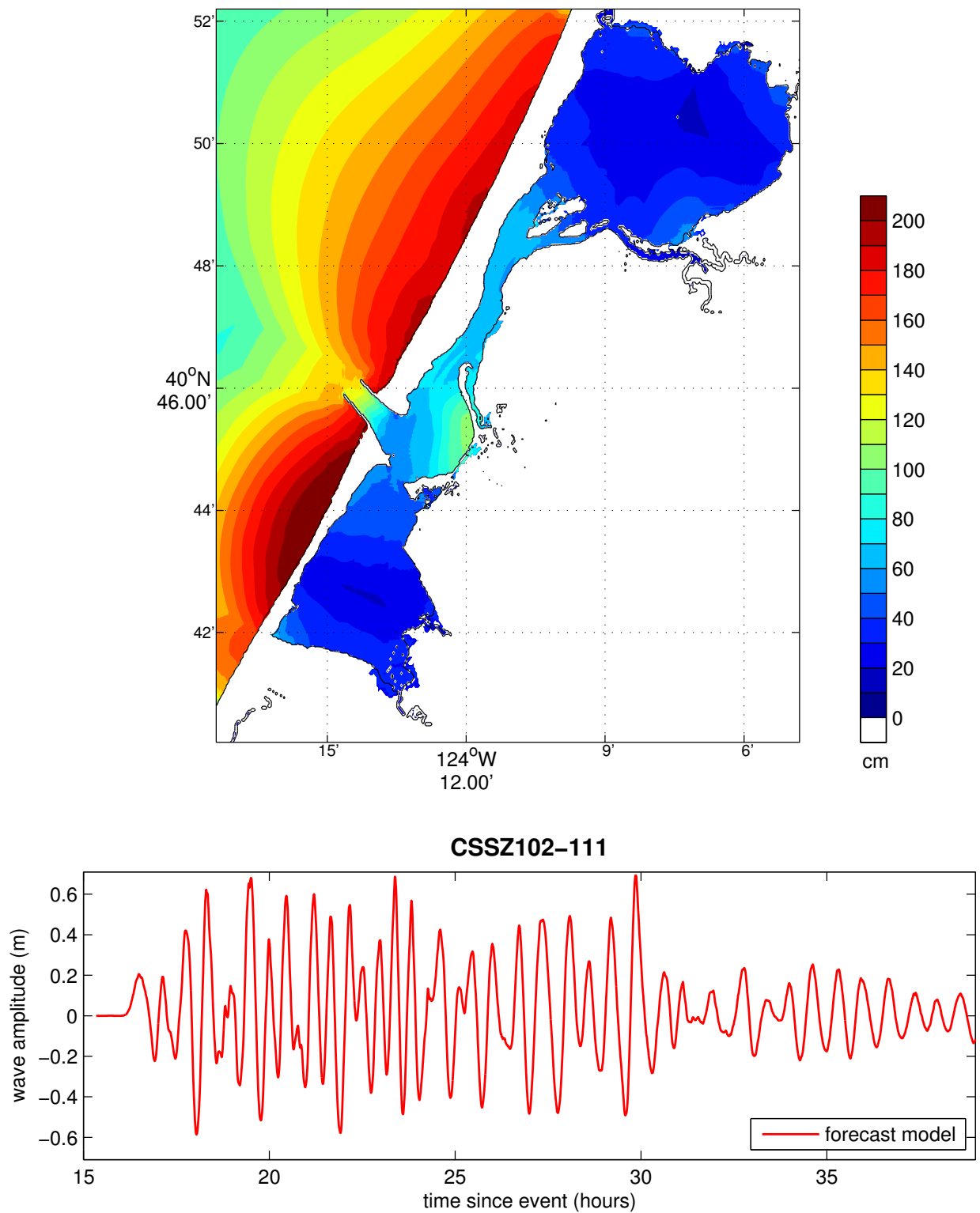
Figure 2.34: Results from the forecast model for the CSSZ 102-111 synthetic event. The upper panel shows the map of predicted maximum wave height in the Eureka C-grid and the lower panel shows the time series of wave amplitude at the tide gauge location.
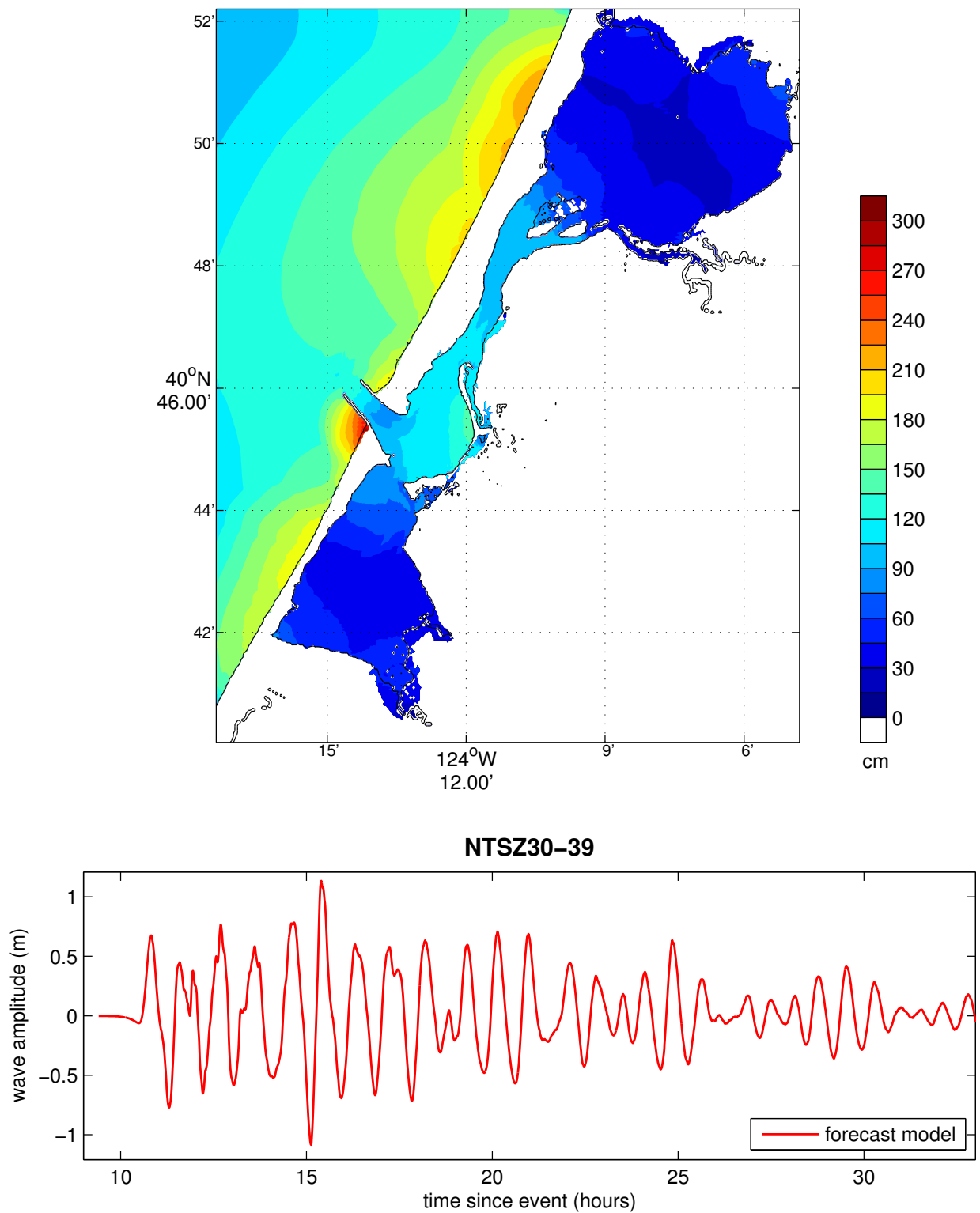
Figure 2.35: Results from the forecast model for the NTSZ 30-39 synthetic event. The upper panel shows the map of predicted maximum wave height in the Eureka C-grid and the lower panel shows the time series of wave amplitude at the tide gauge location.
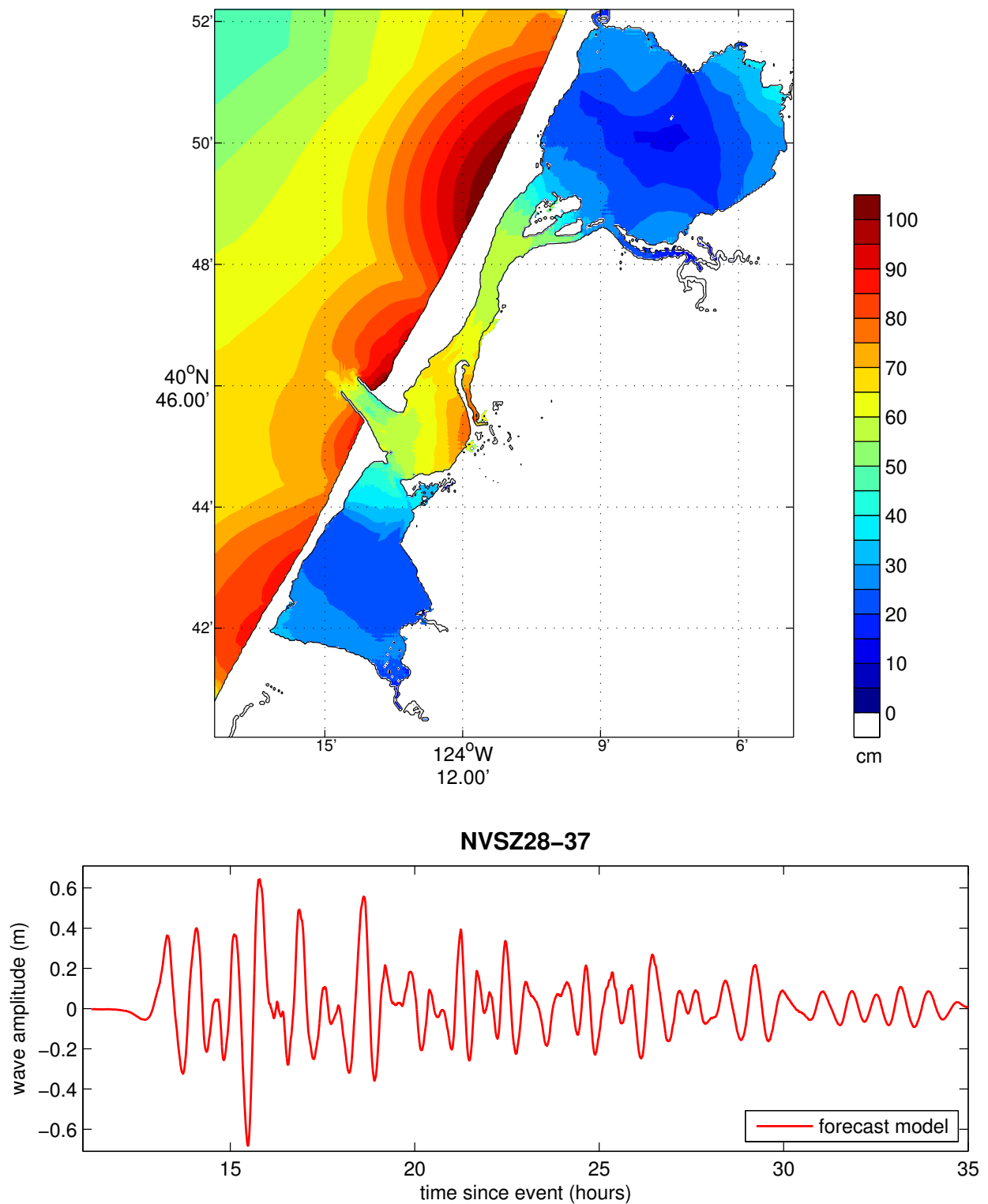
Figure 2.36: Results from the forecast model for the NVSZ 28-37 synthetic event. The upper panel shows the map of predicted maximum wave height in the Eureka C-grid and the lower panel shows the time series of wave amplitude at the tide gauge location.
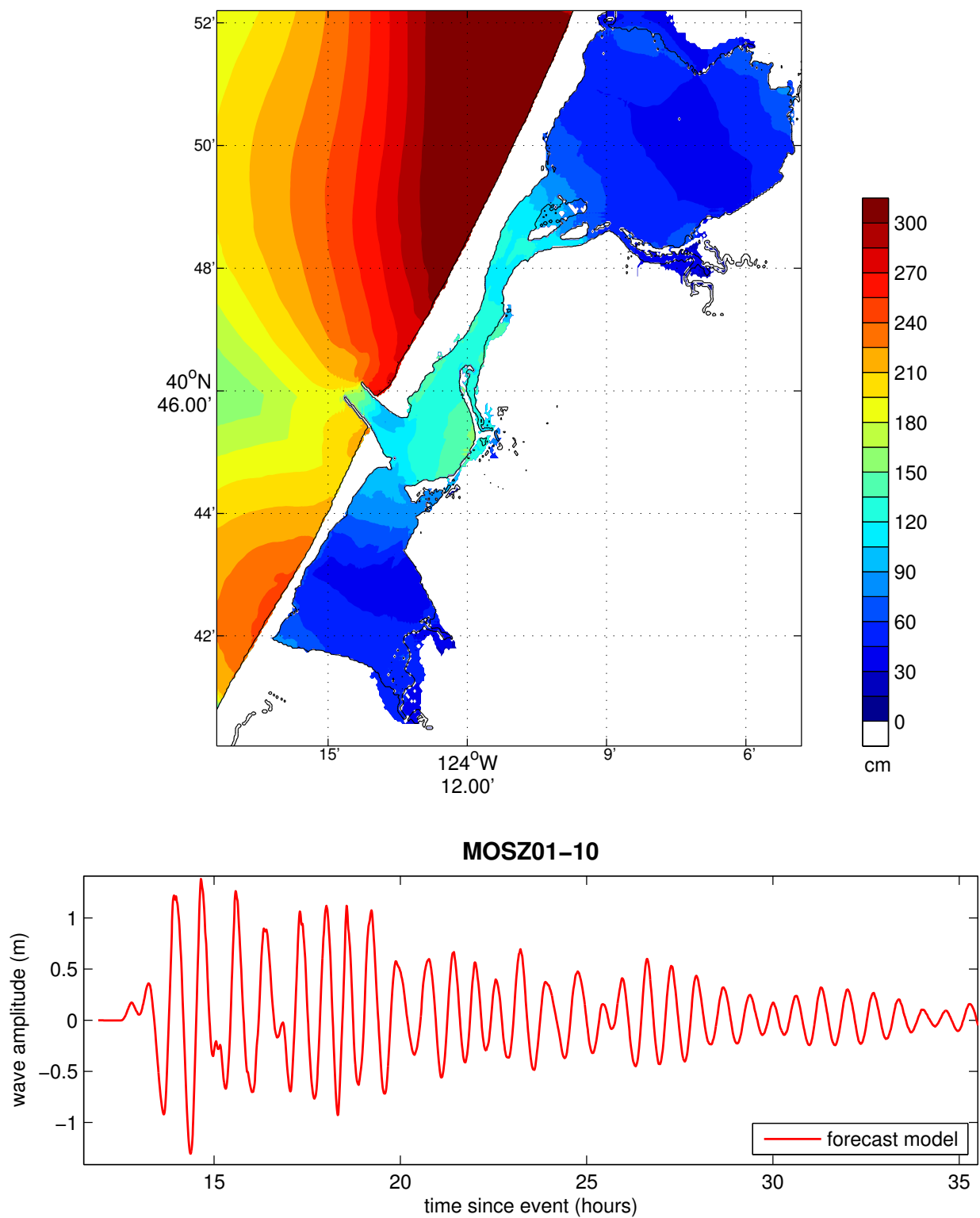
Figure 2.37: Results from the forecast model for the MOSZ 1-10 synthetic event. The upper panel shows the map of predicted maximum wave height in the Eureka C-grid and the lower panel shows the time series of wave amplitude at the tide gauge location.
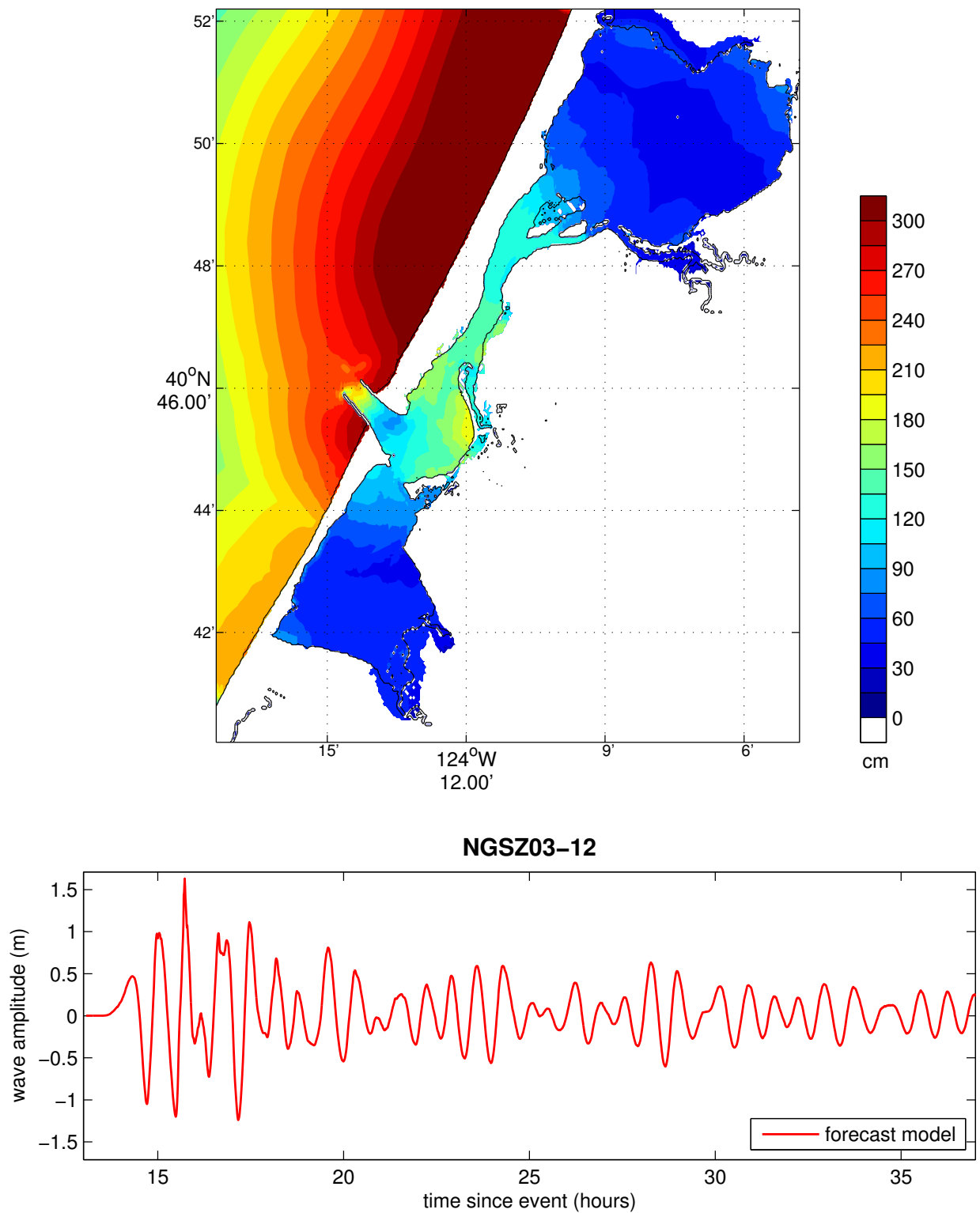
Figure 2.38: Results from the forecast model for the NGSZ 3-12 synthetic event. The upper panel shows the map of predicted maximum wave height in the Eureka C-grid and the lower panel shows the time series of wave amplitude at the tide gauge location.
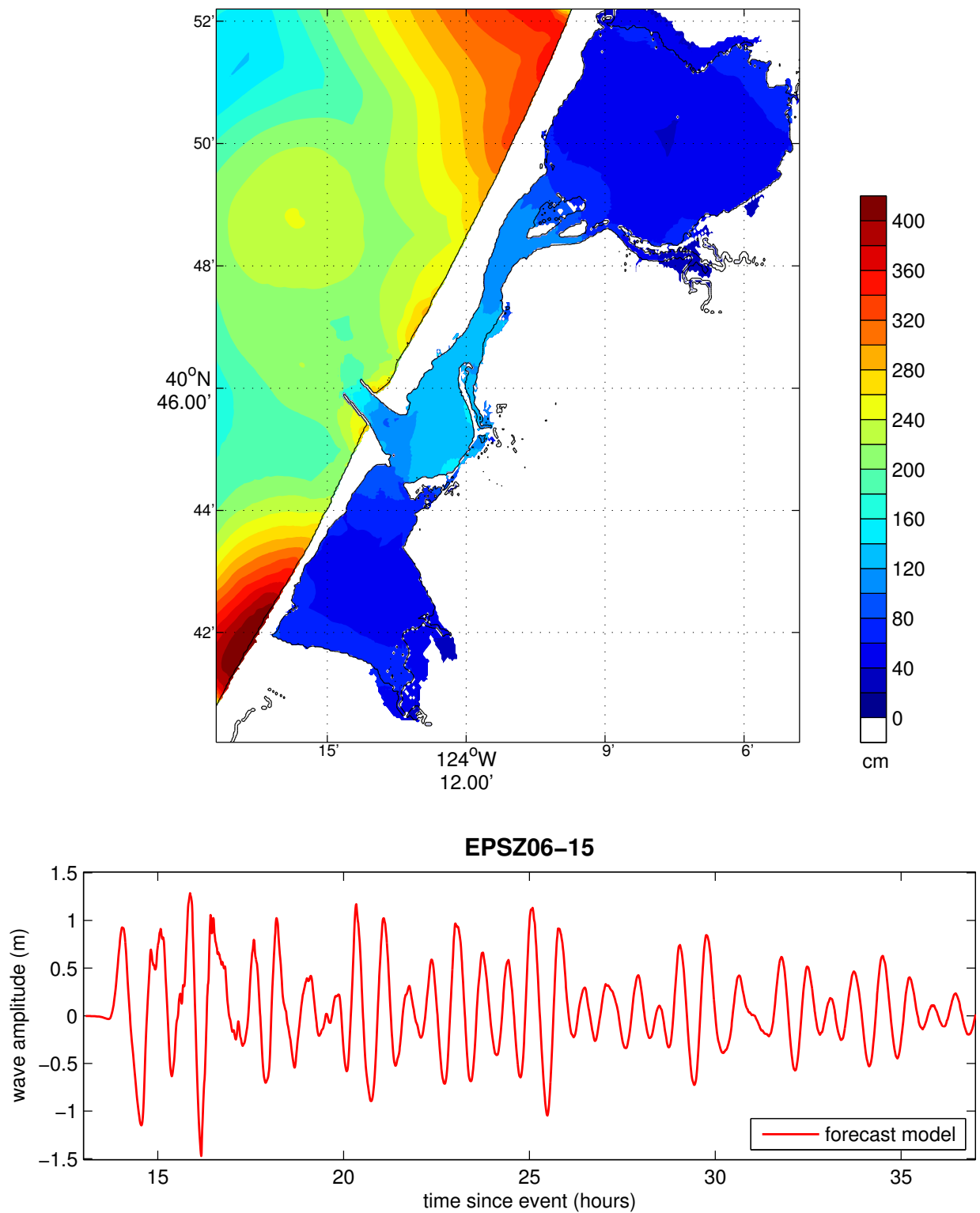
Figure 2.39: Results from the forecast model for the EPSZ 6-15 synthetic event. The upper panel shows the map of predicted maximum wave height in the Eureka C-grid and the lower panel shows the time series of wave amplitude at the tide gauge location.
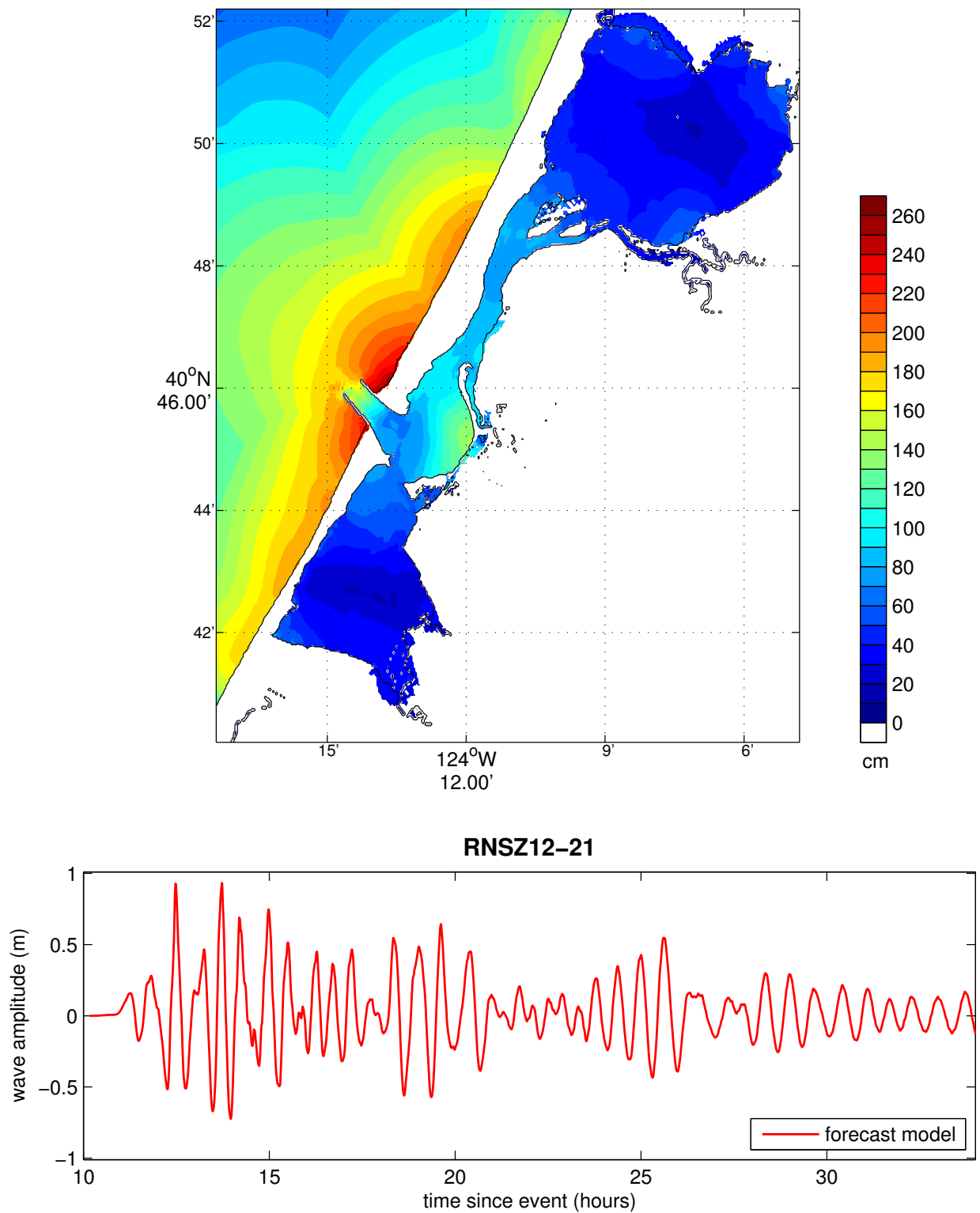
Figure 2.40: Results from the forecast model for the RNSZ 12-21 synthetic event. The upper panel shows the map of predicted maximum wave height in the Eureka C-grid and the lower panel shows the time series of wave amplitude at the tide gauge location.
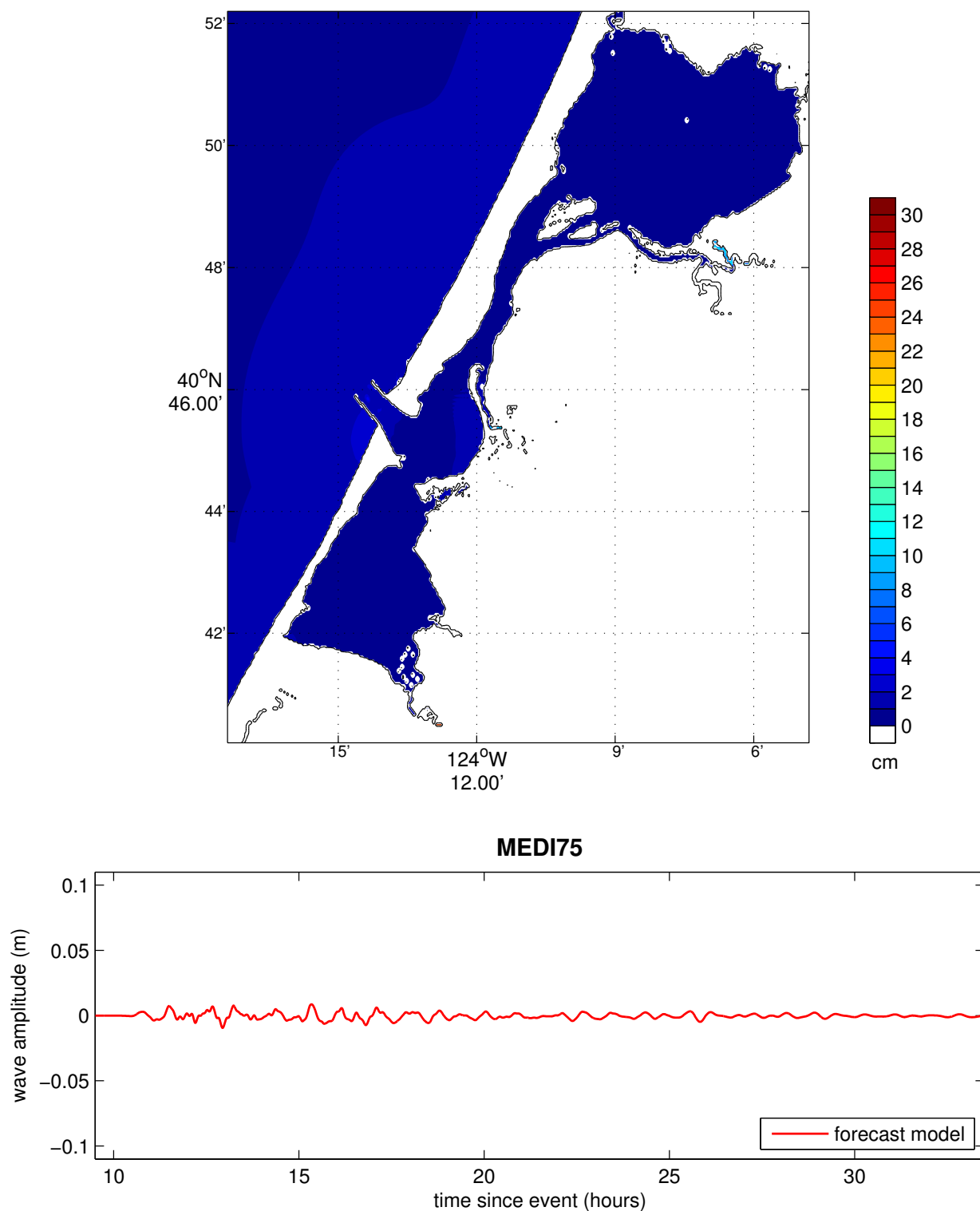
Figure 2.41: Results from the forecast model for the medium synthetic event, with a 1*NTSZb36 source. The upper panel shows the map of predicted maximum wave height in the Eureka C-grid and the lower panel shows the time series of wave amplitude at the tide gauge location.
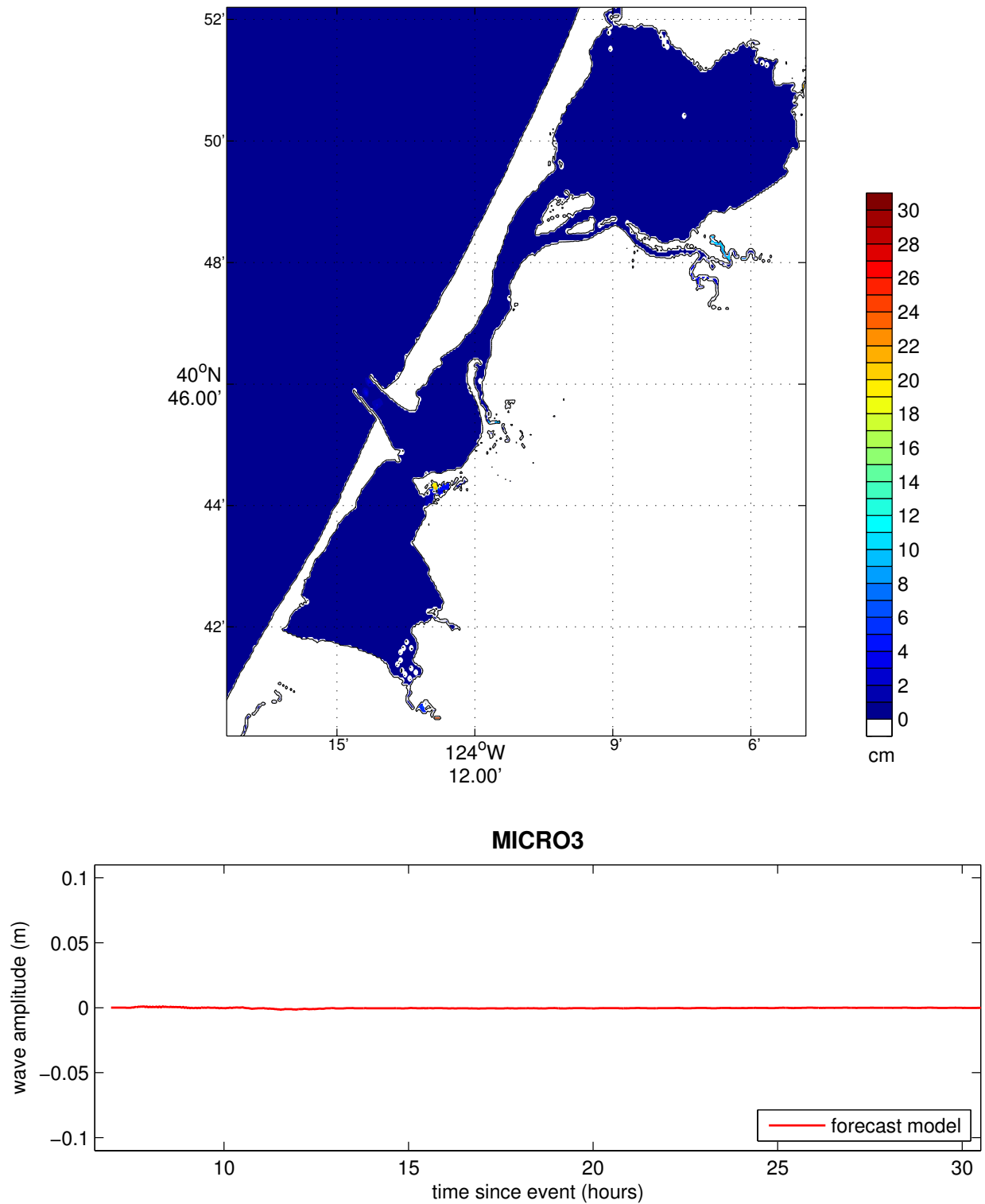
Figure 2.42: Results from the forecast model for the micro synthetic event which uses a source combination of 0.05*ACSZ b6. The upper panel shows the map of predicted maximum wave height in the Eureka C-grid and the lower panel shows the time series of wave amplitude at the tide gauge location.
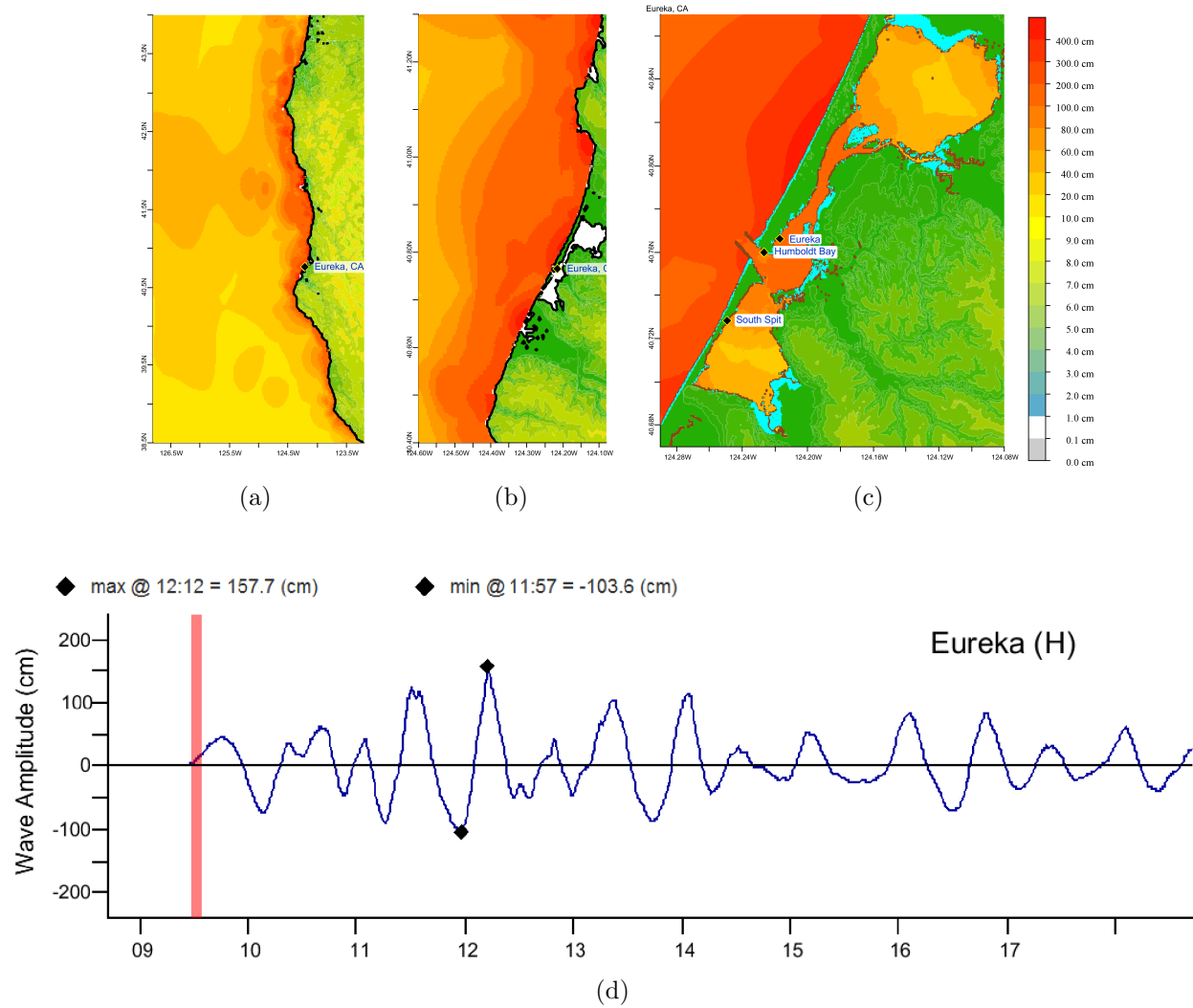
Figure S2.1: Response of the Eureka forecast model to synthetic scenario KISZ 22-31 (α=25 m). In upper plates from left to right are maximum sea surface elevations for A, B, and C-grids, respectively. The lower plate shows the time series of sea surface elevations at the C-grid warning point, with x-axis indicating time since earthquake in hours.
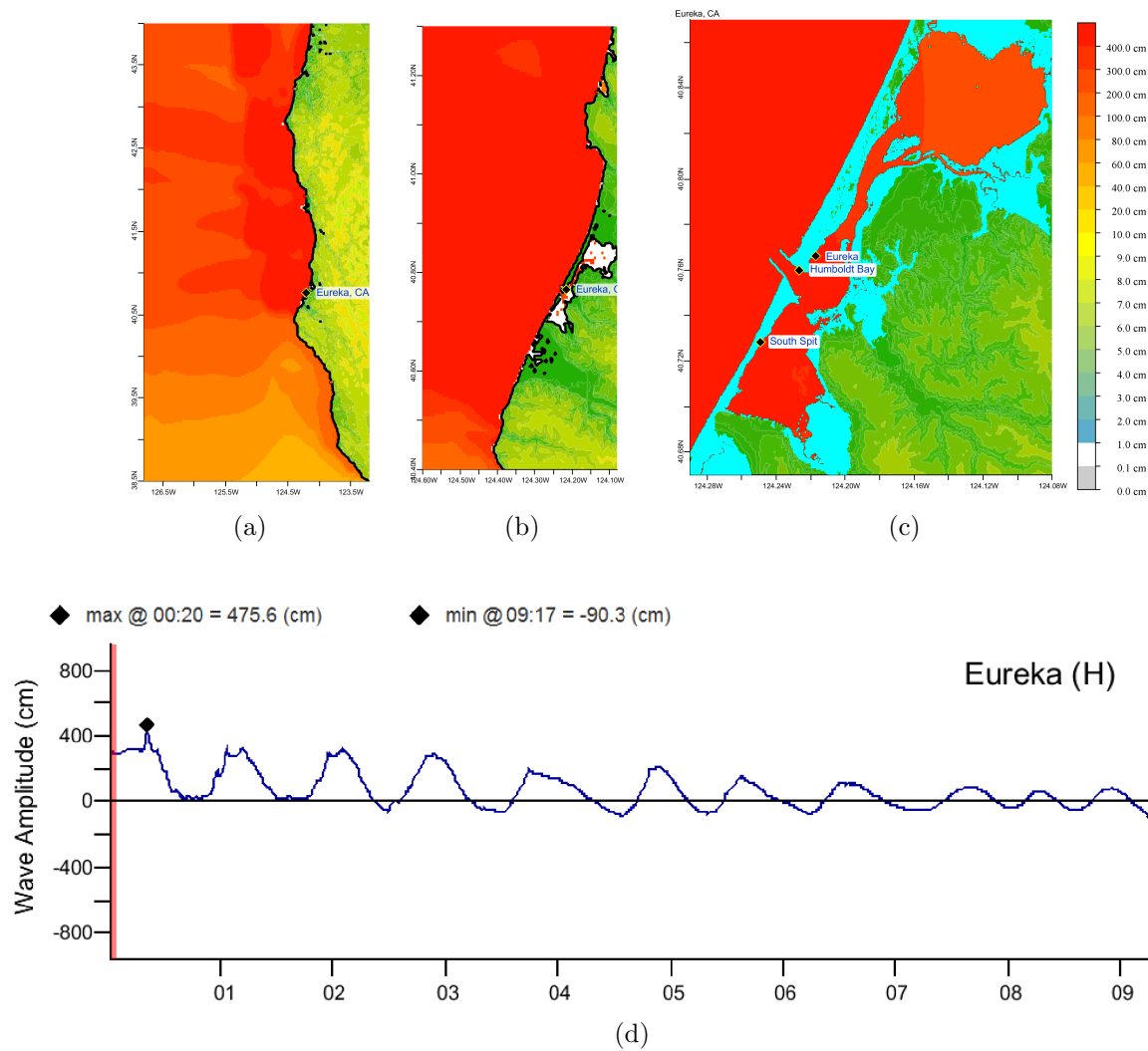
Figure S2.2: Response of the Eureka forecast model to synthetic scenario ACSZ 56-65 (α=25 m). In upper plates from left to right are maximum sea surface elevations for A, B, and C-grids, respectively. The lower plate shows the time series of sea surface elevations at the C-grid warning point, with x-axis indicating time since earthquake in hours.
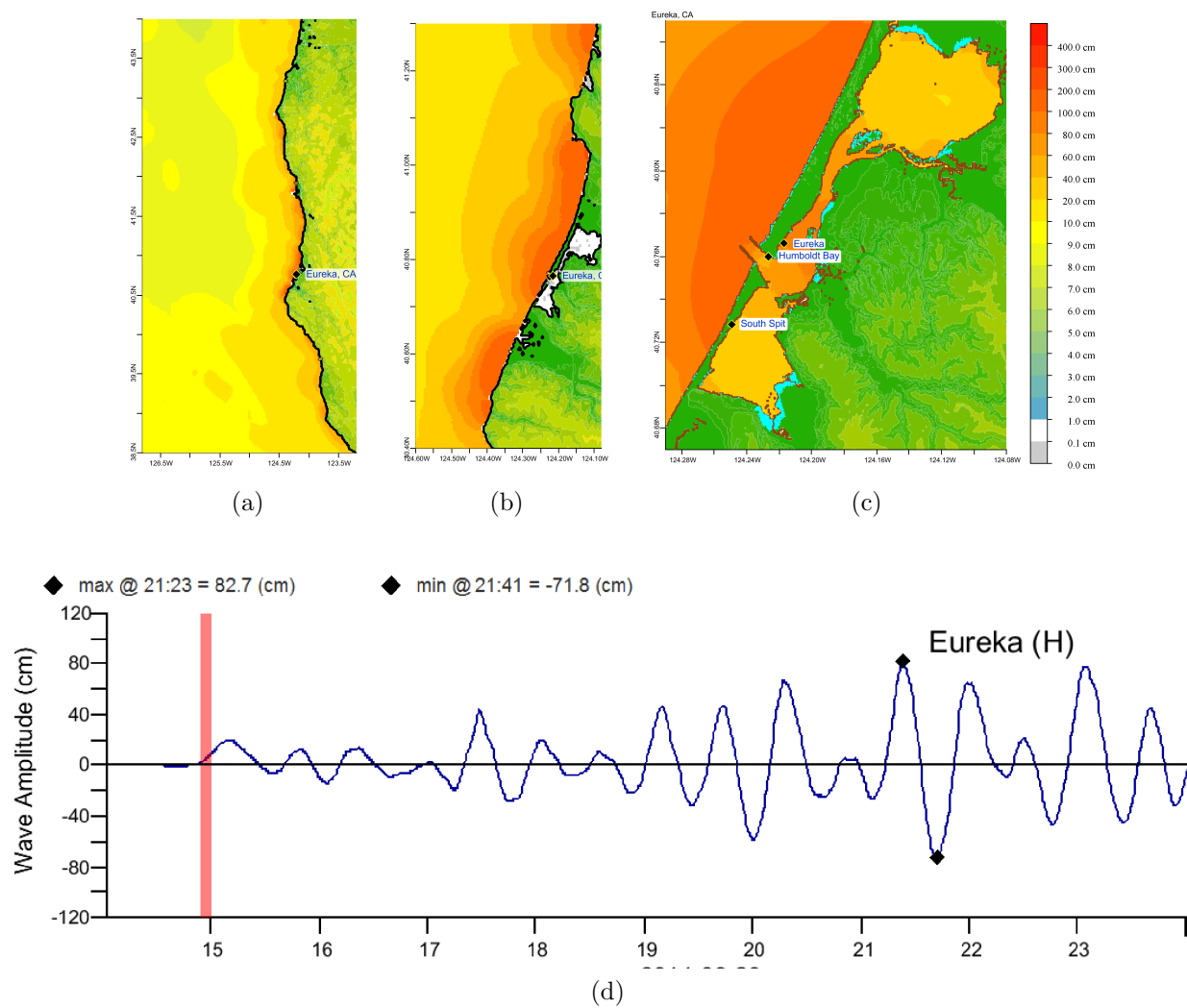
Figure S2.3: Response of the Eureka forecast model to synthetic scenario CSSZ 89-98 (α=25 m). In upper plates from left to right are maximum sea surface elevations for A, B, and C-grids, respectively. The lower plate shows the time series of sea surface elevations at the C-grid warning point, with x-axis indicating time since earthquake in hours.
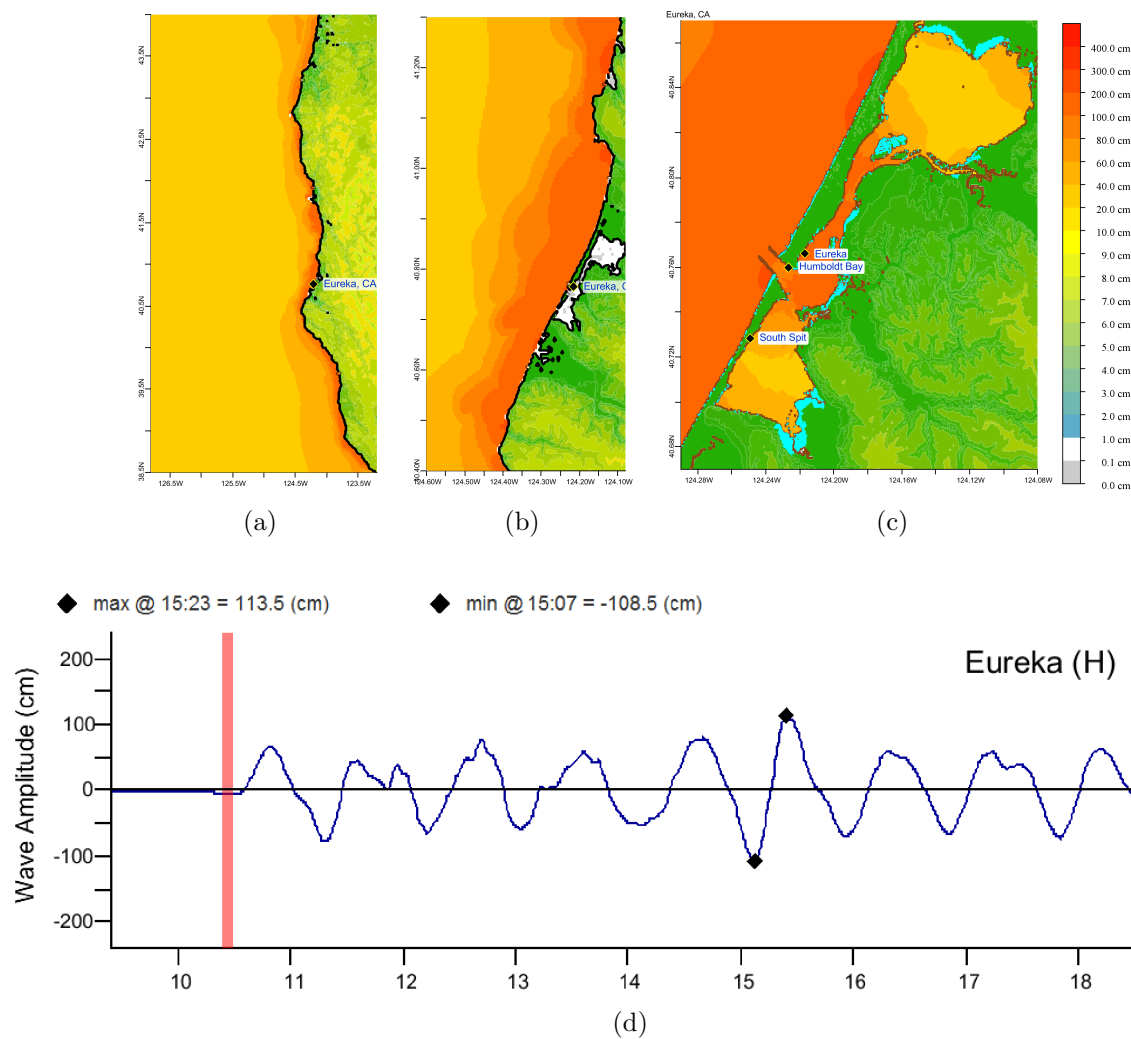
Figure S2.4: Response of the Eureka forecast model to synthetic scenario NTSZ 30-39 (α=25 m). In upper plates from left to right are maximum sea surface elevations for A, B, and C-grids, respectively. The lower plate shows the time series of sea surface elevations at the C-grid warning point, with x-axis indicating time since earthquake in hours.
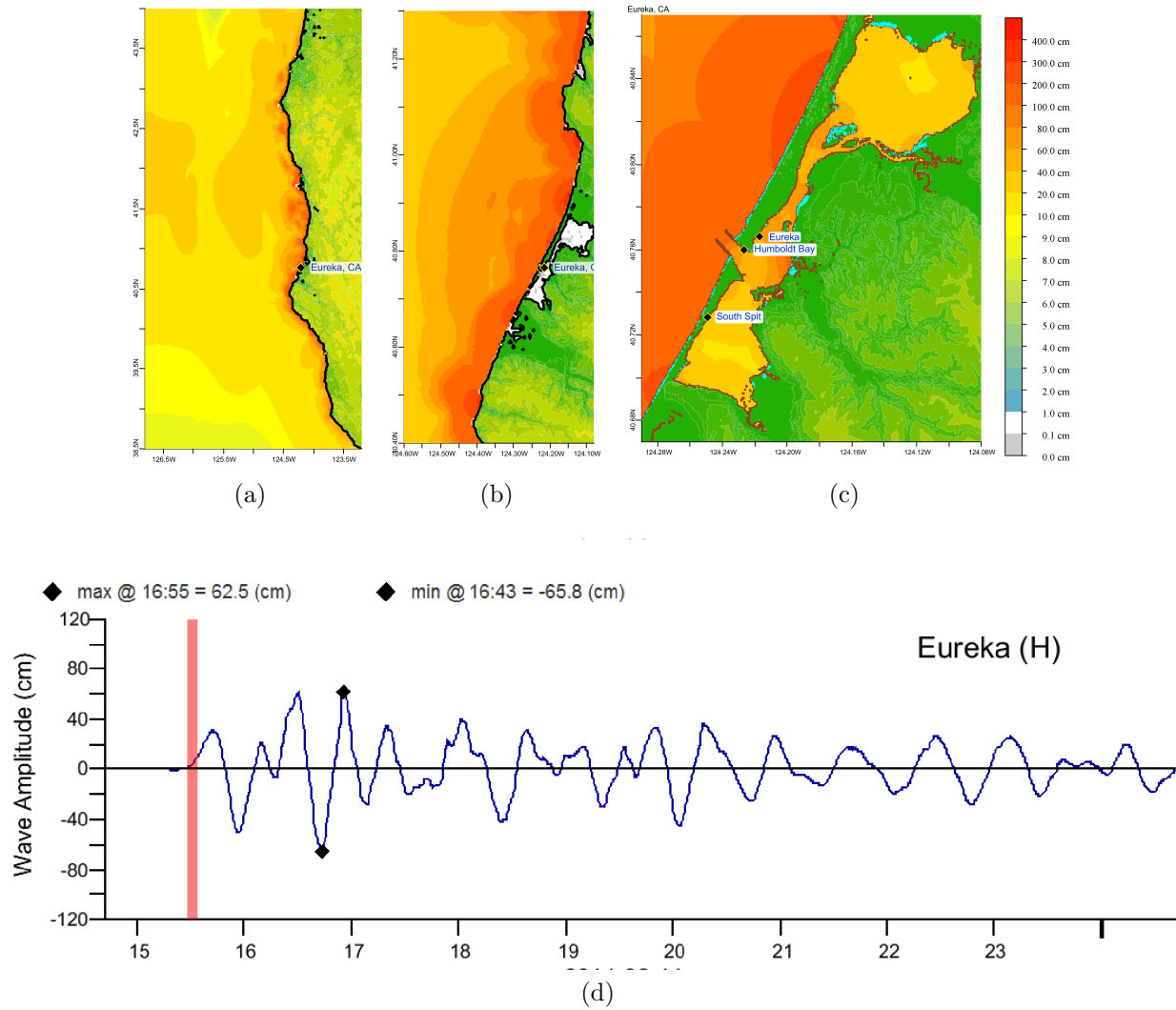
Figure S2.5: Response of the Eureka forecast model to the 2011 Tohoku tsunami. In upper plates from left to right are maximum sea surface elevations for A, B, and C-grids, respectively. The lower plate shows the time series of sea surface elevations at the C-grid warning point, with x-axis indicating time since earthquake in hours.

Tables

Table 2.1: MOST setup of the reference and forecast models for Eureka, California.

		Reference Model				Forecast Model			
Grid	Region	Coverage Lat. (°N) Lon. (°W)	Resolution Lat. Lon.	nx×ny	Time Step (sec.)	Coverage Lat. (°N) Lon. (°W)	Resolution Lat. Lon.	nx×ny	Time Step (sec)
A	US West Coast	38.5–44.0 126.8–123.2	36″ 36″	361×551	2.7	38.5–44.0 126.8–123.2	72″ 72″	181×276	8.0
B	Northern California	40.3–41.3 124.7–124.05	6″ 6″	391×601	0.9	40.4–41.3 124.6–124.08	18″ 18″	105×181	3.2
C	Humboldt Bay	40.67–40.87 124.29–124.08	0.5″ 0.5″	1513×1441	0.3	40.67–40.87 124.29–124.08	2.0″ 2.0″	378×361	1.6
Minimum amp. of input offshore wave (m)			0.0001						0.0001
Minimum offshore depth (m)			5.0						5.0
Water depth for dry land (m)			0.1						0.1
Friction coefficient (n^2)			0.0009						0.0009
Runup in A and B-grids (0: yes, 1:no)			1						1
Max. wave height (m)			100.0						100.0
Time step (sec)			0.3						1.6
Input number of steps			120000						54000
Compute "A" arrays every n-th time step			9						5
Compute "B" arrays every n-th time step			3						2
Input number of steps between snapshots			360						20
... starting from			0						0
... saving grid every n-th node			1						1
CPU time for a 6-hr simulation			11.6 hr						9.8 min

Note: Computations were performed on a single Intel Xeon processor at 3.6 GHz, Dell PowerEdge 1850.

Table 2.2: Historical events used for validation of the Eureka, California, models.

| | Earthquake/Seismic | | | | Model | |
| | USGS | GMT | Magnitude Mw | Tsunami Magnitude[1] | | |
Even	Date Time (UTC) Epicenter	Date Time (UTC) Centroid			Subduction Zone	Tsunami Source
1946 Unimak	01 Apr 12:28:56 52.75°N 163.50°W	01 Apr 12:28:56 53.32°N 163.19°W	[2]8.5	8.5	Aleutian–Alaska–Cascadia (ACSZ)	$7.5 \times b23 + 19.7 \times b24 + 3.7 \times b25$
1960 Chile	22 May 19:11:14 [3]38.29°S 73.05°W	04 Nov 16:58:26.0 52.75°N 159.50°E	[4]9.5		Central-South america (CSSZ)	Kanamori and Cipar (1974)
1964 Alaska	28 Mar 03:36:00 [3]61.02°N 147.65°W	28 Mar 03:36:14 61.10°N 147.50°W	[3]9.2	9.0	Aleutian-Alaska-Cascadia (ACSZ)	$15.4 \times a34 + 19.4 \times a35 + 48.3 \times z34$ $+18.3 \times b34 + 15.1 \times b35$
1994 East Kuril	04 Oct 13:22:58 43.73°N 147.321°E	04 Oct 13:23:28.5 43.60°N 147.63°E	[4]8.3	8.1	Kamchatka–Kuril–Japan - -Izu–Marian–Yap (KISZ)	$9.0 \times a20$
1996 Andreanof	10 Jun 04:03:35 51.56°N 175.39°W	10 Jun 04:04:03.4 51.10°N 177.410°W	[4]7.9	7.8	Aleutian–Alaska–Cascadia (ACSZ)	$2.40 \times a15 + 0.80 \times b16$
2003 Rat Island	17 Nov 06:43:07 51.13°N 178.74°E	17 Nov 06:43:31.0 51.14°N 177.86°E	[5]7.7	7.8	Aleutian-Alaska-Cascadia (ACSZ)	[6]$2.81 \times b11$
2006 Tonga	03 May 15:26:39 20.13°S 174.161°W	03 May 15:27:03.7 20.39°S 173.47°W	[5]8.0	8.0	New Zealand–Kermadec –Tonga (NTSZ)	$6.6 \times b29$
2006 Kuril	15 Nov 11:14:16 46.607°N 153.230°E	15 Nov 11:15:08 46.71°N 154.33°E	[5]8.3	8.1	Kamchatka–Kuril–Japan -Izu–Marian–Yap (KISZ)	[6]$4 \times a12 + 0.5 \times b12 + 2.0 \times a13$ $+1.5 \times b13$
2007 Kuril	13 Jan 04:23:20 46.272°N 154.455°E	13 Jan 04:23:48.1 46.17°N 154.80°E	[5]8.1	7.9	Kamchatka–Kuril–Japan -Izu–Marian–Yap (KISZ)	$-3.64 \times b13$
2007 Solomon	01 Apr 20:39:56 8.481°S 156.978°E	01 Apr 20:40:38.9 7.76°S 156.34°E	[3]8.1	8.2	New Britain-Solomons -Vanuatu (NVSZ)	$12.0 \times b10$
2009 Samoa	29 Sep 17:48:10 15.509°S 172.034°W	29 Sep 17:48:26.8 15.13°S 171.97°W	[5]8.1	8.1	New Zealand–Kermadec –Tonga (NTSZ)	[6]$3.96 \times a34 + 3.96 \times b34$
2010 Chile	27 Feb 06:34:14 33.909°S 72.733°W	27 Feb 06:35:15.4 35.95°S 73.15°W	[5]8.8	8.8	Central–South America (CSSZ)	[6]$17.24 \times a88 + 8.82 \times a90 + 11.86 \times b88$ $+18.39 \times b89 + 16.75 \times b90$ $+20.78 \times z88 + 7.06 \times z90$
2011 Tohoku	11 Mar 05:46:23.82 38.308°N 142.383°E	11 Mar 05:47:47.20 38.486°N 142.597°E	[5]9.0	8.8	Kamchatka-Kuril-Japan -Izu-Mariana-Yap (KISZ)	$4.66 \times b24 + 12.23 \times b25 + 26.31 \times a26$ $+21.27 \times b26 + 22.75 \times a27 + 4.98 \times b27$

[1] Preliminary source–derived from source and deep-ocean observations.

[2] López and Okal (2006)

[3] United States Geological Survey (USGS)

[4] Kanamori and Cipar (1974)

[5] Centroid Moment Tensor

[6] Tsunami source was obtained in real time and applied to the forecast.

Table 2.3: Unit source combinations used to generate synthetic tsunami scenarios for robustness and stability testing of the Eureka forecast model.

Scenario Name	Source Zone	Tsunami Source	Slip (m)
Mega-tsunami Scenario			
KISZ 1-10	Kamchatka-Yap-Mariana-Izu-Bonin	A1-A10, B10-B10	25
KISZ 22-31	Kamchatka-Yap-Mariana-Izu-Bonin	A22-A31, B22-B31	25
KISZ 32-41	Kamchatka-Yap-Mariana-Izu-Bonin	A32-A41, B32-B41	25
KISZ 56-65	Kamchatka-Yap-Mariana-Izu-Bonin	A56-A65, B56-B65	25
ACSZ 6-15	Aleutian-Alaska-Cascadia	A6-A15, B6-B15	25
ACSZ 16-25	Aleutian-Alaska-Cascadia	A16-A25, B16-B25	25
ACSZ 22-31	Aleutian-Alaska-Cascadia	A22-A31, B22-B31	25
ACSZ 50-59	Aleutian-Alaska-Cascadia	A50-A59, B50-B59	25
ACSZ 56-65	Aleutian-Alaska-Cascadia	A56-A65, B56-B65	25
CSSZ 1-10	Central and South America	A1-A10, B1-B10	25
CSSZ 37-46	Central and South America	A37-A46, B37-B46	25
CSSZ 89-98	Central and South America	A89-A98, B89-B98	25
CSSZ 102-111	Central and South America	A102-A111, B102-B111	25
NTSZ 30-39	New Zealand-Kermadec-Tonga	A30-A39, B30-B39	25
NVSZ 28-37	New Britain-Solomons-Vanuatu	A28-A37, B28-B37	25
MOSZ 1-10	ManusOCB	A1-A10, B1-B10	25
NGSZ 3-12	North New Guinea	A3-A12, B3-B12	25
EPSZ 6-15	East Philippines	A6-A15, B6-B15	25
RNSZ 12-21	Ryukus-Kyushu-Nankai	A12-A21, B12-B21	25
Mw 7.5 Scenario			
NTSZ B36	New Zealand-Kermadec-Tonga	B36	1
Micro-tsunami Scenario			
ACSZ B6	Aleutian-Alaska-Cascadia	B6	0.05

Table S2.1: Table of maximum and minimum amplitudes (cm) at the Eureka, California, warning point for synthetic and historical events tested using SIFT 3.2 and obtained during development.

Scenario Name	Source Zone	Tsunami Source	α [m]	SIFT Max (cm)	Development Max (cm)	SIFT Min (cm)	Development Min (cm)
Mega-tsunami Scenarios							
KISZ 22-31	Kamchatka–Yap–Mariana–Izu–Bonin	A22-A31, B22-B31	25	157.7	157.8	-103.6	-103.5
ACSZ 56-65	Aleutian–Alaska–Cascadia	A56-A65, B56-B65	25	475.6	475.6	-90.3	-30.4
CSSZ 89-98	Central and South America	A89-A98, B89-B98	25	82.7	82.7	-71.8	-71.8
NTSZ 30-39	New Zealand–Kermadec–Tonga	A30-A39, B30-B39	25	113.5	113.5	-108.5	-108.5
Historical Events							
2011 Tohoku2011	Kamchatka–Yap–Mariana–Izu–Bonin	$4.66 \times b24 + 12.23 \times b25 + 26.31 \times a26$ $21.27 \times b26 + 22.75 \times a27 + 4.98 \times b27$		62.5	62.8	-65.8	-64.8

Bibliography

Carignan, K.S., L.A. Taylor, B.W. Eakins, R.R. Warnken, R.J. Caldwell, D.Z. Friday, E. Lim, and P.R. Grothe (2010): Digital Elevation Models of Eureka, California: Procedures, Data Sources and Analysis, NOAA Technical Memorandum NESDIS NGDC-38, U.S. Dept. of Commerce, Boulder, CO, 41 pp.

U.S. Census Bureau (2010): State and County Quickfacts: Eureka (city), California. Retrieved Sep. 22, 2015, from `http://quickfacts.census.gov`.

U.S. Census Bureau (2010b): State and County Quickfacts: Arcata (city), California. Retrieved Sep. 22, 2015, from `http://quickfacts.census.gov`.

Kanamori, H., and J.J. Cipar (1974): Focal process of the great Chilean earthquake, May 22, 1960. *Phys. Earth Planet. In.*, *9*, 128–136.

López, A.M., and E.A. Okal (2006): A seismological reassessment of the source of the 1946 Aleutian 'tsunami' earthquake. *Geophys. J. Int.*, *165*(3), 835–849.

3. PMEL Tsunami Forecast Model for Arena Cove, California

Michael Spillane

Table of Contents

LIST OF FIGURES

LIST OF TABLES

3.1 Background and Objectives

3.1.1 The setting

Arena Cove is a semi-circular indentation some 450 m in diameter flanked by cliffs, lying south of the rocky headland whose northernmost point is the site of the Point Arena lighthouse. The cove appears about one-third of the way above the lower edge of **Figure 1** (based on the 2005 National Agricultural Imagery Program image from the United States Geological Survey (USGS) 7.5 arc min quadrangle: 38123h6, available online at atlas.ca.gov/quads). Apart from a pier (better seen in **Figure 2**), raised high above water level on pilings and the focus of local commercial fishing and tourist activity, the waterfront area of Arena Cove is almost devoid of infrastructure, though it lies within the city limits of Point Arena.

This small city's population of about 450 mainly reside at elevations that place them above the level likely to be impacted by even the most severe tsunamis. Population is sparse both to the south and north of Point Arena, but inundation of Manchester Beach State Park, north of the lighthouse, and the low-lying area near the mouth of the Garcia River (crossed by State Highway 1) needs consideration. A comprehensive study of potential tsunami inundation for the entire California coastline was conducted by the University of Southern California Tsunami Research Center. Funded through the California Emergency Management Agency (CalEMA) by the National Tsunami Hazard Program, the study (Barberopoulou *et al.*, 2011) produced a set of inundation maps for emergency planning purposes, accessible in various forms including an online tool, MyHazards (myhazards. calema.ca.gov), which enables users to acquire information specific to their site of interest. The CalEMA inundation results are available in GIS form, and those specific to the Arena Cove area are used throughout this report. In addition to underpinning the modeling effort, the digital elevation model (DEM) for the region, provided by the National Geophysical Data Center (NGDC), includes a 3-D oblique view that assists greatly in visualizing the study area. In **Figure 3**, the CalEMA inundation information is overlaid together with descriptive labels on an extract from the NGDC image, available in full in the DEM Report (Friday *et al.*, 2009).

Arena Cove, both in appearance (**Figure 2**) and population, has not changed substantially since the nineteenth and early twentieth centuries, when it was one of the "Dog Hole" ports of the Mendocino Coast (Haugan, 2005). So named for their small size, these ports nonetheless served an important role in the provision of lumber in the building of the cities of California and in the rebuilding of San Francisco in the wake of the 1906 earthquake and fire (see the inset to **Figure 2**, reproduced by permission of the Mendocino County Historical Society). The Point Arena lighthouse and its namesake city were seriously damaged by the earthquake, and the San Andreas Fault (SAF) dominates the local topography. The SAF intersects the coast just north of Point Arena en route to the triple junction near Cape Mendocino, the southern limit of the Cascadia Subduction Zone, which constitutes a major earthquake and tsunami hazard to the U.S. West Coast.

Unlike the other ports of the Mendocino Coast, whose mouths have sand bars, the channeling northward of the Garcia River by the SAF leaves a limited watershed to supply sediment to Arena Cove via Point Arena Creek, entering the cove through a small, steep-sided valley. The current pier, rebuilt in 1986 following the damage to its predecessor by a series of storms in 1983, stands

on pilings high above water level. It houses a crane to lower boats to the water and the instrumentation for the tide gauge whose sensor is adjacent to the pier. In earlier days, piers and wire chutes atop the flanking cliffs delivered lumber products to coastal schooners. Today's pier supports local commercial fishing and sightseeing; surfing and pier fishing are popular tourist activities.

Apart from the pier and some riprap, the cove remains in its natural state. A congressional study (US Secretary of War, 1914) considered the possibility of engineering works to make Arena Cove a "harbor of refuge" between San Francisco and Humboldt Bay but concluded that this was neither feasible nor a serious need. Consequently, sea level data from the tide gauge represent coastal conditions, unaffected by infrastructure. Port Road links the pier, the parking area, and some buildings housing fishing and tourist amenities to the city proper. Accommodations in the immediate pier area are confined to an inn that is well elevated from the waves associated with winter storms and, as this report will document, even the most severe tsunami.

South of Arena Cove, as illustrated in a striking series of aerial photographs by the California Coastal Records Project (californiacoastline.org), the source of the main frame of **Figure 2**, high cliffs limit potential impact by tsunamis. To the north of the lighthouse, however, and stretching as far as the Irish Beach community, lies Manchester Beach State Park. Inland from the point of entry to the ocean of the Garcia River is the Manchester-Point Arena Rancheria of the federally recognized Band of Pomo Indians. While the historical record of tsunamis does not include mention of this area, its risk for inundation is evident in the CalEMA chart, and the results of this study indicate that it may be prone to inundation in severe tsunami events. Thus, while the study focuses on Arena Cove, and the validation of the forecast model is provided by the tide gauge there, the analysis of the most severe scenarios will consider potential impacts to the Manchester area. The community of Manchester itself appears to be immune to direct impact, though State Highway 1 (also called the Shoreline Highway) may be inundated where it crosses the Garcia River. Queries to the CalEMA "MyHazards" site for Point Arena and Manchester show flooding and earthquake as other hazards to which they are prone, in addition to tsunami.

3.1.2 Natural hazards

Several instances of mild tsunami signals are evident in the tide gauge records for Arena Cove, whose name appears several times in the records compiled by Lander and Lockridge (1989) and the NGDC Tsunami Hazard Database (Dunbar, 2007; see www.ngdc.noaa.gov/hazard/). The historical record first mentions Mendoci County with a 1 m wave height associated with the Sanriku event of 1896. O'Brien (1946) described a 2.4 m wave (4.3 m above mean lower low water, or MLLW) at Arena Cove during the 1946 Unimak tsunami, while Noyo Harbor adjacent to Fort Bragg, the largest coastal community in the county (2010 population: 7273; Census Bureau, 2010), endured "100 fishing boats thrown 1.8 m up beach and some damage to pier." While Arena Cove was not explicitly mentioned in connection with the 1957 Andreanof event, there was a report from Noyo Harbor. Similarly, during the 1960 Chile event, Noyo Harbor reported "6 boats broke mooring… pier damaged" and a height of 0.61 m was observed at Gualala River near the southern boundary of Mendocino County. During the 1964 Alaska tsunami, a runup height of 1.83 m occurred at Arena Cove. Several instances of mild response to tele-tsunamis are available, following the installation of a tide gauge in 1978, with which to validate model predictions.

2

The Mw 7.2 earthquake north of Cape Mendocino on 25 April 1992 was a very mild foretaste of a Cascadia Subduction Zone (CSZ) event. It produced wave heights of 0.14 m at Arena Cove and 0.50 m at Crescent City. Large-scale events on the CSZ are simulated later in the report, but the weak 1992 event will be examined to see whether the presence of the Point Arena headland provides protection to Arena Cove, which lies in its lee for waves propagating along the coast from the north.

Combining events impacting northern California with those that have occurred since the Arena Cove tide gauge was upgraded to 1 min sampling, a total of 27 historical events are available for study. Nineteen of these, listed in **Table 1a**, are the standards for forecast model testing in the Pacific because their seafloor deformation is reasonably well known, either from the literature or, more recently, derived from direct observation of the wave trains they generated. The remaining eight, listed in **Table 1b**, have source characteristics that are less well known; they are included to expand the geographical coverage or because of their special relevance to Arena Cove. The 1992 Mendocino event (discussed in Section 4.5), for example, was the most recent subduction-type event in Cascadia. Others, due to significant noise in the tide gauge, do not produce a clear signal but shed light on Arena Cove as a reference point for coastal impacts. **Figure 4** illustrates the distribution of the 27 historical sources. Those highlighted in red were employed for intercomparison of the reference and forecast versions of the model.

Direct seismic impact is another natural hazard to which Point Arena area is exposed. Its proximity to the rupture zone of the SAF in the San Francisco earthquake of 1906 resulted in significant damage to the town and the destruction of the lighthouse. While the SAF enters the ocean at Manchester Beach, its strike-slip nature reduces the likelihood of severe tsunami wave generation should ruptures occur in the immediate vicinity. Submarine landslides or collapse of sections of sea cliff are a potential local source for tsunami damage. Landslides triggered by seismic events caused significant loss of life during the 1929 Newfoundland event (Fine *et al.*, 2005) and accentuated the 1996 New Guinea tsunami. Landslide-generated tsunami waves are not currently included in the SIFT (Short-term Inundation Forecasting for Tsunamis) forecast methodology, nor are those generated meteorologically. However, to the extent that the waves they produce are detected by the DART (Deep-ocean Assessment and Reporting of Tsunami) array, some warning of their presence may be available.

Another local hazard that has been a frequent cause of damage to Arena Cove has been ocean wave action. Originating locally, or as swell from distant storms, such waves caused severe damage to the pier in 1983 that necessitated its replacement. Another impact of ocean waves, of relevance to tsunami detection and modeling, is in the noise they produce in the tide gauge record that can mask weaker tsunami signals. Harbor resonance in the case of Crescent City can amplify the tsunami and may be a factor too in the Arena Cove response.

3.1.3 Tsunami warning and risk assessment

The forecast model development described here will permit Arena Cove to be incorporated into the tsunami forecasting system, developed at NOAA's Center for Tsunami Research (NCTR) and now in operational use at the U.S. Tsunami Warning Centers (TWCs). The system has had

Table 1. Source characterization for historical tsunami events employed for Arena Cove, California, model testing. Events in bold text were used to compare the reference and forecast model versions. Sources identified as "preliminary" or "ad hoc" may not be identically defined in other forecast model reports. (a) The standard set for Pacific Ocean models; and (b) supplementary historical tsunami events employed for forecast model testing.

Table 1: Source characterization for historical tsunami events employed for Arena Cove, California, model testing. Events in bold text were used to compare the reference and forecast model versions. Sources identified as "preliminary" or "ad hoc" may not be identically defined in other forecast model reports. (a) The standard set for Pacific Ocean models; and (b) supplementary historical tsunami events employed for forecast model testing.

| Event | Earthquake / Seismic | | | | | Model | |
	USGS Date Time (UTC) Epicenter	CMT Date Time (UTC) Centroid	Magnitude Mw	Tsunami Magnitude	Subduction Zone	Tsunami Source (Reference/Derivation)	
(a) Standard set for Pacific Ocean models:							
1946 Unimak	01 Apr 12:28:56 52.75°N 163.50°W	Not Available	8.5	8.5	ACSZ	7.5 × B23 + 19.7 × B24 + 3.7 × B25 (López and Okal, 2006)	
1952 Kamchatka	04 Nov 16:58:26.0 52.76°N 160.06°E	Not Available	9.0	9.0	KISZ	19.71 × (A4 + Y4 + Z4 + A5 + Y5 + Z5 + A6 + Y6 + Z6) [ad hoc]	
1957 Andreanof	09 Mar 14:22:31 51.56°N 175.39°W	Not Available	8.6	8.7	ACSZ	31.4 × A15 + 10.6 × A16 + 12.2 × A17 [preliminary]	
1960 Chile	22 May 19:11:14 38.29°S 73.05°W	Not Available	9.5	9.5	CSSZ	125 × (A93 + B93 + Z93 + A94 + B94 + Z94 + A95 + B95) (Kanamori and Cipar, 1974)	
1964 Alaska	28 Mar 03:36:00 61.02°N 147.65°W	Not Available	9.2	8.9	ACSZ	15.4 × A34 + 18.3 × B34 + 48.3 × Z34 + 19.4 × A35 + 15.1 × B35 (Tang *et al.* 2006, 2009)	
1994 East Kuril	04 Oct 13:22:58 43.73°N 147.321°E	04 Oct 13:23:28.5 43.60°N 147.63°E	8.3	8.1	KISZ	9.0 × A20 [ad hoc]	
1996 Andreanof	10 Jun 04:03:35 51.56°N 175.39°W	10 Jun 04:04:03.4 51.10°N 177.410°W	7.9	7.8	ACSZ	2.40 × A15 + 0.80 × B16 [preliminary]	
2001 Peru	23 Jun 20:33:14 16.265°S 73.641°W	23 Jun 20:34:23.3 17.28°S 72.71°W	8.4	8.2	CSSZ	5.7 × A15 + 2.9 × B16 + 1.98 × A16 [preliminary]	
2003 Hokkaido	25 Sep 19:50:06 41.775°N 143.904°E	25 Sep 19:50:38.2 42.21°N 143.84°E	8.3	8.3	KISZ	3.95 × (A22 + B22 + A23 + B23) [ad hoc]	
2003 Rat Island	17 Nov 06:43:07 51.13°N 178.74°E	17 Nov 06:43:31.0 51.14°N 177.86°E	7.7	7.8	ACSZ	2.81 × B11 [real-time]	
2006 Tonga	03 May 15:26:39 20.13°S 174.161°W	03 May 15:27:03.7 20.39°S 173.47°W	8.0	8.0	NTSZ	6.6 × b29 [ad hoc]	
2006 Kuril	15 Nov 11:14:16 46.607°N 153.230°E	15 Nov 11:15:08 46.71°N 154.33°E	8.3	8.1	KISZ	4.0 × A12 + 0.5 × B12 + 2.0 × A13 + 1.5 × B13 [real-time]	
2007 Kuril	13 Jan 04:23:20 46.272°N 154.455°E	13 Jan 04:23:48.1 46.17°N 154.80°E	8.1	7.9	KISZ	−3.64 × B13 [real-time]	
2007 Solomon	01 Apr 20:39:56 8.481°S 156.978°E	01 Apr 20:40:38.9 7.76°S 156.34°E	8.1	8.2	NVSZ	12.0 × B10 [preliminary]	
2007 Peru	15 Aug 23:40:57 13.354°S 76.509°W	15 Aug 23:41:57.9 13.73°S 77.04°W	8.0	8.1	CSSZ	0.9 × A61 + 1.25 × B61 + 5.6 × A62 + 6.97 × B62 + 3.5 × Z62 [preliminary]	

4

Table 1. *continued*.

Table 1: *Continued*.

Event	USGS Date Time (UTC) Epicenter	CMT Date Time (UTC) Centroid	Magnitude Mw	Tsunami Magnitude	Subduction Zone	Tsunami Source (Reference/Derivation)
(a) Standard set for Pacific Ocean models, continued:						
2007 Chile	14 Nov 15:40:50 22.204°S 69.869°W	14 Nov 15:41:11.2 22.64°S 70.62°W	7.7	7.6	CSSZ	1.65 × Z73 [real-time]
2009 Samoa	29 Sep 17:48:10 15.509°S 172.034°W	29 Sep 17:48:26.8 15.13°S 171.97°W	8.1	8.1	NTSZ	3.96 × A34 + 3.96 × B34 [real-time]
2010 Chile	27 Feb 06:34:14 35.909°S 72.733°W	27 Feb 06:35:15.4 35.95°S 73.15°W	8.8	8.8	CSSZ	17.24 × A88 + 8.82 × A90 + 11.84 × B88 + 18.39 × B89 + 16.75 × B90 + 20.78 × Z88 + 7.06 × Z90 [real-time]
2011 Tohoku	11 Mar 05:46:24 38.297°N 142.372°E	11 Mar 05:47:47.1 38.486°N 142.597°E	9.0	9.0	KISZ	4.66 × B24 + 12.23 × B25 + 26.31 × A26 + 21.27 × B26 + 22.75 × A27 + 4.98 × B27 (Tang *et al.*, 2012) [real-time]
(b) Supplementary historical tsunami events employed for forecast model testing:						
1896 Sanriku	15 Jun 10:33:00 39.5°N 144.0°E		7.6	7.6	KISZ	1.413 × b25 [ad hoc]
1992 Mendocino	25 Apr 18:06:04 40.368°N 124.316°W	25 Apr 18:06:11.8 38.56°N 123.31°W	7.2	7.2	ACSZ	0.355 × a65 *or* 0.355 × b65 [ad hoc]
1995 Chile	30 Jul 05:11:24 23.340°S 70.294°W	30 Jul 05:11:56.9 24.17°S 70.74°W	8.0	8.0	CSSZ	2.812 × (a75 + b75) [ad hoc]
1995 Kuril	03 Dec 18:01:09 44.663°N 149.300°E	03 Dec 18:01:36.1 44.82°N 150.17°E	7.9	7.9	KISZ	1.991 × (a17 + z17) [ad hoc]
1996 Irian Jaya	17 Feb 05:59:31 0.891°S 136.952°E	17 Feb 06:00:02.8 0.67°S 136.62°E	8.2	8.2	NGSZ	2.7984 × (a9 + b9 + a10 + b10) [ad hoc]
2009 Papua NG	03 Jan 19:43:51 0.414°S 132.885°E	03 Jan 19:44:09.0 0.38°S 132.83°E	7.6	7.6	NGSZ	0.7046 × (b13 + b14) [ad hoc]
2009 Kuril	15 Jan 17:49:39 46.857°N 155.154°E	15 Jan 17:49:48.3 46.97°N 155.39°E	7.4	7.4	KISZ	0.7063 × b12 [ad hoc]
2009 Vanuatu/	07 Oct 22:03:15 13.052°S 166.187°E	07 Oct 22:03:28.9 12.59°S 166.27°E	7.6	7.6	NVSZ	1.2 × B24 + 0.26 × A23 *followed after 15 minutes by*
Santa Cruz	07 Oct 22:18:26 12.554°S 166.320°E	07 Oct 22:19:15.3 11.86°S 166.01°E	7.8	7.9	NVSZ	2.6 × B23 + 0.9 × A23 [preliminary] (Yong Wei, 2009 personal communication)

considerable success in accurately forecasting the impact of both moderate and severe tsunami events in recent years, and in the following section, the methodology that permits such forecasts is discussed as prelude to a description of forecast model development for Arena Cove. With the model in hand, validated with historical events and with its stability verified by extensive testing against extreme scenarios, real-time forecasts will be available to inform local emergency response. Additionally, the synthetic scenarios investigated during model development and reported here provide an initial tsunami risk assessment, as described in Section 3.3.

3.2 Model development

3.2.1 Digital elevation models

Water depth determines local tsunami wave speed, and subaerial topography determines the extent to which tsunami waves inundate the land. Thus, a prerequisite for credible tsunami modeling is the availability of accurate gridded bathymetric and topographic datasets, termed digital elevation models, or DEMs. Given their expertise in this area and the number of coastal communities needing tsunami forecast capability, NCTR relies heavily on the NGDC to provide the DEMs needed. In the case of Arena Cove, California, the DEM was produced and documented by Friday *et al*. (2009). The DEM is a composite of multiple data sources merged and converted to a common datum of mean high water (MHW); the use of MHW as the "zero level" is standard in forecast models. The version of MOST currently employed does not explicitly include tidal fluctuations, and, since a tsunami may arrive at any stage of the tide, it is best to employ a "worst-case" approach by assuming high tide when forecasting inundation. For some forecast models, grounding of vessels and the strong and rapidly varying currents often associated with even mild tsunamis are of concern. For Arena Cove, which lacks a marina and shoreline infrastructure, low water impacts are less important.

The DEM provided by NGDC for the Arena Cove area is illustrated in **Figure 3**; its salient features listed in **Table 2** are reproduced from DEM documentation (Friday *et al*., 2009). The NGDC report thoroughly describes the data sources and methods employed in constructing the DEM. With 1/3 arc sec (10 m) resolution, the DEM provides the basis for the B and C grids developed for both the reference and forecast models. NCTR maintains an atlas of lower-resolution gridded bathymetries that can be used for the A grids, as described in Section 3.4. All of the DEMs employed were verified for consistency with charts, satellite imagery, and other datasets during the course of MOST grid development.

The elevations and depths used in the development of this forecast model were based on the DEM provided by the NGDC; the author considers it to be a good representation of the local topography and bathymetry. As new DEMs become available, forecast models will be updated and report updates will be posted at nctr.pmel.noaa.gov/forecast_reports/.

3.2.2 Tides and sea level variation

Arena Cove's history of tidal observations dates back only to 1978. The tide station (9416841, 38°54.8′N, 123°42.4′W) is located near the end of the pier, whose concrete pilings raise the deck

about 7.7 m above sea level and do not impede water movement within the cove. The instrumentation was upgraded in 2006 to include a tsunami-capable gauge sampling at 1 min intervals; some earlier data were sampled at 6 min intervals, and several historical events are only available as marigrams on microfiche. An ongoing project at NGDC will digitize the more critical images in this archive.

Table 2. The main features of the Arena Cove digital elevation model (DEM).

Table 2: The main features of the Arena Cove digital elevation model (DEM).

Grid Area	Arena Cove, California
Coverage Area	123.43° to 124.43°W; 38.40° to 39.40°N
Coordinate System	Geographical decimal degrees
Horizontal Datum	World Geodetic System 1984 (WGS84)
Vertical Datum	Mean High Water (MHW)
Vertical Units	Meters
Cell Size	1/3 arc sec
Grid Format	ESRI Arc ASCII grid

Station characteristics for 9416841 are provided in **Table 3**, based on the wealth of online tidal information available at NOAAs CO-OPS (Center for Operational Oceanographic Products and Services) website (tidesandcurrents.noaa.gov). Note the sizeable diurnal range of over 1.7 m, and that, while the long-term rate of change in sea level is low (compared to more tectonically active areas), there is substantial seasonal, interannual, and short-term variability. Owing to the relatively short history of the Arena Cove tide gauge, trends and cycles are reported for Crescent City to the north and Point Reyes to the south.

Table 3. Tidal characteristics of the Arena Cove tide gauge.
Arena Cove, California: Station 9416841 (38° 54.8'N, 123° 42.4'W)

Table 3: Tidal characteristics of the Arena Cove tide gauge.

Arena Cove, California: Station 9416841 (38°54.8'N, 123°42.4'W)

Tidal Datum and Range Values (Epoch 1983–2001)

MHHW (Mean Higher High Water)	10.609 m		
MHW (Mean High Water)	10.405 m	Great Diurnal Range	Mean Range
MSL (Mean Sea Level)	9.779 m	1.787 m	1.232 m
MLW (Mean Low Water)	9.174 m		
MLLW (Mean Lower Low Water)	8.822 m		

Sea Level Trends and Cycles from Point Reyes, California, Station 9415020

Long-term Sea Level Trend	Increasing 2.10 ± 1.52 mm/yr
Seasonal Cycle Range	Min. −89 mm (April); Max. +59 mm (September)
Interannual Variation (from 1980)	Min. −20 mm (1988); Max. +21 mm (1997)

Sea Level Trends and Cycles from Crescent City, California, Station 9419750

Long-term Sea Level Trend	Decreasing 0.65 ± 0.36 mm/yr
Seasonal Cycle Range	Min. −87 mm (May); Max. +85 mm (January)
Interannual Variation (from 1980)	Min. −20 mm (1989); Max. +28 mm (1998)

Extremes (1991–2011)

Maximum	11.461 m on 6 February 1998
Minimum	8.017 m on 18 May 2003

A sample section of the tide gauge record, again extracted from the CO-OPS website, is reproduced in **Figure 5**. Deviations (or residuals) from the astronomically predicted tide can be several cm and the variability strong. In particular, the highest water level reported for the Arena Cove gauge is 1.056 m above MHW (6 February 1998), so the use of MHW as the zero level of modeled sea level may underestimate the truly worst case. While the simultaneous arrival of the crest of a large tsunami at high tide during a storm surge has low probability, a feature of the simulated events reported below is that sustained oscillations at a resonant period may extend the duration of the threat. This effect is notorious at Crescent City, California, which is frequently the most heavily impacted U.S. West Coast location for remote events.

3.2.3 The CFL condition and other considerations for grid design

Water depth-dependent wave speed, in conjunction with the spacing of the spatial grid representation, places an upper limit on the time step permissible for stable numerical solutions employing an explicit scheme. This is the CFL (Courant-Friedrichs- Levy) limit, which requires careful consideration when the grids employed for a reference or forecast model are being designed. Finer-scale spatial grids, or greater water depths, require shorter time steps, thereby increasing the amount of computation required to simulate a specific real-time interval.

Another feature of the application of gridded numerical solutions to the tsunami wave problem is the shortening that the wave train encounters in moving from deep water onto the shelf. In deep water, a grid spacing of 4 arc min (of latitude and longitude, corresponding to ~7 km) is normally used to represent propagating wave trains with a typical wavelength of the order of a few hundred kilometers. The stored results of such propagation model runs are typically decimated by a factor of 4, resulting in a database of ~30 km spacing (and 1 min temporal sampling) with which to generate the boundary conditions for the outermost (A grid) of the nested grids in a model solution. The extraction of the boundary conditions (of wave height and the two horizontal velocity components) is achieved by linear interpolation in space and time. To provide realistic interpolated values, the stored fields for these variables must be smoothly varying and have adequate sampling in space and time to resolve their structure. This necessitates the placement of the outer boundary of the forecast model domain well offshore. The presence of the Mendocino Escarpment is another incentive to do so, to ensure that its role in topographic steering of trans-Pacific wave trains is adequately represented.

Figure 6 illustrates the placement of the model domain in its west coast setting. The outermost A grid covers the entire region shown; embedded in it is the B grid, which covers most of Mendocino County. The innermost C grid, with the finest spatial resolution, spans the region north and south of Point Arena. A number of nearby communities where runups are mentioned in the historical record are marked in red. The tsunami-capable tide gauges of the region, the closest of which are Point Reyes to the south and North Spit to the north, are indicated as black triangles. Almost directly offshore is DART 46411. This would play a major role in the detection of regionally generated waves. Its offshore location cleanly registers moderate to large tele-tsunamis and could, potentially, refine a local forecast that was initially based on DART array elements closer to the source. Red, green, and magenta lines indicate, using the color-convention employed in the USGS/NEIC (National Earthquake Information Center) online earthquake resources, the three

types of fault that radiate from the triple junction off Cape Mendocino. To the south is the strike-slip San Andreas Fault, skirting the coastline north of San Francisco Bay before entering the ocean within the C-grid domain. The Mendocino Escarpment is dramatic evidence of the ridge fault extending offshore, but of most concern as a local source of tsunamis is the Cascadia Subduction Zone. The two southernmost pairs of the unit source set used to represent it fall within the A-grid domain. A "beachball" that visually represents the source mechanism marks the location of the 1992 Mendocino event, which was the last significant subduction event in Cascadia (at the time this report was written).

3.2.4 Specifics of the model grids

After several rounds of experimentation, the extents and resolutions of the nested grids for the reference and forecast models were chosen; these are illustrated in **Figures 7** and **8** and details are provided in **Tables 4** and **5**. The reference and forecast model grid pairs (A and B level) have the same extent, differing only in resolution. The C grid domain is, however, slightly larger for the reference than for the forecast model; the dimensions of the latter being reduced to achieve a shorter run time appropriate to operational use. The corresponding panels in the figures employ the same depth contours and color palette. Rectangles drawn in red for the A and B grid panels indicate the extent of the embedded grid; where appropriate the blue rectangles indicate the less extensive forecast model C grid. Superimposed in the C-grid panels is the network of rivers, creeks, and roads. The thick red line marks State Hwy 1, also called the Shoreline Highway.

Both C grids lie entirely within the NGDC-provided DEM; A and B grids include bathymetry and topography from other DEM datasets available at NCTR. Some smoothing and editing were necessary to eliminate erroneous points or grid features that tend to cause model instability. For example, "point" islands, where an isolated grid cell stands above water, are eliminated, as are narrow channels or inlets one grid-unit wide; these tend to resonate in the numerical solution. Large depth changes between adjacent grid cells can also cause numerical problems; customized tools (such as "bathcorr") are available to correct many of these grid defects.

Details of the model grids are provided in **Tables 4** and **5**. The latter lists the maximum depth, the CFL time step requirement that must not be exceeded, and the actual time steps chosen for the reference and forecast model runs. Since the numerical solutions in the three grids proceed simultaneously in the current version of MOST employed by SIFT, there is a requirement that the A- and B-grid time steps be integer multiples of the (innermost) C-grid time step, in addition to satisfying the appropriate CFL requirement. For both reference and forecast models, the CFL requirement of the C grid was the most stringent. The values chosen are shown in **Table 5**, and are such that an integer multiple of each time step ($20\times$ for the forecast model; $50\times$ for the reference model) is identically 30 sec, the chosen output time interval for both models. When run on an Intel® Xeon® E5670 2.93 GHz processor, the forecast model produces 4 hr of simulation in 9.5 min, within the desired 10 min value for this metric.

3.2.5 Model run input and output files

In addition to providing the bathymetry file names, the appropriate time step, and A and B grid multiples as provided in **Table 5** above, it is necessary to provide a number of additional parameters in an input file. These include the Manning friction coefficient (n), a depth threshold to determine when a grid point becomes inundated, and the threshold amplitude at the A-grid boundary that will start the model. An upper limit on wave amplitude is specified in order to terminate the run if the waves grow beyond reasonable expectation. Standard MOST values are used: $n2 = 0.0009$ for the friction coefficient (appropriate for natural channels and flood plains) and 0.1 m for the inundation threshold. The latter causes the inundation calculation to be avoided for insignificant water encroachments that are probably below the level of uncertainty in the topographic data. Inundation can, optionally, be ignored in the A and B grids, as is the norm in the (non-nested) MOST model runs that generate the propagation database. When A- and B-grid inundation is excluded, water depths less than a specified "minimum offshore depth" are treated as land; in effect, a "wall" is placed at the corresponding isobath. When invoked, a value of 1 m is applied as the threshold, although A and B inundation is normally permitted as a way to gain some knowledge of tsunami impact beyond the scope of the C-grid domain. Other parameter settings allow decimation of the output in space and/or time. As noted above, 30 sec output has been the target and output at every spatial node is preferred. These choices avoid aliasing in the output fields that may be suggestive of instability (particularly in graphical output) when none, in fact, exists.

Table 4. Specifics of the reference and forecast model grids employed for Arena Cove, California. For the paired values in the resolution and grid points columns, the zonal (east to west) value is listed first, followed by the meridional (north to south).

Table 4: Specifics of the reference and forecast model grids employed for Arena Cove, California. For the paired values in the resolution and grid points columns, the zonal (east to west) value is listed first, followed by the meridional (north to south).

Reference Model for Arena Cove, California

Minimum offshore depth: 1.0 m; Water depth for dry land: 0.1 m; Friction coefficient (n^2): 0.0009; CPU time for a 4-hr simulation: 326 min

Grid	Zonal Extent		Meridional Extent		Resolution	Grid Points
A	128.00°W	121.50°W	36.00°N	42.50°N	30" × 30"	781 × 781
B	124.55°W	123.00°W	38.35°N	39.80°N	6" × 6"	931 × 871
C	123.85°W	123.60°W	38.82°N	39.03°N	1" × 1"	901 × 757

Forecast Model for Arena Cove, California

Minimum offshore depth: 1.0 m; Water depth for dry land: 0.1 m; Friction coefficient (n^2): 0.0009; CPU time for a 4-hr simulation: 9.5 min

Grid	Zonal Extent		Meridional Extent		Resolution	Grid Points
A	128.00°W	121.50°W	36.00°N	42.50°N	60" × 60"	391 × 391
B	124.55°W	123.00°W	38.35°N	39.80°N	24" × 24"	234 × 291
C	123.78°W	123.65°W	38.89°N	39.02°N	2" × 2"	235 × 313

CPU times for a 4-hr simulation are based on use of a single Intel® Xeon® E5670 2.93GHz processor.

Table 5. Grid file names and grid-related parameters for Arena Cove, California. The time steps for the A and B grids must be integer multiples of the basic time step chosen for the C grid

Table 5: Grid file names and grid-related parameters for Arena Cove, California. The time steps for the A and B grids must be integer multiples of the basic time step chosen for the C grid.

Grid	File Name	Maximum Depth (m)	Minimum CFL (s)	Model Time Step (s)	Water Cells
A	ArenaCoveCA_RM_A	5002	3.350	3.0 (5×)	436,966
	ArenaCoveCA_FM_A	5005	6.689	6.0 (4×)	109,323
B	ArenaCoveCA_RM_B	3781	0.7559	0.6 (1×)	485,760
	ArenaCoveCA_FM_B	3776	2.893	1.5 (1×)	40,535
C	ArenaCoveCA_RM_C	143.6	0.6423	0.6	434,701
	ArenaCoveCA_FM_C	94.4	1.526	1.5	37,611

Finally, the input file (**Table 6**) provides options that control the output produced. Output of the three variables—wave amplitude, zonal (positive to the east) velocity, and meridional (positive to the north) velocity—can be written (in netCDF format) for any combination of A, B, and C grids. These files can be very large. A separate file, referred to as a SIFT file, contains the time series of wave amplitude at each time step at discrete cells of a selected grid. Normally, the time series at a "reference" or warning point, typically the location of a tide gauge, is selected to permit validation in the case of future or historical events. The SIFT file output also includes the distribution of the overall minimum and maximum wave amplitude and speed in each grid. By contrast with the complete space-time results of a run, the SIFT file (also netCDF) is very compact, and, if more than a single grid point is specified, a broader view of the reponse is provided.

Table 6. Model input file for Arena Cove, California.

Parameters	Reference model	Forecast model
Minimum amplitude of input offshore wave (m)	0.001	0.001
Input minimum depth for offshore (m)	1	1
Input "dry land" depth for inundation (m)	0.1	0.1
Input friction coefficient (n^2)	0.0009	0.0009
A and B grid runup flag (0 = disallow, 1 = allow)	1	1
Blow-up limit/max eta before blow-up (m)	900.0	900.0
Input time step (sec)	0.6	1.5
Input number of steps	48000	19200
Compute "A" arrays every nth time step, n=	5	4
Compute "B" arrays every nth time step, n=	1	1
Input number of steps between snapshots	50	20
…Starting from	0	0
…Saving grid every nth node n=	1	1
A-grid bathymetry file	ArenaCoveCA_RM_A.most	ArenaCoveCA_FM_A.most
B-grid bathymetry file	ArenaCoveCA_RM_B.most	ArenaCoveCA_FM_B.most
C-grid bathymetry file	ArenaCoveCA_RM_C.most	ArenaCoveCA_FM_C.most
Directory of source files	./	./
Directory of output files	./	./
netCDF output for A, B, C, SIFT	1 1 1 1	1 1 1 1
Number of time series locations	1	1
Grid & cell indices for reference point	3 500 417	3 125 254

By default, two additional output files are generated. A "listing" file summarizes run specifications, progress, and performance in terms of run time, as well as information to determine the reason, should a run not start or terminate early. A "restart" file is produced so that a run can be resumed from the time it ended, either normally or by operator intervention.

The input files described above are specific to the model itself. For an actual run, the program must be pointed toward the files that contain the boundary conditions of wave amplitude (H) and velocity components (U, V) to be imposed at the A-grid boundary. Time-varying conditions are generally extracted as a subset of a basin-wide propagation solution (either a single unit source or several, individually scaled and linearly combined) that mimics a particular event. These boundary forcing files typically consist of 24 hr of values (beginning at the time of the earthquake), sampled at 1 min intervals and available on a 16 arc min grid. Occasionally, for more remote seismic sources or when delayed arrival of secondary waves due to reflections are a concern (as has been seen at Hawaii), the time span of the propagation run available for forcing is extended beyond one day.

3.3 Results and Discussion

Before proceeding to an extensive suite of model runs that explore the threat from various source regions to the Point Arena area in California, the stability of the model is tested in both low and extreme amplitude situations. The former we refer to as "micro-tsunami" testing, where the boundary forcing is at such a low level (but not precisely zero) that the response is expected to be negligible. These tests can be highly valuable in revealing localized instabilities that may result from undesirable features in the discretized bathymetric representation. Inlets or channels that are only one grid-cell wide may "ring" or resonate in a non-physical way in the numerical solution. An instability may not grow large enough to cause the model to fail but, in a run with typical tsunami amplitudes, may be masked by actual wave variability.

Forcing by extreme events, termed "mega-tsunami" events, is also tested. In addition to the need to test model stability under such circumstances, there is a parameter in the input file that truncates the run if a prescribed threshold is exceeded. For operational use, the threshold must be set high enough so that an extreme event run is not unnecessarily terminated. Both tests should be performed for test sources whose waves enter the model domain from different directions since, although stable for one set of incoming waves, an instability may be encountered for another. The micro- and mega-tsunami testing of the forecast and reference models is reported in the following subsections. Further evidence of stability is provided by the extensive set of scenarios, aimed at exploring the dependence of impact to source location, described later in the report and used in independent testing by other members of the NCTR team prior to the model's release for operational use.

3.3.1 The micro-tsunami tests

Three micro-tsunami test cases (see **Table 7**) were run representing sources in the western Aleutians, the Philippines, and south of Japan. Based on sources from the propagation database (Gica *et al*., 2008), their amplitudes were scaled down by a factor of 100 to mimic a Mw 6.1667 / Slip 0.01 m source rather than the Mw 7.5 / Slip 1 m standard. A number of grid cells in the B and C grids emerged as potential sources of instability. Generally, these were minor indentations of the coastline, barely resolved by the grids, or narrow channels. Also to be tested further is the area northwest of the Point Arena Light where the rugged seabed reveals several past water level stands. A limited number of grid cells in the outermost (A) grid required correction. These were generally associated with non-physical features in the topographic database, such as a track of ship-based soundings that were improperly merged with other data sources. After an iterative process of grid correction and retesting using these micro-tsunami sources, both the reference and forecast model grids were deemed satisfactory (as illustrated in the upper panel of **Figure 9**) and the testing of extreme and historical events could begin. The lower panel of **Figure 9** illustrates a step in the process where a deficiency in the reference model grid generated a mild instability (in the EPSZ B19 microtsunami scenario—see **Table 7**), causing the reference model time series at the reference point, initially in close agreement with the forecast model, to develop unrealistic, high-frequency oscillations. Though still generally tracking the forecast model result and not growing without bound, the feature could behave erratically in simulating real events. Modification of the reference model bathymetry eliminated the problem, and tests involving other micro-tsunami sources (RNSZ B14 and ACSZ B6) did not reveal other issues.

3.3.2 The mega-tsunami tests

The record of tsunami impact on the northern California coast discussed in this report reveals that sources around the entire periphery of the Pacific can be felt. Indeed, the catastrophic Indian Ocean tsunami of 2004 was detectable at Arena Cove, as it was throughout the global ocean. A broad suite of 19 extreme events (termed mega-tsunamis), whose locations are standard for Pacific basin forecast model testing, are listed in **Table 7**, and their locations are shown in **Figure 10**. Unit source subduction zone acronyms (e.g., ACSZ, stretching from the Aleutians to Cascadia) are provided in Appendix B. To simulate each mega-tsunami source, 10 A–B pairs of unit sources are used with an evenly distributed slip of 25 m. As described by Gica *et al*. (2008), each unit source represents a 100×50 km area of the fault surface, with the long axis parallel to the plate boundary. Row B is shallowest, sloping from a nominal depth of 5 km (unless the USGS provides a depth estimate based on the earthquake catalogs). Row A is deeper, followed by rows Z, Y, X, etc. where appropriate. Thus, the mega-tsunami sources represent 1000 km long ruptures with a width of 100 km and corresponding magnitude of Mw 9.3.

Discussion of the entire set in greater detail is provided once the validity of the forecast model has been established. Here we focus on a subset of three synthetic cases, highlighted in **Figure 10** and **Table 7**, to contrast the forecast model with the more highly resolved reference model. The results are presented in **Figures 11–13**, with the time series at the reference point (the Arena Cove tide gauge) shown in the upper panel and the amplitude and current pattern at a selected time shown below. The black and red curves represent the reference and forecast model, respectively; the green line identifies the time at which the comparison in the lower panel was made. Inset in the lower

panels are enlargements of the area around Arena Cove. It is noticeable that, in all three of the cases shown, the reference model tends to oscillate longer and have somewhat larger amplitude than does the forecast model, although the two solutions are in close agreement for the first few tsunami waves. This is likely a physical reality: the more highly resolved bathymetry and coastline of the reference model provides greater scope for nonlinear features or reflected waves to develop. This observation suggests a caveat to operational use of the forecast model: while accurate portrayal of the early history of an event is to be expected, the duration of the event and the amplitude of later waves may be underestimated.

The snapshot comparisons in the lower panels of **Figures 11** and **12** are quite reasonable, illustrating that the solutions match not just at the reference point. It is worth noting too that, although the ACSZ 56–65 mega-tsunami event represents a massive Cascadia tsunami, the scale of impact to the Arena Cove area (~3 m) is not substantially greater than from trans-Pacific locations (KISZ 1–10 off Kamchatka and NTSZ 30–39 near Samoa.) The Crescent City response to the same synthetic Cascadia mega-tsunami event exceeds 10 m (Arcas and Uslu, 2010). It would appear that the energy propagated alongshore to the south, possibly with some sheltering by Cape Mendocino, is reduced, and that perhaps the greatest impact to Arena Cove may be associated with source regions elsewhere in the Pacific basin.

In **Figure 13**, the comparison time was intentionally chosen later in the event as a counterexample. At the warning point and nearby, the forecast and reference models may be in reasonable agreement, but the broader wave patterns may have substantial phase differences. The comparisons in these lower panels are restricted to the portion of C-grid area common to both models. Waves generated by reflections in the larger reference model C grid will impinge on the common domain as the solution proceeds, so the greatest disparities are to be expected at the northern and southern forecast model boundaries. However, **Figure 13** and other "snapshot" comparisons show that the effect is quite minor.

Before proceeding to validate the model with historical events, one other synthetic event is standard in the testing protocol: a moderate source of Mw 7.5 at a remote location. A single unit source near Samoa (NTSZ B36) is employed, and its representation by the reference and forecast model are compared in **Figure 14**. Such an event results in a response of about 2 cm in Arena Cove sea level, and there is excellent agreement between both model representations in the earlier portion of the event.

Overall, the close agreement between the first wave arrival time and waveform and the general range of variation of the two model representations in synthetic scenarios (even though the amplitude and phase is not always well-matched for later waves) suggest that the forecast model is performing well, and that we can confidently proceed to model real events.

Table 7. Synthetic tsunami events employed in Arena Cove model testing.

Scenario	Source Zone	Tsunami Source	α [m]
Mega-tsunami (Mw 9.3) Scenario			
KISZ 1–10	Kamchatka-Kuril-Japan-Izu-Mariana-Yap	A1–10, B1–10	25
KISZ 22–31	Kamchatka-Kuril-Japan-Izu-Mariana-Yap	A22–31, B22–31	25
KISZ 32–41	Kamchatka-Kuril-Japan-Izu-Mariana-Yap	A32–41, B32–41	25
KISZ 56–65	Kamchatka-Kuril-Japan-Izu-Mariana-Yap	A56–65, B56–65	25
ACSZ 6–15	Aleutian-Alaska-Cascadia	A6–15, B6–15	25
ACSZ 16–25	Aleutian-Alaska-Cascadia	A16–25, B16–25	25
ACSZ 22–31	Aleutian-Alaska-Cascadia	A22–31, B22–31	25
ACSZ 50–59	Aleutian-Alaska-Cascadia	A50–59, B50–59	25
ACSZ 56–65	Aleutian-Alaska-Cascadia	A56–65, B56–65	25
CSSZ 1–10	Central and South America	A1–10, B1–10	25
CSSZ 37–46	Central and South America	A37–46, B37–46	25
CSSZ 89–98	Central and South America	A89–98, B89–98	25
CSSZ 102–111	Central and South America	A102–111, B102–111	25
NTSZ 30–39	New Zealand-Kermadec-Tonga	A30–39, B30–39	25
NVSZ 28–37	New Britain-Solomons-Vanuatu	A28–37, B28–37	25
MOSZ 1–10	Manus–Oceanic Convergent Boundary	A1–10, B1–10	25
NGSZ 3–12	North New Guinea	A3–12, B3–12	25
EPSZ 6–15	East Philippines	A6–15, B6–15	25
RNSZ 12–21	Ryukyu-Kyushu-Nankai	A12–21, B12–21	25
Mw 7.5 Scenario			
NTSZ 36	New Zealand-Kermadec-Tonga	B36	1
Micro-tsunami (Mw 6.5) Scenario			
EPSZ B19	East Philippines	B19	0.01
RNSZ B14	Ryukyu-Kyushu-Nankai	B14	0.01
ACSZ B6	Aleutian-Alaska-Cascadia	B6	0.01

3.3.3 Model validation with historical events

We now proceed to examine, for the historical cases highlighted in **Table 1a** and **Figure 4**, how well the reference and forecast model solutions compare with observation. Since the observations are limited to the tide gauge records or runup reports in Arena Cove, the purpose of the lower panels is only to illustrate the agreement between the models.

The results displayed and described below represent the large 1946 Unimak and 1964 Alaska events and three more recent ones: 2006 Kuril (which has been extensively studied), 2009 Samoa, and 2010 Chile. The latter three events occurred subsequent to the installation of an improved tide gauge at Arena Cove. In Section 4.6, the Tohoku tsunami of 11 March 2011 is discussed. The event occurred while this report was undergoing internal review at NCTR, but the forecast model was available for use in real-time circumstances. Another difference between the earlier and more recent events is that the source characterization for the former is based on the literature, with the source mechanism estimated from the seismic record. The 2006 Kuril event was the first

15

substantial event for which direct observation of the tsunami wave train was available from multiple deep-water DART sites. As such, its source characteristics, and those for the 2009 Samoa, 2010 Chile, and 2011 Tohoku events are better suited to tsunami modeling and forecast; those based on seismic data only may suffer from the defect that earthquakes differ in their ability to generate tsunami waves. An extreme case of this is the 1896 Sanriku event, which is modeled and briefly discussed in Section 4.4. It was referred to as a "tsunami-earthquake" (Dudley and Lee, 1998), causing devastating losses in Japan despite its modest magnitude and scant warning in the form of ground motion.

Even in the case of source characterizations based on DART detection and inversion, one should bear in mind that perfect agreement between the model wave and observation is unlikely. For one thing, the DART sites used in the inversion process may be well described by a linear combination of unit source functions but their placement may limit the ability to predict basin-wide energy propagation. Ideally, one might hope to refine the model solution in light of DART observations closer to the impact site. The deep-water waves in the far field (e.g., 46411, for Arena Cove) may, however, fall below the DART detection threshold. Neither are the tide gauge observations, available for comparison with model prediction, perfect. They may include noise, possibly amplified by harbor resonances and wind wave activity.

The 1946 Unimak and 1964 Alaska events were widely felt along the U.S. West Coast, although the greatest impact was to the Hawaiian Islands. Reported runups at Arena Cove were 2.40 and 1.83 m, respectively, comparable in the case of 1964 Alaska (but somewhat lower for 1946 Unimak) to the modeled responses shown in **Figures 15** (1946 Unimak) and **16** (1964 Alaska). The reference and forecast model solutions match well, both in the time series and in the amplitude and velocity field at the selected comparison time.

For the more recent events, where time series at Arena Cove permit direct intercomparison with the reference and forecast model predictions, the results are presented in **Figures 17–19**. For the 2006 Kuril event (**Figure 17**), the reported 61 cm runup at Arena Cove exceeds, by a factor of about 2, the amplitude of the tide gauge oscillations. Particularly for the early waves, the model gives a reasonable representation of both the amplitude and timing of the observations. The time axis is in model hours and the discrepancy in the first wave arrival time is about 5 min, just 1% of its transoceanic travel time.

For the 2009 Samoa event (**Figure 18**), the reported runup at Arena Cove is 44 cm, which may correspond to later in the record when harbor resonances may have been excited. For the early waves, the amplitude of the observations is closer to 20 cm, and, though it does reasonably well in predicting the early timing and the sequence of waves, the model underestimates the amplitude by about a third. For the 2010 Chile event (**Figure 19**), the amplitude of the observations is replicated more closely. Again though, the reported runup of 35 cm is substantially greater than the greatest positive excursion of the de-tided observations as displayed.

Considering the above results, the main discrepancy appears to be the mismatch between reported runup and the processed sea level time series. Some possible explanations come to mind. Runup is defined as maximum elevation above the predicted tide, which may not include seasonal or meteorologically driven departures, which, as illustrated in **Figure 5**, can be several centimeters.

Another possibility is that the overall maximum of the tide gauge record may be aliased by high-frequency variability, which was smoothed somewhat by a 3-point running average in the preparation of these graphics.

3.3.4 Further historical simulations

The above analysis has documented good agreement between the forecast model and the slower-running reference version. This permits us to simulate the balance of historical cases where impacts to Arena Cove and northern California have been reported with the forecast model alone. These runs are used to further validate the stability of the forecast model, but also provide some information on the exposure of the region to tsunamis generated at various points on the periphery of the Pacific.

In **Figures 20–24**, the full set of observed records at Arena Cove (or proxy sites in some cases) are compared with forecast model prediction. Also provided for each event is the state of the tide at Arena Cove. While probably of little concern for weak events, this may be a factor in the impact of larger ones. Reported runup is included in each case, but as noted earlier, this may be only loosely related to the plotted series. In each case, the forecast model series is shown in black and the observations are drawn in red. Although studies of the global ocean response to the 2004 Indian Ocean tsunami suggest a runup of 19 cm in Arena Cove, the signal is largely obscured by noise. An attempt was made to employ global ocean model results (on a coarser grid than is available for the Pacific propagation database) to drive the Arena Cove forecast model; the results were unsatisfactory and will not be presented. When a better-resolved global solution is available, this event may be added to the suite employed for forecast model testing, since it should shed light on the extent to which bathymetric resolution may impact arrival time accuracy.

The sequence begins with a cautionary tale: the "tsunami-earthquake"-induced 1896 Sanriku event (upper left panel, **Figure 20**). This was modeled by a suitably positioned unit source (KISZ B25) with the slip appropriate to the reported Mw 7.6 magnitude. As shown, such an event would be expected to generate only a few centimeters signal at Arena Cove. Large runups occurred (1 m in the case of the nearby town of Mendocino), illustrating the fact that direct observation of deep water waves is needed for realistic forecasting. The depth and frequency of seafloor motion for this event was such that the earthquake magnitude poorly indicated its devastating tsunami-generating potential to Japan's Sanriku coast.

Next, we consider the set of events from 1946 to 1964 that were felt in or near Arena Cove. During this time, a tide gauge had not yet been installed and the DART array was still in the future. (1946 Unimak and 1964 Alaska were shown earlier.) In each case the source was represented by a weighted group of unit sources from the propagation database or constructed to match source characteristics appearing in the literature (see **Table 1**; Tang *et al.*, 2006).

A number of other events between 1994 (East Kuril) and 2003 (Rat Island), listed in **Table 1** and illustrated in **Figures 21** and **22**, generated weak responses in Arena Cove. In the case of the 1994 East Kuril event, although the match is quite good, the presence of substantial noise in the tide gauge record in advance of the waves' arrival suggests a limitation on the detection of weak tsunami signals. Particularly in winter months, the tide gauge record at Arena Cove can be

17

extremely noisy. This is true for the 1996 Irian Jaya event; the tide gauge records for the Chile and Kuril events of 1995 are not readily available. For the 1996 Andreanof event, the model seems to capture the timing and periodicity of the Arena Cove 2003 Hokkaido events, the match is less convincing. The 2003 Rat Island event is notable in the history of tsunami forecasting and the DART array. Based on data from early elements of the DART array of the Aleutian Islands and without the conveniences of the SIFT system for inversion, an estimate for the likely impact of this event on the Hawaiian Islands (Titov *et al.*, 2005) demonstrated the utility of direct sea level observation in tsunami forecasting.

The next set of Pacific basin historical events, depicted in **Figure 23**, are the 2006 Tonga through 2007 Peru events. The previously examined Kuril event of 15 November 2006, excluded from this set, was observed at several DART sites; it serves as a benchmark event for NCTR. The 2006 Tonga event is reported by NGDC as producing a 27 cm runup at Crescent City, California, but unfortunately, only 6 min sampled tide gauge data are available at Arena Cove. Though the arrival time and first wave shape correspond reasonably well, the amplitude of the observations is considerably less that the model predicts. For the 2006 Kuril event, the tsunami-capable instrument, with its 1-min sampling, was in place and the early waves of the event were well represented by the forecast model. The same is true of the 2007 Kuril event, which also played an important role in the development of the SIFT forecast tool. Unlike most preceding events, whose source mechanism is a reverse-thrust fault sending a leading peak toward the offshore DART sites, this was a "normal" thrust event from which a leading trough propagated. As seen in **Figure 23**, this observed time series at Arena Cove is well matched by the model.

For the 2007 Solomon event, the observations were weak and intermittent, although the amplitude of the model signal and its inclusion of larger late waves seems consonant with the data. Also shown in **Figure 23**, the 2007 Peru event was only weakly felt at Arena Cove, and one might be tempted to view the observations as noise. By shifting the model result to the right by about 10 min, it is suggested that the early event history is mimicked. Waves traveling from South America to the U.S. West Coast occasionally arrive later than the propagation model predicts, perhaps due to the model bathymetry being smoother than the real ocean. Tsunami waves travel slower in shallower water, and therefore real waves may be delayed in passing through rugged ocean regions, such as the Galapagos. Similar delays have been encountered in other forecasts, and it remains to be seen whether, as more accurate bathymetric data become available, arrival time forecasts will improve. It should be emphasized that, as a percentage of the overall travel time, these delays are quite minor.

Another event off South America, 2007 Chile, occurred late in the same year. The Arena Cove response, shown in **Figure 24**, was quite weak and difficult to match with model prediction. Two events from early 2009, also appearing in **Figure 24**, are available for study. The predicted signal from the first, near Bird's Head in Papua New Guinea, arrived at a noisy period at the Arena Cove tide gauge, and little, if anything, can be gleaned from the comparison. Two weeks later, an event of similar magnitude occurred off the Kuril Islands where tsunami waves impacting the west coast frequently originate. As seen in the lower left panel of **Figure 24**, the Arena Cove forecast model is reasonably successful in representing that response. The final event in this set, 2009 Vanuatu, is discussed below.

We now arrive at the events that were most recent at the time this report was initially written. The 2009 Samoa event was the most damaging to U.S. territory in recent years, and, although the DART array performed well in providing data to provide an accurate forecast, the proximity of the source to U.S. and Western Samoa did not permit any lead time there. This was a sizeable event, and, even as far away as Arena Cove, a runup of 44 cm was reported. As seen in **Figure 25**, the Arena Cove forecast model performs very well in replicating the early waves, though the later waves may be underestimated. This is an instance in which the reference model (see **Figure 18**) may, in light of the substantial lead-time inherent in such remote source situations, be a worthwhile option. With a workstation-level computer, the run time of the forecast model is presently about 9.5 min of wallclock time for 4 hr of simulation. With advances in computing power, or the migration of operational computing to supercomputers, it may be possible to depart from the current standard of about 10 min per 4 hr of simulation with a forecast model, perhaps even to run the basin-wide solution in real time with enhanced resolution.

Just days after the 2009 Samoa event, another occurred off Vanuatu. Though much less damaging, this event had a new feature to exercise the tsunami community. The 2009 Vanuatu case was a composite event with two earthquakes in a 15 min period. Though not yet part of the standard set of historic events for forecast model evaluation, the separate source characterizations have been established at NCTR (Yong Wei, personal communication). Blending the two forcing histories with an appropriate time delay provides the input needed for a forecast (or reference) model run, and the result for the mild response at Arena Cove is quite good. The final historical event analyzed for the initial development of this report is associated with the major earthquake that struck Chile on 27 February 2010. Causing major damage and loss of life locally, the tsunami waves propagated widely throughout the Pacific. The waves, seen at DART 32412, provided a good estimate of the remote hazard, particularly to Hawaii, indicating that wide-scale evacuation was not necessary. On the U.S. West Coast, noticeable tsunami effects were observed matching predictions. At Arena Cove, had this model been available and included in the SIFT system then, it would have been another point of success for the forecast system in the emergency response to the 2010 Chile event. As seen in **Figure 25**, there is very close agreement between the forecast model hindcast and tide gauge observation. On 11 March 2011, as this report was undergoing internal review, the Tohoku region of Honshu, Japan, was struck by a huge earthquake, generating a tsunami that caused local devastation and serious impacts throughout the Pacific basin. The forecast model for Arena Cove was employed in real time, and the results are described briefly in Section 3.3.6.

3.3.5 The Mendocino earthquake of 25 April 1992

Of special interest to northern California is the Mendocino earthquake of 25 April 1992. This has the distinction of being the most recent substantial thrust event on the Cascadia Subduction Zone. Strike-slip events are commonplace offshore in this region, as shown in **Figure 26**. The upper panels show earthquake epicenters and some fault mechanisms from the USGS/NEIC catalogs in the period 1900–2010. Most are strike-slip, with only the 1991 and 1992 events having the signature of thrust faulting, with the greater potential to generate significant vertical displacements of the seafloor. The epicenter of the 1992 event was on land to the southeast of the plate triple junction off Cape Mendocino. Uplift on the order of 1 m of a 25 km stretch of the nearshore, between Cape Mendocino and Punta Gorda to the south, was evident in a die-off of intertidal organisms, reported by Carver *et al*. (1994). Presumably extending offshore too, this deformation

is not well represented by either of the southernmost unit sources now available in the propagation database (ACSZ A65 and B65). The model predictions based on either of these unit sources with an appropriate scale factor for the magnitude 7.2 event underestimate the tide gauge signal at Arena Cove, as seen in **Figure 26**. Another feature of interest for this event, described by González *et al*. (1995), is that its proximity to shore may have generated a train of coastal-trapped edge waves. Traveling slower than normal tsunami waves taking a deep-water route, the edge waves may have extended the duration of the event at nearby locations to the north and south. This possibility, and the suggestion that the ACSZ source line should be extended at least one unit farther south, make this an event worth further study. The reference and forecast models for Arena Cove and other existing or planned West Coast models (Eureka, Crescent City, etc.) have a major role in ongoing risk assessment studies for Cascadia.

3.3.6 The Tohoku tsunami of 11 March 2011

As this report was in development, a severe earthquake and consequent tsunami occurred in the Tohoku region off the east coast of Honshu, Japan. The SIFT forecast system, ingesting timely data from nearby DART sites, performed well and provided the basis for appropriate response at those sites for which forecast models were available. Among these was Arena Cove, so it seems appropriate to add 2011 Tohoku (alternately referred to as 2011 Honshu) to the suite of historical events for which observations, and both forecast model and reference model results, are available. The results appear in **Figure 27** where, in the upper panel, the reference and forecast model time series at the Arena Cove tide gauge (black and red lines, respectively) are compared with the 1 min tide gauge record (in blue).

While the largest tsunami waves fortuitously arrived near low water for the U.S. West Coast, and the NCTR models employ MHW to represent "worst case" conditions, the agreement is excellent. As at other sites, there was a slight discrepancy in the arrival time (9 min in the case of Arena Cove); this has been compensated for in **Figure 27**. This error is < 1.6% of the overall travel time and is believed to be associated with the relatively coarse grid of the propagation database, which provides the boundary conditions of the finer-scale nested forecast and reference model grids.

After the first few waves, the timing and amplitude of crests and troughs lose synchronicity, both between the reference and forecast model and between these and the observations. Nonetheless, the character of the response is well replicated and the maximum runup agrees well with the reported 1.55 m provided by NGDC. The latter is the difference between actual and predicted sea level and suggests that, in the case of Arena Cove itself, the forecast wave height is not overly sensitive to the state of the tide, although the extent of inundation may be overstated.

The second row of **Figure 27** contrasts the reference and forecast model solutions at a time, indicated by the green line in the upper panel, where the solutions have begun to diverge. It illustrates that both wave amplitude and tsunami-induced currents are in good agreement through most of the region shown. As before, there is some nearshore discrepancy at the northern and southern limits of the C grid and near the complex topography off Point Arena Light. The lower panels of the figure contrast the reference and forecast model predictions for maximum wave amplitude. No reports of amplitude or inundation are available for comparison with these predictions, but the agreement would appear to be best near shore for this event. The maxima, in

particular, predicted for Arena Cove and the inundation near the mouth of the Garcia River and much of Manchester Beach match well. If there is error, the forecast model appears to err on the conservative side, overstating the likely impact. Other historical cases, comparing reference and forecast model predictions to observation, may weaken this as a general conclusion though it does come from the event generating the strongest signal. In the upper panels of **Figures 18** and **19** the reference model may be a better match, particularly for later waves, while for the 2006 Kuril case (**Figure 17**), neither model replicates well what may be noise in the tide gauge record.

To summarize the analysis of historical events, it would appear that the Arena Cove forecast model is capable of producing accurate forecasts for this open coast site on the U.S. West Coast. Though the tsunami waves may be difficult to detect amid the noise at the tide gauge during winter storms, the objective of producing credible forecasts of tsunami impact appears to have been met.

3.3.7 Simulation of the remaining synthetic mega-tsunami events

We conclude this section with a summary of other model runs, included to verify its stability, that provide useful information on the exposure of Arena Cove to potentially hazardous future events within the Pacific. As noted earlier, the sparse instrumental record of actual events needs to be augmented with credible scenarios to permit risk assessment. While not pretending to be a full-blown risk assessment for the Arena Cove–Manchester Beach area, the full set of mega-tsunami events modeled during stability testing can provide some early estimates.

Results for the set of 19 mega-tsunami events based on the forecast model are presented in **Figure 28**. At the center of each source zone (1000 × 100 km in extent, with the long axis aligned with the local plate boundary and a uniform slip distribution corresponding to an event magnitude of 9.3) a color-coded square represents the impact at Arena Cove. The measure of impact employed is the maximum amplitude of the predicted time series at the reference point (for the Arena Cove forecast model, the tide gauge location near the head of the pier.) There is not any simple relationship between source orientation, location, or great circle distance to Arena Cove; focusing associated with seafloor features can more than compensate for the decay associated with geometric spreading. In **Figure 29**, forecast model prediction of the inundation that might result from some of these scenarios are drawn together with (in the lower right panel) an ensemble representing the selection employed in the CalEMA study, whose inundation line is drawn in red.

3.4 Conclusions

In conclusion, good agreement between observations and model predictions for a subset of historical events, including the recent 2011 Tohoku tsunami, has been established, and the stability of the model for numerous synthetic events has been demonstrated. The reliability of the forecast model, designed to run rapidly in real-time emergency conditions, has been proven by the favorable comparison with reference model predictions, particularly during the early hours of an event. The model will be included in the SIFT system employed operationally at the Tsunami Warning Centers, and will permit the Point Arena–Manchester area of California to be added to

the coastal communities for which forecast capability is available. Additionally, this model provides a useful tool in risk assessment for the Arena Cove area.

Further tests have been made by other members of the group at NCTR, and will continue to be made by staff at the Tsunami Warning Centers and others, perhaps in training situations. Among the many related tools developed at NCTR is ComMIT (the Community Model Interface for Tsunamis; Titov *et al*., 2011), which provides a highly intuitive graphical environment in which to exercise and explore forecast models for any combination of propagation database unit sources. Were any of these avenues to reveal a problem with the model, its origin (most likely in some quirk of the bathymetric files) would be located and corrected, and the revised version would then be re-installed for operational use. The development of the forecast system is a dynamic process, with new models added (and old ones revisited) from the current list of U.S. interests and globally. As algorithms and methodologies to represent meteo- or landslide-generated tsunamis become available in the coming years, the utility of current forecast models beyond purely seismic events could well expand.

Acknowledgments

FIGURES

Figure 1. The Point Arena area of southern Mendocino County, California. Arena Cove is indicated by the red arrow.

Figure 2. Views of present-day Arena Cove, California (Photographer: Kenneth Adelman) and its appearance in the early 1900s (inset).
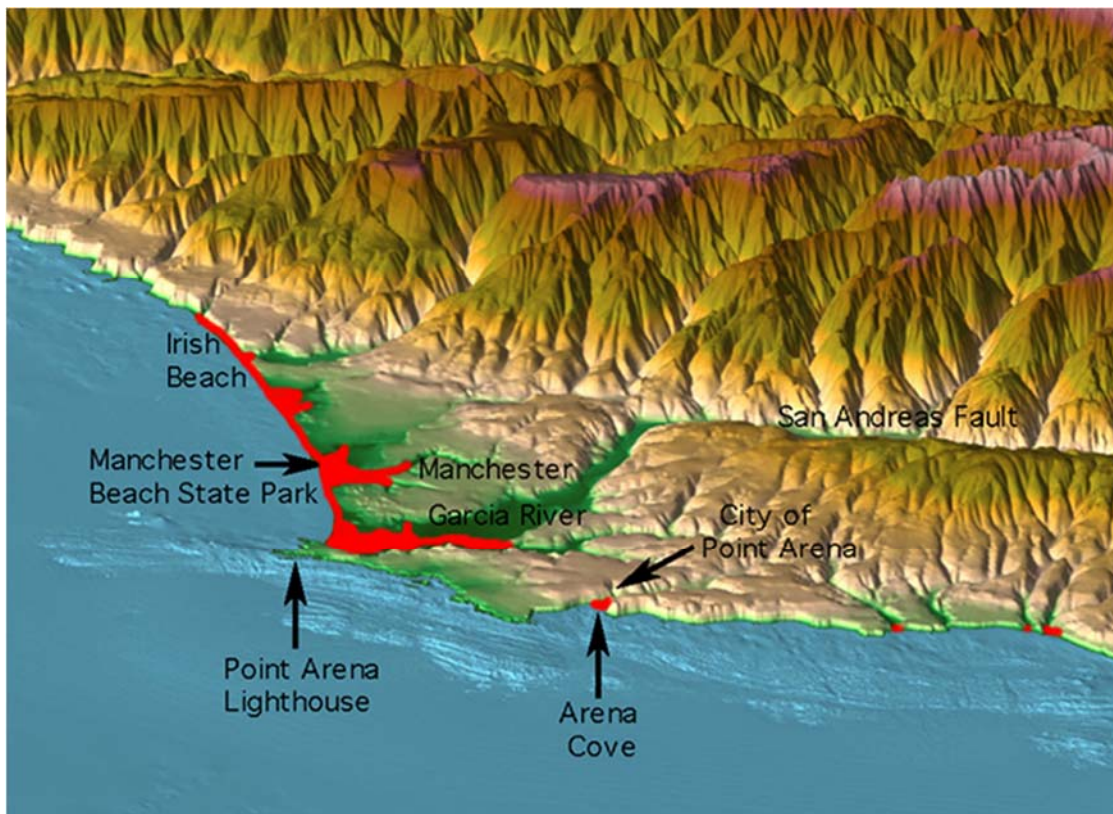
Figure 3. Extract from the oblique 3-D view of the Arena Cove digital elevation model provided by NGDC; sites of potential inundation identified by CalEMA are highlighted in red.
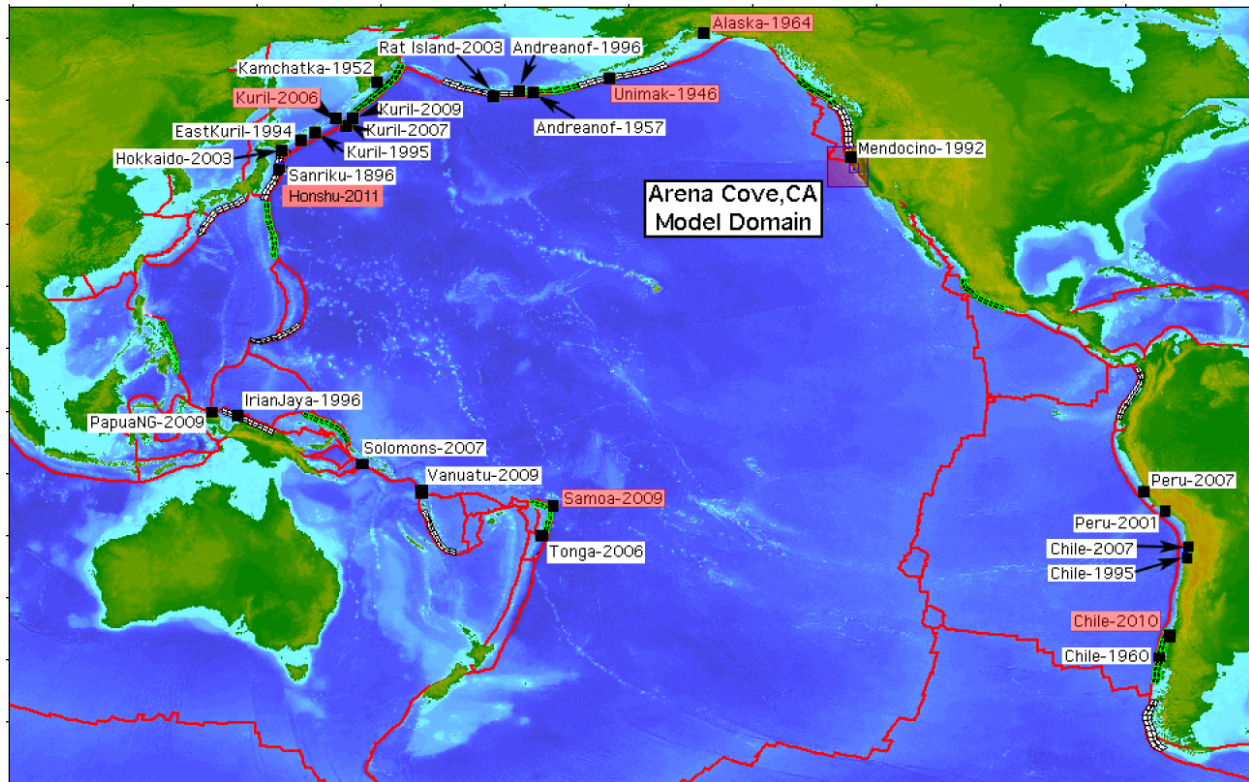
Figure 4. Distribution of the historical tsunami sources employed for the development of the Arena Cove forecast model. Those highlighted in red are more extensively investigated using the reference model.
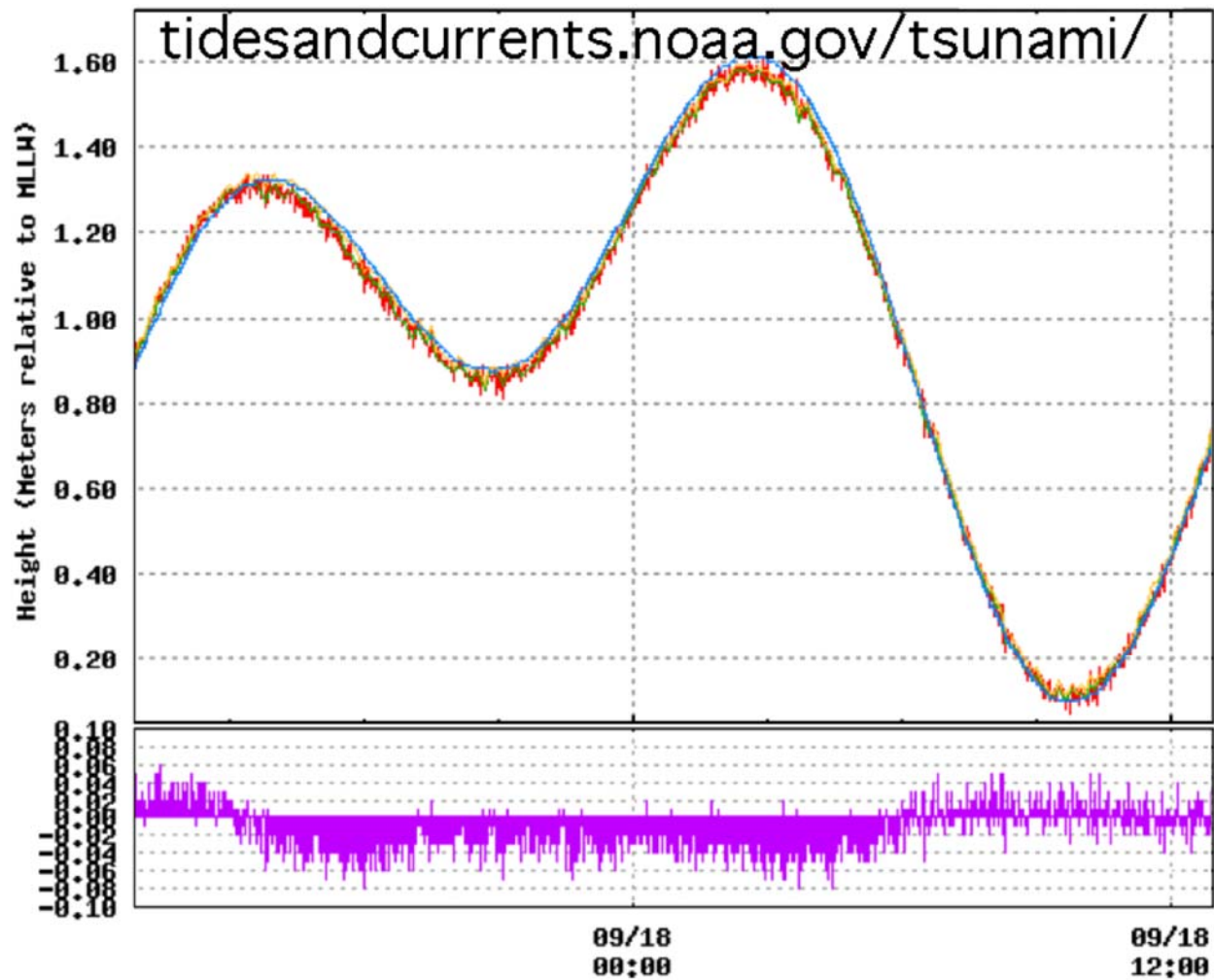
Figure 5. A sample time interval from the tsunami-capable tide gauge at Arena Cove, California, unrelated to tsunami activity.
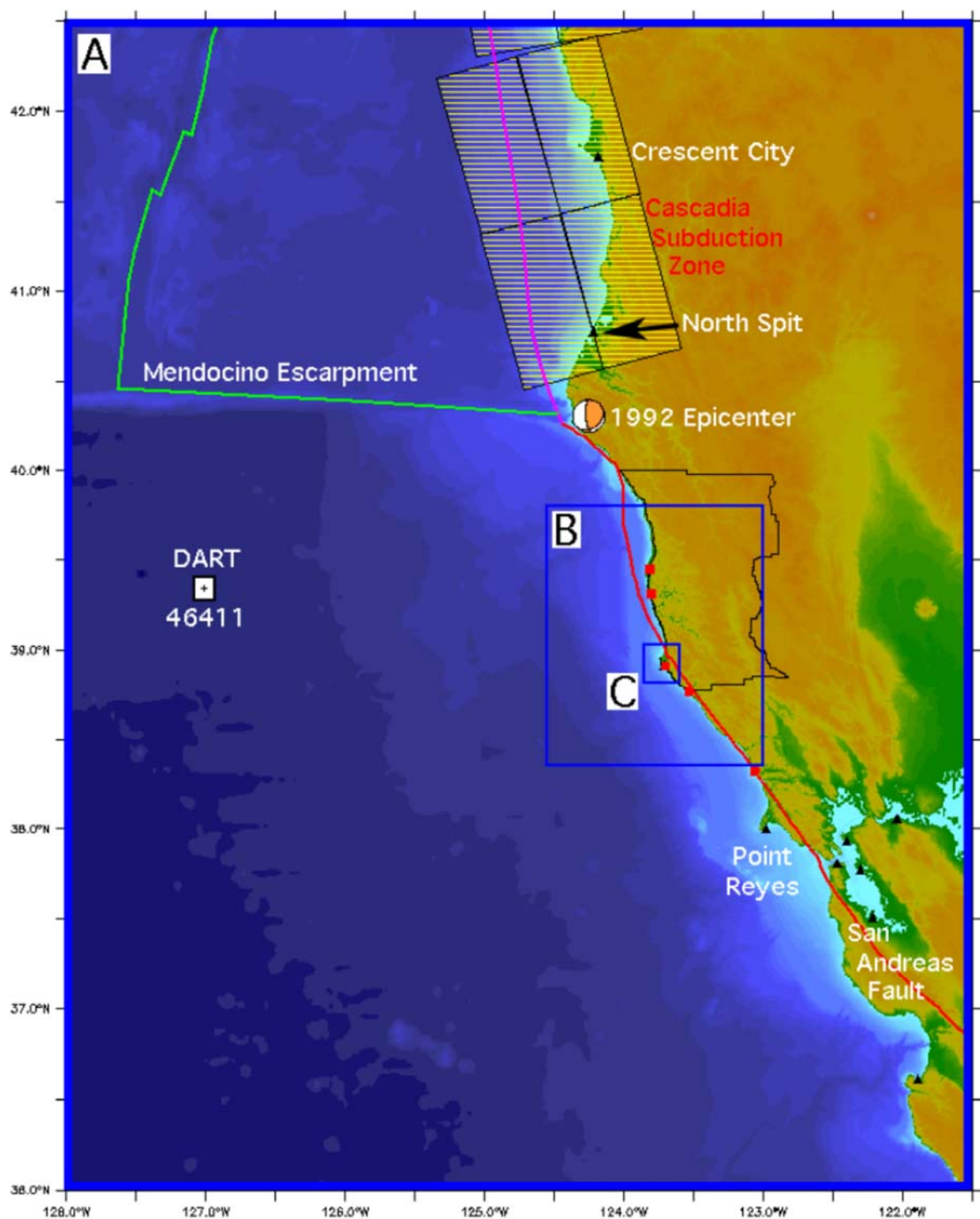
Figure 6. The setting of the Arena Cove model. Rectangles indicate the extents of the nested grids; communities within the model domain are marked in red. Tide gauge locations are drawn as black triangles; 46411 is the closest DART. Plate boundaries are shown, as are the southernmost unit sources representing Cascadia.
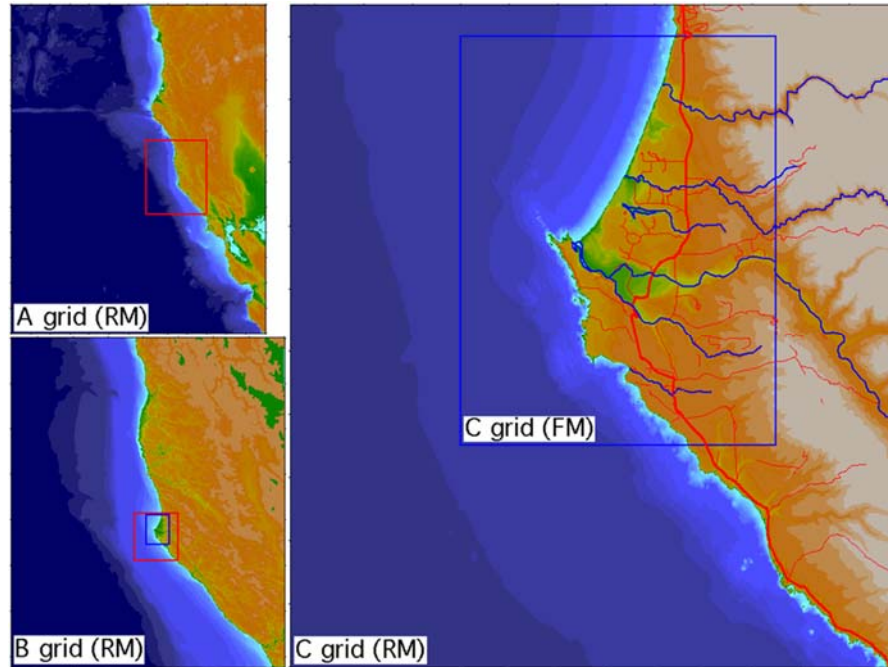
Figure 7. Nested grid representation for the Arena Cove, California, reference model (RM). Rectangles, drawn in red, indicate the placement of the next nesting level. Blue rectangles delineate the forecast model (FM) grid boundaries. Rivers and roads are marked in the C grid panel.
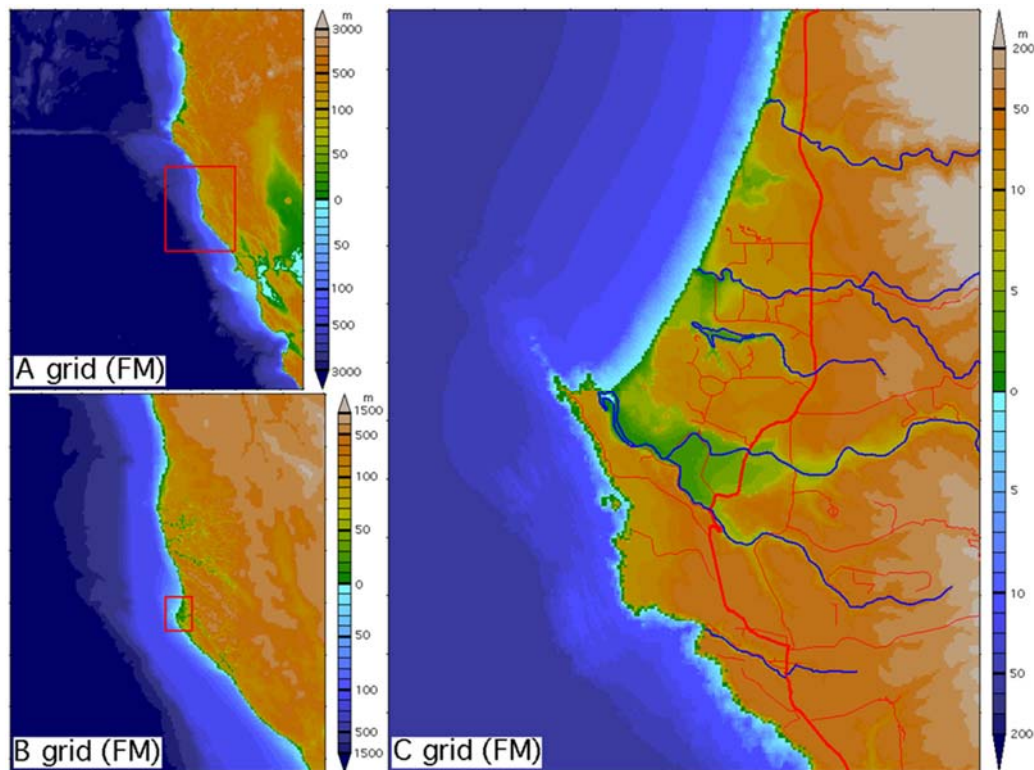
Figure 8. Nested grid representation for the Arena Cove, California, forecast model (FM). Rectangles are drawn to indicate the placement of the next nesting level. Rivers and roads are marked in the C grid panel.
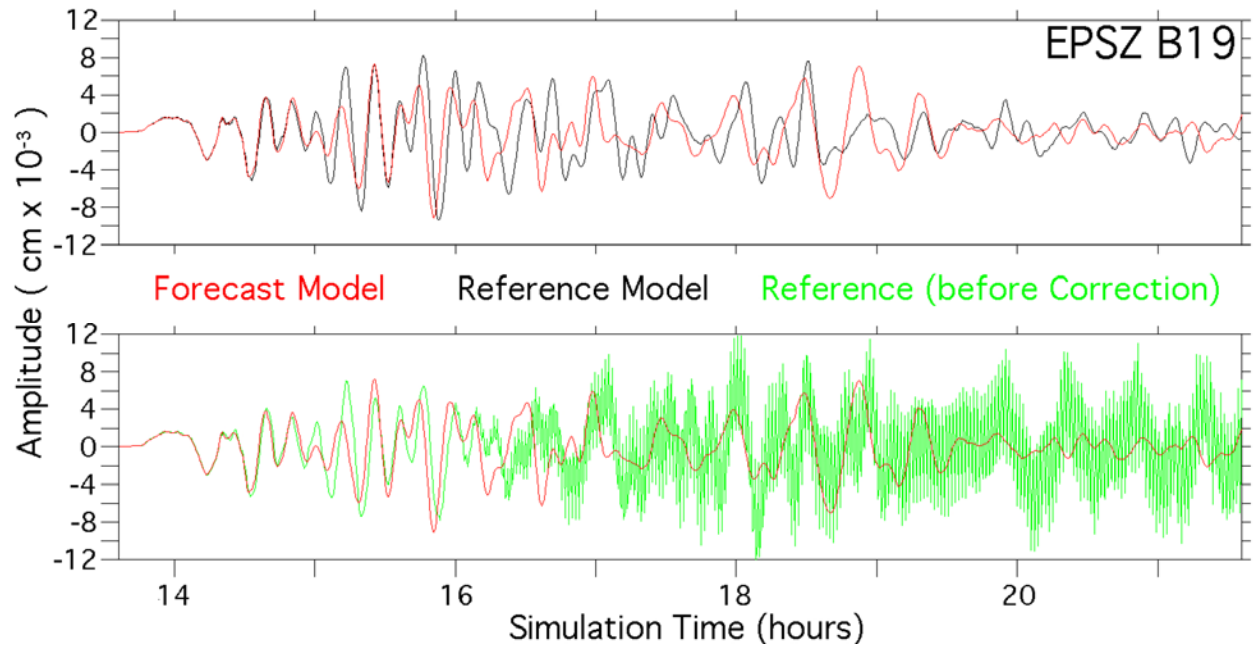
Figure 9. Comparison of the reference and forecast model time series at the warning point for micro-tsunami scenario EPSZ B19. Upper panel: Illustration of the close agreement between the reference (black) and forecast (red) model responses. Lower panel: The signature of model instability in the reference model (green) prior to finalization of its bathymetry.
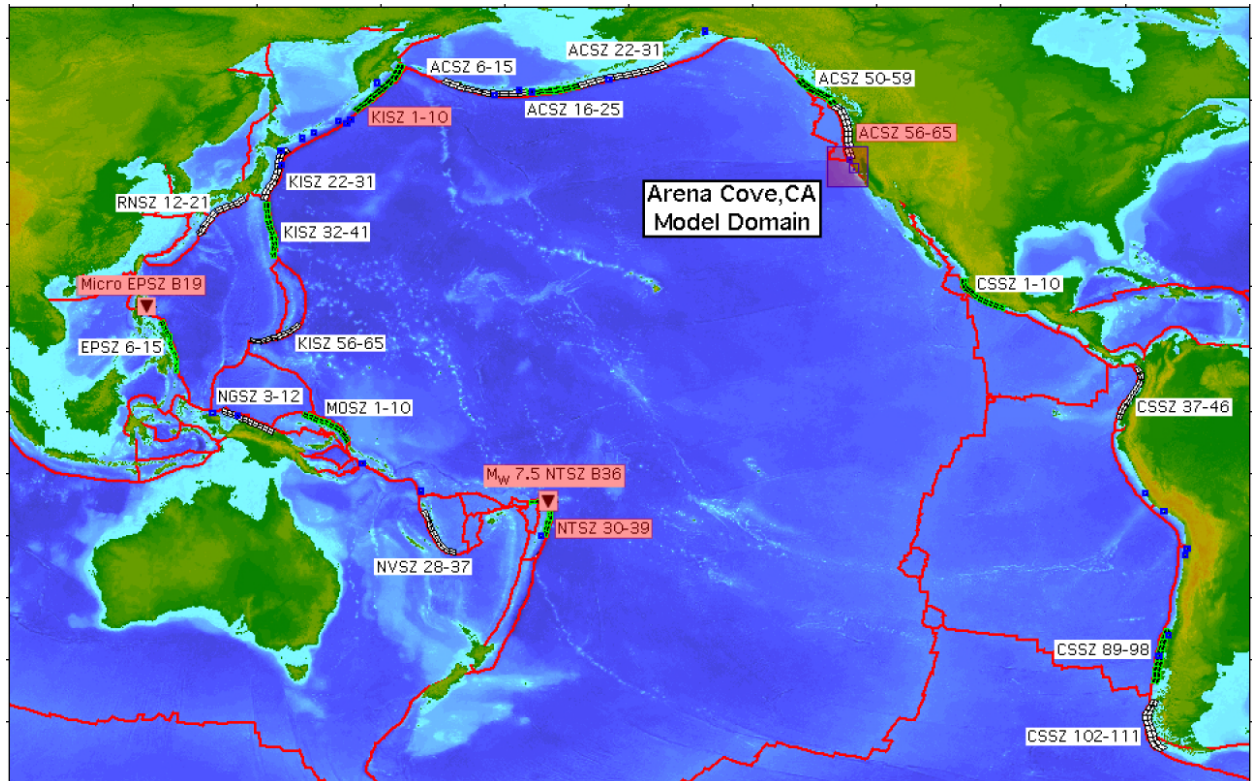
Figure 10. Locations of synthetic tsunami scenarios employed in the development of the Arena Cove model. Those highlighted in red are more extensively investigated in this report.
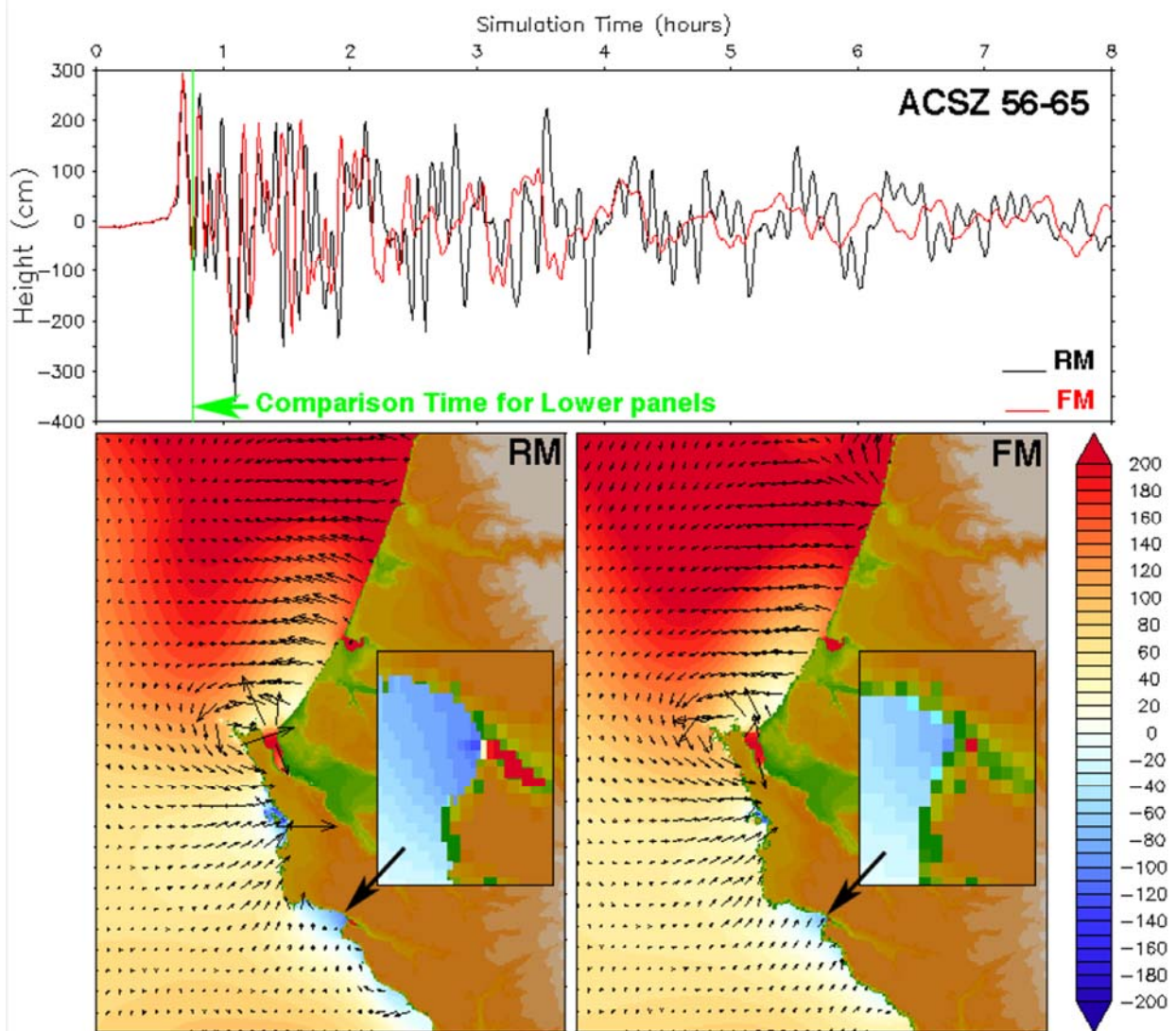
Figure 11. Comparison of reference and forecast model results for the synthetic ACSZ 56–65 mega-tsunami event representing the Cascadia Subduction Zone. Time series at the tide gauge location in Arena Cove are shown in the upper panel. The lower panels contrast the reference (RM) and forecast (FM) model amplitude and velocity fields at the time indicated in the upper panel. Insets are enlargements of Arena Cove, left pixilated to reflect the discrete grid resolution.
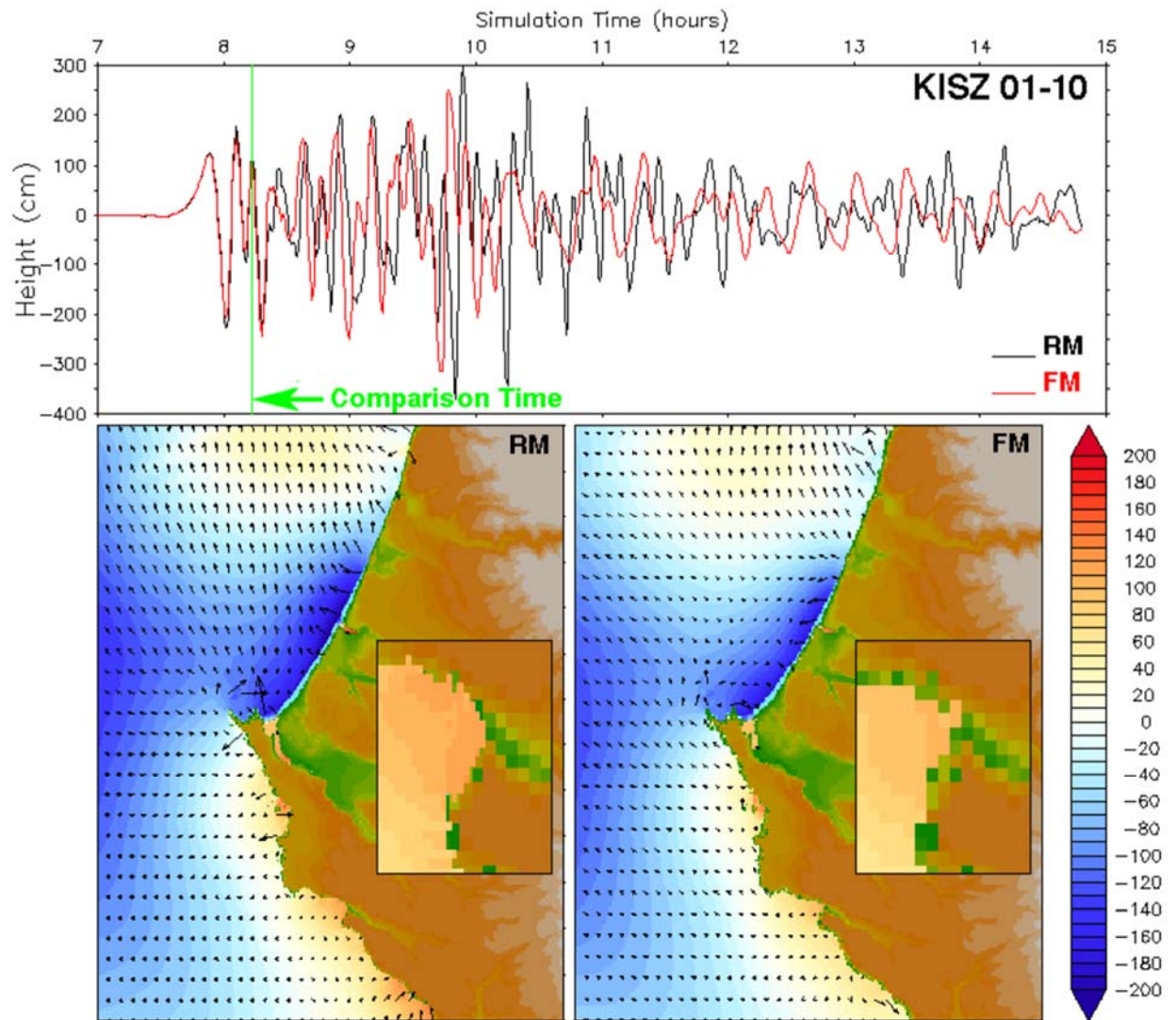
Figure 12. Comparison of reference and forecast model results for the synthetic KISZ 01–10 mega-tsunami event representing Kamchatka. Time series at the tide gauge location in Arena Cove are shown in the upper panel. The lower panels contrast the reference (RM) and forecast (FM) model amplitude and velocity fields at the time indicated in the upper panel. Insets are enlargements of Arena Cove, left pixilated to reflect the discrete grid resolution.
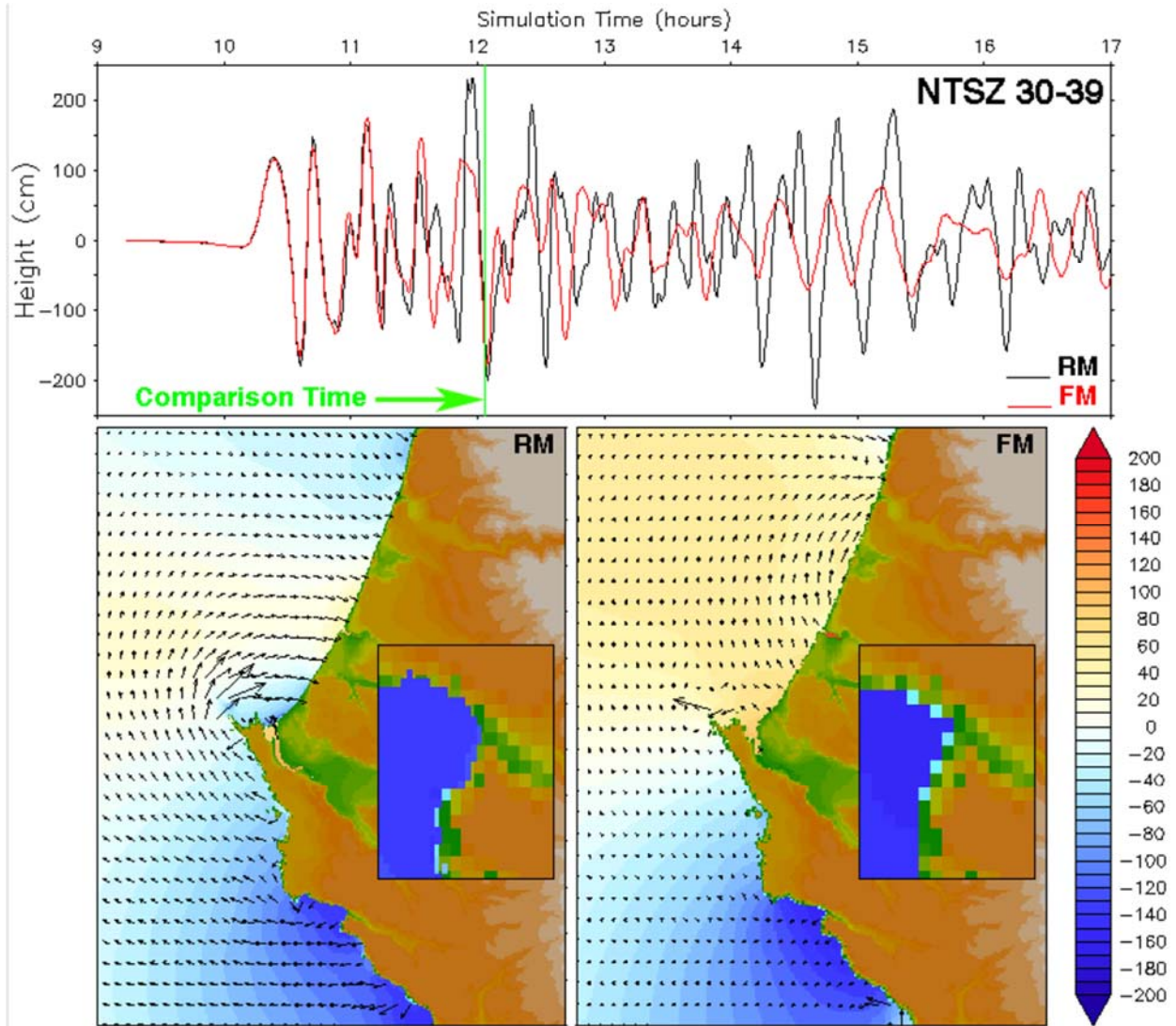
Figure 13. Comparison of reference and forecast model results for the synthetic NTSZ 30–39 mega-tsunami event representing Samoa. Time series at the tide gauge location in Arena Cove are shown in the upper panel. The lower panels contrast the reference (RM) and forecast (FM) model amplitude and velocity fields at the time indicated in the upper panel. Insets are enlargements of Arena Cove, left pixilated to reflect the discrete grid resolution.
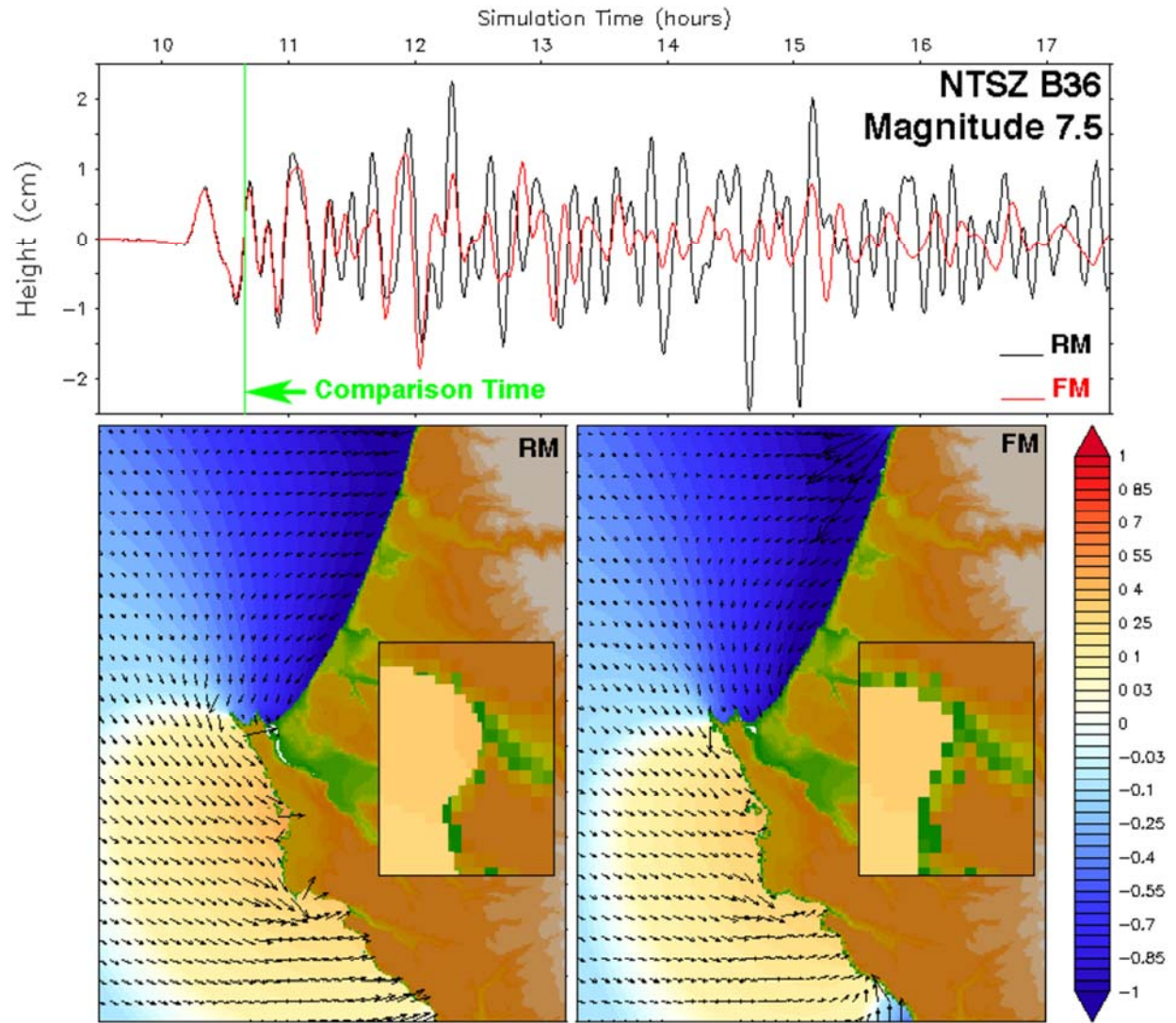
Figure 14. Comparison of reference and forecast model results for the synthetic moderate event at NTSZ B36 near Samoa. Time series at the tide gauge location in Arena Cove are shown in the upper panel. The lower panels contrast the reference (RM) and forecast (FM) model amplitude and velocity fields at the time indicated in the upper panel. Insets are enlargements of Arena Cove, left pixilated to reflect the discrete grid resolution.

34
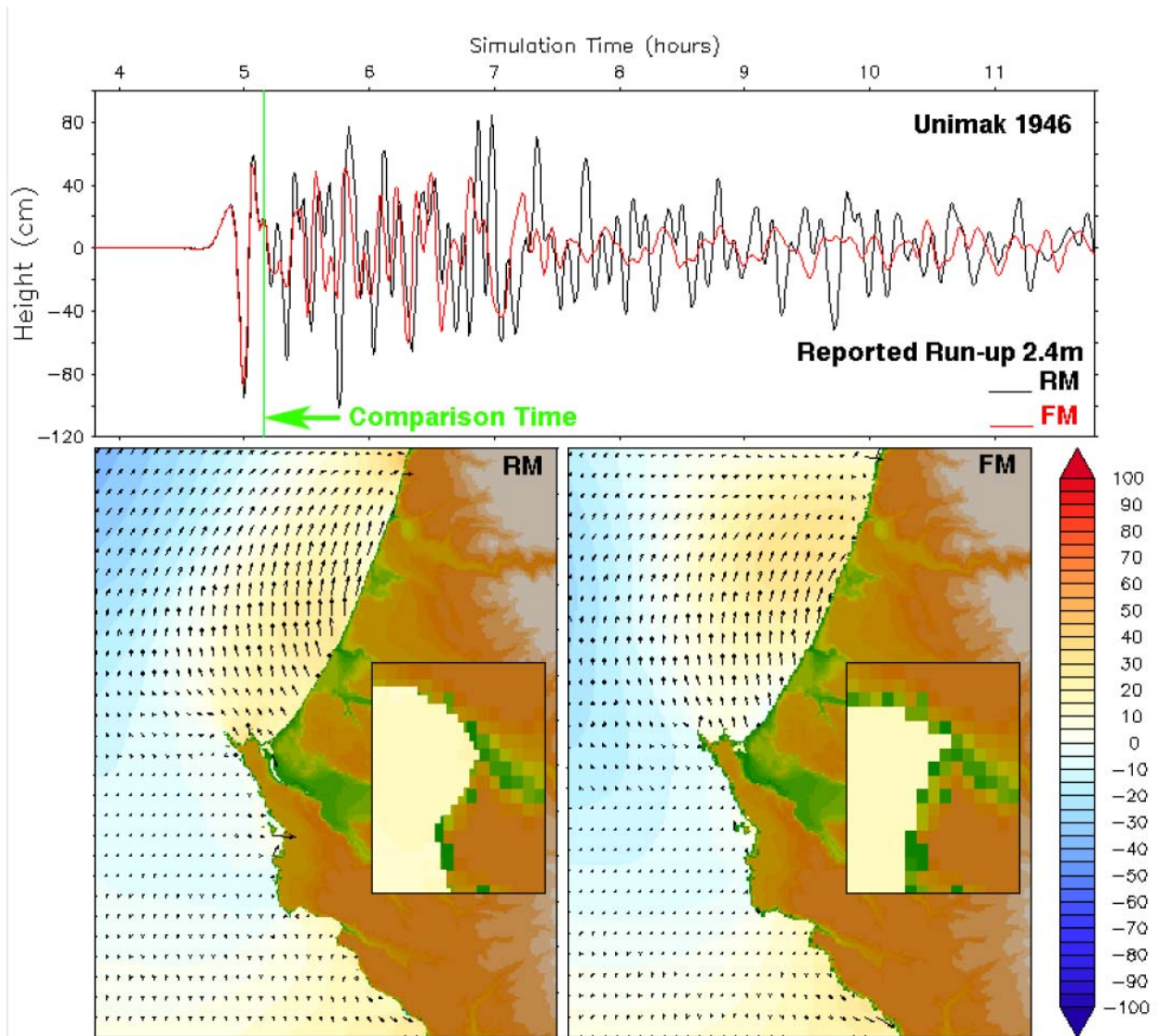
Figure 15. Comparison of reference (RM) and forecast (FM) model results for the historical 1946 Unimak tsunami (prior to tide gauge installation).
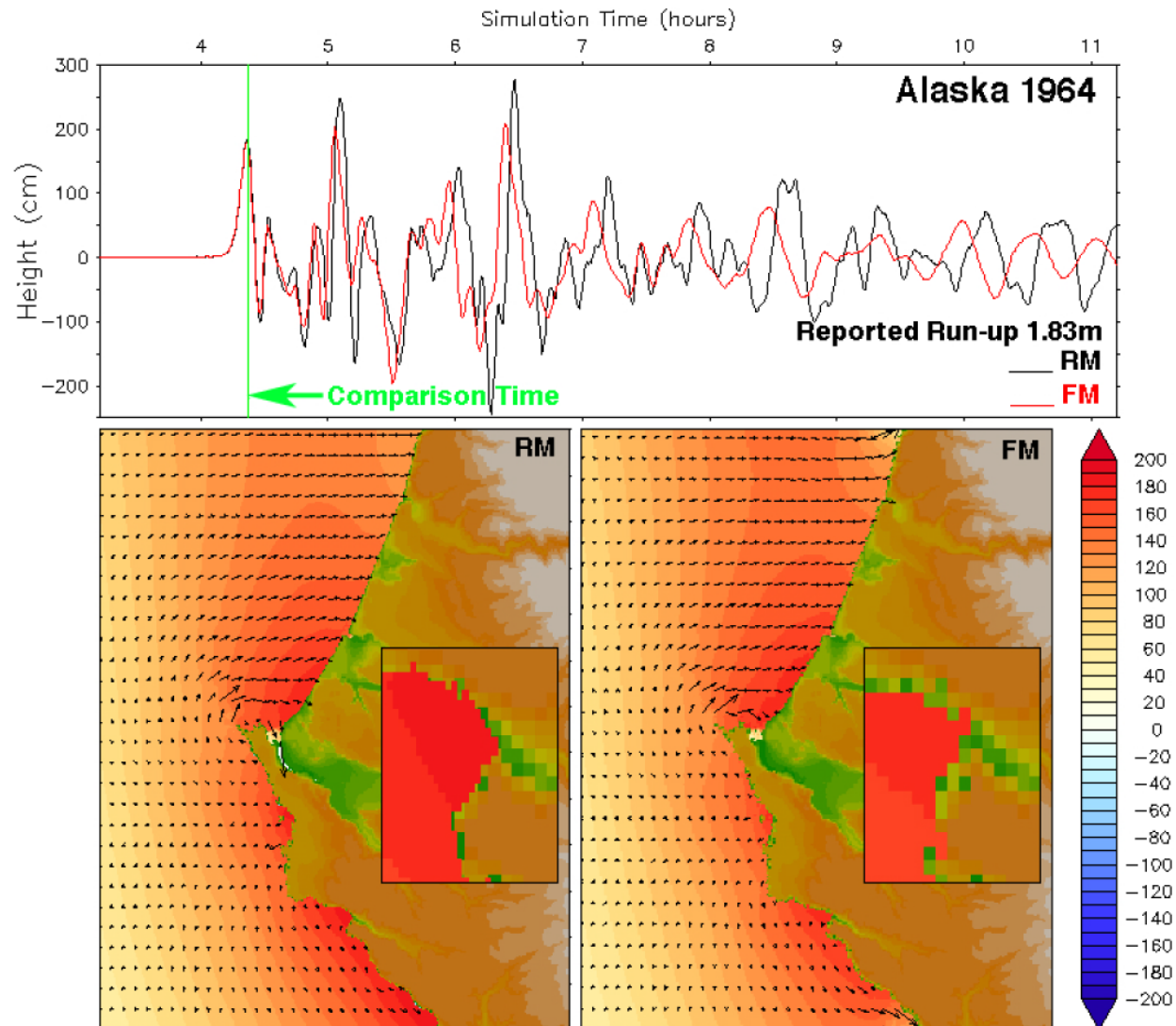
Figure 16. Comparison of reference (RM) and forecast (FM) model response for the historical 1964 Alaska tsunami (prior to tide gauge installation).
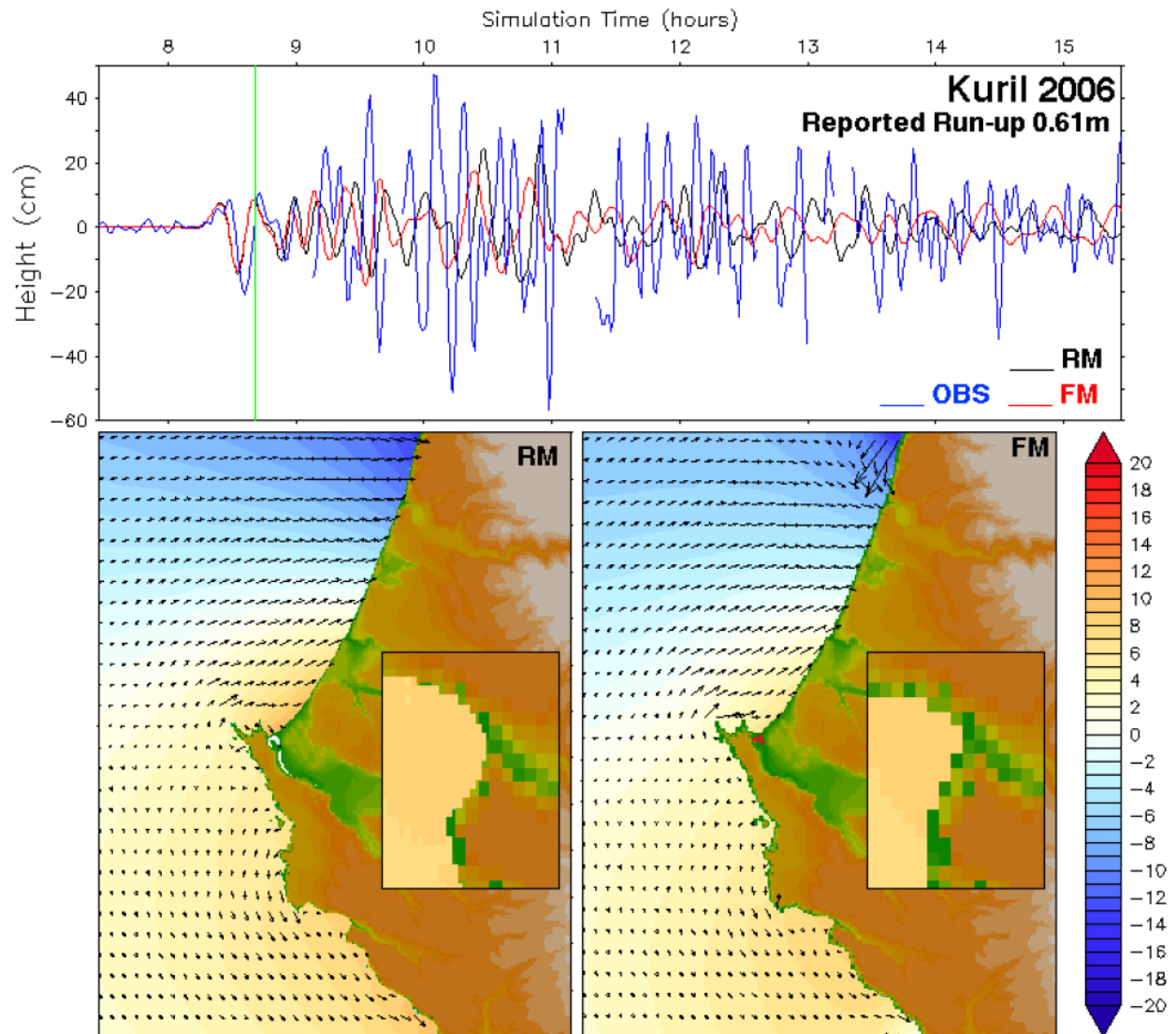
Figure 17. Comparison of reference (RM) and forecast (FM) model results for the 2006 Kuril event with sea level fluctuations, observed by the tsunami-capable Arena Cove tide gauge.
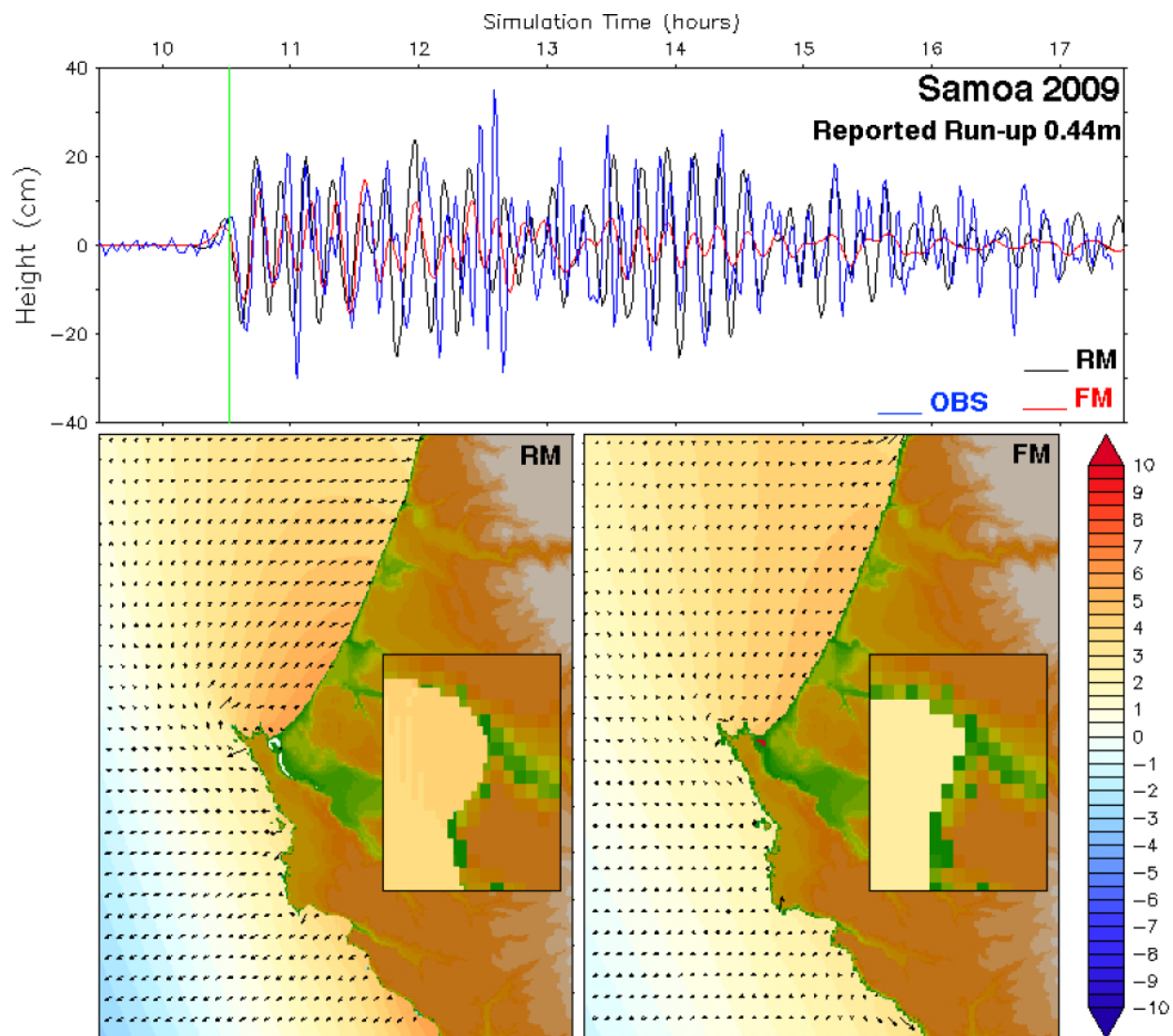
Figure 18. Comparison of reference (RM) and forecast (FM) model hindcasts of the 2009 Samoa event with sea level fluctuations in Arena Cove.
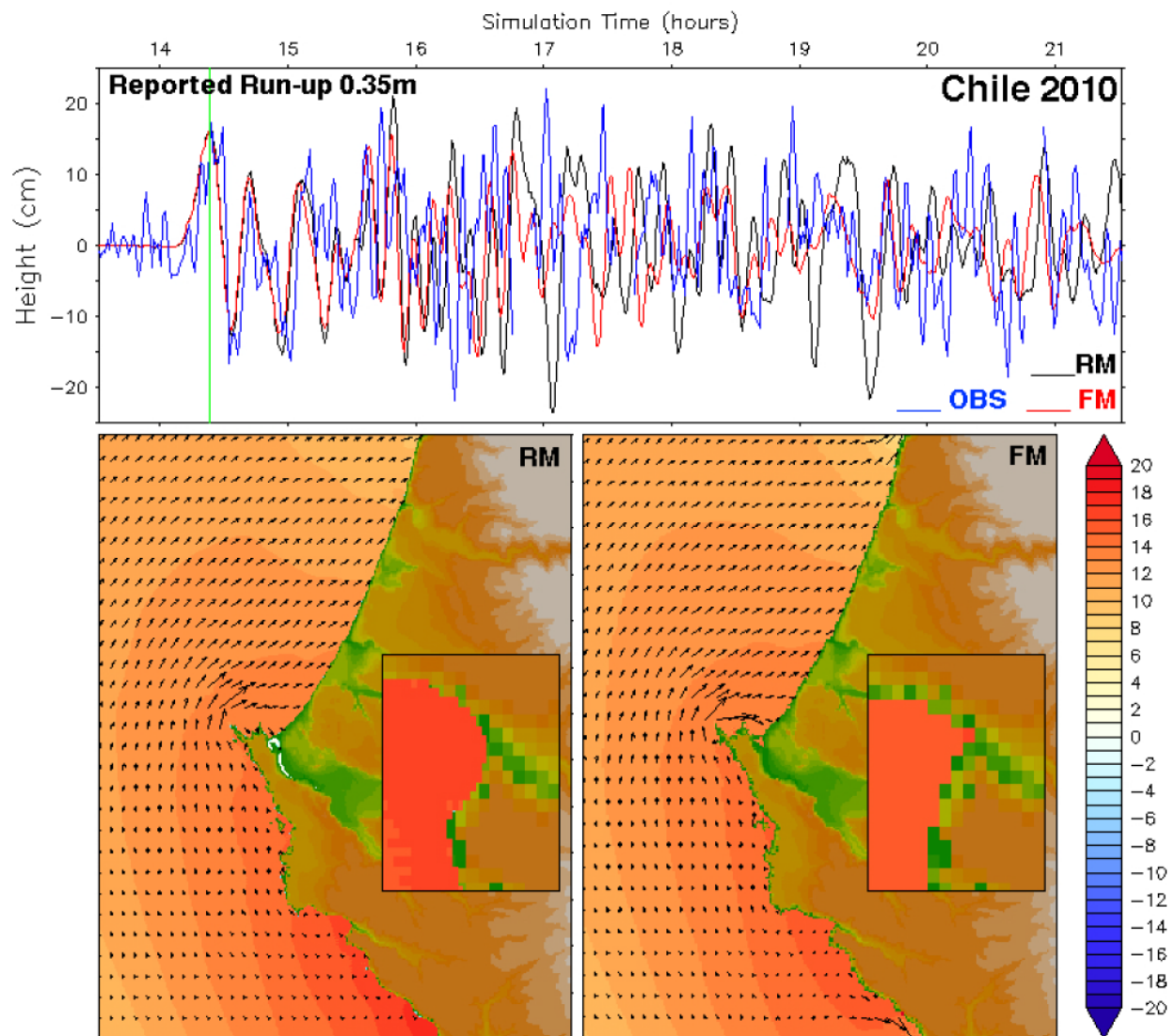
Figure 19. Comparison of reference (RM) and forecast (FM) model hindcasts of the 2010 Chile event with sea level fluctuations in Arena Cove.
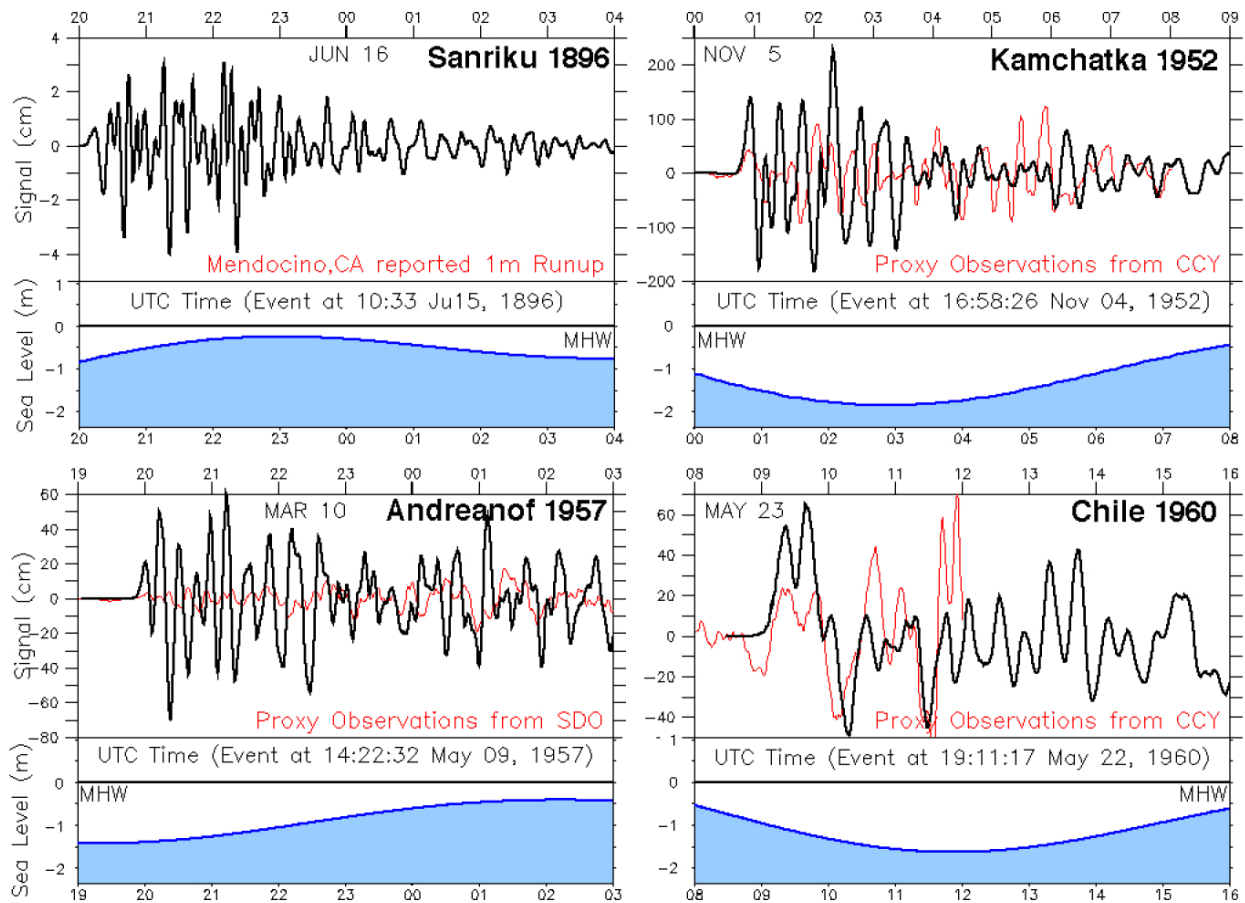
Figure 20. Simulated model response to the historical 1896 Sanriku, 1952 Kamchatka, 1957 Andreanof, and 1960 Chile events. Proxy observations (in red) are provided, where available, from other California locations. The 1896 Sanriku result is not expected to match the observed runup at nearby Mendocino. The state of the tide is shown, and times are given as UTC.
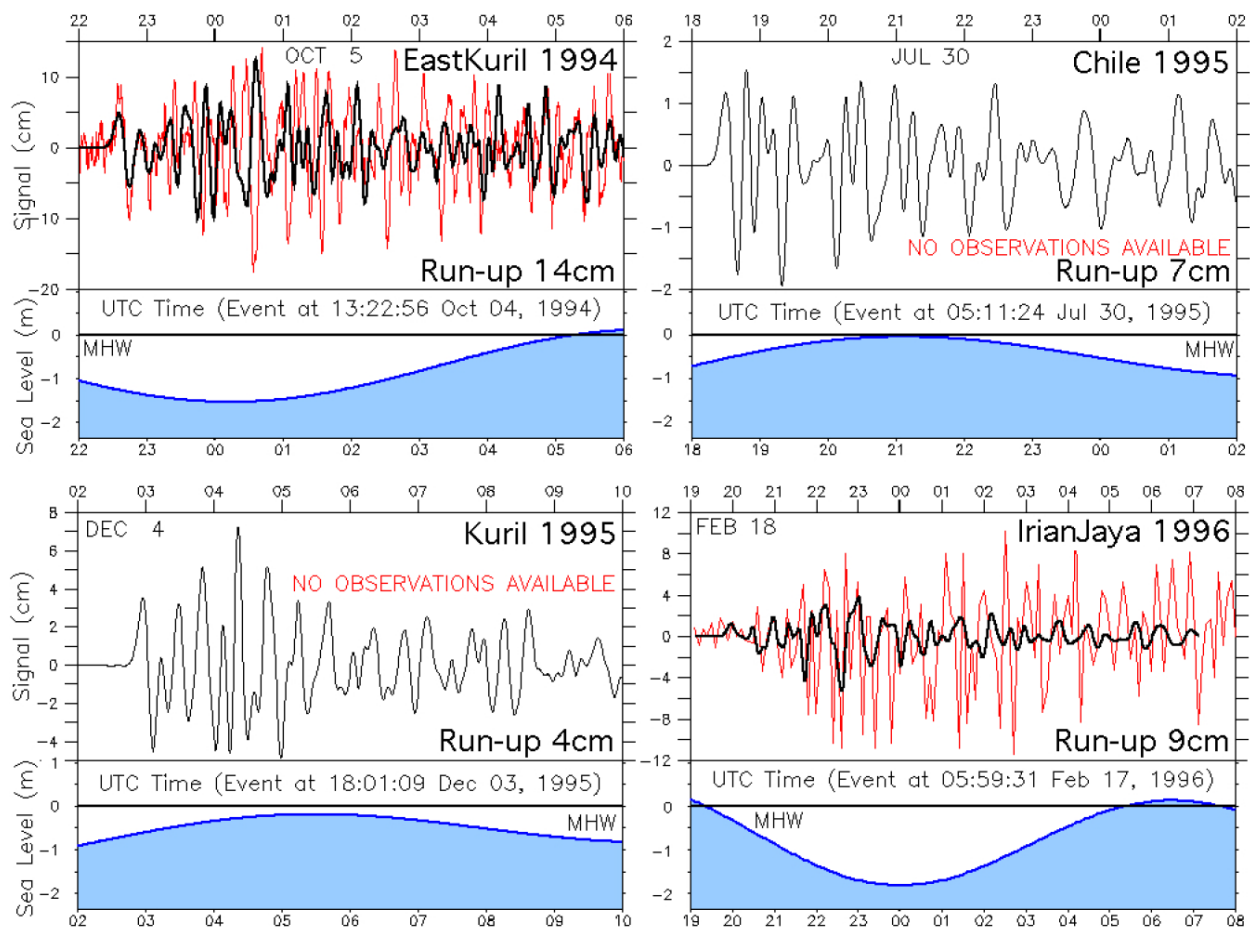
Figure 21. Forecast model response to the 1994 East Kuril, 1995 Chile, 1995 Kuril, and 1996 Irian Jaya events. Tide gauge data (in red), where available, are from Arena Cove.
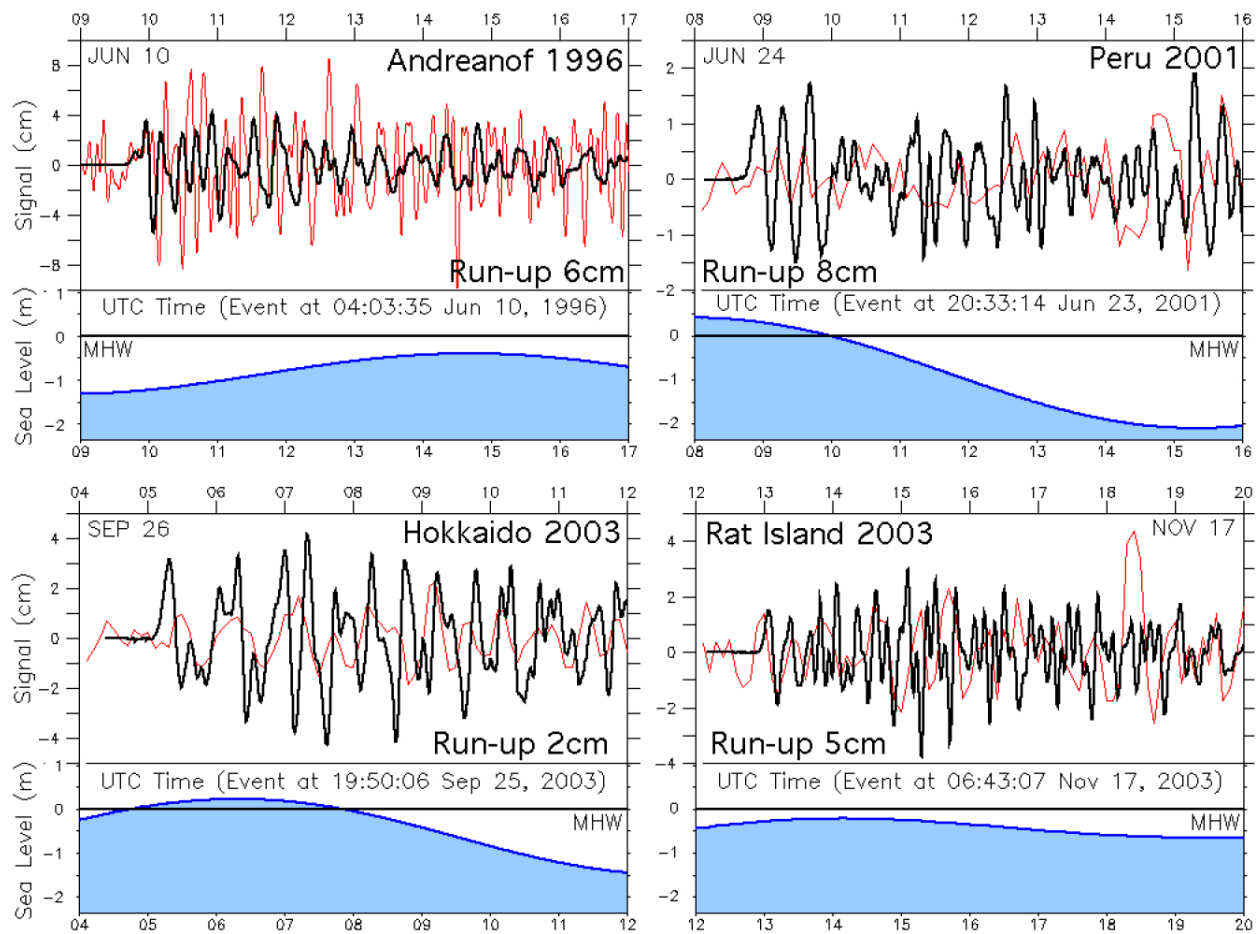
Figure 22. Forecast model response to the 1996 Andreanof, 2001 Peru, 2003 Hokkaido, and 2003 Rat Island events. Tide gauge data (in red) are from Arena Cove.
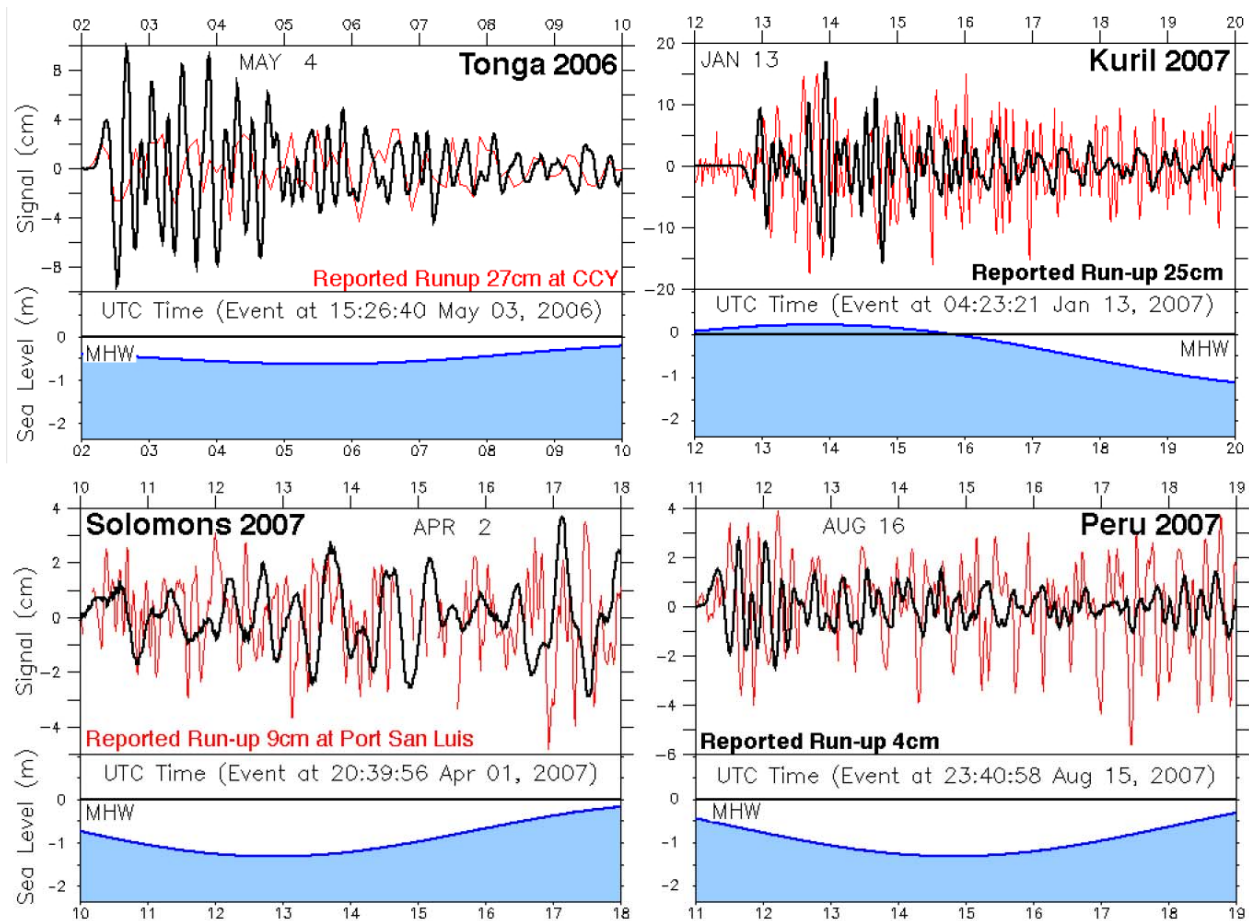
Figure 23. Forecast model response to the 2006 Tonga, 2007 Kuril, 2007 Solomons, and 2007 Peru events. Tide gauge data (in red) are from Arena Cove.
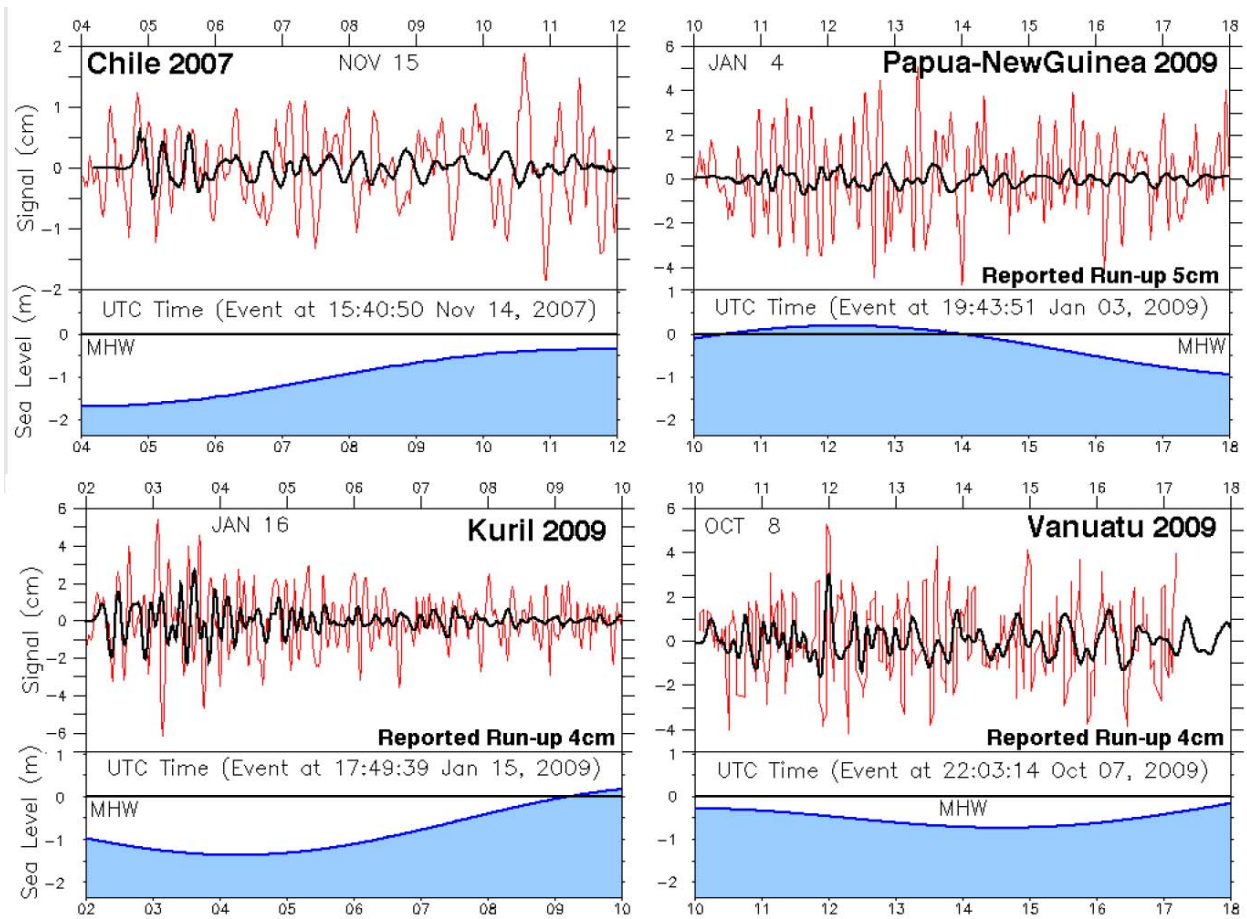
Figure 24. Forecast model response to the 2007 Chile, 2009 Papua New Guinea, 2009 Kuril, and 2009 Vanuatu events. Tide gauge data (in red) are from Arena Cove.
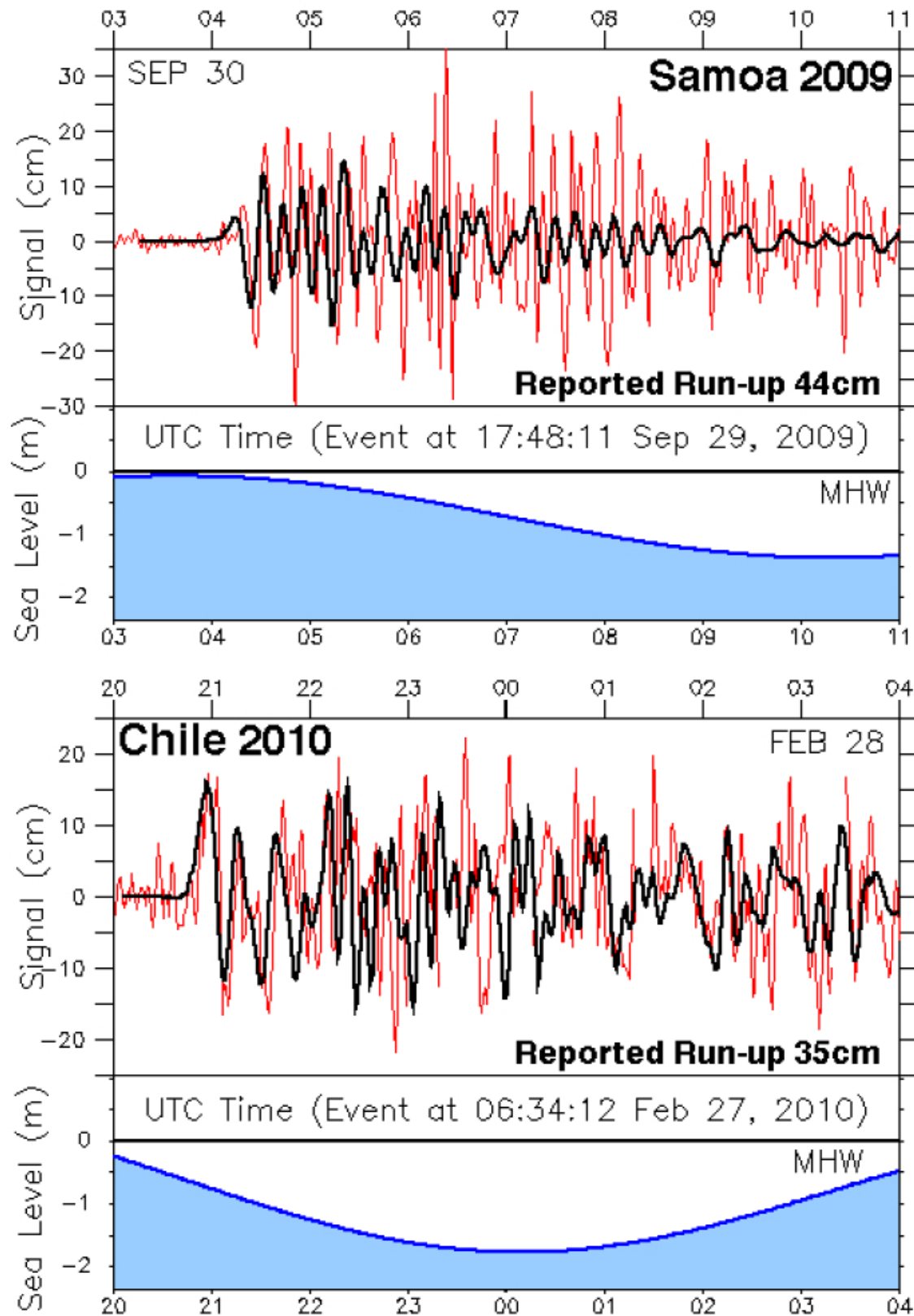
Figure 25. Forecast model response to the 2009 Samoa and 2010 Chile events. Tide gauge data (in red) are from Arena Cove.
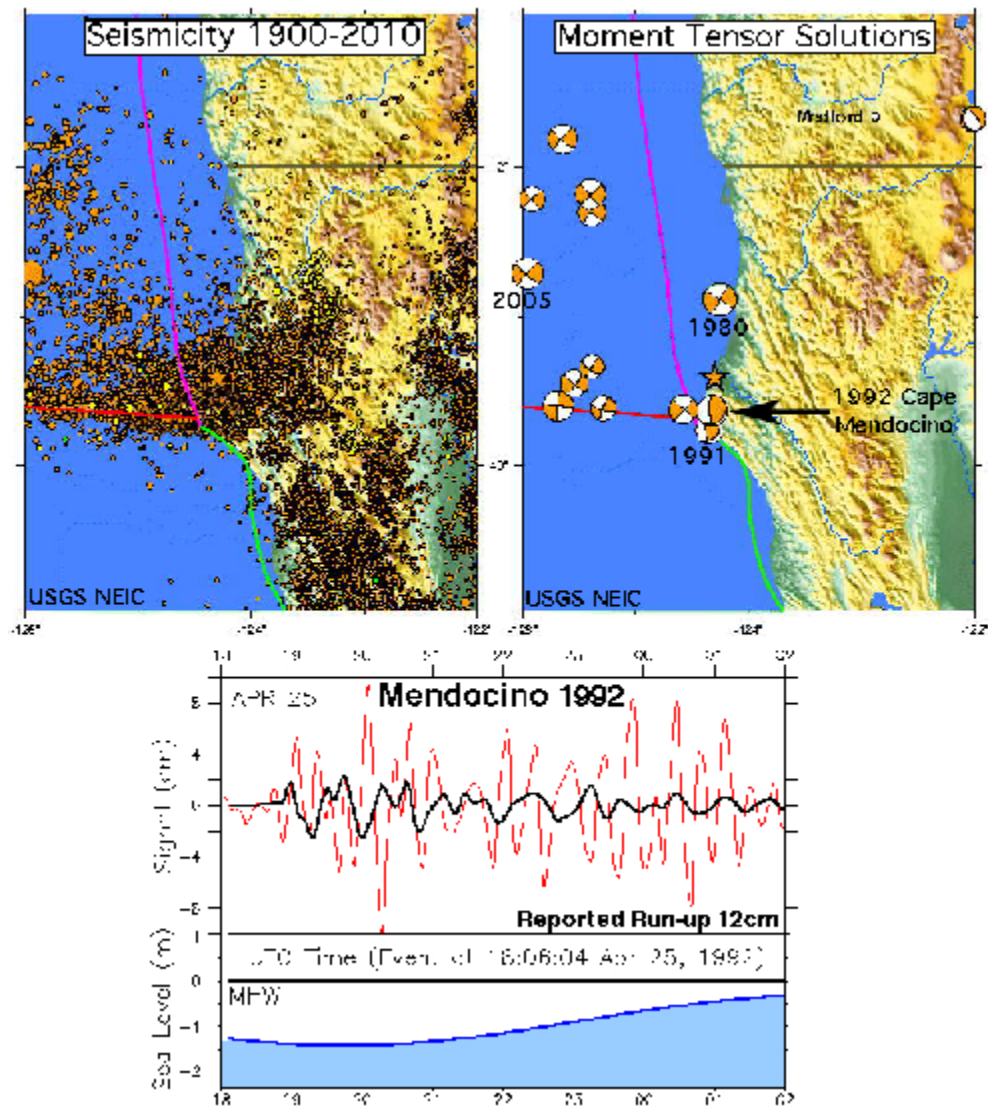
Figure 26. Seismicity in the vicinity of Cape Mendocino and the source mechanisms of recent earthquakes, adapted from USGS/NEIC products. The lower panel shows the poor agreement between the model and Arena Cove tide gauge observations that is likely due to inadequate source representation in the model.
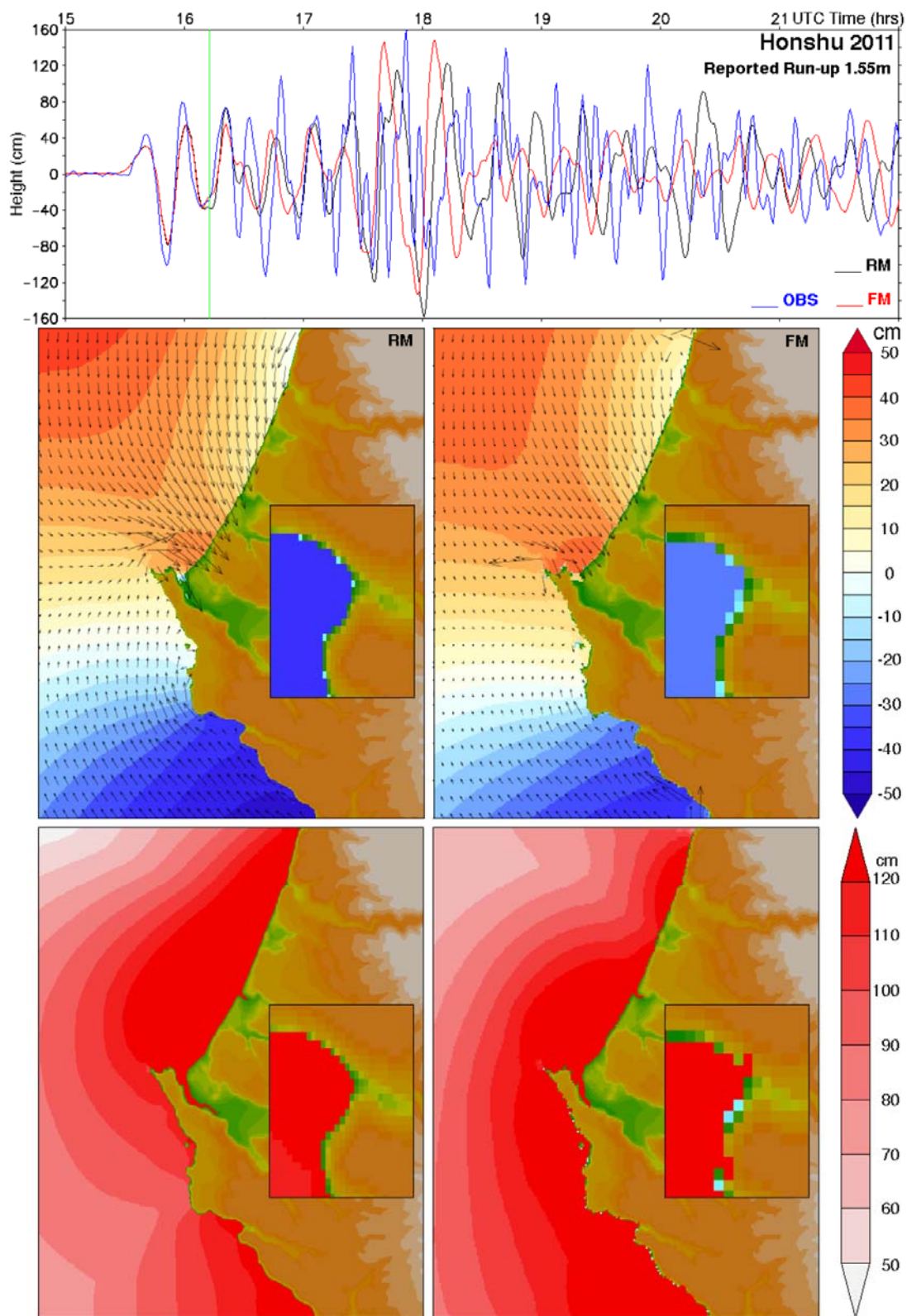
Figure 27. Comparison of real-time forecast (FM) and hindcast reference (RM) model representations of the 2011 Tohoku (Honshu) event with sea level observations in Arena Cove.
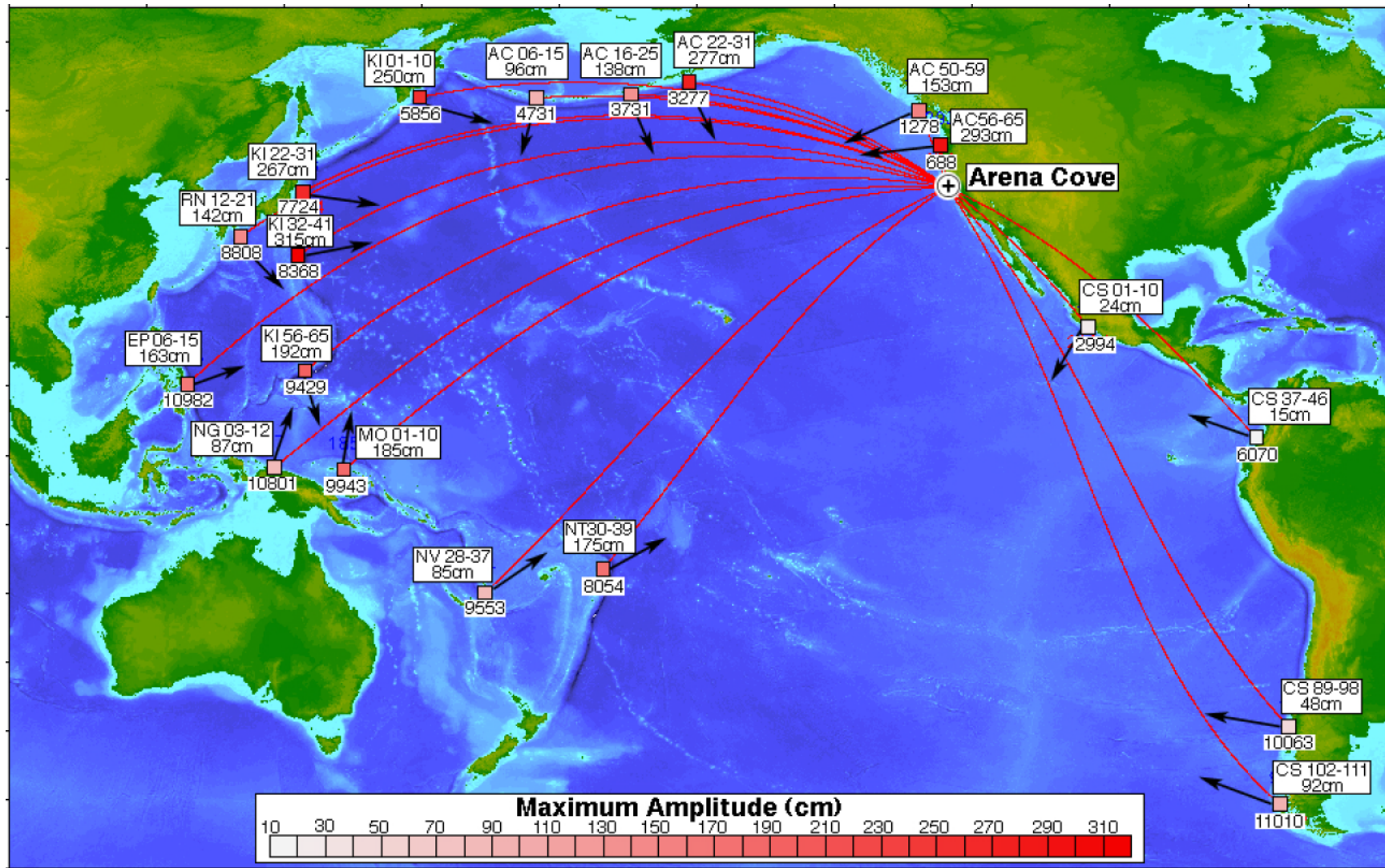
Figure 28. Predicted maximum sea level (from the forecast model) at the Arena Cove tide gauge for the mega-tsunami scenarios described in **Table 6**. Great circle routes are shown in red (with distances in km); black arrows indicate the normal to the strike direction.
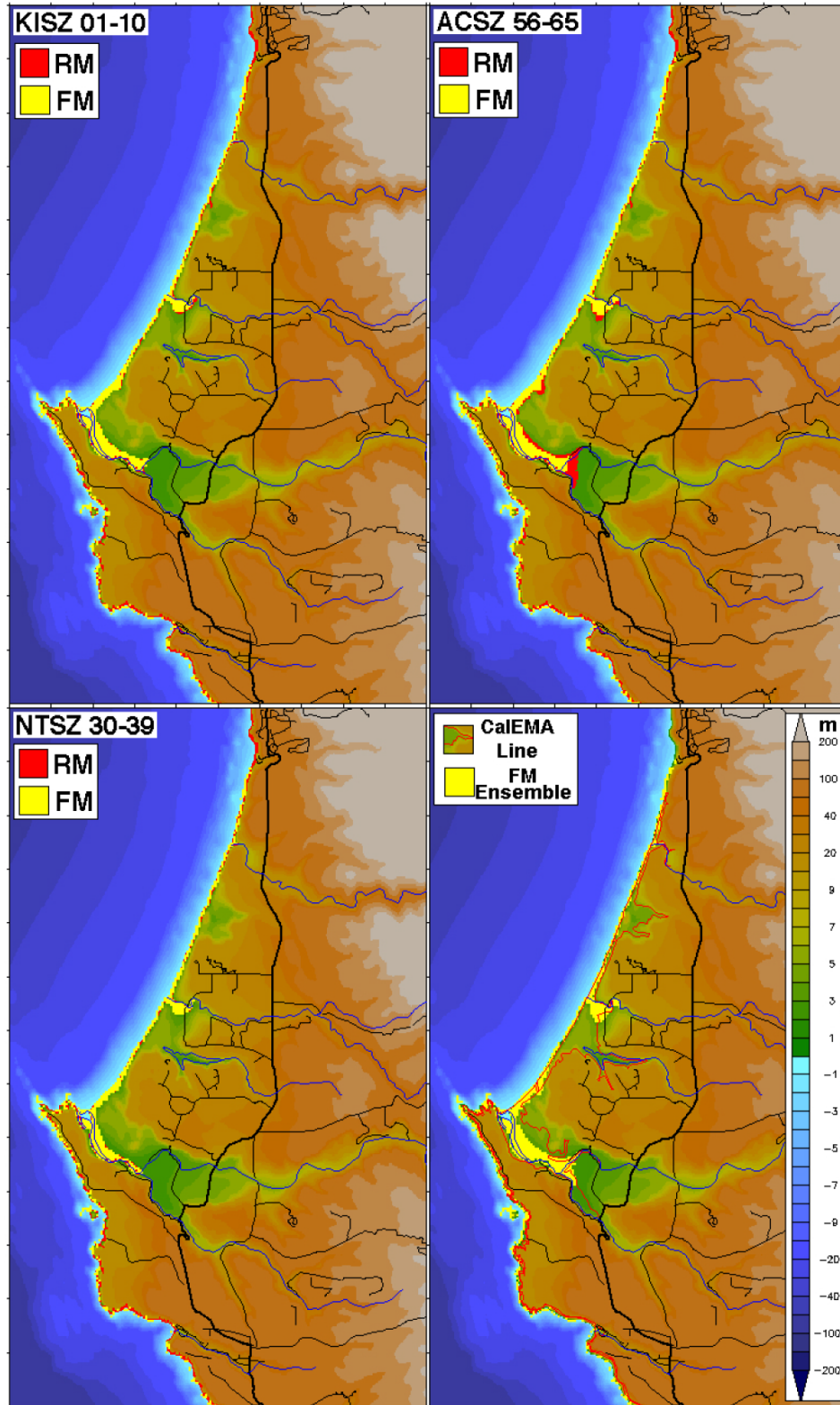
Figure 29. Comparison of reference (RM) and forecast (FM) model predictions for inundation of the Arena Cove / Manchester Beach region for selected mega-tsunami scenarios and (lower right) for the ensemble employed in the CalEMA study.

Supplement: Synthetic testing — Arena Cove, California

The Arena Cove forecast model was tested with NOAA's tsunami forecast system, SIFT. Test results from the forecast system and comparisons with the results obtained during the forecast model development are shown numerically in **Table S1** and graphically in **Figures S1**–S**6** as described below. The results show that the forecast model is stable and robust, with consistent and high-quality results across geographically distributed tsunami sources and mega-tsunami event magnitudes. The model run time (wall-clock time) for all six cases was under 19 min for 8 hr of simulation, and under 10 min for 4.0 hr, thereby satisfying the criterion of 10 min run time per 4 hr of simulation time for operational efficiency.

A suite of five synthetic events and one historical case were run on the Arena Cove forecast model. The modeled scenarios were stable for all cases tested, with no instabilities or ringing. Results show that the largest modeled height (see **Table S1**) was 295.03 cm, originating from the Cascadia source ACSZ 56–65. Amplitudes greater than 100 cm were recorded for four of the five mega-tsunami scenarios; the smallest signal of 47.67 cm originated from the far-field South American source CSSZ 89–98. Direct comparisons of output from the forecast tool with results of both the historical event (2011 Tohoku, alternately referred to as 2011 Honshu) and available development synthetic events demonstrated that the wave patterns were similar in shape, pattern, and amplitude. Where available, the figure captions in this appendix point to the relevant figures of the main report. Where time series in the main text were not available, the extrema reported in **Table S1** were obtained from the output files saved during model development.

Table S1. Maximum and minimum tsunami amplitudes (cm) at the Arena Cove, California, warning point for synthetic and historical events tested using SIFT 3.2 and obtained during development.

Scenario Name	Source Zone	Tsunami Source	α [m]	SIFT Max (cm)	Development Max (cm)	SIFT Min (cm)	Development Min (cm)
Mega-tsunami Scenarios							
KISZ 1-10	Kamchatka-Yap-Mariana-Izu-Bonin	A1-A10, B1-B10	25	250.055	250.055	-368.491	-315.426
KICZ 22-31	Kamchatka-Yap-Mariana-Izu-Bonin	A22-A31, B22-B31	25	266.764	266.764	-198.325	-198.325
ACSZ 56-65	Aleutian-Alaska-Cascadia	A56-A65, B56-B65	25	295.027	292.952	-226.995	-231.452
CSSZ 89-98	Central and South America	A89-A98, B89-B98	25	47.673	47.673	-47.978	-47.978
NTSZ 30-39	New Zealand-Kermadec-Tonga	A30-A39, B30-B39	25	175.210	175.210	-179.082	-179.082
Historical Events							
2011 Tohoku	Kamchatka-Yap-Mariana-Izu-Bonin	4.66 b24 + 12.23 b25 + 26.31 a26 + 21.27 b26 +22.75 a27 + 4.98 b27		147.809	147.957	-133.476	-133.518
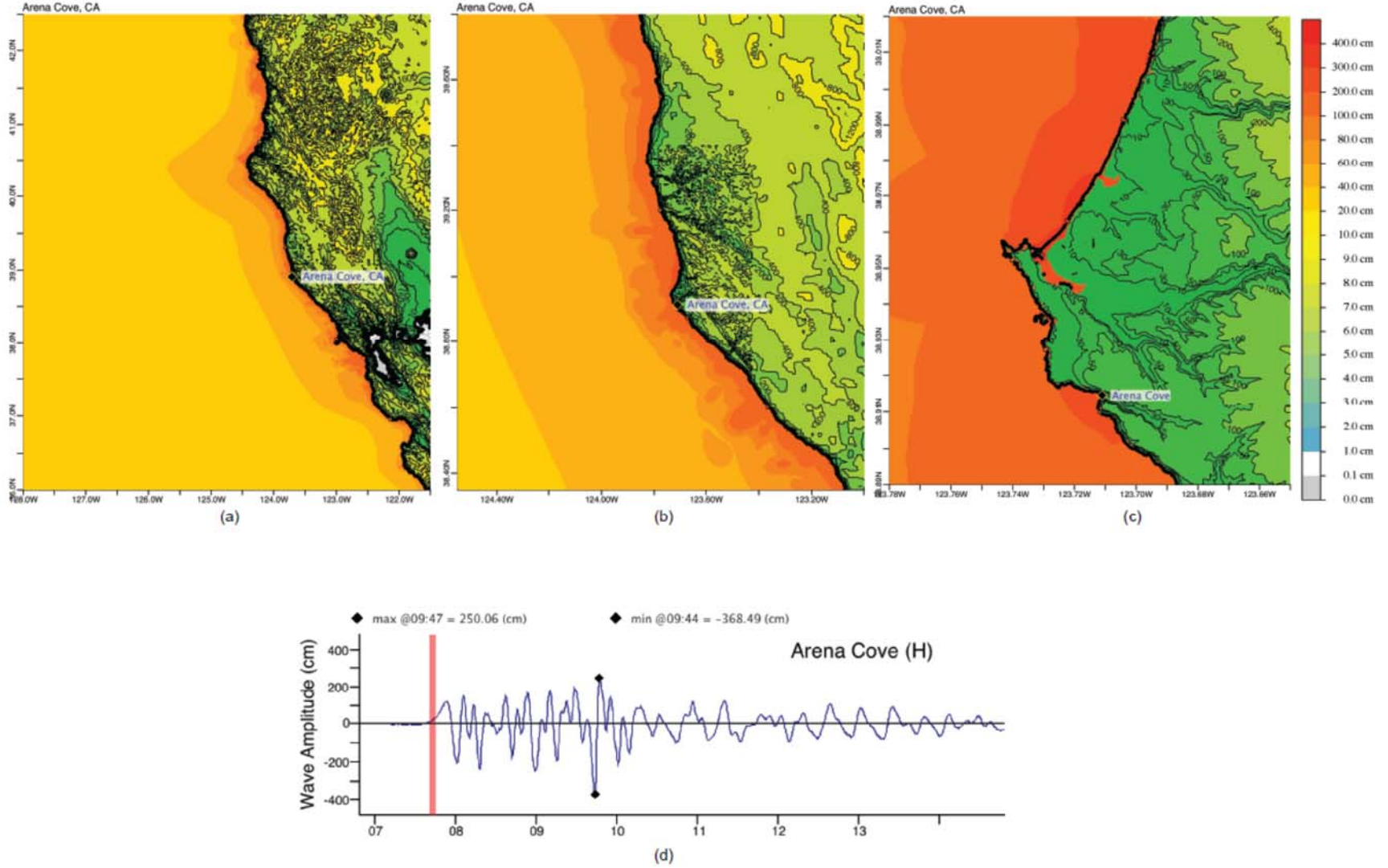
Figure S1. Response of the Arena Cove forecast model to synthetic scenario KISZ 1–10 (α=25). Maximum sea surface elevation for (a) A grid, (b) B grid, and (c) C grid. Sea surface elevation time series at the C-grid warning point (d). Panel (d) can be compared with the equivalent values obtained during model development, displayed in **Figure 12**.
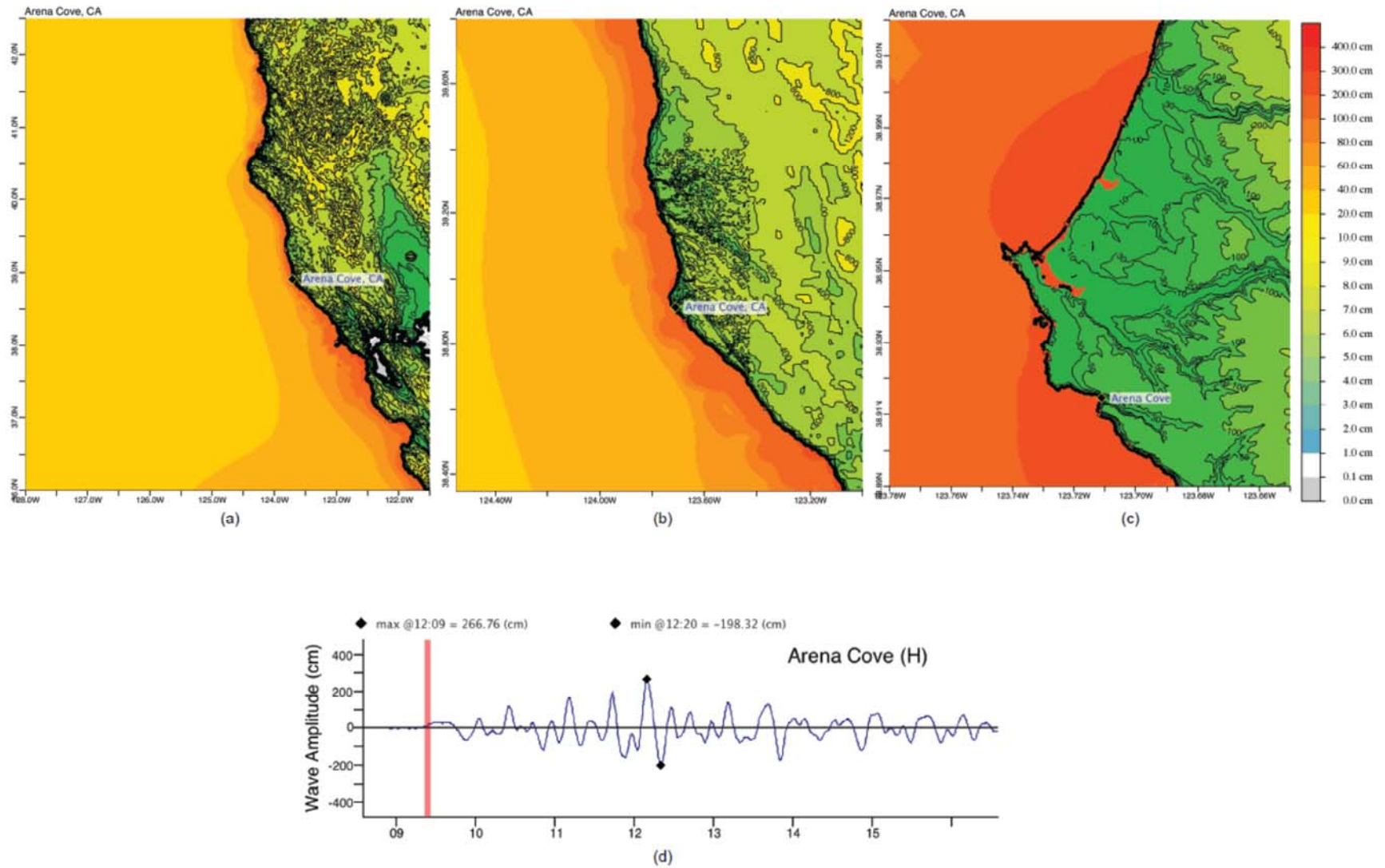
Figure S2. Response of the Arena Cove forecast model to synthetic scenario KISZ 22-31 (=25). Maximum sea surface elevation for (a) A grid, (b) B grid, (c) C grid. Sea surface elevation time series at the C grid warning point (d). For extrema computed during model development, see **Table S1**.

Figure S3. Response of the Arena Cove forecast model to synthetic scenario ACSZ 56–65 (α=25). Maximum sea surface elevation for (a) A grid, (b) B grid, and (c) C grid. Sea surface elevation time series at the C-grid warning point (d). Panel (d) can be compared with the equivalent results, obtained during model development, displayed in **Figure 11**.

Figure S4. Response of the Arena Cove forecast model to synthetic scenario CSSZ 89–98 (α=25). Maximum sea surface elevation for (a) A grid, (b) B grid, and (c) C grid. Sea surface elevation time series at the C-grid warning point (d). For extrema computed during model development, see **Table S1**.

Figure S5. Response of the Arena Cove forecast model to synthetic scenario NTSZ 30–39 (α=25). Maximum sea surface elevation for (a) A grid, (b) B grid, (c) C grid. Sea surface elevation time series at the C-grid warning point (d). Panel (d) can be compared with the equivalent results, obtained during model development, displayed in **Figure 13**.

Figure S6. Response of the Arena Cove forecast model to the 11 March 2011 Tohoku tsunami. Maximum sea surface elevation for (a) A-grid, (b) B-grid, and (c) C-grid. Sea surface elevation time series at the C-grid warning point (d). Panel (d) can be compared with the equivalent results, obtained during model development, displayed in **Figure 27.**

4. PMEL Tsunami Forecast Model for Point Reyes, California

Michael Spillane

Table of Contents

LIST OF FIGURES

LIST OF TABLES

4.1 Background and Objectives

4.1.1 The setting

Point Reyes, California, lying to the northwest of the entrance to San Francisco Bay, is a prominent navigational landmark. As illustrated in **Figure 1**, composed of orthographic images from "Marin-Maps" (mmgis.marinmap.org/OrthoGrid/viewer.htm), the headland is the site of a lighthouse, and, in Drakes Bay in its lee, adjacent to the historic Point Reyes Lifeboat Station is the tide gauge bearing the same name. All lie within the Point Reyes National Seashore (PRNS), composing most of west Marin County, which is essentially unpopulated and in a natural state, with the exception of some agricultural activity that was allowed to continue when the PRNS was established in 1962. As seen in the inset to **Figure 1**, the San Andreas Fault (SAF) strongly delineates the eastern boundary of the region, though it is submerged in Tomales Bay in the north and Bolinas Lagoon in the south. In the neck of land between them are the communities of Olema and Point Reyes Station, which are close to the epicenter of the 1906 San Francisco earthquake. Several small communities lie on the shores of Tomales Bay (20.4 km in length but with a mean depth of only 3.1 m; Niemi and Hall, 1996). The entrance is shallow and constricted. To the south, Bolinas and Stinson Beach, with communities of 1620 and 632 residents, respectively (Census Bureau, 2010), have greater exposure to damage from tsunami or winter storm waves. Between Stinson Beach and Point Bonita, the southernmost point of Marin County, lies Muir Beach, a community of about 310 (Census Bureau, 2010). It is notable, from the tsunami perspective, in that it reported major runups during the 1946 Unimak and 1964 Alaska events.

North of Tomales Bay is Bodega Bay (population: 1077; Census Bureau, 2010), whose shores lie both in Marin and Sonoma counties. Apart from the shallow Bodega Harbor and the communities of Bodega Bay and Doran Beach extending onto the spit at its mouth, this area too is sparsely populated. The natural beauty of the region, with its mild climate and proximity to the San Francisco area and other urban centers, provides outstanding recreational opportunities resulting in large numbers of visitors throughout the year.

Normally, in selecting the domain of a tsunami forecast model, the location of a tide gauge provides the focus, but in this case, a somewhat larger region is included to provide forecast capability to population centers and primary recreational assets. Initially it was hoped that a forecast model could cover the entire region from Bodega Bay to Muir Beach. This proved to be impossible, given the time constraints on model run time imposed by emergency usage, without an unacceptable reduction in spatial resolution. While the innermost area of study used in the reference model does include Tomales Bay and a portion of Bodega Bay, these are excluded from the forecast model, which focuses on the south and southwest area of Marin County (http://xenon.colorado.edu/spotlight/).

The University of Southern California Tsunami Research Center conducted a comprehensive study of potential tsunami inundation for the entire California coastline. Funded through the California Emergency Management Agency (CalEMA) by the National Tsunami Hazard Program, the study (Barberopoulou *et al*., 2011) has produced a set of inundation maps for emergency planning purposes, accessible online in various forms, including "MyHazards" (myhazards.calema.ca.gov),

which enables users to acquire information specific to their site of interest. The CalEMA inundation results are available in GIS form and those specific to the Point Reyes area are used throughout this report. In addition to underpinning the modeling effort, the digital elevation model (DEM) for the San Francisco region, provided by the National Geophysical Data Center (NGDC), includes a 3-D oblique view that assists greatly in visualizing the study area. In **Figure 2**, the CalEMA inundation information is overlaid with descriptive labels on an extract from the NGDC image. The full 3-D image is available in the San Francisco DEM Report (Carignan *et al*., 2010).

A striking series of aerial photographs (www.californiacoastline.org) shows that the study region contains both high cliffs (also seen in **Figure 3**), which limit potential impact by tsunamis, and broad beaches and shallow coastal inlets that are more exposed. Queries to the CalEMA My Hazards site show, in addition to tsunamis, that flooding and earthquakes are hazards to which Bolinas and Stinson Beach are prone. Available online is a video, "Marin Tsunami" (Loeffler and Gesell, 2010), produced for the U.S. Geological Survey (USGS) in cooperation with the Marin County Sheriff's Office of Emergency Services. In addition to providing an overview of the comprehensive level of preparedness for tsunami impact on the communities of Bolinas, Stinson Beach, Dillon Beach/Lawson's Landing, and the National Park Service's popular Limantour Beach, this excellent resource for residents and visitors alike gives insight into the character of the area.

4.1.2 Natural hazards

Instances of mild tsunami signals are evident in the tide gauge records for Point Reyes (established in 1975), and Marin County sites appear several times in the records compiled by Lander and Lockridge (1989) and their regularly updated online equivalent, the NGDC Tsunami Hazard Database (Dunbar, 2007; see ngdc.noaa.gov/hazard/). The historical record first mentions Marin County with a wave observed at Sausalito, on the north shore of the Golden Gate, from a Chilean event in 1877. The earliest time series currently available for analysis is a digitized marigram from Sausalito, recorded during the Sanriku event of 1896 and available in the National Tsunami Warning Center (NTWC) archives. O'Brien (1946) described a 2.6 m wave above Mean Lower Low Water (MLLW) in Drakes Bay during the 1946 Unimak tsunami, with a boat washed onto the highway. While Marin County sites are not explicitly mentioned in connection with the 1952 Kamchatka or 1957 Andreanof events, waves were observed at Bodega Bay and within San Francisco Bay. During the 1960 Chile event, a 1.5 m runup was reported at Stinson Beach, and during the 1964 Alaska tsunami, waves were observed at several sites within Marin County, including Drakes Beach. Time series from several tsunamis are available from the Point Reyes tide gauge in recent years, culminating in the major event east of Japan's island of Honshu on 11 March 2011 (also referred to as the Tohoku earthquake). The latter will be discussed extensively in this report.

Combining events impacting northern California with those that have occurred since the Point Reyes tide gauge was upgraded to 1 min sampling, a total of 27 historical events are available for study. Nineteen of these, listed in **Table 1a**, are among the preferred cases for forecast model testing in the Pacific because their seafloor deformation is reasonably well known, either from the literature or more recently derived from direct observation of the wave trains they generated. The remaining eight, listed in **Table 1b**, have source characteristics that are less well known; they are

included to expand the geographical coverage or because of their special relevance to the U.S. West Coast. The Mw 7.2 earthquake north of Cape Mendocino on 25 April 1992 was a very mild foretaste of a Cascadia Subduction Zone event, but was registered in marigrams at Arena Cove and Point Reyes. Others, due to significant noise in the tide gauge, do not produce a clear signal but shed light on Point Reyes as a reference point for coastal impacts. **Figure 4** illustrates the distribution of the 27 historical sources. Those highlighted in red were employed for intercomparison of the reference and forecast versions of the model.

Direct seismic impact is another natural hazard to which Marin County is exposed. Its proximity to the rupture zone of the SAF in the San Francisco earthquake of 1906 resulted in significant lateral displacements and some damage in the inland towns. The lighthouse on the Point Reyes headland suffered only mild damage. While the SAF enters the ocean at Bolinas, its strike-slip nature reduces the likelihood of severe tsunami wave generation should ruptures occur in the immediate vicinity. Submarine landslides or collapse of sections of sea cliff are, however, a potential local source for tsunami damage. Landslides triggered by seismic events caused significant loss of life during the 1929 Newfoundland event and accentuated the 1996 New Guinea tsunami. Landslide-generated tsunami waves are not currently included in the forecasting system SIFT (Short-term Inundation Forecasting for Tsunamis), developed at NOAA Center for Tsunami Research (NCTR) and now in operational use at the U.S. Tsunami Warning Centers (TWCs), nor are those that are generated meteorologically. However, to the extent that the waves they produce are detected by the DART® array, some warning of their presence may be available.

Another local hazard that has been a frequent cause of damage in the Bolinas–Stinson Beach area is ocean wave action. Originating locally, or as swell from distant storms, such waves in the winters of 1977–78 and 1982–83 caused the loss of several beachfront homes. Another impact of ocean waves, of relevance to tsunami detection and modeling, is in the noise they produce in the tide gauge records. Although the Point Reyes tide gauge is in the lee of the headland, excessive wave action and resonance can mask weak tsunami signals.

4.1.3 Tsunami warning and risk assessment

The forecast model development described here will permit Point Reyes to be incorporated into the tsunami forecasting system, SIFT. The system has had considerable success in accurately forecasting the impact of both moderate and severe tsunami events in recent years, and in the following section, the methodology that permits such forecasts is discussed as prelude to a description of forecast model development for Point Reyes. With the model in hand, validated with historical events and with its stability verified by extensive testing against extreme scenarios, real-time forecasts will be available to inform local emergency response. Additionally, the synthetic scenarios investigated during model development and reported here provide an initial tsunami risk assessment, as described in Section 4.4.

Table 1. Source characterization for historical tsunami events employed for Point Reyes, California, model testing. Events in bold text were used to compare the reference and forecast model versions. Sources identified as "preliminary" or "ad hoc" may not be identically defined in other forecast model reports (a) The standard set for Pacific Ocean models; and (b) supplementary tsunami events for forecast model testing.

| | Earthquake / Seismic | | | | | Model | |
Event	USGS Date Time (UTC) Epicenter	CMT Date Time (UTC) Centroid	Magnitude Mw	Tsunami Magnitude	Subduction Zone	Tsunami Source (Reference/Derivation)	
(a) Standard set for Pacific Ocean models:							
1946 Unimak	01 Apr 12:28:56 52.75ºN 163.50ºW	Not Available	8.5	8.5	ACSZ	7.5 × B23 + 19.7 × B24 + 3.7 × B25 (López and Okal, 2006)	
1952 Kamchatka	04 Nov 16:58:26.0 52.76ºN 160.06ºE	Not Available	9.0	9.0	KISZ	19.71 × (A4 + Y4 + Z4 + A5 + Y5 + Z5 + A6 + Y6 + Z6) [ad hoc]	
1957 Andreanof	09 Mar 14:22:31 51.56ºN 175.39ºW	Not Available	8.6	8.7	ACSZ	31.4 × A15 + 10.6 × A16 + 12.2 × A17 [preliminary]	
1960 Chile	22 May 19:11:14 38.29ºS 73.05ºW	Not Available	9.5	9.5	CSSZ	125 × (A93 + B93 + Z93 + A94 + B94 + Z94 + A95 + B95) (Kanamori and Cipar, 1974)	
1964 Alaska	28 Mar 03:36:00 61.02ºN 147.65ºW	Not Available	9.2	8.9	ACSZ	15.4 × A34 + 18.3 × B34 + 48.3 × Z34 +19.4 × A35 + 15.1 × B35 (Tang *et al.* 2006, 2009)	
1994 East Kuril	04 Oct 13:22:58 43.73ºN 147.321ºE	04 Oct 13:23:28.5 43.60ºN 147.63ºE	8.3	8.1	KISZ	9.0 × A20 [ad hoc]	
1996 Andreanof	10 Jun 04:03:35 51.56ºN 175.39ºW	10 Jun 04:04:03.4 51.10ºN 177.410ºW	7.9	7.8	ACSZ	2.40 × A15 + 0.80 × B16 [preliminary]	
2001 Peru	23 Jun 20:33:14 16.265ºS 73.641ºW	23 Jun 20:34:23.3 17.28ºS 72.71ºW	8.4	8.2	CSSZ	5.7 × A15 + 2.9 × B16 + 1.98 × A16 [preliminary]	
2003 Hokkaido	25 Sep 19:50:06 41.775ºN 143.904ºE	25 Sep 19:50:38.2 42.21ºN 143.84ºE	8.3	8.3	KISZ	3.95 × (A22 + B22 + A23 + B23) [ad hoc]	
2003 Rat Island	17 Nov 06:43:07 51.13ºN 178.74ºE	17 Nov 06:43:31.0 51.14ºN 177.86ºE	7.7	7.8	ACSZ	2.81 × B11 [real-time]	
2006 Tonga	03 May 15:26:39 20.13ºS 174.161ºW	03 May 15:27:03.7 20.39ºS 173.47ºW	8.0	8.0	NTSZ	6.6 × b29 [ad hoc]	
2006 Kuril	15 Nov 11:14:16 46.607ºN 153.230ºE	15 Nov 11:15:08 46.71ºN 154.33ºE	8.3	8.1	KISZ	4.0 × A12 + 0.5 × B12 + 2.0 × A13 + 1.5 × B13 [real-time]	
2007 Kuril	13 Jan 04:23:20 46.272ºN 154.455ºE	13 Jan 04:23:48.1 46.17ºN 154.80ºE	8.1	7.9	KISZ	-3.64 × B13 [real-time]	
2007 Solomon	01 Apr 20:39:56 8.481ºS 156.978ºE	01 Apr 20:40:38.9 7.76ºS 156.34ºE	8.1	8.2	NVSZ	12.0 × B10 [preliminary]	
2007 Peru	15 Aug 23:40:57 13.354ºS 76.509ºW	15 Aug 23:41:57.9 13.73ºS 77.04ºW	8.0	8.1	CSSZ	0.9 × A61 + 1.25 × B61 + 5.6 × A62 + 6.97 × B62 + 3.5 × Z62 [preliminary]	

Table 1. *Continued.*

	Earthquake / Seismic					Model	
	USGS Date Time (UTC) Epicenter	CMT Date Time (UTC) Centroid	Magnitude Mw	Tsunami Magnitude	Subduction Zone		
Event						Tsunami Source (Reference/Derivation)	
(a) Standard set for Pacific Ocean models, continued:							
2007 Chile	14 Nov 15:40:50 22.204°S 69.869°W	14 Nov 15:41:11.2 22.64°S 70.62°W	7.7	7.6	CSSZ	$1.65 \times Z73$ [real-time]	
2009 Samoa	29 Sep 17:48:10 15.509°S 172.034°W	29 Sep 17:48:26.8 15.13°S 171.97°W	8.1	8.1	NTSZ	$3.96 \times A34 + 3.96 \times B34$ [real-time]	
2010 Chile	27 Feb 06:34:14 35.909°S 72.733°W	27 Feb 06:35:15.4 35.95°S 73.15°W	8.8	8.8	CSSZ	$17.24 \times A88 + 8.82 \times A90 + 11.84 \times B88 + 18.39 \times B89 +$ $16.75 \times B90 + 20.78 \times Z88 + 7.06 \times Z90$ [real-time]	
2011 Honshu	11 Mar 05:46:24 38.297°N 142.372°E	11 Mar 05:46:23 38.486°N 142.597°E	9.0	9.0	KISZ	$4.66 \times B24 + 12.23 \times B25 + 26.31 \times A26 + 21.27 \times B26 +$ $22.75 \times A27 + 4.98 \times B27$ (Tang *et al.*, 2012) [real-time]	
(b) Supplementary historical tsunami events employed for forecast model testing:							
1896 Sanriku	15 Jun 10:33:00 39.5°N 144.0°E		7.6	7.6	KISZ	$b25 \times 1.413$ [ad hoc]	
1992 Mendocino	25 Apr 18:06:04 40.368°N 124.316°W	25 Apr 18:06:11.8 38.56°N 123.31°W	7.2	7.2	ACSZ	$a65 \times 0.355$ **or** $b65 \times 0.355$ [ad hoc]	
1995 Chile	30 Jul 05:11:24 23.340°S 70.294°W	30 Jul 05:11:56.9 24.17°S 70.74°W	8.0	8.0	CSSZ	$2.812 \times (a75 + b75)$ [ad hoc]	
1995 Kuril	03 Dec 18:01:09 44.663°N 149.300°E	03 Dec 18:01:36.1 44.82°N 150.17°E	7.9	7.9	KISZ	$1.991 \times (a17 + z17)$ [ad hoc]	
1996 Irian Jaya	17 Feb 05:59:31 0.891°S 136.952°E	17 Feb 06:00:02.8 0.67°S 136.62°E	8.2	8.2	NGSZ	$2.7984 \times (a9 + b9 + a10 + b10)$ [ad hoc]	
2009 Papua NG	03 Jan 19:43:51 0.414°S 132.885°E	03 Jan 19:44:09.0 0.38°S 132.83°E	7.6	7.6	NGSZ	$0.7046 \times (b13 + b14)$ [ad hoc]	
2009 Kuril	15 Jan 17:49:39 46.857°N 155.154°E	15 Jan 17:49:48.3 46.97°N 155.39°E	7.4	7.4	KISZ	$b12 \times 0.7063$ [ad hoc]	
2009 Vanuatu/	07 Oct 22:03:15 13.052°S 166.187°E	07 Oct 22:03:28.9 12.59°S 166.27°E	7.6	7.6	NVSZ	$1.2 \times B24 + 0.26 \times A23$ *followed after 15 minutes by*	
Santa Cruz	07 Oct 22:18:26 12.554°S 166.320°E	07 Oct 22:19:15.3 11.86°S 166.01°E	7.8	7.9	NVSZ	$2.6 \times B23 + 0.9 \times A23$ [preliminary] (Yong Wei, personal communication)	

4.2 Model Development

4.2.1 Digital elevation models

Water depth determines local tsunami wave speed, and subaerial topography determines the extent to which tsunami waves inundate the land. Thus, a prerequisite for credible tsunami modeling is the availability of accurate gridded bathymetric and topographic datasets, termed digital elevation models, or DEMs. Given their expertise in this area and the number of coastal communities needing tsunami forecast capability, NCTR relies heavily on the NGDC to provide the DEMs needed. In the case of Point Reyes, California, a subregion of the San Francisco DEM is employed. This DEM, a composite of multiple data sources merged and converted to a common datum of mean high water (MHW), was produced and documented by Carignan *et al*. (2010). MHW is employed as the "zero level" in all forecast models. The MOST model does not include tidal fluctuations, and, since a tsunami may arrive at any stage of the tide, it is best to employ a "worst-case" approach by assuming high tide when forecasting inundation. For some forecast models, grounding of vessels and the strong and rapidly varying currents often associated with even mild tsunamis are of concern. For Point Reyes, which lacks a marina and shoreline infrastructure, low water impacts are less important.

The Point Reyes subregion of the San Francisco DEM is illustrated in **Figure 2**; its salient features listed in **Table 2** are reproduced from DEM documentation (Carignan *et al*., 2010). The NGDC report thoroughly describes the data sources and methods employed in constructing the DEM. With 1/3 arc sec (10 m) resolution, the DEM provides the basis for the B and C grids for both reference and forecast model usage. NCTR maintains an atlas of lower-resolution gridded bathymetries that can be used for the A grids, as described later. All of the DEMs employed were verified for consistency with charts, satellite imagery, and other datasets during the course of MOST grid development.

Table 2. The main features of the San Francisco digital elevation model (DEM), which includes Point Reyes, California.

Grid Area	San Francisco, California
Coverage Area	123.30° to 121.85°W; 37.32° to 38.48°N
Coordinate System	Geographical decimal degrees
Horizontal Datum	World Geodetic System 1984 (WGS84)
Vertical Datum	Mean High Water (MHW)
Vertical Units	Meters
Cell Size	1/3 arc sec
Grid Format	ESRI Arc ASCII grid
Version Employed	24 February 2011 update

The elevations and depths used in the development of this forecast model were based on the DEM provided by the NGDC; the author considers it to be a good representation of the local topography

and bathymetry. As new DEMs become available, forecast models will be updated and report updates will be posted at nctr.pmel.noaa.gov/forecast_reports/.

4.2.2 Tides and sea level variation

9415020 is located near the end of a pier projecting into Drakes Bay, just west of the historic Lifeboat Station. The pilings raise the deck well above sea level and do not impede water movement. The instrumentation was upgraded in 2006 to include a tsunami-capable gauge sampling at 1 min intervals (and on demand at 15 sec intervals); some earlier data were sampled at 6 min intervals, and several historical events are only available as marigrams on microfiche. An ongoing project at NGDC will be to digitize the more critical images in this archive; a few are available in digitized form in the NTWC archives.

Station characteristics for 9415020 are provided in **Table 3**, based on the wealth of online tidal information available at NOAA's CO-OPS (Center for Operational Oceanographic Products and Services) website, tidesandcurrents.noaa. gov. Note the sizeable diurnal range of about 1.7 m and, while the long-term rate of change in sea level is low (compared to more tectonically active areas), there is substantial seasonal, interannual, and short-term variability.

Table 3. Tidal characteristics of the Point Reyes tide gauge.

Point Reyes, California: Station 9415020 (37°59.7´N, 122°58.6´W)

Tidal Datum and Range Values (Epoch 1983–2001)

MHHW (Mean Higher High Water)	2.964 m		
MHW (Mean High Water)	2.760 m	Great Diurnal Range 1.758 m	Mean Range 1.193 m
MSL (Mean Sea Level)	2.152 m		
MLW (Mean Low Water)	1.567 m		
MLLW (Mean Lower Low Water)	1.206 m		

Sea Level Trends and Cycles

Long-term Sea Level Trend	Increasing 1.39 ± 1.05 mm/yr
Seasonal Cycle Range	Min. −90 mm (April); Max. +60 mm (September)
Interannual Variation (from 1980)	Min. −19 mm (1989); Max. +22 mm (1997)

Extremes to Date (October 2014)

Maximum	3.810 m on 6 February 1998
Minimum	0.387 m on 19 January 1988

An analysis of the 11 March 2011 Honshu event in the Point Reyes model is given in Section 4.3, with time series data extracted from the CO-OPS website to illustrate patterns of inundation. In a several hour section of 1 min data, the signature of an arriving tsunami is generally a burst of higher-frequency energy with a sudden onset. However, during winter months in particular, similar bursts unrelated to tsunami activity are quite common. In January 2011, for example, several occurred, one of which is illustrated in **Figure 5**. The tidal signal has been removed with a Butterworth band-pass filter with cutoff periods at 5 and 120 min. (This filter is used throughout the report to pre-process tide gauge records for comparison with model prediction.) The lower

panel of **Figure 5** is the spectral wave energy at hourly intervals from NDBC buoy 46026, 18 nm west of San Francisco. There is a clear correlation between enhanced swell at this site and the detided residuals in Drakes Bay, suggesting that surface waves can excite a coastal response. For the example shown, the amplitude of this noise (perhaps 10–20 cm) would likely obscure a mild tsunamis signature were one to arrive during such an episode. Deviations (or residuals) from the astronomically predicted tide can be several centimeters and the variability strong. In particular, the highest water level reported for the Point Reyes tide gauge is 1.05 m above MHW (6 February 1998), so the use of MHW as the zero level of modeled sea level may underestimate the truly worst case. While the simultaneous arrival of the crest of a large tsunami at high tide during a storm surge has low probability, a feature of the simulated events reported below is that sustained oscillations at a resonant period may extend the duration of the threat. This effect is notorious at Crescent City, California, which is frequently the most heavily impacted U.S. West Coast location for remote events.

4.2.3 The CFL condition and other considerations for grid design

Water depth-dependent wave speed, in conjunction with the spacing of the spatial grid representation, places an upper limit on the time step permissible for stable numerical solutions employing an explicit scheme. This is the CFL (Courant-Friedrichs- Levy) limit, which requires careful consideration when the grids employed for a reference or forecast model are being designed. Finer-scale spatial grids, or greater water depths, require shorter time steps, thereby increasing the amount of computation required to simulate a specific real-time interval.

Another feature of the application of gridded numerical solutions to the tsunami wave problem is the shortening that the wave train encounters in moving from deep water onto the shelf. In deep water, a grid spacing of 4 arc min (of latitude and longitude, corresponding to ~7 km) is normally used to represent propagating wave trains with a typical wavelength of the order of a few hundred kilometers. The stored results of such propagation model runs are typically decimated by a factor of 4, resulting in a database of ~30 km spacing (and 1 min temporal sampling) with which to generate the boundary conditions for the outermost (A grid) of the nested grids in a model solution. The extraction of the boundary conditions (of wave height and the two horizontal velocity components) is achieved by linear interpolation in space and time. To provide realistic interpolated values, the stored fields for these variables must be smoothly varying and have adequate sampling in space and time to resolve their structure. This necessitates the placement of the outer boundary of the forecast model domain well offshore. The presence of the Mendocino Escarpment is another incentive to do so, to ensure that its role in topographic steering of trans-Pacific wave trains is adequately represented.

4.2.4 Specifics of the model grids

After several rounds of experimentation, the extents and resolutions of the nested grids were chosen; these are illustrated in **Figures 6–8** and details are provided in **Tables 4** and **5**. The reference model grid extents were set early in the process when the objective was to provide forecast results from Bodega Bay to Muir Beach, but they have further value in ensuring adequate representation of waves entering the domain from remote sources. The reference model grids are displayed in **Figure 7;** in the A- and B-grid panels, rectangles show the nested grid domain within.

8

In the case of the reference model C-grid panel, the reduced extent of the equivalent forecast model grid is indicated. **Figure 8** depicts the nested grids of the forecast model itself. The main focus of the forecast model, and of this report, is on the southwestern and southern portions of Marin County. Some mention of the northern portion will be made as appropriate but with the exception of some results that can be derived from the A grid, comprehensive forecasts for Bodega Bay will require a dedicated model.

Table 4. Specifics of the reference and forecast model grids employed for Point Reyes, California. For the paired values in the resolution and grid points columns, the zonal (east to west) value is listed first, followed by the meridional (north to south).

Reference Model for Point Reyes, California

Minimum offshore depth: 1.5 m; Water depth for dry land: 0.1 m; Friction coefficient (n^2): 0.0009; CPU time for a 4-hr simulation: 305 min

Grid	Zonal Extent		Meridional Extent		Resolution	Grid Points
A	128.000°W	121.500°W	36.000°N	42.500°N	30" × 30"	781 × 781
B	123.300°W	122.100°W	37.475°N	38.475°N	4" × 3"	1081 × 1201
C	123.150°W	122.533°W	37.825°N	38.350°N	4/3" × 1"	1666 × 1891

Forecast Model for Point Reyes, California

Minimum offshore depth: 2.5 m; Water depth for dry land: 0.1 m; Friction coefficient (n^2): 0.0009; CPU time for a 4-hr simulation: 8 min

Grid	Zonal Extent		Meridional Extent		Resolution	Grid Points
A	125.000°W	122.000°W	37.000°N	39.000°N	60" × 60"	181 × 121
B	123.300°W	122.100°W	37.550°N	38.475°N	18" × 15"	241 × 233
C	123.130°W	122.533°W	37.825°N	38.100°N	4" × 3"	538 × 331

CPU times for a 4-hr simulation are based on use of a single Intel® Xeon® E5670 2.93GHz processor.

Table 5. Grid file names and grid-related parameters for Point Reyes, California. The time steps for the A and B grids must be integer multiples of the basic time step chosen for the C grid.

Grid	File Name	Maximum Depth (m)	Minimum CFL (s)	Model Time Step (s)	Water Cells
A	PtReyesCA_RM_A	5002	3.350	1.2 (2×)	436,723
	PtReyesCA_FM_A	4379	7.137	6.0 (3×)	15,977
B	PtReyesCA_RM_B	2166	0.637	0.6 (1×)	664,682
	PtReyesCA_FM_B	2114	3.062	2.0 (1×)	26,598
C	PtReyesCA_RM_C	98.6	0.995	0.6	1,411,698
	PtReyesCA_FM_C	94.7	3.045	2.0	103,086

Both C grids lie entirely within the NGDC-provided DEM; A and B grids include bathymetry and topography from other DEM datasets available at NCTR. Some smoothing and editing were necessary to eliminate erroneous points or grid features that tend to cause model instability. For example, "point" islands, where an isolated grid cell stands above water, are eliminated, as are narrow channels or inlets one grid-unit wide; these tend to resonate in the numerical solution. Large depth changes between adjacent grid cells can also cause numerical problems; customized

tools (such as "bathcorr") are available to correct many of these grid defects. An additional constraint on the bathymetry (Elena Tolkova, personal communication), which identifies excessive depth changes in the discrete representation, was applied.

Details of the model grids are provided in **Tables 4** and **5**. The latter lists the maximum depth, the CFL time step requirement that must not be exceeded, and the actual time steps chosen for the reference and forecast model runs. Since the numerical solutions in the three grids proceed simultaneously in the current version of MOST employed by SIFT, there is a requirement that the A- and B-grid time steps be integer multiples of the (innermost) C-grid time step, in addition to satisfying the appropriate CFL requirement. For both reference and forecast models, the CFL requirement of the C grid was the most stringent. The values chosen are shown in **Table 5** and are such that an integer multiple of each time step (15 × for the forecast model; 50 × for the reference model) is identically 30 sec, the chosen output time interval for both models. When run on an Intel® Xeon® E5670 2.93 GHz processor, the forecast model produces 4 hr of simulation in 7.46 min, within the desired 10 min value for this metric.

4.2.5 Model Run Input and Output Files

In addition to providing the model grid file names, the appropriate time step, and A and B grid multiples as provided in the tables above, it is necessary to provide a number of additional parameters in an input file. These include the Manning friction coefficient (n), a depth threshold to determine when a grid point becomes inundated, and the threshold amplitude at the A-grid boundary that will start the model. An upper limit on wave amplitude is specified in order to terminate the run if the waves grow beyond reasonable expectation. Usual MOST values are used: 0.0009 for the squared friction coefficient (n2)and 0.1 m for the inundation threshold. The latter causes the inundation calculation to be avoided for insignificant water encroachments that are probably below the level of uncertainty in the topographic data. Inundation can, optionally, be ignored in the A and B grids, as is the norm in the (non-nested) MOST model runs that generate the propagation database. When A- and B-grid inundation is excluded, water depths less than a specified "minimum offshore depth" are treated as land; in effect, a "wall" is placed at the corresponding isobath. When invoked, a typical value of 1–5 m is applied as the threshold, although A and B inundation is normally permitted as a way to gain some knowledge of tsunami impact beyond the scope of the C-grid domain. Other parameter settings allow decimation of the output in space and/or time. As noted above, 30 sec output has been the target and output at every spatial node is preferred. These choices avoid aliasing in the output fields that may be suggestive of instability (particularly in graphical output), when none, in fact, exists.

Finally, the input file (**Table 6**) provides options that control the output produced. Output of the three variables—wave amplitude, zonal (positive to the east) velocity, and meridional (positive to the north) velocity—can be written (in netCDF format) for any combination of grids A, B, and C. These files can be very large. A separate file, referred to as a SIFT file, contains the time series of wave amplitude at each time step at discrete cells of a selected grid. Normally, the time series at a "reference" or warning point, typically the location of a tide gauge, is selected to permit validation in the case of future or historical events. As noted earlier, several additional sites within the model domain were specified during development and are discussed in Section 4 of this report. The SIFT file output also includes the distribution of the overall minimum and maximum wave amplitude

and speed in each grid. By contrast with the complete space-time results of a run, the SIFT file (also netCDF) is very compact.

Table 6. Model input file for Point Reyes, California.

Parameters	Reference model	Forecast model
Minimum amplitude of input offshore wave (m)	0.001	0.001
Input minimum depth for offshore (m)	1.5	2.5
Input "dry land" depth for inundation (m)	0.1	0.1
Input friction coefficient (n^2)	0.0009	0.0009
A and B grid runup flag (0 = disallow, 1 = allow)	1	1
Blow-up limit/max eta before blow-up (m)	900.0	900.0
Input time step (sec)	1.0	2.0
Input number of steps	28800	32400
Compute "A" arrays every nth time step, n=	2	3
Compute "B" arrays every nth time step, n=	1	1
Input number of steps between snapshots	30	15
…Starting from	0	0
…Saving grid every nth node n=	1	1
A-grid bathymetry file	PtReyesCA_RM_A.most	PtReyesCA_FM_A.most
B-grid bathymetry file	PtReyesCA_RM_B.most	PtReyesCA_FM_B.most
C-grid bathymetry file	PtReyesCA_RM_C.most	PtReyesCA_FM_C.most
Directory of source files	./	./
Directory of output files	./	./
netCDF output for A, B, C, SIFT	1 1 1 1	1 1 1 1
Number of time series locations	1	1
Grid & cell indices for reference point	3 335 967	3 139 125

By default, two additional output files are generated. A "listing" file summarizes run specifications, progress, and performance in terms of run time, as well as information to determine the reason, should a run not start or terminate early. A "restart" file is produced so that a run can be resumed from the time it ended, either normally or by operator intervention.

The input files described above are specific to the model itself. For an actual run, the program must be pointed toward the files that contain the boundary conditions of wave amplitude (H) and velocity components (U, V) to be imposed at the A-grid boundary. Time-varying conditions are generally extracted as a subset of a basin-wide propagation solution (either a single unit source or several, individually scaled and linearly combined) that mimics a particular event. These boundary forcing files typically consist of 24 hr of values (beginning at the time of the earthquake), sampled at 1 min intervals and available on a 16 arc min grid. Occasionally, for more remote seismic sources or when delayed arrival of secondary waves due to reflections are a concern (as has been seen at Hawaii), the time span of the propagation run available for forcing is extended beyond one day.

4.3 Results and Discussion

Before proceeding to an extensive suite of model runs that explore the threat to Marin County, California, from various source regions, the stability of the Point Reyes model is tested in both low and extreme amplitude situations. The former we refer to as "micro-tsunami" testing, where the

boundary forcing is at such a low level (but not precisely zero) that the response is expected to be negligible. These tests can be highly valuable in revealing localized instabilities that may result from undesirable features in the discretized bathymetric representation. Inlets or channels that are only one grid-cell wide may "ring" or resonate in a nonphysical way in the numerical solution. An instability may not grow large enough to cause the model to fail but, in a run with typical tsunami amplitudes, may be masked by actual wave variability.

Forcing by extreme events, which we refer to as "mega-tsunami" events, is also tested. In addition to the need to test model stability under such circumstances, there is a parameter in the input file that truncates the run if a prescribed threshold is exceeded. For operational use, the threshold must be set high enough so that an extreme event run is not unnecessarily terminated. Both tests should be performed for test sources whose waves enter the model domain from different directions since, although stable for one set of incoming waves, an instability may be encountered for another. The micro- and mega-tsunami testing of the forecast and reference models is reported in the following subsections. Further evidence of stability is provided by the extensive set of historical (Sections 4.3–4.6) and synthetic (Section 4.7) scenarios, aimed at exploring the dependence of impact to source location and used in independent testing by other members of the NCTR team prior to the model's release for operational use.

4.3.1 The micro-tsunami tests

Three cases (see **Table 7**) were run representing micro-tsunami sources in the western Aleutians, the Philippines, and south of Japan (see **Figure 10**). Based on sources from the propagation database (Gica *et al*., 2008), their amplitudes were scaled down by a factor of 100 so as to mimic a Mw 6.167 / Slip 0.01 m source rather than the Mw 7.5 / Slip 1 m of a unit source. A number of grid cells in the B and C grids emerged as potential sources of instability. Generally, these were minor indentations of the coastline barely resolved by the grids, or narrow channels. The region contains several inlets (called *esteros*) extending far inland that, at a practical level of spatial resolution, proved difficult to accommodate. Among these are the upper reaches of the multiple arms of Drakes Estero and, feeding into Bodega Bay, Estero Americano and Estero de San Antonio. A limited number of grid cells in the outermost (A) grid required correction. These were generally associated with non-physical features in the topographic database, such as a track of ship-based soundings that were improperly merged with other data sources. After an iterative process of grid correction and retesting using these sources, both the reference and forecast model grids were deemed satisfactory and the testing of extreme and historical events could begin. **Figure 9** illustrates a step in the process where a deficiency in the reference model grid generated a mild instability (in the EPSZ B19 micro-tsunami scenario—see **Table 7**) causing the reference model time series at the reference point, initially in close agreement with the forecast model, to develop unrealistic, high-frequency oscillations. Though still generally tracking the forecast model result, and not growing without bound, the feature could behave erratically in simulating real events. Modification of the reference model bathymetry eliminated the problem, as seen in the lower panel of **Figure 9**, and micro-tsunami tests involving other sources (RNSZ B14 and ACSZ B6) did not reveal other issues.

Table 7. Synthetic tsunami events employed in Point Reyes model testing.

Scenario	Source Zone	Tsunami Source	α [m]
Mega-tsunami (Mw 9.3) Scenario			
KISZ 1–10	Kamchatka-Kuril-Japan-Izu-Mariana-Yap	A1–10, B1–10	25
KISZ 22–31	Kamchatka-Kuril-Japan-Izu-Mariana-Yap	A22–31, B22–31	25
KISZ 32–41	Kamchatka-Kuril-Japan-Izu-Mariana-Yap	A32–41, B32–41	25
KISZ 56–65	Kamchatka-Kuril-Japan-Izu-Mariana-Yap	A56–65, B56–65	25
ACSZ 6–15	Aleutian-Alaska-Cascadia	A6–15, B6–15	25
ACSZ 16–25	Aleutian-Alaska-Cascadia	A16–25, B16–25	25
ACSZ 22–31	Aleutian-Alaska-Cascadia	A22–31, B22–31	25
ACSZ 50–59	Aleutian-Alaska-Cascadia	A50–59, B50–59	25
ACSZ 56–65	Aleutian-Alaska-Cascadia	A56–65, B56–65	25
CSSZ 1–10	Central and South America	A1–10, B1–10	25
CSSZ 37–46	Central and South America	A37–46, B37–46	25
CSSZ 89–98	Central and South America	A89–98, B89–98	25
CSSZ 102–111	Central and South America	A102–111, B102–111	25
NTSZ 30–39	New Zealand-Kermadec-Tonga	A30–39, B30–39	25
NVSZ 28–37	New Britain-Solomons-Vanuatu	A28–37, B28–37	25
MOSZ 1–10	Manus-Oceanic Convergent Boundary	A1–10, B1–10	25
NGSZ 3–12	North New Guinea	A3–12, B3–12	25
EPSZ 6–15	East Philippines	A6–15, B6–15	25
RNSZ 12–21	Ryukyu-Kyushu-Nankai	A12–21, B12–21	25
Mw 7.5 Scenario			
NTSZ 36	New Zealand-Kermadec-Tonga	B36	1
Micro-tsunami (Mw 6.5) Scenario			
EPSZ B19	East Philippines	B19	0.01
RNSZ B14	Ryukyu-Kyushu-Nankai	B14	0.01
ACSZ B6	Aleutian-Alaska-Cascadia	B6	0.01

4.3.2 The mega-tsunami tests

The record of tsunami impact on the northern California coast discussed later reveals that sources around the entire periphery of the Pacific can be felt. Indeed, the catastrophic Indian Ocean tsunami of 2004 was detectable at Point Reyes, as it was throughout the global ocean. A broad suite of 19 extreme events (so-called mega-tsunamis) are part of the NCTR protocol for the testing of Pacific basin forecast models. These are listed in **Table 7**, and their locations are included in **Figure 10**. To simulate each mega-tsunami source, 10 A–B pairs of unit sources are used, with an evenly

distributed slip of 25 m. As described by Gica *et al*. (2008), each unit source represents a 100 × 50 km area of the fault surface, with the long axis parallel to the plate boundary. Row B is shallowest, sloping from a nominal depth of 5 km (unless a depth estimate has been provided by the USGS based on the earthquake catalogs), row A is deeper, followed by rows Z, Y, X, etc. where appropriate. Thus, the mega-tsunami event sources represent 1000 km long ruptures with a width of 100 km; the corresponding magnitude is Mw 9.3.

Discussion of the entire set in greater detail is provided (Section 4.7) once the validity of the forecast model has been established. Here we focus on a subset of three synthetic cases, highlighted in **Figure 10** and **Table 7**, to contrast the forecast model with the more highly resolved reference model. In **Figures 11–13**, the reference model results (from the subregion spanned by the forecast model) are shown in the upper panel. The corresponding forecast model results in the lower panel employ the same scale. Insets are used to show the time series (black for reference model, red for forecast model) of H, U, and V at the warning point (the Point Reyes tide gauge). The lagged correlation of H at the reference point is drawn in the lower inset and illustrates that there is generally only a few minutes lag between the time series, with the reference model lagging behind the forecast model. This behavior is repeated in other scenarios investigated in this chapter. It is a general feature of MOST and is due to the tendency of more finely resolved features in the bathymetry slowing the progress of long waves, and arises in the context of model validation using observations.

The agreement between the reference and forecast model results for the three mega-tsunami events is good, both for the maximum amplitude and speed distributions, the reference point time series, and the discrete "snapshots" of the amplitude and vector velocity fields. The earliest waves show the best agreement; later in the solution the reference and forecast model results begin to diverge as multiple reflections with the coastline occur. A qualitative difference between the solutions is often seen along the straight coastline north of Point Reyes Lighthouse (see **Figures 1** and **2**). The straight shoreline, bounded by rocky headlands at the south and north, supports edge waves that appear most noticeably in the reference model results almost as a standing wave pattern, but generally do not propagate around the headland and into Drakes Bay.

It is noticeable that, in all three of the cases shown, the reference model tends to oscillate longer and have somewhat larger amplitude than does the forecast model although the two solutions are in close agreement for the first few tsunami waves. This is likely a physical reality: the more highly resolved bathymetry and coastline of the reference model provides greater scope for nonlinear features or reflected waves to develop (as, for example, near the rocky headland west of Bodega Bay). This observation suggests a caveat to operational use of the forecast model: while accurate portrayal of the early history of an event is to be expected, the duration of the event and the amplitude of later waves may be underestimated. Tide gauge data will be needed to verify this conjecture, which is pursued later in this report.

The snapshot comparisons in the lower panels of **Figures 11** and **12** are quite reasonable, illustrating that the solutions match not just at the reference point. It is worth noting too that, although the ACSZ 56–65 mega-tsunami event represents a massive Cascadia tsunami, the scale of impact to the Point Reyes area (~3 m) is not substantially greater than from trans-Pacific locations (KISZ 1–10 off Kamchatka and NTSZ 30–39 near Samoa.) The Crescent City response

to the same synthetic Cascadia mega-tsunami event exceeds 10 m (Arcas and Uslu, 2010). It would appear that the energy propagated alongshore to the south, perhaps due to sheltering by Cape Mendocino, is reduced, and that perhaps the greatest impact to Marin County may be associated with source regions elsewhere in the Pacific basin.

In **Figure 13**, the comparison time was intentionally chosen later in the event as a counterexample. While the warning point amplitudes and the nearby fields of the forecast and reference model may be in reasonable agreement, the broader wave patterns may have substantial phase differences. The comparisons in these lower panels are restricted to the portion of C-grid area common to both models, there is a suggestion that the nearshore velocity fields at the north and south forecast model boundaries differ somewhat from the reference model for which these are internal points.

Before proceeding to validate the model with historical events, one other synthetic event is standard in the testing protocol: a mild source of Mw 7.5 at a remote location. A single unit source near Samoa (NTSZ B36, see **Figure 10**) is employed here and its representation by the reference and forecast model are compared in **Figure 14**. Such an event results in a response of about 4 cm in Point Reyes sea level and again, there is excellent agreement between both model representations in the earlier portion of the event.

The results presented above, for a variety of synthetic events, suggest that the reference and forecast versions of the model are in good agreement. The match is particularly good in the early stages of a wave train; later, as reflections and other interactions with the coastline occur, the solutions may diverge. The next task is to ascertain whether the models replicate observations from actual tsunami events. Given the manner in which the MOST model is forced, at its boundary (with wave amplitudes and currents not available in real observations), it is not possible to validate the model independently. Rather, as described in Section 2.2, the validation will rely on the results of an external model, based perhaps on DART observations or on a description of the tsunami source in the literature. As a result, the success of the model in replicating observations within its domain is, in part, dependent on the adequacy of the forcing employed to represent the actual external wave field. For historical events preceding the DART array, the unit source representations are based on seismic observations or coastal tide gauge data. Past experience suggests that, in the far field at least, the propagation solution is not overly sensitive to variation in the unit source weights. Nonetheless, imperfections in forecast model predictions of coastal observations will not necessarily indicate a defect in the model itself. Neither are the tide gauge observations, available for comparison with model prediction, perfect. They may include noise from wind wave activity, possibly amplified by harbor resonances.

4.3.3 Model validation: The 2011 Honshu tsunami

In addition to its disastrous impact on the coast of Japan, the Honshu tsunami of 11 March 2011 radiated waves throughout the Pacific basin. Those arriving at nearby DARTs were of unprecedented amplitude and their signal-to-noise ratios facilitated accurate and early source characterization. Further afield, the waves were detectable at all operational DARTs in the basin and, while major damage was mainly confined to Japan, significant signals were obtained at multiple coastal tide gauges. Prior to this event, the 2006 Kuril tsunami event was the best available for model validation. For the U.S. West Coast at least, that role has now been taken by the 2011

Honshu tsunami. The adequacy of the composite propagation solution can be assessed by comparison with the BPR signals from the West Coast DARTs. An additional BPR record is available for this purpose: the MARS cabled observatory in Monterey Canyon included, between July 2010 and November 2011, a pair of bottom pressure sensors at a depth of about 870 m. One was a typical BPR, reporting at the standard DART 15 sec recording interval. The other was an experimental sensor—the "Nano" (Paros *et al.*, 2011)—sampling at 40 Hz with enhanced sensitivity. For this report, we employ only data from the typical BPR.

The locations of the West Coast BPRs, reporting during the 2011 Honshu event, are shown in **Figure 15**. To the left of the locator chart, the actual and simulated propagation model results, interpolated to the BPR locations, are compared. There is clearly a strong agreement but even for the earliest waves, there are two points of difference. Firstly, the model "waves" (drawn in black) arrive about eight minutes early, a difference that is small compared to the transit time of over nine hours. Early arrival in the model is typical and is associated with the limited resolution of the basin-wide bathymetry. Finer-scale features in the actual bathymetry slow down the real wave trains (the red curves). The other feature of the modeled versus observed comparison is that the model underestimates the observed signal by about 20% at all locations. In the right-hand panel of **Figure 15**, the lagged and scaled-up versions of the model time series are seen to be in excellent agreement with observations. Since these results are likely the best obtainable with the current state of the DART array and inversion methodology, less than perfect agreement between the forecast model and observations is not necessarily indicative of a major defect in the forecast model itself.

With that caveat, we proceed with the model validation. The prime location for this purpose is the Point Reyes tide gauge itself, the "reference point" for the current model. Other coastal locations termed "warning points" are of interest to the TWCs though they may not have their own dedicated forecast model. In its basic form, SIFT's coastal forecast for warning points is generated by extrapolating offshore values from the propagation solution to the coast using Green's law. Based on simple assumptions, this law indicates that the waves should grow in inverse proportion to the one-fourth power of the depth ratio. The assumption is crude at best, and it makes sense that, when a forecast model has been run, the predictions within its domain are likely to be superior to the Green's law equivalent and should replace them in an enhanced coastal forecast. For the Point Reyes model, tide gauge observations are available at several points within the domain and, in the case of the 2011 Honshu event, all of these had detectable signals. The auxiliary sites are Bolinas, lying within the C grid but within the lagoon and with only 6 min sampling; San Francisco, Alameda, and Richmond, within San Francisco Bay and the model B grid, with 1 min sampling; Arena Cove, near the northern bound of the forecast model A grid, also with 1 min sampling. The results of the comparison may be seen in **Figure 16** where the reference (black) and forecast (red) versions of the model response are compared to the observations (green.) The model curves have been lagged to facilitate the comparison but, unlike the 20% enhancement needed to bring the propagation results into conformity with the DART observations (see **Figure 15**), the amplitude within the forecast model has not been adjusted. For the first six hours of the event, the agreement between observation and model is quite gratifying, particularly at Point Reyes itself and at San Francisco. For Arena Cove, the agreement is limited more to the early waves. Perhaps as a result of resonance associated with local geometry, the observed response grows and shifts to a higher frequency than appears in the model signals. The reference model solution is a better match in

amplitude to the observations from Arena Cove than is the forecast model, whose representation of the geometry is quite coarse.

The good agreement between the model amplitude and observation at Point Reyes, particularly for the first wave, is an apparent contradiction of the situation at the offshore sites. There, as noted above in the discussion of **Figure 15**, the model forcing underestimated the observations by some 20%. The explanation lies in an unfortunate data loss in the 1 min data stream from the coastal tide gauges during the early part of the event. At most sites, the loss was 18 min, 16:03 to 16:20 UTC (slightly longer at San Francisco), as highlighted in yellow in **Figure 16**. During the event, and in the days that followed, 15 sec data were downloaded from some tide gauges to bridge the gap. At Point Reyes, these supplementary 15 sec data were unavailable prior to 18:19 UTC. A few points from the 6 min data stream were employed in the bridging and filtering operations that resulted in the observed Point Reyes time series. Six minute data badly alias the short time scales of the tsunami waves and, as a result, the apparent close agreement of model amplitude and observation for the first wave peak is probably fortuitous.

Progressing deeper into San Francisco Bay, at Alameda and Richmond, the match between the models themselves and the observations is degraded compared with the better agreement near the entrance. Nonetheless, the agreement is quite good and shows promise for an improved "coastal forecast" usage of Point Reyes' forecast model results. Least satisfying, but understandable, is the comparison at Bolinas. The tide gauge there lies within the mouth of the lagoon, and an adequate representation of the narrow entrance channel is difficult, particularly in the forecast model. As is common with narrow-mouthed entrances to enclosed regions, there is a tendency for the model to retain water (red curve in the upper panel of **Figure 16b**) where Bolinas Lagoon increasingly does not empty during the "ebb" phase of the tsunami wave train. The reference model solution, perhaps as a result of excessive modifications or inaccurate representation of entrance geometry in the DEM, seems to resonate far more than the observational record. It is possible, however, that with its 6 min sampling and placement, the Bolinas tide gauge is not well suited to tsunami detection. On a positive note, the timing and amplitude are not grossly dissimilar to the data. The purpose of the forecast model is more to predict the impact on the seaward side of the Stinson Beach spit, and, based on the success at San Francisco, forecasts outside constricted regions of the model domain are likely to be quite useful for warning purposes.

We now step back in order to verify the agreement between the reference and forecast model solutions throughout the common portion of the C-grid domain. In **Figure 17**, as was done for the purely synthetic scenarios, the solutions are compared, based on their maximum amplitude and speed fields, and the time series and lagged correlation at the Point Reyes tide gauge site. The distribution patterns of the maximum fields are comparable and it is not unexpected, based on the Point Reyes time series sample, that the reference model should be the greater, with the mismatch coming perhaps for the later waves. A pointwise (zero lag) correlation distribution (not shown) between reference and forecast model throughout the forecast model C-grid domain indicates that over 60% of the variance is explained, except in constricted areas. The lagged correlation inset confirms a phase difference of only a few minutes between the reference and forecast model time series at the tide gauge. As a further means of comparing the reference and forecast model solutions, snapshots of the amplitude and velocity fields are also provided in **Figure 17**. A common scale is used for both the reference (upper panel) and forecast (lower panel) model. The agreement

is particularly close when the comparison time (indicated by the green line) is close to the first peak's arrival at the tide gauge. Two later sample times are shown in **Figures 17d** and **17e**, illustrating that phase differences can increase as the event unfolds.

The analysis of the 2011 Honshu event in the Point Reyes model is concluded with an examination of the pattern of inundation in **Figure 18**. For this purpose, the full reference model C-grid domain is drawn. The model suggests that, had the waves arrived at or above MHW, both the Limantour Spit and much of Stinson Beach and the low-lying parts of Bolinas may have been inundated. In fact, as illustrated in the inset based on the observed water level at the Point Reyes tide gauge, the waves barely attained MHW. Though the reporting of the impact on the U.S. may have been somewhat muted, given the gravity of the imagery from Japan, it appears that on the U.S. West Coast, the main evidence of the tsunami was in excessive currents, notably in California at Santa Cruz and Crescent City. As designed, with model sea level set at MHW, the forecast erred on the side of conservatism. In the northern portion of the reference model domain (excluded in the forecast model C grid), the greatest response was predicted with inundation of the Doran Beach spit and the Dillon Beach / Lawson's Landing area at the north and south ends of Bodega Bay. Although in reality no actual inundation occurred due to the state of the tide, video clips posted online document strong currents beneath the Lawson's Landing pier, and oscillations of 2–3 ft with 20 min periodicity were reported for Dillon Beach. Examination of the model time series, both the reference and forecast versions, from Bodega Bay (not shown) indicate that the northern and southern portions were rising and falling together, so the large amplitudes responsible for the inundation pattern were not associated with the excitation of an alongshore standing wave mode. Also shown in **Figure 18** is the CalEMA Inundation Line, based on an ensemble of synthetic mega-tsunami scenarios. The MHW-based model prediction does impact, albeit at a lesser level, the regions that the CalEMA study identifies as vulnerable.

4.3.4 Model validation with other preferred historical events

We now proceed to examine, for several other historical cases highlighted in **Table 1a** and **Figure 6**, how well the reference and forecast model solutions compare with observation. These are among the preferred cases in the NCTR protocol to be applied in the validation of Pacific Ocean forecast models. The reference and forecast model time series are intercompared at Point Reyes tide gauge, Arena Cove, and San Francisco, and are validated where possible with observation, and the same representations of maximum amplitude, pointwise correlation, and snapshots of the reference and forecast model fields are drawn.

The results, displayed and described below, represent other DART-detected and well-documented recent events: 2010 Chile, 2009 Samoa, and 2006 Kuril, the latter being the first substantial event for which direct observation of the tsunami wave train was available from multiple deep water DART sites. These events occurred subsequent to the installation of the tide gauge at Point Reyes. Two pre- DART cases are included in this section: 1964 Alaska and 1946 Unimak, whose large amplitudes caused severe damage to Hawaii and provided the impetus for the establishment of the TWCs. Source characterization for these events is based on the literature, with the source mechanism estimated from the seismic record.

For the 2010 Chile event, the direct comparison of the reference and forecast model appears in **Figure 19** with satisfactory results, both in terms of reference to forecast model intercomparison and agreement with the observed time series at the three locations displayed in **Figure 20**. The amplitude series match well throughout the six-hour period shown, and there is strong pointwise correlation throughout the common domain. Comparisons of observations with predictions based on the dedicated forecast models are to be found in the forecast model reports for Arena Cove (Spillane, *in press*) and San Francisco (Uslu *et al.*, 2010) and in post-event reports online at the NCTR website. Excellent agreement is seen for Point Reyes and San Francisco, although the leading wave at Point Reyes is overestimated and the timing of some later features at San Francisco is less than perfect. The observational record at Arena Cove is noisier, although the amplitude of the first wave is captured well by both models.

For the 2009 Samoa event, the equivalent set of results is shown in **Figures 21** and **22**. Despite the considerably more complex structure of the maximum amplitude field, the forecast model pattern is in good agreement with that from the reference model and the time series for the first few hours agree well. Later, the forecast model solution appears to decay faster than that from the reference model. Considering the Point Reyes observations in **Figure 22**, the reference model is in better agreement with the amplitude of later waves. At San Francisco, the situation is less clear, with the reference model perhaps overestimating the observed response, while at Arena Cove, neither model (as extracted from the A grid) reproduces the severe ringing evident in the observations.

Figures 23 and **24** represent the 2006 Kuril event. Agreement between the models is strong, both for the early and later portions of the record shown. However, in comparisons with observations, the models underestimate later features in the San Francisco observations, and the forecast model response decays far too rapidly at Arena Cove. At both locations outside the C grid, the predicted maxima are less than 50% of what was observed. To summarize these three events, with weaker impacts than the 2011 Honshu event, the accuracy of a revised "coastal forecast" based on the A and B grids may be reduced. It remains to be demonstrated whether they are significantly better than those based on Green's law.

The 1964 Alaska and 1946 Unimak events were widely felt along the U.S. West Coast, although the greatest impact was to the Hawaiian Islands. The model representations of these major pre-DART events are illustrated in **Figures 25–28**. The reference and forecast model representations of the 1964 Alaska event in the C grid are seen (**Figure 25**) to be in close agreement, both in terms of their maxima and at the arrival of the first wave peak. During the 1964 Alaska event, a runup of 240 cm was reported for Drakes Bay (Point Reyes) with 274 cm at Muir Beach and 113 cm at San Francisco. Arena Cove and Bodega Bay experienced runups of 183 cm and 76 cm, respectively. The maxima of the model time series (**Figure 26**) are in good agreement with these reports, although both the reference and forecast model amplitudes for the first wave at San Francisco are about twice the observed value.

The representation of the 1946 Unimak event is also satisfactory, with close agreement of the pattern of reference and forecast model maxima, the time series of wave amplitude and velocity at the Point Reyes reference point, and for the instantaneous "snapshots" of these fields an hour after the leading peak (**Figure 27**). Reported runups associated with the 1946 Unimak event were 240 cm at Arena Cove, 130 cm at Bolinas, and 256 cm at Muir Beach; runup at San Francisco and

Alameda were 26 cm and 20 cm, respectively. The model hindcasts for San Francisco (**Figure 28**) are in reasonable agreement with the observation, and the model maximum at Point Reyes is consistent with the reported runup at nearby Bolinas. The model result for Arena Cove considerably underestimates the reported value. This may be due to the coarse representation of Arena Cove in the A grid of the present model, with the better result for the 1964 Alaska event being fortuitious, or indicative of directionality as a factor in model fidelity. However, for both events, the results support the usefulness of model results beyond the C grid for forecast purposes.

4.3.5 Other historical simulations of interest at Point Reyes, California

The above analysis has documented good agreement between the forecast model and the slower-running reference version. This permits us to simulate the balance of the historical cases (and the remaining mega-tsunami scenarios) in **Table 1a**, where impacts to the study area have been reported with the forecast model alone. These runs are intended to further validate the stability of the forecast model but also provide some information on the exposure of the region to tsunamis generated at various points on the periphery of the Pacific.

The quality of the modeling of the historical events highlighted above is likely to be the result of good characterizations of the source, based on DART observations in the case of recent tsunamis or extensive post-event analysis in the case of the historical examples. In the absence of direct and timely observations, the successes of the forecast models are likely to be much reduced. An extreme case in point is the 1896 Sanriku event, a so-called "tsunami-earthquake" (Dudley and Lee, 1998), causing devastating losses in Japan despite its modest magnitude and scant warning in the form of ground motion. A digitized marigram from Sausalito (across the Golden Gate from San Francisco) is available from the NTWC archives and is drawn in the lower panel of **Figure 29**. While the timing is reasonably represented, the amplitude considerably underestimates the reported runup of 10 cm at Sausalito and 20 cm at San Francisco. The nearest location outside the bay to report runup for this event was Santa Cruz, at 150 cm.

For the 1957 Andreanof event, reported runup values of 29 cm at Bodega Bay, 26 cm at San Francisco, and 18 cm at Alameda are in reasonable agreement with the model results (35 cm, 46 cm, and 23 cm, respectively). No observed time series is available for comparison for this event, nor for the 1994 East Kuril event. For the latter, only a 4 cm runup reported at Alameda is available for validation; the maximum model amplitude for Alameda at 2.5 cm is in good agreement. For the remaining events in **Table 1a**, time series are available for more thorough validation and are displayed in **Figures 30–36** with limited comment; runup values from the NGDC database, where available, are added as annotations to the graphics.

The impact of the 1952 Kamchatka Mw 9.0 event is available as a marigram from San Francisco (**Figure 30**). Its amplitude there is well represented by the model, suggesting that a runup of 3 m or more may have occurred at Point Reyes and elsewhere in Marin County. For the 1960 Chile Mw 9.5 event, the character of the observed response is quite different from the model representation. As seen in **Figure 31**, the model exceeds the observed amplitude response by a factor of 2–3, and lacks the higher frequency components evident in the observations some hours into the event. The model wave arrives about 20 min early. At Alameda, also within San Francisco Bay, the maximum amplitude of the model, at 68 cm, is about twice the reported runup of 31 cm.

At Stinson Beach, the model exaggeration is less severe: 217 cm compared to the observed 152 cm, but is again large (68 cm compared to the observed 25 cm) near Bodega Bay.

Figure 32 presents the validation results for the 1996 Andreanof event. At Point Reyes the agreement is quite good, and at Alameda the weak model waves seem to capture some of the features of the observed series. At Arena Cove, however, the signal is far too weak to be visible against the high noise background. For the 2001 Peru (**Figure 33**) and 2003 Hokkaido (**Figure 34**) events, the validation is quite satisfactory, but for the winter 2003 Rat Island event, as seen in **Figure 35**, there is considerable noise at the validation sites, limiting the visibility of signals as weak as the model predicts. This event is, however, notable in that, aided by direct observations of bottom pressure from precursors to the DART array, useful forecasts were provided to inform Hawaii's emergency response. The 2006 Tonga event proved useful for validation of the Point Reyes model, with a strong response, shown in **Figure 36**, that agrees well with observation.

The year 2007 brought several events with which to validate the model, beginning with the normal thrust earthquake seaward of the Kuril Trench in January 2007. As seen in **Figure 37**, the model correctly captured the leading trough and amplitude seen at Point Reyes and San Francisco, although at Arena Cove, the background noise limits the usefulness of the observations. The 2007 Solomon event hindcast (**Figure 38**) is reasonably satisfactory but the signal in both the model and the observations is weak. In August, an event off Peru (**Figure 39**) appears to match well the observations at Point Reyes, but at Arena Cove and San Francisco, while the model seems to capture the amplitude and timing of the early waves, the later portion of the event is less satisfactory. The final event to be treated, among those listed in **Table 1a**, is the weak winter 2007 Chile event. Not surprisingly, since the forecast amplitudes are very small off California, there is not a lot to be learned from this event, displayed in **Figure 40**.

Several additional events, listed in **Table 1b**, are available for analysis. Of these, the 1896 Sanriku event has been presented earlier, and the Cape Mendocino tsunami of 1992 as the sole, albeit weak, representative of a Cascadia event, is described in the next Section. The remainder, generally weak in terms of their impact and most occurring in winter where the noise background limits the signalto- noise ratio, are not reported other than to state that all ran without difficulty or evidence of instability.

4.3.6 The Mendocino earthquake of 25 April 1992

Of special interest to northern California is the Mendocino earthquake of 25 April 1992. This has the distinction of being the most recent substantial thrust event on the Cascadia Subduction Zone. While strike-slip events are commonplace offshore in this region, as shown in the upper right panel of **Figure 41**, it is thrust faults that have the potential to generate significant vertical displacements of the seafloor that cause large tsunamis. The epicenter of the 1992 event was on land to the southeast of the plate triple-junction off Cape Mendocino. Uplift on the order of a meter of a 25 km stretch of the nearshore, between Cape Mendocino and Punta Gorda to the south, was evident in a die-off of intertidal organisms, reported by Carver *et al*. (1994). Presumably extending offshore too, this deformation is not well represented by either of the southernmost unit sources (ACSZ A/B65) now available in the propagation database (see **Figure 6**, where the epicenter is marked by the seismic "beach ball"). A custom source, available from NCTR but not part of the

propagation database, is used to model the event for comparison with two digitized marigrams, obtained from the NTWC archives and plotted in the lower panels of **Figure 41**. The model performs reasonably in representing the leading wave, though the model series had to be delayed by 30 min to achieve alignment. This time offset, greater both in actual time units and as a percentage of travel time than those typically necessary to adjust transbasin predictions, may be the result of the coarse representation of the nearshore bathymetry. Another possible explanation is that this event, described by González *et al.* (1995), may have generated a train of coastal-trapped edge waves. Traveling slower than normal tsunami waves taking a deep water route, the edge waves may have resulted in a delayed arrival and an extended duration for the event. This possibility, and the suggestion that the ACSZ source line should be extended at least one unit further south, make this an event worth further study. The reference and forecast models for Point Reyes and other West Coast models (Eureka, Crescent City, etc.) have a major role in ongoing risk assessment studies for Cascadia.

To summarize the analysis of historical events in the preceding sections, it would appear that the Point Reyes forecast model is capable of producing accurate forecasts for this open coast site on the U.S. West Coast. Though the actual waves may be difficult to observe accurately at the tide gauge during winter storms, the objective of producing credible forecasts of sizeable tsunami impacts appears to have been met. Enhanced "coastal forecast" estimates for locations within the Point Reyes B grid can be useful, while sites in the A grid (as illustrated by Arena Cove) may have less utility.

4.3.7 Simulation of the remaining synthetic mega-tsunami events

We conclude this section with a summary of other model runs, included to verify the stability of the Point Reyes model, that provide useful information on the exposure of Point Reyes to potentially hazardous future events within the Pacific. As noted earlier, the sparse instrumental record of actual events needs to be augmented with credible scenarios to permit risk assessment. While not pretending to be a full-blown risk assessment for the Point Reyes and southwest Marin County area, the full set of mega-tsunamis modeled during stability testing can provide some early estimates.

Results for the set of 19 mega-tsunami events based on the forecast model are presented in **Figure 42**. Each source is a composite of 20 unit sources from the A and B rows with an evenly distributed slip of 25 m, representing a Mw 9.3 event. A color-coded square, drawn at the geometric center of each synthetic source, is used to represent the impact at Point Reyes resulting from that source. The measure of impact employed in **Figure 42** is the maximum amplitude of the predicted time series at the reference point. There is no simple relationship apparent between source orientation, location, or great circle distance to Point Reyes; focusing associated with seafloor features can more than compensate for the decay associated with geometric spreading. It is notable that the greatest impact at Point Reyes comes from transbasin sources rather than from those representing Cascadia. The latter apparently beam most of their energy directly onshore or offshore into the open ocean; arrows normal to the plate boundary are used in **Figure 42** as an approximate indicator of main beam direction.

Further results from the suite of mega-tsunami event scenarios are presented in **Table 7**. Seven sites within the C and B grids of the forecast model are represented, with the first being the Point Reyes tide gauge, illustrated graphically in **Figure 42**. Limatour Beach is a well-visited recreational site within the Point Reyes National Seashore; Stinson Beach, adjacent to Bolinas, and Muir Beach are coastal communities between Point Reyes and the southern limit of the forecast model C grid at Point Bonita. Doran Beach and Lawson's Landing represent communities within Bodega Bay, which is only represented in the forecast model B grid. San Francisco, also in the B grid, is included owing to the wealth of tsunami records available there. While Point Reyes has the most (10) instances of the greatest amplitude among the selected sites, for the mega-tsunami events treated here, Muir Beach, with seven instances and the two overall greatest impacts, is clearly threatened. These results are consistent with the large runup reported at Muir Beach in the historical record. Lawson's Landing, with the remaining two cases (one representing the southern end of Cascadia, the other the mid-Aleutians), is also clearly at risk. Given the inundation that might have resulted had the 2011 Honshu waves arrived under adverse tidal conditions (**Figure 18**) and statements by emergency responders in the "Marin Tsunami" video, Bodega Bay perhaps warrants a dedicated forecast model, although it lacks an instrumented reference point. Given the linear geometry and orientation of Bodega and Tomales bays, version 4 of MOST, which is not limited to north-south and east-west grid lines, should be well suited.

Finally, the set of 19 mega-tsunami scenarios evaluated here is an approximate match to the set employed in the CalEMA study that established an inundation line for California. In **Figure 43**, an ensemble of the inundation predictions by the Point Reyes forecast model is compared with the CalEMA results. The forecast model C-grid cells inundated by one or more of the mega-tsunami scenarios are colored red; the CalEMA inundation line is drawn in blue. (The flooded area, in square kilometers, associated with each scenario is included in **Table 8**.) The underlying topography in **Figure 43** uses the reference model grid to better indicate coastal indentations. The forecast model provides a reasonable match in most of the threatened areas, particularly the Limantour Spit and Beach areas and Stinson Beach. In some areas, such as Muir Beach, the reduced resolution of the forecast model limits the penetration of flooding there. No attempt has been made to adequately represent Tomales Bay in the forecast model. Its shallowness and the constrictions at its mouth cannot be adequately represented at the spatial resolution necessitated by the run-time constraints for emergency usage.

4.4 Conclusions

To conclude, good agreement between observations and model predictions for a subset of historical events, including the recent 2011 Honshu tsunami, has been established, and the stability of the model for numerous synthetic events has been demonstrated. In particular, the reliability of the forecast model, designed to run rapidly in real-time emergency conditions, has been proven by the favorable comparison with reference model predictions, particularly during the early hours of an event. The model will be included in the SIFT system employed operationally at the Tsunami Warning Centers, and will permit the Point Reyes, California beaches and the communities of Bolinas, Stinson Beach, and Muir Beach to be added to the coastal communities for which forecast

capability is available. Additionally, this model will provide a tool for use in risk assessment studies.

In addition to the scenarios run by the author and reported here, further tests have been made by other members of the group at NCTR, and will continue to be made by staff at the Tsunami Warning Centers and others, perhaps in training situations. Among the many related tools developed at NCTR is ComMIT (the Community Model Interface for Tsunamis; Titov *et al.*, 2011), which provides a highly intuitive graphical environment in which to exercise and explore forecast models for any combination of propagation database unit sources. Were any of these avenues to reveal a problem with the model, its origin (most likely in some quirk of the bathymetric files) would be located and corrected, with the revised version then re-installed for operational use. The development of the forecast system will be a dynamic process, with new models added (and old ones revisited) from the current list of U.S. interests nationally and globally. As algorithms and methodologies to represent meteo- or landslide-generated tsunamis become available in the coming years, the utility of current forecast models beyond purely seismic events could well expand.

Table 8. Mega-tsunami scenario impacts, represented by flooding and maximum amplitude at several sites within the model domain.

Scenario	Flooding		Impact Sites							Amp.
(Great Circle, km)	Area	Rank	PTR[1]	LIM[2]	STN[3]	MUR[4]	DOR[5]	LAW[6]	SFO[7]	Rank
ACSZ 56–65 (688)	5.18	7	159	152	160	182	201	224	115	13
ACSZ 50–59 (1278)	4.72	11	202	106	217	373	194	193	203	4
CSSZ 1–10 (2994)	1.18	18	99	69	64	72	48	52	37	18
ACSZ 22–31 (3277)	6.34	4	239	221	288	227	251	333	150	6
ACSZ 16–25 (3731)	4.97	8	266	121	234	275	162	194	102	8
ACSZ 6–15 (4731)	2.55	17	134	87	117	136	118	120	81	17
KISZ 1–10 (5856)	4.93	10	354	152	184	245	144	189	90	6
CSSZ 37–46 (6070)	0	19	42	36	38	35	37	38	25	19
KISZ 22–31 (7724)	4.24	12	251	129	170	231	212	182	74	11
NTSZ 30–39 (8054)	7.00	2	402	226	263	277	239	309	127	3
KISZ 32–41 (8368)	6.39	3	318	169	288	502	361	440	159	2
RNSZ 12–21 (8808)	3.27	15	209	84	115	162	110	121	57	14
KISZ 56–65 (9429)	3.94	13	166	96	145	233	171	204	87	12
NVSZ 28–37 (9553)	4.96	9	258	131	149	149	173	202	88	10
MOSZ 1–10 (9943)	**7.71**	1	460	295	324	513	240	277	200	1
CSSZ 89–98 (10063)	3.48	14	140	134	102	78	102	136	43	16
NGSZ 3–12 (10801)	3.15	16	162	107	143	145	133	131	104	15
EPSZ 6–15 (10932)	6.31	5	246	160	264	296	211	235	137	7
CSSZ 102–111 (11010)	3.27	6	265	132	156	193	157	172	77	9
	Overall Max.		**402**	**295**	**324**	**513**	**361**	**440**	**203**	

1–Point Reyes Tide Gauge; 2–Limantour Beach; 3–Stinson Beach; 4–Muir Beach;
B-Grid: 5–Doran Spit; 6–Lawson's Landing; 7–San Francisco Tide Gauge

Acknowledgments

FIGURES

Figure 1. The Point Reyes area of west and south Marin County, California.
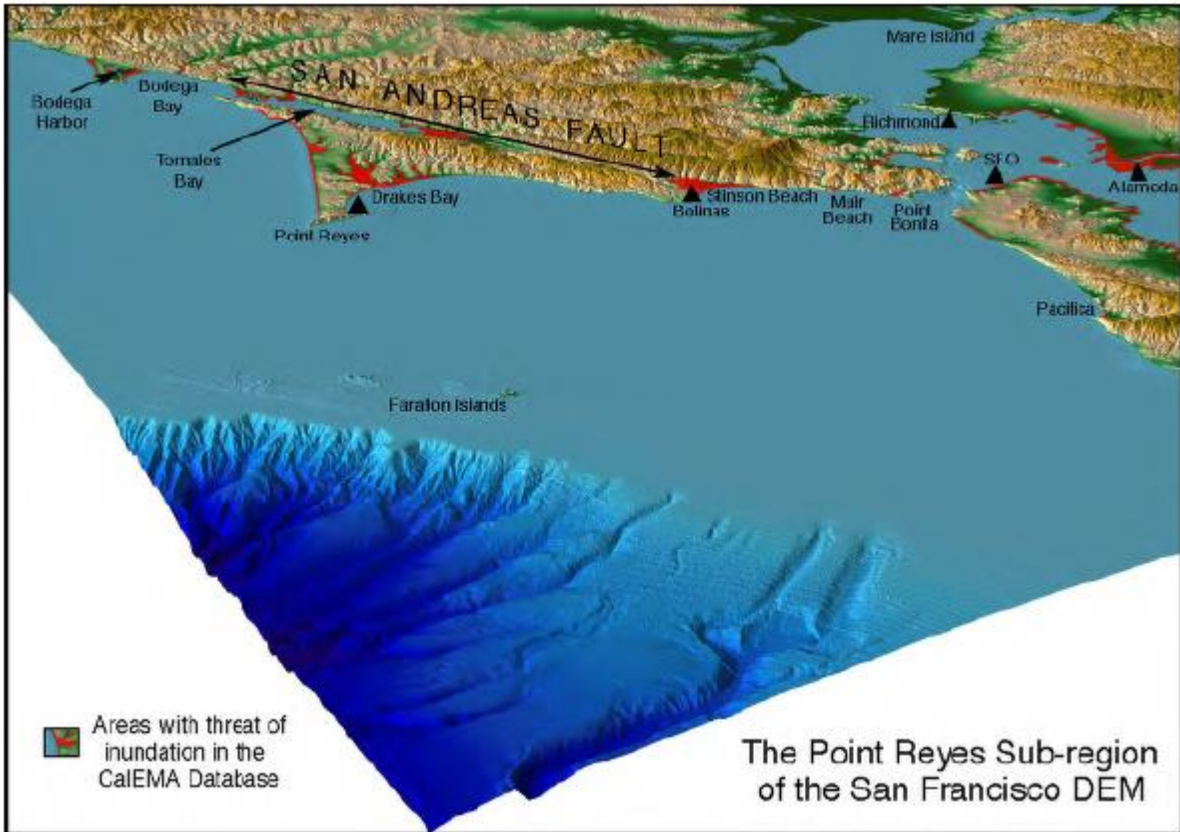
Figure 2. Extract from the oblique 3-D view of the San Francisco DEM provided by NGDC. The focus is Point Reyes; areas of potential inundation identified by CalEMA are highlighted in red.

Figure 3. View of the Point Reyes headland and Drakes Bay in its lee.
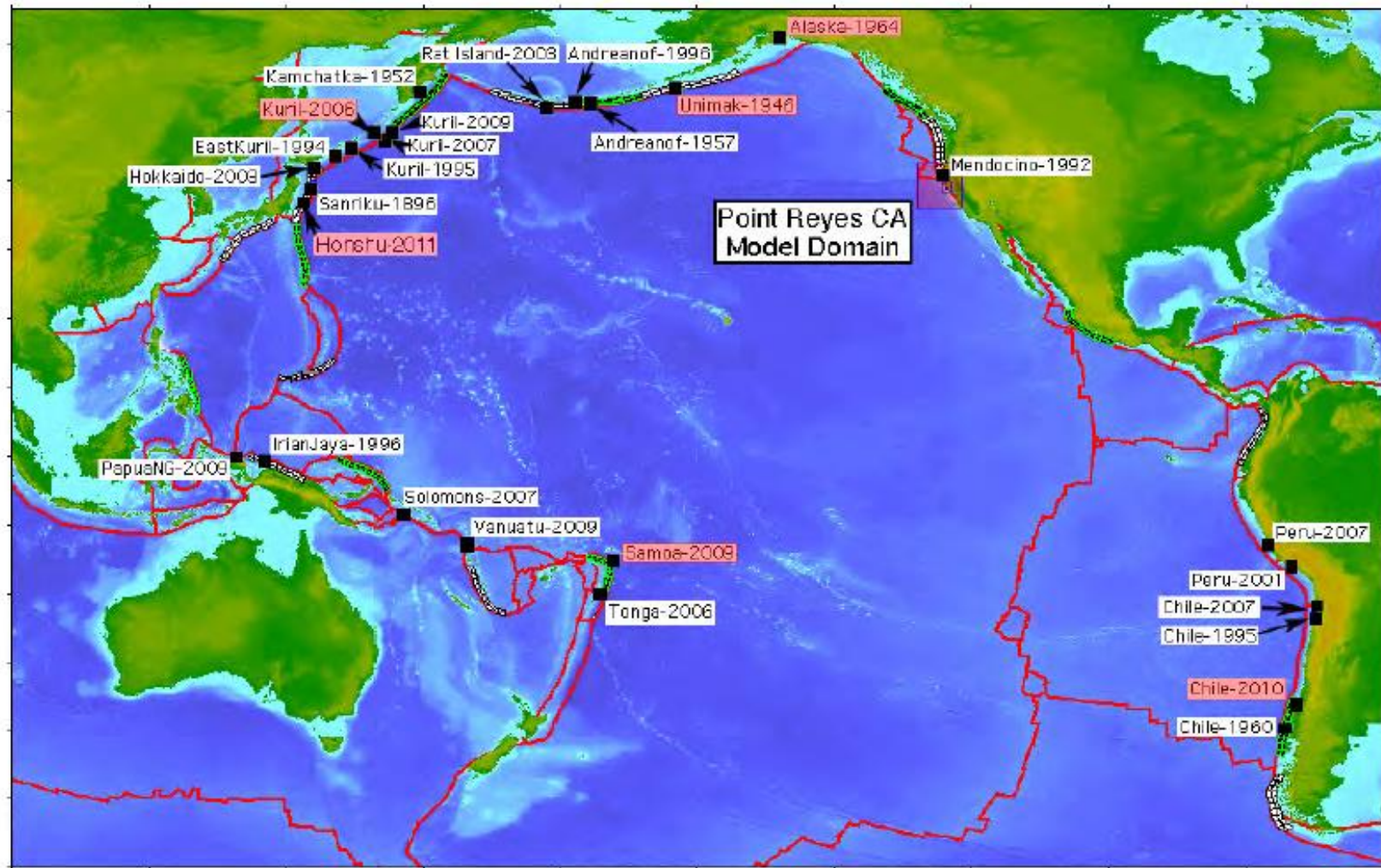
Figure 4. Distribution of the historical tsunami sources employed for the development of the Point Reyes forecast model. Those highlighted in red are more extensively investigated using the reference model.
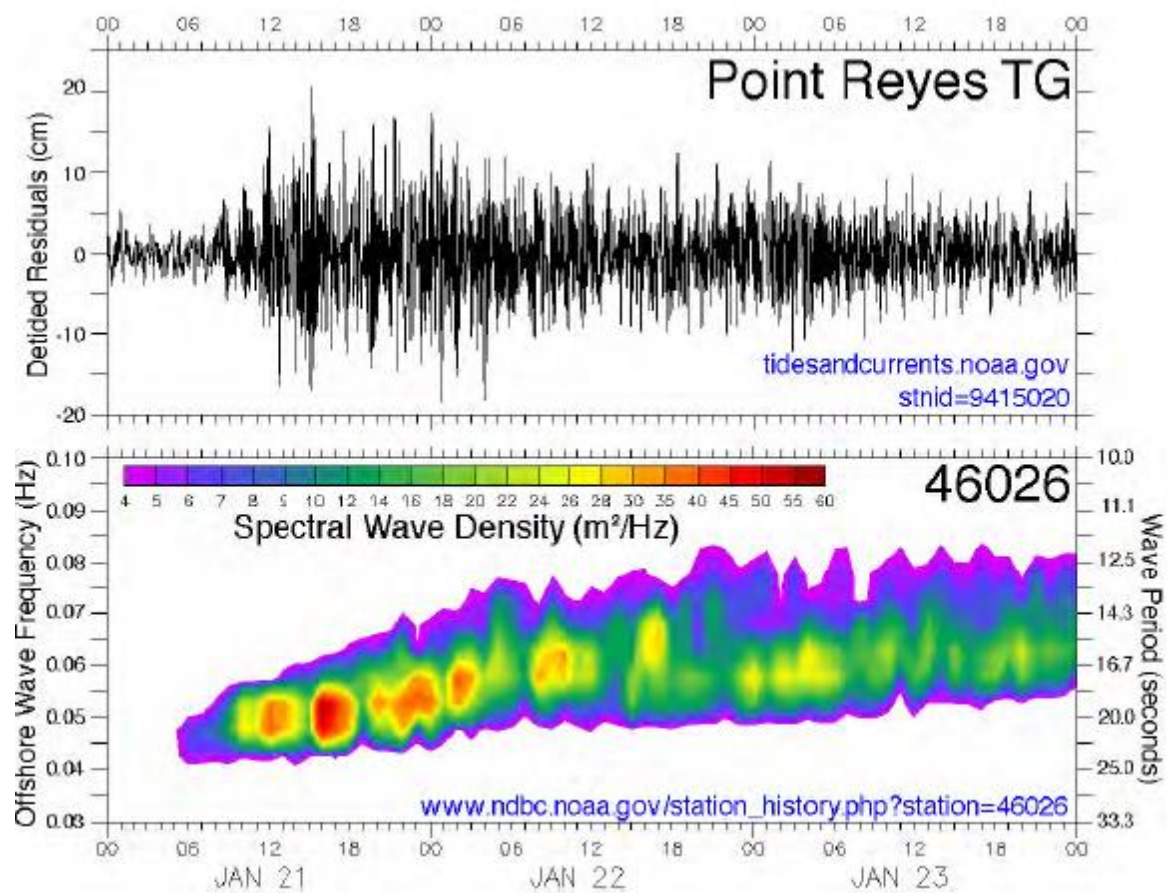
Figure 5. A sample time interval from the Point Reyes tsunami-capable tide gauge, unrelated to tsunami activity. The evolving surface wave spectrum is shown in the lower panel.
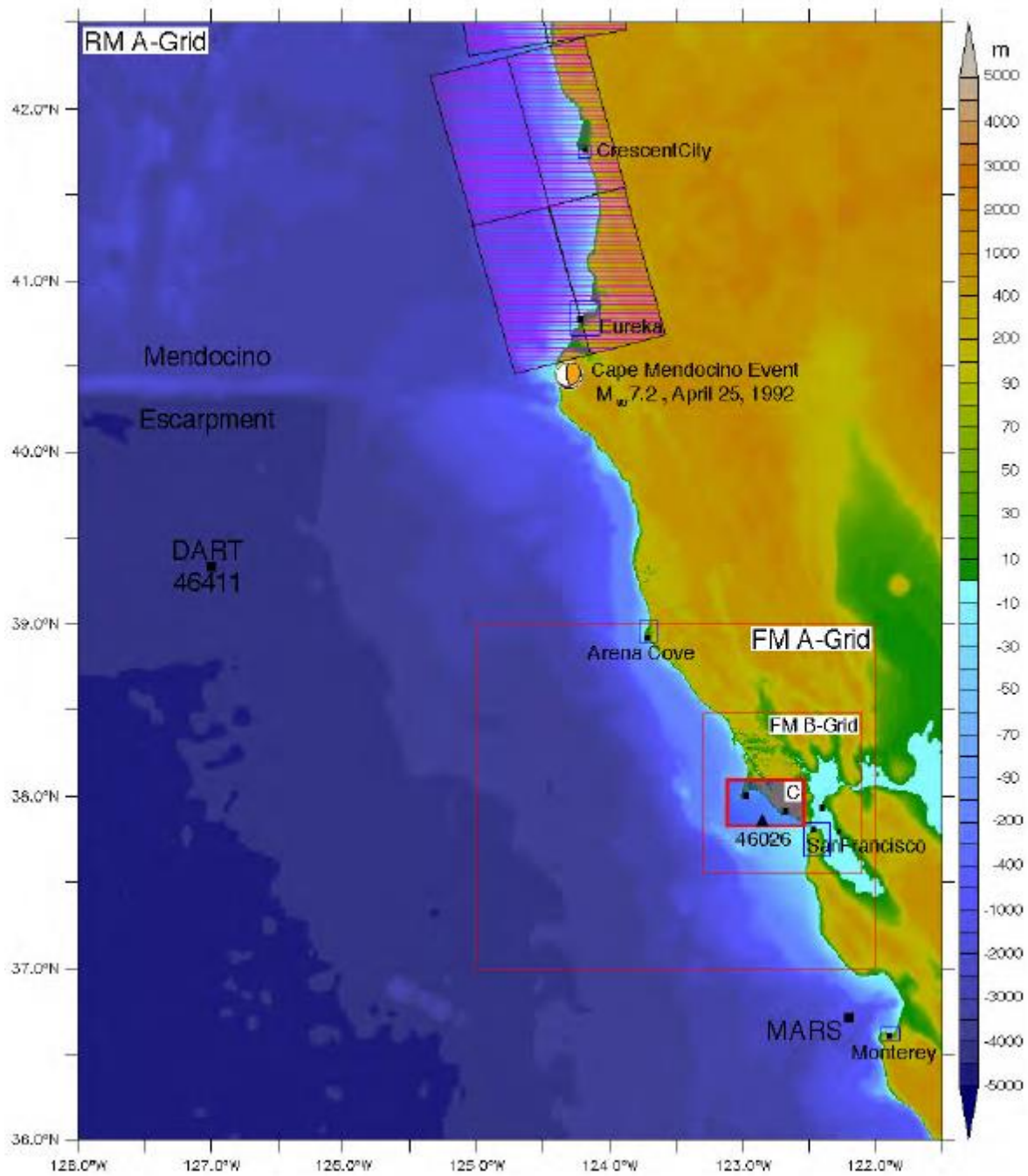
Figure 6. The setting of Point Reyes and its nested forecast model grids. The C grids of other West Coast forecast models are marked, as are various sites with data available for this study. The closest unit sources of the propagation database lie north of Cape Mendocino, and the epicenter of the most recent Cascadia thrust event is marked.
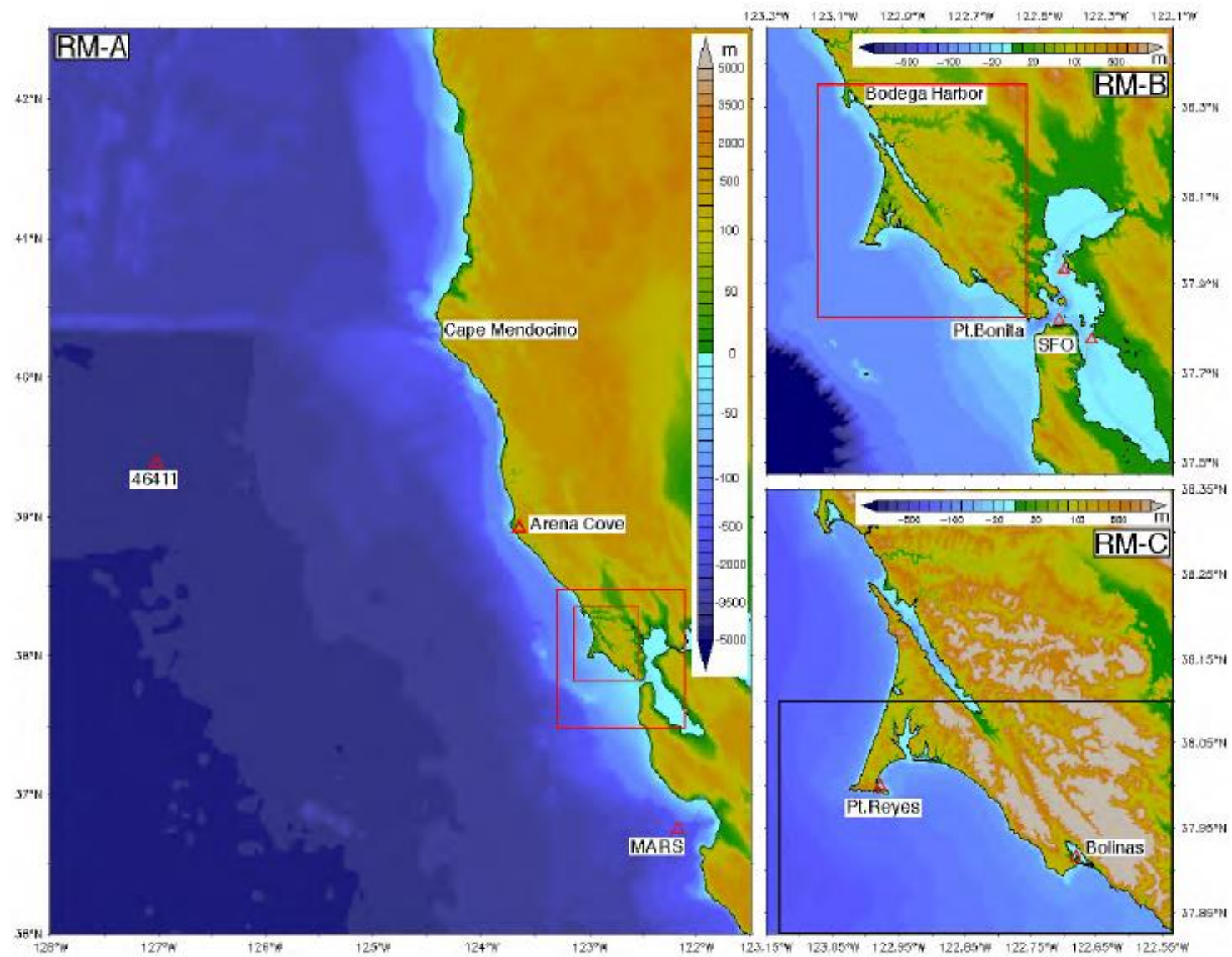
Figure 7. Nested grid representation for the Point Reyes reference model (RM).
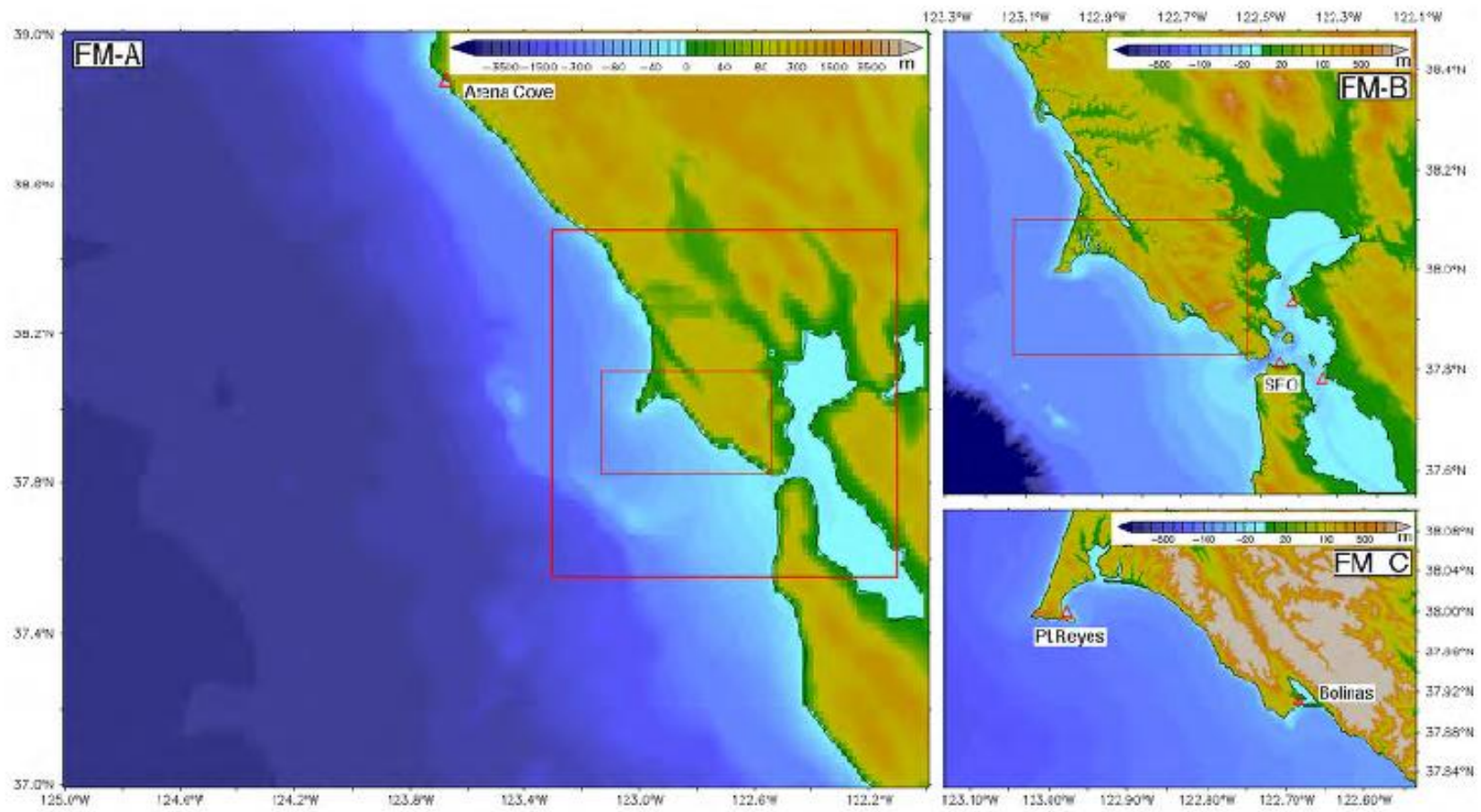
Figure 8. Nested grid representation for the Point Reyes forecast model (FM).
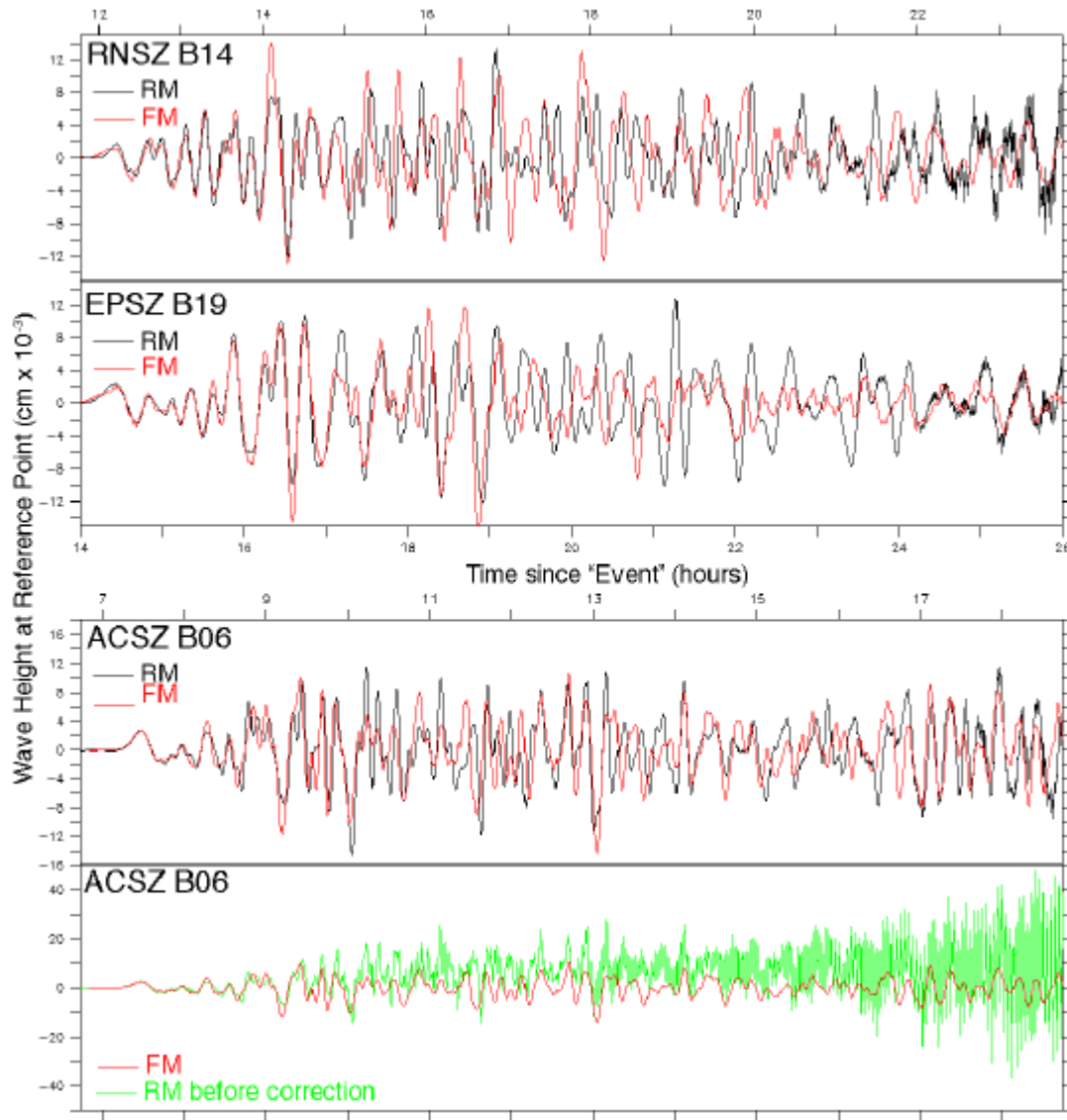
Figure 9. Comparison of the reference (RM) and forecast model (FM) time series at the warning point for three "micro-tsunami" sources in the Western Pacific. The lowest panel illustrates the appearance of model instability before the reference model C-grid bathymetry was finalized.
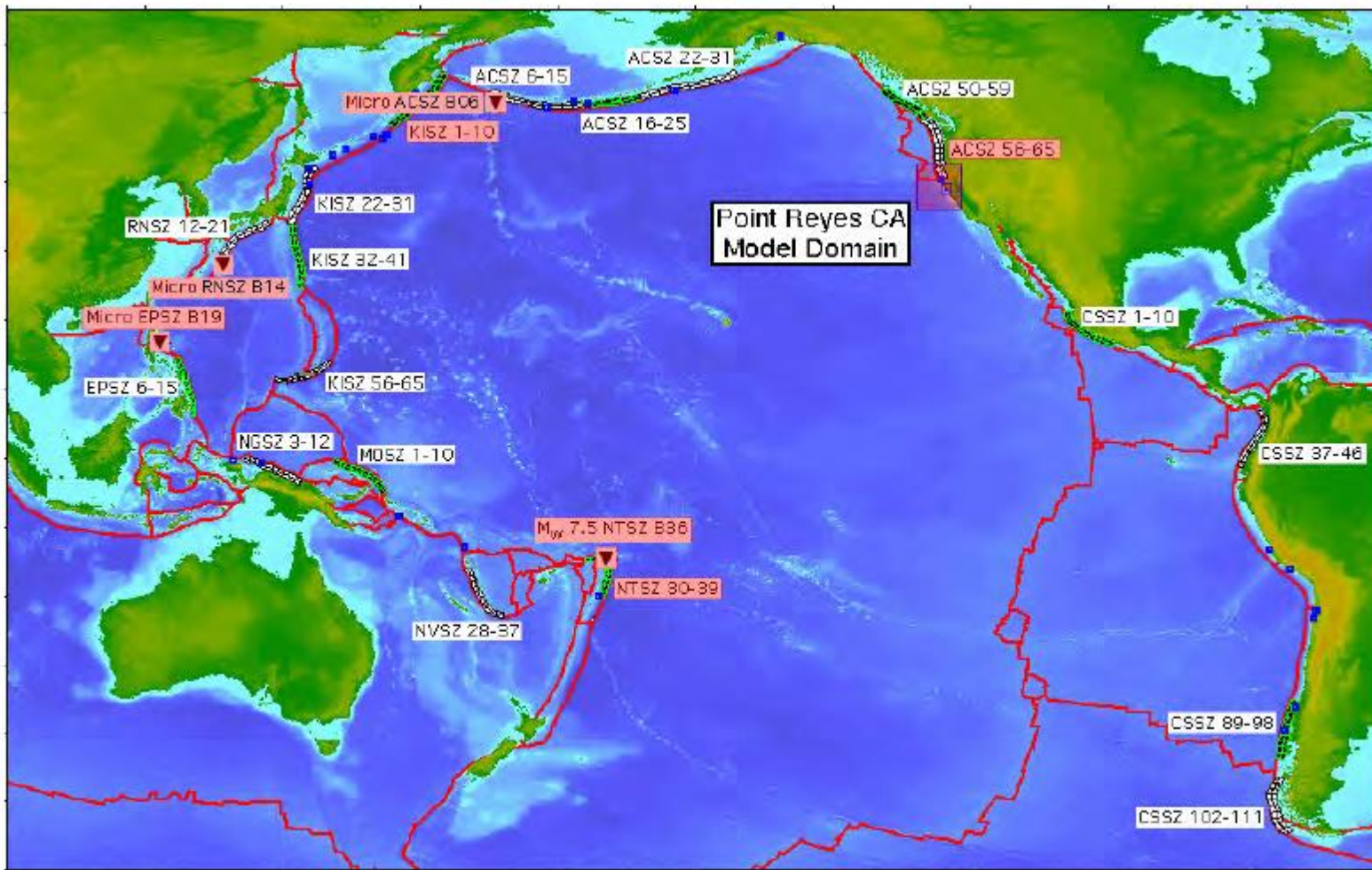
Figure 10. Locations of synthetic tsunami scenarios employed in model development. Three micro-tsunami scenarios and the magnitude 7.5 case employ a single unit source; 19 combine 10 pairs of unit sources to model mega-tsunamis. Details are provided in Table 6. Cases highlighted in red have both forecast and reference model solutions.
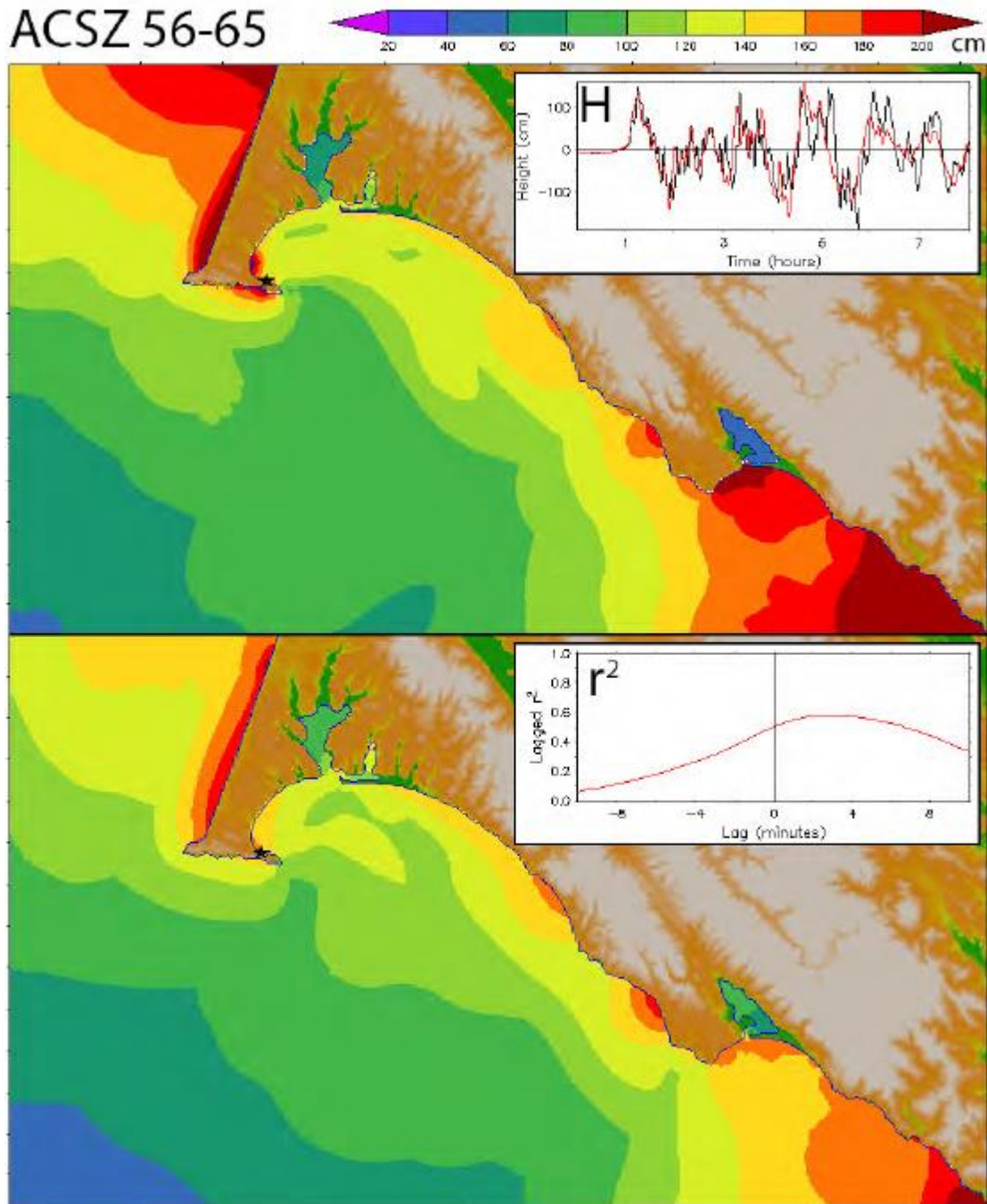
Figure 11. Comparison of reference and forecast model results for the ACSZ 56–65 synthetic mega-tsunami, representing the Cascadia Subduction Zone. (a) Distributions of maximum amplitude in the reference (upper panel) and forecast (lower panel) model results with their time series (reference model–black, forecast model–red) and lagged correlation at the Point Reyes tide gauge as insets.
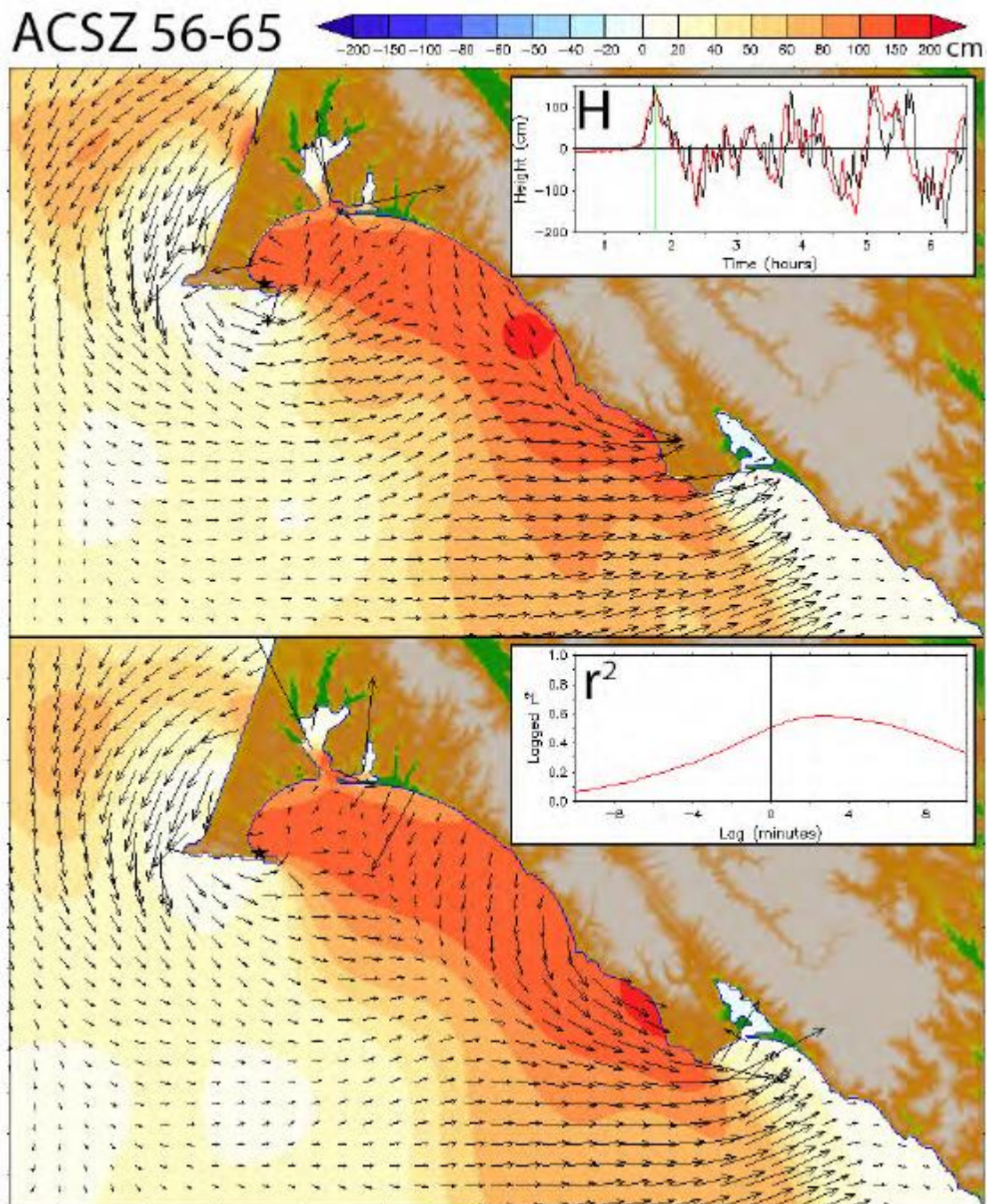
Figure 11. **continued**: (c) comparison of the wave amplitude and currents in the reference (upper panel) and forecast (lower panel) model results at the time indicated in the upper panel inset (the first wave peak).

(d)

Figure 11. **continued**: (d) as in (c) but at the later time when the reference and forecast model solutions have diverged somewhat.
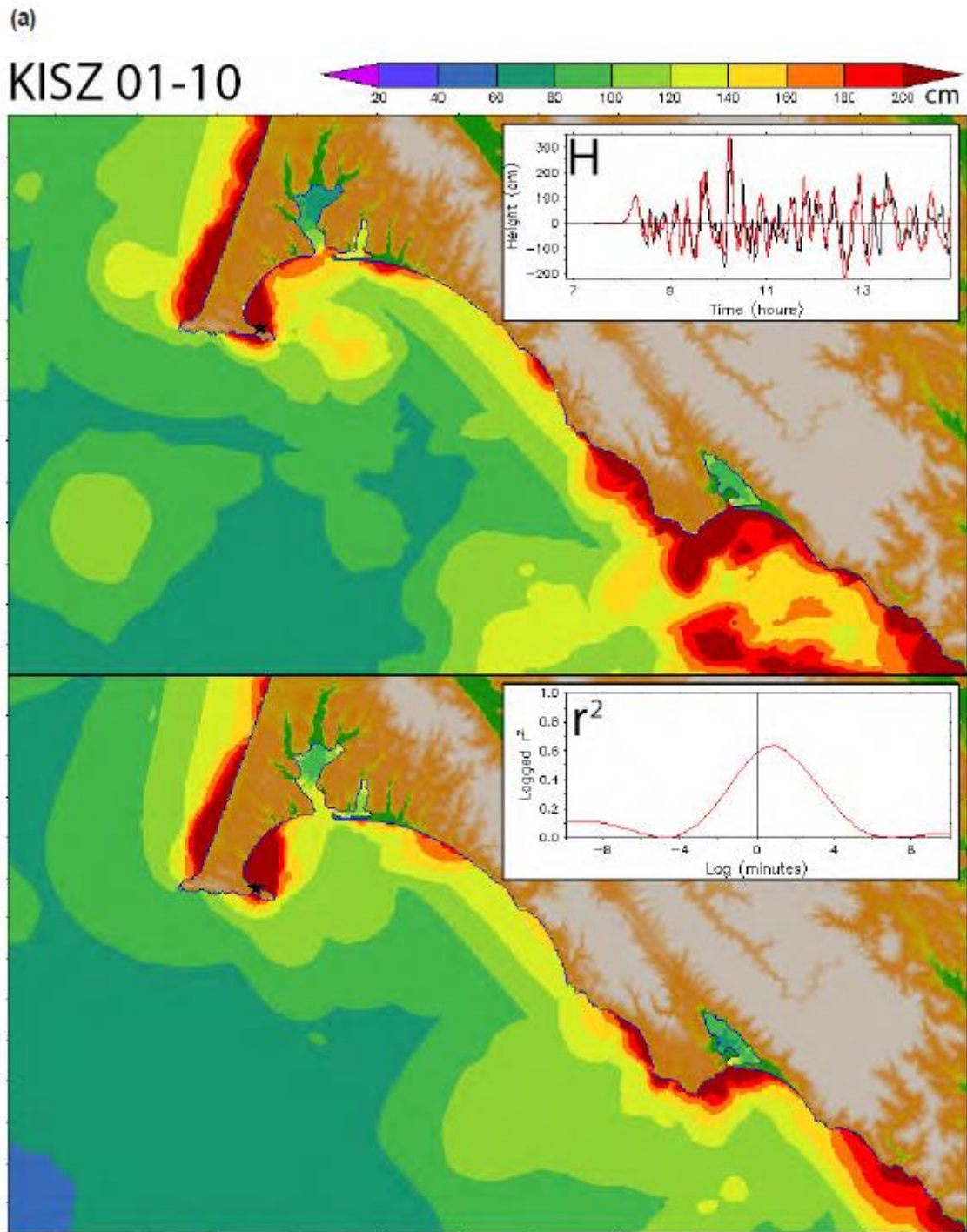
Figure 12. Comparison of reference and forecast model results for the synthetic KISZ 01–10 mega-tsunami, representing Kamchatka. (a) Distributions of maximum amplitude in the reference (upper panel) and forecast (lower panel) model results with their time series (reference model–black, forecast model–red) and lagged correlation at the Point Reyes tide gauge as insets.

40
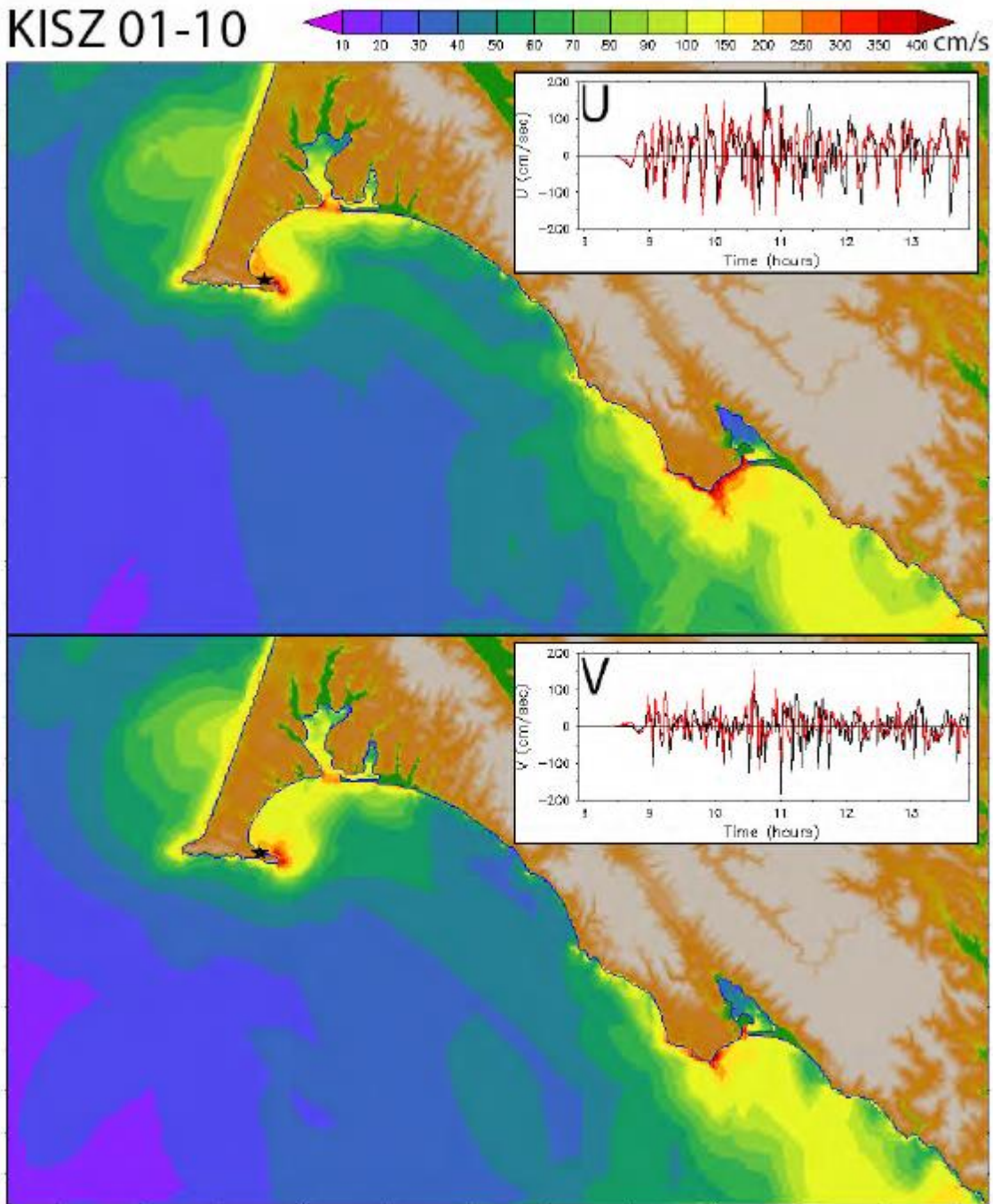
Figure 12. continued: (b) distributions of maximum speed in the reference (upper panel) and forecast (lower panel) model results with the time series of the vector components at the Point Reyes tide gauge as insets.

Figure 12. **continued**: (c) comparison of the wave amplitude and currents in the reference (upper panel) and forecast (lower panel) model results at the time indicated in the upper panel inset (the first wave peak).

42

Figure 13. Comparison of reference and forecast model results for the synthetic NTSZ 30–39 event representing Samoa. (a) Distributions of maximum amplitude in the reference (upper panel) and forecast (lower panel) model results with their time series (reference model–black, forecast model–red) and lagged correlation at the Point Reyes tide gauge as insets.

43
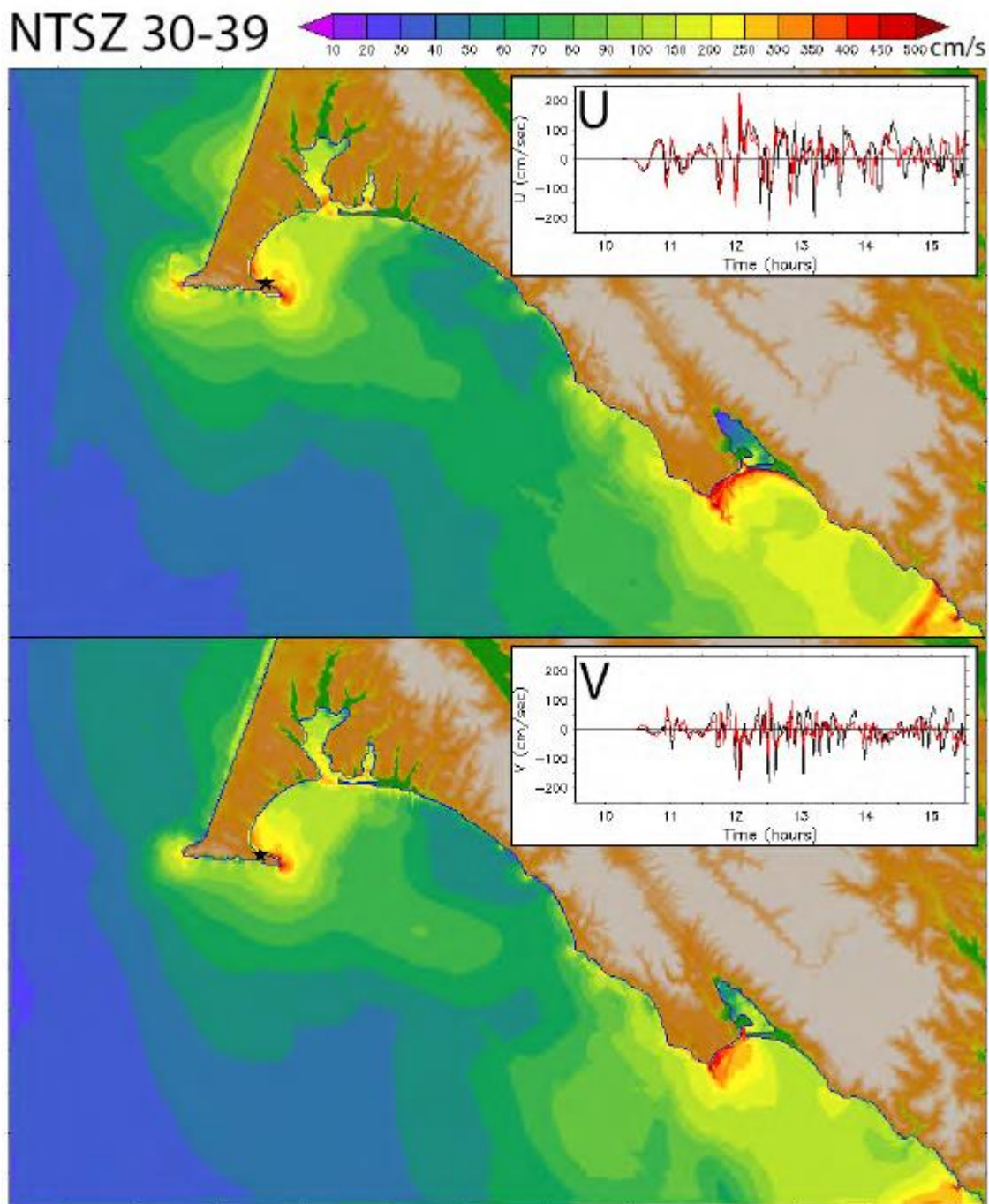
Figure 13. **continued**: (b) distributions of maximum speed in the reference (upper panel) and forecast (lower panel) model results with the time series of the vector components at the Point Reyes tide gauge as insets.
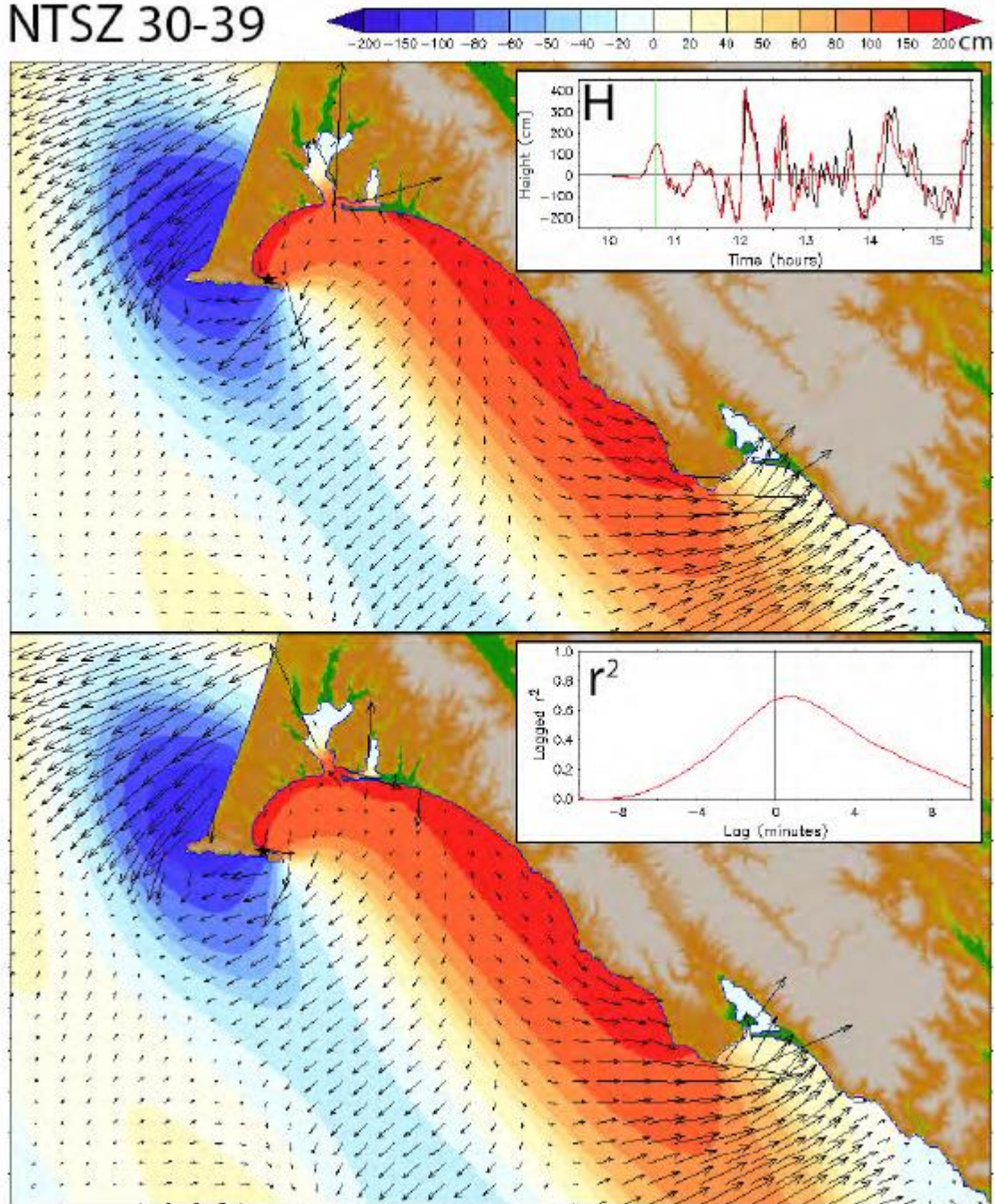
Figure 13. **continued**: (c) comparison of the wave amplitude and currents in the reference (upper panel) and forecast (lower panel) model results at the time indicated in the upper panel inset (the first wave peak).
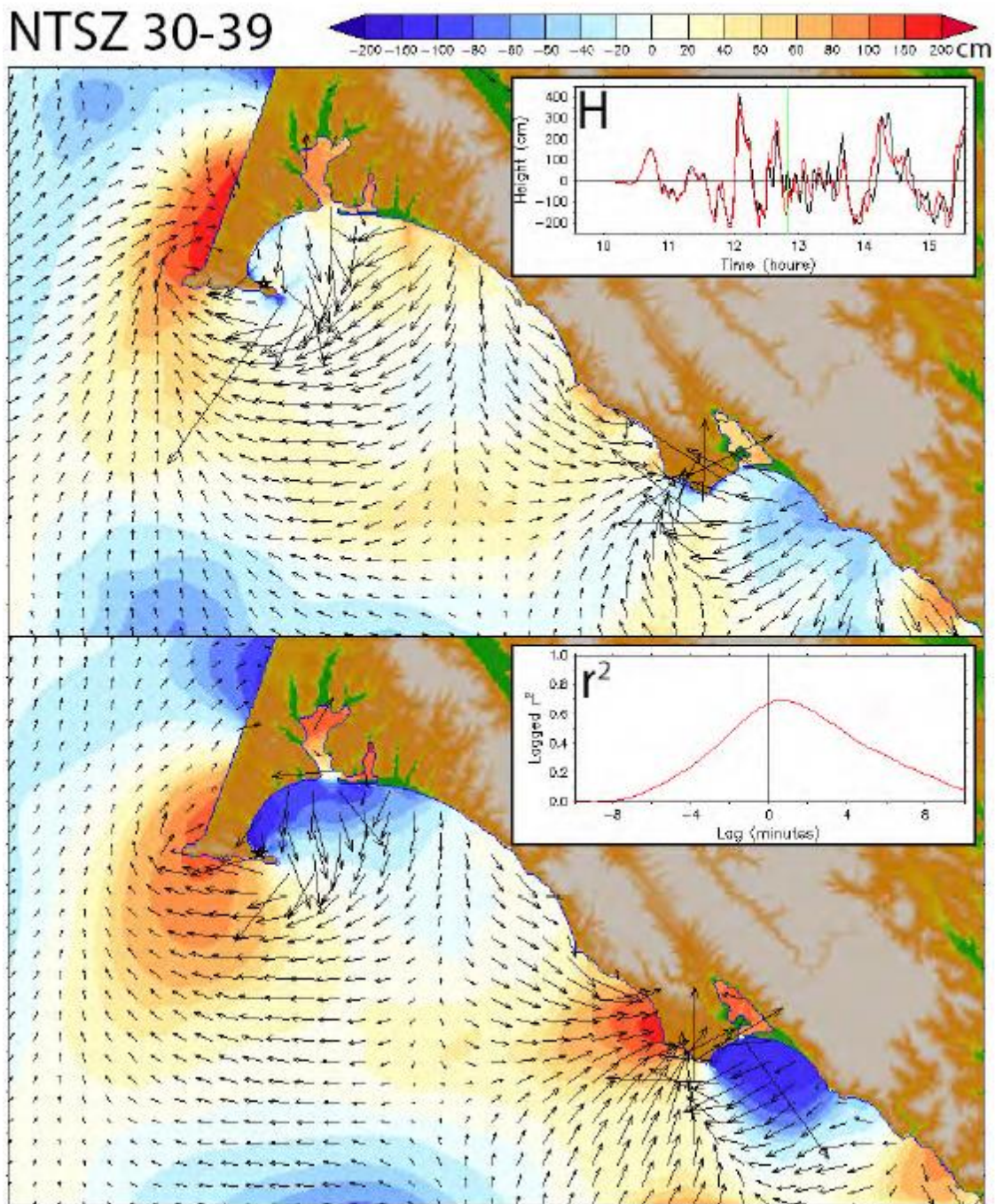
Figure 13. **continued**: (d) as in (c) but at the later time when the reference and forecast model solutions have diverged somewhat.
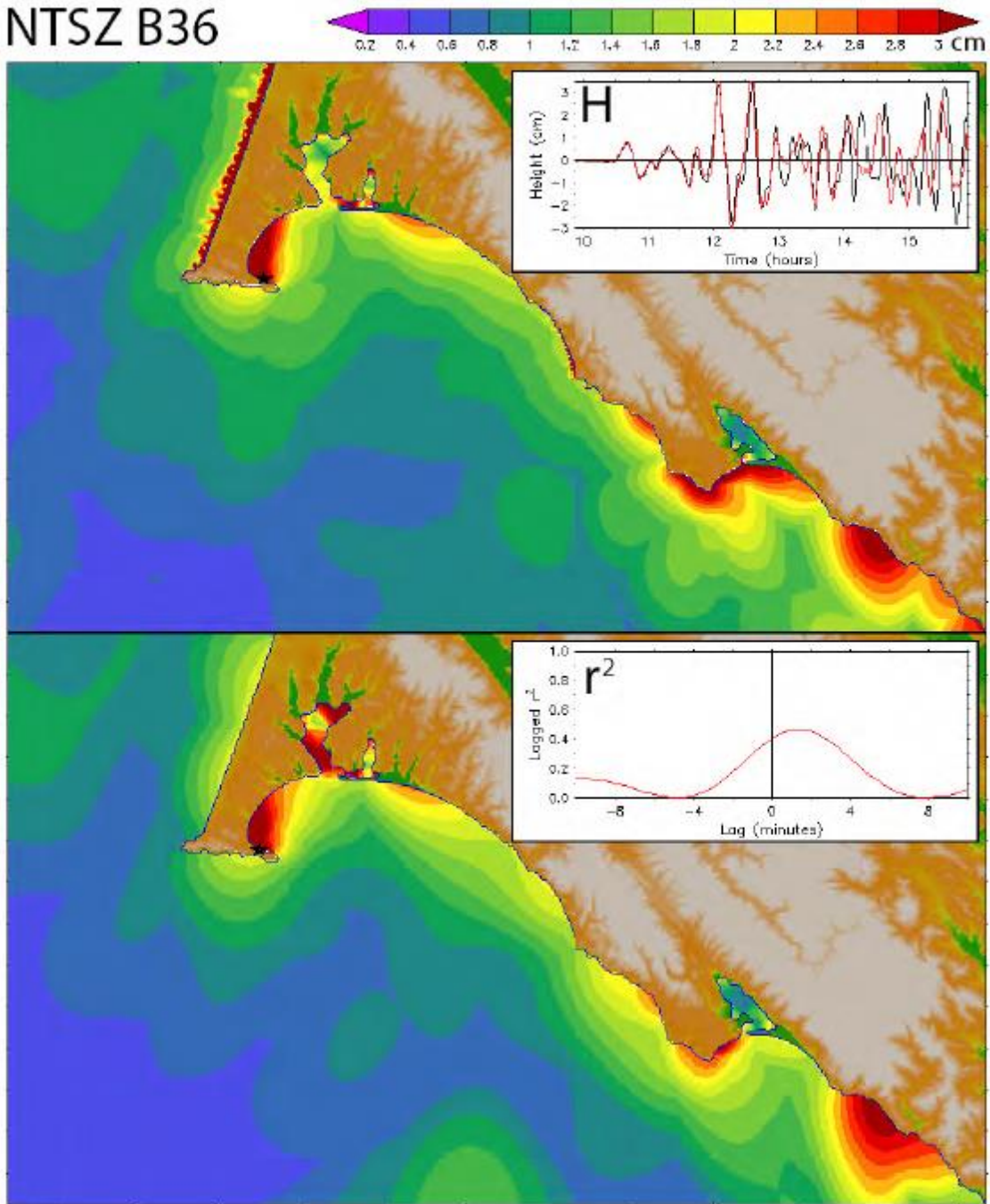
Figure 14. Comparison of reference and forecast model results for a moderate synthetic event at NTSZ B36 near Samoa. (a) Distributions of maximum amplitude in the reference (upper panel) and forecast (lower panel) model results with their time series (reference model–black, forecast model–red) and lagged correlation at the Point Reyes tide gauge as insets.
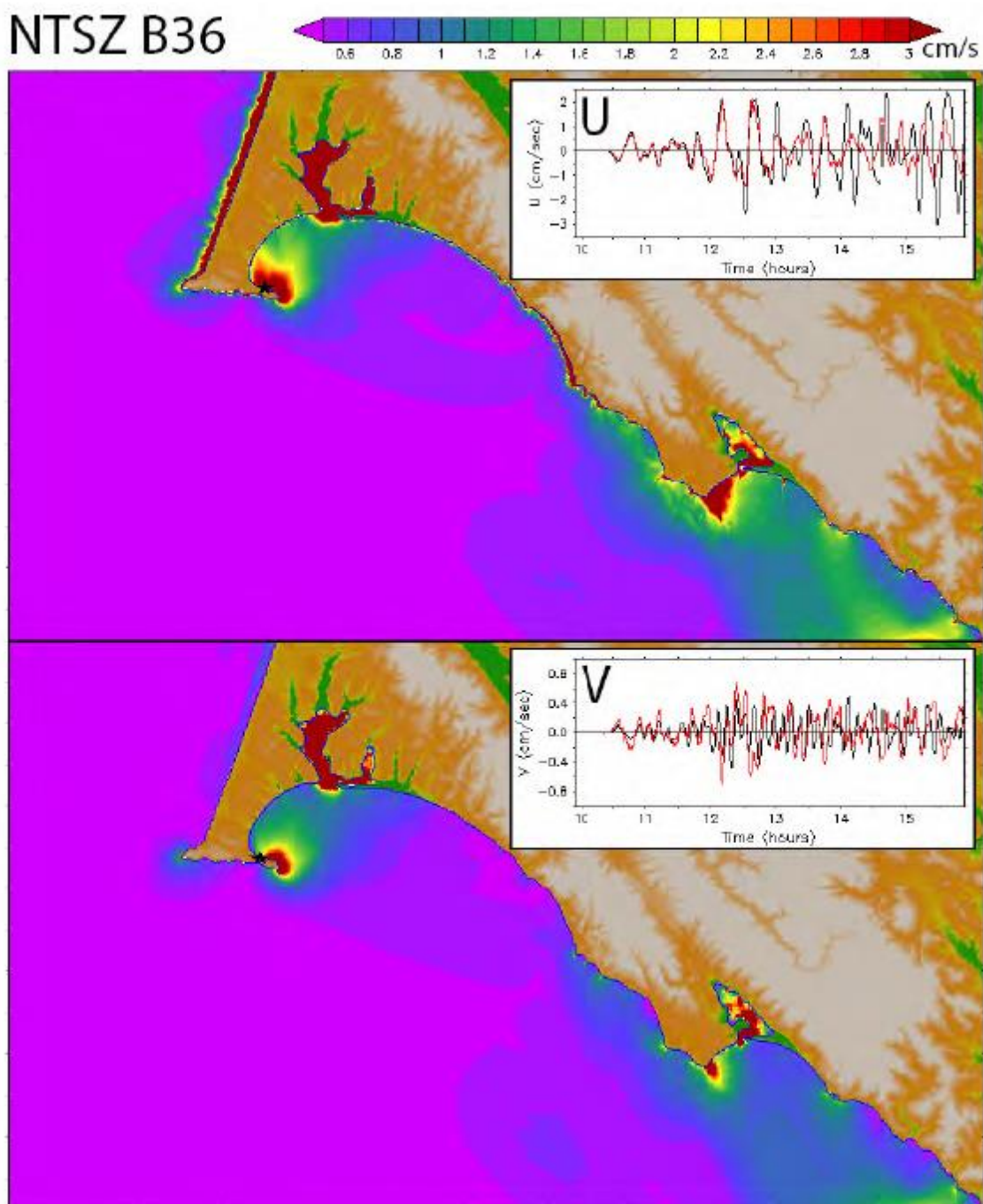
Figure 14. **continued**: (b) distributions of maximum speed in the reference (upper panel) and forecast (lower panel) model results with the time series of the vector components at the Point Reyes tide gauge as insets.
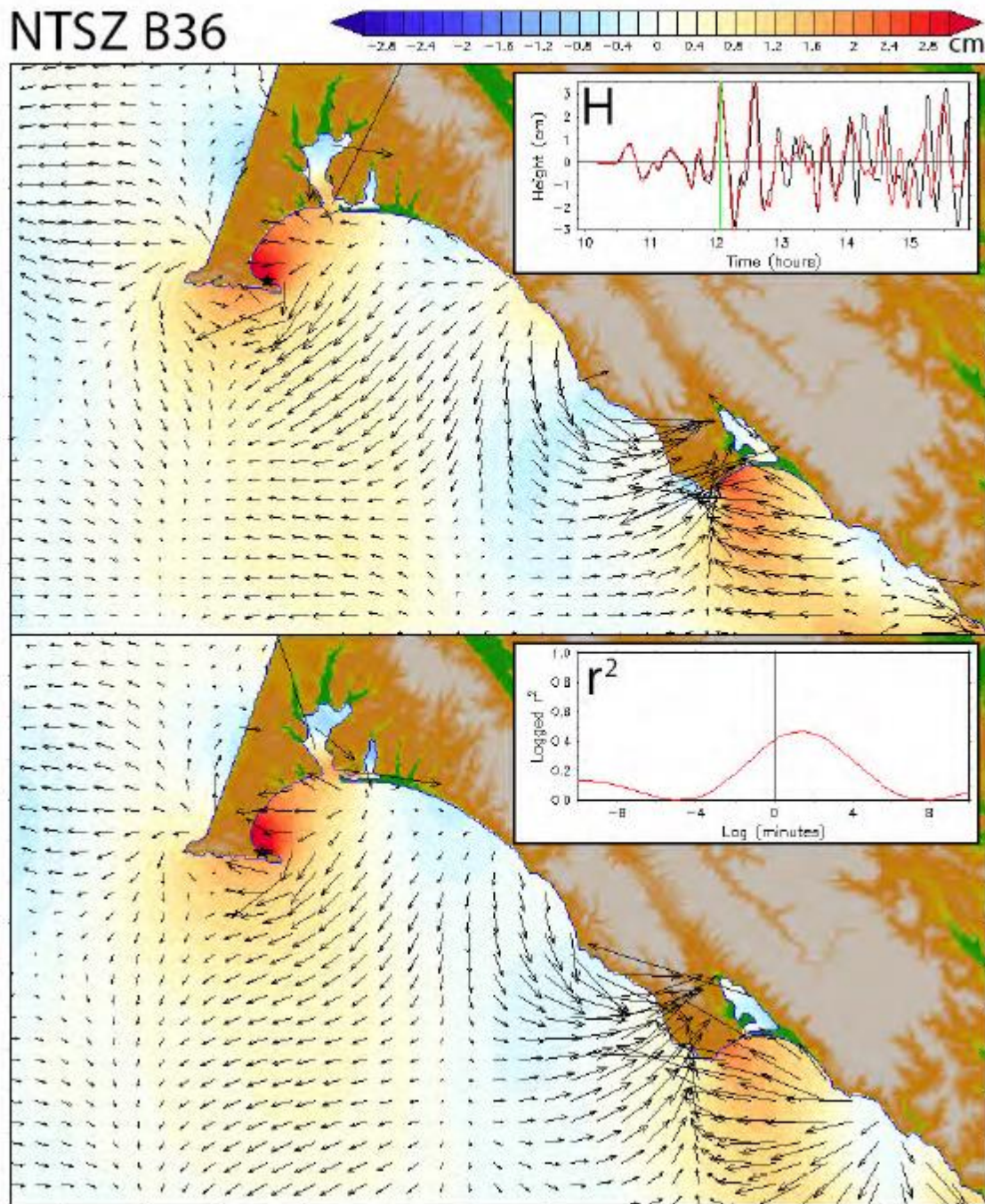
Figure 14. **continued**: (c) comparison of the wave amplitude and currents in the reference (upper panel) and forecast (lower panel) model results at the time indicated in the upper panel inset (the first major wave peak).

49
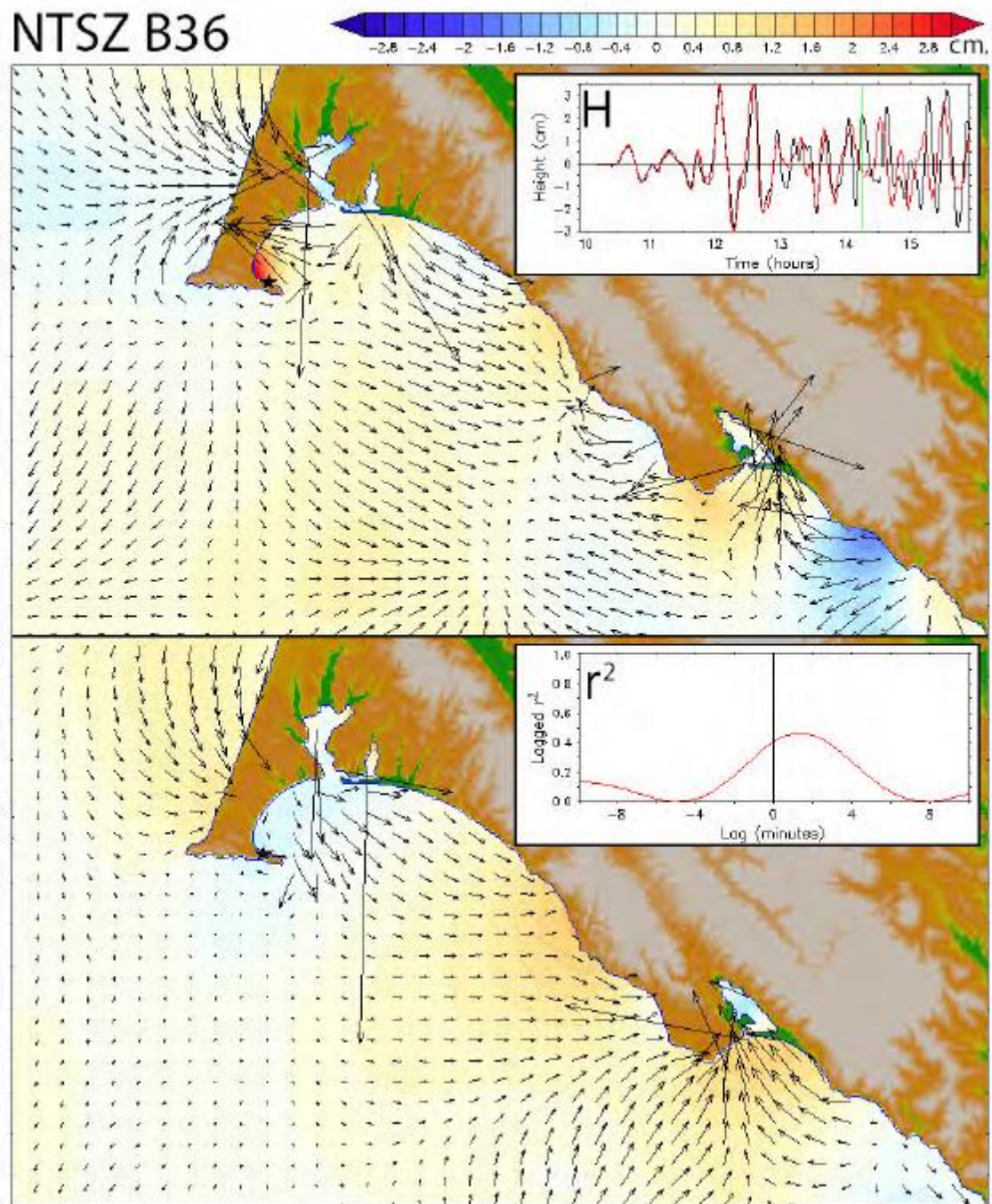
Figure 14. **continued**: (d) as in (c) but at the later time when the reference and forecast model solutions have diverged somewhat.
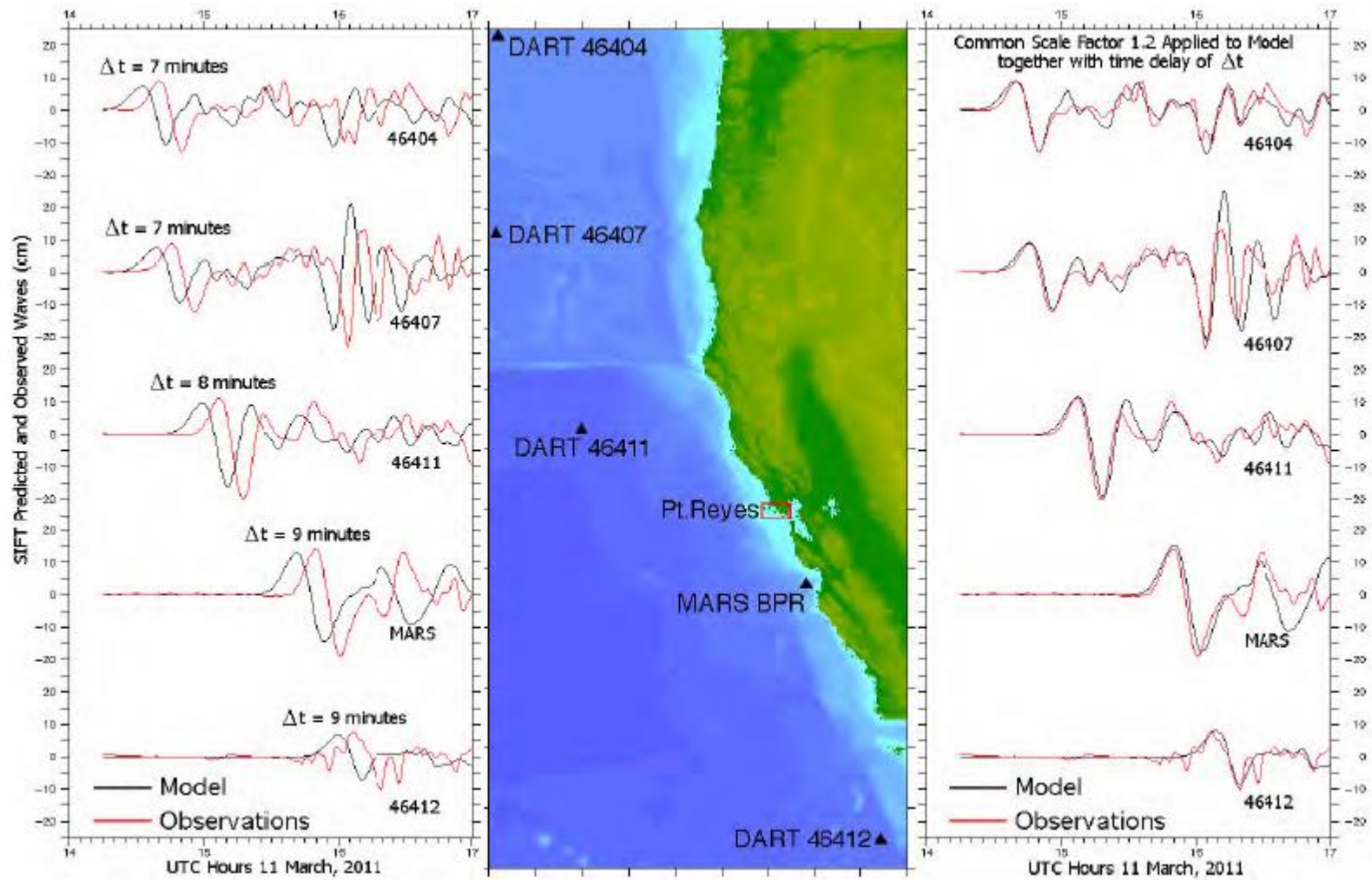
Figure 15. Observed time series (red curves) from DART® and MARS bottom pressure sensors during the 2011 Honshu event, compared with the forecast model representation (black curves) based on the propagation database (see Table 1(a)). Model time series in the right-hand panel have been lagged, and a common scale factor of 1.2 applied.
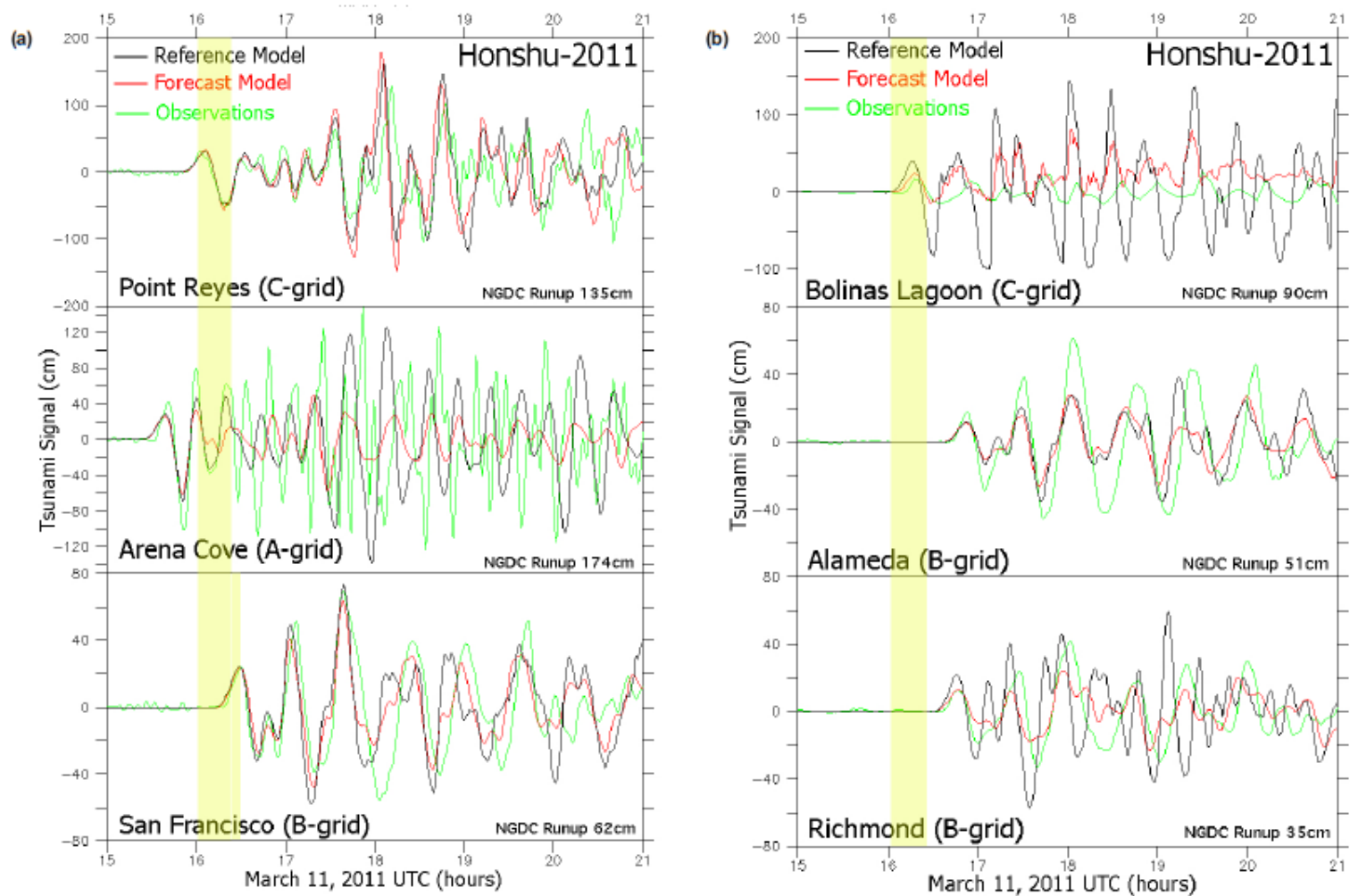
Figure 16. Comparison of observations with reference and forecast model-predicted time series for the historical 2011 Honshu event at selected locations where tide gauge data are available: (a) Point Reyes, Arena Cove, and San Francisco; (b) Bolinas (6-min data), Alameda, and Richmond. The time period highlighted in yellow marks an outage of 18 min or more that occured for the 1-min data streams along the entire West Coast during the event. Runup values from the NGDC catalog, when available, are indicated in the lower right of each panel for this and subsequent figures.
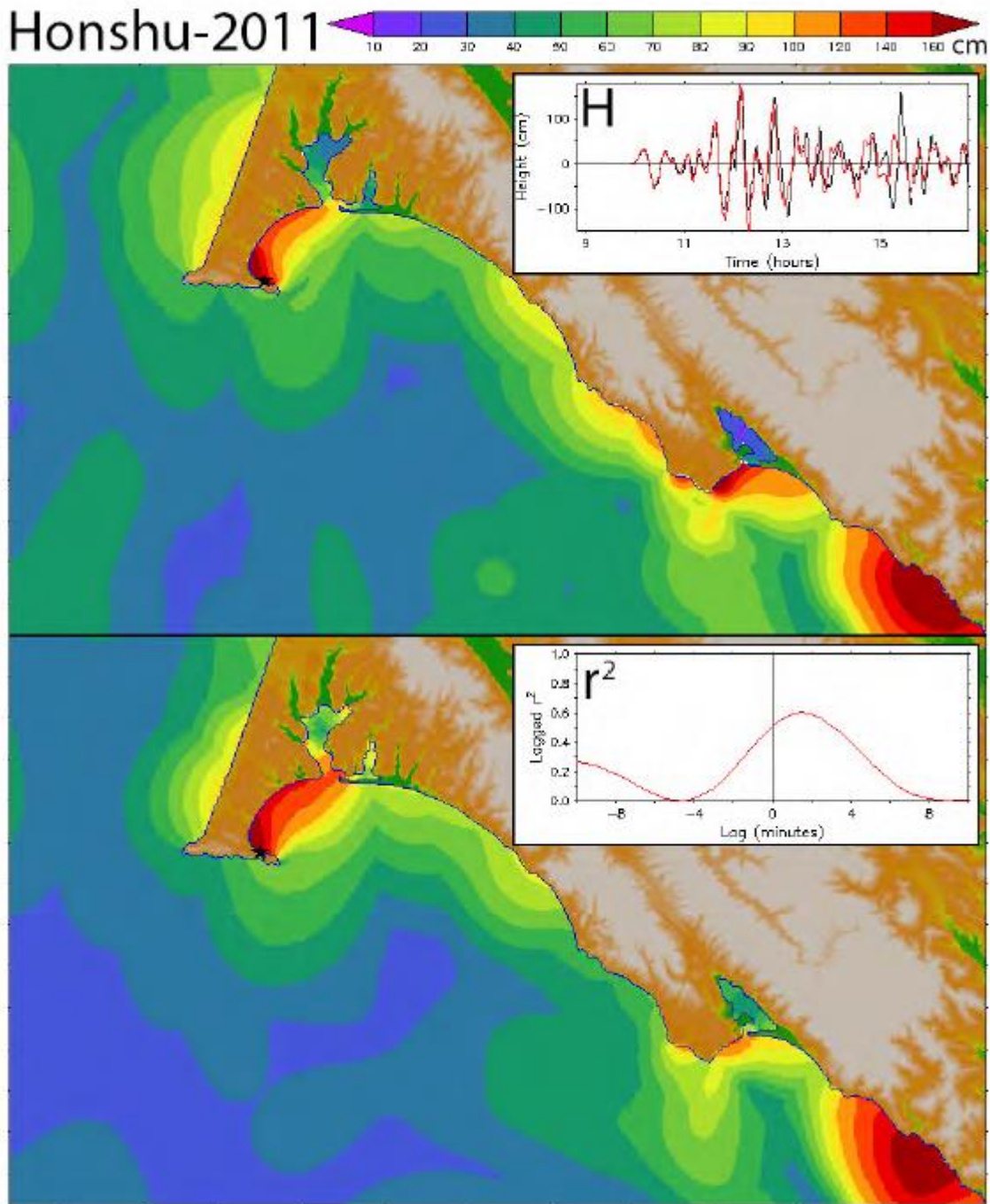
Figure 17. Comparison of reference and forecast model results for the historical 2011 Honshu event. (a) Distributions of maximum amplitude in the reference (upper panel) and forecast (lower panel) model results with their time series (reference model–black, forecast model–red) and lagged correlation at the Point Reyes tide gauge as insets.
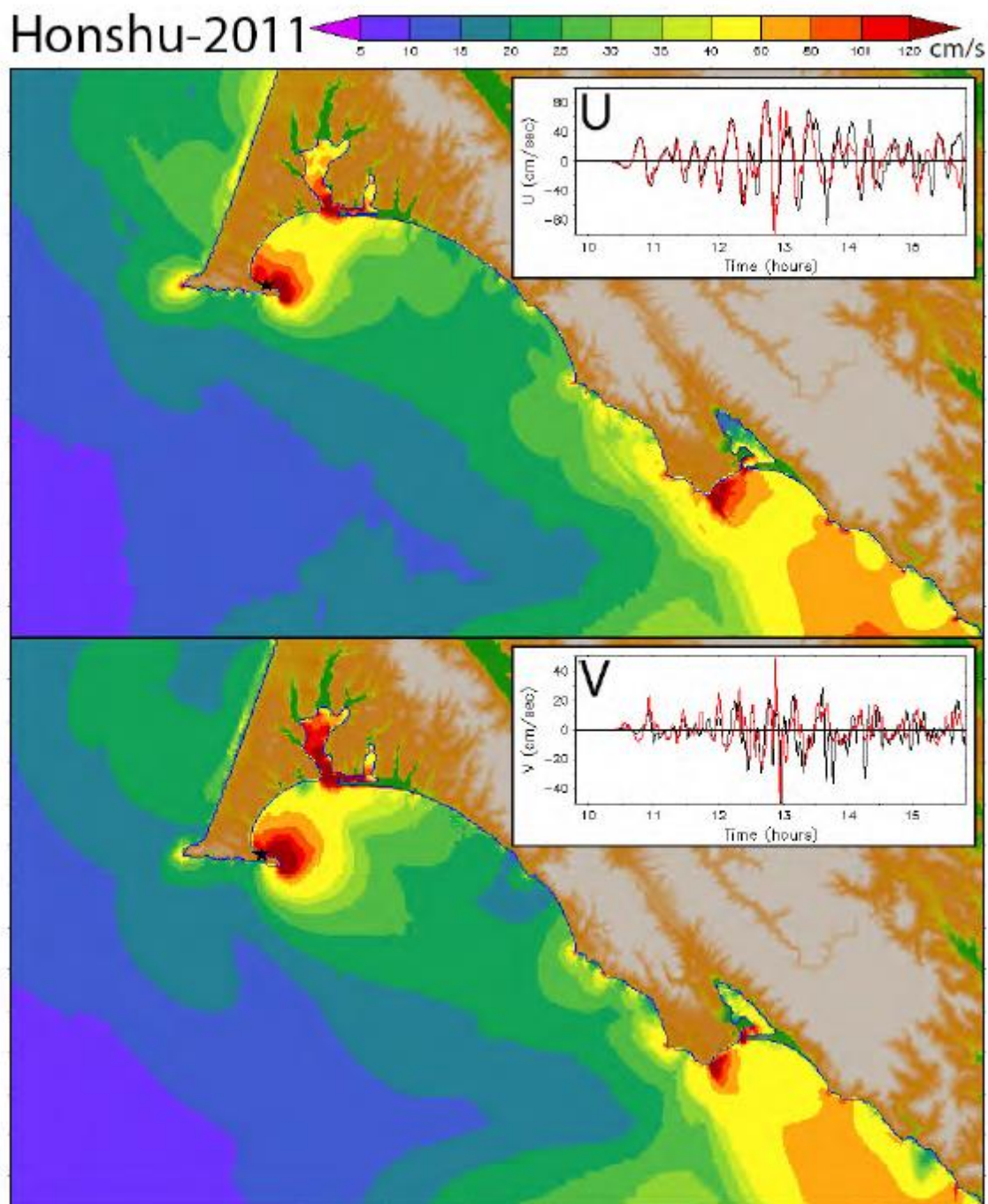
Figure 17. **continued**: (b) distributions of maximum speed in the reference (upper panel) and forecast (lower panel) model results with the time series of the vector components at the Point Reyes tide gauge as insets.
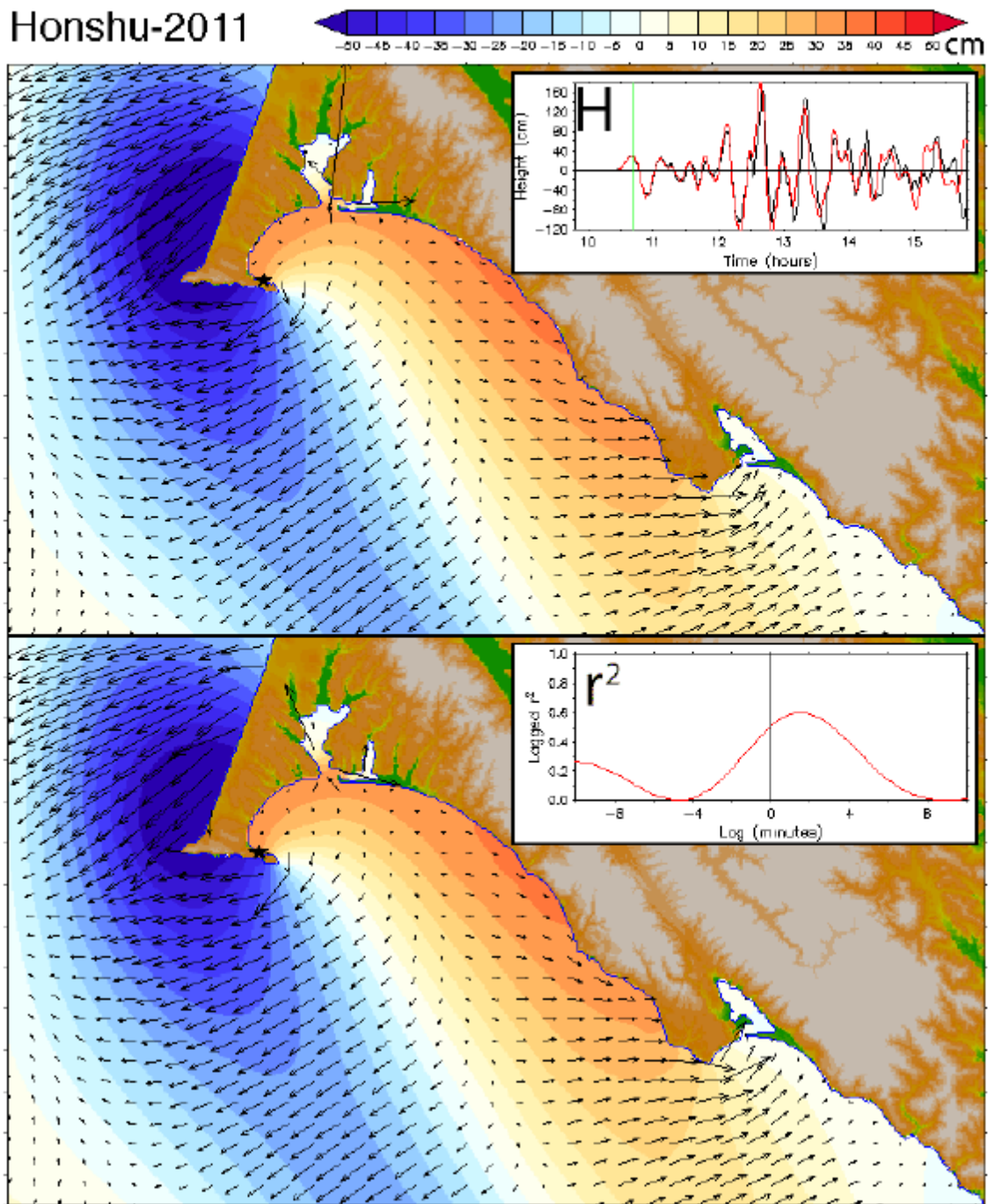
Figure 17. **continued**: (c) comparison of the wave amplitude and currents in the reference (upper panel) and forecast (lower panel) model results at the time indicated in the upper panel inset (the first wave peak).
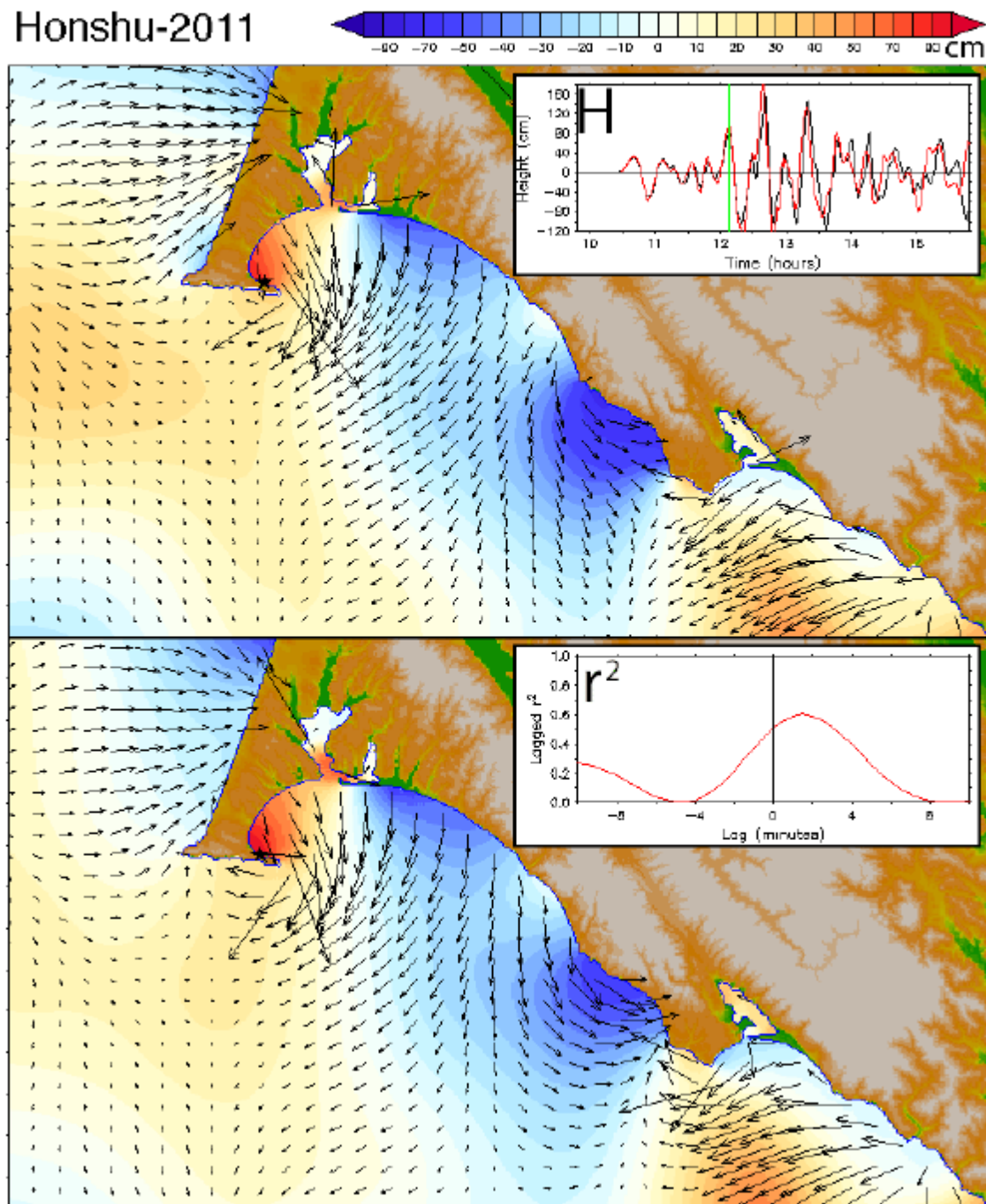
Figure 17. **continued**: (d) as in (c) but during a later wave peak.
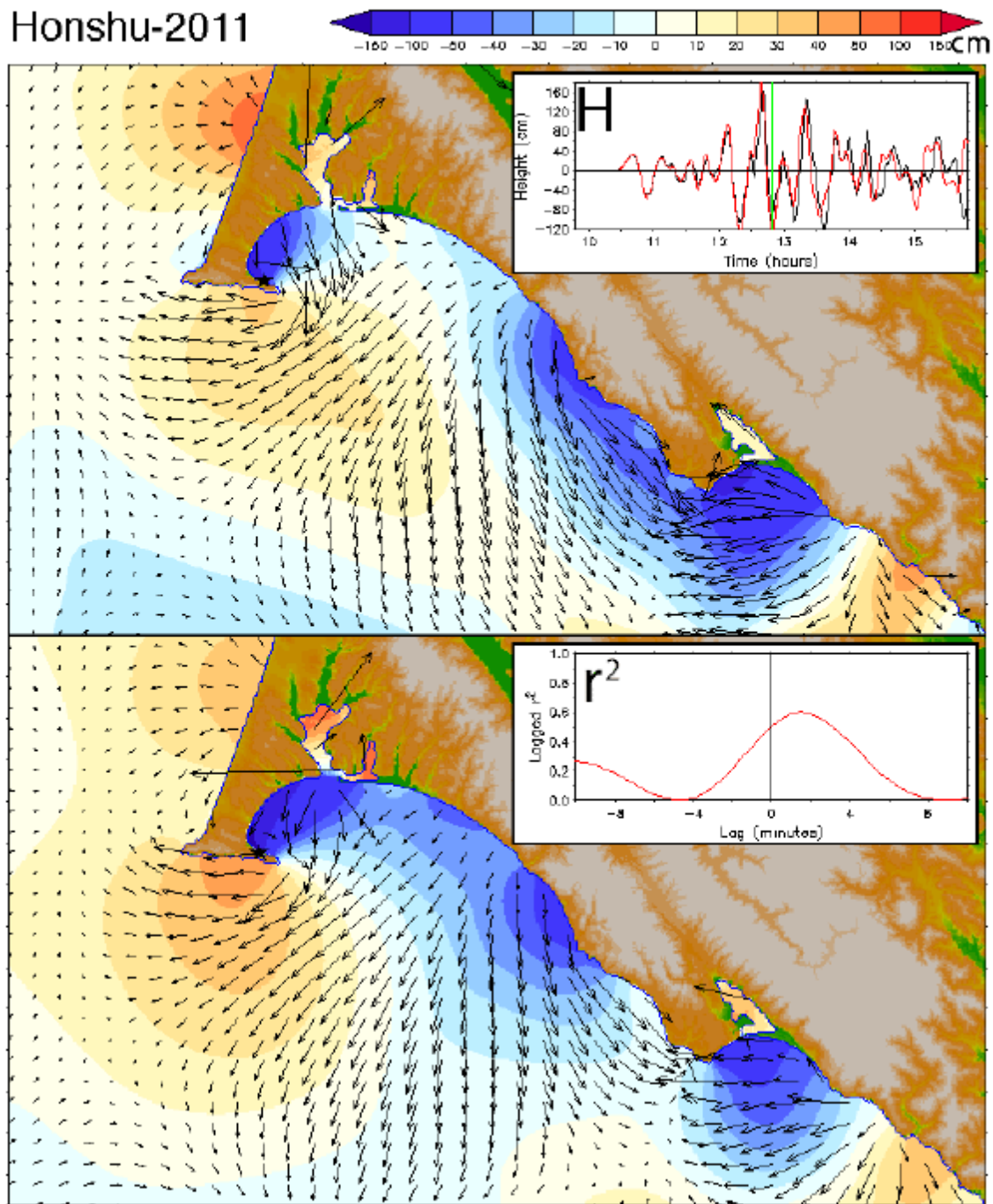
Figure 17. **continued**: (e) as in (c) and (d) but during a later wave trough.
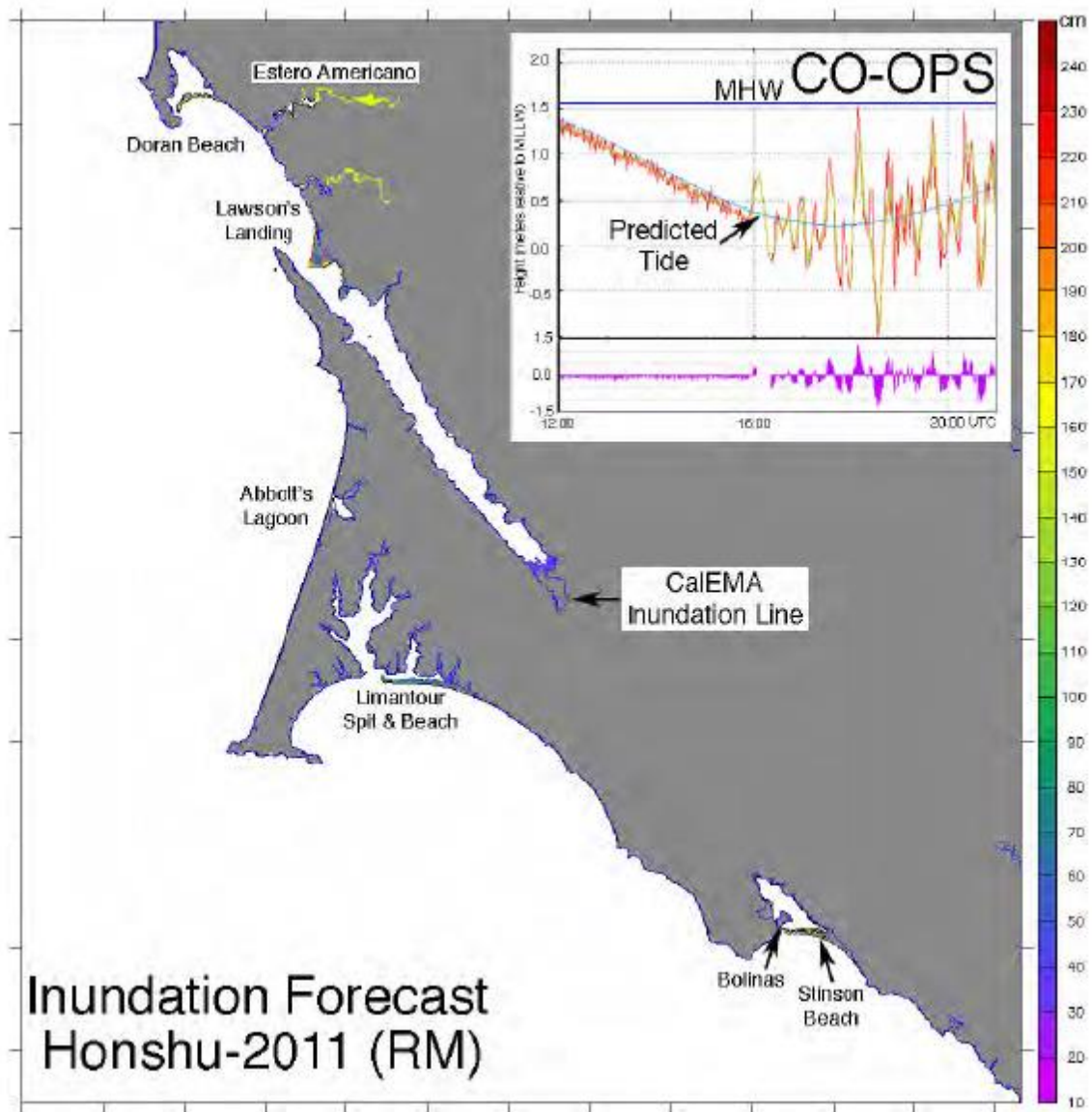
Figure 18. Inundation forecast from the reference model (RM) C grid for the 2011 Honshu event, compared with the CalEMA inundation line. The inset in the upper right shows tide gauge data from Point Reyes. Actual tides were well below MHW so the inundation forecast was overly conservative.
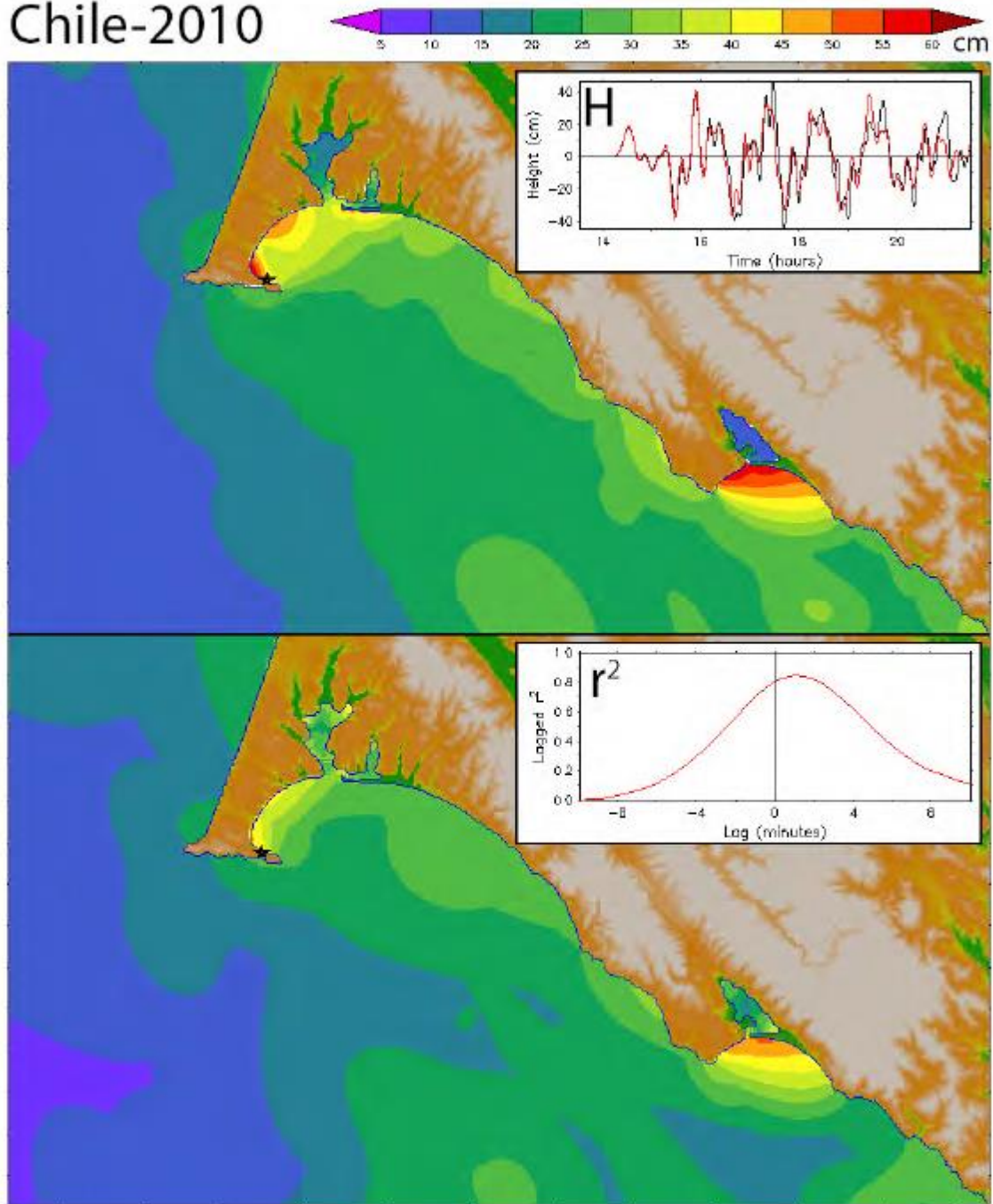
Figure 19. Comparison of reference and forecast model results for the historical 2010 Chile event. (a) Distributions of maximum amplitude in the reference (upper panel) and forecast (lower panel) model results with their time series (reference model–black, forecast model–red) and lagged correlation at the Point Reyes tide gauge as insets.
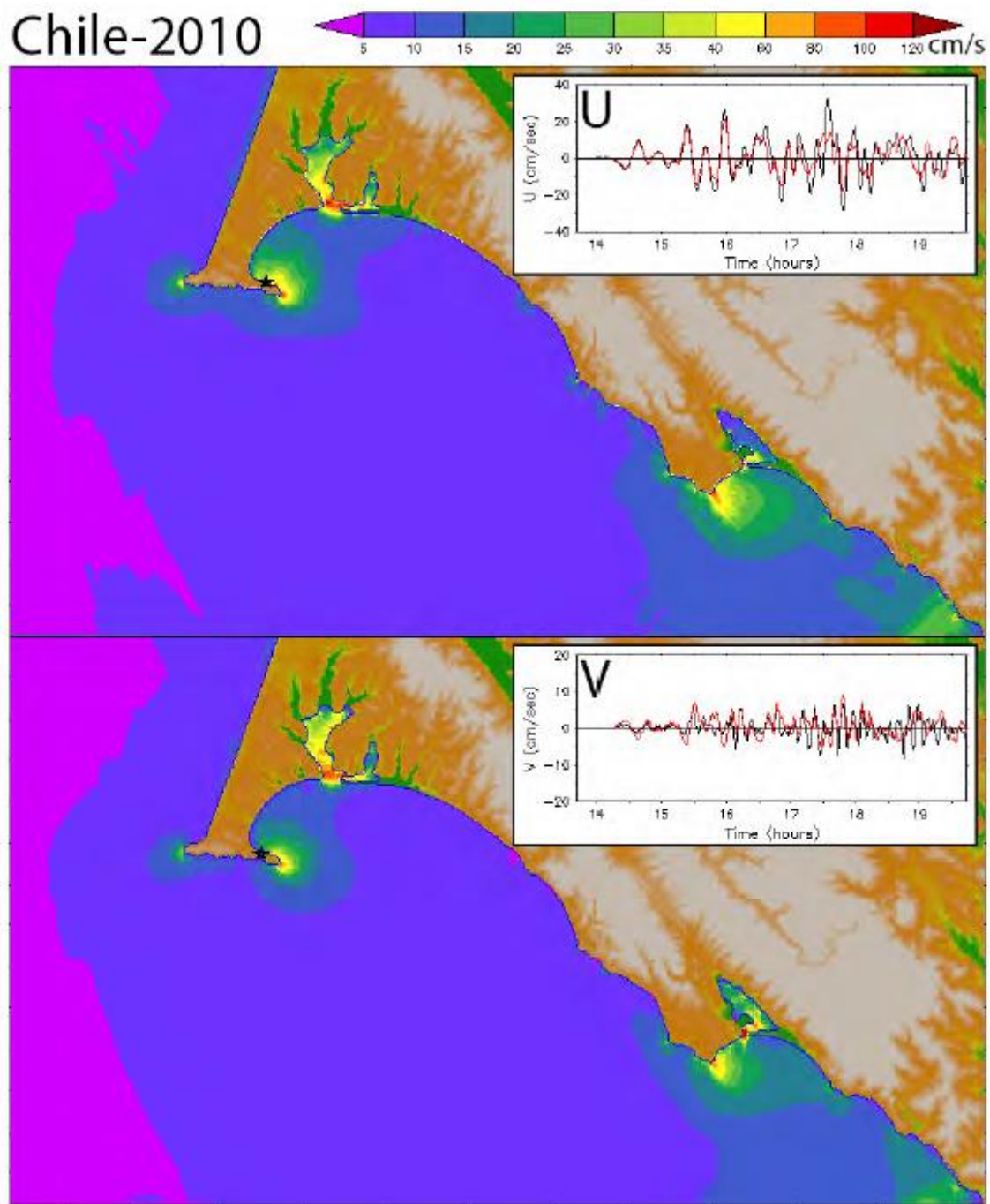
Figure 19. **continued**: (b) distributions of maximum speed in the reference (upper panel) and forecast (lower panel) model results with the time series of the vector components at the Point Reyes tide gauge as insets.
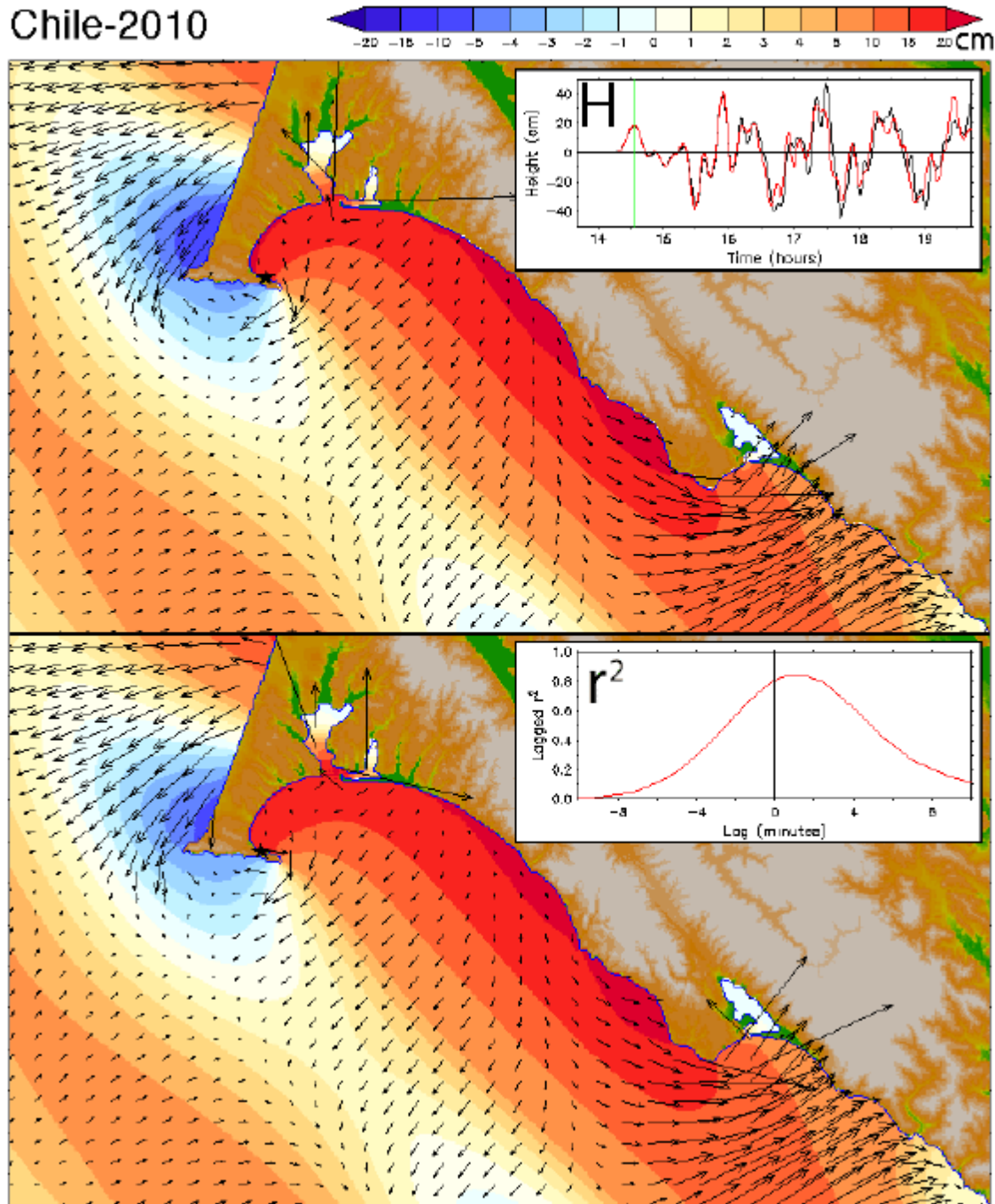
Figure 19. continued: (c) comparison of the wave amplitude and currents in the reference (upper panel) and forecast (lower panel) model results at the time indicated in the upper panel inset (the first wave peak).
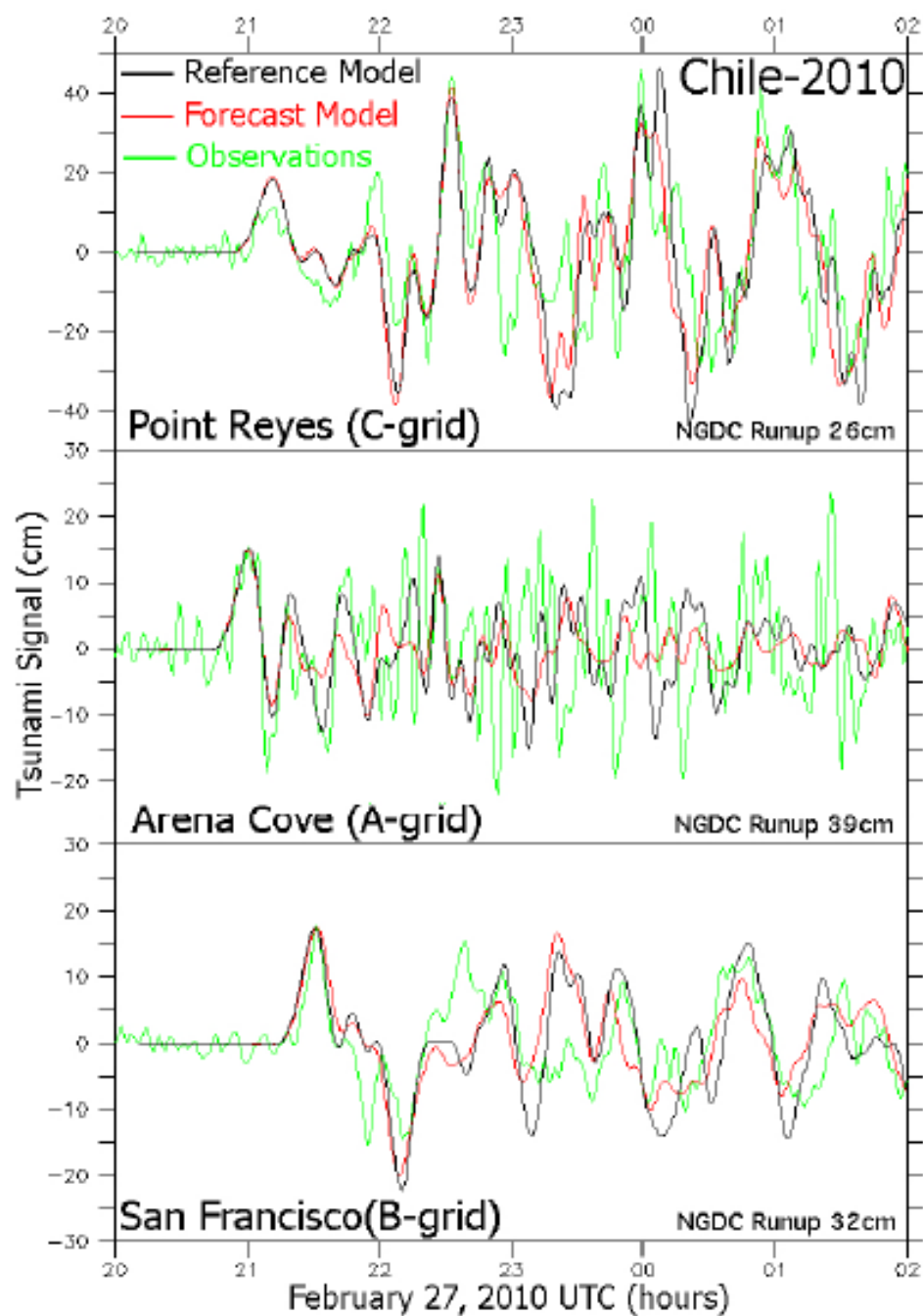
Figure 20. Modeled and observed time series comparison for the historical 2010 Chile event.
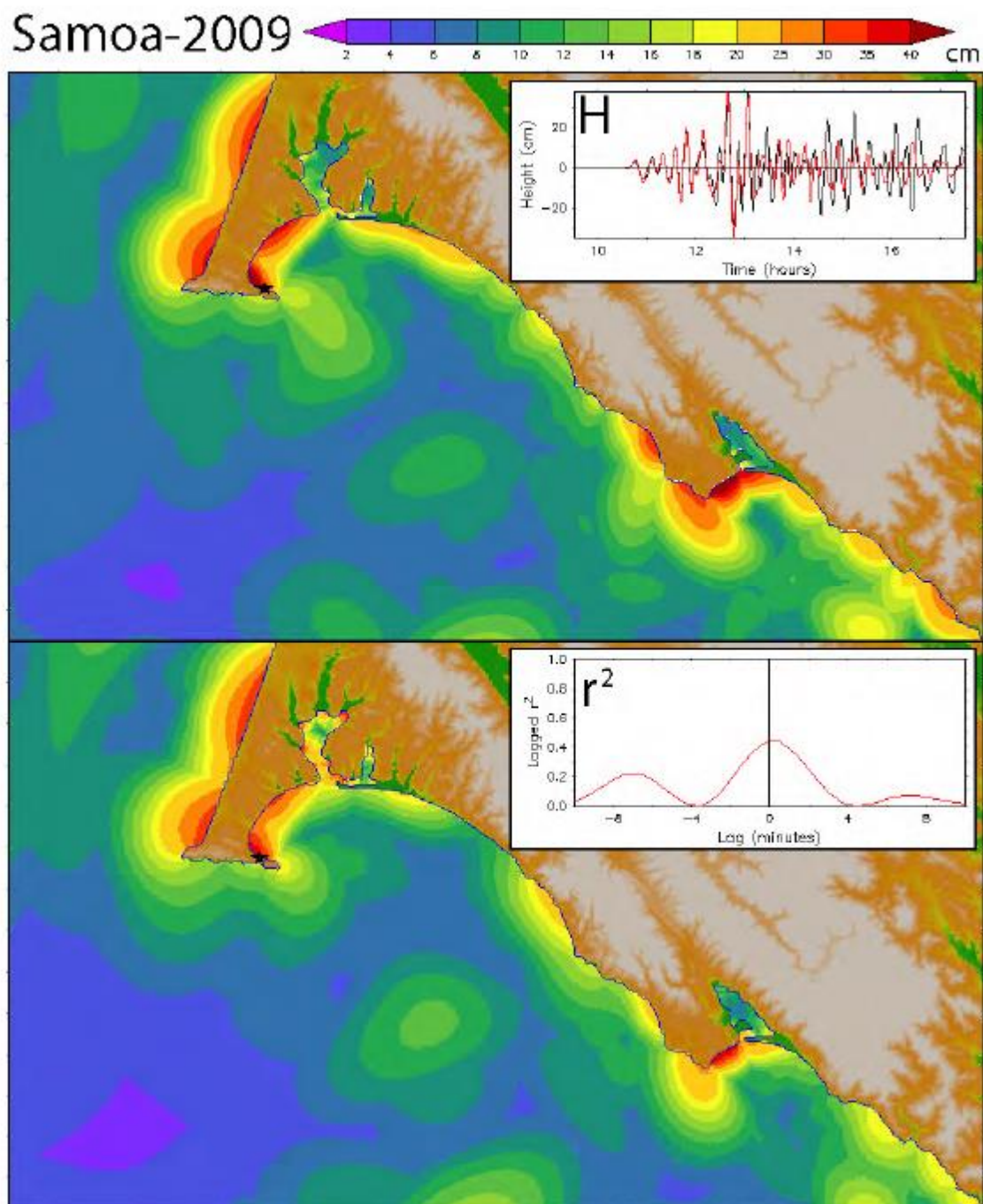
Figure 21. Comparison of reference and forecast model results for the historical 2009 Samoa event. (a) Distributions of maximum amplitude in the reference (upper panel) and forecast (lower panel) model results with their time series (reference model–black, forecast model–red) and lagged correlation at the Point Reyes tide gauge as insets.
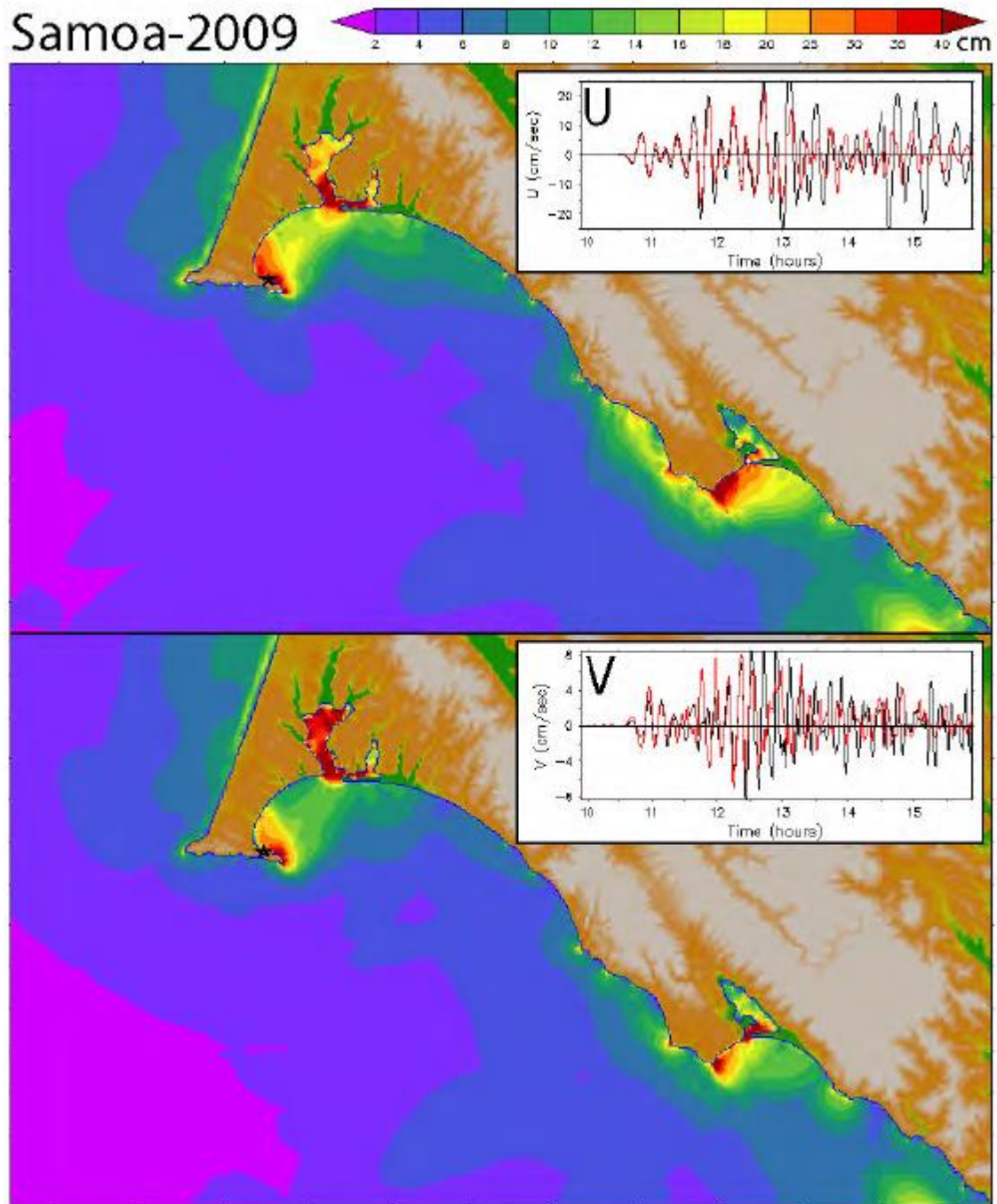
Figure 21, **continued**: (b) distributions of maximum speed in the reference (upper panel) and forecast (lower panel) model results with the time series of the vector components at the Point Reyes tide gauge as insets.
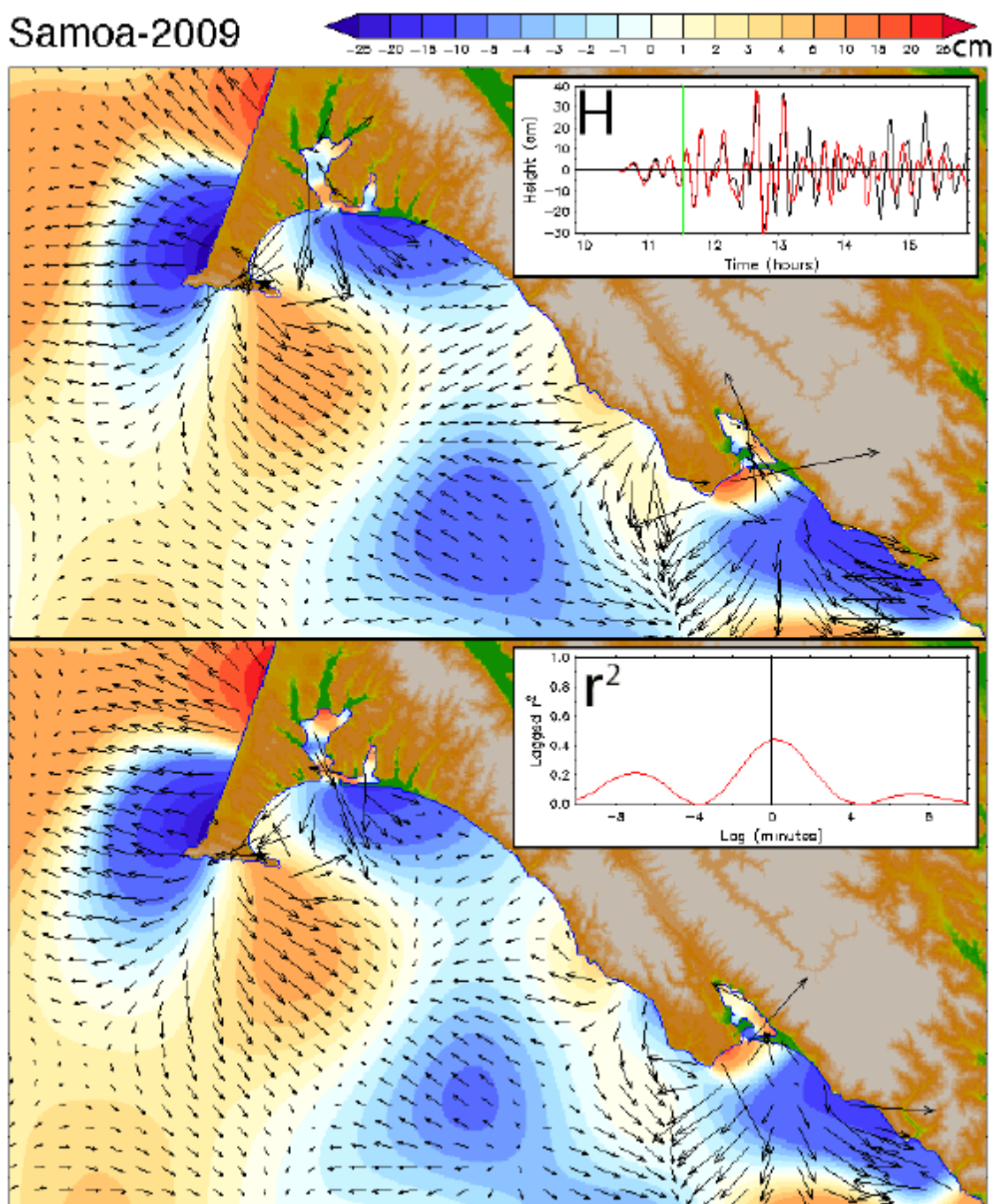
Figure 21, **continued**: (c) comparison of the wave amplitude and currents in the reference (upper panel) and forecast (lower panel) model results at a time between waves at the reference point.
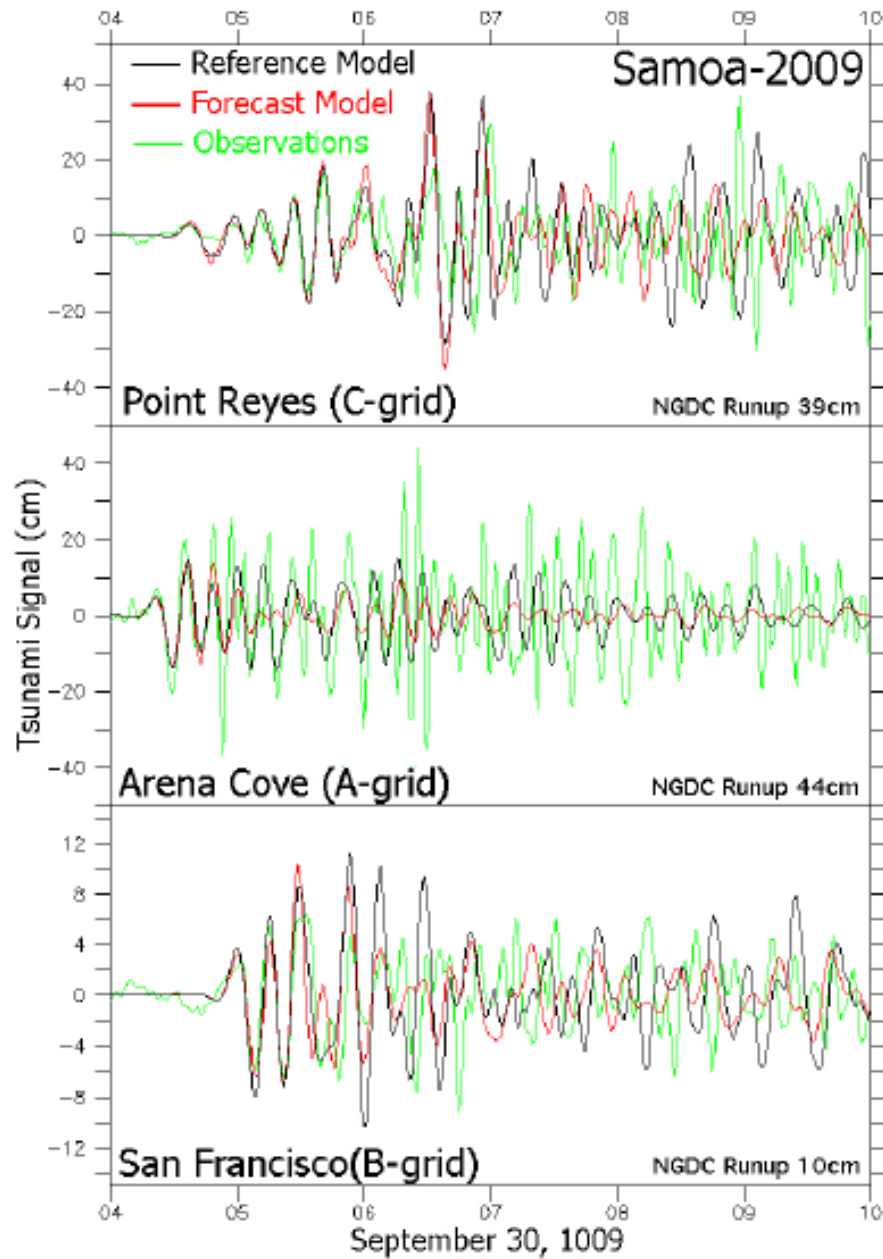
Figure 22. Modeled and observed time series comparison for the historical 2009 Samoa event.
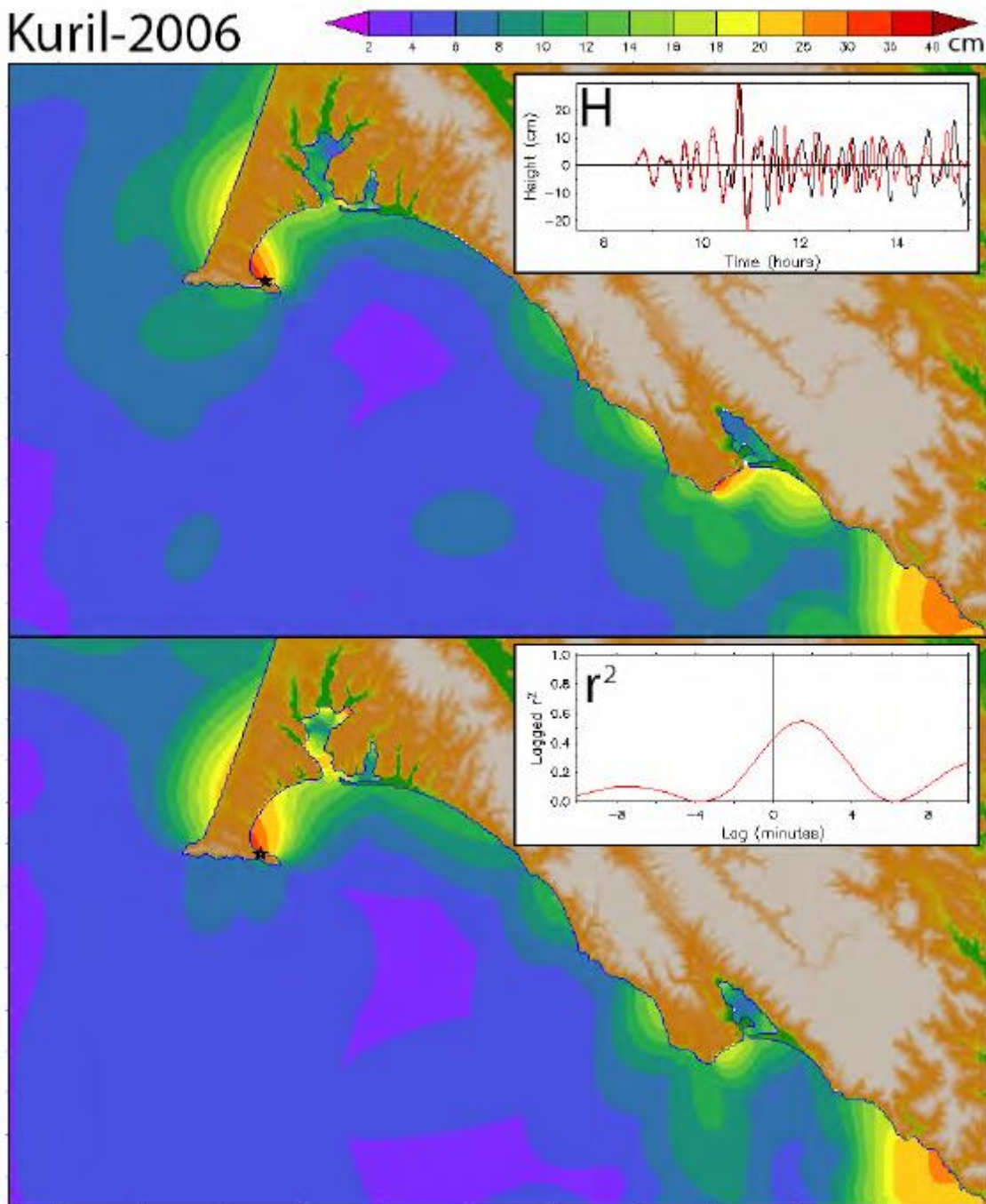
Figure 23. Comparison of reference and forecast model results for the historical 2006 Kuril event. (a) Distributions of maximum amplitude in the reference (upper panel) and forecast (lower panel) model results with their time series (reference model–black, forecast model–red) and lagged correlation at the Point Reyes tide gauge as insets.
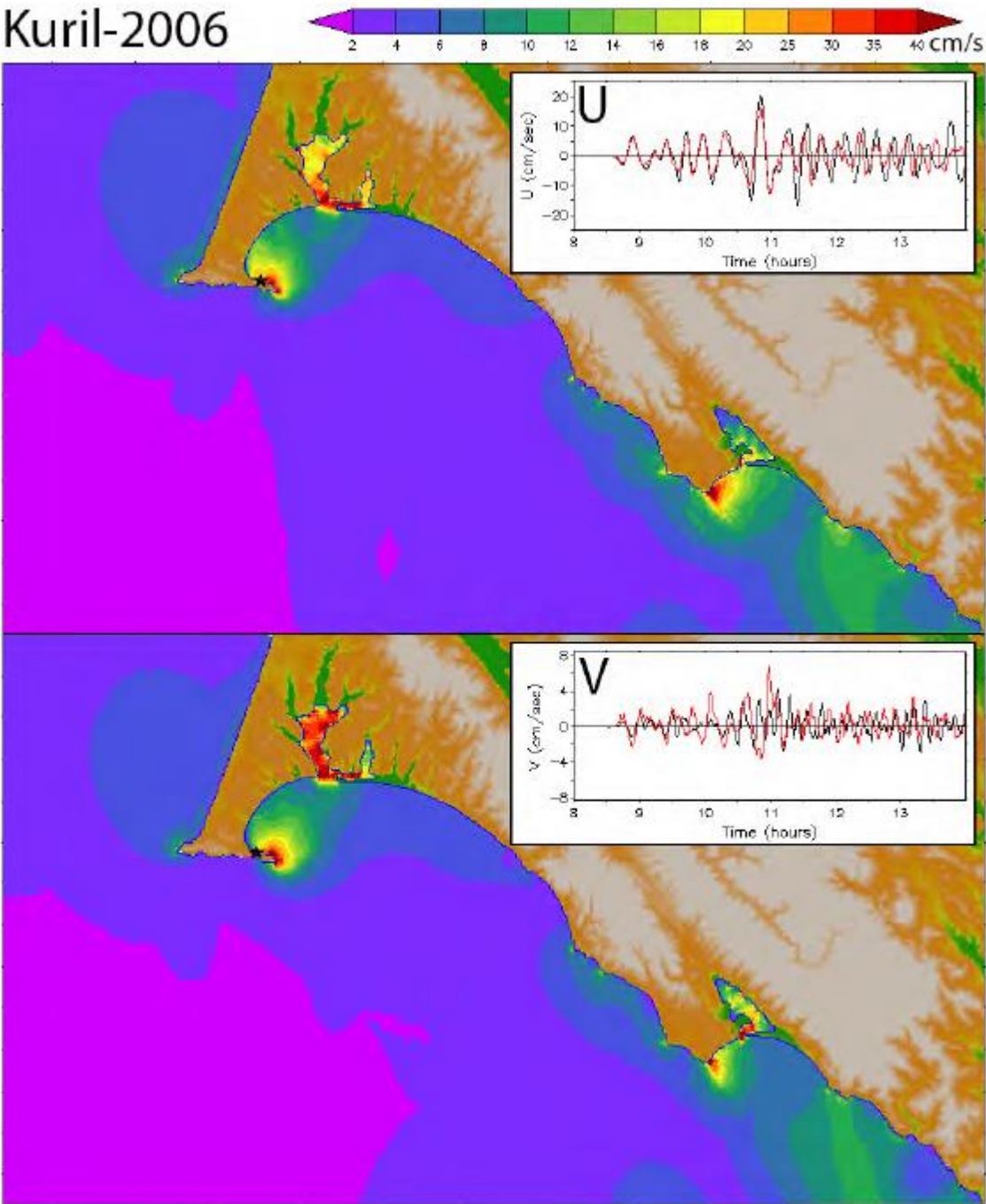
Figure 23, **continued**: (b) distributions of maximum speed in the reference (upper panel) and forecast (lower panel) model results with the time series of the vector components at the Point Reyes tide gauge as insets.
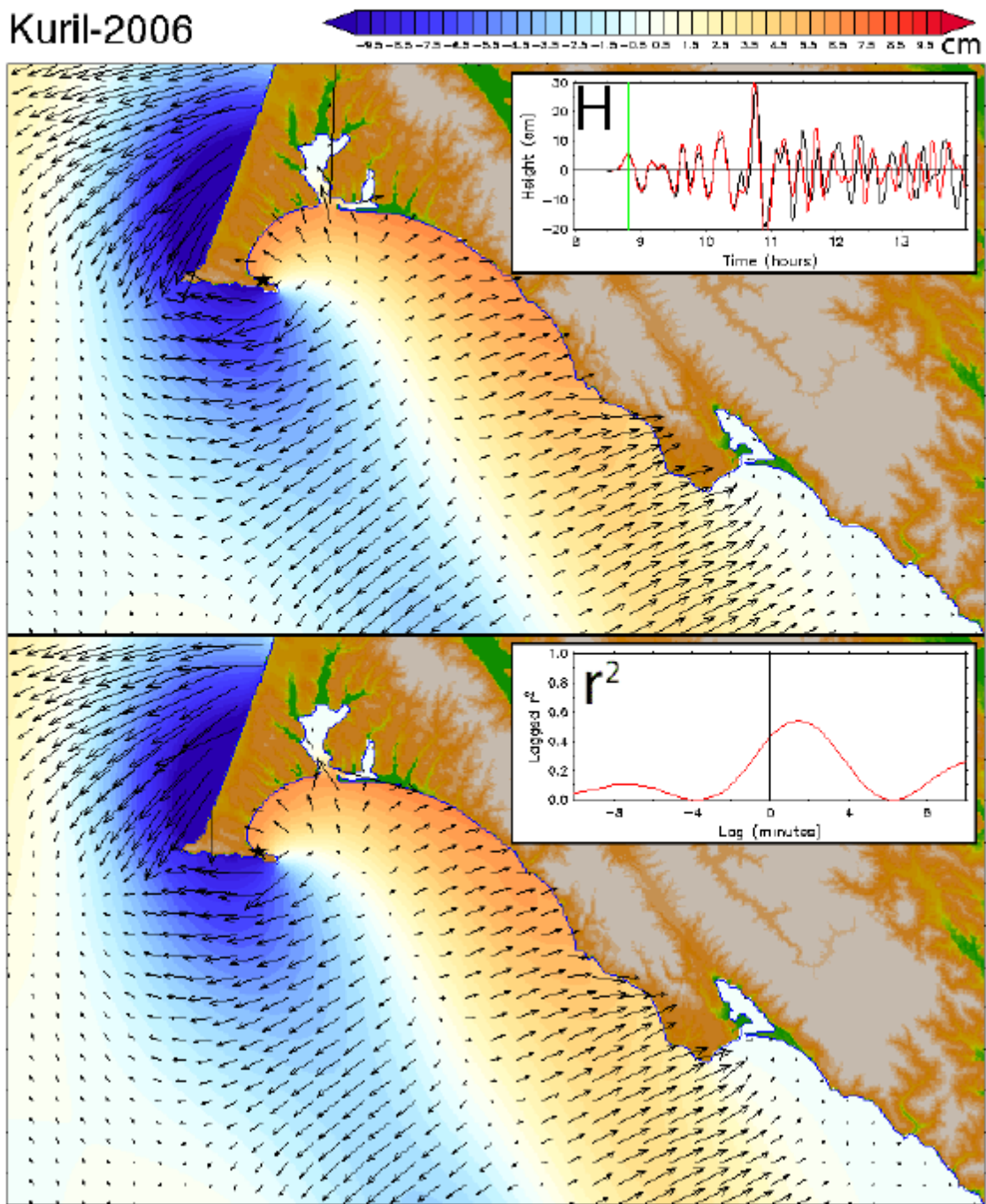
Figure 23, **continued**: (c) comparison of the wave amplitude and currents in the reference (upper panel) and forecast (lower panel) model results at the time indicated in the upper panel inset (the first wave peak).
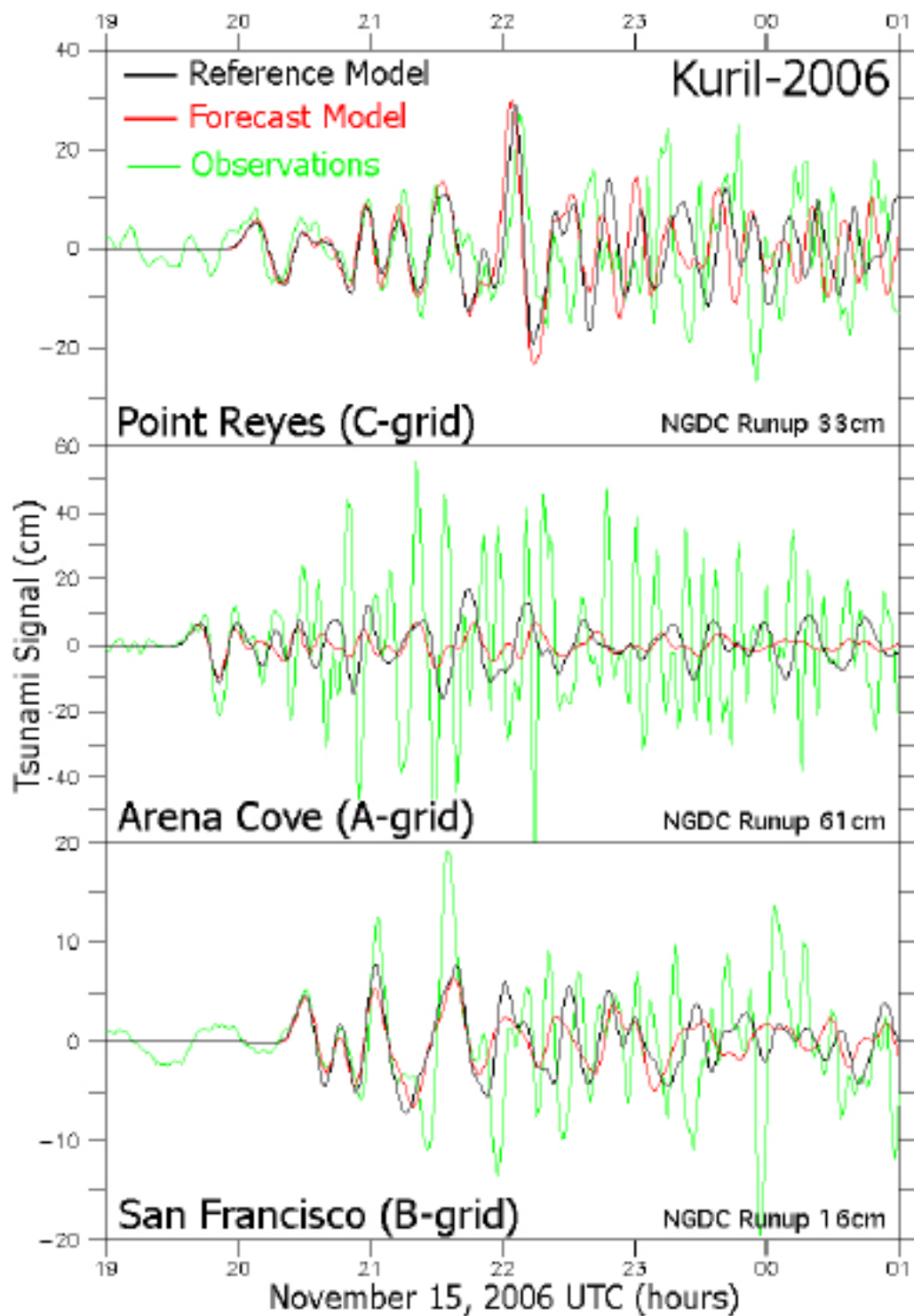
Figure 24. Modeled and observed time series comparison for the historical 2006 Kuril event.
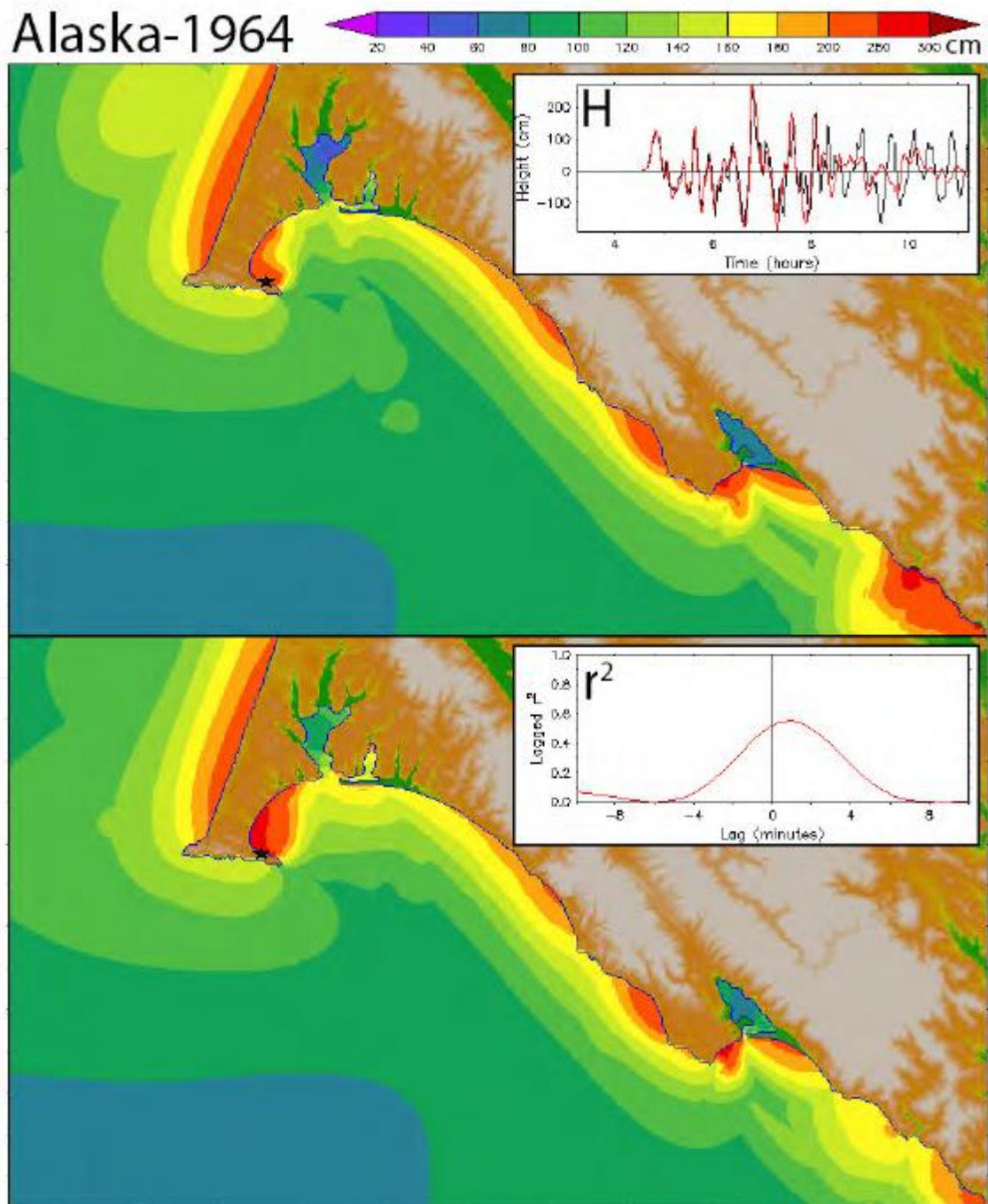
Figure 25. Comparison of reference and forecast model results for the historical 1964 Alaska event. (a) Distributions of maximum amplitude in the reference (upper panel) and forecast (lower panel) model results with their time series (reference model–black, forecast model–red) and lagged correlation at the Point Reyes tide gauge as insets.
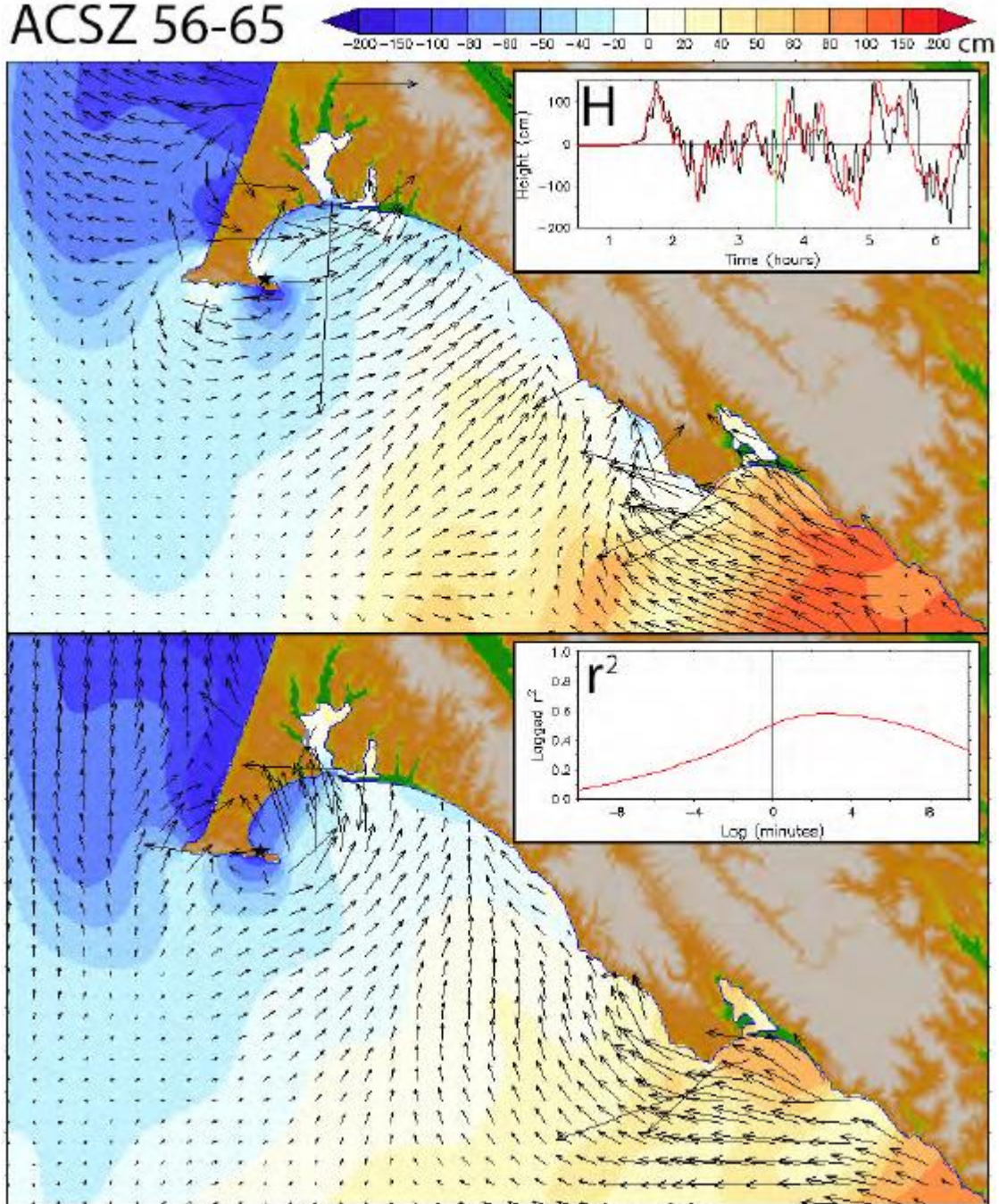
71
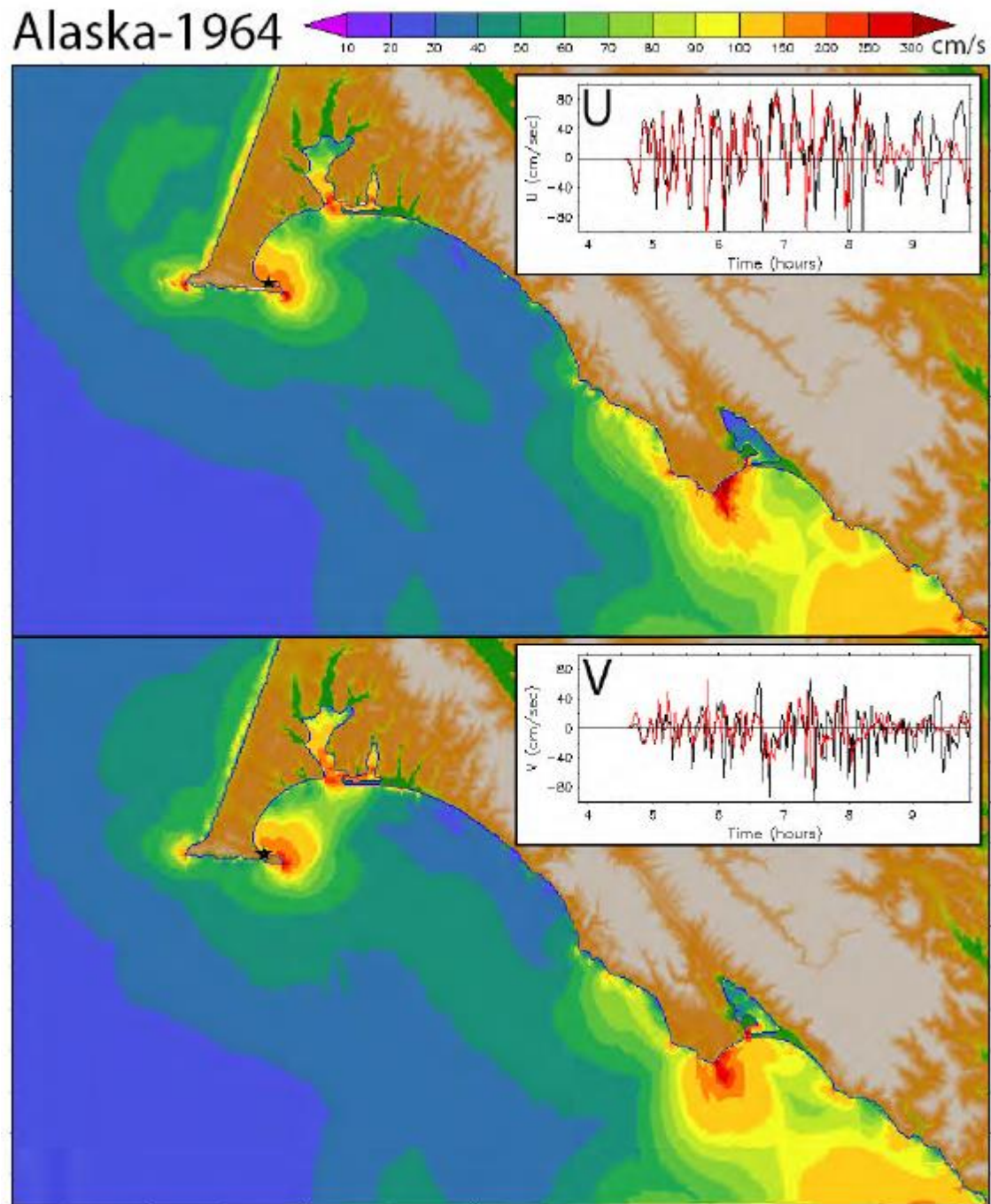
Figure 25, **continued**: (b) distributions of maximum speed in the reference (upper panel) and forecast (lower panel) model results with the time series of the vector components at the Point Reyes tide gauge as insets.
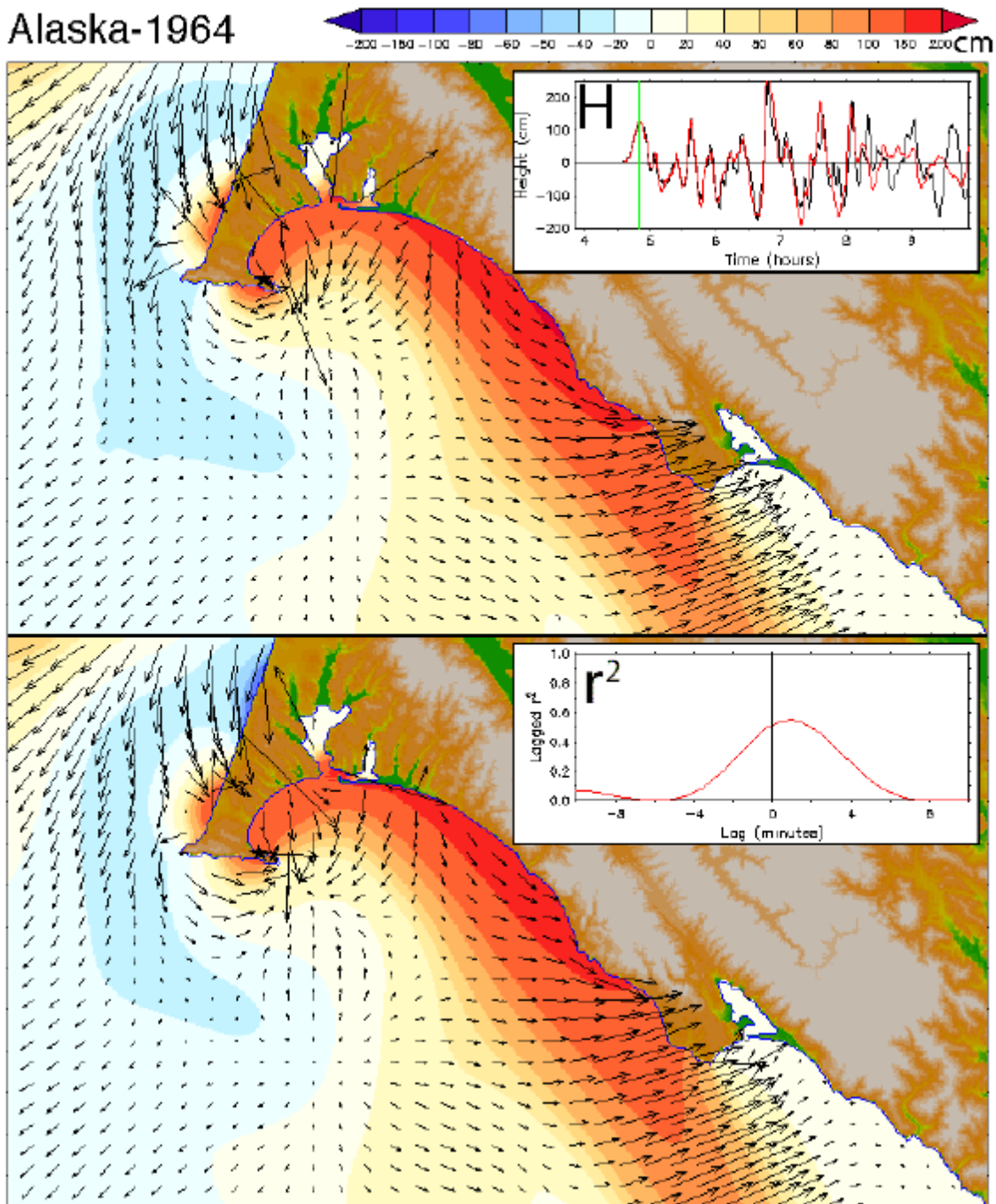
Figure 25, **continued**: (c) comparison of the wave amplitude and currents in the reference (upper panel) and forecast (lower panel) model results at the time indicated in the upper panel inset (the first wave peak).
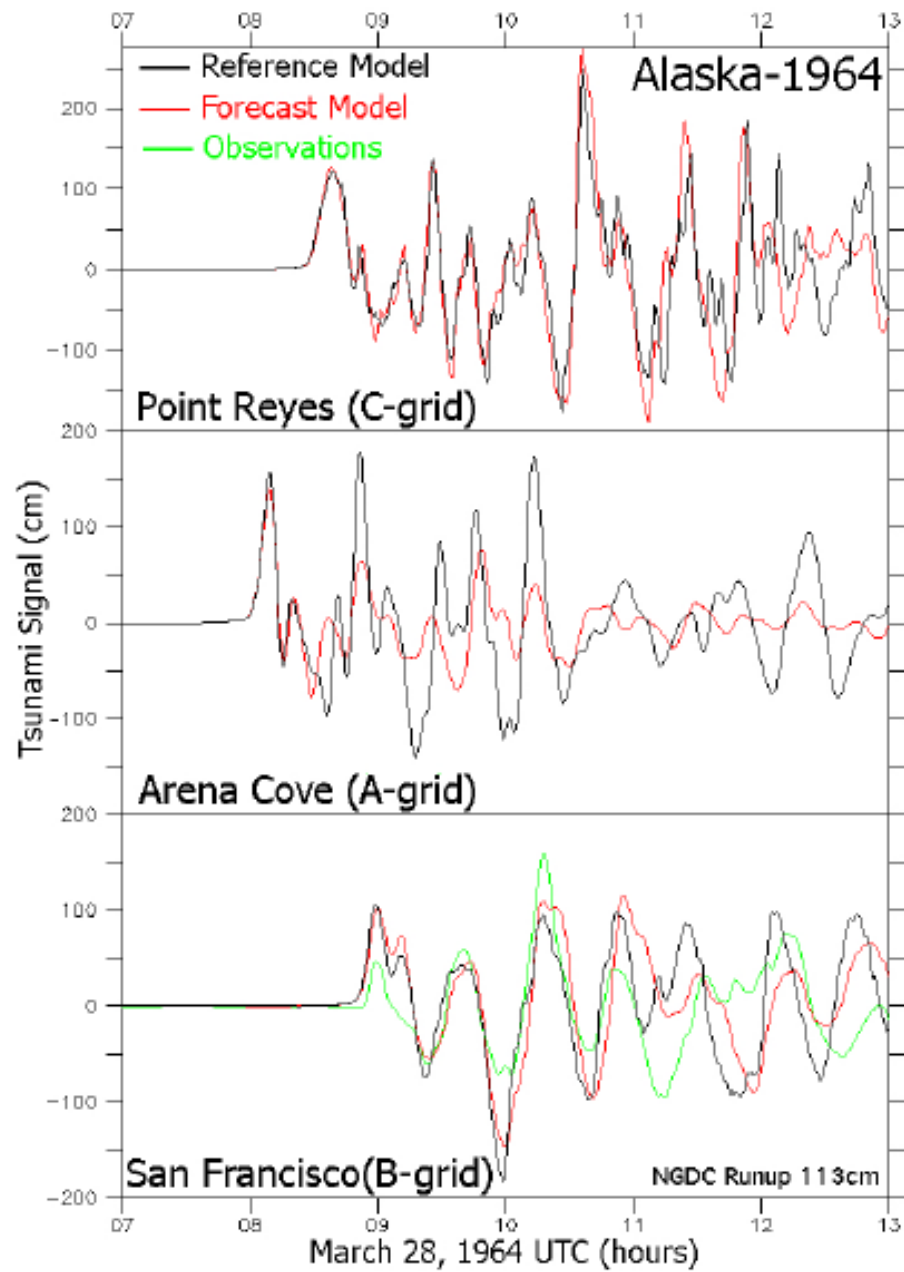
Figure 26. Modeled and observed time series comparison for the historical 1964 Alaska event.
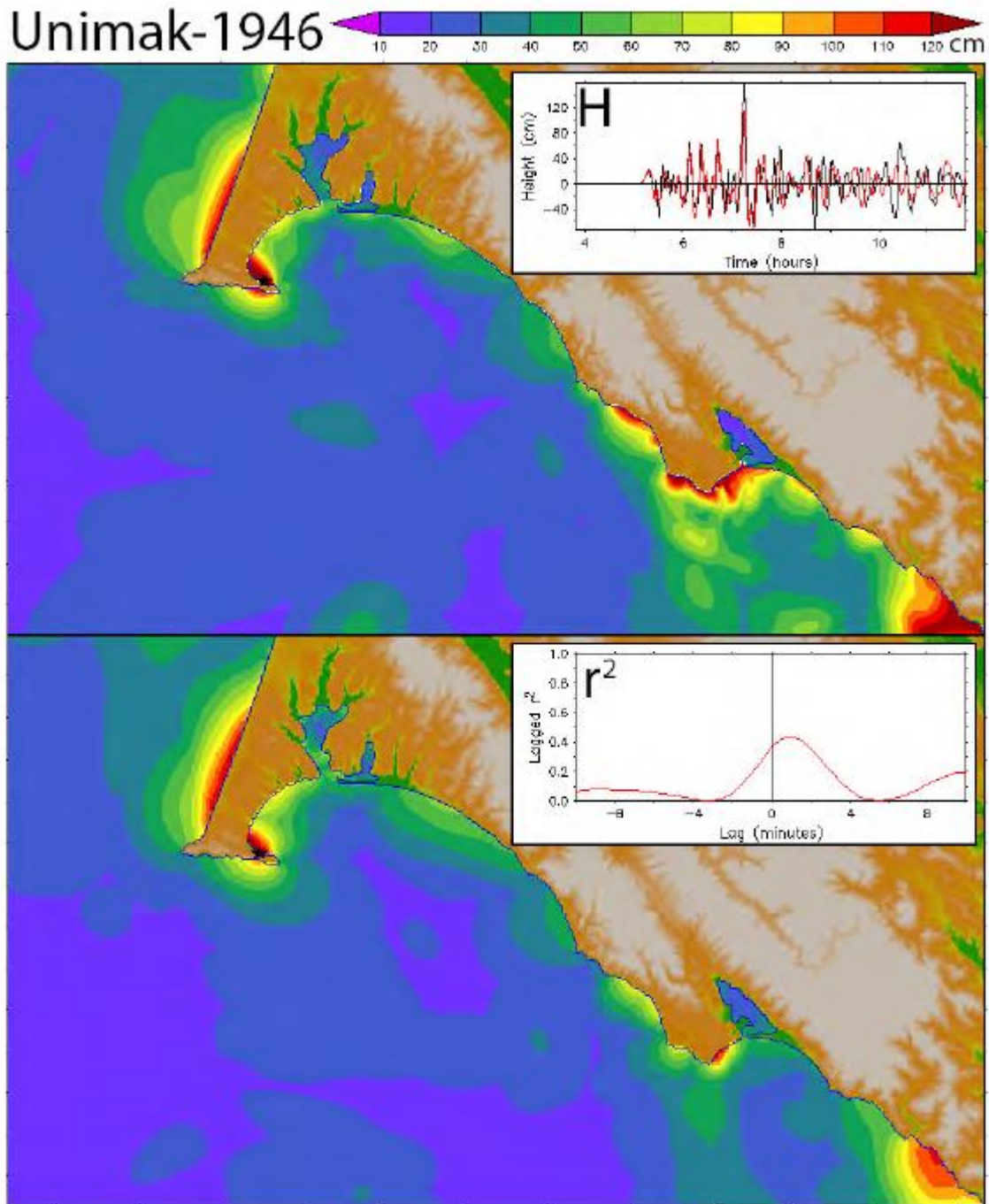
Figure 27. Comparison of reference and forecast model results for the historical 1946 Unimak event. (a) Distributions of maximum amplitude in the reference (upper panel) and forecast (lower panel) model results with their time series (reference model–black, forecast model–red) and lagged correlation at the Point Reyes tide gauge as insets.
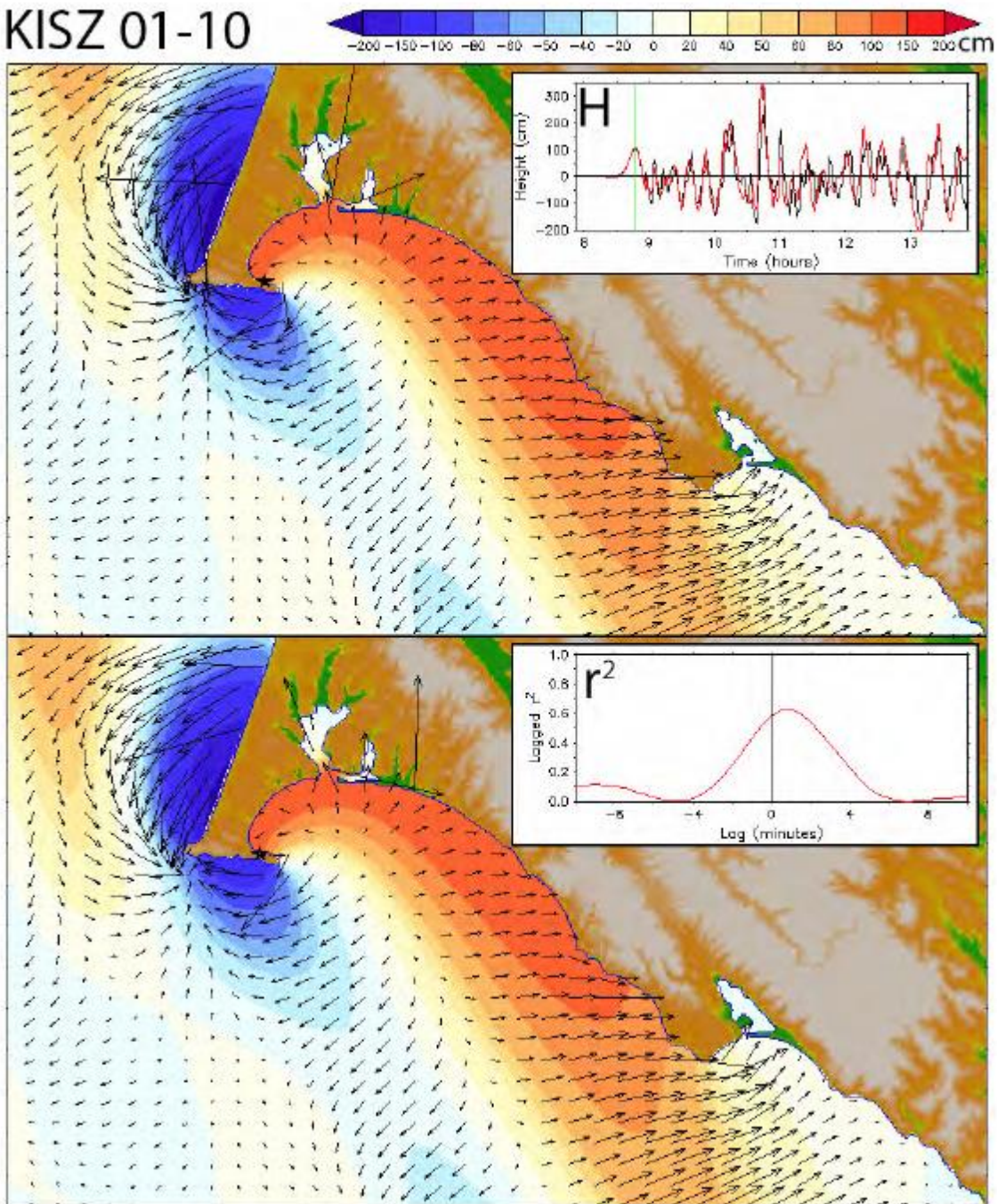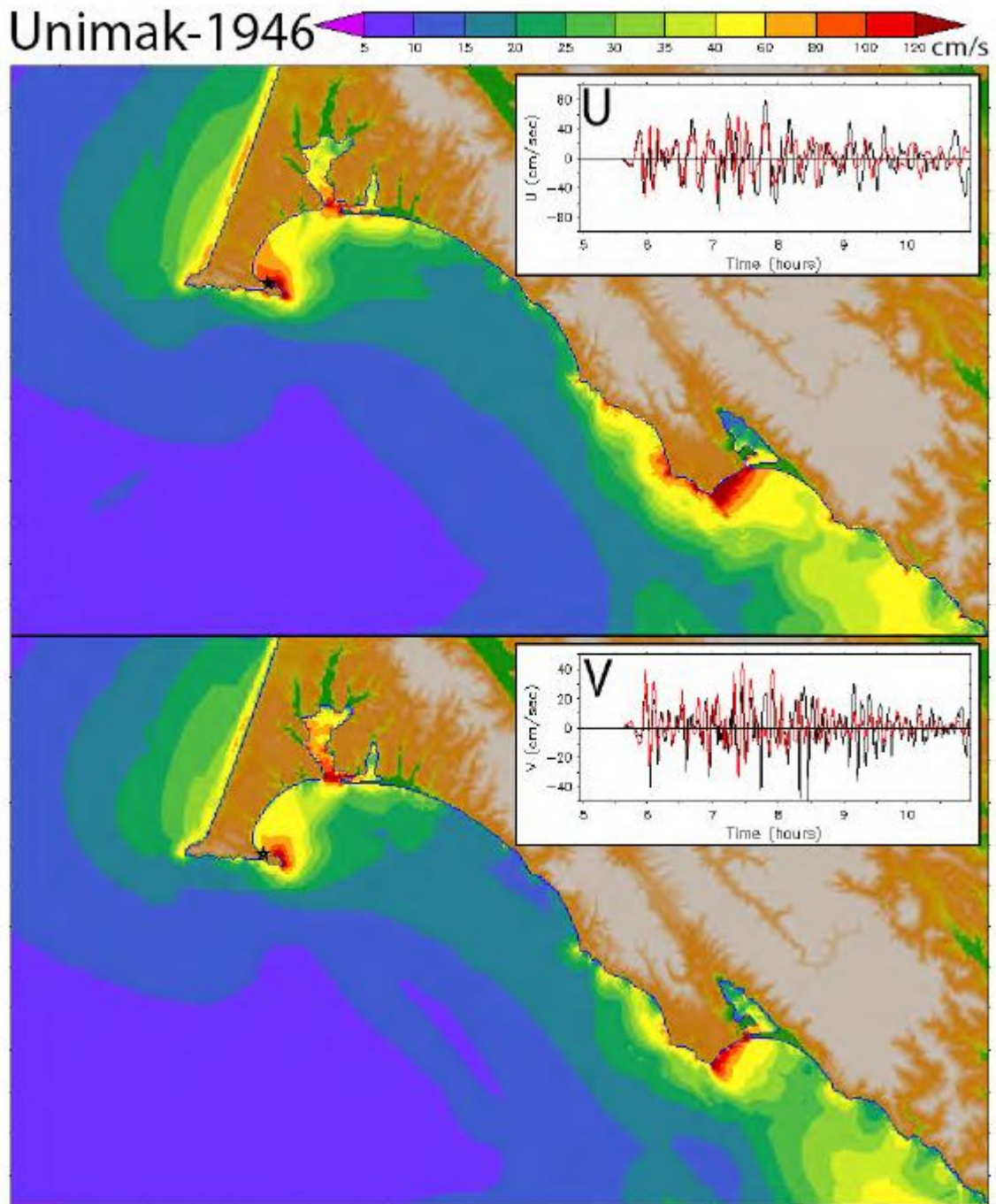
Figure 27, **continued**: (b) distributions of maximum speed in the reference (upper panel) and forecast (lower panel) model results with the time series of the vector components at the Point Reyes tide gauge as insets.

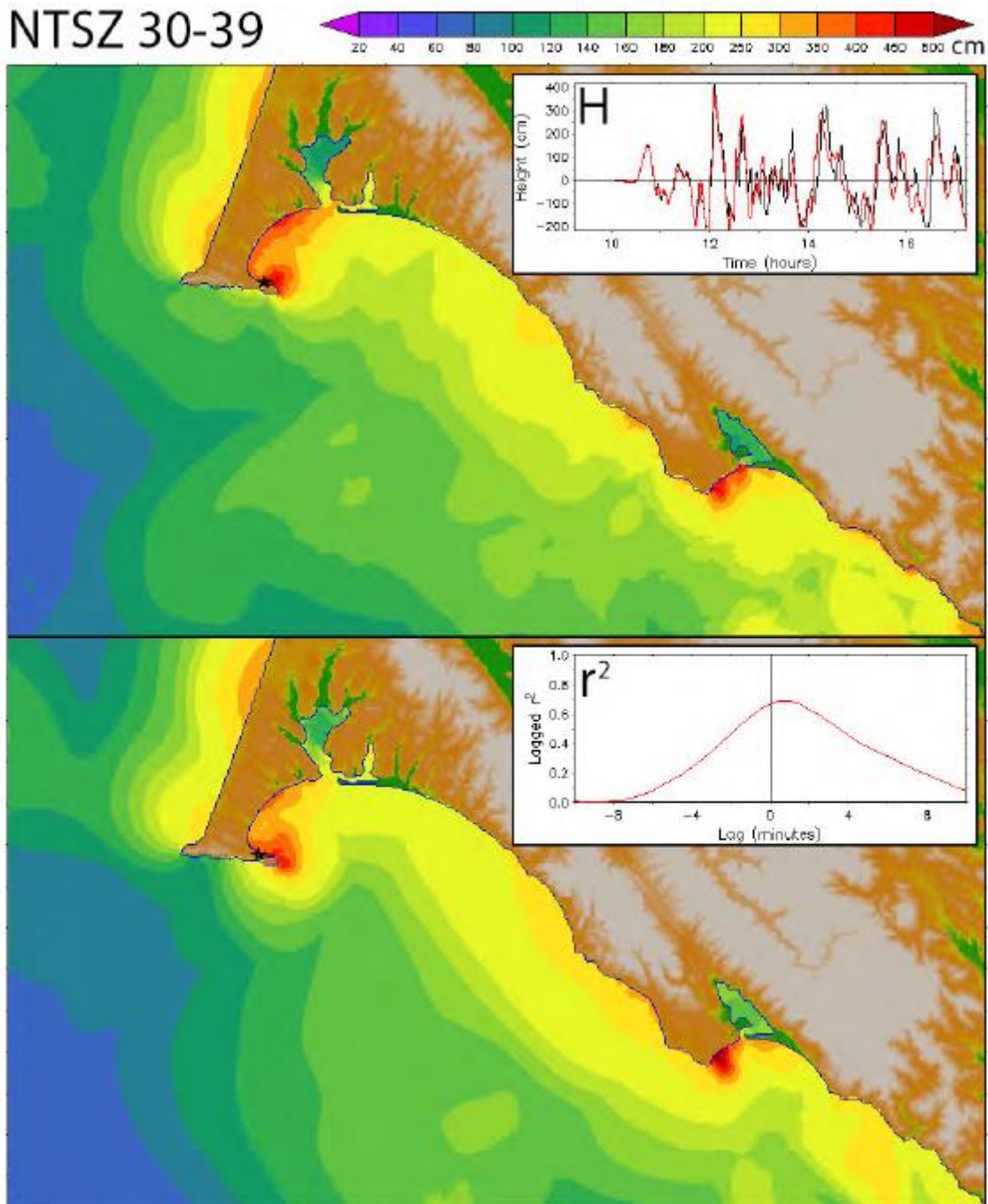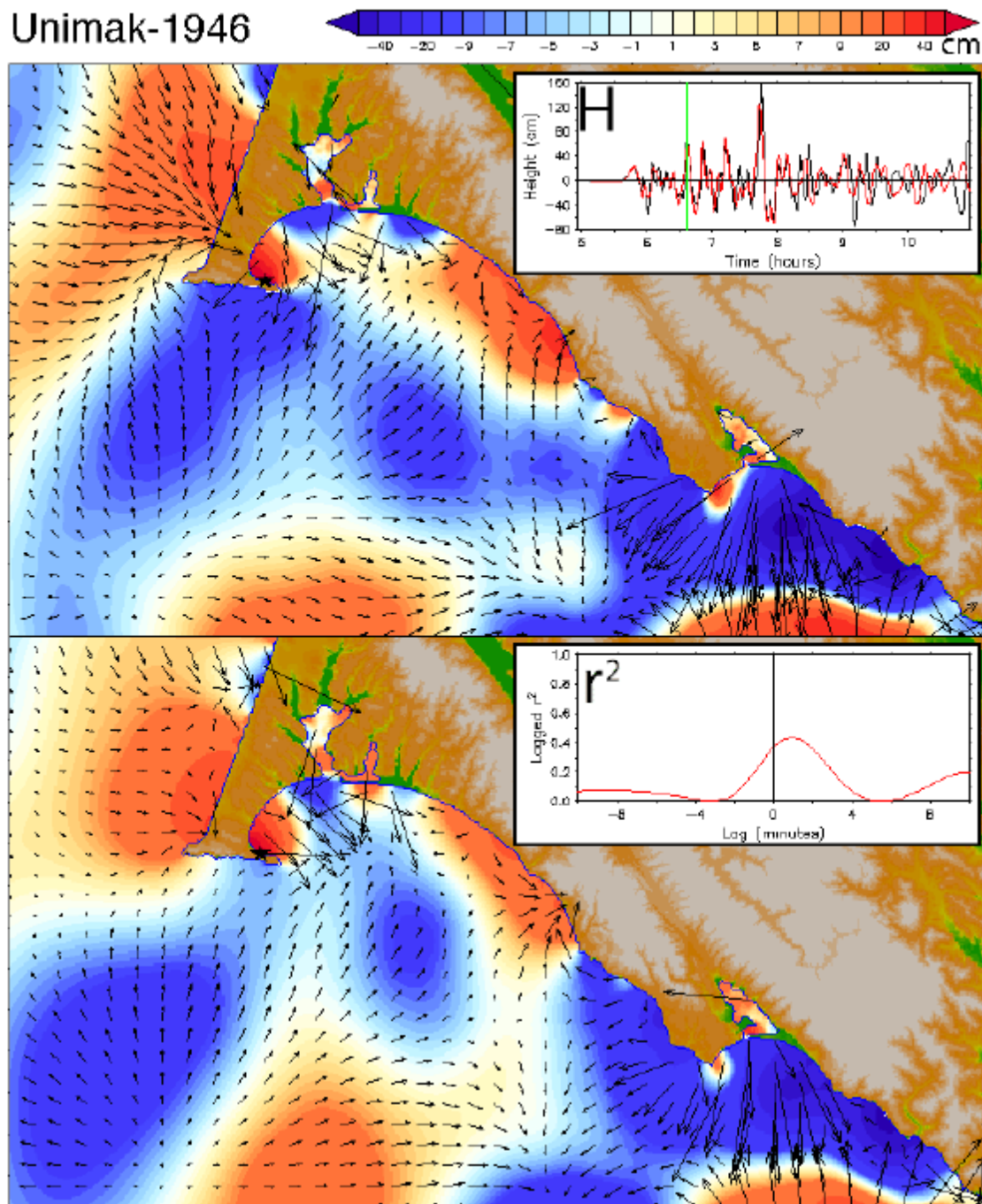**Figure 27**, **continued**: (c) comparison of the wave amplitude and currents in the reference (upper panel) and forecast (lower panel) model results at a later wave peak.
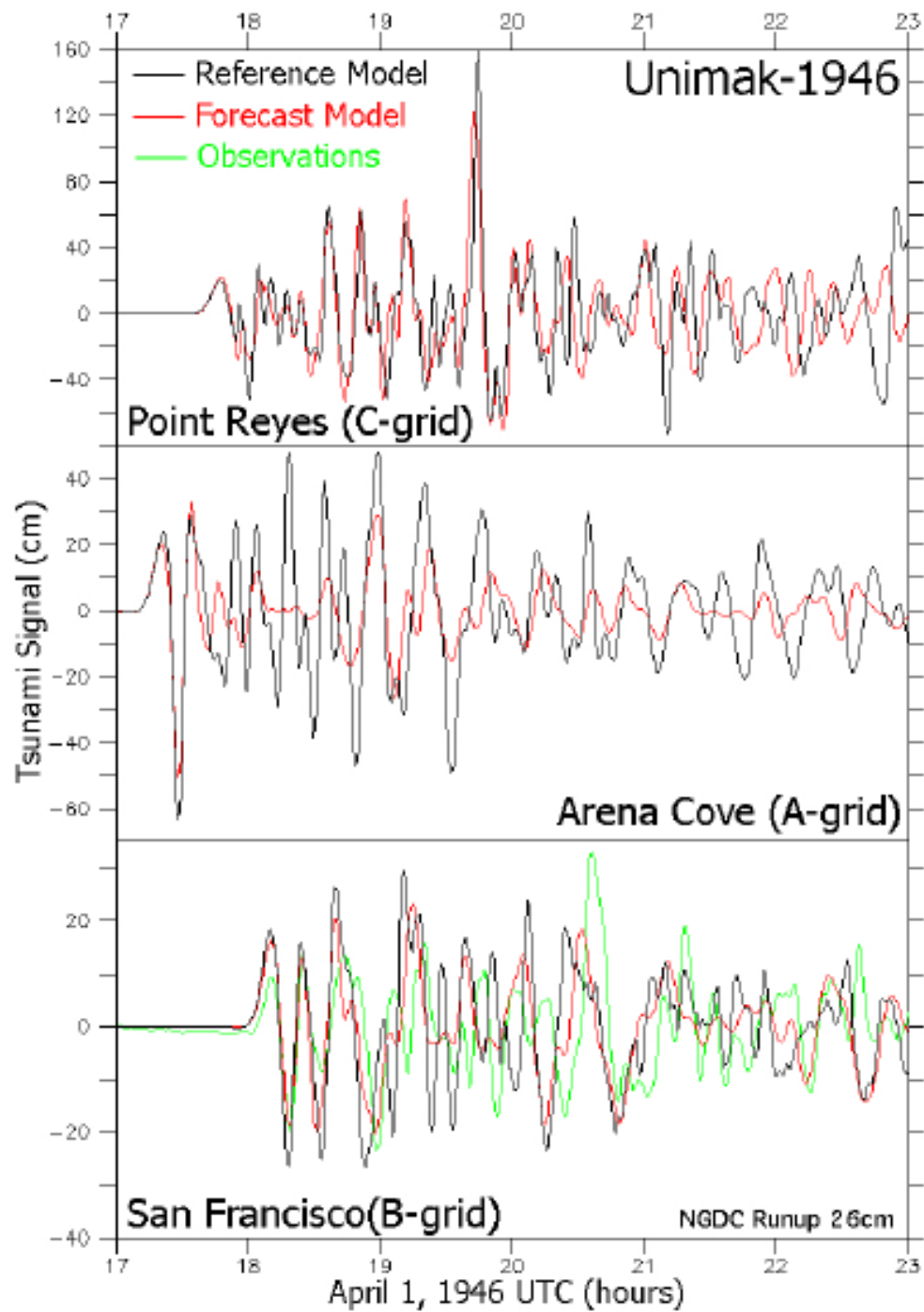
Figure 28. Modeled and observed time series comparison for the historical 1946 Unimak event.
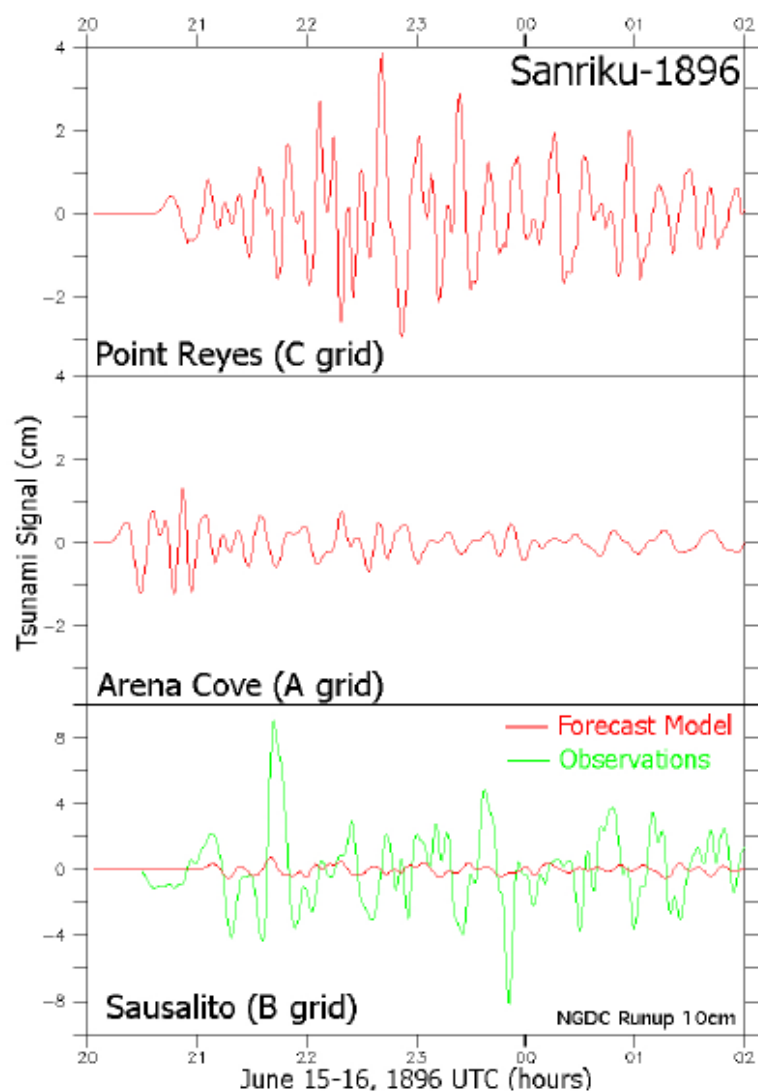
Figure 29. Modeled and observed time series comparison for the Sanriku event of 15 June 1896.
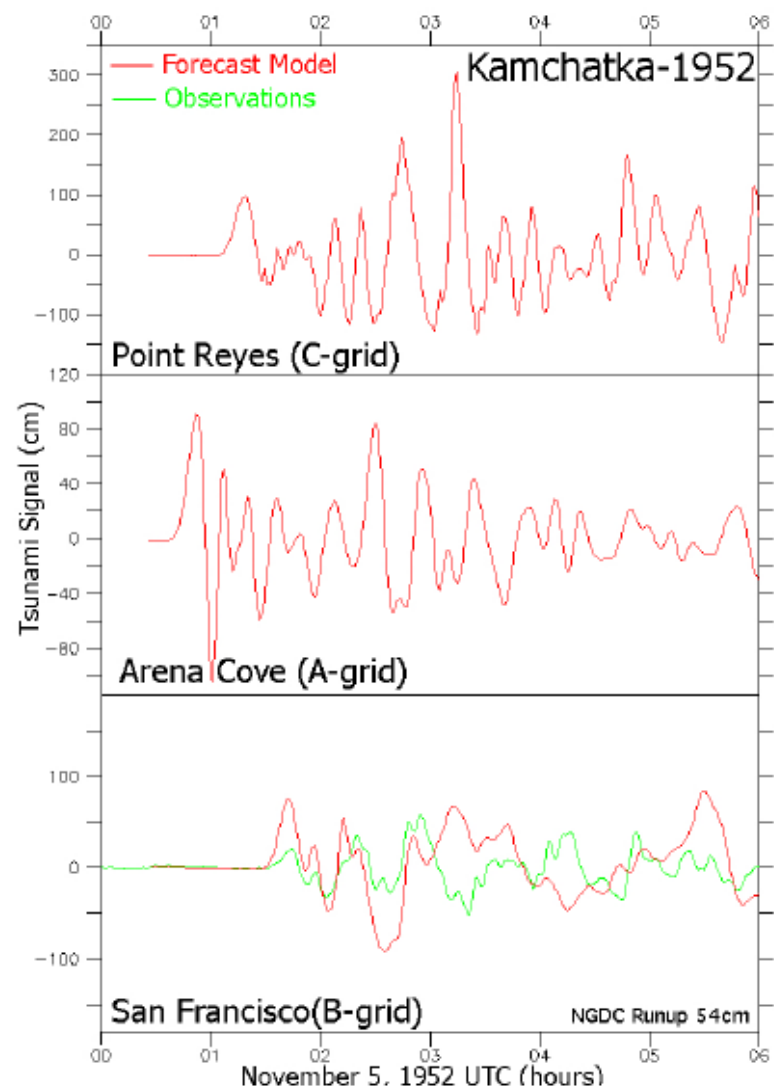
Figure 30. Modeled and observed time series comparison for the Kamchatka event of 4 November 1952.
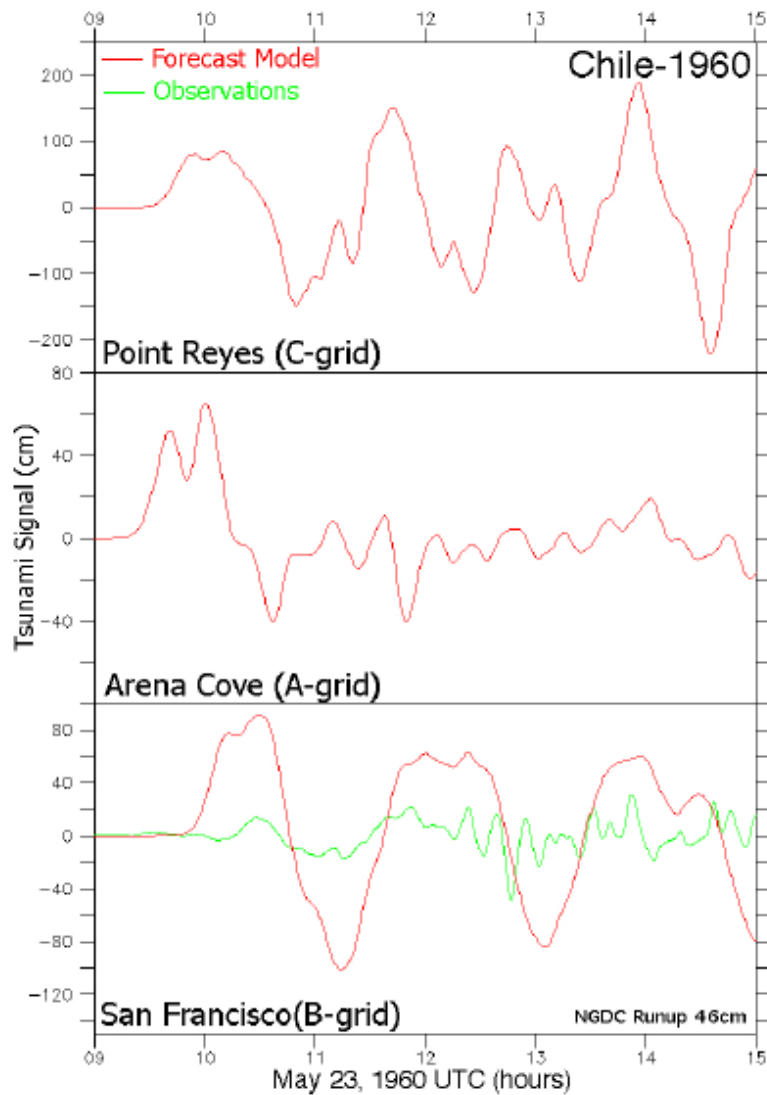
Figure 31. Modeled and observed time series comparison for the Chile event of 22 May 1960.
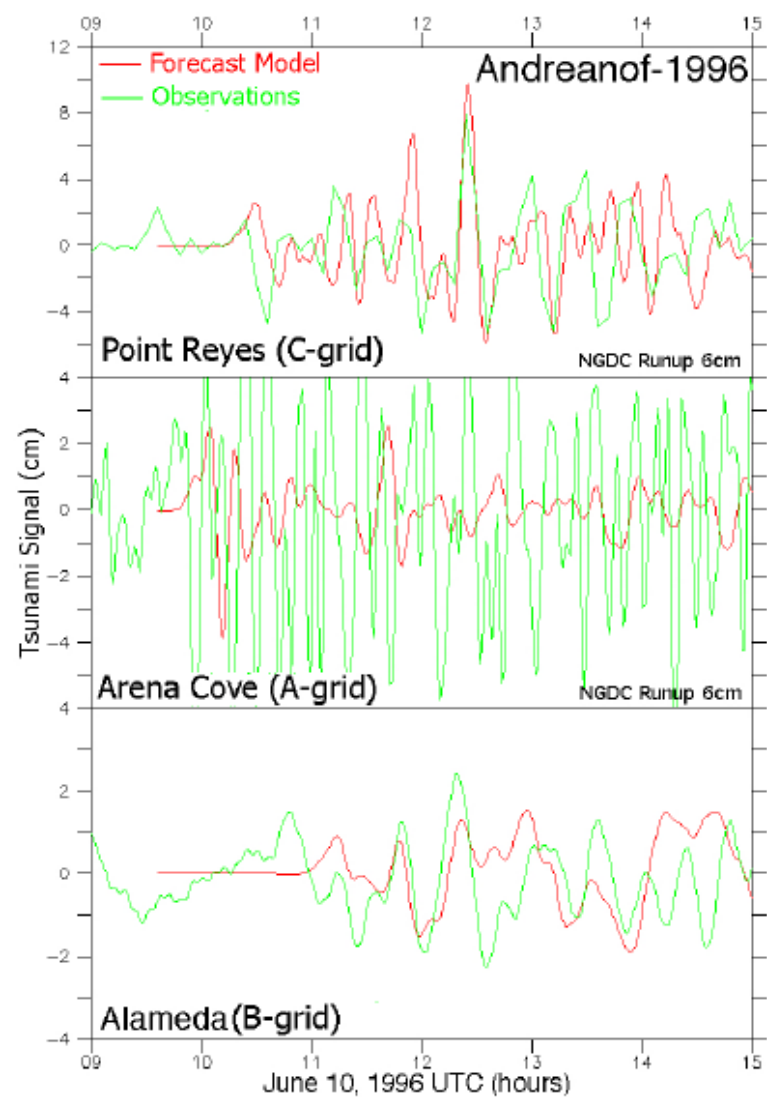
Figure 32. Modeled and observed time series comparison for the Andreanof event of 10 June 1996.
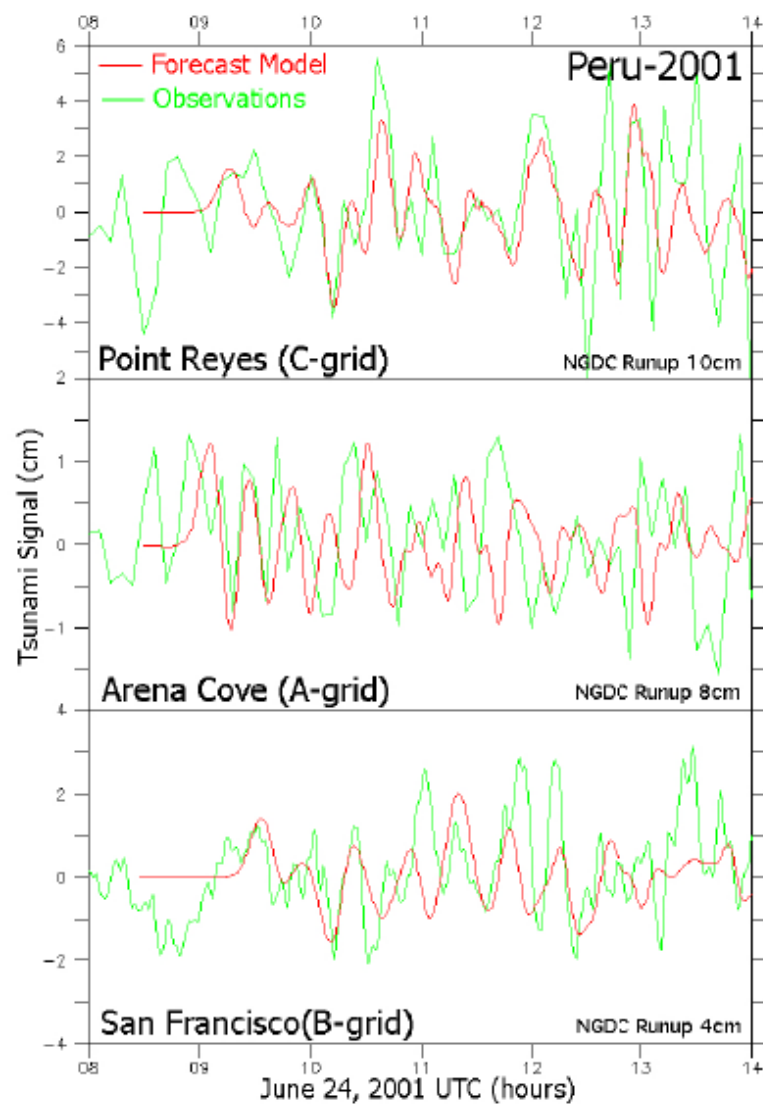
Figure 33. Modeled and observed time series comparison for the Peru event of 23 June 2001.
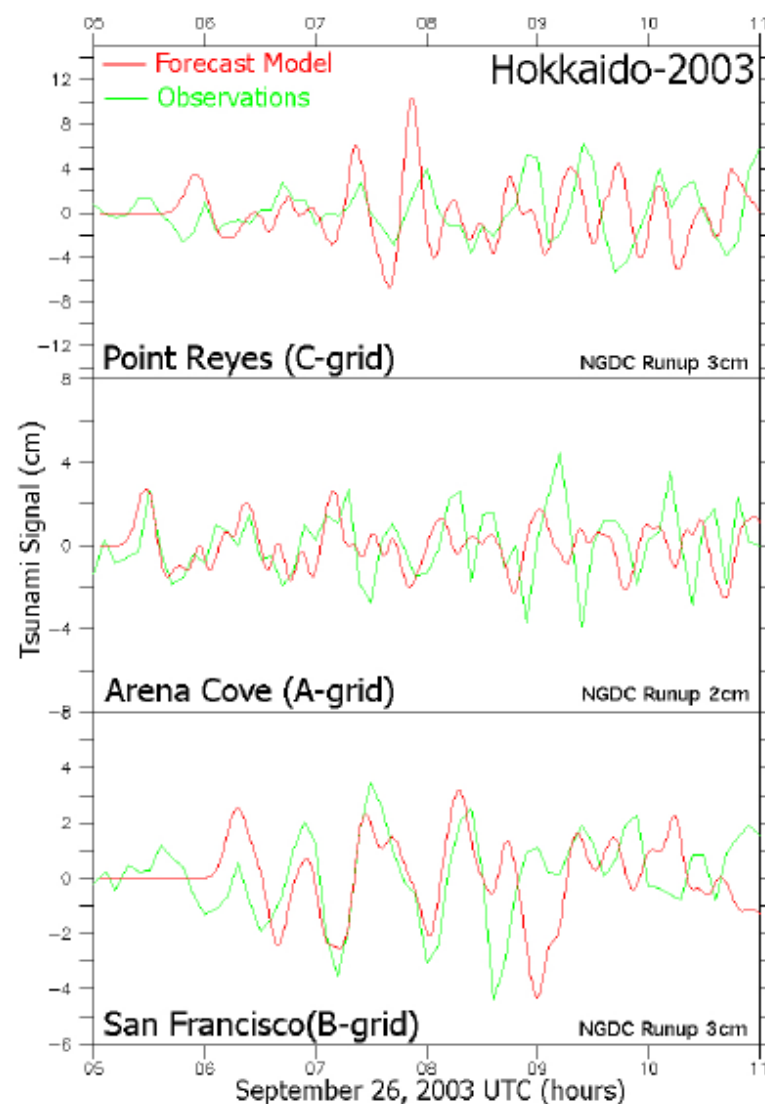
Figure 34. Modeled and observed time series comparison for the Hokkaido event of 25 September 2003.
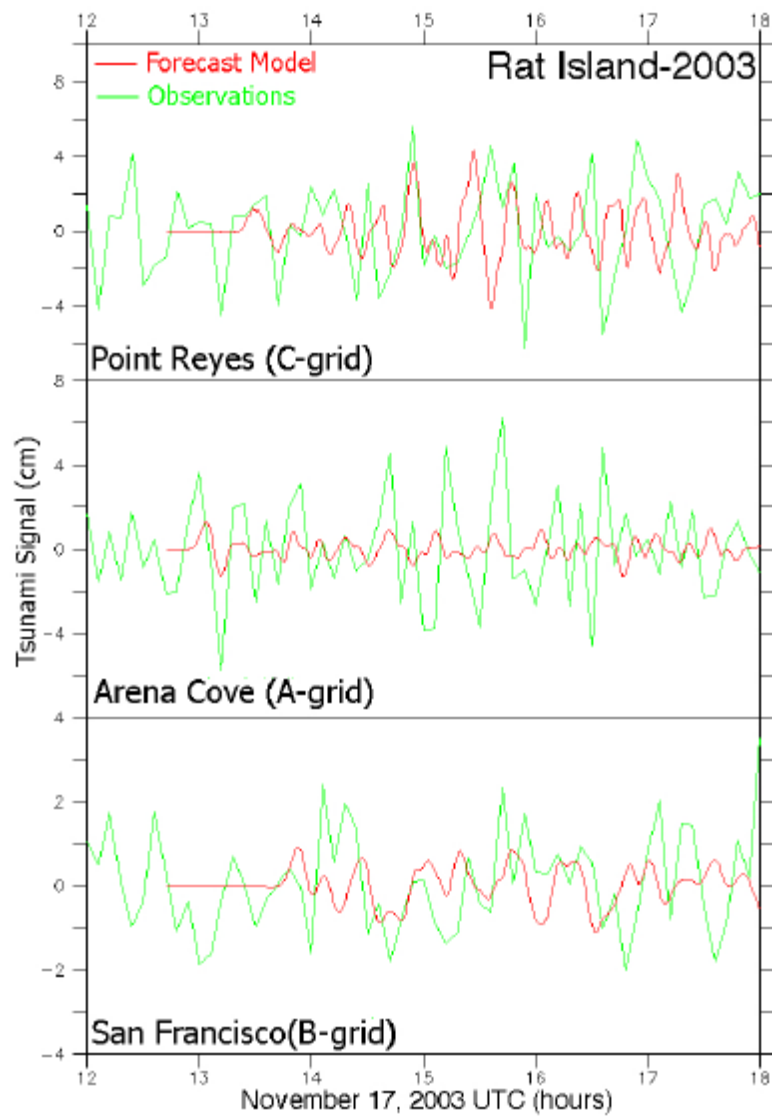
Figure 35. Modeled and observed time series comparison for the Rat Island event of 17 November 2003.
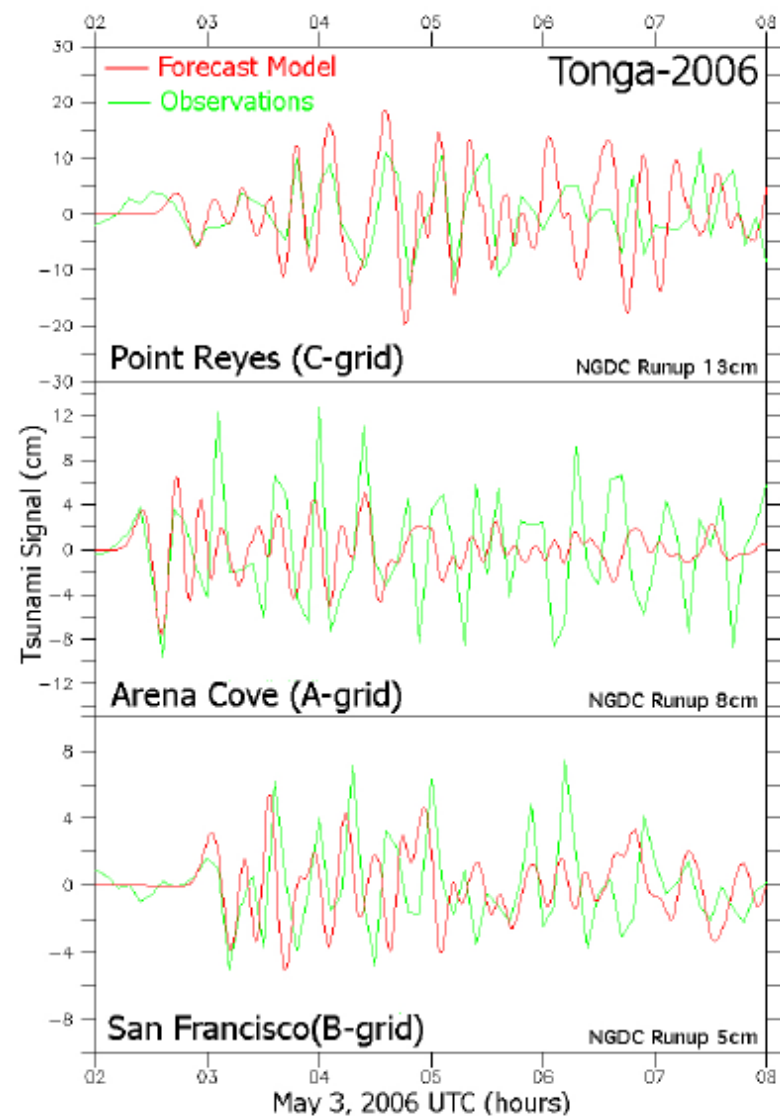
Figure 36. Modeled and observed time series comparison for the Tonga event of 3 May 2006.
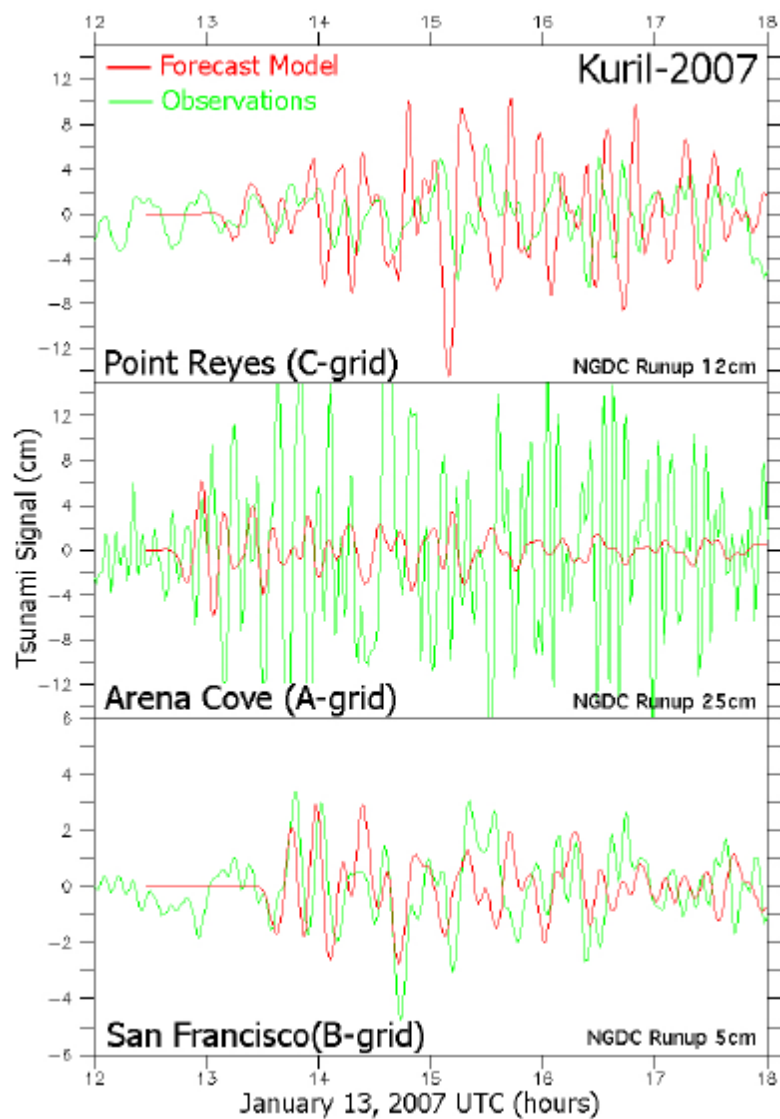
Figure 37. Modeled and observed time series comparison for the normal thrust event off the Kuril Islands on 13 January 2007.
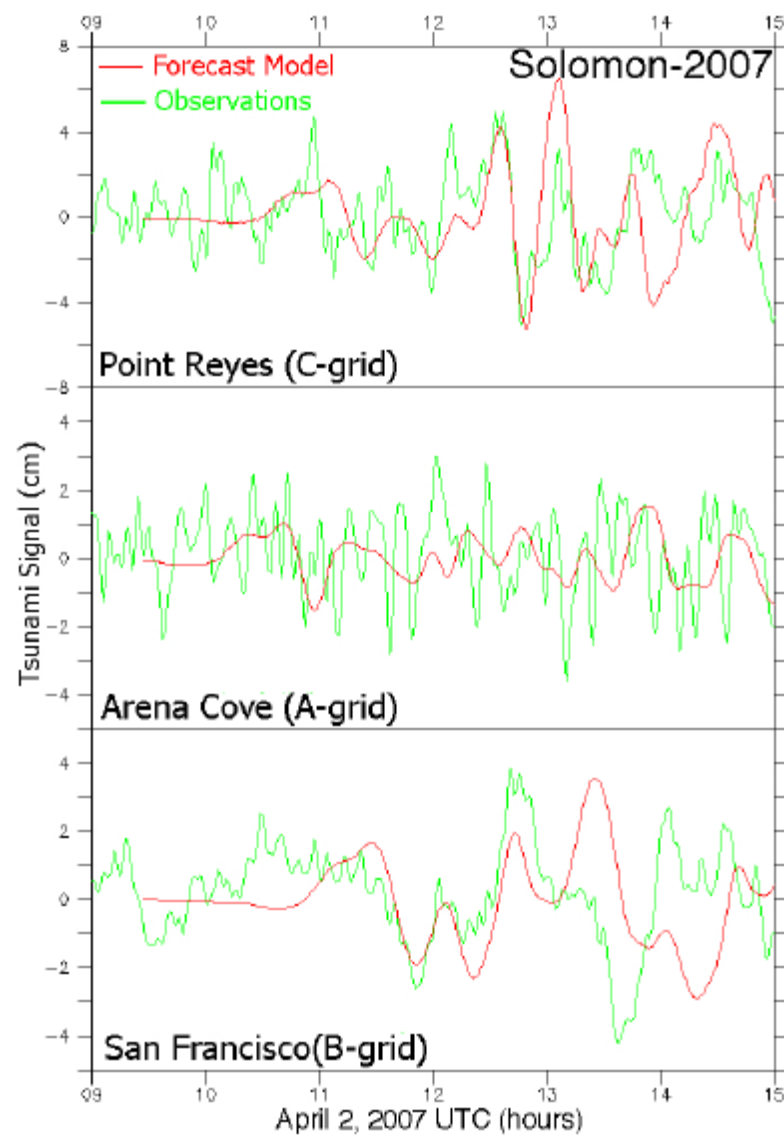
Figure 38. Modeled and observed time series comparison for the Solomon event of 1 April 2007.

83
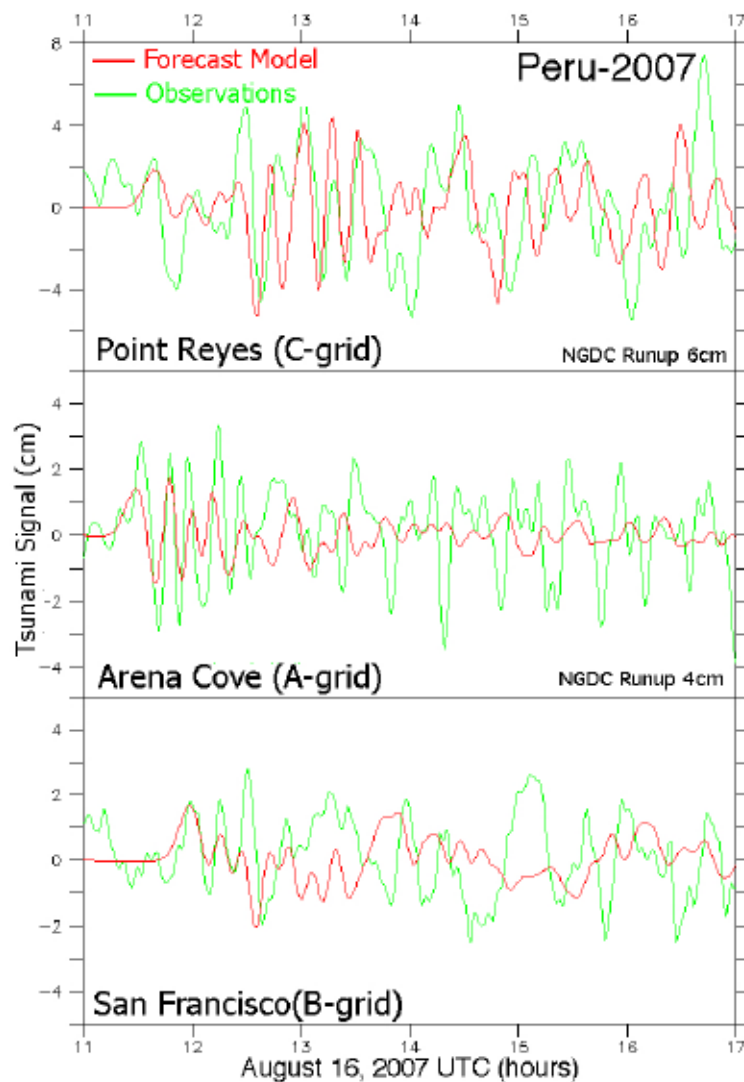
Figure 39. Modeled and observed time series comparison for the Peru event of 15 August 2007.
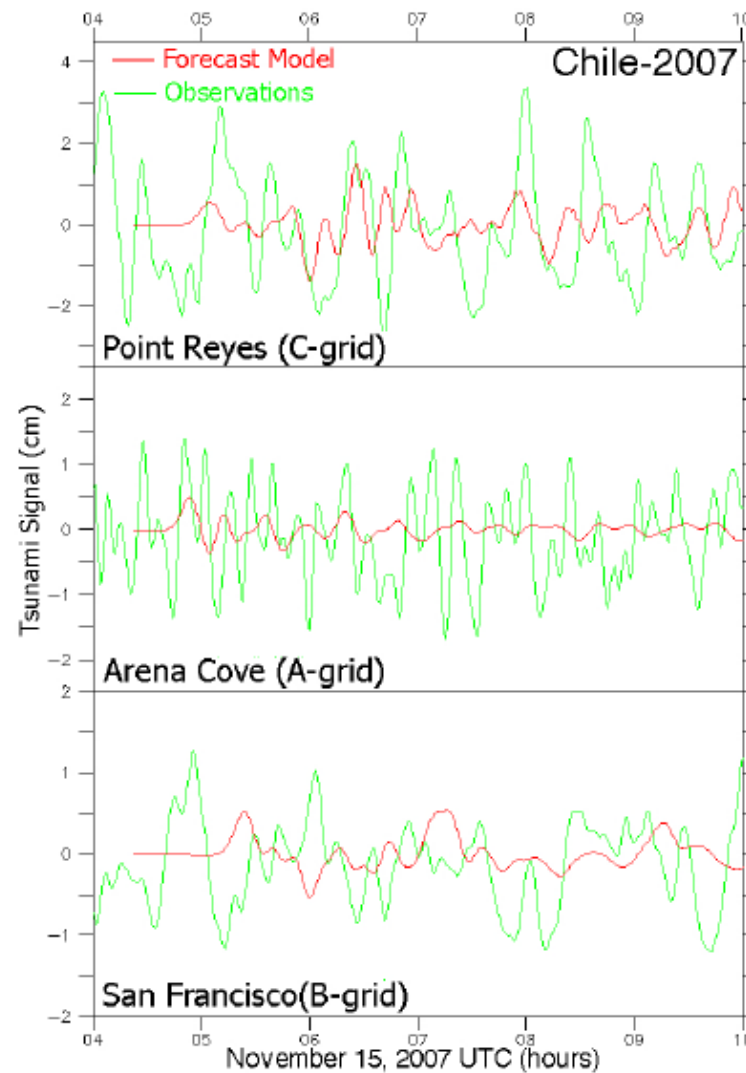
Figure 40. Modeled and observed time series comparison for the Chile event of 14 November 2007.
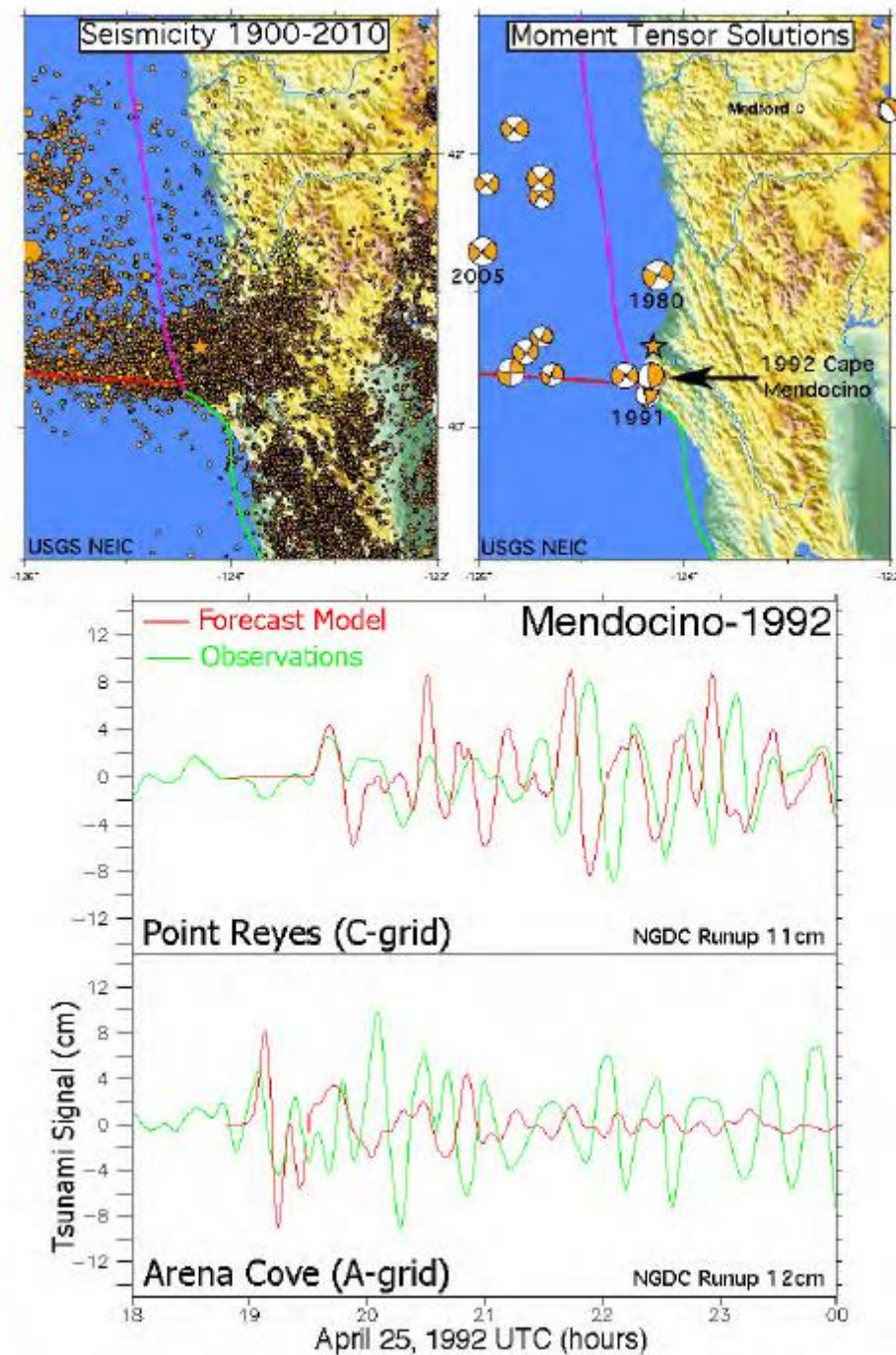
Figure 41. The Cape Mendocino event of 25 April 1992. The upper panels show the frequency of non-thrust events in the vicinity, with only two having a focal mechanism characteristic of subduction. The lower panels show a comparison of the forecast model with observations at Arena Cove and Point Reyes.
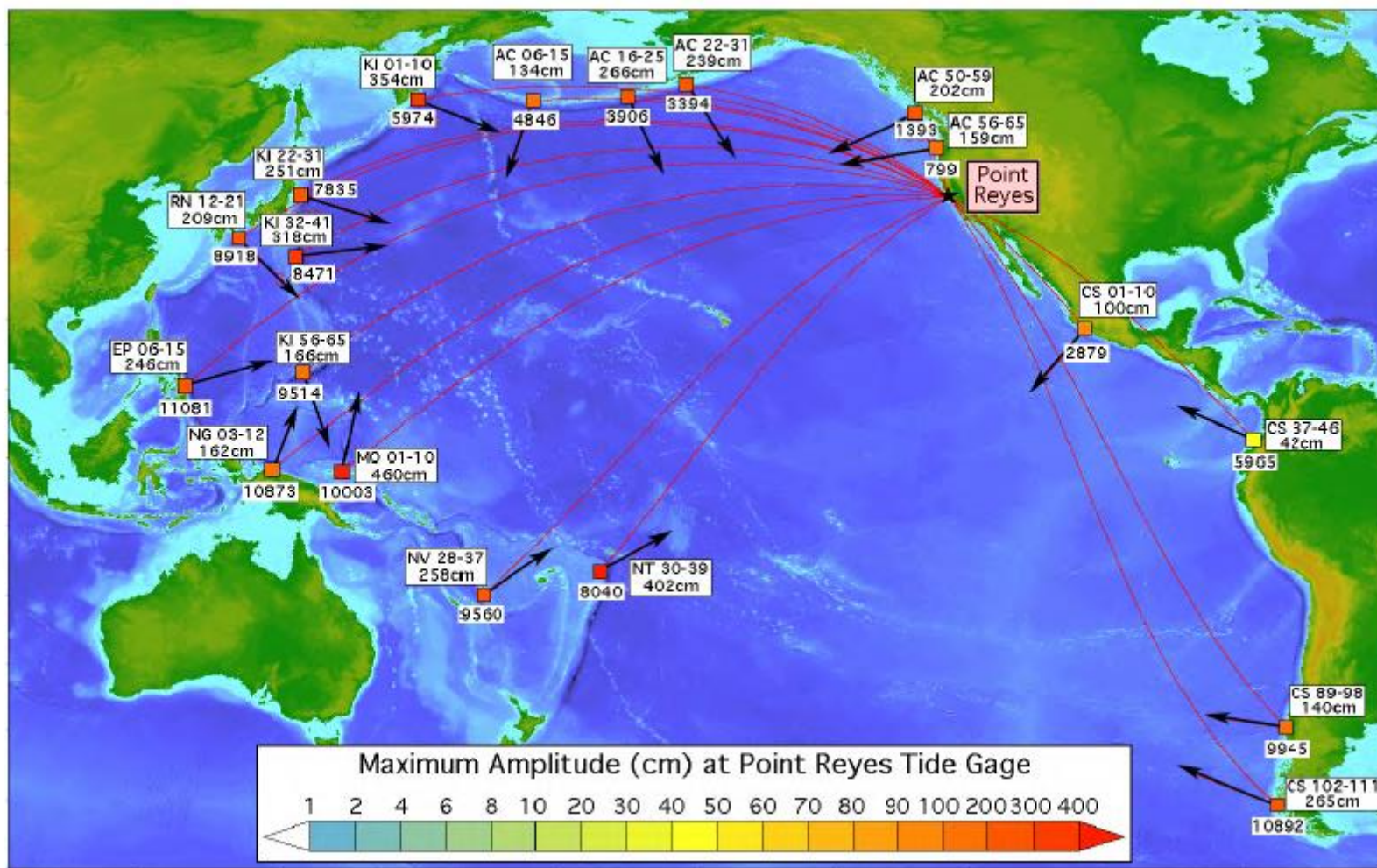
Figure 42. Predicted maximum sea level (from the forecast model) at the Point Reyes tide gauge that might result were "mega-tsunamis" to occur at various locations around the Pacific basin.

Supplement: Synthetic testing of Point Reyes, California

The Point Reyes forecast model was tested with five synthetic scenarios and one historical tsunami event. Test results from the forecast system and comparisons with the results obtained during the forecast model development are shown numerically in **Table S1** and graphically in **Figures S1**–**S6**. The results show that the forecast model is stable and robust, with consistent and high-quality results across geographically distributed tsunami sources and mega-tsunami event magnitudes. The model run time (wall-clock time) was under 18 min for 8 hr of simulation time, and under 8 min for 4.0 hr, thereby satisfying the required time criterion of 10 min run time per 4 hr of simulation time for operational efficiency.

Time series plots for two of the synthetic cases (CSSZ 89–98 and KISZ 22–31) were not present in the main report and their statistics were extracted from the original model output files from the development stage. The modeled scenarios were stable for all cases tested, with no instabilities or ringing. Results show that the largest modeled height was 401.25 cm, originating in the New Zealand-Kermadec- Tonga (NTSZ 30–39) source. Amplitudes greater than 100 cm were recorded for all synthetic test sources. The smallest signal of 119.8 cm was recorded for the far-field Central and South American (CSSZ 89–98) source. Direct comparisons of output from the forecast tool with results of the historical event (Tohoku, previously referred to as 2011 Honshu in this report) and available development synthetic events demonstrated that the wave patterns were similar in shape, pattern, and amplitude.

Table S1. Maximum and minimum amplitudes (cm) at the Point Reyes, California, warning point for synthetic and historical events tested using SIFT 3.2 and obtained during development.

Scenarios	Source Zone	Tsunami Source	a [m]	Maxima (cm)		Minima (cm)	
				SIFT	Development	SIFT	Development
Mega-tsunami Scenarios							
KISZ 1–10	Kamchatka-Kuril-Japan-Izu-Mariana-Yap	A1–10, B1–10	25	354.127	354	-175.953	-219
KISZ 22–31	Kamchatka-Kuril-Japan-Izu-Mariana-Yap	A22–31, B22–31	25	250.248	251	-176.243	-214
ACSZ 56–65	Aleutian-Alaska-Cascadia	A56–65, B56–65	25	157.536	159	-158.122	-156
CSSZ 89–98	Central and South America	A89–98, B89–98	25	119.796	119	-141.905	-142
NTSZ 30–39	New Zealand-Kermadec-Tonga	A30–39, B30–39	25	401.252	402	-177.000	-219
Historical Event							
2011 Tohoku	Kamchatka-Kuril-Japan-Izu-Mariana-Yap	4.66 b24 + 12.23 b25 + 26.31 a26 +21.27 b26 + 22.75 a27 + 4.98 b27		178.215	182	-148.389	-136
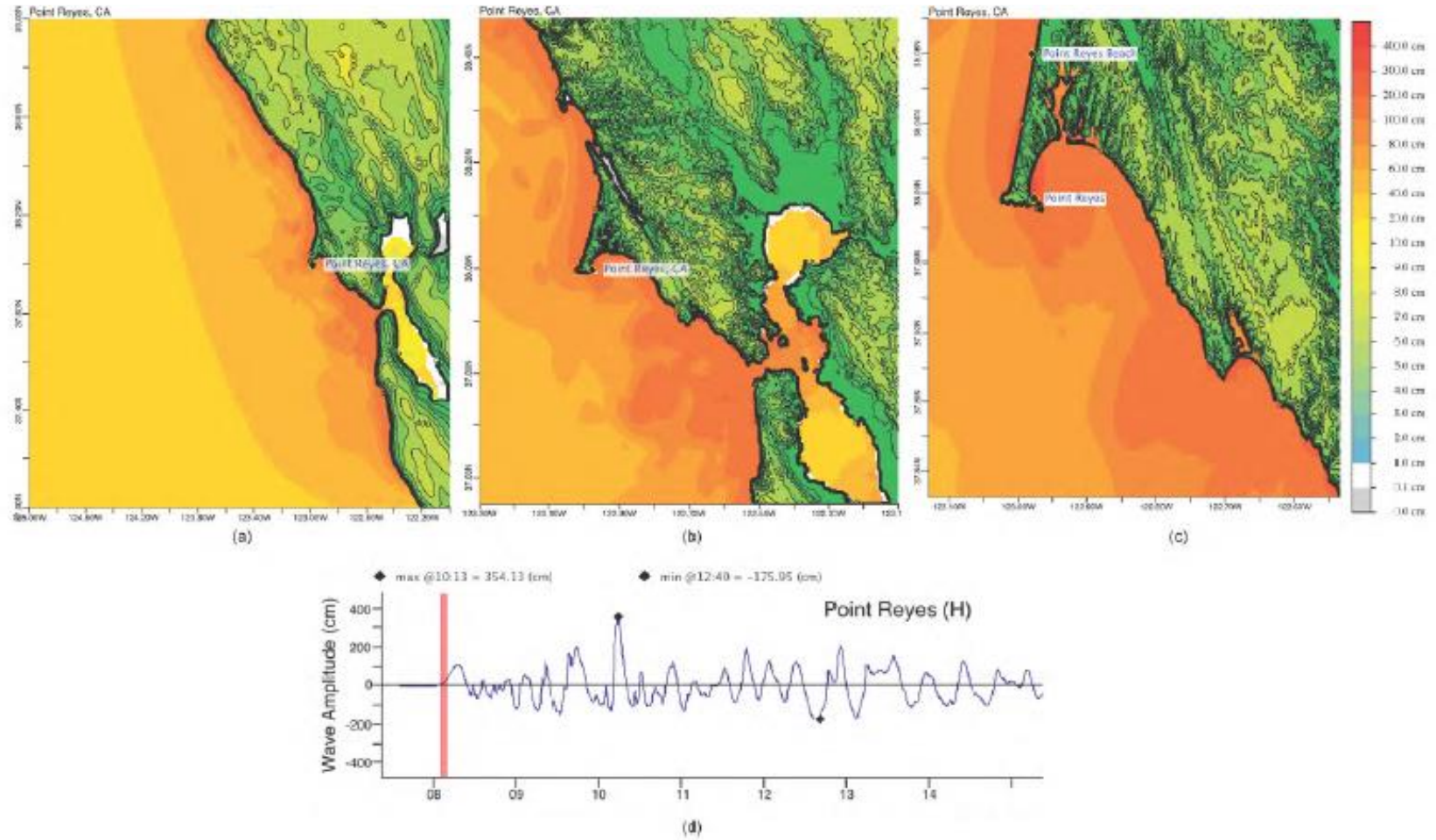
Figure S1. Response of the Point Reyes forecast model to synthetic scenario KISZ 1-10 (α=25). Maximum sea surface elevation for (a) A grid, (b) B grid, and (c) C grid. Sea surface elevation time series at the C-grid warning point (d). The extrema at the reference point are compared with the equivalent values obtained during model development in **Figure 12**.

Figure S2. Response of the Point Reyes forecast model to synthetic scenario KISZ 22-31 (α=25). Maximum sea surface elevation for (a) A grid, (b) B grid, and (c) C grid. Sea surface elevation time series at the C-grid warning point (d). The extrema at the reference point are compared with the equivalent values obtained during model development listed in **Table S1**.

Figure S3. Response of the Point Reyes forecast model to synthetic scenario ACSZ 56–65 (α=25). Maximum sea surface elevation for (a) A grid, (b) B grid, and (c) C grid. Sea surface elevation time series at the C-grid warning point (d). Panels (c) and (d) can be compared with the equivalent results, obtained during model development, displayed in **Figure 11**.

Figure S4. Response of the Point Reyes forecast model to synthetic scenario CSSZ 89–98 (α=25). Maximum sea surface elevation for (a) A grid, (b) B grid, and (c) C grid. Sea surface elevation time series at the C-grid warning point (d). Panels (c) and (d)can be compared with the equivalent results, obtained during model development, listed in **Table S1**.

Figure S5. Response of the Point Reyes forecast model to synthetic scenario NTSZ 30–39 (α=25). Maximum sea surface elevation for (a) A grid, (b) B grid, (c) C grid. Sea surface elevation time series at the C-grid warning point (d). Panels (c) and (d) can be compared with the equivalent results, obtained during model development, displayed in **Figure 13**.

Figure S6. Response of the Poiint Reyes forecast model to the 11 March 2011 Tohoku (Honshu) tsunami. Maximum sea surface elevation for (a) A-grid, (b) B-grid, and (c) C-grid. Sea surface elevation time series at the C-grid warning point (d). Panels (c) and (d) can be compared with the equivalent results, obtained during model development, displayed in **Figures 17(a)** and **16**, respectively.

5. PMEL Tsunami Forecast Report for San Francisco, California

Burak Uslu
Diego Arcas
Vasily V. Titov
Angie J. Venturato

Table of Contents

LIST OF FIGURES

LIST OF TABLES

5. San Francisco, California

San Francisco, California, is located along the west coast of North America at approximately 37.8∘N latitude and 122.5∘W longitude, as shown in **Figure 1**. The San Francisco metropolitan area has a population of 7,039,362, ranking it fifth largest metropolis in the country (Census, 2000). Together with San Pablo Bay, the Bay area encompasses approximately 4,100 square km of water (Borrero *et al*., 2006), lending itself to shipping operations. The San Francisco Bay is home to one of the United States' most economically important and major west coast ports. According to the Pacific Merchant Shipping Association (PMSA, 2003), the Port of San Francisco, along with the ports of Los Angeles harbor and Long Beach, California, together offload 95% of Asian imports. The high volumes of goods that pass through these ports ensure stable employment that contributes to the California economy. California port activity supports more than 500,000 jobs, generating up to $30.5 billion in income (Uslu, 2008). An aerial view of the Port of San Francisco, with the city skyline in the distance, is shown in **Figure 2**. The San Francisco Bay area is internationally important in terms of commerce and tourism and is one of the most densely populated communities in the United States, second only to New York City. In addition, the region is important to the economic health of the entire State of California. In addition to San Francisco, numerous populous California communities, including Oakland, Alameda, Hayward, and Redwood City, call the shores of the bay home.

The region is seismically active with numerous faults bisecting the landscape. To the west, the northern segment of the San Andreas strike-slip fault system runs parallel to San Francisco Bay. To the east, the bay is flanked by the Hayward Fault that continues north-northwest bisecting the city of Oakland. These two fault systems effectively bracket the entire Bay area between them. At the northernmost extent of the Hayward Fault lies the San Pablo Bay, a depression formed from the step-over between Rodgers Creek and the Hayward Fault. San Francisco Bay itself is separated from the open Pacific Ocean by a narrow channel at Golden Gate. Below the Golden Gate Bridge, the channel depth reaches up to 113 m. The average depth through San Francisco Bay, however, is on the order of 4.2 m. The overall shallow bathymetry that dominates the area is a factor in the wave dynamics and has been discussed in Magoon (1966) and Ritter and Dupre (1972). Borrero *et al*. (2006) and Uslu (2008) have studied the dynamics of the bay in relation to average depth.

The objective of the present work~~, then,~~ is to develop an operational forecast model for San Francisco, California, for the purpose of minimizing false alarms that disrupt port activities and to provide the region with accurate and timely information necessary to make decisions in the event of tsunami generation. This report details the development of a tsunami forecast model for San Francisco, California. Development includes construction of a digital elevation model based on available bathymetric and topographic data, model validation with historic events, and sensitivity testing of the models with a suite of mega tsunami events the origin of which were from representative subduction zones rimming the Pacific Ocean.

5.1. Model Development

Modeling of coastal communities is accomplished by development of a set of three nested grids that telescope down from a large spatial extent to a grid that finely defines the ~~localized~~ community. The basis for these grids is a high resolution digital elevation model constructed by NCTR or, more commonly, by the National Geophysical Data Center using best available bathymetric, topographic, and coastal shoreline data for an at-risk community. For each community, data are compiled from a variety of sources to produce a digital elevation model referenced to Mean High Water in the vertical and to the World Geodetic System 1984 in the horizontal (http://ngdc.noaa.gov/mgg/inundation/ tsunami/inundation.html). From these digital elevation models, a set of three high-resolution, "reference" models are constructed which are then "optimized" to run in an operationally specified period of time.

5.1.1. Historical events and data

The San Francisco tide gauge station is the oldest continuously operating tide gauge station in the United States and has provided the longest record of tides at one location in the western hemisphere. Originally installed at Fort Point in 1854, the gauge was relocated to Sausalito in 1877 when the Fort Point pier came into disrepair. Great care was taken to level the gauge and match bench marking so that the integrity of the record would be maintained. The gauge was again moved to a temporary location when the Sausalito pier, too, came into disrepair. In 1897, 20 years after the Sausalito move, the San Francisco tide gauge was relocated to the Presidio on the southeast side of Golden Gate. The tide gauge has resided at this Presidio location ever since (Borrero *et al.*, 2006; Bromirski *et al.*, 2002).

The San Francisco tide gauge has recorded numerous tsunamis throughout its history of operation. Soon after initial installation in 1854, the gauge recorded a series of tsunami waves generated by an earthquake that occurred off of Japan. The 1964 Alaska tsunami had the greatest impact on the United States west coast; responsible for 11 fatalities and damage exceeding $17 million in the State of California alone (Lander *et al.*, 1993). In the San Francisco Bay region and the communities of Sausalito, San Rafael, and Berkeley, the 1964 tsunami caused approximately $1 million in damage.

5.1.2. Model setup

High-resolution 1-sec digital elevation models constructed by the NOAA Center for Tsunami Research were used to develop a high-resolution reference inundation model for San Francisco. The reference model consists of three nested grids; Grid A covering Monterey to Sonoma County with 30-sec resolution. Grid B covering the greater San Francisco Bay Area with 6-sec resolution, and Grid C covering the city of San Francisco with 1-sec resolution. From this high resolution reference model, an optimized tsunami forecast model was developed as discussed by Tang *et al.* (2009). The forecast model A and B grid extents retain the same resolution as those of the reference model, but to increase model run time while retaining accuracy requirements, the C Grid extents were lowered to 4 arc sec in the forecast model. **Table 1** provides specific details for both reference and forecast model grids, including extents. Reference and forecast model extents are graphically presented in **Figure 3**.

Table 1. MOST setup parameters for reference and forecast models for San Francisco Bay.

Grid	Region	Reference Model				Forecast Model			
		Coverage Lat. [°N] Lon. [°W]	Cell Size ["]	nx × ny	Time Step [sec]	Coverage Lat. [°N] Lon. [°W]	Cell Size ["]	nx × ny	Time Step [sec]
A	Monterey to Sonoma Counties	38.9992–36.0075 124–121.0083	30 × 30	360 × 360	3.5	38.4992–36.4992 123.4917–121.9917	30 × 30	181 × 241	3.6
B	San Francisco Bay	38.3331–37.3347 122.5833–121.4183	6 × 6	700 × 600	3.5	37.9497–37.4997 122.5833–122.20	6 × 6	231 × 271	3.6
C	San Francisco City	37.85–37.58 122.55–122.35	1 × 1	723 × 973	0.7	37.85–37.6494 122.54–122.35	4 × 2	172 × 362	1.8
Minimum offshore depth [m]				5				5	
Water depth for dry land [m]				0.1				0.1	
Friction coefficient (n^2)				0.0009				0.0009	
CPU time for a 4-hr simulation				2.77 hr				11 min	

Computations were performed on a single Intel Xeon processor at 3.6 GHz, Dell PowerEdge 1850.

The San Francisco tsunami forecast model was optimized in computation time for use in hazard assessment and real-time tsunami forecasting during an event. Relative computation times for both the reference and forecast model are provided in **Table 1**. CPU time for a 4-hr model simulation is cut significantly when the forecast model is run. For the same 4-hr model simulation, the reference model requires 2.77 hr of CPU time while the tsunami forecast model runs in 11 min. Validation of this forecast model was accomplished by testing model grids against historical sources and by comparing results with those of the companion San Francisco reference model. **Table 2** lists the MOST model input files used for the reference and forecast models. Quality records during the 11 historical events listed in **Table 3** and shown in **Figure 4** provide the basis for validation of the San Francisco tsunami forecast model. Synthetic scenarios were developed and used for stability testing and to model likely worst-case scenarios at the San Francisco Presidio tide gauge. Specific information about each synthetic scenario, including subduction zone and tsunami source referenced to the NOAA propagation database unit sources provided in Appendix B, is provided in **Table 4**. A plot showing the location of each synthetic scenario modeled is provided in **Figure 5** to visually show the coverage represented by these scenarios.

5.2. Results and Discussions

The San Francisco reference and tsunami forecast models were each validated by modeling the 11 historical events listed in **Table 3** and shown in **Figure 2**. Model results were compared with observations recorded by the Presidio tide gauge during the historical events for which data were recorded and available. Specifically, the tsunamis generated during the 1946 Unimak, 2001 Peru, 2006 Kuril, and 2007 Kuril Islands events were each recorded and compared to both reference and forecast model run results. A discussion of results and comparisons follows in the results of tested events section of this chapter.

Table 2. MOST model input files for San Francisco Bay.

Parameters	Reference model	Forecast model
Minimum amplitude of input offshore wave (m)	0.001	0.0001
Input minimum depth for offshore (m)	5	1
Input "dry land" depth for inundation (m)	0.1	0.1
Input friction coefficient (n^2)	0.0009	0.0009
A and B grid runup flag (0 = disallow, 1 = allow)	1	1
Blow-up limit/max eta before blow-up (m)	100.0	300.0
Input time step (sec)	0.7	1.8
Input number of steps	61715	16000
Compute "A" arrays every nth time step, n=	5	2
Compute "B" arrays every nth time step, n=	5	2
Input number of steps between snapshots	150	18
…Starting from	0	0
…Saving grid every nth node n=	1	1

5.2.1. Model stability and reliability

Artificial ringing and a high level of background noise obscuring a tsunami signal could be an issue with tsunami modeling in the San Francisco Bay area. For this reason, the model was tested with 11 historical event scenarios and 18 simulated tsunami scenarios. The scenarios were chosen from various subduction zones with a likelihood of probable tsunami generation. By running the model for an extended duration with historical tsunami events, low-level background noise and ringing in the harbor are smoothed. In addition to testing with historical events, testing was performed with simulated mega tsunamis again from various sources as a test of forecast model stability. No problems or instabilities were noted after reference model scenario tests up to 12 hr and optimized forecast model tests up to 24 hr were performed.

5.2.2. Results of tested events

San Francisco reference and forecast model results are compared with observations recorded during the 1946 Unimak, 2001 Peru, 2006 Kuril, and 2007 Kuril Islands tsunamis. The 1946 Unimak tsunami signal is compared to the computed reference and forecast model siñgnals in **Figure 6**. There is good agreement between the two models, giving confidence in the performance of the forecast model. Differences noted between the two model results in later wave amplitudes point to the non-linearity of the wave processes. Comparisons with observations show a general trend toward overestimation of wave amplitude by the models as well as a lag in model arrival time. **Figures 7 and 8** show the computed maximum wave height simulated at the Presidio tide gauge from the respective reference and forecast models. Wave amplitudes as high as 40 cm are predicted in these results. The results of a simulated tsunami from an Mw 9.3 event from Japan (synthetic case KISZ 22–31) are shown in **Figure 9**. A 2- m maximum wave height at Ocean Beach and a wave height greater than 1 m at the Presidio are predicted if this scenario were to occur. Comparisons of time series results from the reference and forecast models run to simulate historical events are shown in **Figures 10–19**. In all plots, forecast model results correlate well with those of the reference model in both amplitude and phase. Model results for the 2001 Peru

Table 3. Historical events used for San Francisco, California.

Event	Earthquake Date Time (UTC)	Lat. (°)	Lon. (°)	Subduction Zone	Seismic Moment Magnitude (Mw)	Tsunami Magnitude[1]	Model Tsunami Source
1946 Unimak	1946-04-01 12:28:56	53.32N	163.19W	Aleutian-Alaska-Cascadia (ACSZ)	[2]8.5	8.5	7.5 × b23 + 19.7 × b24 + 3.7 × b25
1994 East Kuril	1994-10-04 13:23:28.5	43.60N	147.63E	Kamchatka-Kuril-Japan-Izu-Mariana-Yap (KISZ)	[3]8.3	8.1	9.0 × a20
1996 Andreanov	1996-06-10 04:04:03.4	51.10N	177.410W	Aleutian-Alaska-Cascadia (ACSZ)	[3]7.9	7.8	2.40 × a15 + 0.80 × b16
2001 Peru	2001-06-23 20:34:23.3	17.28S	72.71W	South America (SASZ)	[3]8.4	8.2	5.70 × a15 + 2.90 × b16 + 1.98 × a16
2003 Rat Island	2003-11-17 06:43:31.0	51.14N	177.86E	Aleutian-Alaska-Cascadia (ACSZ)	[3]7.7	7.8	2.81 × b11
2006 Tonga	2006-05-03 15:27:03.7	20.39S	173.47W	New Zealand-Kermadec-Tonga (NTSZ)	[3]8.0	8.0	6.6 × b29
2006 Kuril	2006-11-15 11:15:08.0	46.71N	154.33E	Kamchatka-Kuril-Japan-Izu-Mariana-Yap (KISZ)	[3]8.3	8.1	4.0 × a12 + 0.5 × b12 + 2.0 × a13 + 1.5 × b13
2007 Kuril	2007-01-13 04:23:48.1	46.17N	154.80E	Kamchatka-Kuril-Japan-Izu-Mariana-Yap (KISZ)	[3]8.1	7.9	−3.64 × b13
2007 Solomon	2007-04-01 20:40:38.9	7.79S	156.34E	New Britain-Solomons-Vanuatu (NVSZ)	8.1	8.2	12.0 × b10
2007 Peru	2007-08-15 23:41:57.9	13.73S	77.04W	South America (SASZ)	[3]8.0	8.1	4.1 × a9 + 4.32 × b9
2007 Chile	2007-11-14 15:41:11.2	22.64S	70.62W	South America (SASZ)	[3]7.7	7.6	0.81 × a22 + 0.3 × a23 + 0.11 × b23

[1]Equivalent tsunami source moment magnitude from model source constrained by tsunami observations.
[2]López and Okal (2006)
[3]Centroid Moment Tensor

Table 4. Synthetic tsunami sources recorded at the Presidio tide station for San Francisco Bay (from Tang et al., 2009).

Scenario Name	Subduction Zone	Tsunami Source
KISZ 22–31	Kamchatka-Yap-Mariana-Izu-Bonin	A22–A31, B22–B3
KISZ 1–10	Kamchatka-Yap-Mariana-Izu-Bonin1	A1–A10, B1–B10
ACSZ 12–21	Aleutian-Alaska-Cascadia	A12–A21, B12–B31
ACSZ 22–31	Aleutian-Alaska-Cascadia	A22–A31, B22–B31
ACSZ 38–47	Aleutian-Alaska-Cascadia	A38–A47, B38–B47
ACSZ 56–65	Aleutian-Alaska-Cascadia	A56–A65, B56–B65a
CASZ 1–10	Central American	A1–A10, B1–B10
ECSZ 1–10	Columbia-Ecuador	A1–A10, B1–B10
SASZ 40–49	South America	A40–A49, B40–B49
SCSZ 3–12	South Chile	A3–A12, B3–B12
NTSZ 20–29	New Zealand-Kermadec-Tonga	A20–A29, B20–B29
NTSZ 30–39	New Zealand-Kermadec-Tonga	A30–A39, B30–B39
NVSZ 28–37	New Britain-Solomons-Vanuatu	A28–A37, B28–B37
MOSZ 1–10	Manus OCB	A1–A10, B1–B10
NGSZ 3–12	North New Guinea	A3–A12, B3–B12
EPSZ 6–15	East Philippines	A6–A15, B6–B15
NRSZ 12–21	Ryukus-Kyushu-Nankai	A12–A21, B12–B21
KISZ 32–41	Kamchatka-Yap-Mariana-Izu-Bonin	A32–A41, B32–B41

event define wave characteristics in the observed time series, with a high noise-to-signal ratio coupled with low observed wave amplitudes as shown in **Figure 12**. Comparisons for the 2006 Kuril Islands event in **Figure 15** shows the predicted tsunami arrival time leading observations. In this case, both reference and forecast models underestimate the amplitudes observed at the Presidio tide gauge. During the 2007 Kuril Islands event, forecast model results reproduce observations in both amplitude and phase, as shown in **Figure 16**. **Figures 20–22** show plots of the maximum wave height computed with the reference model for the historical events tested and **Figures 23–25** show plots of maximum wave height computed with the forecast model for the same historical events.

5.2.3. Sensitivity study

A sensitivity study for the San Francisco Bay area was conducted with the 18 scenarios listed in **Table 4** to determine the variation of tsunami impact due to generation of a tsunami during a large magnitude earthquake in source regions around the Pacific. For all scenario runs, earthquake magnitude was kept constant, while source regions were varied across all potential tsunamagenic subduction zones. Each scenario was modeled to determine the maximum wave heights expected at the Presidio tide gauge. This study uses the NOAA propagation database to model a tsunami triggered by an Mw 9.3 earthquake having a rupture length of 20 source units, for a total area of

1000 km × 100 km, and a 30-m slip. Thirty-six events from the Aleutian-Alaska-Cascadia Subduction Zone, 26 from the Kuril-Kamchatka Subduction Zone and Japan Trench, 27 from Central American sources, and 40 from South American sources are considered (Gica *et al.*, 2008).

Sensitivity study results show that the San Francisco Bay area is at greatest risk from a tsunami generated in the eastern portion of the Aleutian-Alaska-Cascadia Subduction Zone. A maximum wave of 7.6 m is predicted for a tsunami generated in Aleutian-Alaska-Cascadia segments 29–38, as shown in **Figure 26**. Tsunami waves from the northern portion of the Kuril and Japan subduction zones and those generated along the southern portion of Chile pose a significant risk to the San Francisco area with waves greater than 1 m predicted. The maximum wave heights computed for each of the 18 synthetic scenarios run as part of the sensitivity study are plotted in **Figure 27–31**.

5.3.   Summary and Conclusions

A set of reference inundation models and optimized forecast models have been prepared for San Francisco Bay, California. Both reference inundation and high-resolution forecast models for San Francisco Bay have robustly modeled the historical scenarios. The computational speed of the forecast models is 16 times faster than that of reference models while retaining accurate wave height estimation at the Presidio tide gauge. The forecast model has been tested extensively by performing a sensitivity study and incorporation of hypothetical scenarios. The San Francisco forecast model has been developed for the purpose of real-time tsunami prediction, to forecast a tsunami generated in far field subduction zones in real time. However, the results are also very beneficial in tsunami hazard assessment. As demonstrated in the sensitivity study, a forecast model can be used to verify the effective source region and worst-case scenarios.

The 1964 Alaska earthquake triggered the largest tsunami that the west coast of the United States has ever recorded since installation of instrumentation to make observations. This study suggests that subduction zones along the Eastern Aleutians and Alaska are the most effective tsunami generating source regions for the San Francisco Bay area and that the hazard posed to this community is significant. A large magnitude earthquake occurring in these identified source regions of Alaska coupled with a favorable orientation could potentially have a greater impact on the Bay area than the tsunami generated after the 1964 Alaska earthquake. Tsunami hazard assessment is not only necessary for protecting the lives of people who live in low-lying coastal regions, but also in identifying the potential impact a tsunami would have on ports and harbors. The optimized forecast model developed for San Francisco, California, provides a 4-hr forecast of first-wave arrival, amplitudes, and inundation tide gauge warning point within 10 min, based on testing with available historical data and simulated events as presented in this report.

Acknowledgments

FIGURES

Figure 1. Topographic map of the San Francisco Bay area with San Francisco and other major population centers shown.

Figure 2. An aerial view of the Port of San Francisco, with the city skyline in the distance.
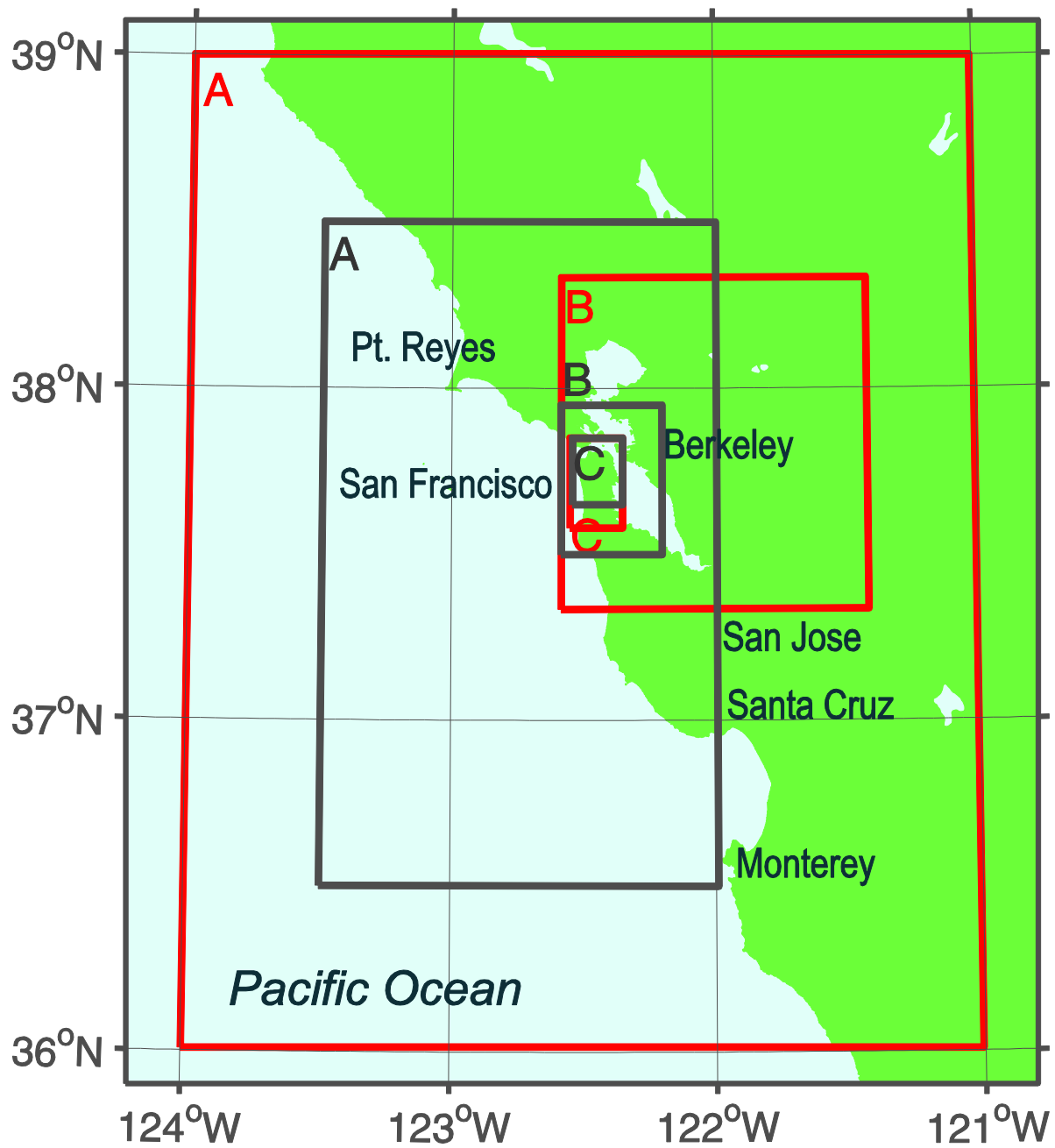
Figure 3. Extents of the reference inundation (red) and optimized forecast (gray) model grids.
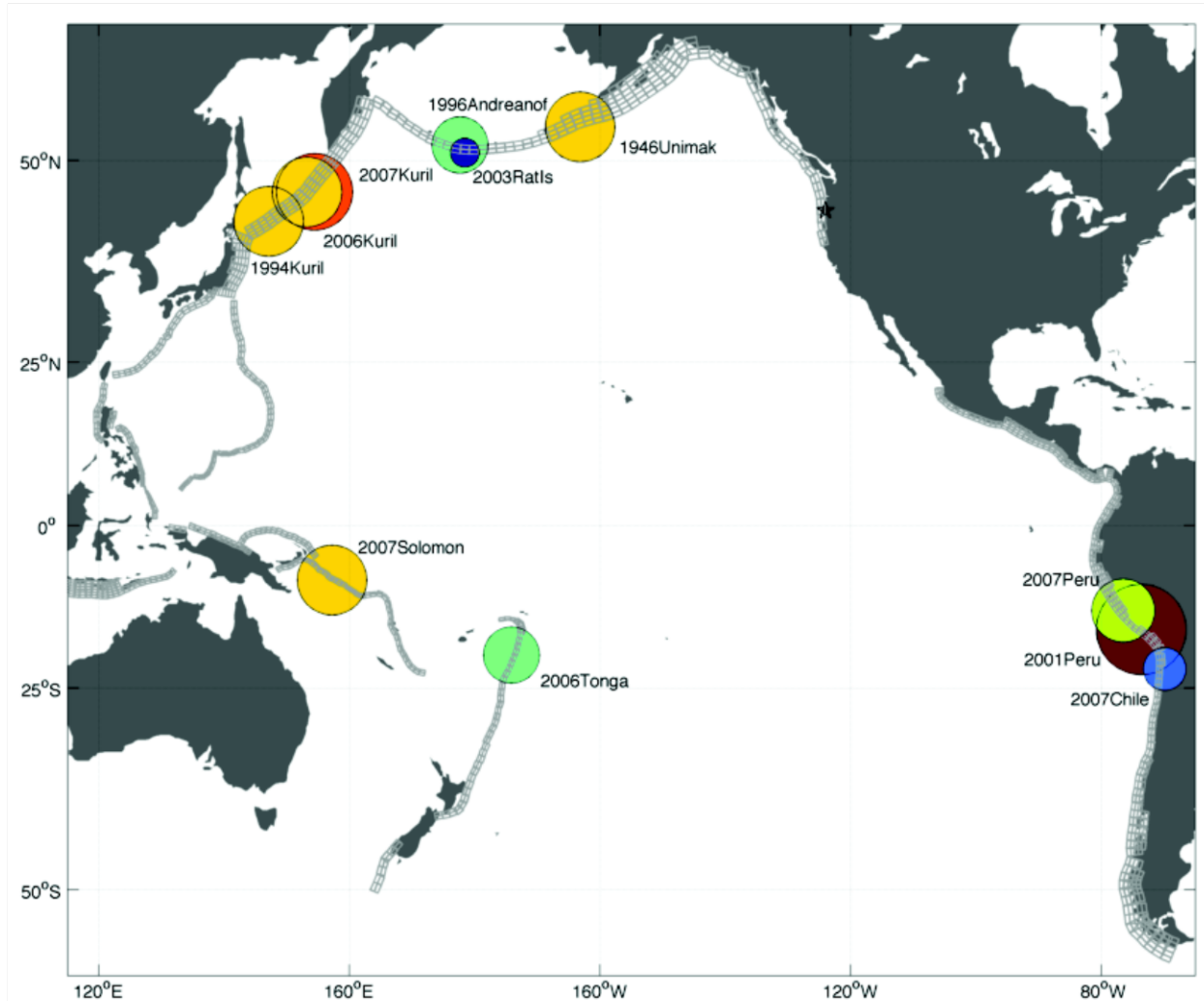
Figure 4. Map of the Pacific Ocean Basin showing the location of the 11 historical events used to test and validate the San Francisco model. Relative earthquake magnitude is shown by the varying sizes and colors of the filled circles. The largest magnitude earthquake used in model validation was the 1946 Unimak Mw 8.5 earthquake, denoted by the red circle.
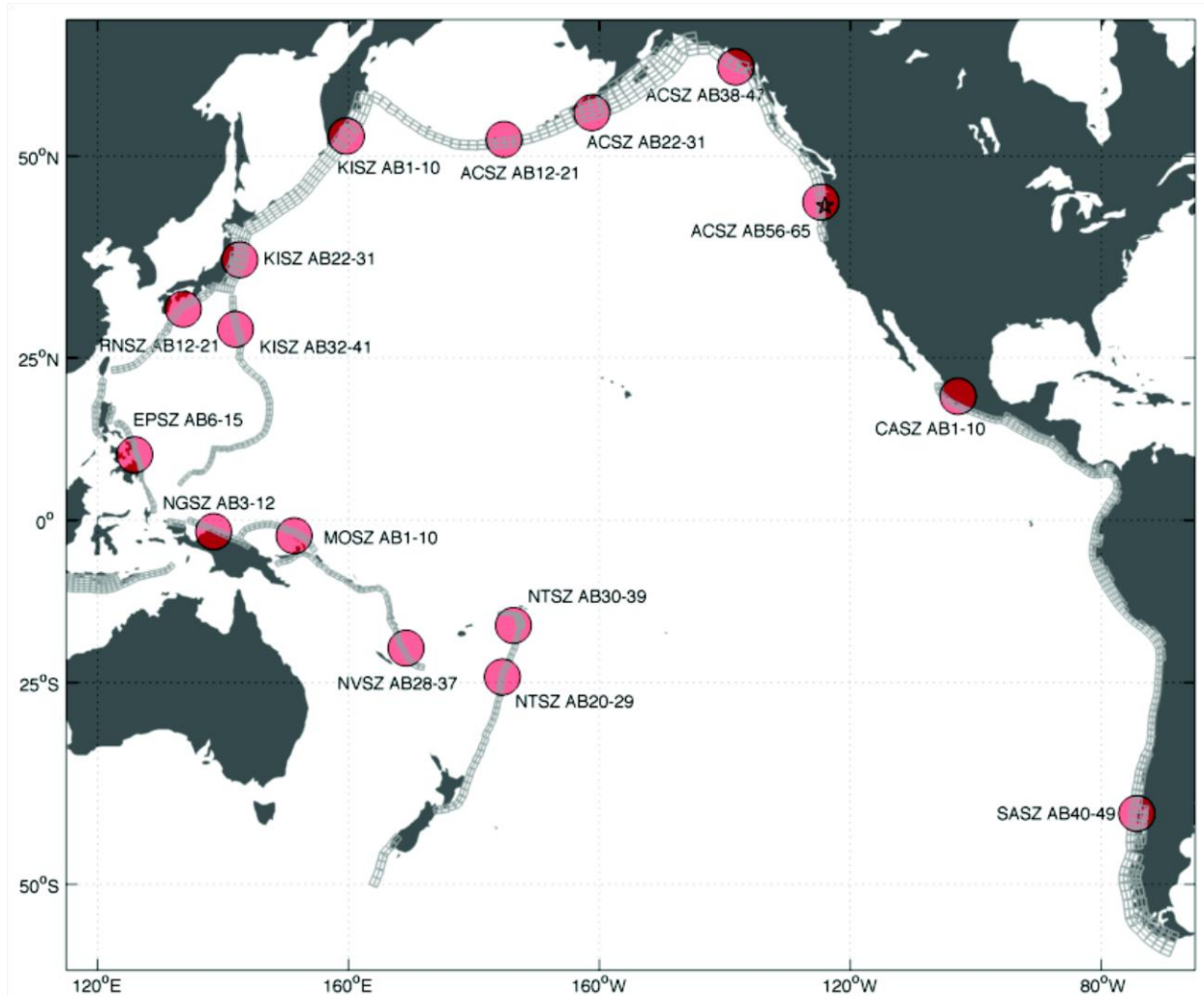
Figure 5. Map of the Pacific Ocean Basin showing the synthetic Mw 9.3 scenarios used to test the San Francisco model. Red circles mark the location of each source relative to one another and to San Francisco, denoted by the solid star. Specific unit source combinations are provided alongside each red circle.
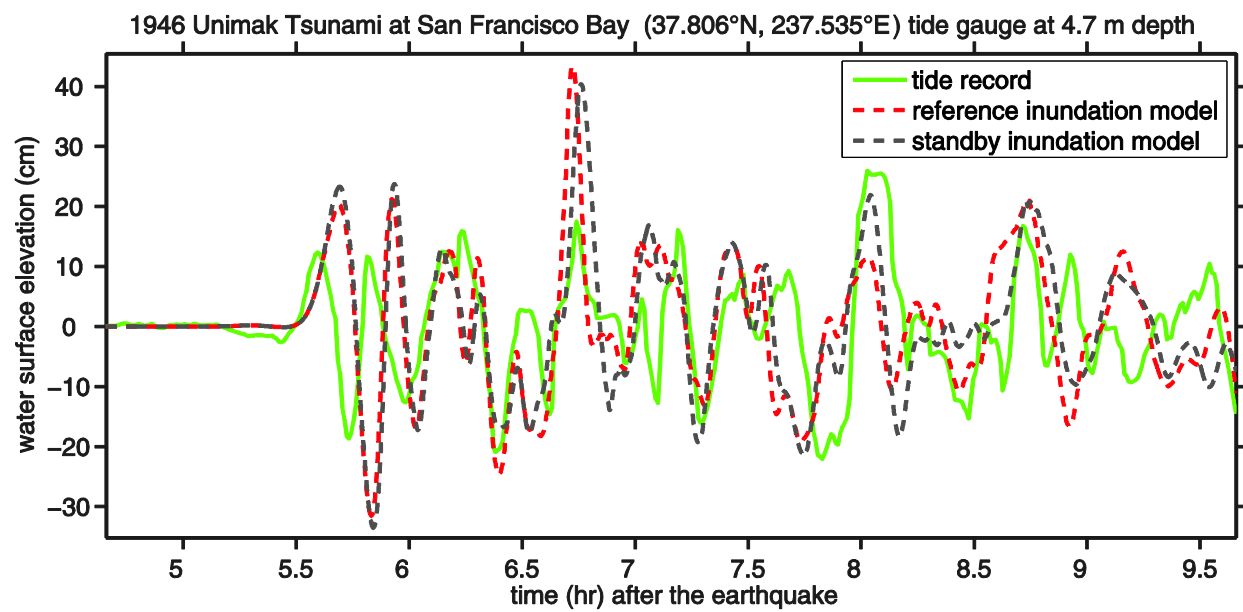
Figure 6. Comparison at the Presidio tide gauge of the modeled and observed tsunami generated during the 1946 Unimak earthquake. The observed tidal record (green) is shown with the reference inundation (red) and optimized forecast (black) model results superimposed.
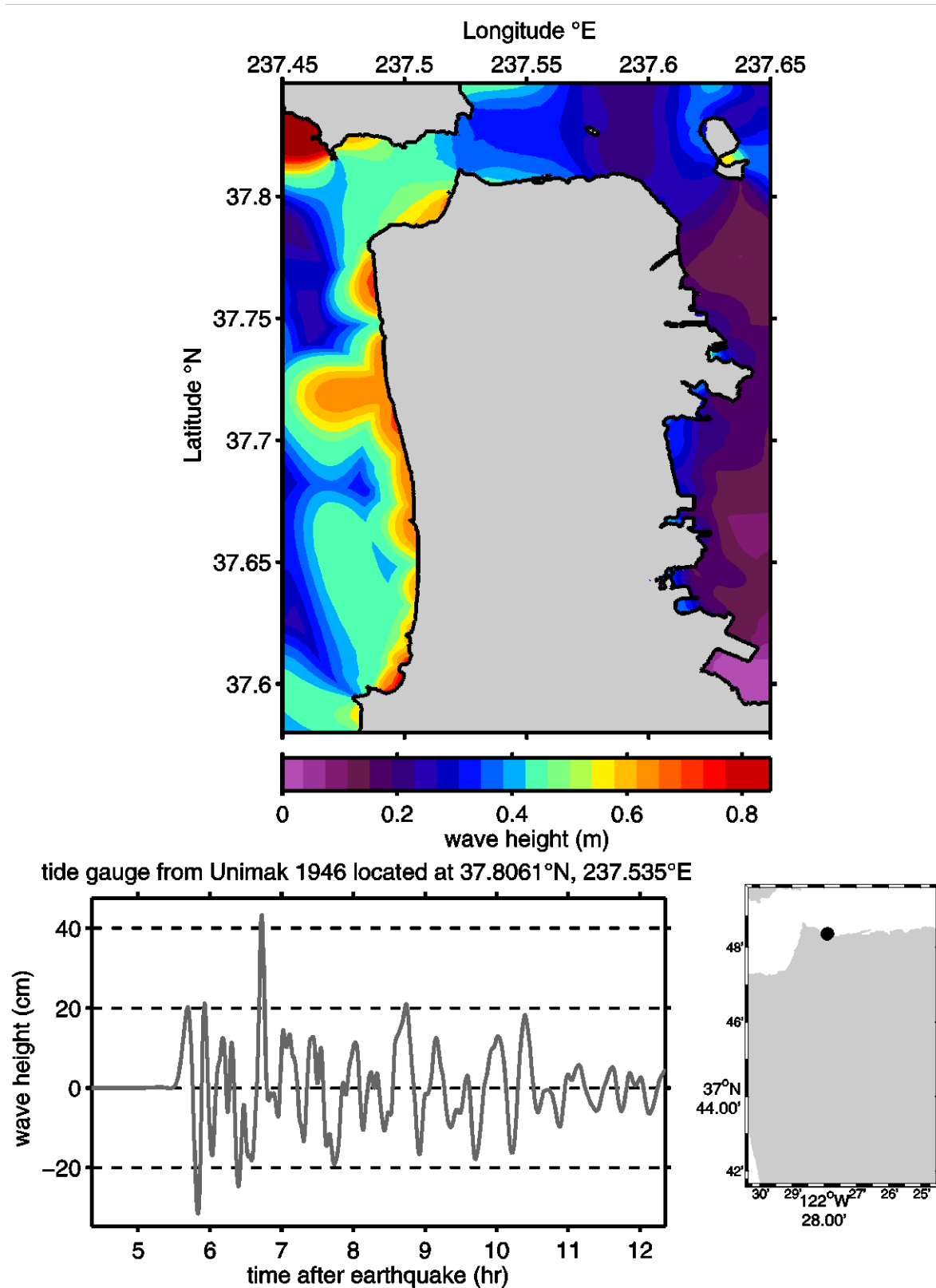
Figure 7. The maximum wave height and tide gauge simulation of the 1946 tsunami at the San Francisco reference model grid.
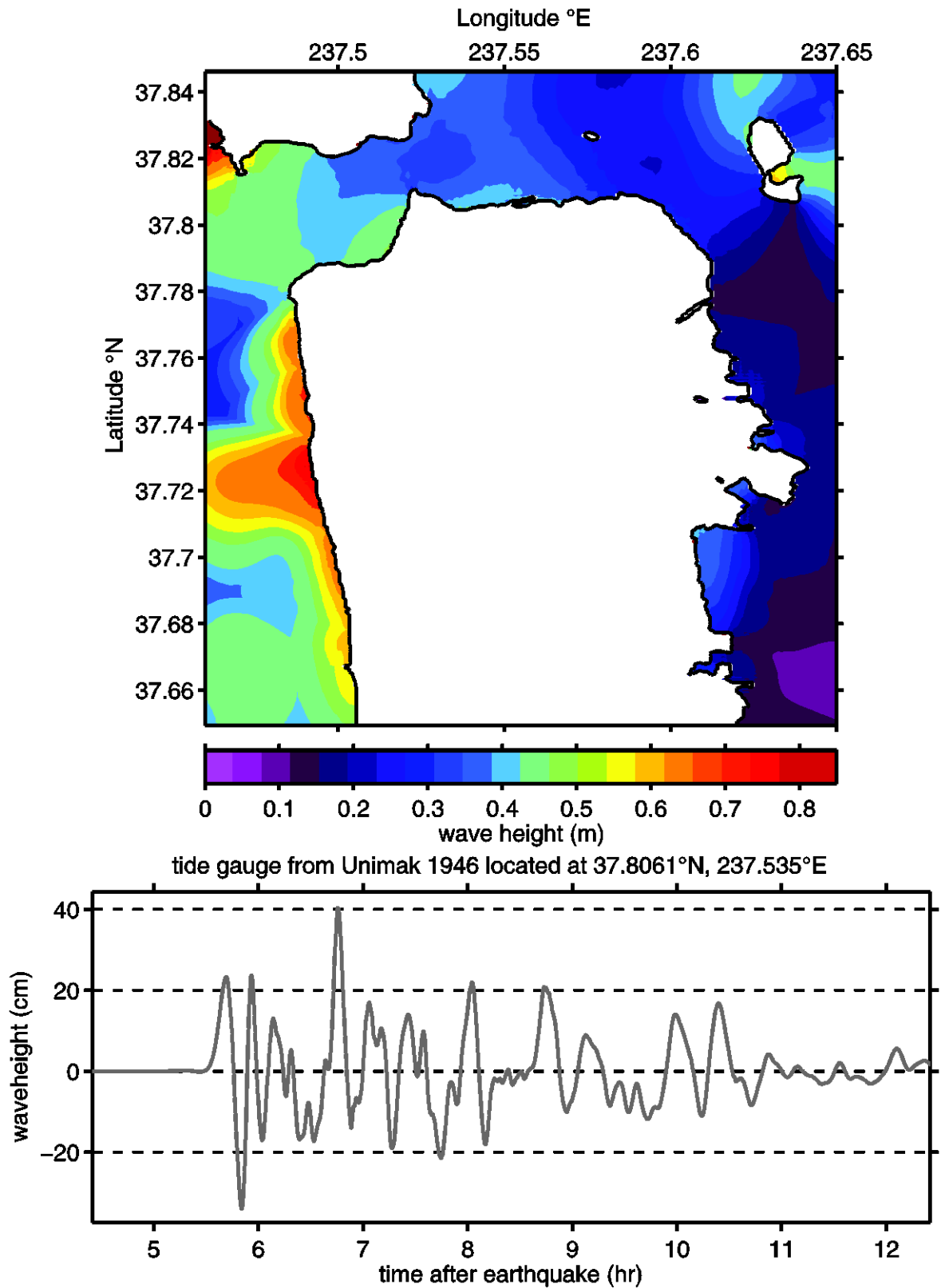
Figure 8. The maximum wave height and tide gauge simulation of the 1946 Unimak tsunami at the San Francisco forecast model grid.
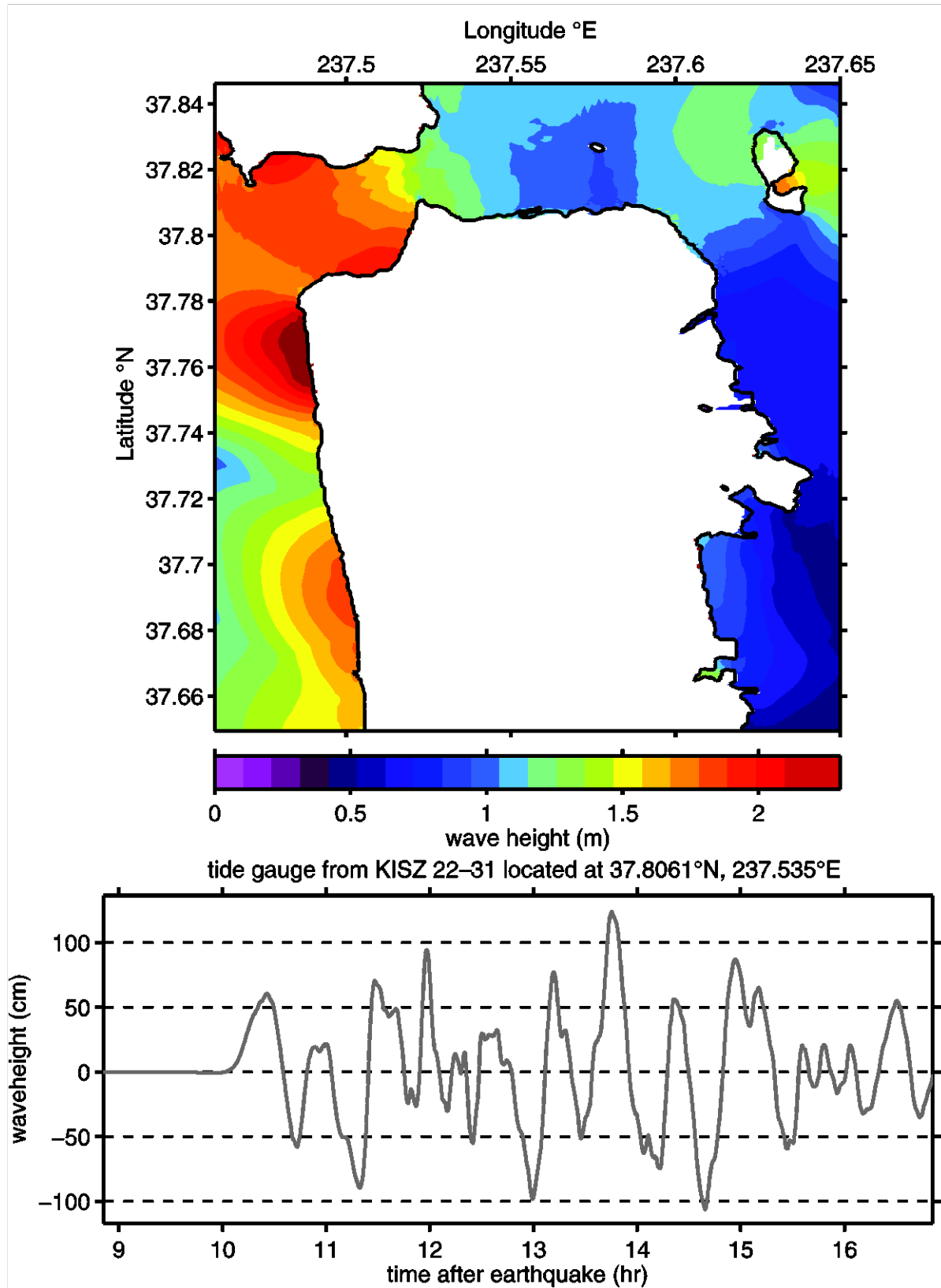
Figure 9. The maximum wave height and tide gauge simulation of a synthetic tsunami from Japan at the San Francisco forecast model grid.
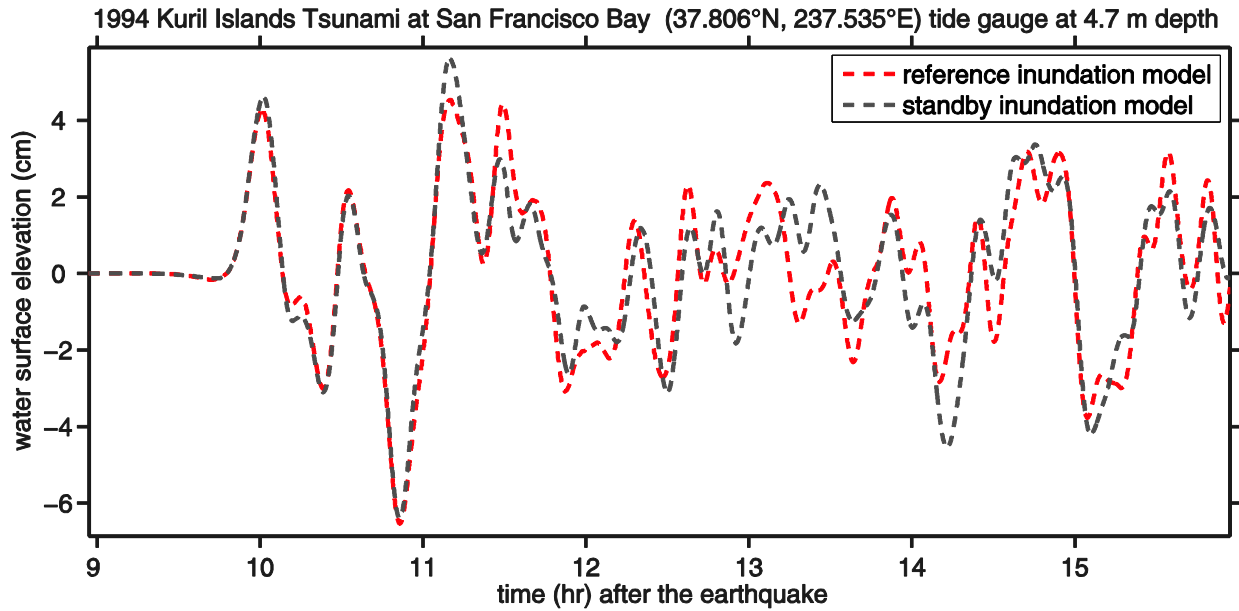
Figure 10. Comparison at the Presidio tide gauge of the modeled and observed tsunami generated during the 1994 Kuril Unimak earthquake. The observed tidal record (green) is shown with the reference inundation (red) and optimized forecast (black) model results superimposed.
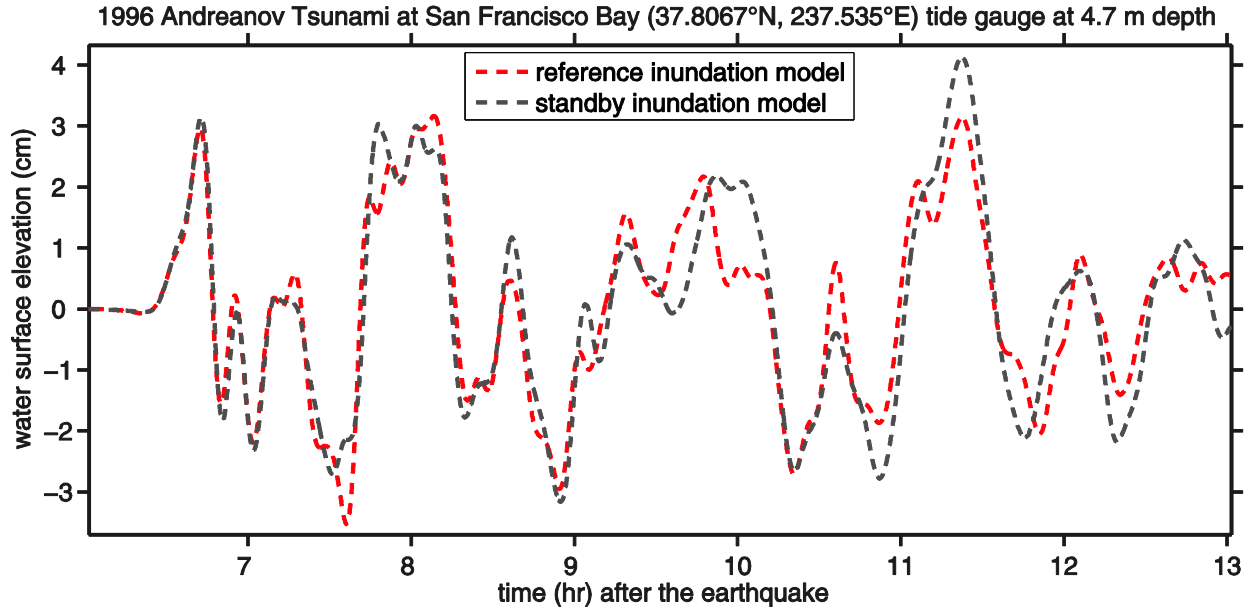
Figure 11. Comparison at the Presidio tide gauge of the modeled and observed tsunami generated during the 1996 Andreanov earthquake. The observed tidal record (green) is shown with the reference inundation (red) and optimized forecast (black) model results superimposed.
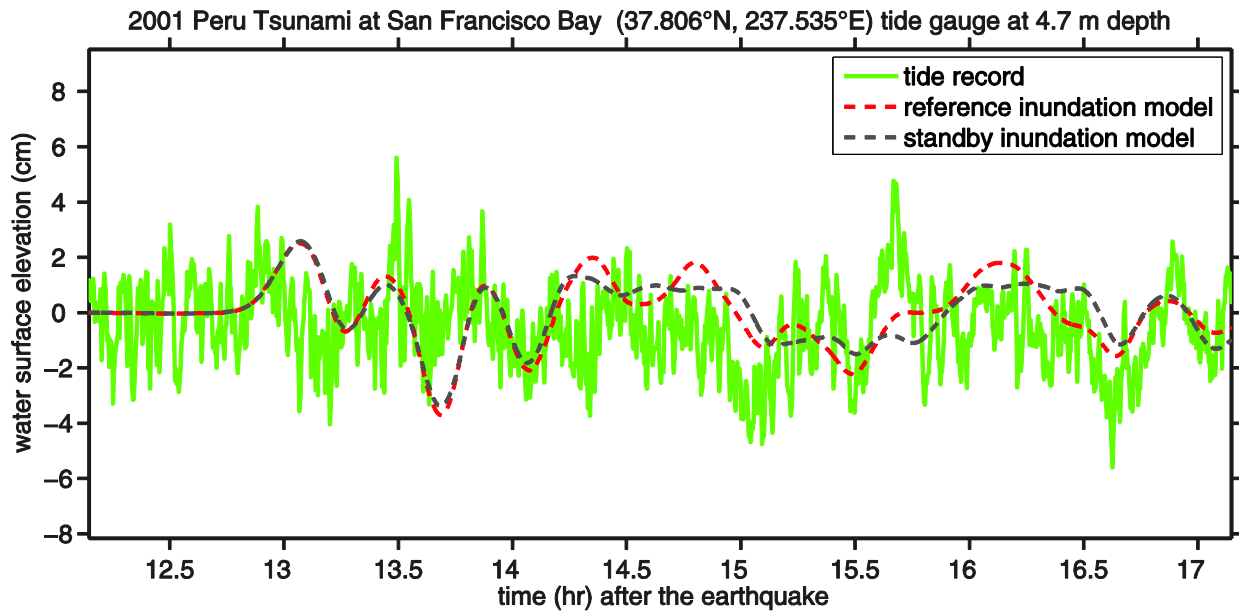
Figure 12. Comparison at the Presidio tide gauge of the modeled and observed tsunami generated during the 2001 Peru earthquake. The observed tidal record (green) is shown with the reference inundation (red) and optimized forecast (black) model results superimposed.
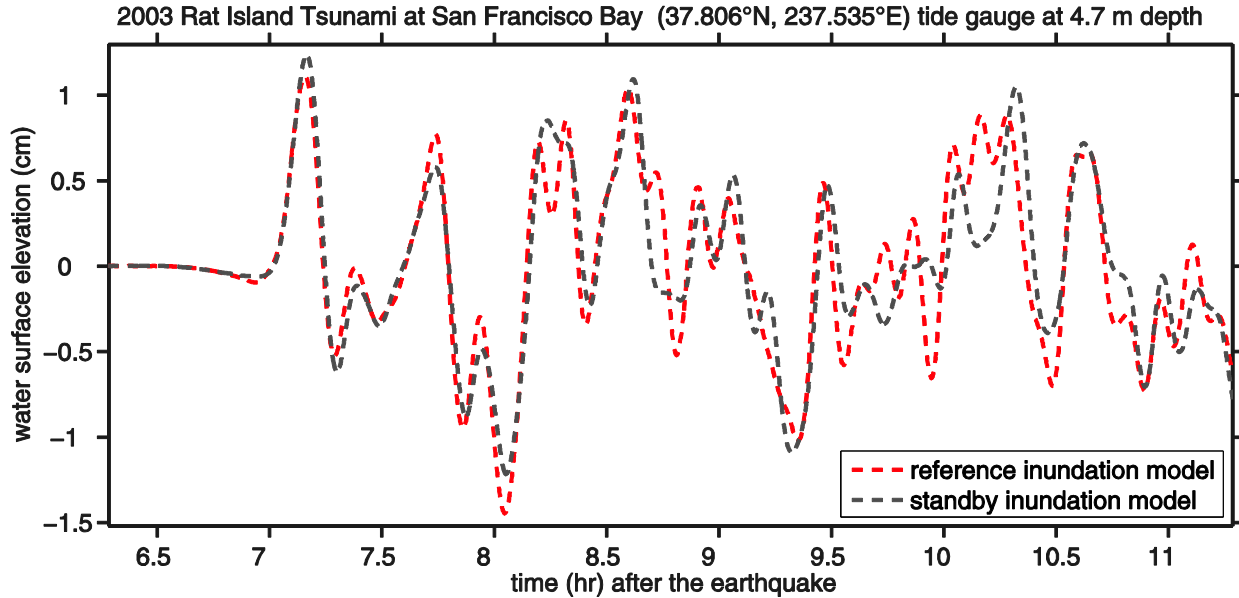
Figure 13. Comparison at the Presidio tide gauge of the modeled and observed tsunami generated during the 2003 Rat Island earthquake. The observed tidal record (green) is shown with the reference inundation (red) and optimized forecast (black) model results superimposed.
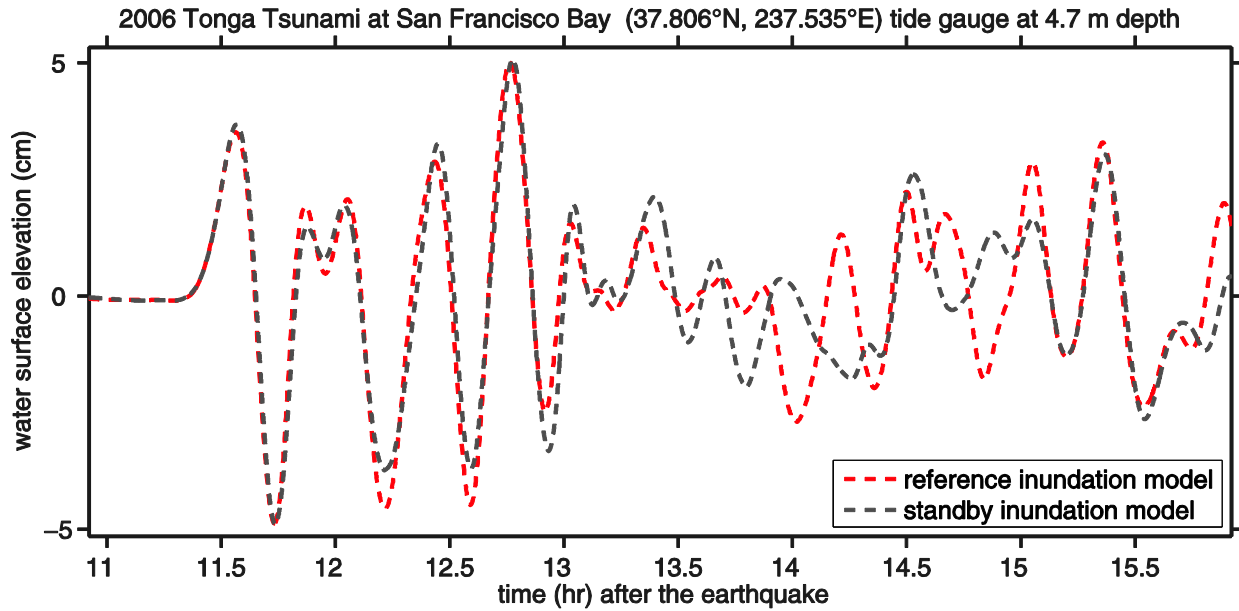
Figure 14. Comparison at the Presidio tide gauge of the modeled and observed tsunami generated during the 2006 Tonga earthquake. The observed tidal record (green) is shown with the reference inundation (red) and optimized forecast (black) model results superimposed.
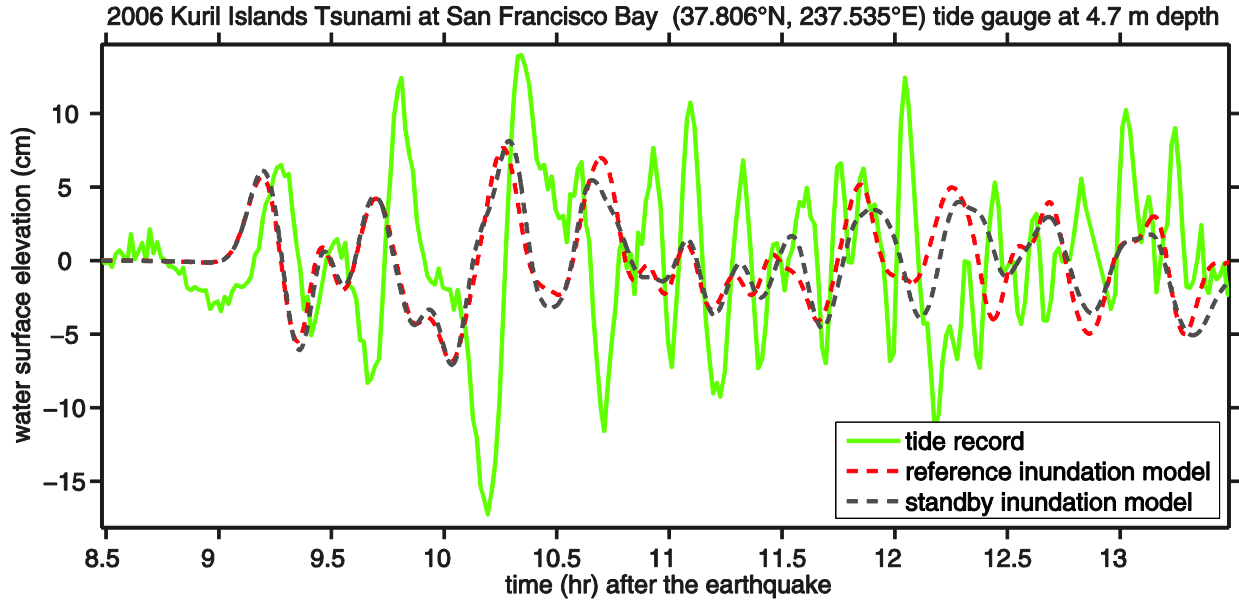
Figure 15. Comparison at the Presidio tide gauge of the modeled and observed tsunami generated during the 2006 Kuril earthquake. The observed tidal record (green) is shown with the reference inundation (red) and optimized forecast (black) model results superimposed.
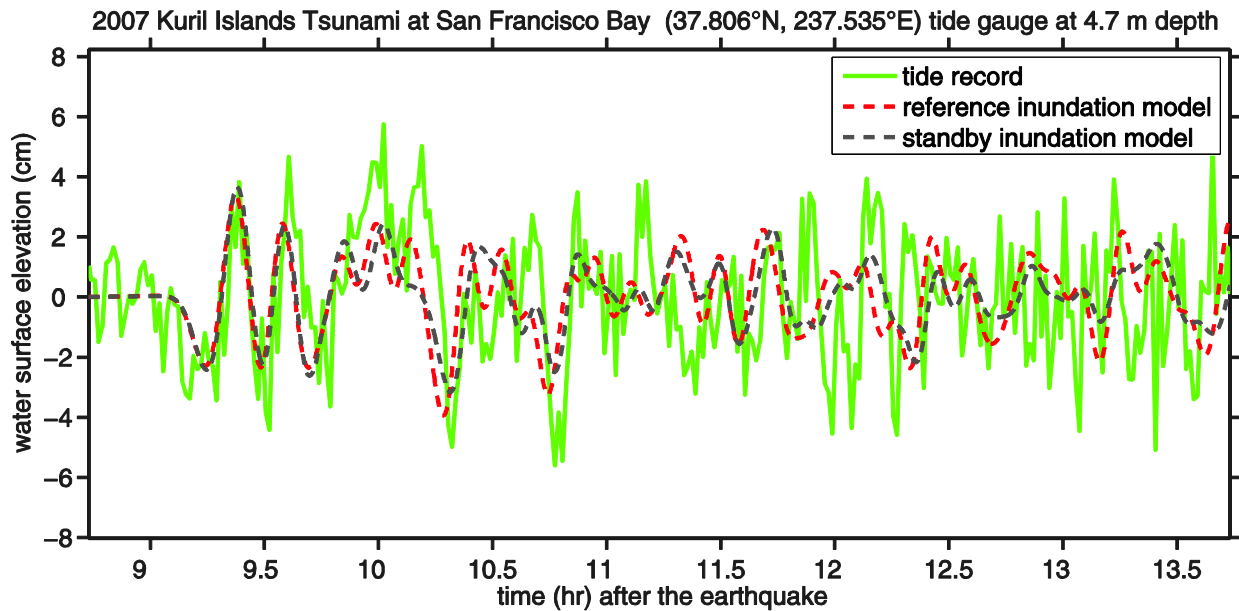
Figure 16. Comparison at the Presidio tide gauge of the modeled and observed tsunami generated during the 2007 Kuril earthquake. The observed tidal record (green) is shown with the reference inundation (red) and optimized forecast (black) model results superimposed.
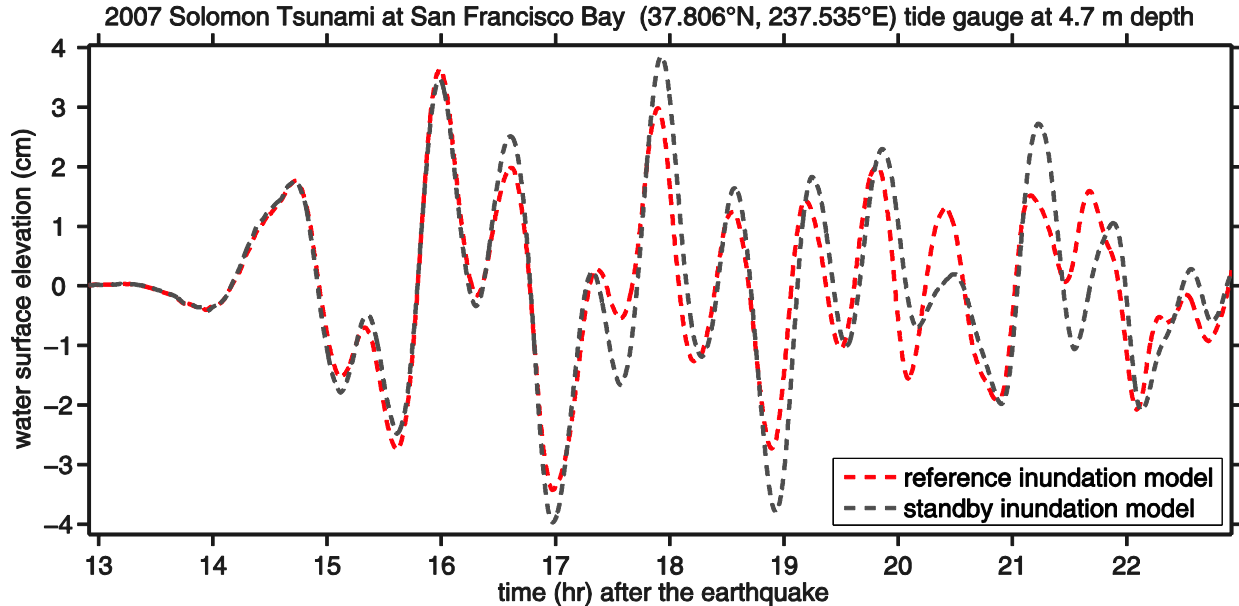
Figure 17. Comparison at the Presidio tide gauge of the modeled and observed tsunami generated during the 2007 Solomon earthquake. The observed tidal record (green) is shown with the reference inundation (red) and optimized forecast (black) model results superimposed.
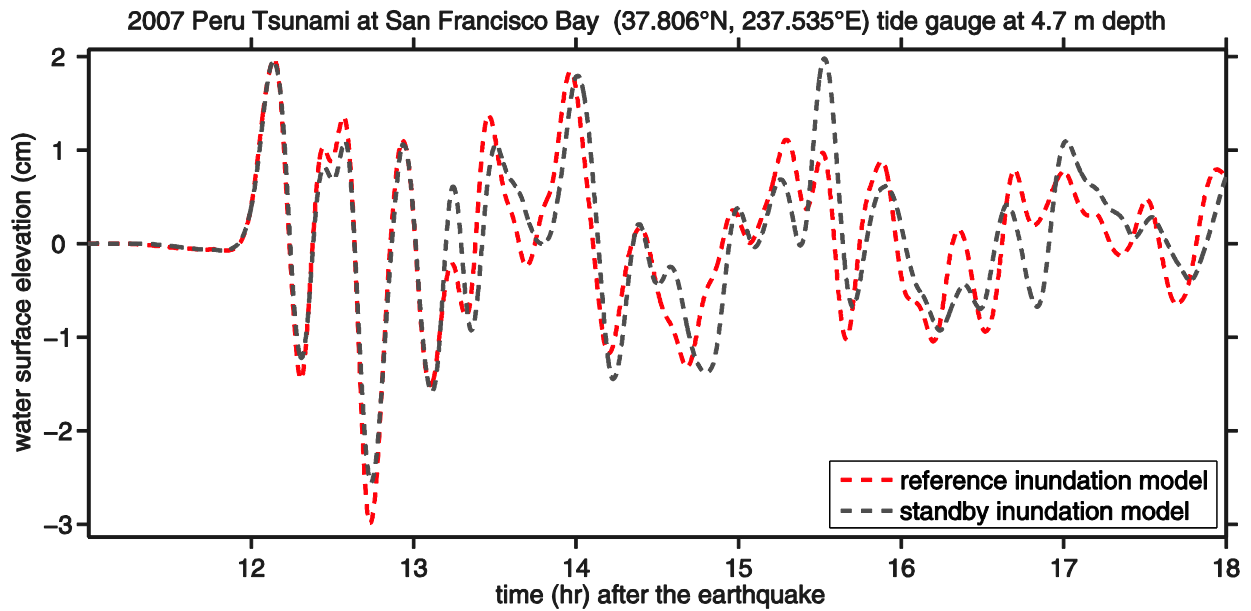
Figure 18. Comparison at the Presidio tide gauge of the modeled and observed tsunami generated during the 2007 Peru earthquake. The observed tidal record (green) is shown with the reference inundation (red) and optimized forecast (black) model results superimposed.
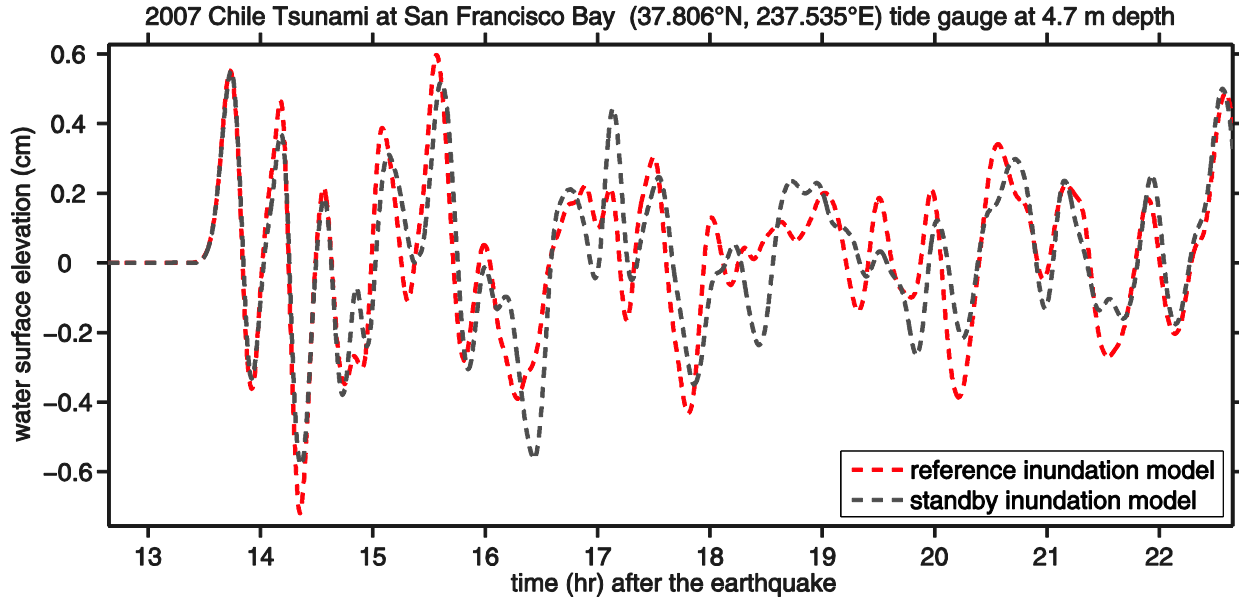
Figure 19. Comparison at the Presidio tide gauge of the modeled and observed tsunami generated during the 2007 Chile earthquake. The observed tidal record (green) is shown with the reference inundation (red) and optimized forecast (black) model results superimposed.

22
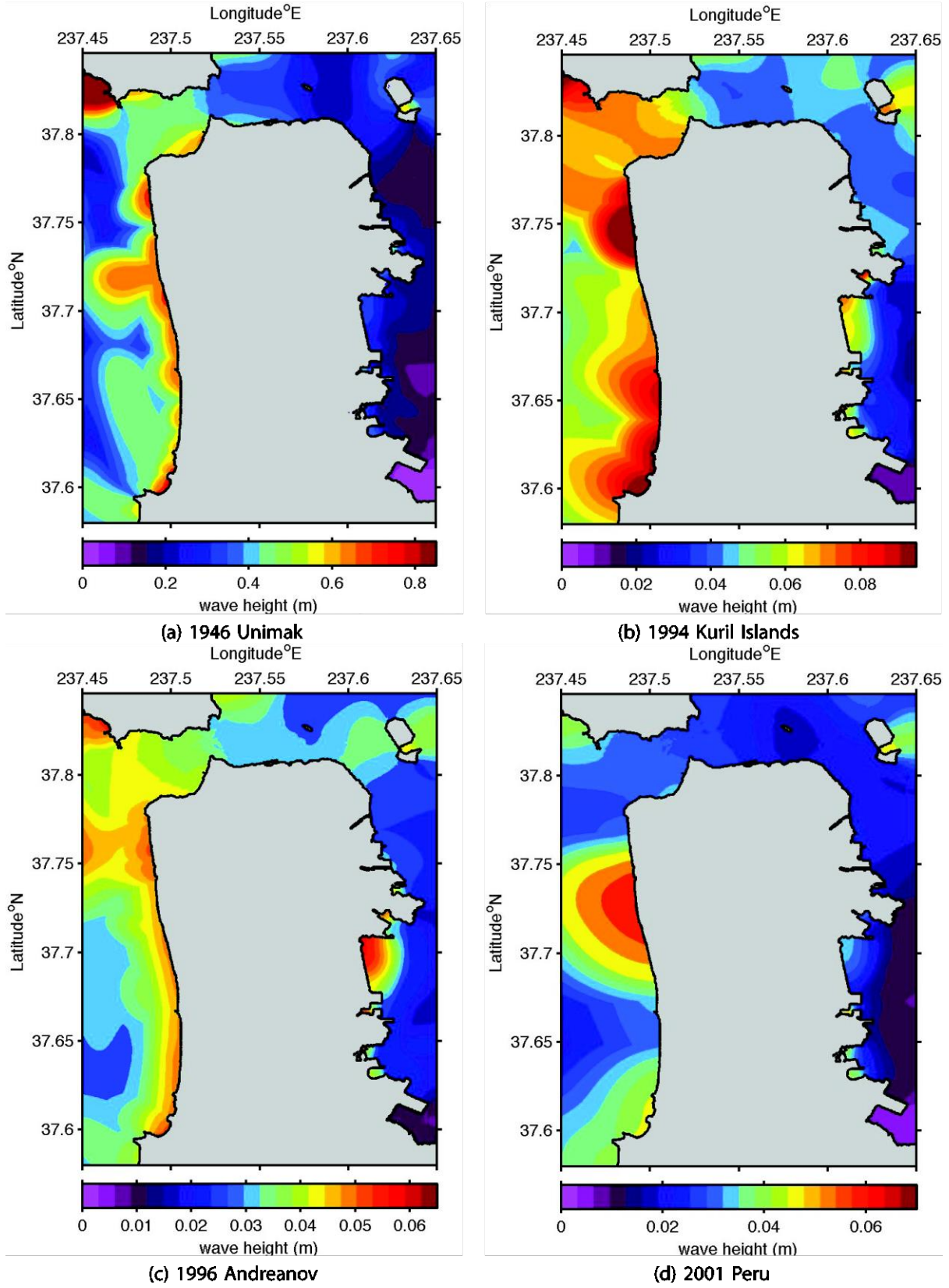
Figure 20. Maximum wave heights computed with reference model grids from (a) 1946 Unimak tsunami, (b) 1994 Kuril Islands tsunami, (c) 1996 Andreanov tsunami and (d) 2001 Peru tsunami.
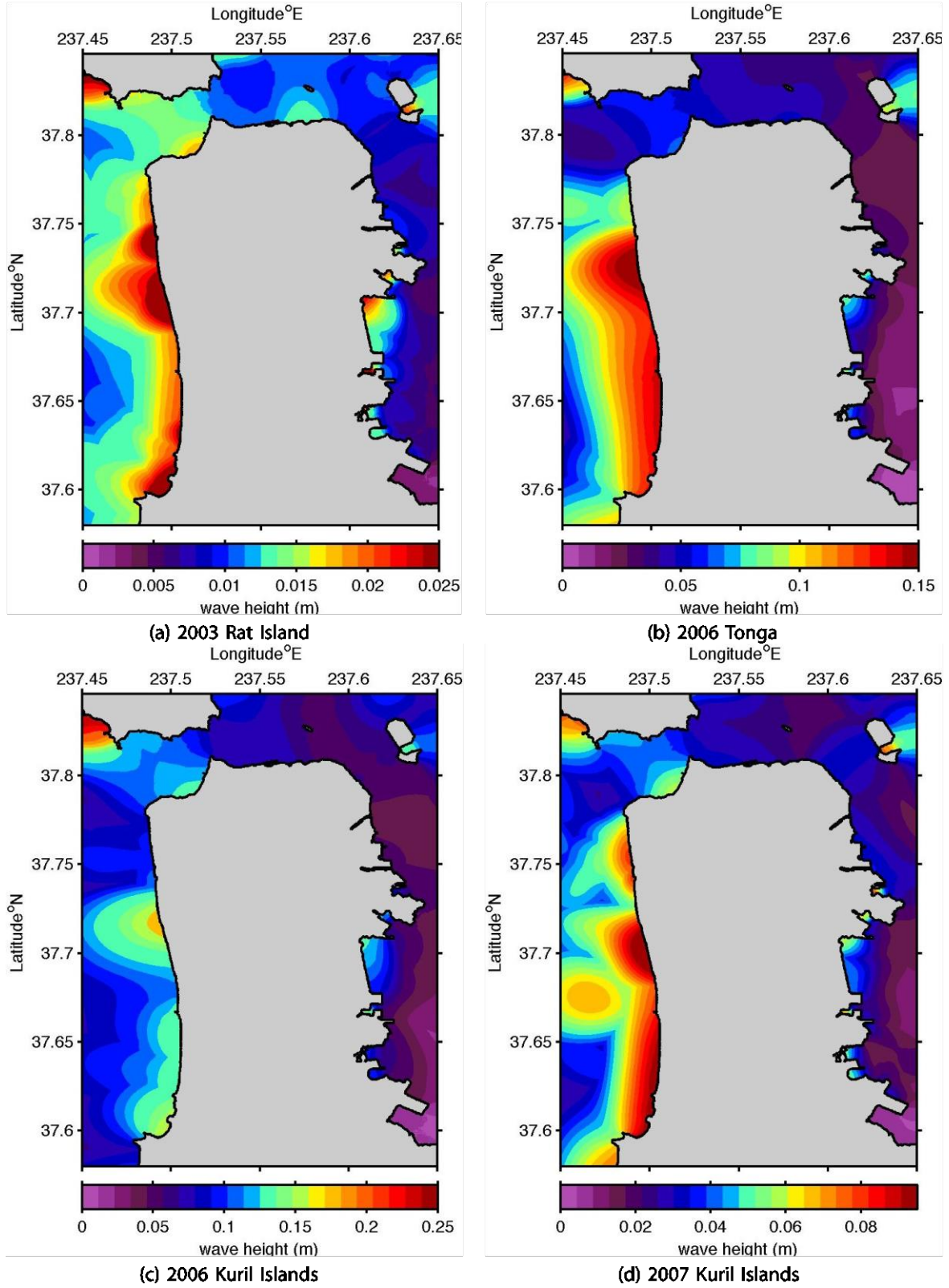
Figure 21. Maximum wave heights computed with reference model grids from (a) 2003 Rat Islands tsunami, (b) 2006 Tonga tsunami, (c) 2006 Kuril Islands tsunami and (d) 2007 Kuril Islands tsunami.
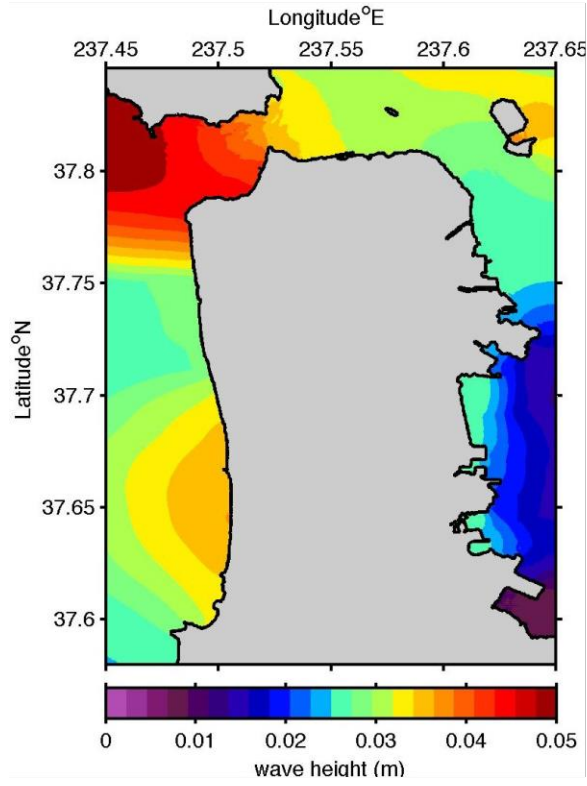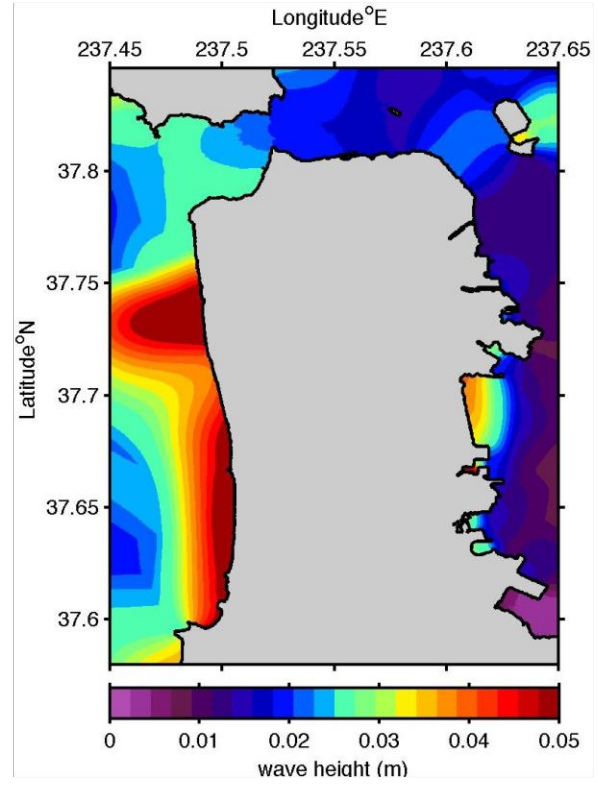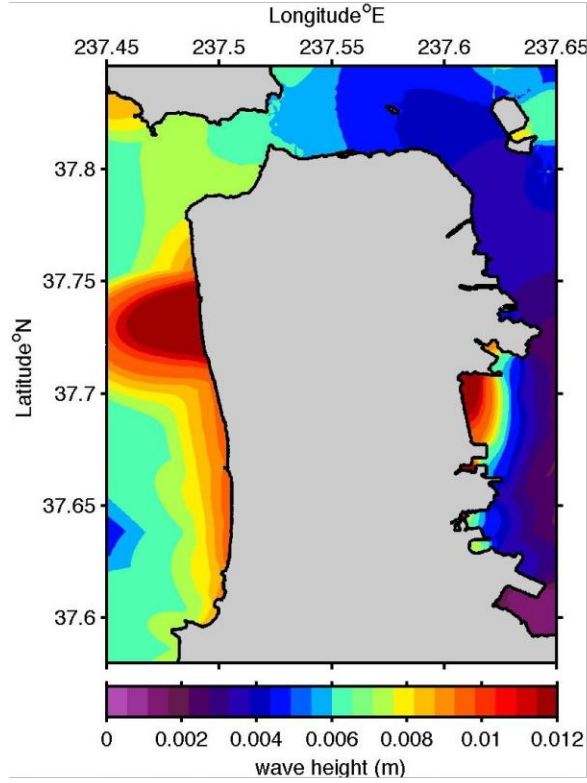
Figure 22. Maximum wave heights computed with reference model grids from (a) 2007 Solomon tsunami, (b) 2007 Peru tsunami and (c) 2007 Chile tsunami.
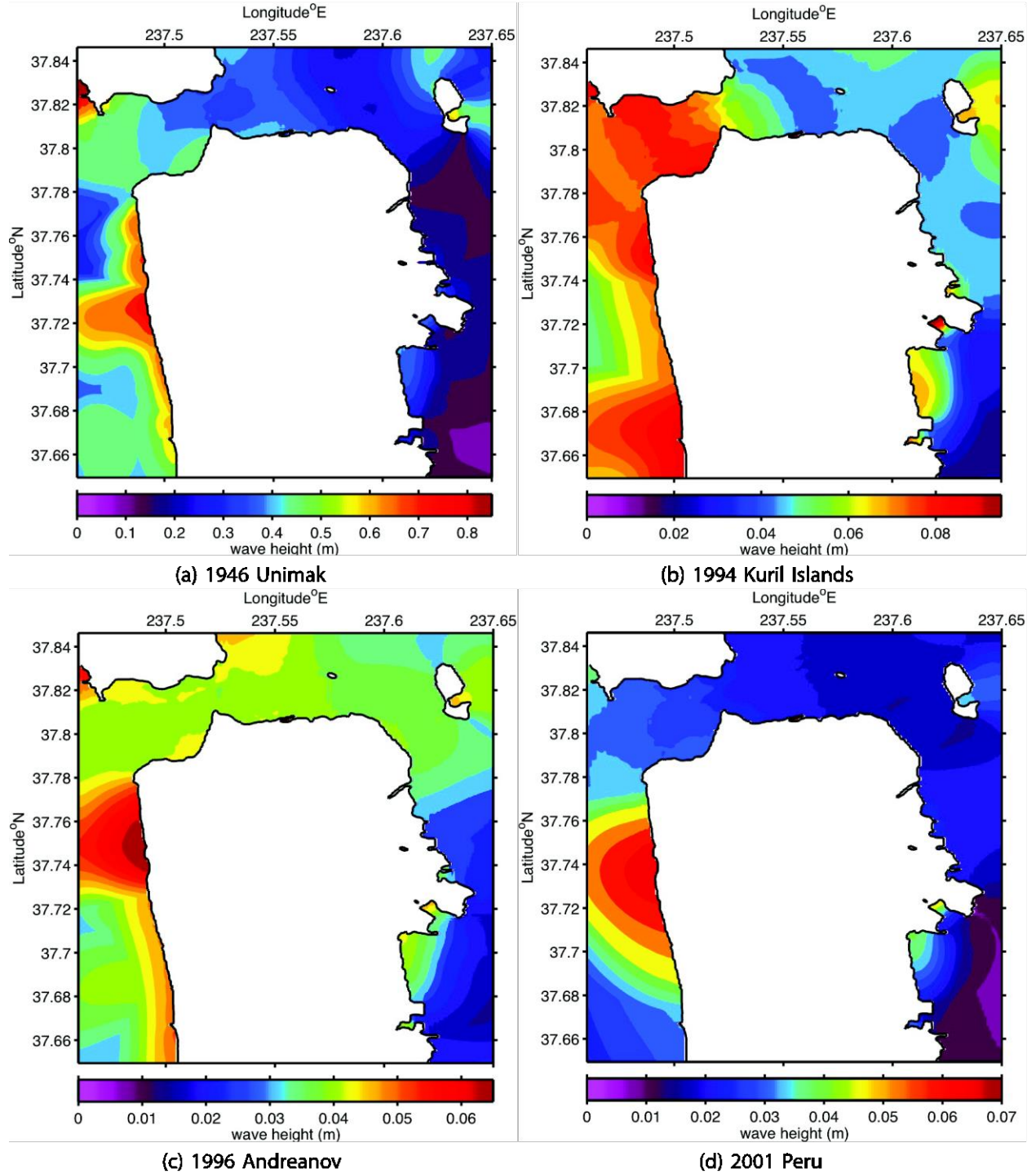
Figure 23. Maximum wave heights computed with forecast model grids from (a) 1946 Unimak tsunami, (b) 1994 Kuril Islands tsunami, (c) 1996 Andreanof tsunami and (d) 2001 Peru tsunami.

Figure 24. Maximum wave heights computed with forecast model grids from (a) 2003 Rat Islands tsunami, (b) 2006 Tonga tsunami, (c) 2006 Kuril Islands tsunami and (d) 2007 Kuril Islands tsunami.
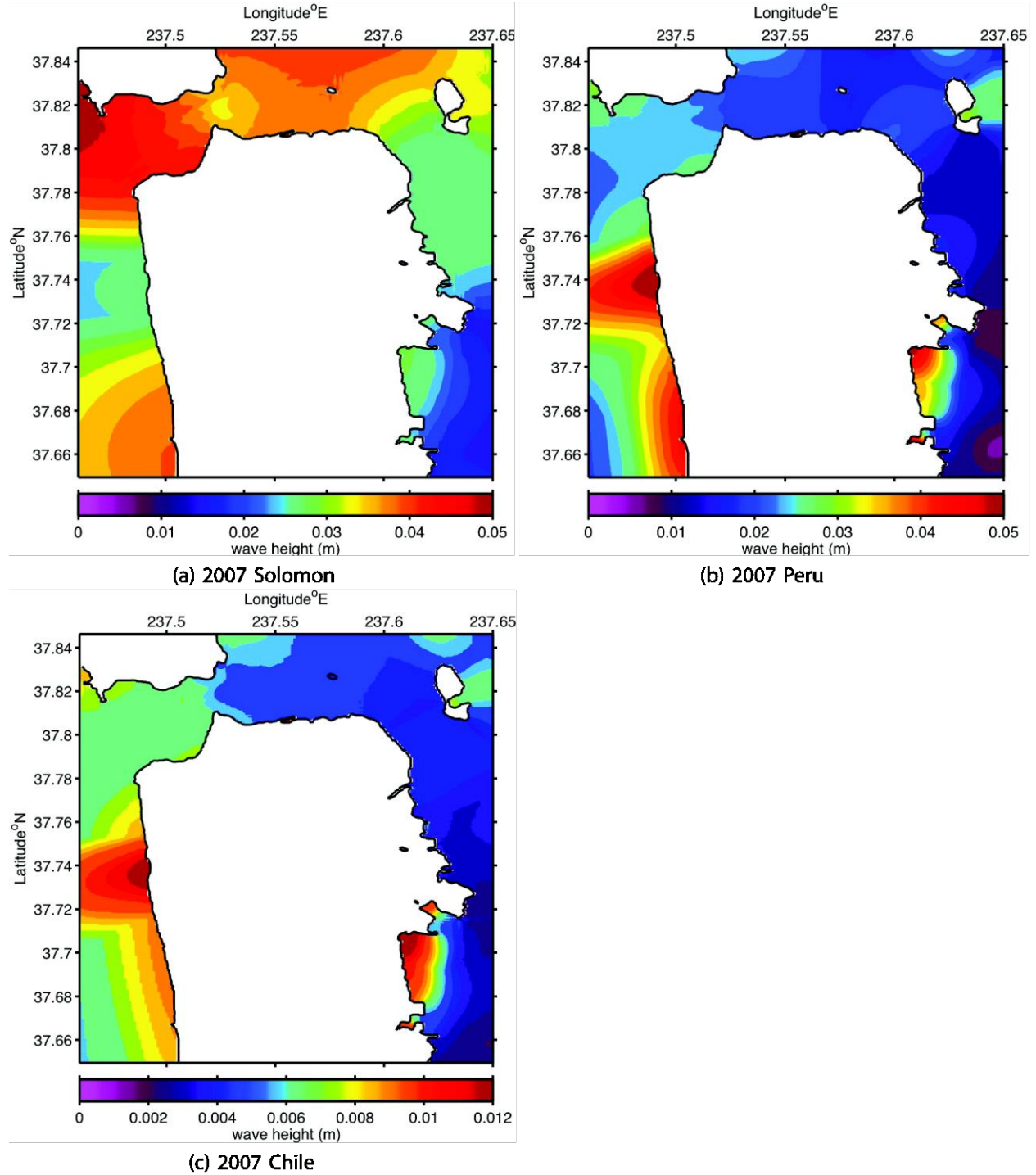
Figure 25. Maximum wave heights computed with forecast model grids from (a) 2007 Solomon tsunami, (b) 2007 Peru tsunami and (c) 2007 Chile tsunami.
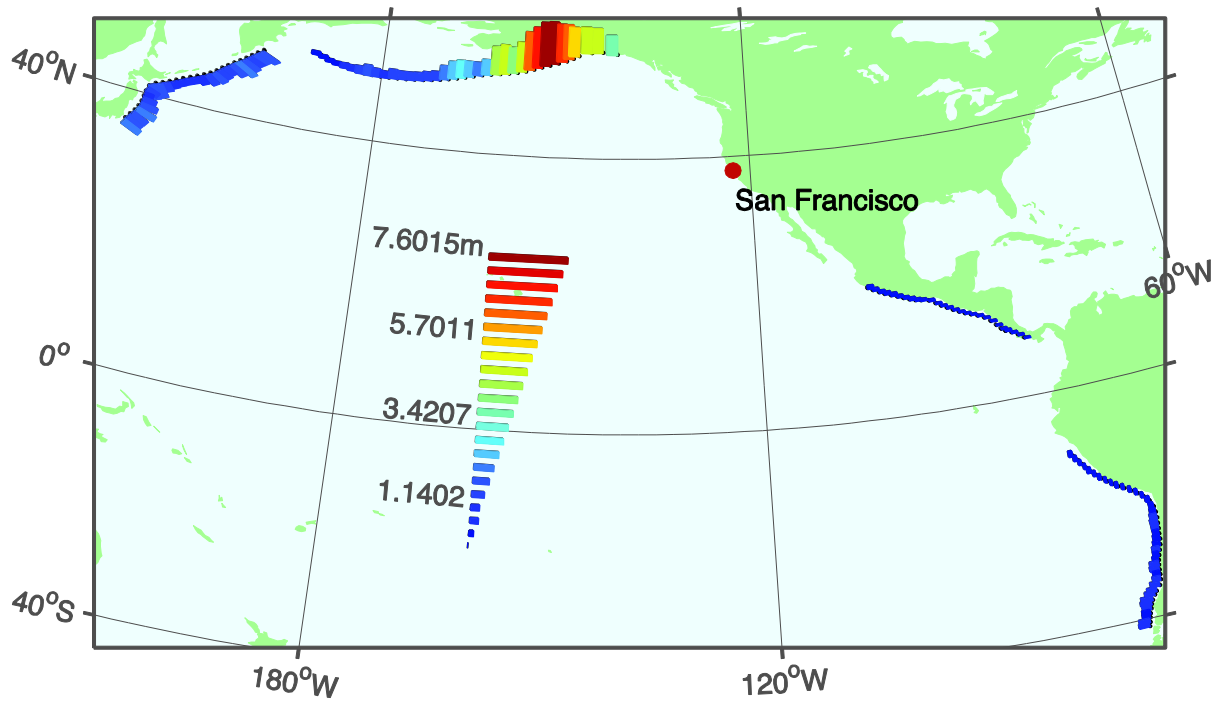
Figure 26. The predicted tsunami wave height response at Presidio tide gauge from Mw 9.3 events modeled from a 1000 km × 100 km source area with 30-m rupture.
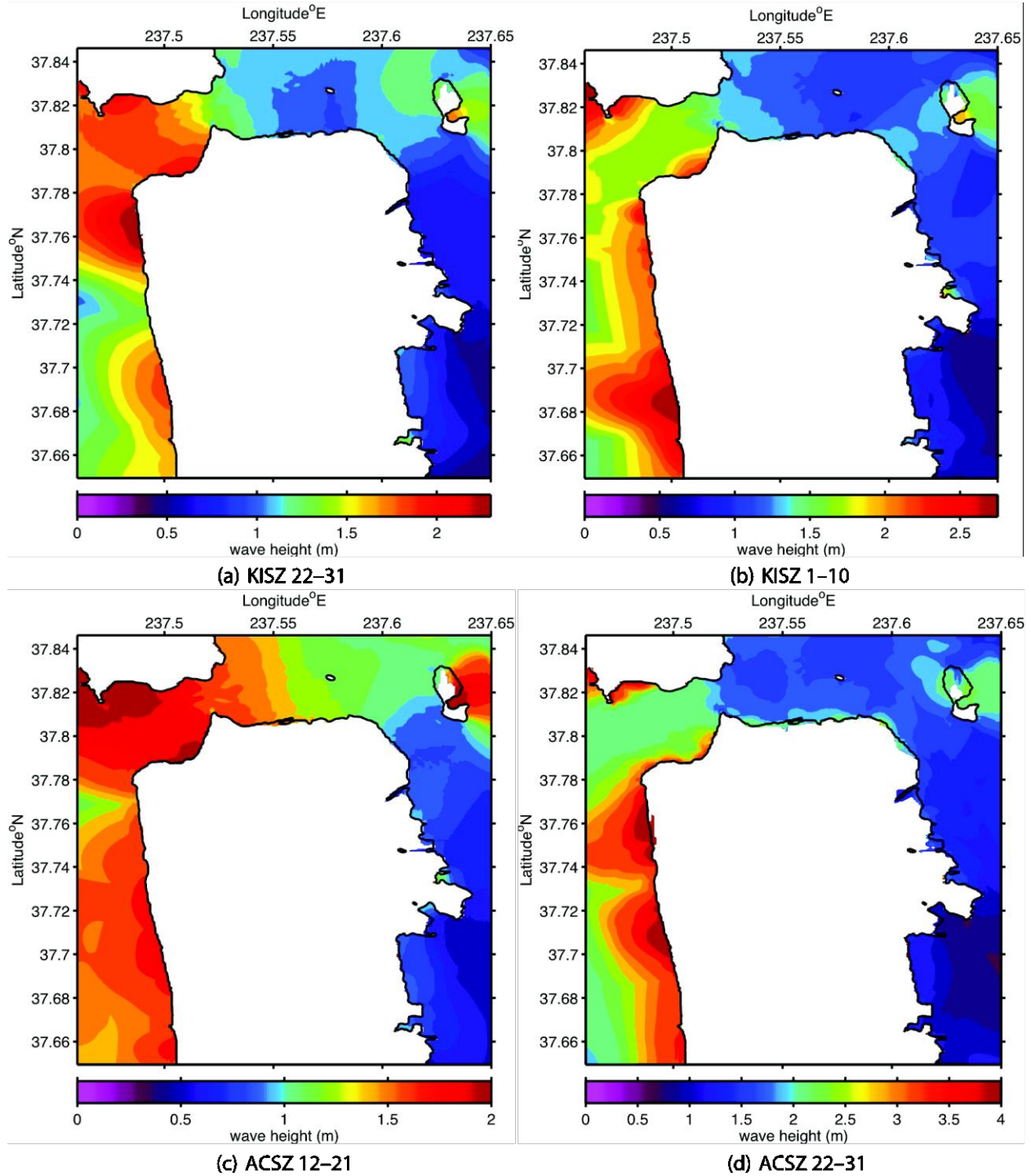
Figure 27. Maximum wave heights computed with forecast model grids from synthetic scenarios 1–4.
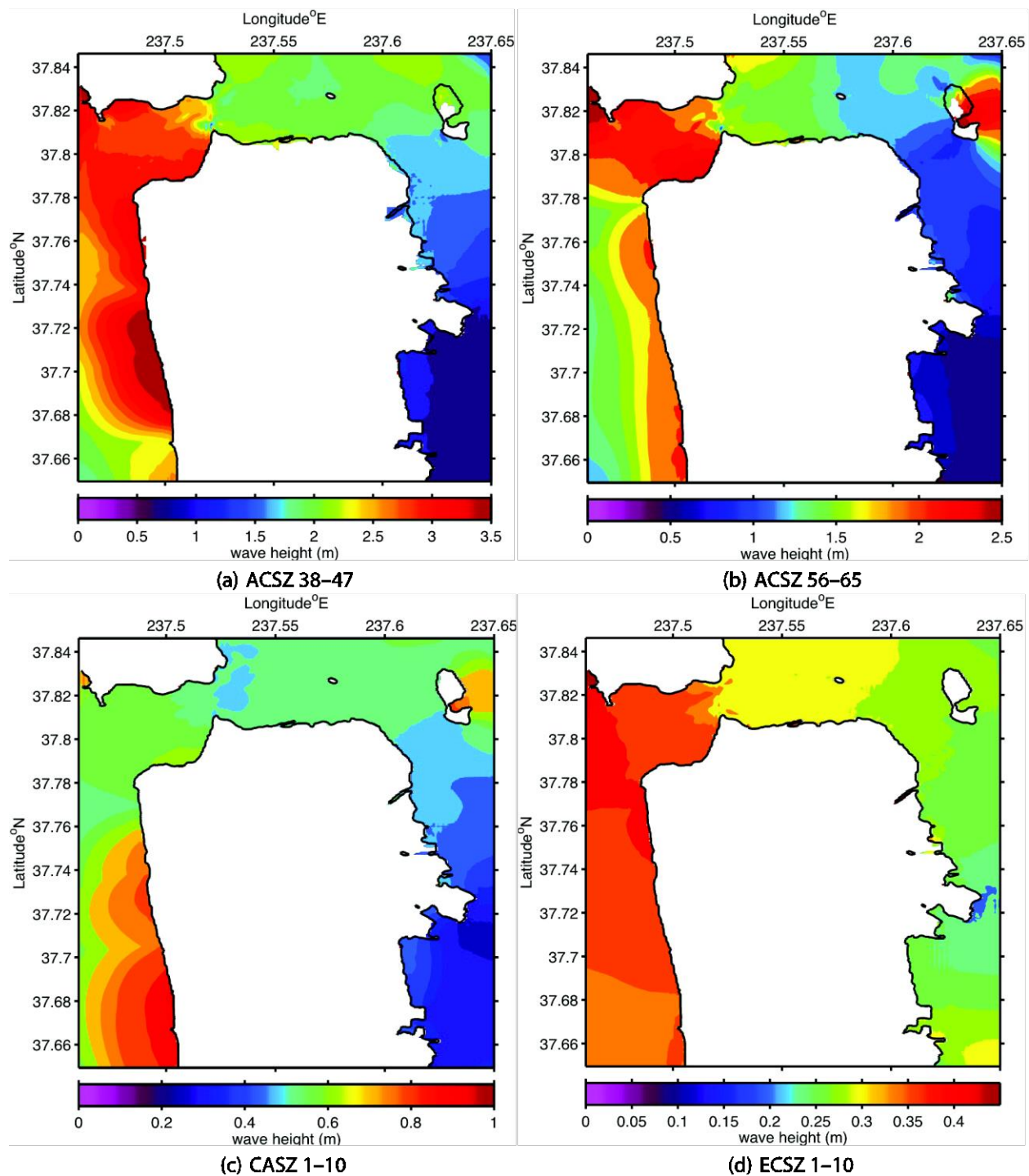
Figure 28. Maximum wave heights computed with forecast model grids from synthetic scenarios 5–8.
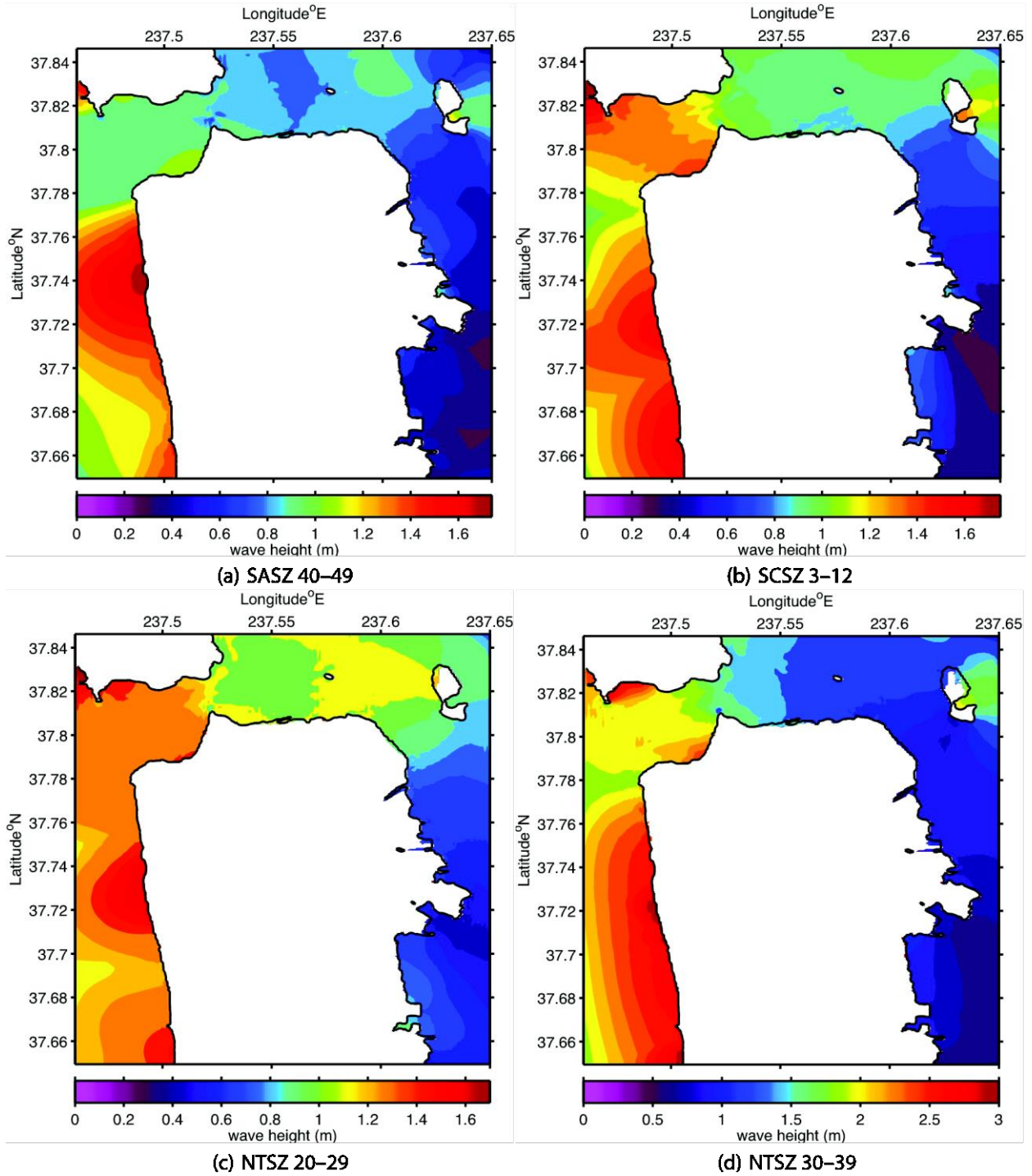
Figure 29. Maximum wave heights computed with forecast model grids from synthetic scenarios 9–12.
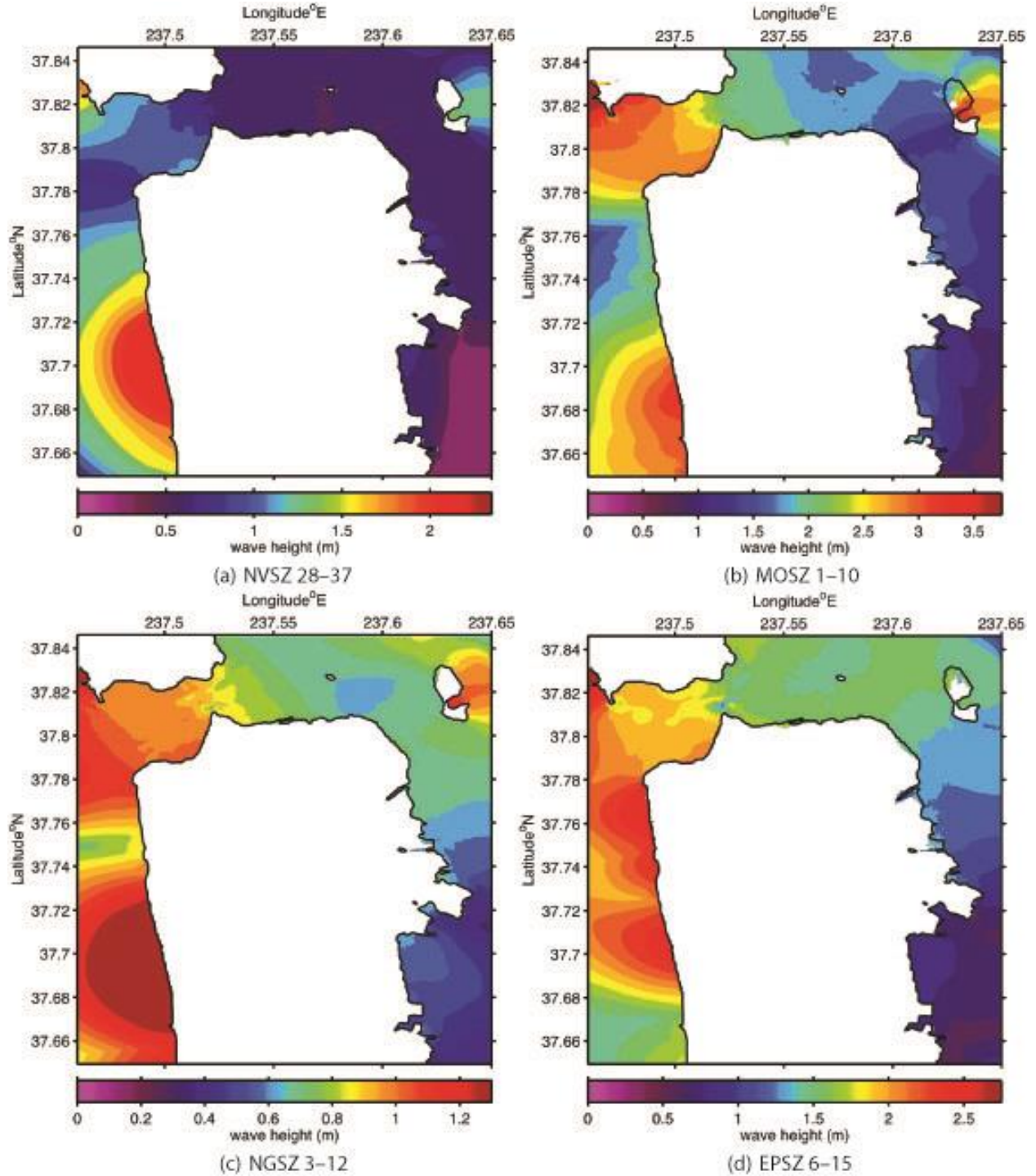
Figure 30. Maximum wave heights computed with forecast model grids from synthetic scenarios 13–16.
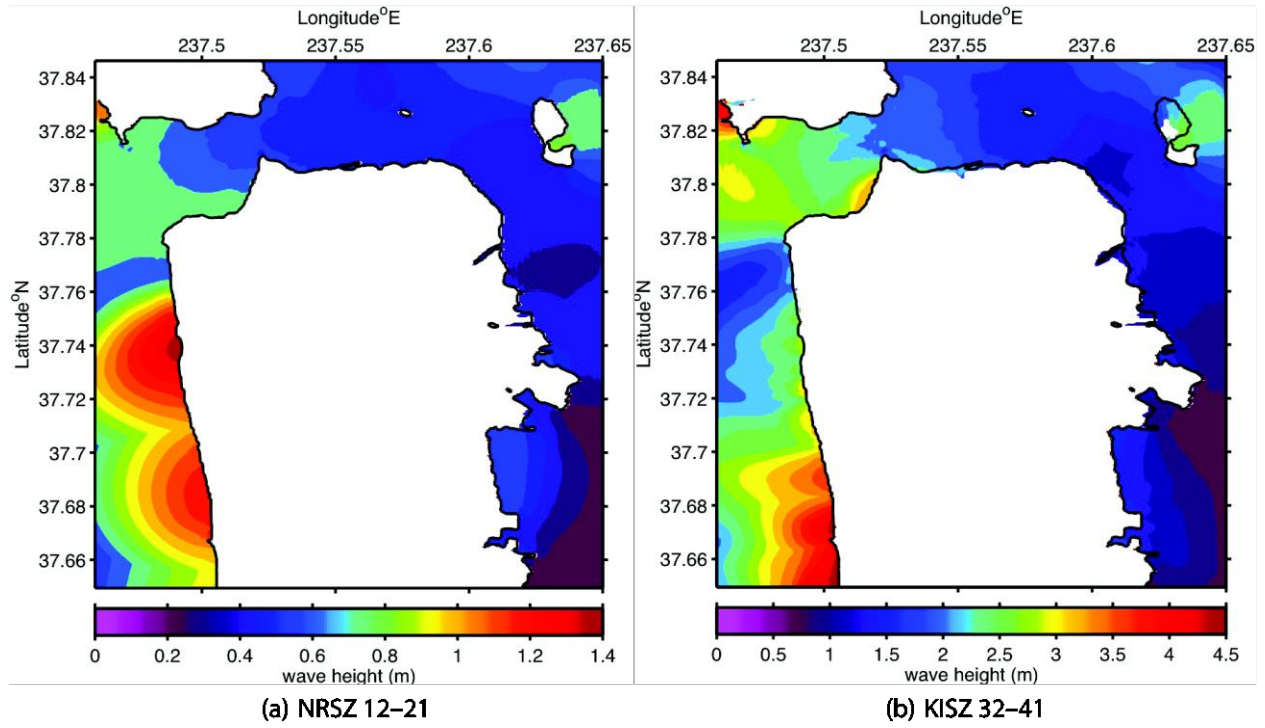
Figure 31. Maximum wave heights computed with forecast model grids from synthetic scenarios 17–18.

SUPPLEMENT: Synthetic Testing — San Francisco, California

The San Francisco forecast model was tested with NOAA's tsunami forecast system version 3.2. The San Francisco forecast model was tested with four synthetic scenarios and one historical tsunami event. Test results from the forecast system and comparisons with the results obtained during the forecast model development are shown numerically in **Table S1** and graphically in **Figures S1 to S5**. The results show that the forecast model is stable and robust, with consistent and high quality results across geographically distributed tsunami sources and mega-event tsunami magnitudes. The model run time (wall clock time) was 5 min for a 4 hr simulation. This run time is within the 10 min run time for 4 hr of simulation time and satisfies time efficiency requirements.

Four synthetic events were run on the Crescent City forecast model. The modeled scenarios were stable for all cases tested, with no instabilities or ringing. Results show that the largest modeled height was 167.5 cm and originated in the New Zealand-Kermadec-Tonga (NTSZ 30-39) source. Amplitudes greater than 50.9 cm were recorded for all of the test sources. The smallest signal of 50.9 cm was recorded at the far field Central and South America (CSSZ 91-100) source. Direct comparisons of output from the forecast tool with results of both the Tohoku 2011 historical event and available development synthetic events demonstrated that the wave patterns were similar in shape, pattern, and amplitude.

Table S1. Maximum and minimum amplitudes (cm) at the San Francisco warning point for synthetic and historical events tested using SIFT 3.2 and obtained during development.

Scenario Name	Source Zone	Tsunami Source	α [m]	SIFT Max (cm)	Development Max (cm)	SIFT Min (cm)	Development Min (cm)
Mega-tsunami Scenarios							
KISZ 22-31	Kamchatka-Yap-Mariana-Izu-Bonin	A22-A31, B22-B31	30	113.7	113.2	-99.3	-99.3
ACSZ 56-65	Aleutian-Alaska-Cascadia	A56-A65, B56-B65	30	142.5	143.2	-160.8	-161.8
CSSZ 91-100	Central and South America	A91-A100, B91-B100	30	50.9	50.9	-51.7	-51.7
NTSZ 30-39	New Zealand-Kermadec-Tonga	A30-A39, B30-B39	30	167.5	167.5	-172.5	-172.5
Historical Events							
2011 Tohoku	New Zealand-Kermadec-Tonga	4.66 b24 + 12.23 b25 + 26.31 a26 + 21.27 b26 +22.75 a27 + 4.98 b27		70.2	70.2	-53.3	-53.3

Figure S1. Response of the San Francisco forecast model to synthetic scenario KISZ 22-31 (α=30). Maximum sea surface elevation for (a) A grid, (b) B grid, and (c) C grid. Sea surface elevation time series at the C-grid warning point (d). The lower time series plot displays the result obtained during model development, shown for comparison with test results.

(a)

(c)

(b)

(d)
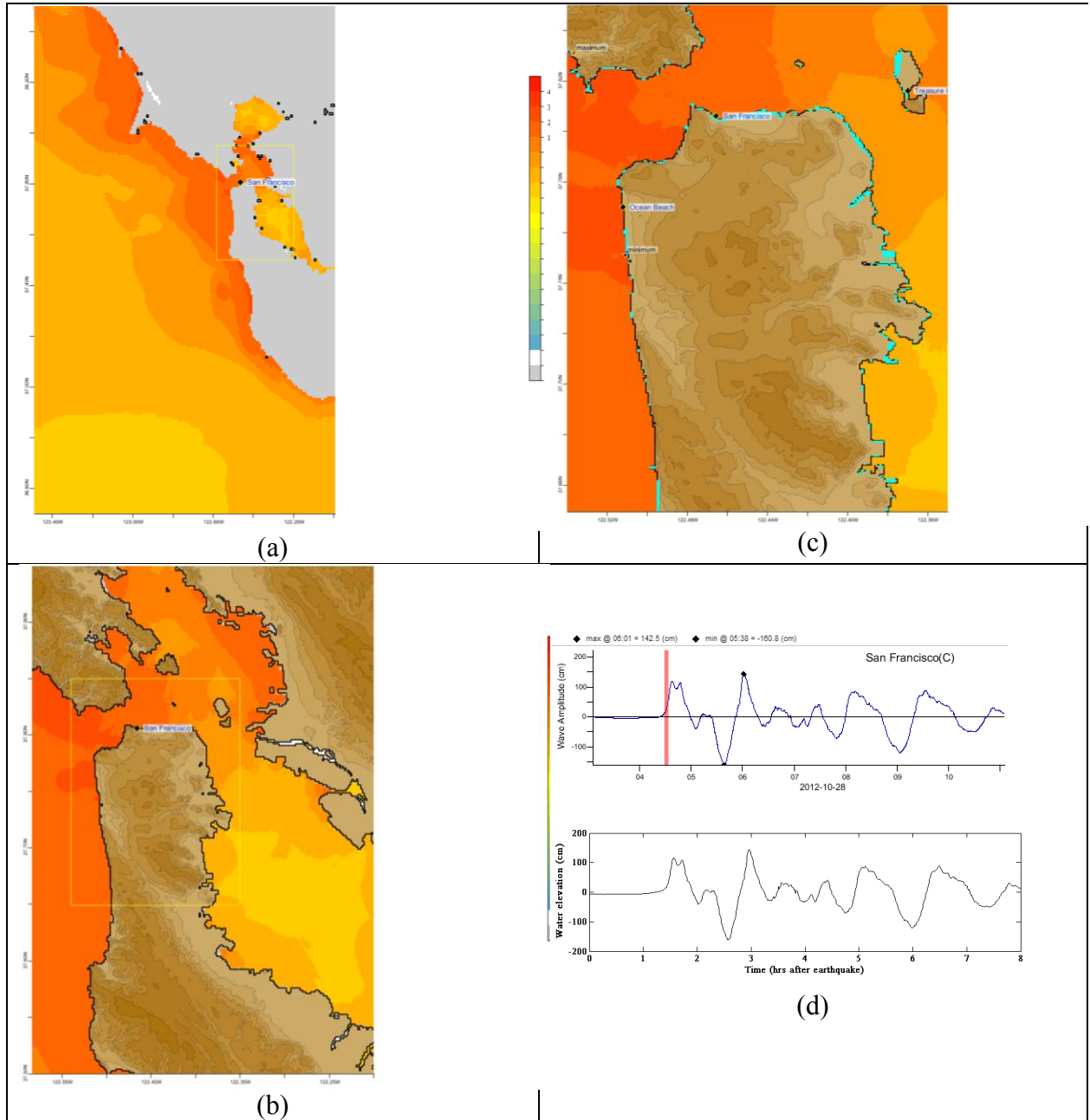
Figure S2. Response of the San Francisco forecast model to synthetic scenario ACSZ 56-65 (α=30). Maximum sea surface elevation for (a) A grid, (b) B grid, and (c) C grid. Sea surface elevation time series at the C-grid warning point (d). The lower time series plot displays the result obtained during model development, shown for comparison with test results.

Figure S3. Response of the San Francisco forecast model to synthetic scenario CSSZ 91-100 (α=30). Maximum sea surface elevation for (a) A grid, (b) B grid, and (c) C grid. Sea surface elevation time series at the C-grid warning point (d). The lower time series plot displays the result obtained during model development, shown for comparison with test results.
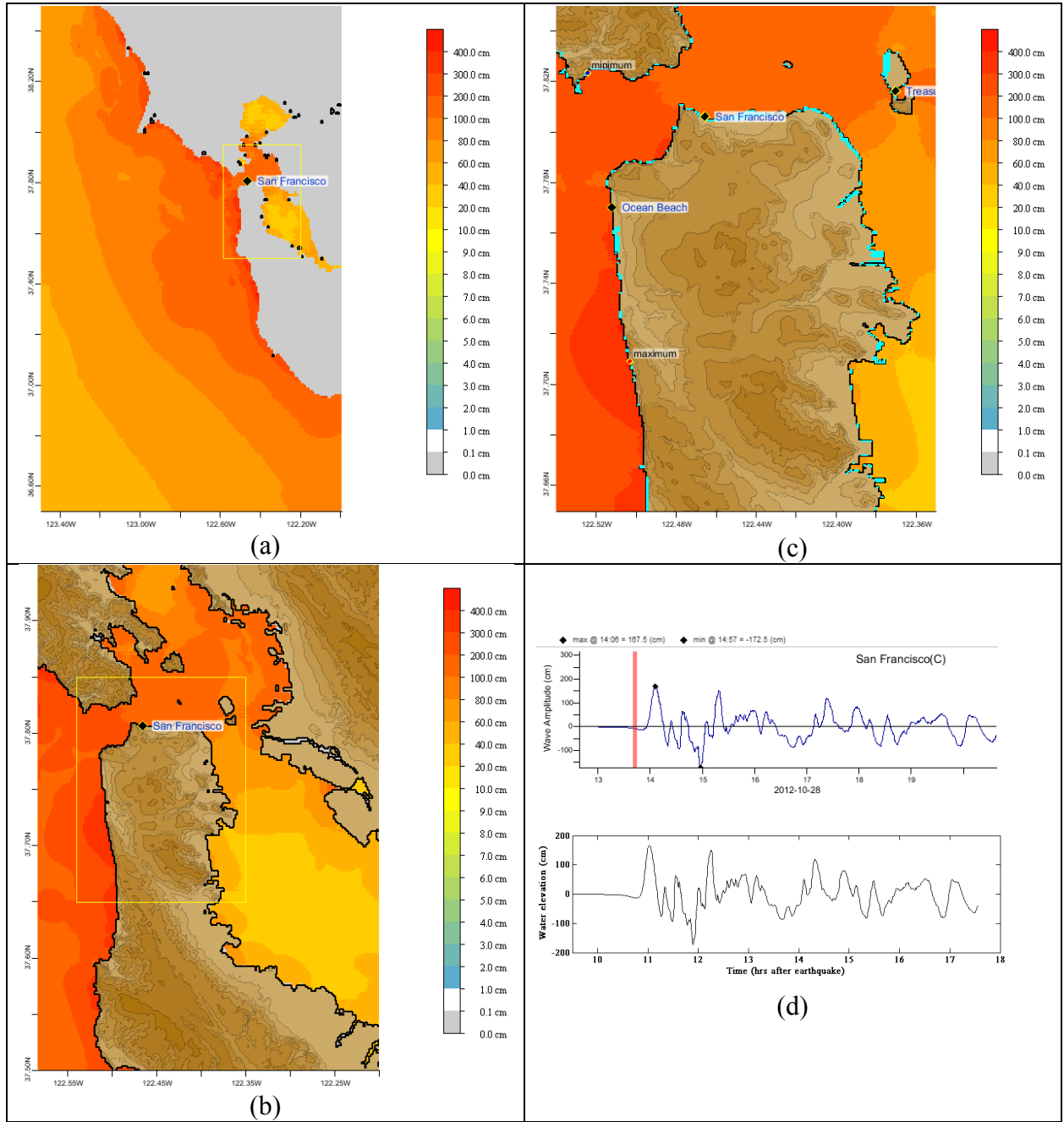
Figure S4. Response of the San Francisco forecast model to synthetic scenario NTSZ 30-39 (α=30). Maximum sea surface elevation for (a) A grid, (b) B grid, and (c) C grid. Sea surface elevation time series at the C-grid warning point (d). The lower time series plot displays the result obtained during model development, shown for comparison with test results.

Figure S5. Response of the San Francisco forecast model to 2011 Tohoku tsunami. Maximum sea surface elevation for (a) A grid, (b) B grid, and (c) C grid. Sea surface elevation time series at the C-grid warning point (d). The lower time series plot displays the result obtained during model development, shown for comparison with test results.

6. PMEL Tsunami Forecast Model for Monterey, California

Yong Wei

Table of Contents

List of Figures:

List of Tables:

6.1 Model development

A tsunami forecast model using MOST usually consists of three nested grids, referred to as A, B, and C-grids, that employ increasing spatial resolutions. Tsunami wave dynamics offshore are predicted using a low-resolution A grid, while the wave dynamics in shallow, near-shore area is computed in C grid, where the model results are compared with observations at tide gauges for historical tsunamis. The goal is to achieve a 4 to 10 hour simulation of tsunami propagation and flooding within 10 min of wall-clock time. NOAA's National Geophysical Data Center (NGDC) provides Digital Elevation Models (DEMs), mostly at a grid resolution of 1/3 arc sec (~ 10 m), for a coastal community at risk. The NGDC's DEMs are integrated from a variety of data sources to use unified vertical datum, Mean High Water (MHW), and horizontal datum, World Geodetic System 1984 (WGS84, http://ngdc.noaa.gov/mgg/inundation/tsunami/inundation.html).

6.1.1 Study area and NOS tide station

The City of Monterey is situated on the Monterey Bay National Marine Sanctuary, a federally protected ocean area extending 450 km along the coast, where the San Andreas fault system traverses in a northwest-southeast direction and controls much of the overall geologic character of the region. This series of sub-parallel faults forms the boundary between the Pacific and North American tectonic plates, the former of which is sliding northwest several centimeters per year relative to the latter. In the vicinity of the sanctuary, the San Andreas fault system is basically composed of four fault zones: the San Gregorio fault that extends from Monterey to Half Moon Bay and is predominantly offshore; the Monterey – Tularcitos fault zone that extends over a wide area from Monterey to Santa Cruz within Monterey Bay; The San Simeon fault; and the infamous San Andreas fault that is almost entirely onshore in this region. An earthquake probability study by the USGS) determined that there is a 62 percent chance of a magnitude 6.7 or greater earthquake occurring on one of the faults in the greater San Francisco Bay Area between 2003 and 2032 (Working Group on California Earthquake Probabilities, 2003). In this time period, there is a 10 percent chance of a magnitude 6.7 or greater earthquake on the San Gregorio fault and a 21 percent chance of a similar earthquake on the San Andreas Fault (**Figure 1**).

Monterey is subject to both distant and local tsunami threats. **Table 1** shows historical tsunamis that have affected Monterey Bay with associated observations of tsunami heights of these events. The 1964 Alaska tsunami affected the entire California coastline. The tsunami waves were particularly high from Crescent City to Monterey with heights on the open coast ranging from 2.1 – 6.4 m. The recorded wave amplitude at Monterey Bay tide gauge, located on the south side on the Monterey Bay, is about 1 m, but reached as high as 3.4 m on the north side of Monterey Bay at Santa Cruz Harbor. The 1946 Unimak tsunami barely produced any noticeable waves at Monterey Harbor but reached over 3 m at Santa Cruz. Other recorded tsunami waves before 2010 are mostly smaller than 0.2 m in amplitude, causing no damage to the coastline. The last major tsunamis hitting Monterey Bay were the 2010 Chile and 2011 Tohoku, causing maximum wave amplitudes of 0.28 m and 0.7 m at the tide gauge, respectively.

The submarine canyon offshore of Monterey Bay has been identified as a region of mass movement features. Slumps, debris flows and other submarine landslides are concentrated along canyon walls and the lower continental slope, with many additional distinct and youthful slumps at the base of the headward walls of Monterey Canyon (Greene et al., 2002). Land mass movement features in the Monterey Bay region suggest that a potential for tsunami generation exists (Greene and Ward, 2003). A small landslide occurred at the head of Monterey Canyon during the 1989 Loma Prieta Mw 6.9 earthquake with a small tsunami about 0.5 m high reported to have entered the Moss Landing Harbor and a turbidity current reported to have traveled down the canyon axis (Greene and Hicks, 1990; Schwing et al., 1990; Garfield et al., 1994). Ward and Simon (2005) showed that a 0.1 km^3 of material failure in Monterey Canyon could induce more than 7 meters of runup over 25 km of the coast, posing severe tsunami threats to the City of Monterey.

The NOS tide station at Monterey Harbor is located at (121.889278W, 36.605056N) with a Mean Sea Level (MSL) water depth of about 2.5 m on wharf #2, north of the main boat harbor (**Figure 2**). The tide station was established in November of 1973, and the present installation occurred in September of 1988. The mean tidal range at Monterey Harbor is about 1 m, and the mean sea level is increasing at the rate of 1.34 +/- 1.35 mm per year. 11 of the 25 historical events listed in **Table 1** are used to validate the present forecast model. The 11 tsunami events include the 26 March 1964 Alaska, 4 October 1994 Kuril, 10 June 1996 Andreanof, 23 June 2001 Peru, 3 May 2007 Tonga, 15 November 2006 Kuril, 13 January 2007 Kuril, 15 August 2007 Peru, 29 September 2009 Samoa, 27 February 2010 Chile, and 11 March 2011 Tohoku.

6.1.2 Digital Elevation Model (DEM) of Monterey, California

Accurate bathymetry and topography in offshore and coastal regions play a key role, both globally and locally, in tsunami generation, propagation and inundation. The global bathymetric and topographic datasets are available for public-domain research. Marks and Smith (2006) conducted an evaluation on 6 publicly available global bathymetry grids: DBDB2 (Digital Bathymetric Data Base by Naval Research Laboratory), ETOPO2 (Earth Topography by National Geophysical Data Center), GEBCO (General Bathymetric Charts of the Oceans by British Oceanographic Data Center), GINA (Geographic Information Network of Alaska), Smith and Sandwell (1997) and S2004. They concluded the original Smith and Sandwell grid might be the best source among these global bathymetric grids. Subsequently, they developed a new 1-min global topography grid S2004 that combines the Smith and Sandwell grid below 1,000 m depth and equatorward of 72°, and GEBCO grids in shallow water and polar regions. NOAA Center for Tsunami Research (NCTR) developed a Pacific-Basin 30sec grid, derived primarily from the Smith and Sandwell grid and the SRTM30_PLUS grid, with amendments in areas where NCTR has better bathymetry. This comprehensive dataset covers the entire Pacific Ocean and part of the Arctic Ocean from E120° to W68°, and S80° to N80°.

While developing bathymetric and topographic grids for specific coastal communities, NCTR has been collaborating with NGDC on the Tsunami Inundation

Gridding Project since 2005 to build high-resolution digital elevation models (DEMs) for more U.S. coastal regions, and satisfy the needs of tsunami forecast model development in the near future. Currently, the finished datasets, along with the associated documentation, are downloadable in ESRI ArcGIS ASCII grid format at http://www.ngdc.noaa.gov/dem/.

The Monterey DEM was delivered to PMEL by NGDC in January of 2008 at a grid resolution of 1/3 arc sec for areas between latitudes of 122.52°W - 121.52°W, and latitudes of 36.09°N - 37.11°N (Taylor et al., 2008). Data sources used by NGDC to derive the Monterey DEM include NOAA's National Ocean Service (NOS), Office of Coastal Survey (OCS) and Coastal Services Center (CSC), California State University Seafloor Mapping Laboratory, the U.S. Geological Survey (USGS), and the California Department of Fish and Game Marine Region GIS unit (CDFG). The horizontal and vertical datum of the dataset are the World Geodetic System 1984 (WGS 84) and the mean high water, respectively. The spatial resolution ranges from 1 m to 1 km for the bathymetric datasets, and 2.5 m to ~ 8.3 m (1/3 arc second) for the topographic datasets (Taylor et al., 2008).

Bathymetry and topography implemented in the Monterey forecast model are derived from NGDC's DEM described above, which is deemed as the best-available elevation model for Monterey at the time when it was developed. When new digital elevation models become available, forecast models may be updated and the new results will be posted at http://nctr.pmel.noaa.gov/forecast_reports/.

6.1.3 Model Setup

Figures 3 to 5 show the computational grids, derived from the aforementioned Monterey DEMs, of the reference inundation model and the optimized forecast model. Figures 3 shows the computational domain of outermost grid, A grid, covers most of coastlines of California. The A grid has a grid resolution of 36 arc seconds (~ 1,080 m) for the reference model (**Figure 3a**), and a grid resolution of 2 arc minutes (~ 3,740 m) for the forecast model (**Figure 3b**). Both A grids are bounded at a water depth greater than 4,000 m at their western boundaries. This way, the inundation models adopt most of the boundary conditions in the deep water from the pre-computed propagation database. For the same reason, the A grid is extended to 30°N to avoid settling the south boundary on the shallow continental shelf. The study area of Monterey is positioned in the middle of the A grid to minimize the influence of boundary forcing.

The intermediate grid, B grid, covers the entire Monterey Bay, and its western boundary is extended to water depths greater than 3,000 m. The B grid has a grid resolution of 3 arc seconds (~ 90 m) for the reference model (**Figure 4a**), and a grid resolution of 18 arc minutes (~ 540 m) for the forecast model (**Figure 4b**). In comparison with the A grids, the B grids provide more details of wave dynamics transitioned from deep water to shallow shelf, where the nonlinearity of waves is amplified the most. It's worth noting that the submarine canyon offshore of Monterey Bay is included in both B grids.

The innermost grid, C grid, covers the south part of Monterey bay and the entire Monterey Harbor. **Figures 5** indicates that the coast of Monterey Bay is featured with with a sloping beach with gradual decrease of water depth cross-shore. The contours of the water depth are nearly parallel to the shoreline, implying less complex directionality and nonlinearity of the tsunami wave dynamics. This bathymetric setting allows us to use a small C-grid coverage for the forecast model (**Figure 5b**) in comparison with that for the reference model (**Figure 5a**) since reducing computational time is also major consideration in development of a forecast model.

Table 2 provides the details of model setup and input parameters for all grids of both models. It's worth noting that the main difference between the forecast model and the reference model lies in the grid resolution implemented in each grid. In comparison with the forecast model, the reference model employs denser grid spacing, and larger computational domains (**Table 2**). The main purpose of developing a reference model is to provide more accurate description of the bathymetry and topography, and thus more accurate modeling results that a corresponding forecast model can refer to. As indicated in this table, the reference model takes about 1,500 min of CPU time to finish a 4-hour simulation because of finer grid resolutions and larger computational domains. The forecast model needs only 10.4 min to accomplish the same 4-hour run, and is therefore much more operationally efficient. This study also examines the model accuracy of the forecast measured in reference to the reference model.

6.2. Results and Discussions

6.2.1 Model Validation
The deep-ocean tsunameter array (also named as Deep-Ocean Assessment and Report of Tsunami (DART) in the United States) has been playing a critical role in tsunami detection and measurements. These real-time waveforms of tsunami are used to estimate tsunami sources while a tsunami is still in progress. As aforementioned, previous studies have shown successful applications of NOAA's tsunami forecast system to obtain the tsunami sources from real-time DART measurements, which is subsequently used to provide real-time propagation and coastal inundation forecast. Since 2003, these real-time inversions of tsunami sources have provided forecast accuracies up to 90% of the tsunami waveforms at distant coastlines. In this study, both the forecast model and the reference model for Monterey will be validated using 11 historical events. These events include the 4 October 1994 Kuril, the 10 June 1996 Andreanof, the 23 June 2011 Peru, the 3 May 2006 Tonga, the 15 November 2006 Kuril, the 13 January 2007 Kuril, the 1 April 2007 Solomon, the 15 August 2007 Peru, the 29 September 2009, the 27 February 2010 Chile, and the 11 March 2011 Japan. Except for the 11 events, the great 1964 Alaska tsunami also produced notable wave amplitude up to 1 m. The distinct tsunami waves registered by Monterey tide station during the 1964 event are valuable to validate the Monterey forecast model due to its high signal-to-noise ratio compared to other events. This study also computed the destructive tsunamis of 1 April 1946 Unimak, to demonstrate the wave dynamics at the coast of Monterey. **Figure 6** provides an overview of the earthquake epicenters of these historical events. **Table 3** provides details of tsunami source configuration for all historical events used for model validation in this study. All tsunami

sources are inverted from tsunami waveforms recorded at deep-ocean DARTs, or at tide gauges for events occurred long before DARTs (such as the 1 April 1946 Unimak and 27 March 1964 Alaska). The last column in Table 3 shows the source combination of each event on the basis of tsunami propagation database. It's worth noting that some of these source combinations were obtained in real time, some were obtained using an older propagation database, and the others were obtained in hindcast studies.

Figures 7 to 18 show good agreement between model results and observations for most of the events with sizable signal-to-noise ratio in the observations. The model time series of the 27 March 1964 Alaska tsunami computed by the forecast model is excellent in comparison with the observations up to hours after tsunami arrival, except for some phase shifts and slightly larger wave amplitude due to the uncertainty of the tsunami source. The time series of the reference model shows larger amplitude with a maximum of 2.3 m in comparison that obtained forecast model and observations. Figure 7 (b) and (d) show that the computed tsunami amplitudes in the reference model are about 40% larger than those in the forecast model along the coastline of Monterey. According to historical accounts at Monterey during the 28 March 1964 Alaska tsunami, there was no noticeable damage along the coastline of Monterey. It gives more credits to the forecast model that shows no inundation at Monterey (Figure 7d), while the reference model shows some flooding in the low-lying areas to the east of Monterey Harbor (Figure 7b). It should be noted here that the model discrepancy between the reference model and forecast model is small for all other historical events validated in this study, meaning it is an event-dependent, instead of a systematic, modeling issue. This issue is currently under investigation and will be addressed in a future update of this report.

Real-time DART measurements were used to derive valid tsunami sources during the events of 3 May 2006 Tonga, 15 November 2006 Kuril Islands, 13 January 2007 Kuril Islands, 15 August 2007 Peru, the 29 September 2009, the 27 February 2010 Chile, and the 11 March 2011 Japan. The computed time series at the Monterey tide station for these events show good agreement with the first several hours of measurements for the 2006 Tonga, 2007 Kuril, 2007 Peru, 2010 Chile and 2011 Tohuku (Figures 11a, 13a, 14a, 16a and 17a). Misfits between model results and measurements for some events are either due to low signal-to-noise ratio of the tsunami waveforms (Figures 8a, 10a, and 15a), or because the tide gauge was not functioning properly during the event, such as the 15 November 2006 tsunami (Figure 12a). It's worth mentioning that the comparison between model and observation is excellent for the 4 October 1994 Kuril tsunami, even though this tsunami source was not inverted from DART measurements.

When comparing modeling results, we can see minor discrepancies in the first 4 to 5 waves between the reference model and forecast model. However, small offsets in both amplitude and phase appear in the late waves, which are expected between models using different spatial and temporal resolutions. The comparison between model and observation for the 2010 Chile (Figure 16) and 2011 Japan (Figure 17) events are excellent, in particular the reference model seems to reproduce the resonance patter well inside Monterey Bay. In comparison with the forecast model, the reference model employs a grid resolution of three times higher to adequately describe the local

bathymetric and topographic features, and thus able to enhance the modeling capability in capture of the late waves. The reference model provides model reference for the computational accuracy of its optimized version, the tsunami forecast model. Despite the differences in the late waves (i.e. six hours after the first tsunami arrival), one can see that the main characteristics of the tsunami waves, such as the maximum wave amplitude and the wave period, are accurately computed in the forecast model. In comparison with a reference model, the major advantage of a forecast model is its computational efficiency, about 150 times less time consuming (**Table 2**), while still able to achieve similar model accuracy.

The maximum computed current speed at Monterey is generally small offshore. In spite of the flow speed at the headland northwest of Monterey Harbor, the computed results show larger current speed at the entrance of Monterey Harbor as well as inside the boat harbor, indicating potential harbor damages due to strong current. Strong current was responsible for significant damage in the Crescent City boat harbor during the 15 November 2006 Kuril Islands tsunami (Kelly et al., 2006; Uslu et al., 2007). For the 1964 Alaska tsunami, the computed wave current speed by forecast model is about $0.8 - 1.0$ m/s ($1.6 - 2.0$ knots) near the entrance of Monterey harbor and inside the boat harbor (**Figure 7e**), whereas the current speed induced by the 1946 Unimak tsunami is about half of that (**Figure 18e**).

6.2.2 Model stability tests using synthetic tsunami events

Model stability of the forecast model is evaluated using 42 synthetic events, 40 large source scenarios of M_w 9.3, 1 small source scenario of M_w 7.5, and one "no-wave" scenario of Mw 4.8, generated in the source zones around the Pacific Rim (**Table 4**). Each M_w 9.3 scenario consists of a combination of 20 unit sources covering a rupture area of 1000 km by 100 km with a uniform 28.4 m slip on each unit source A M_w 9.3 scenario imitates an equivalent or greater event of the 2004 Indian tsunami, which caused severe devastation along the coastline of Indian Ocean and accounted for hundreds of thousands of deaths. Our modeling experiences have shown that the singularities in the bathymetry and topography may cause model instabilities not only when the waves are large, but also when they are small enough to be taken over by accumulated numerical errors induced by those singularities. For such a reason, the present study also evaluates model stabilities due to a small synthetic tsunami scenario of M_w 7.5, which applies one-meter slip on one unit source (a source area of 100 km $\times$ 50 km). Another key test is the "no wave" scenario, 0.0001 m slip on one unit source in the present study, to examine the model stability under extremely small (close to null) wave forcing along the model boundaries. A successful no-wave test expects only wave activities in the same order of the boundary forcing without unreasonable amplification.

Figures 19 to 58 show the computational results of maximum computed wave amplitude and current speed for all synthetic scenarios. Each figure shows the computed time series at a warning point that best represents the location of the tide station, the results of maximum wave amplitude in all A, B, C grids, and the maximum current speed in the C grid. We note that no model instabilities were observed in all of these model runs, with or without tsunami inundation occurring. The M_w 9.3 scenario ACSZ 31-40

18

from central Aleutian-Alaska Subduction Zone produces the most severe tsunami strike along the Monterey coastline, while a M_w 9.3 event generated in the northern region of South America, such as CSSZ 41-50, has almost no impact at Monterey. Among all the M_w 9.3 scenarios, the computed maximum wave amplitude at the warning point ranges from 0.19 m in scenario CSSZ 41-50 to 5.2 m in scenario ACSZ 31-40. Similarly, the computed maximum wave trough at the warning point ranges from -0.23 m in CSSZ 41-50 to -7.6 m in scenario ACSZ 31-40. The computed maximum tsunami runup height reaches 7.3 m above mean high water (~ 7.8 m above mean sea level) in Monterey for scenario ACSZ 31-40. Considering most of the Monterey area has a land elevation of 8 m, a potential M_w 9.3 mega tsunami from central Aleutian-Alaska Subduction Zone may be catastrophic for this area. The fault area of ACSZ 31-40 is similar to the rupture area of the earthquake (M_w 9.2) that triggered the destructive 1964 Alaska tsunami, which however did not cause much damage in Monterey. The Mw 9.3 tsunami scenarios also reveal another two noticeable phenomena: (1) The B grid, covering the entire Monterey Bay, clearly shows that the tsunamis from all directions in the Pacific will tend to induce larger waves at north end of the Monterey Bay, where the City of Santa Cruz is located at, than at its south end where situates the City of Monterey. This has been confirmed by the historical destructive tsunamis of 1946 and 1964. The resonance modes of Monterey Bay triggered by tsunamis may be responsible for these effects (Tolkova and Power, 2011). (2) The modeling results show that the tsunamis from NTSZ, NVSZ, MOSZ and KISZ can induce large late waves that arrive 8 to 12 hours after the first arrival, and even 20 hours later if from CSSZ. Most of these late waves are possibly due to the reflected waves by the ocean ridges or islands in the Pacific.

The small synthetic scenarios generated negligible waves less than 1 cm at the warning point, and show no modeling instabilities (**Figures 59 and 60**). With little boundary forcing, the no-wave scenario produces negligible ripples at the order of 10^{-5} cm throughout the entire computational domain, meaning the present forecast model is robust to produce results without numerical amplification.

6.3. Summary and Conclusions

This study develops a tsunami forecast model for the community of Monterey, California. The developed model will be implemented into NOAA's tsunami forecast system to provide real-time modeling forecast of the water elevation, current speed, runup, and inundation for the coastal community at Monterey and its vicinity. This study discusses details of each individual component of the tsunami forecast model, including the bathymetry and topography, the basic model setup and model parameters. The forecast model employs grids as fine as 30 m and can accomplish 4-hour simulation after tsunami arrival in 10 minutes of CPU time. Using grids as fine as 8 m, a reference inundation model is also developed to provide model reference for the forecast model.

Model validations are carried out for both the Monterey forecast model and the reference model using 13 historical tsunami events to compare modeling results and the observations at the tide station. The computed time series are comparable with historical records at the Monterey tide gauge, especially those of sizable signal-to-noise ratio. Model validation using historical tsunamis shows these events did not cause serious

inundation along the coastline of Monterey. This study tests the model stability of the forecast model using a total of 42 synthetic source scenarios from major subduction zones in the Pacific, including 40 Mw 9.3 scenarios, one Mw 7.5 scenario, and a Mw 4.8 scenario. These tests ensure the stability of the developed forecast model under the strike up to wave amplitude of 7.3 m along the coastlines of Monterey.

All model validation and stability tests demonstrated that the developed tsunami forecast model and reference model for Monterey are accurate, robust and efficient. The forecast model of Monterey Bay is ready to be implemented in short-term real-time tsunami forecast. Both the forecast model and the reference model also have potential values for long-term tsunami inundation study.

Acknowledgments

Figures:

Figure 1. Probabilities of Mw 6.7 or stronger earthquakes occurring on faults in the San Francisco Bay Region during 2001-2031, where the probability of occurrence on each fault in indicated in ovals, and colors indicate the corresponding probabilities of each fault segment. Credit: Working Group on California Earthquake Probabilities (2003)

Figure 2 Aerial photo overlooking Monterey Harbor.

(a)

(b)

Figure 3 Bathymetry and topography of the outermost A grid for (a) the reference model and (b) the forecast model at Monterey, CA.

(a)
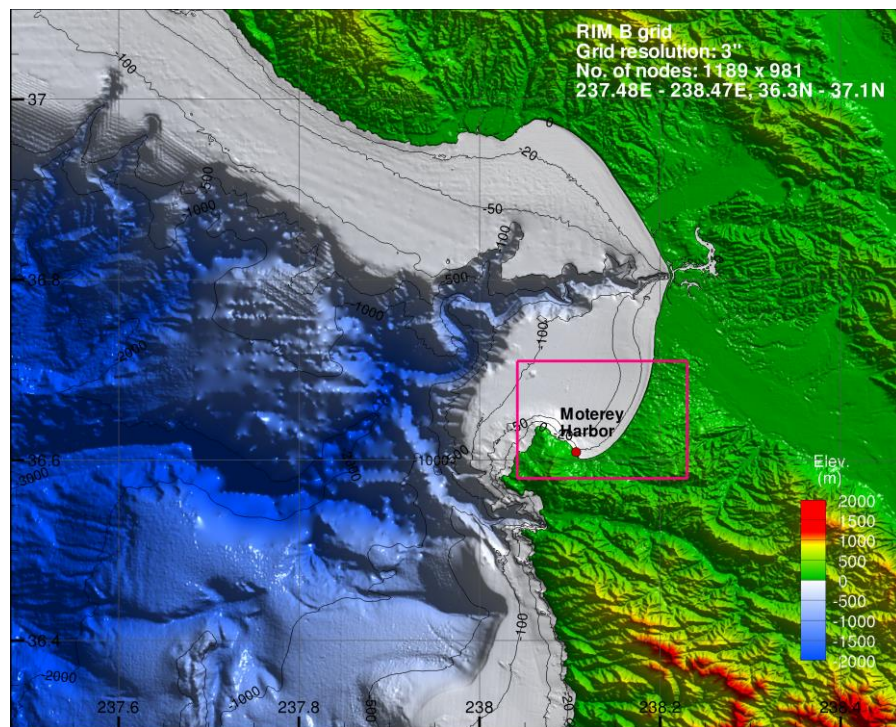
(b)
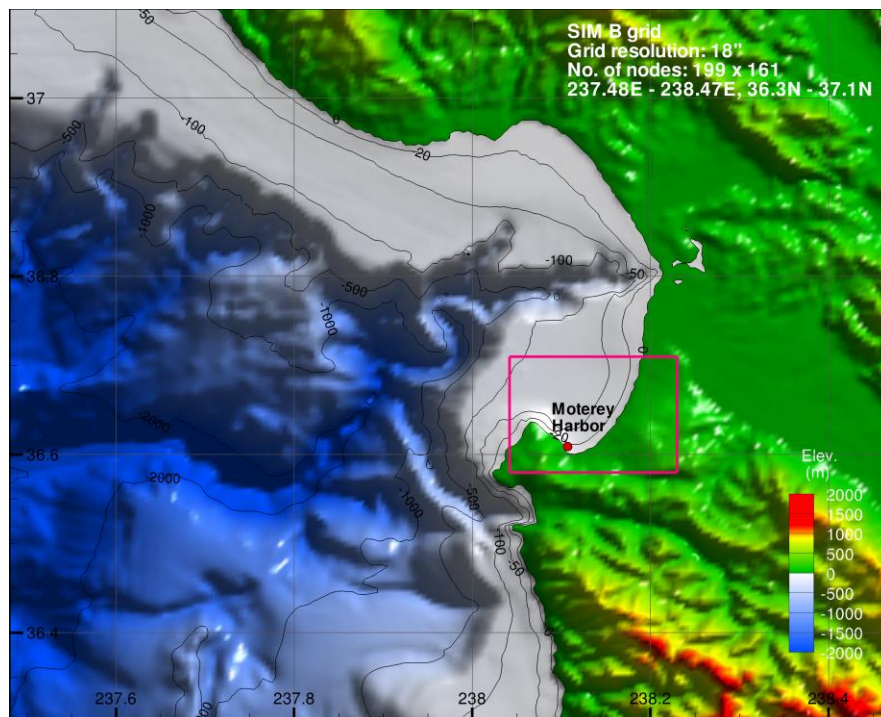
Figure 4 Bathymetry and topography of the intermediate B grid for (a) the reference model and (b) the forecast model at Monterey, CA.

(a)
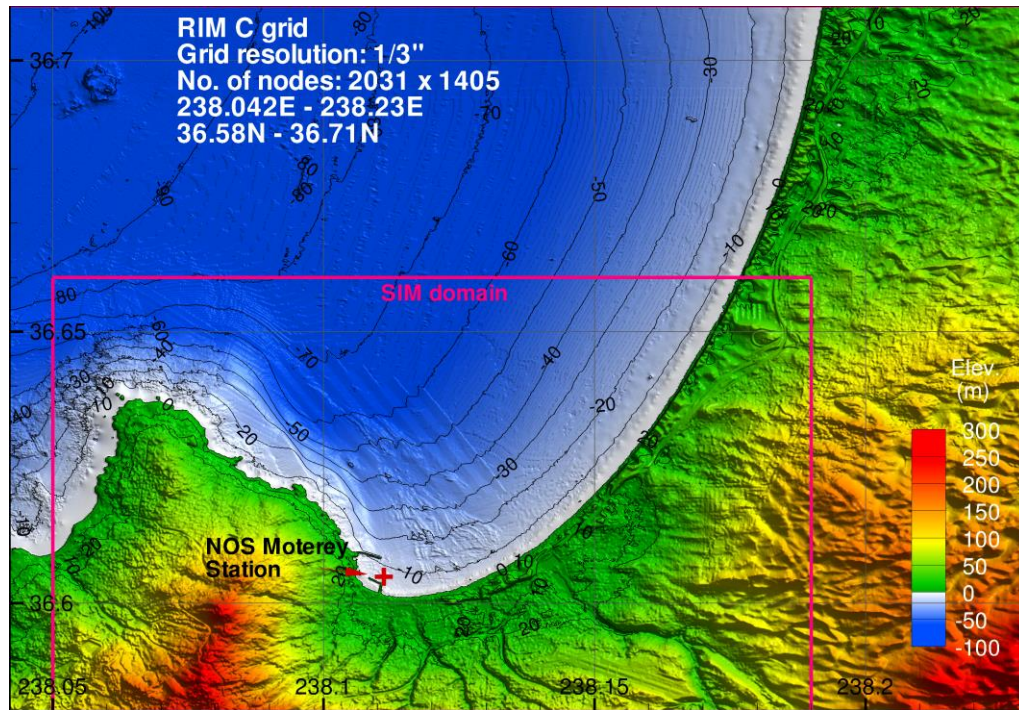
(b)
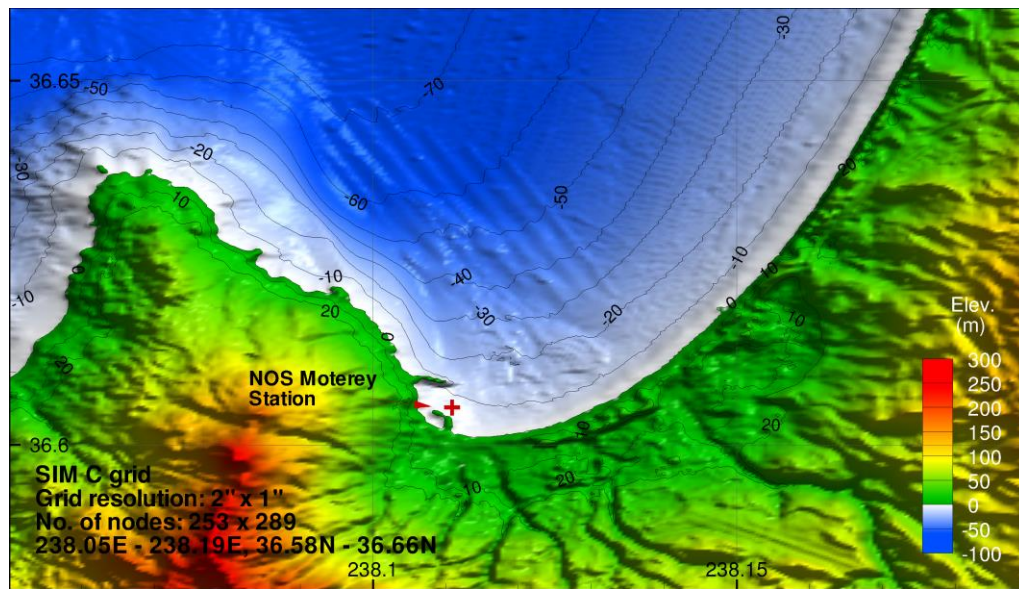
Figure 5 Bathymetry and topography of the innermost C grid for (a) the reference model and (b) the forecast model at Monterey, CA. The red box shown in (a) indicates the model domain of the C grid of the forecast model, shown in (b).
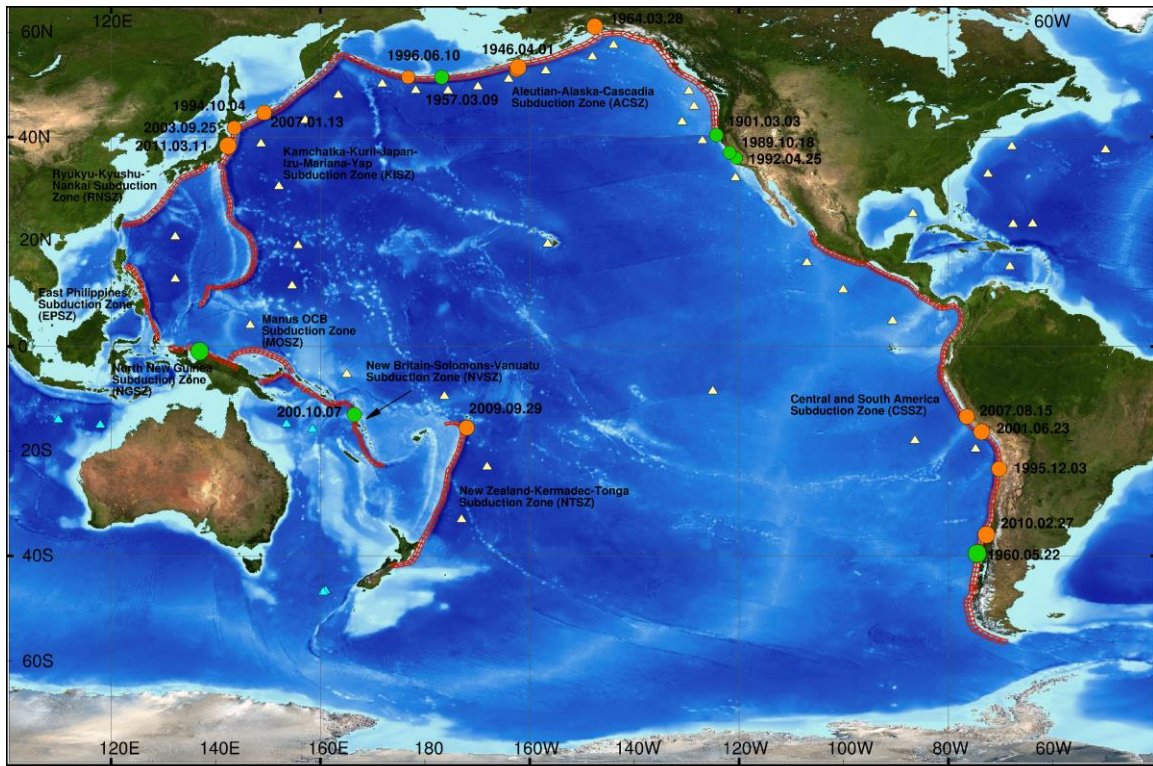
Figure 6 Location map of historical events.
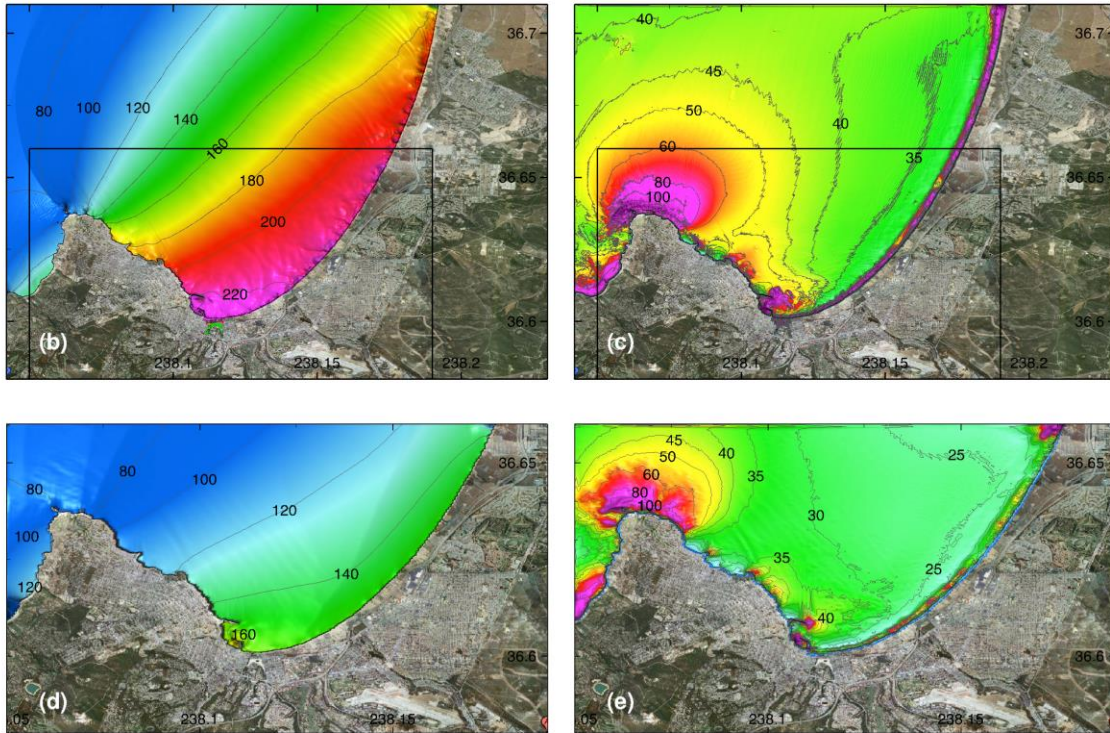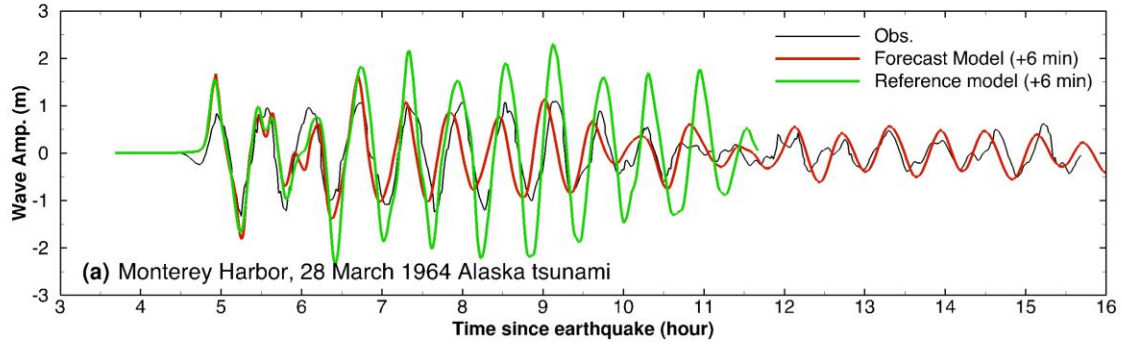
Figure 7 Model validation at Monterey for 28 March 1964 Alaska tsunami. (a) Computed and observed time series at Monterey tide station; (b) Computed maximum wave amplitude in grid C of the reference model; (c) Computed maximum current speed in grid C of the reference model; (d) Computed maximum wave amplitude in grid C of forecast model; (e) Computed current speed in grid C of forecast model. The black rectangular in (b) and (c) indicates the computational domain of forecast model grid C in (d) and (e).
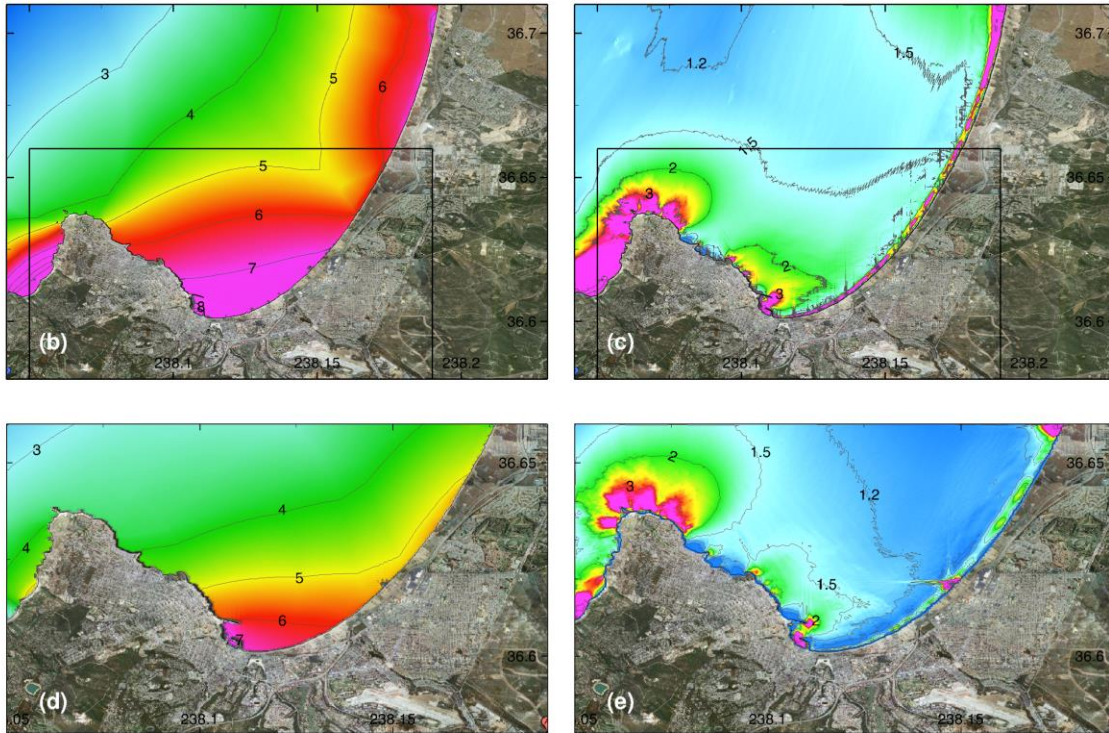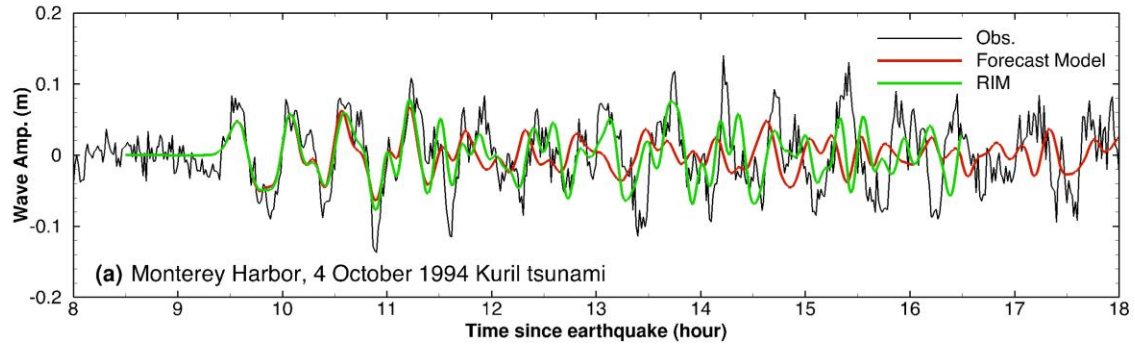
Figure 8 Model validation at Monterey for 4 October 1994 Kuril Islands tsunami. (a) Computed and observed time series at the Monterey tide station; (b) Computed maximum wave amplitude in C grid of the reference model; (c) Computed maximum current speed in C grid of the reference model; (d) Computed maximum wave amplitude in C grid of forecast model; (e) Computed current speed in C grid of forecast model. The black rectangular in (b) and (c) indicates the computational domain of forecast model C grid in (d) and (e).
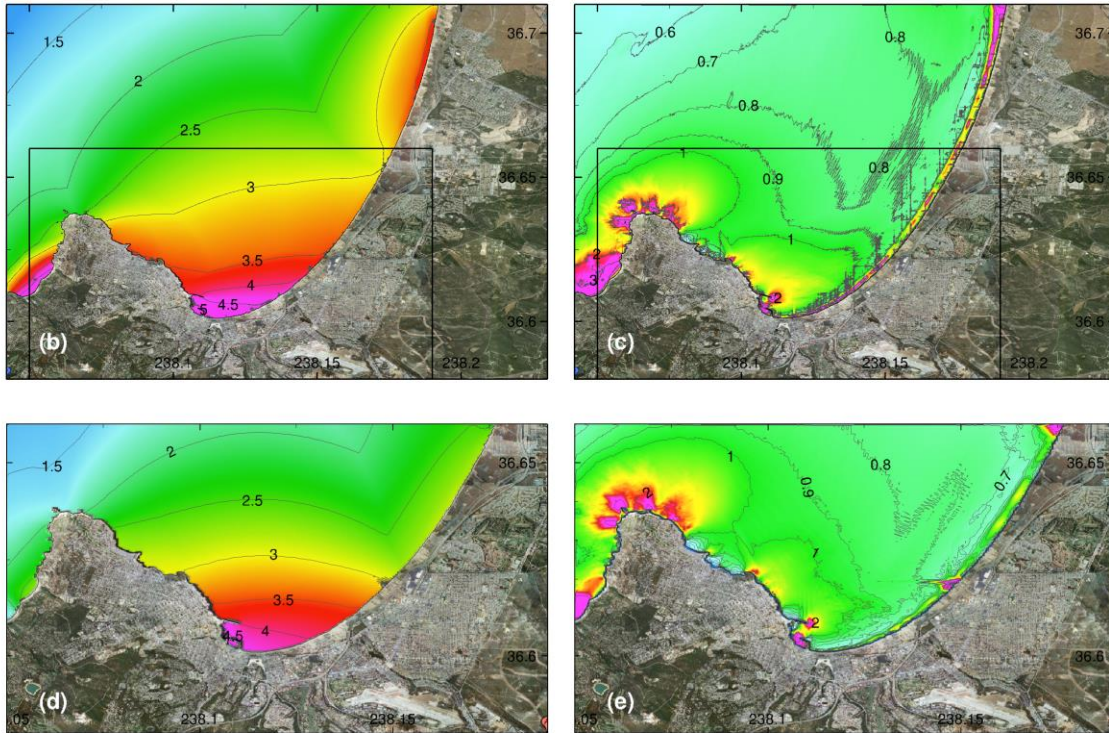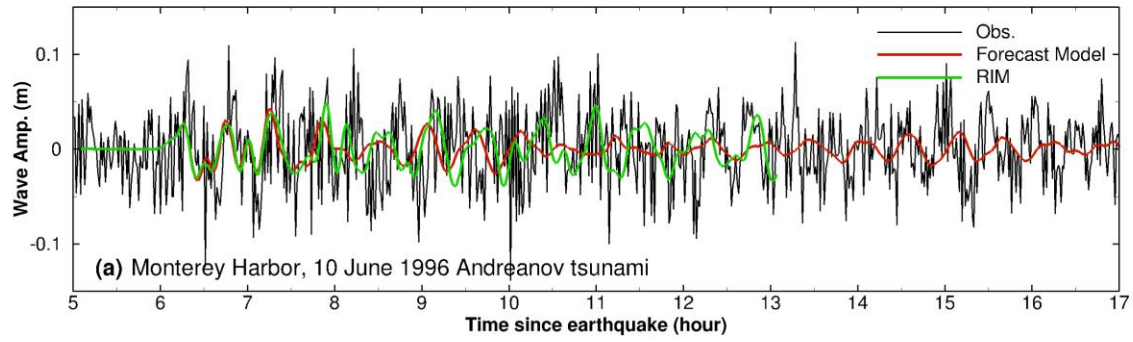
Figure 9 Model validation at Monterey for 4 October 1994 Kuril Islands tsunami. (a) Computed and observed time series at the Monterey tide station; (b) Computed maximum wave amplitude in C grid of the reference model; (c) Computed maximum current speed in C grid of the reference model; (d) Computed maximum wave amplitude in C grid of forecast model; (e) Computed current speed in C grid of forecast model. The black rectangular in (b) and (c) indicates the computational domain of forecast model C grid in (d) and (e).
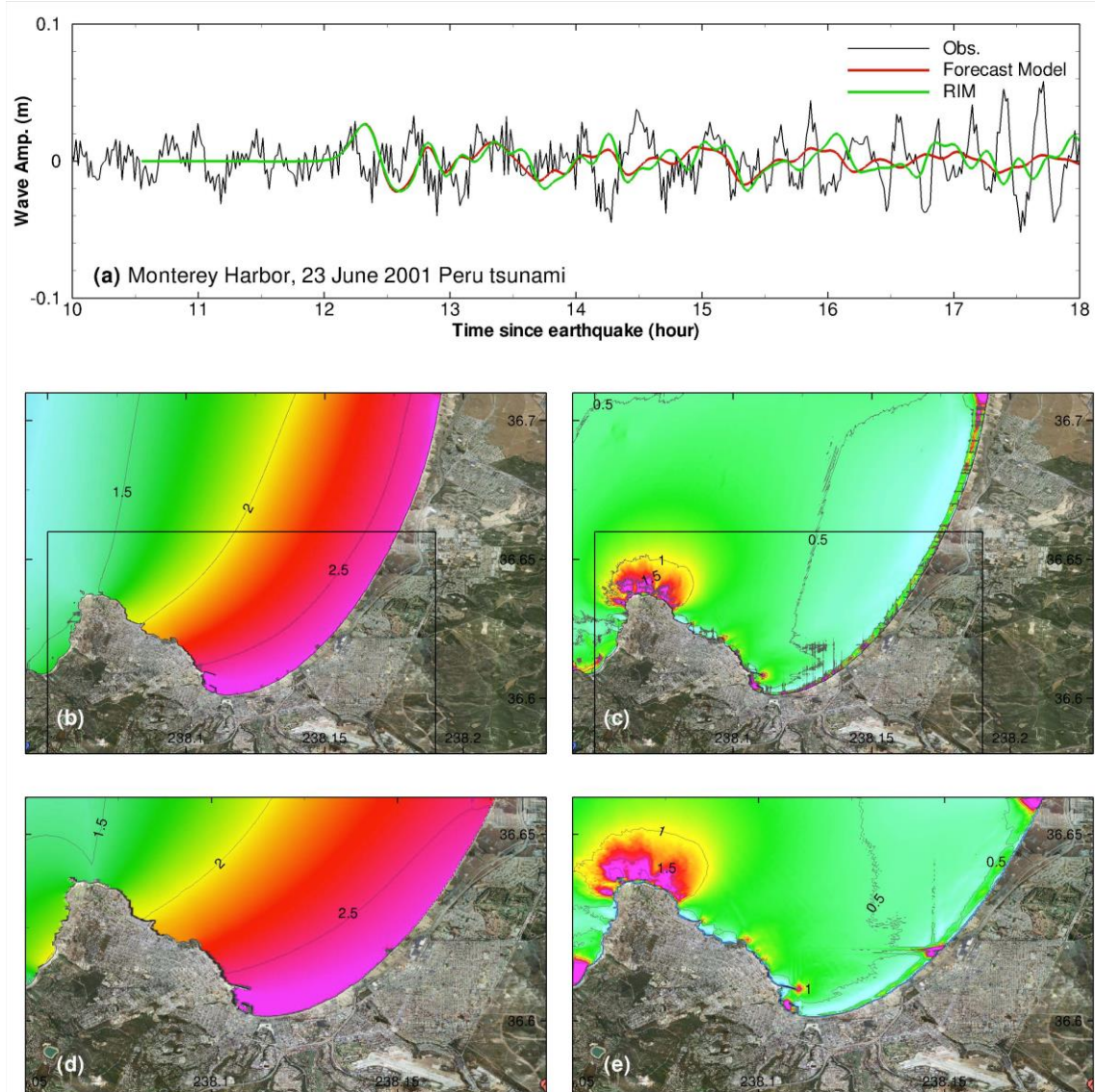
Figure 10 Model validation at Monterey for 23 June 2001 Peru tsunami. (a) Computed and observed time series at the Monterey tide station; (b) Computed maximum wave amplitude in C grid of the reference model; (c) Computed maximum current speed in C grid of the reference model; (d) Computed maximum wave amplitude in C grid of forecast model; (e) Computed current speed in C grid of forecast model. The black rectangular in (b) and (c) indicates the computational domain of forecast model C grid in (d) and (e).
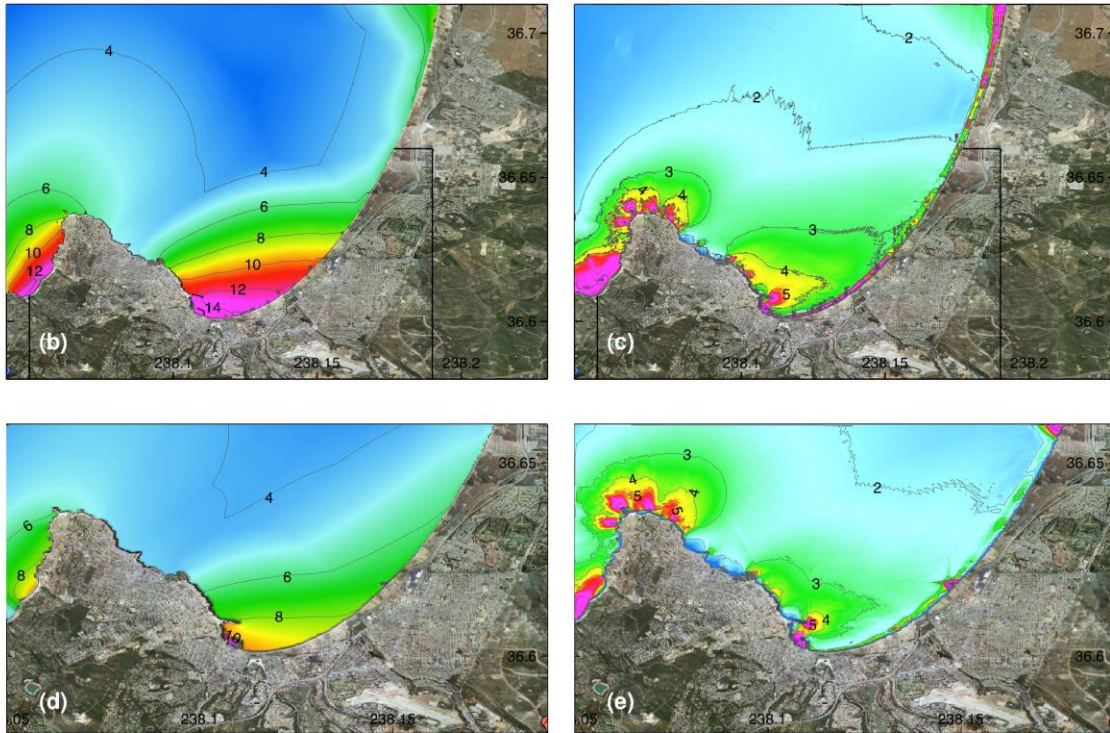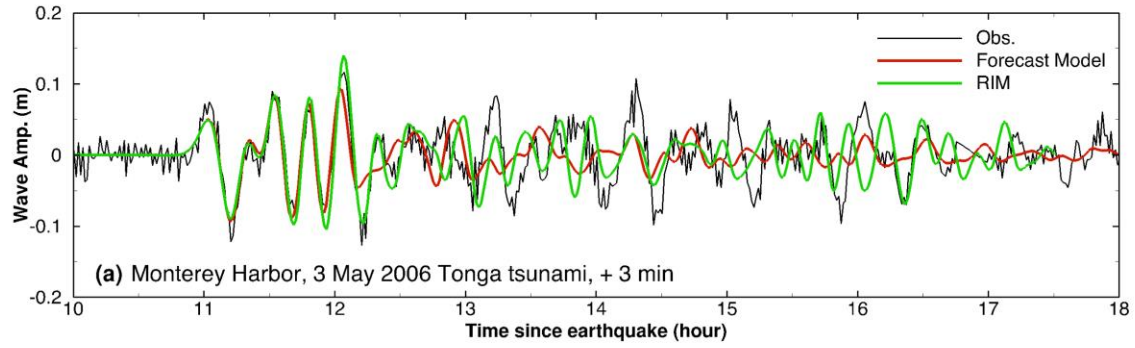
Figure 11 Model validation at Monterey for 3 May 2006 Tonga tsunami. (a) Computed and observed time series at the Monterey tide station; (b) Computed maximum wave amplitude in C grid of the reference model; (c) Computed maximum current speed in C grid of the reference model; (d) Computed maximum wave amplitude in C grid of forecast model; (e) Computed current speed in C grid of forecast model. The black rectangular in (b) and (c) indicates the computational domain of forecast model C grid in (d) and (e).
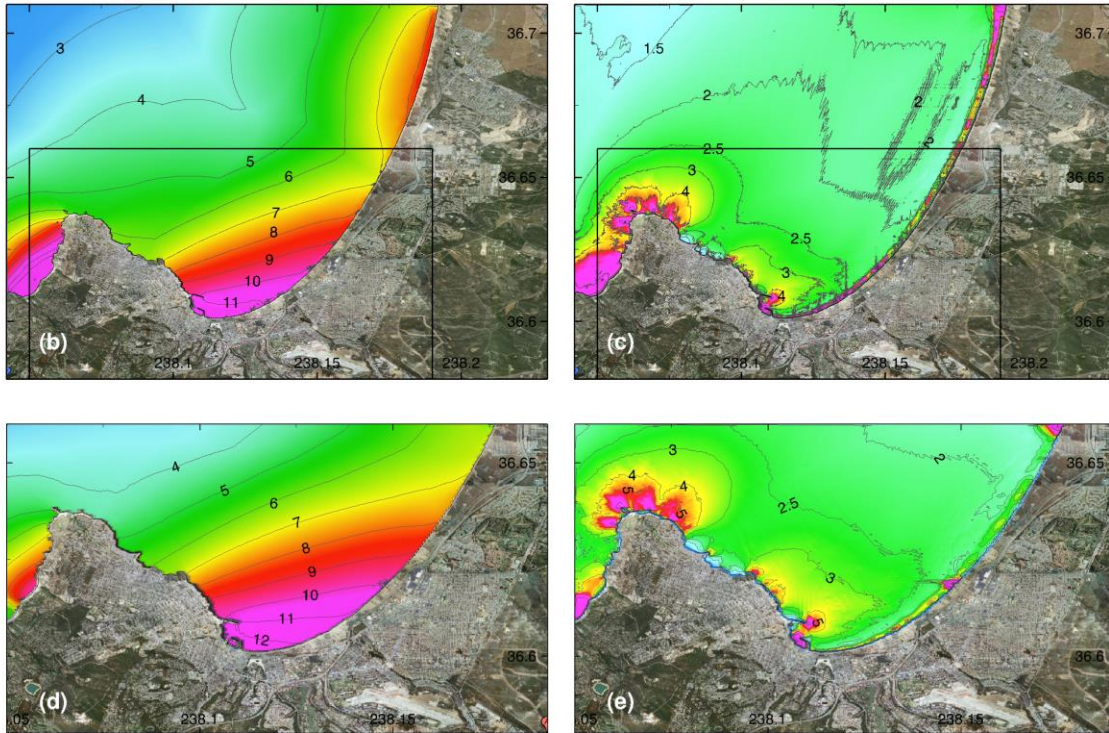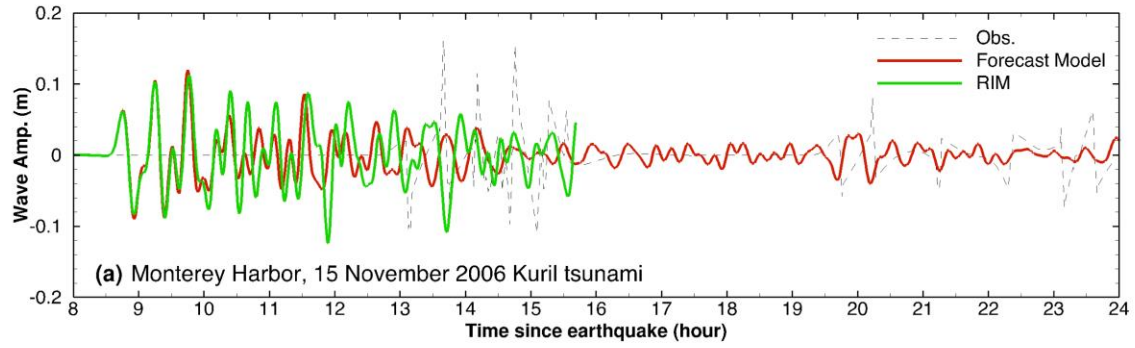
Figure 12 Model validation at Monterey for 11 November 2006 Kuril Islands tsunami. (a) Computed and observed time series at the Monterey tide station; (b) Computed maximum wave amplitude in C grid of the reference model; (c) Computed maximum current speed in C grid of the reference model; (d) Computed maximum wave amplitude in C grid of forecast model; (e) Computed current speed in C grid of forecast model. The black rectangular in (b) and (c) indicates the computational domain of forecast model C grid in (d) and (e).
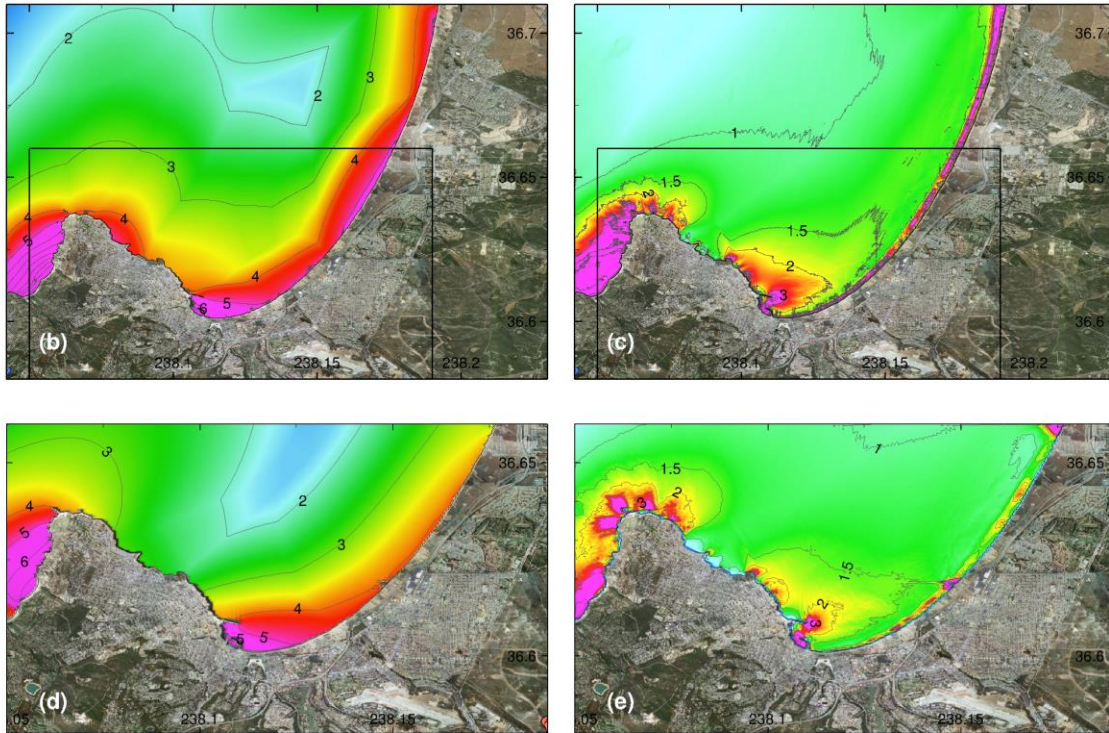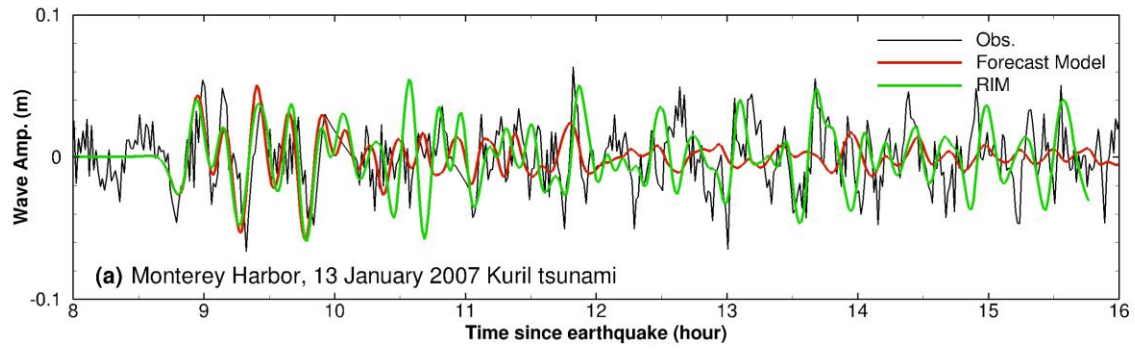
Figure 13 Model validation at Monterey for 13 January 2007 Kuril Islands tsunami. (a) Computed and observed time series at the Monterey tide station; (b) Computed maximum wave amplitude in C grid of the reference model; (c) Computed maximum current speed in C grid of the reference model; (d) Computed maximum wave amplitude in C grid of forecast model; (e) Computed current speed in C grid of forecast model. The black rectangular in (b) and (c) indicates the computational domain of forecast model C grid in (d) and (e).
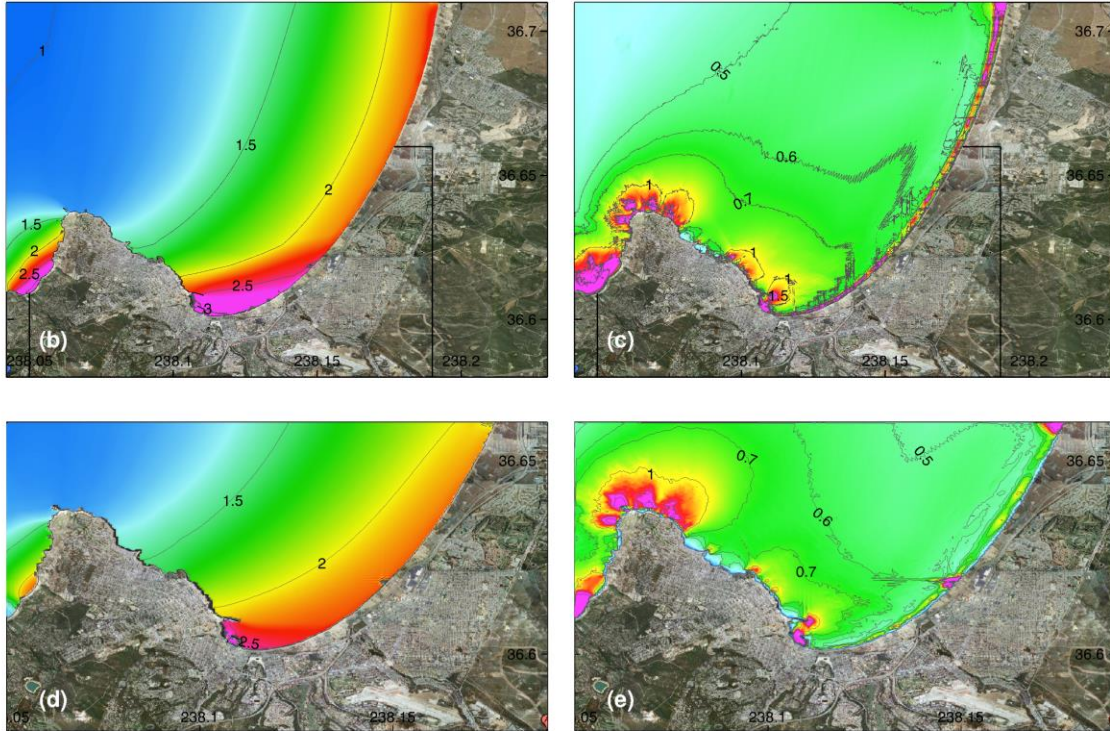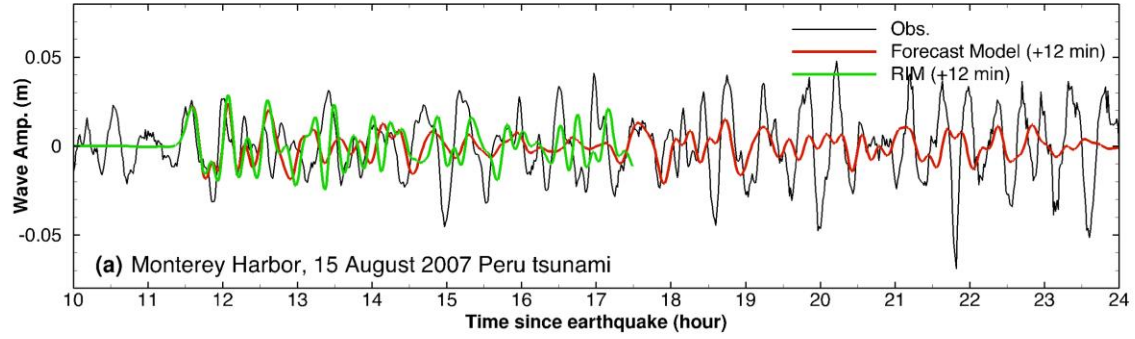
Figure 14 Model validation at Monterey for 15 August 2007 Peru tsunami. (a) Computed and observed time series at the Monterey tide station; (b) Computed maximum wave amplitude in C grid of the reference model; (c) Computed maximum current speed in C grid of the reference model; (d) Computed maximum wave amplitude in C grid of forecast model; (e) Computed current speed in C grid of forecast model. The black rectangular in (b) and (c) indicates the computational domain of forecast model C grid in (d) and (e).
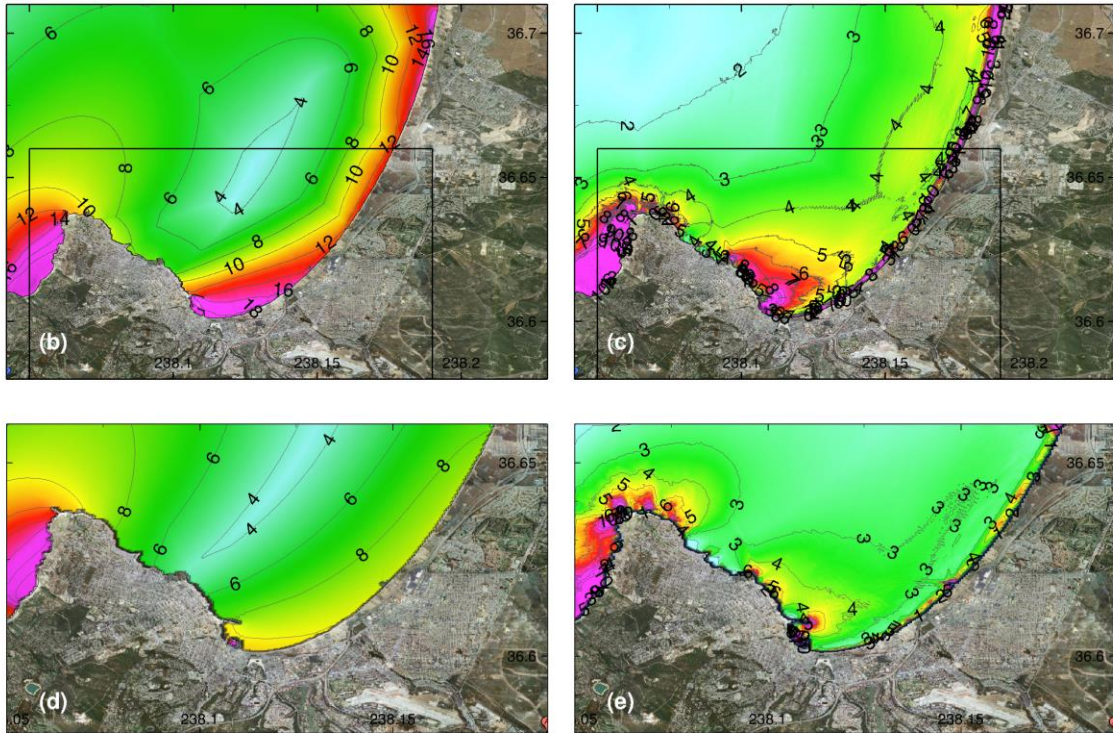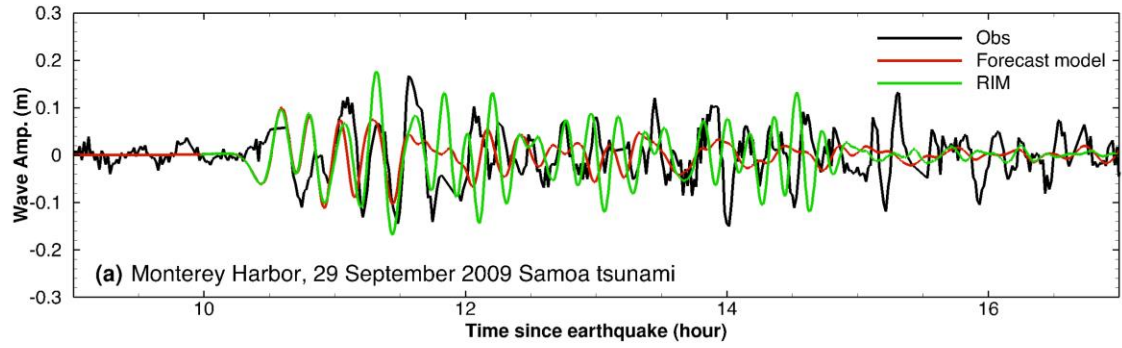
Figure 15 Model validation at Monterey for 29 September 2009 Samoa tsunami. (a) Computed and observed time series at the Monterey tide station; (b) Computed maximum wave amplitude in C grid of the reference model; (c) Computed maximum current speed in C grid of the reference model; (d) Computed maximum wave amplitude in C grid of forecast model; (e) Computed current speed in C grid of forecast model. The black rectangular in (b) and (c) indicates the computational domain of forecast model C grid in (d) and (e).
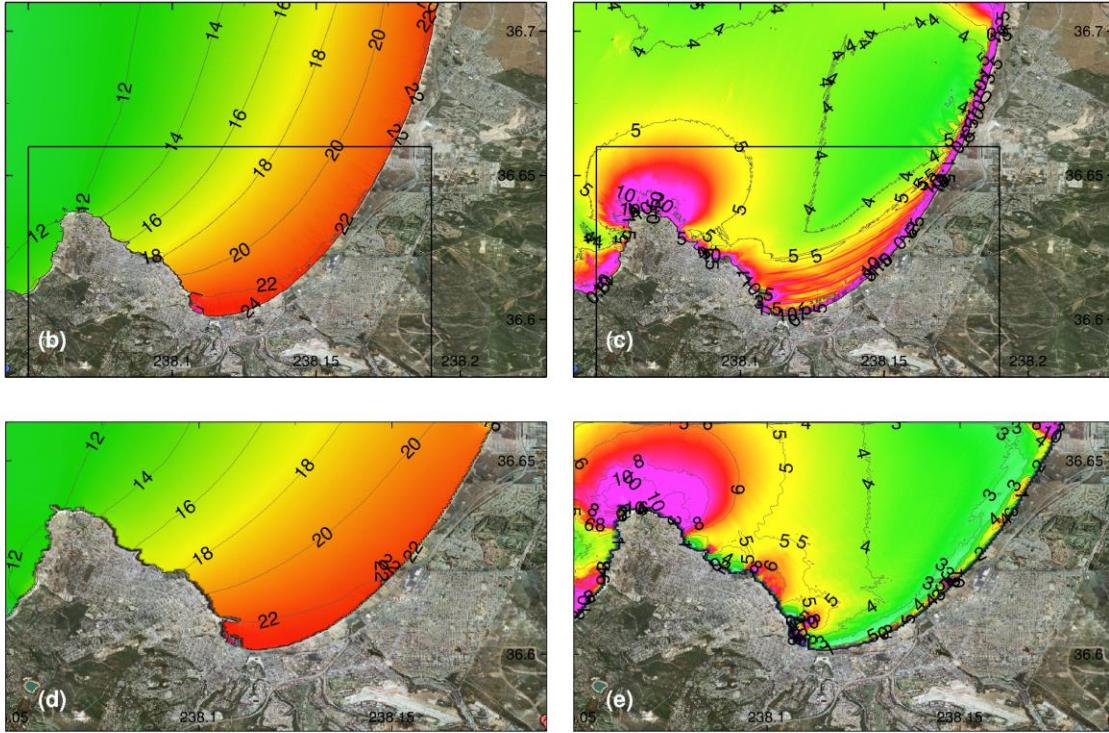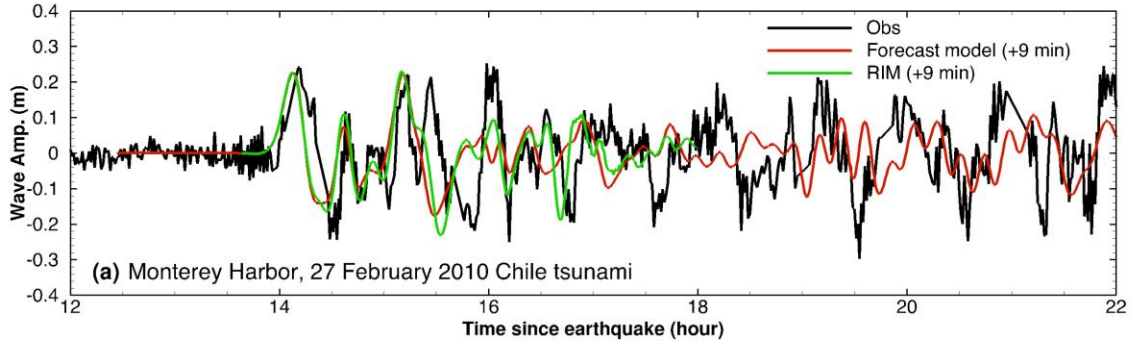
Figure 16 Model validation at Monterey for 27 February 2010 Chile tsunami. (a) Computed and observed time series at the Monterey tide station; (b) Computed maximum wave amplitude in C grid of the reference model; (c) Computed maximum current speed in C grid of the reference model; (d) Computed maximum wave amplitude in C grid of forecast model; (e) Computed current speed in C grid of forecast model. The black rectangular in (b) and (c) indicates the computational domain of forecast model C grid in (d) and (e).
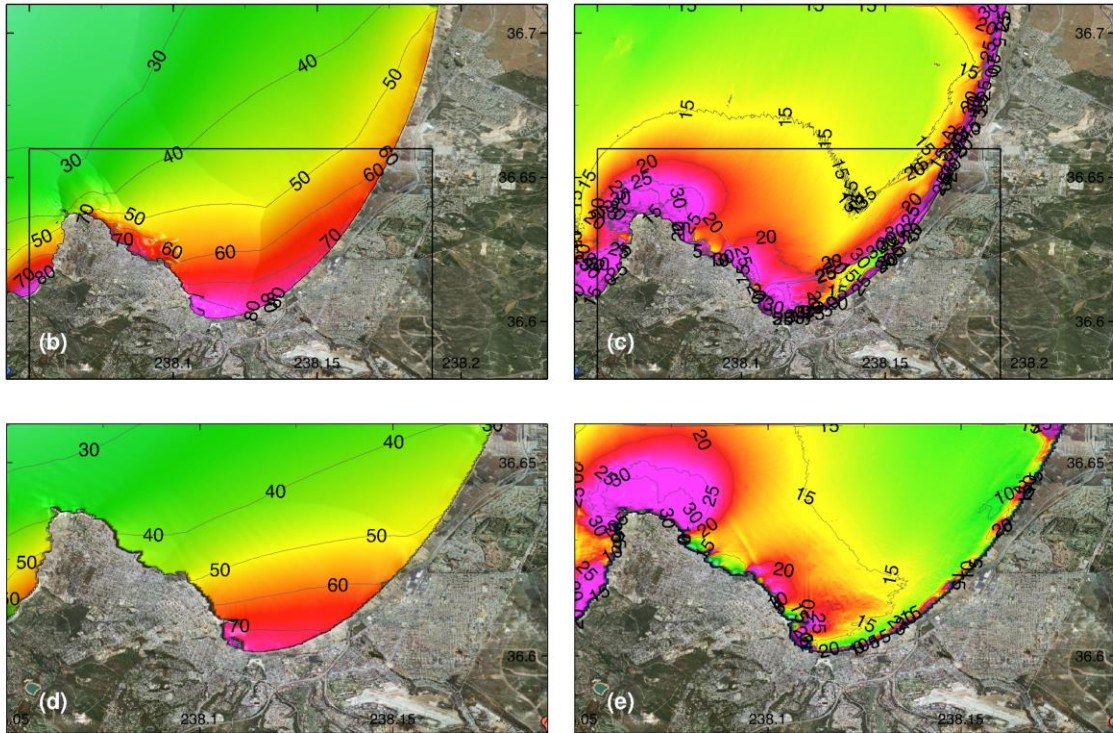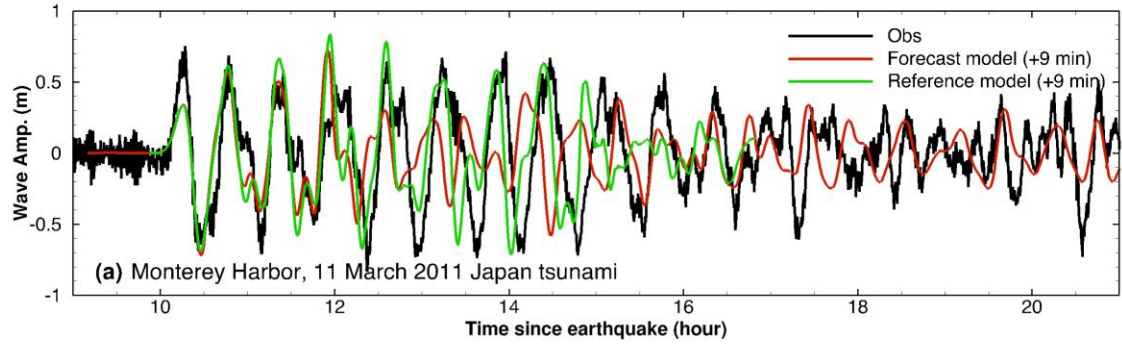
Figure 17 Model validation at Monterey for 11 March 2011 Japan tsunami. (a) Computed and observed time series at the Monterey tide station; (b) Computed maximum wave amplitude in C grid of the reference model; (c) Computed maximum current speed in C grid of the reference model; (d) Computed maximum wave amplitude in C grid of forecast model; (e) Computed current speed in C grid of forecast model. The black rectangular in (b) and (c) indicates the computational domain of forecast model C grid in (d) and (e).
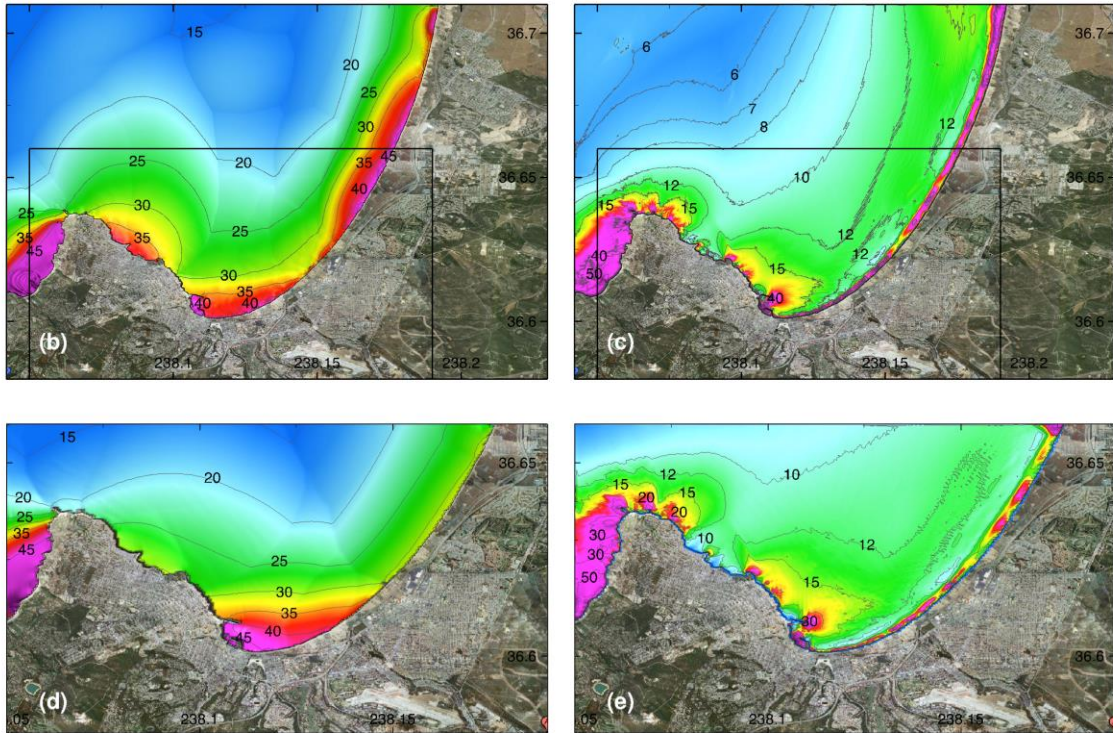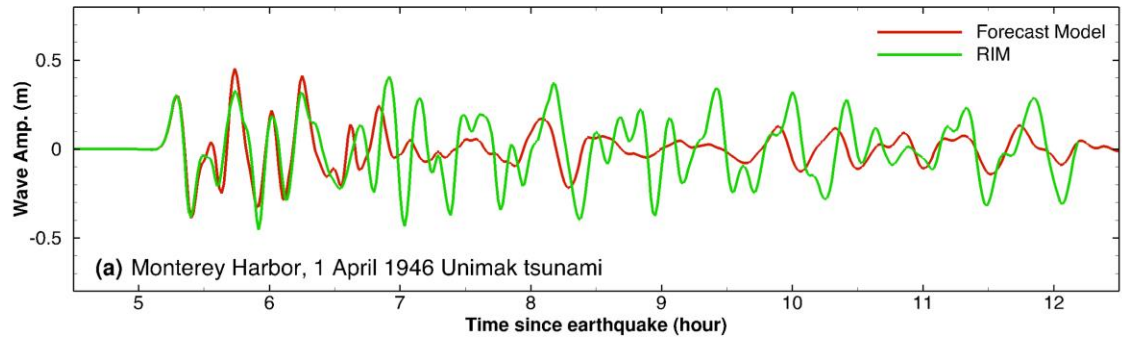
Figure 18 Model results at Monterey for 1 April 1946 Alaska tsunami. (a) Computed and observed time series at the Monterey tide station; (b) Computed maximum wave amplitude in C grid of the reference model; (c) Computed maximum current speed in C grid of the reference model; (d) Computed maximum wave amplitude in C grid of forecast model; (e) Computed current speed in C grid of forecast model. The black rectangular in (b) and (c) indicates the computational domain of forecast model C grid in (d) and (e).
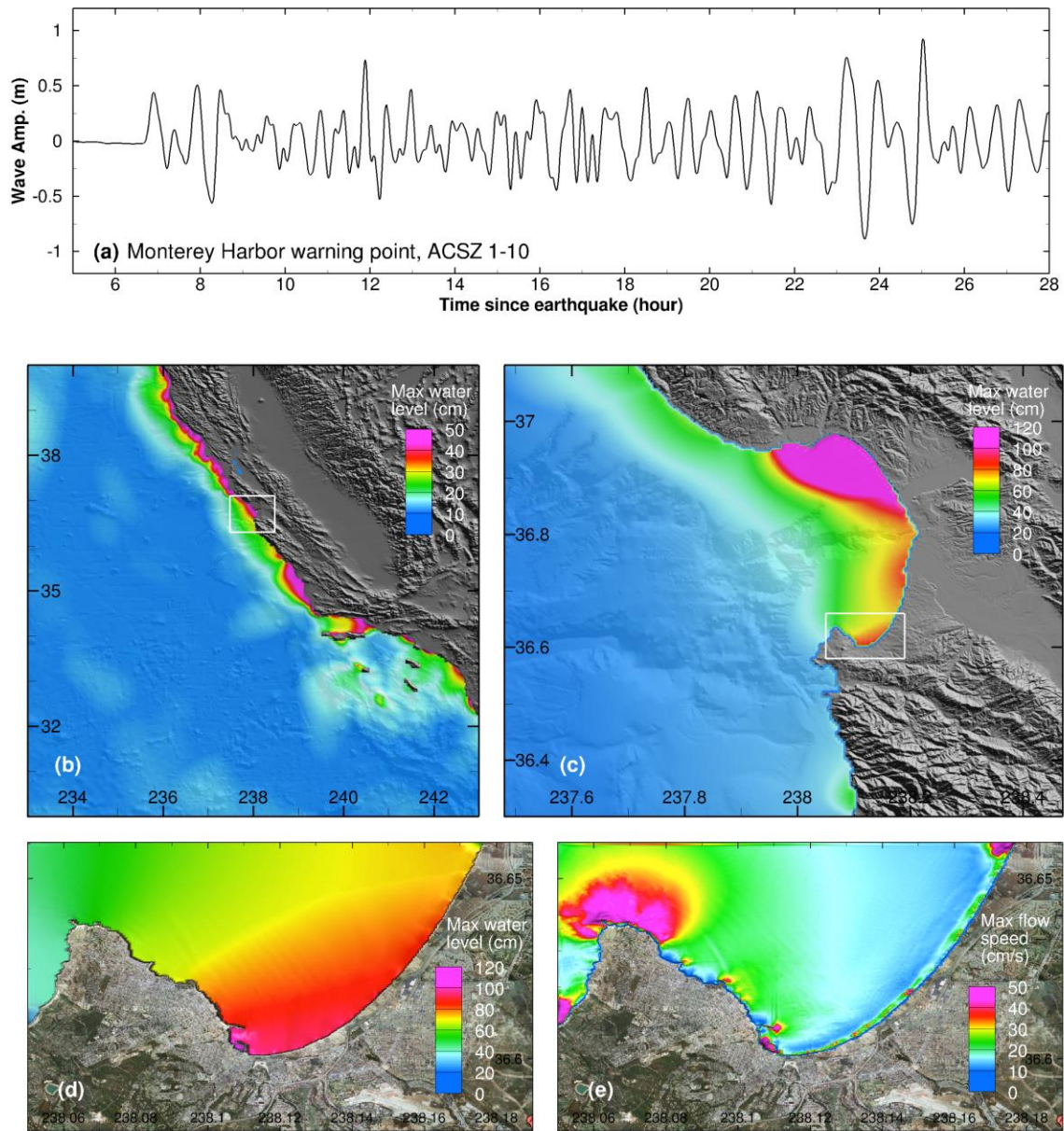
Figure 19 Model stability testing results at Monterey for synthetic mega tsunami scenario ACSZ 1-10. (a) Computed time series at the Monterey warning point; (b) Computed maximum wave amplitude in A grid of the forecast model; (c) Computed maximum current speed in B grid of the forecast model; (d) Computed maximum wave amplitude in C grid of the forecast model; (e) Computed current speed in C grid of the forecast model.
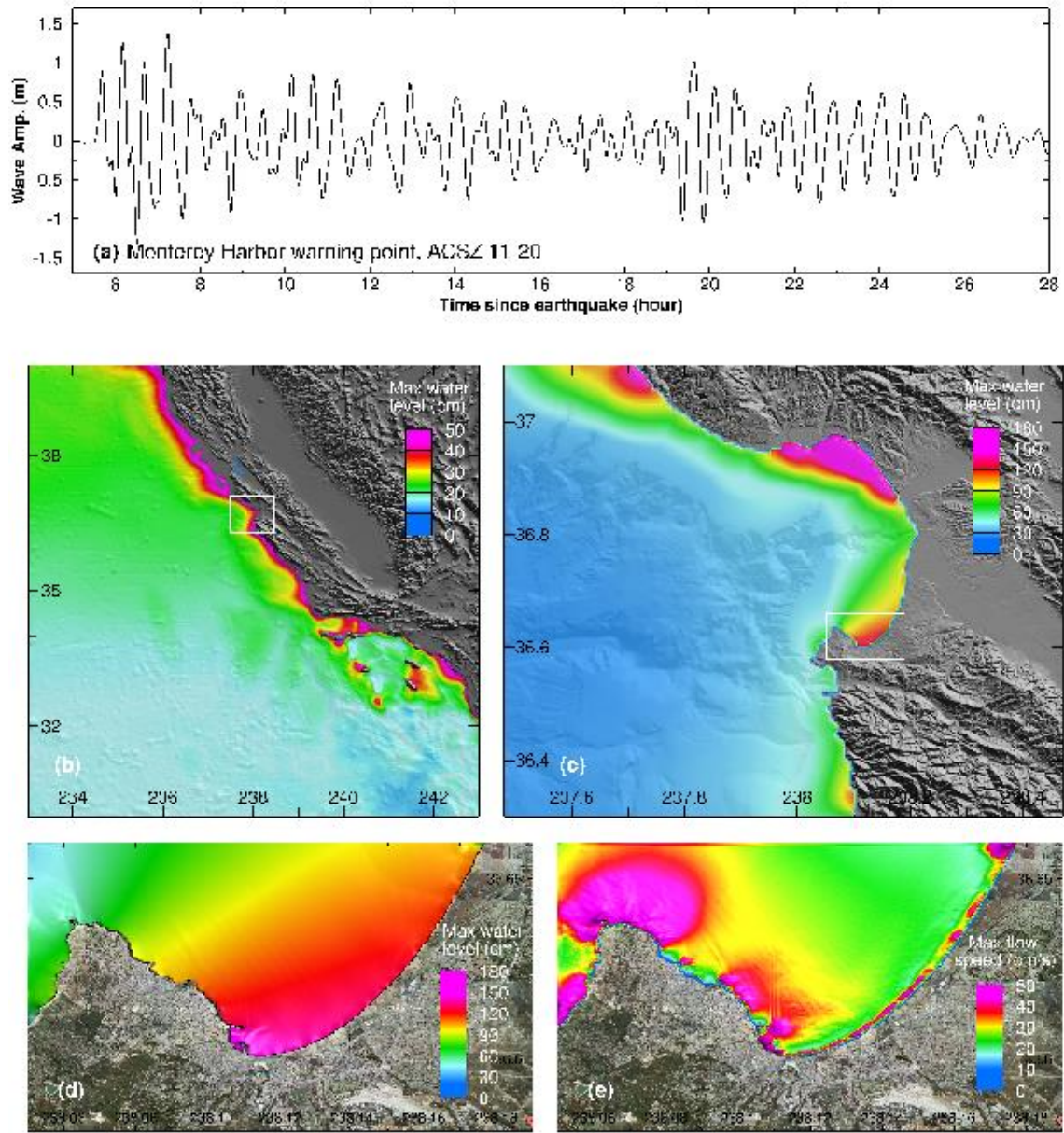
Figure 20 Model stability testing results at Monterey for synthetic mega tsunami scenario ACSZ 11-20. (a) Computed time series at the Monterey warning point; (b) Computed maximum wave amplitude in A grid of the forecast model; (c) Computed maximum current speed in B grid of the forecast model; (d) Computed maximum wave amplitude in C grid of the forecast model; (e) Computed current speed in C grid of the forecast model.
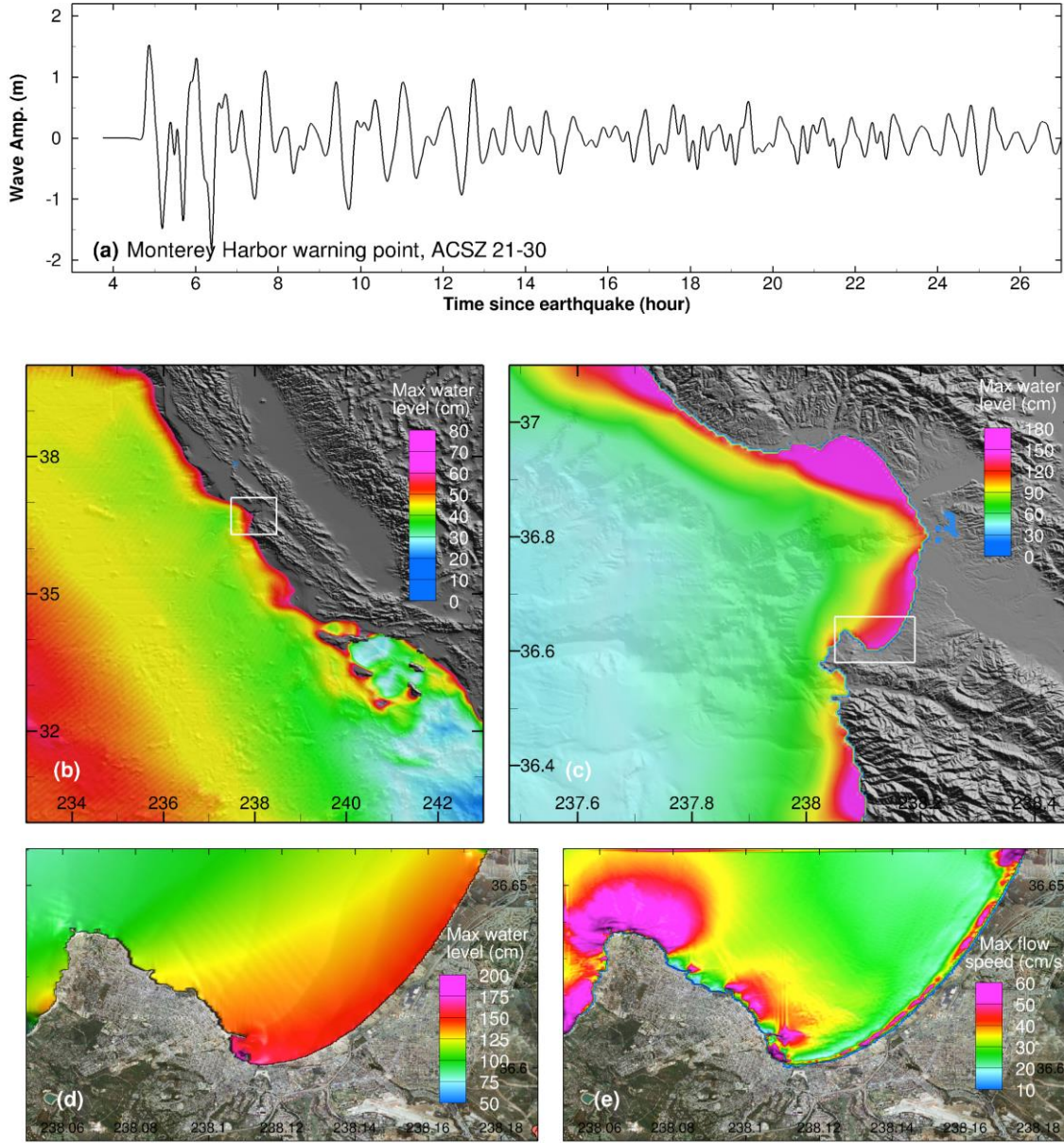
Figure 21 Model stability testing results at Monterey for synthetic mega tsunami scenario ACSZ 21-30. (a) Computed time series at the Monterey warning point; (b) Computed maximum wave amplitude in A grid of the forecast model; (c) Computed maximum current speed in B grid of the forecast model; (d) Computed maximum wave amplitude in C grid of the forecast model; (e) Computed current speed in C grid of the forecast model.
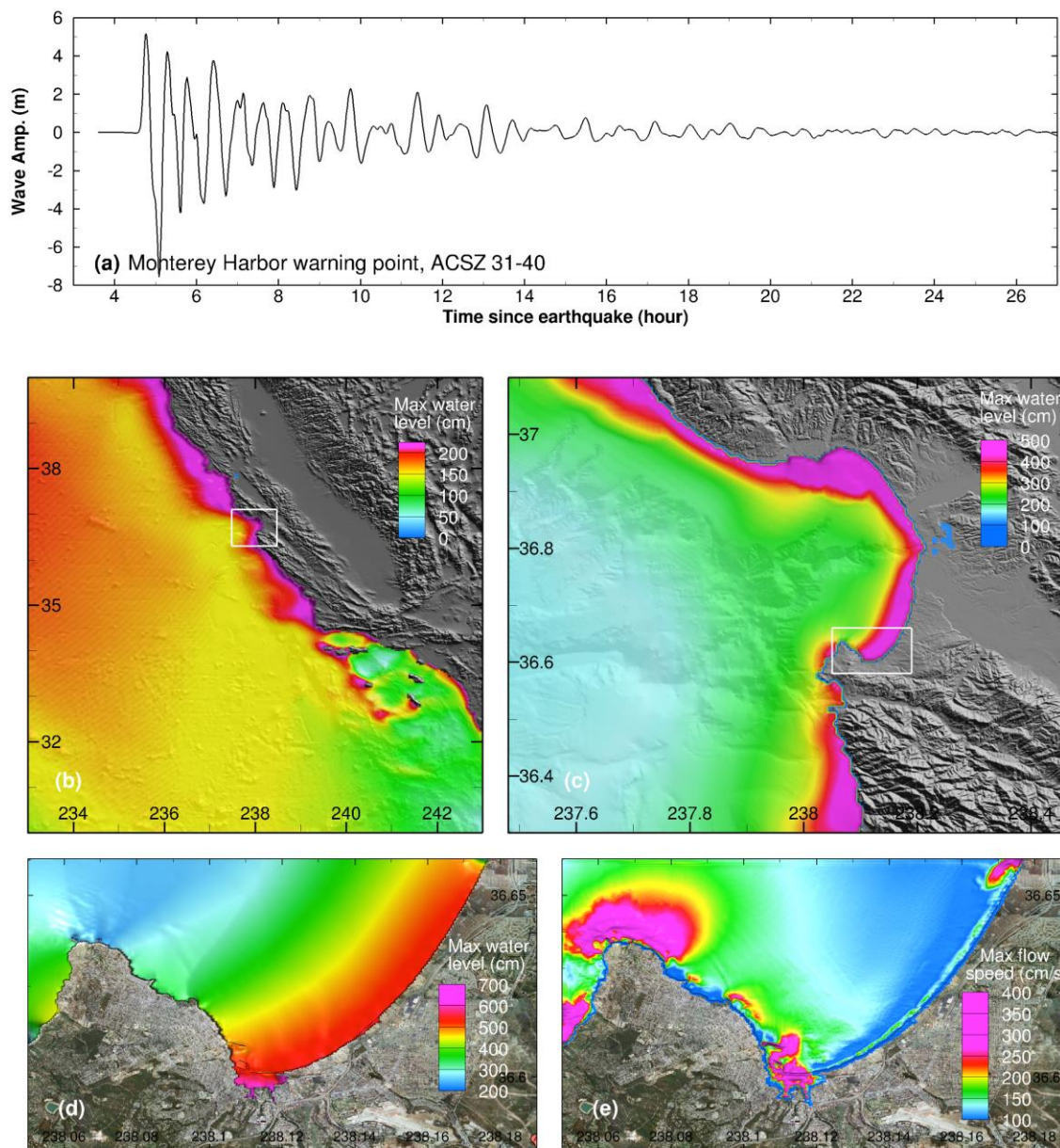
Figure 22 Model stability testing results at Monterey for synthetic mega tsunami scenario ACSZ 31-40. (a) Computed time series at the Monterey warning point; (b) Computed maximum wave amplitude in A grid of the forecast model; (c) Computed maximum current speed in B grid of the forecast model; (d) Computed maximum wave amplitude in C grid of the forecast model; (e) Computed current speed in C grid of the forecast model.
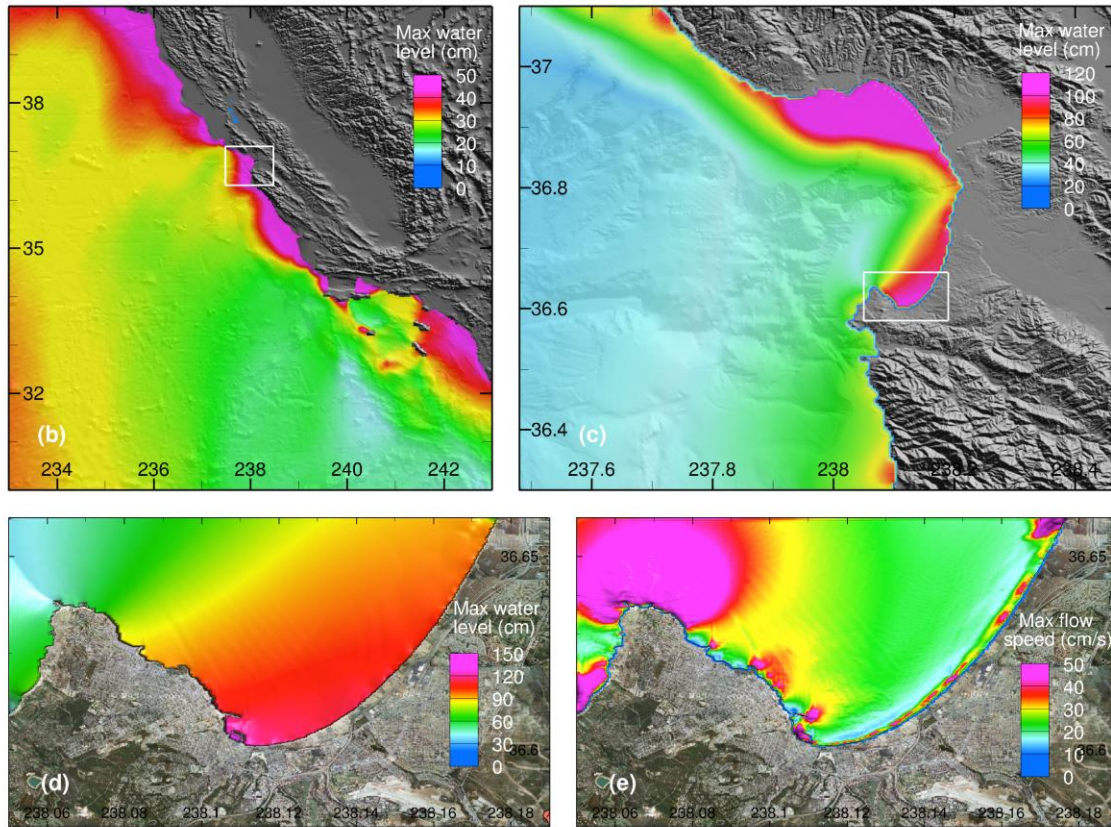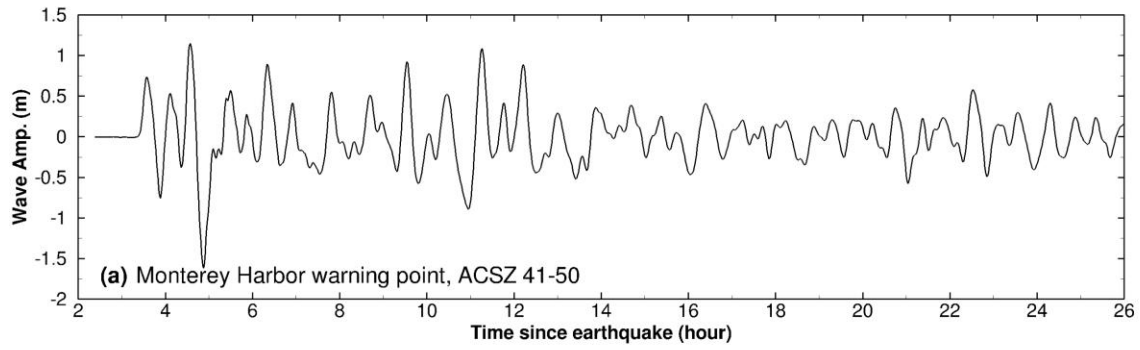
Figure 23 Model stability testing results at Monterey for synthetic mega tsunami scenario ACSZ 41-50. (a) Computed time series at the Monterey warning point; (b) Computed maximum wave amplitude in A grid of the forecast model; (c) Computed maximum current speed in B grid of the forecast model; (d) Computed maximum wave amplitude in C grid of the forecast model; (e) Computed current speed in C grid of the forecast model.
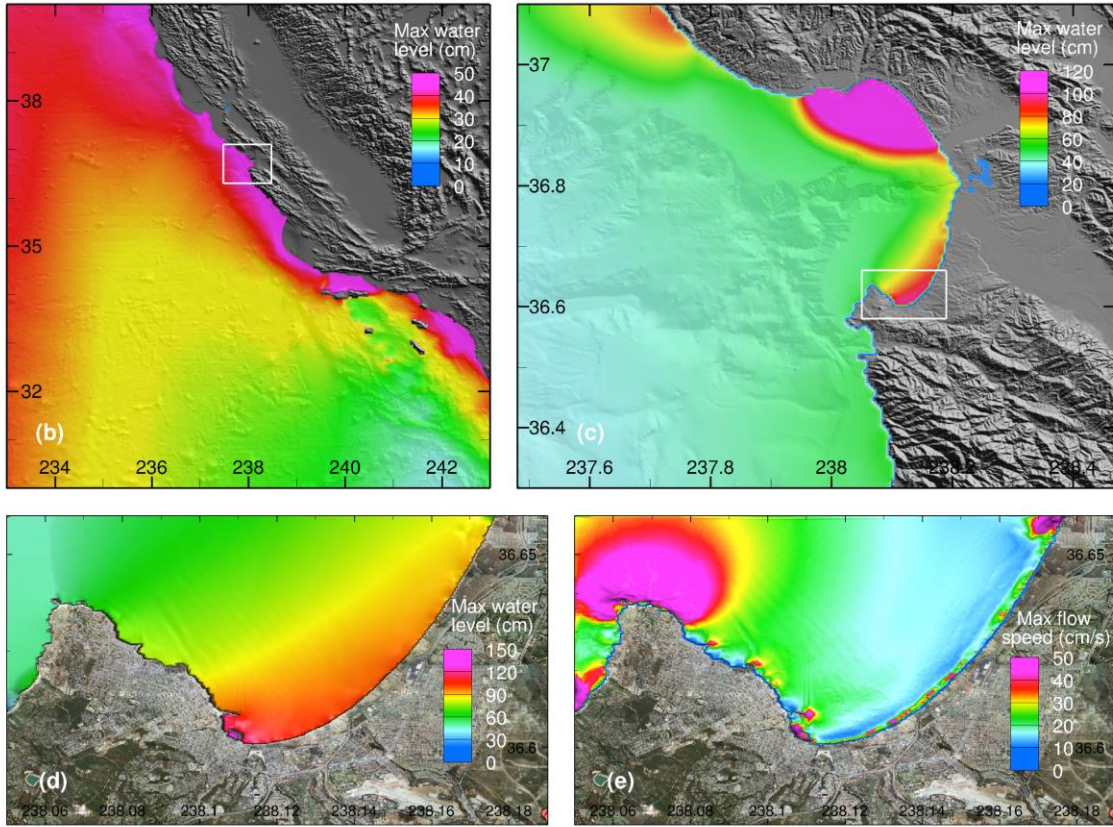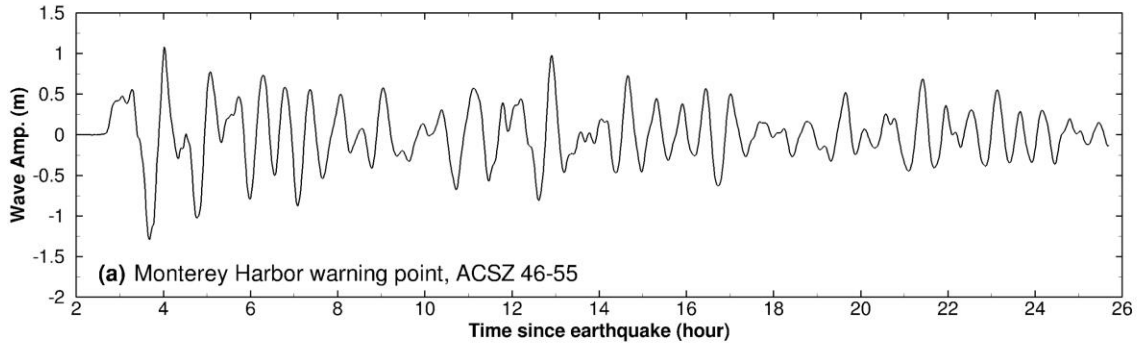
Figure 24 Model stability testing results at Monterey for synthetic mega tsunami scenario ACSZ 46-55. (a) Computed time series at the Monterey warning point; (b) Computed maximum wave amplitude in A grid of the forecast model; (c) Computed maximum current speed in B grid of the forecast model; (d) Computed maximum wave amplitude in C grid of the forecast model; (e) Computed current speed in C grid of the forecast model.
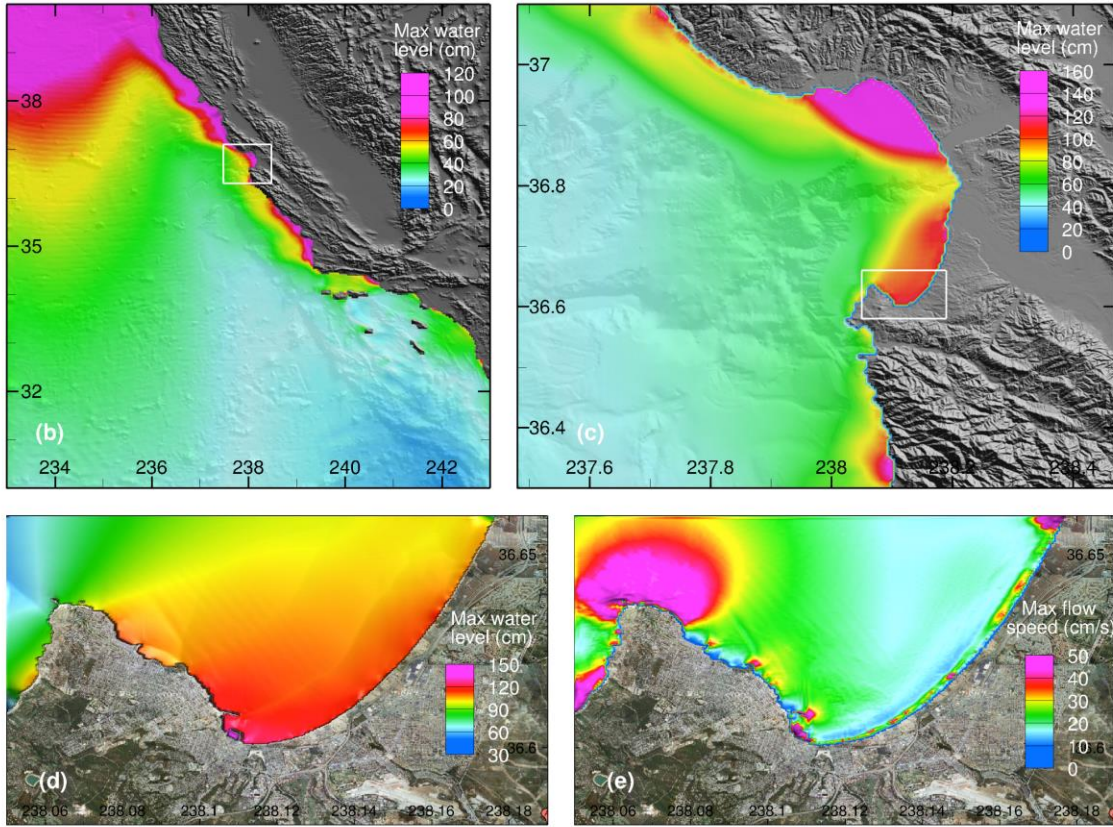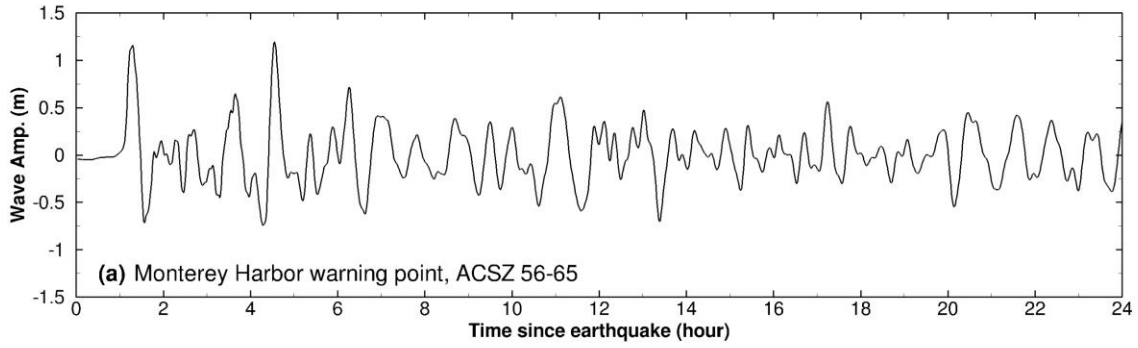
Figure 25 Model stability testing results at Monterey for synthetic mega tsunami scenario ACSZ 56-65. (a) Computed time series at the Monterey warning point; (b) Computed maximum wave amplitude in A grid of the forecast model; (c) Computed maximum current speed in B grid of the forecast model; (d) Computed maximum wave amplitude in C grid of the forecast model; (e) Computed current speed in C grid of the forecast model.
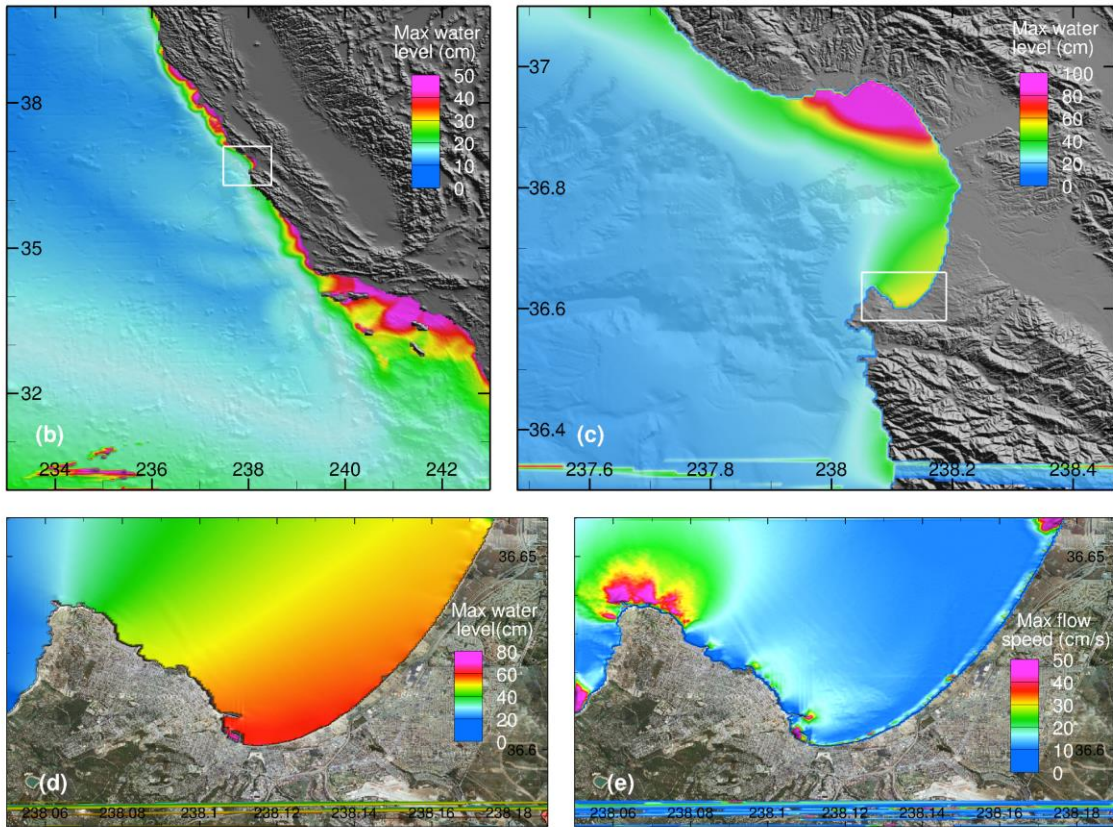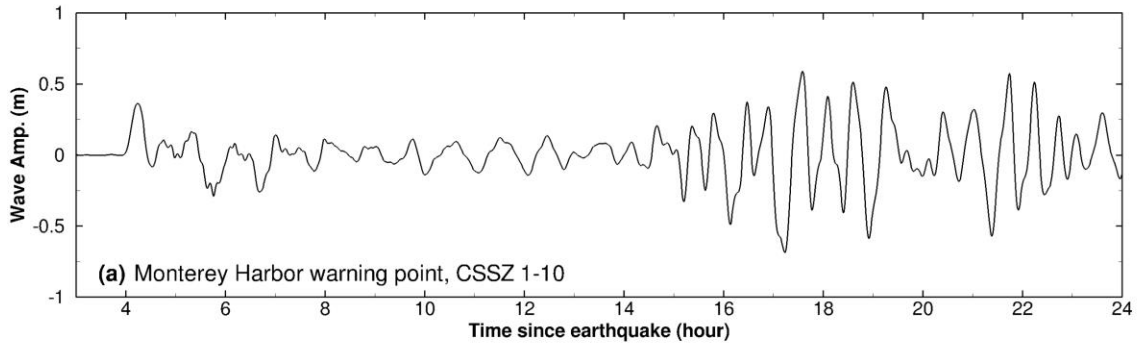
Figure 26 Model stability testing results at Monterey for synthetic mega tsunami scenario CSSZ 1-10. (a) Computed time series at the Monterey warning point; (b) Computed maximum wave amplitude in A grid of the forecast model; (c) Computed maximum current speed in B grid of the forecast model; (d) Computed maximum wave amplitude in C grid of the forecast model; (e) Computed current speed in C grid of the forecast model.
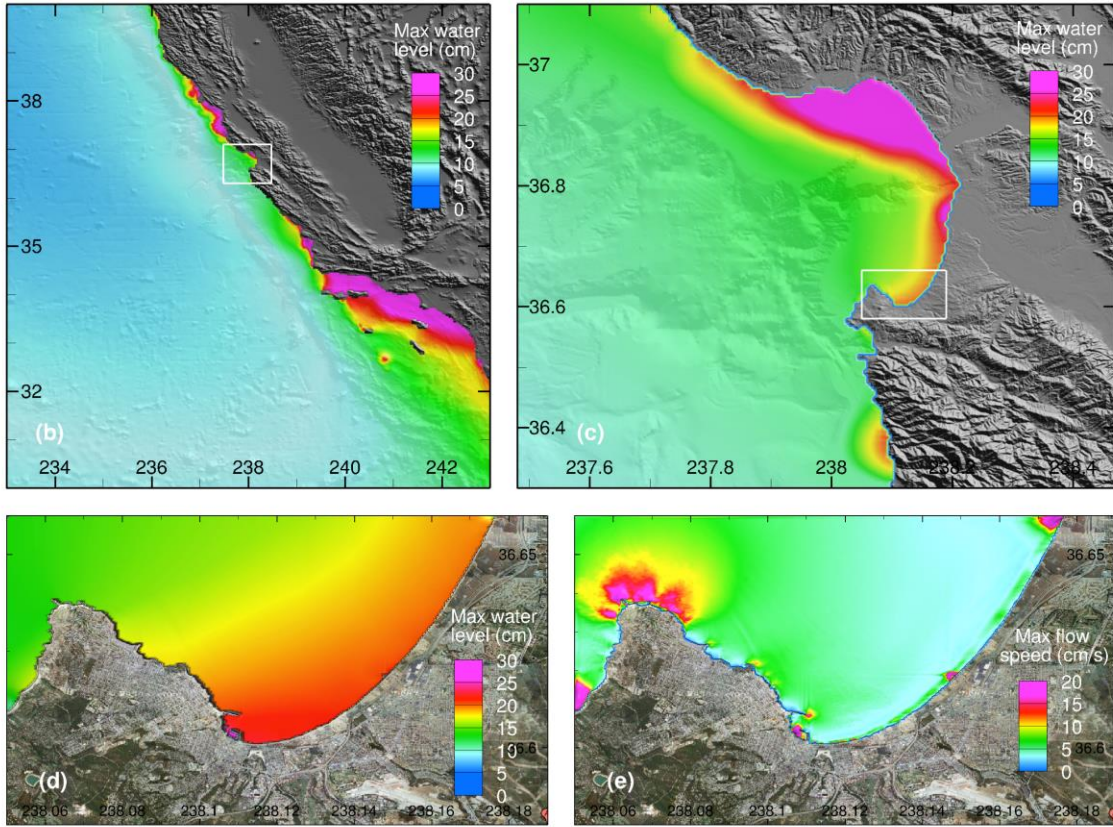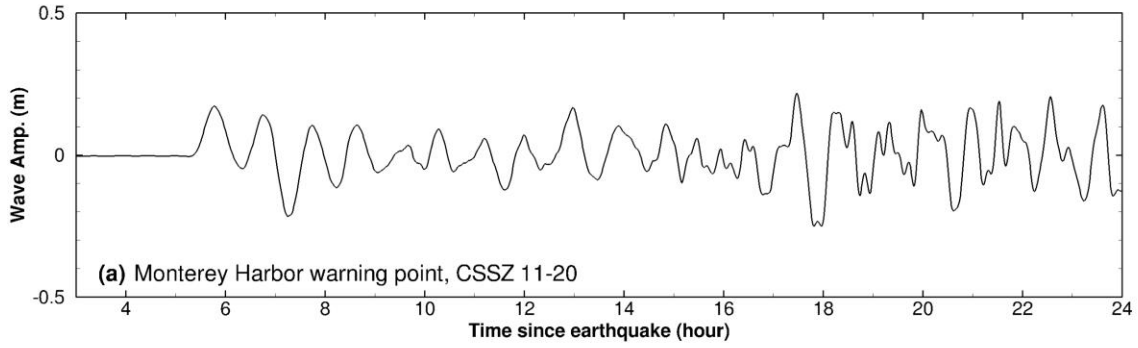
Figure 27 Model stability testing results at Monterey for synthetic mega tsunami scenario CSSZ 11-20. (a) Computed time series at the Monterey warning point; (b) Computed maximum wave amplitude in A grid of the forecast model; (c) Computed maximum current speed in B grid of the forecast model; (d) Computed maximum wave amplitude in C grid of the forecast model; (e) Computed current speed in C grid of the forecast model.
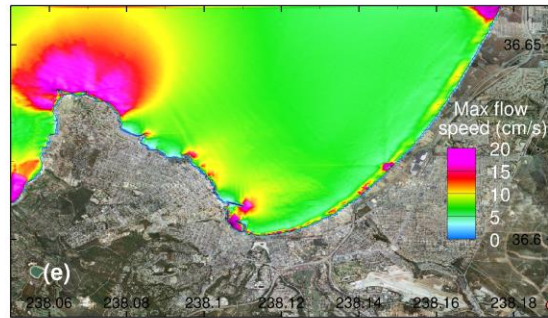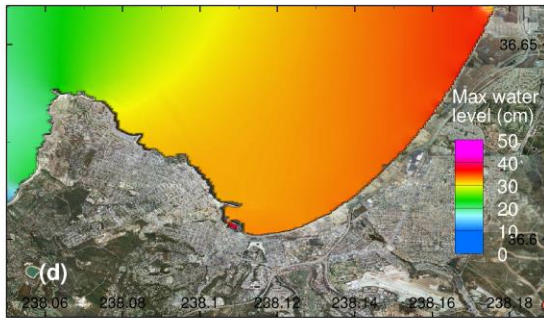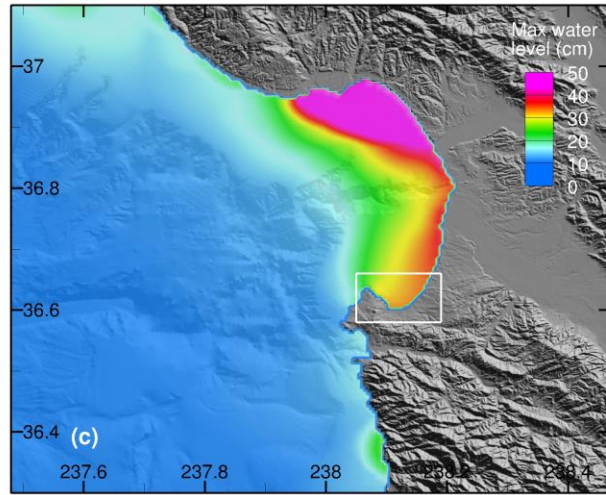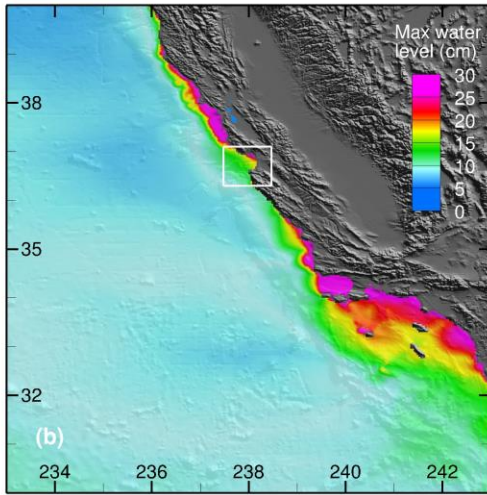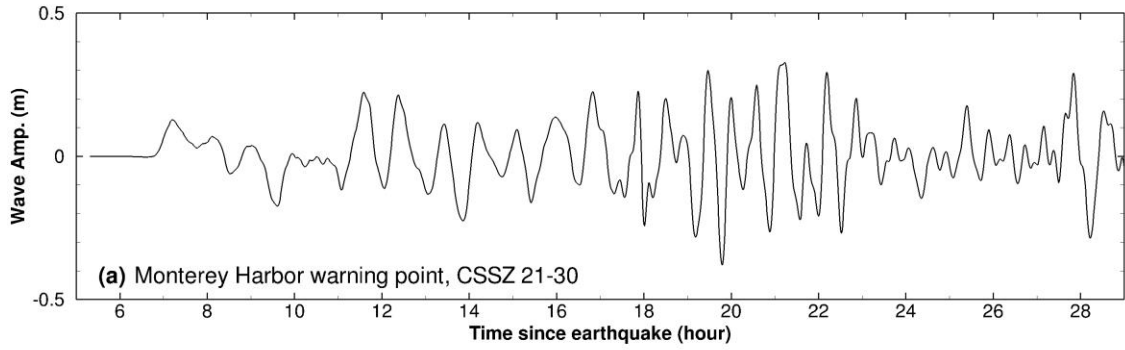
Figure 28 Model stability testing results at Monterey for synthetic mega tsunami scenario CSSZ 21-30. (a) Computed time series at the Monterey warning point; (b) Computed maximum wave amplitude in A grid of the forecast model; (c) Computed maximum current speed in B grid of the forecast model; (d) Computed maximum wave amplitude in C grid of the forecast model; (e) Computed current speed in C grid of the forecast model.
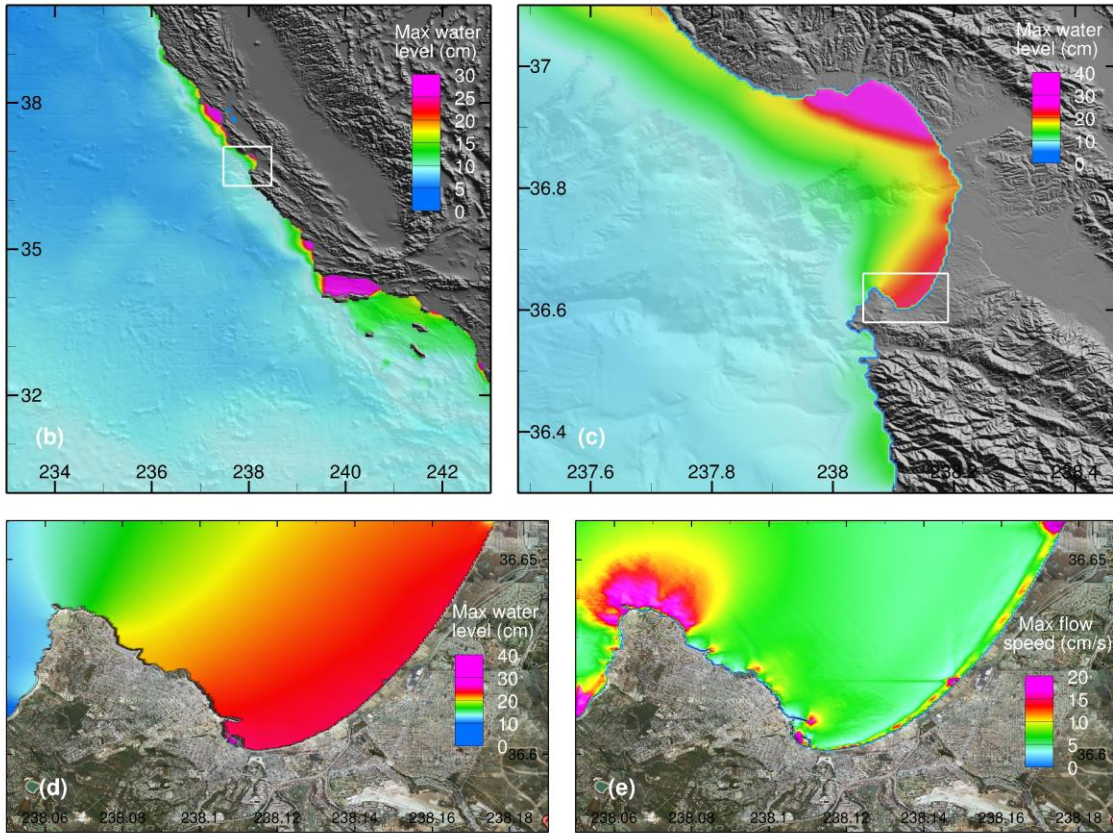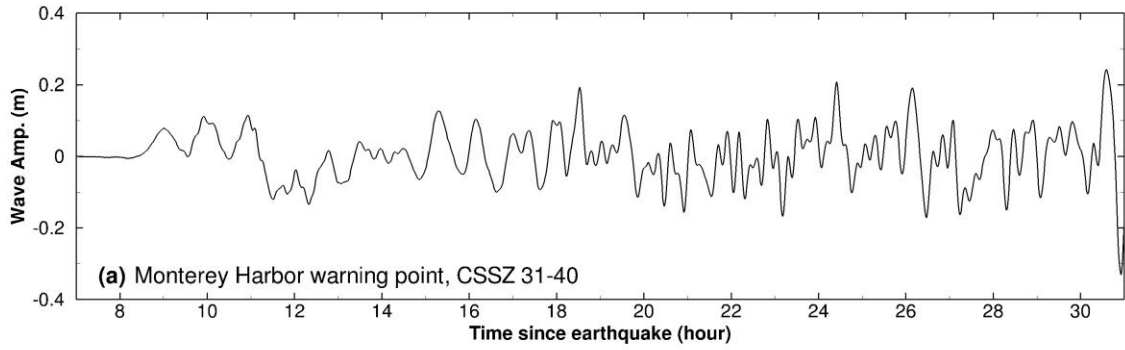
Figure 29 Model stability testing results at Monterey for synthetic mega tsunami scenario CSSZ 31-40. (a) Computed time series at the Monterey warning point; (b) Computed maximum wave amplitude in A grid of the forecast model; (c) Computed maximum current speed in B grid of the forecast model; (d) Computed maximum wave amplitude in C grid of the forecast model; (e) Computed current speed in C grid of the forecast model.
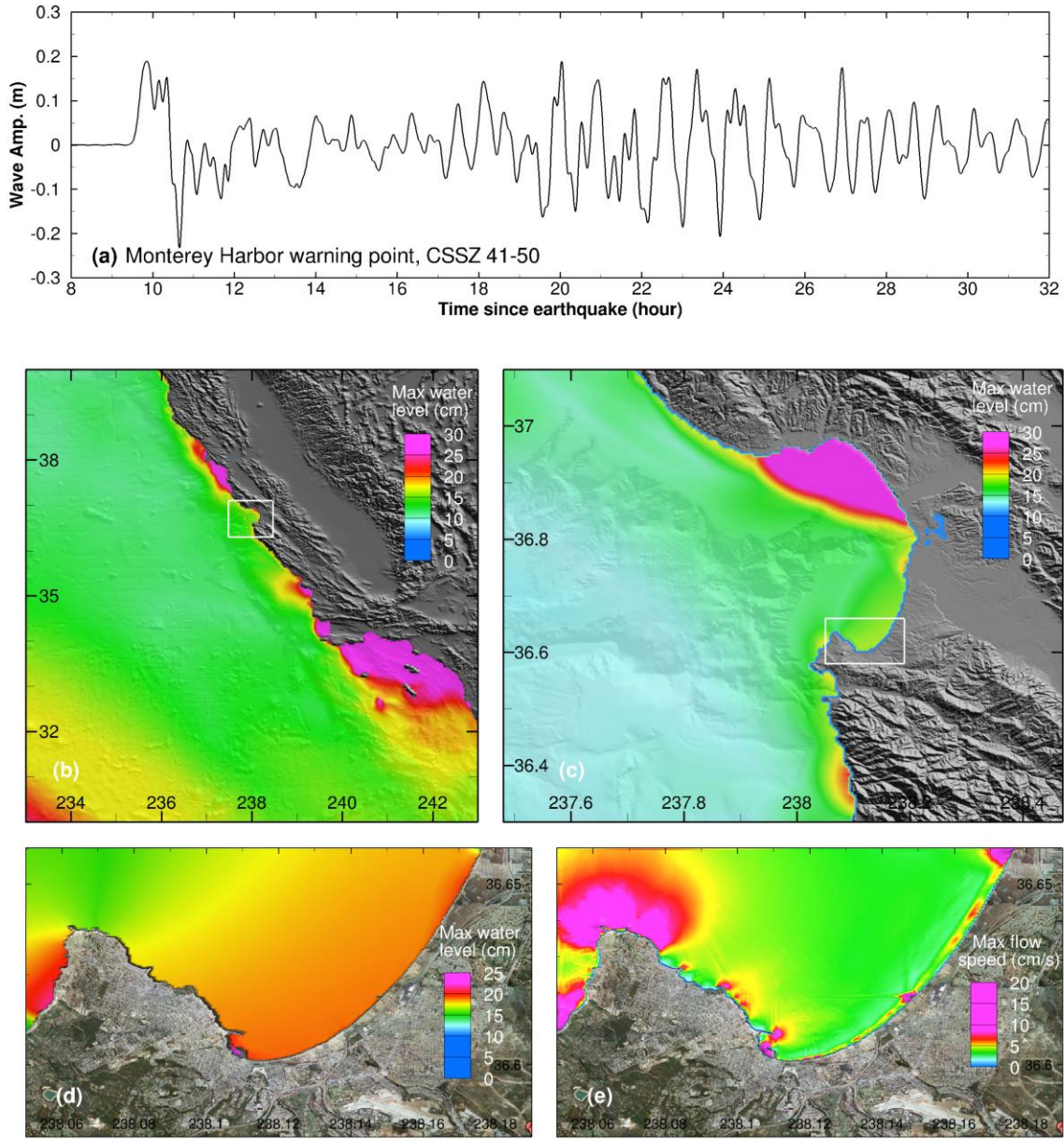
Figure 30 Model stability testing results at Monterey for synthetic mega tsunami scenario CSSZ 41-50. (a) Computed time series at the Monterey warning point; (b) Computed maximum wave amplitude in A grid of the forecast model; (c) Computed maximum current speed in B grid of the forecast model; (d) Computed maximum wave amplitude in C grid of the forecast model; (e) Computed current speed in C grid of the forecast model.
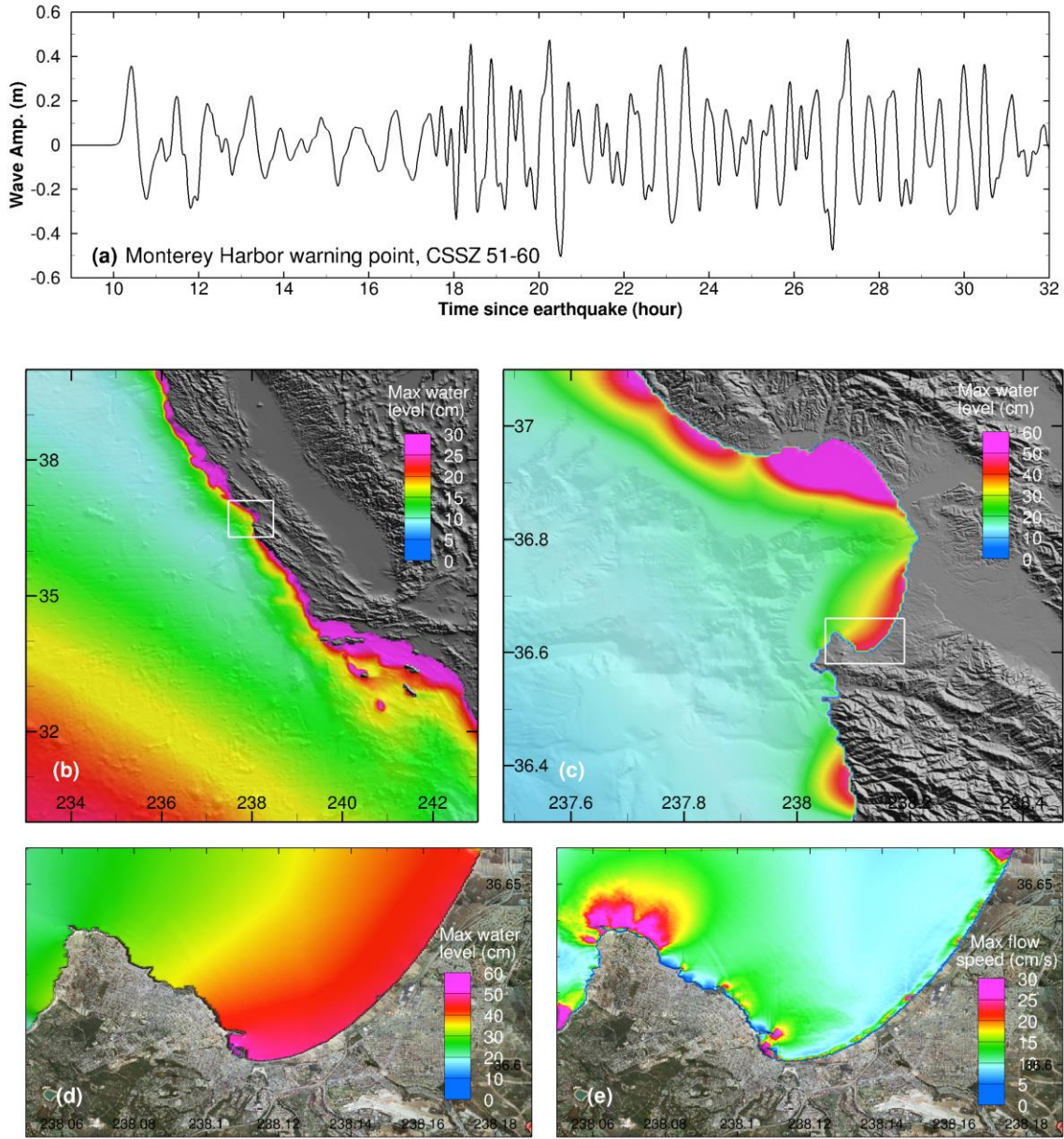
Figure 31 Model stability testing results at Monterey for synthetic mega tsunami scenario CSSZ 51-60. (a) Computed time series at the Monterey warning point; (b) Computed maximum wave amplitude in A grid of the forecast model; (c) Computed maximum current speed in B grid of the forecast model; (d) Computed maximum wave amplitude in C grid of the forecast model; (e) Computed current speed in C grid of the forecast model.
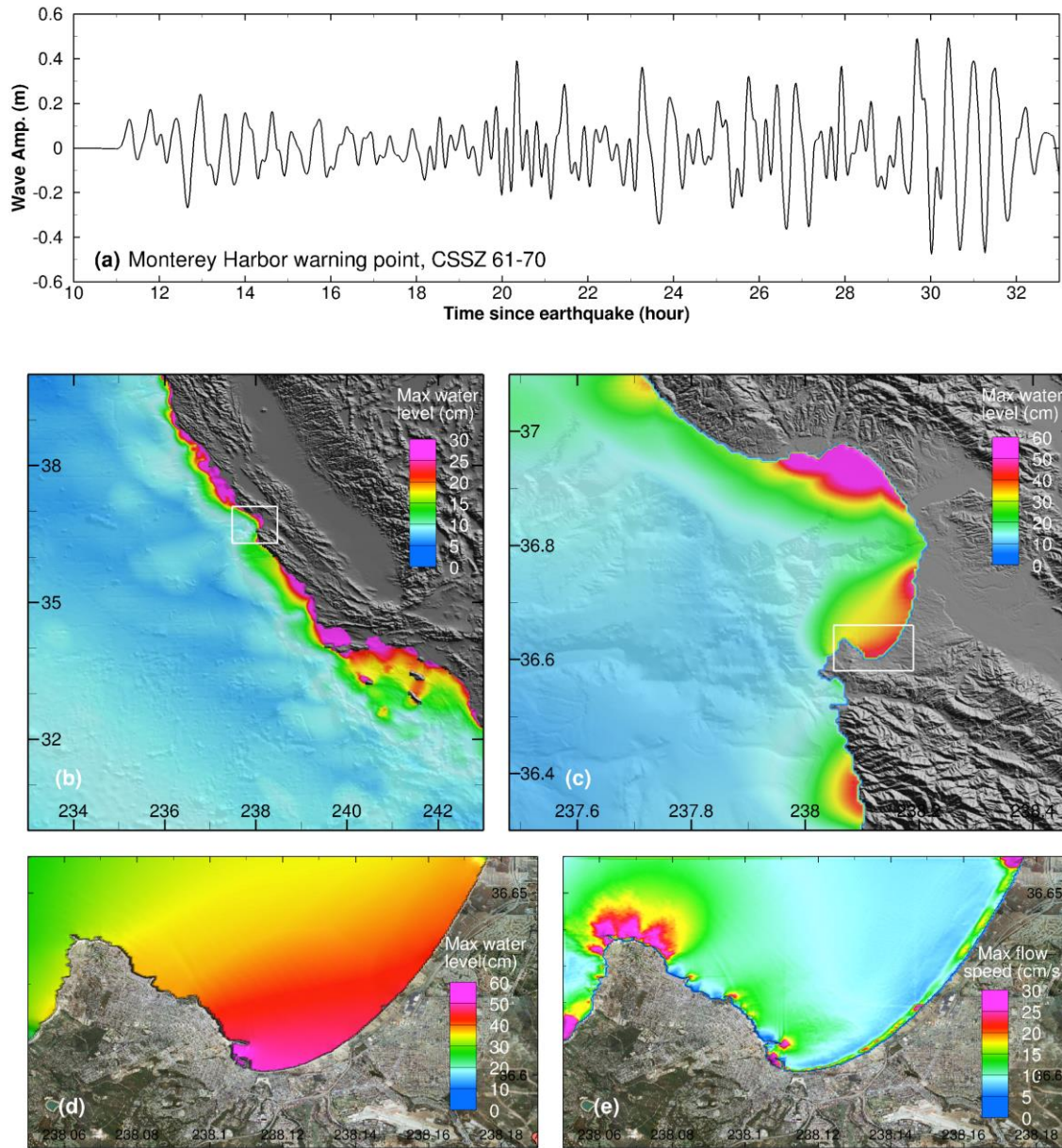
Figure 32 Model stability testing results at Monterey for synthetic mega tsunami scenario CSSZ 61-70. (a) Computed time series at the Monterey warning point; (b) Computed maximum wave amplitude in A grid of the forecast model; (c) Computed maximum current speed in B grid of the forecast model; (d) Computed maximum wave amplitude in C grid of the forecast model; (e) Computed current speed in C grid of the forecast model.
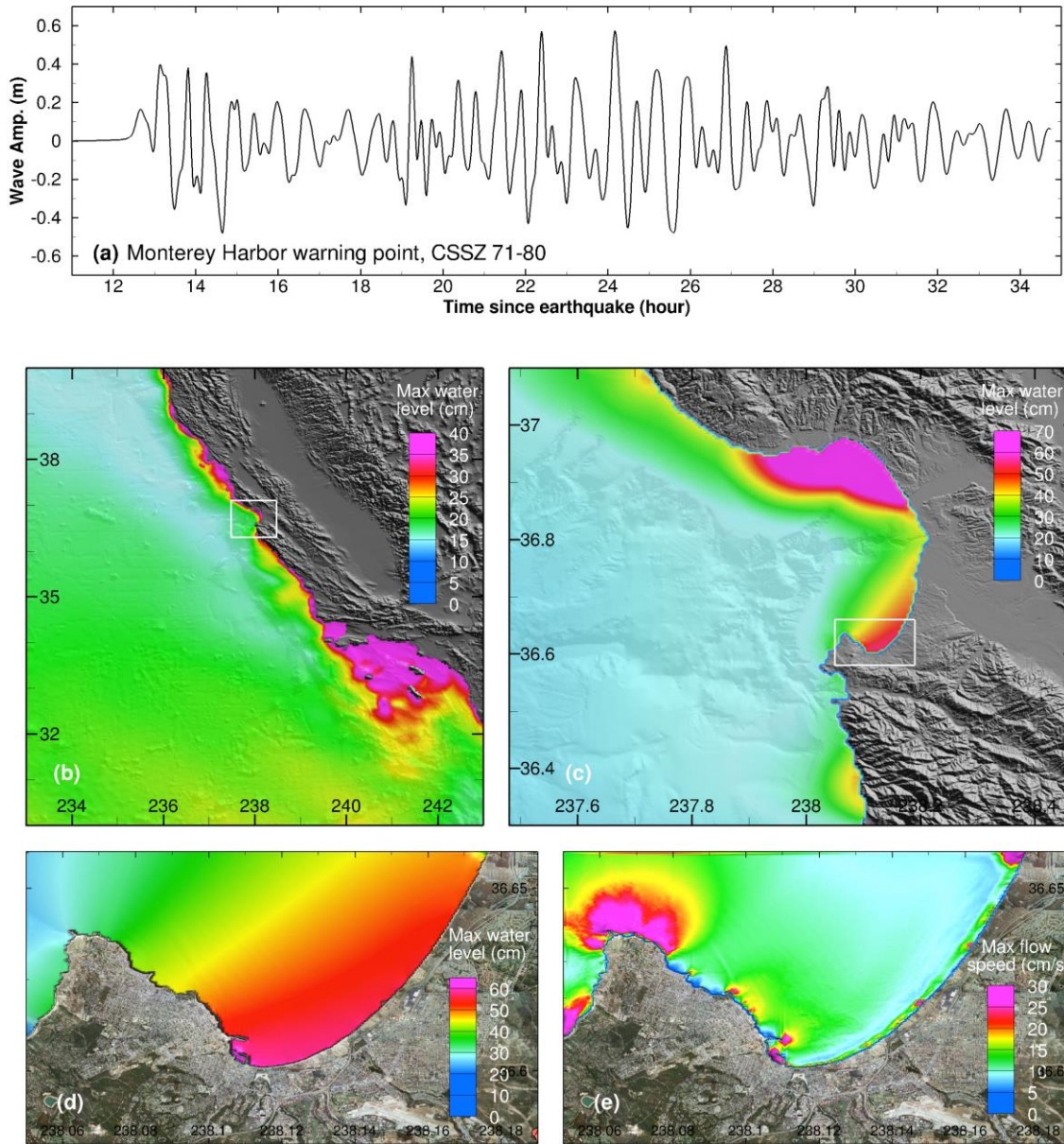
Figure 33 Model stability testing results at Monterey for synthetic mega tsunami scenario CSSZ 71-80. (a) Computed time series at the Monterey warning point; (b) Computed maximum wave amplitude in A grid of the forecast model; (c) Computed maximum current speed in B grid of the forecast model; (d) Computed maximum wave amplitude in C grid of the forecast model; (e) Computed current speed in C grid of the forecast model.
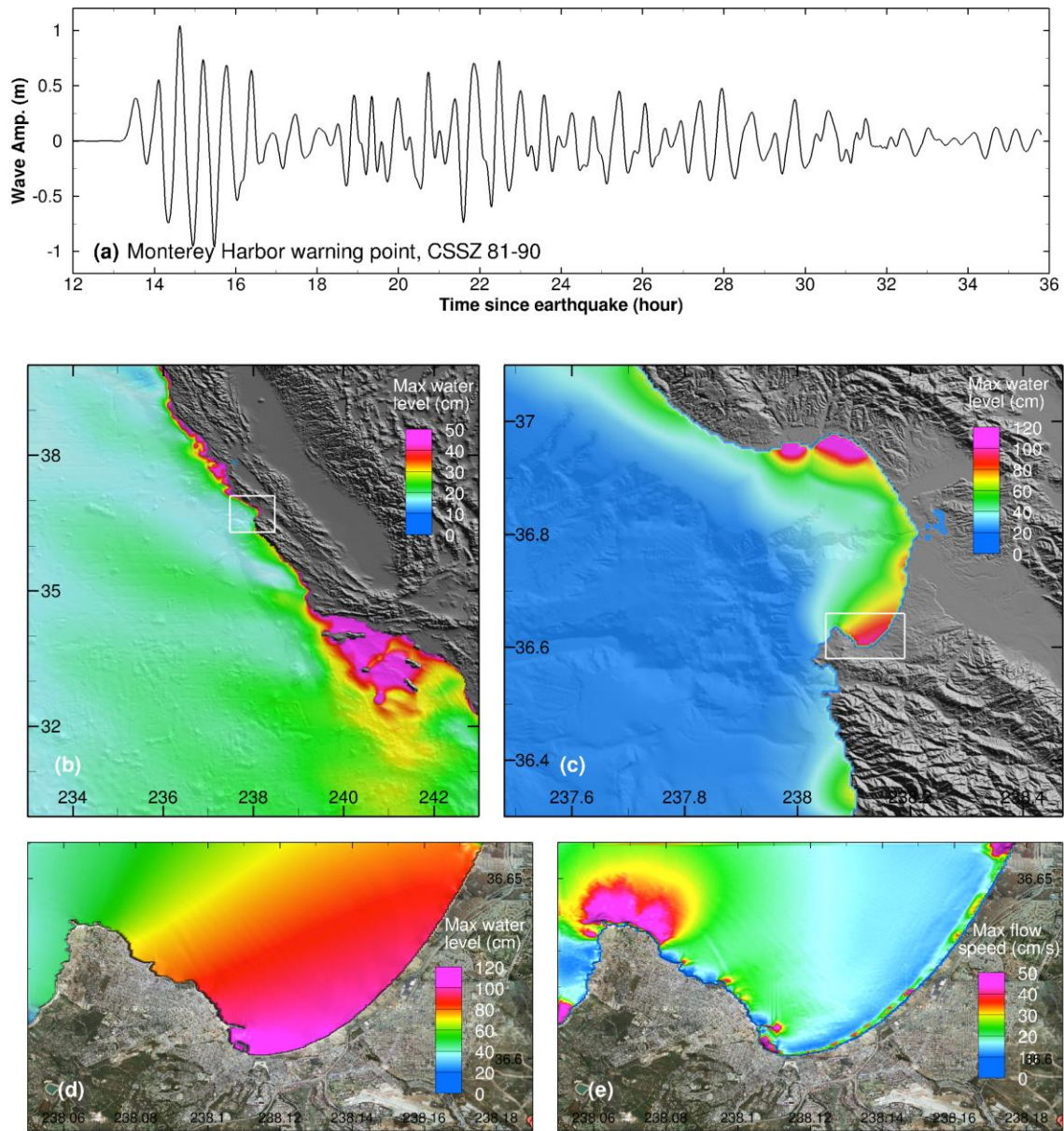
Figure 34 Model stability testing results at Monterey for synthetic mega tsunami scenario CSSZ 81-90. (a) Computed time series at the Monterey warning point; (b) Computed maximum wave amplitude in A grid of the forecast model; (c) Computed maximum current speed in B grid of the forecast model; (d) Computed maximum wave amplitude in C grid of the forecast model; (e) Computed current speed in C grid of the forecast model.
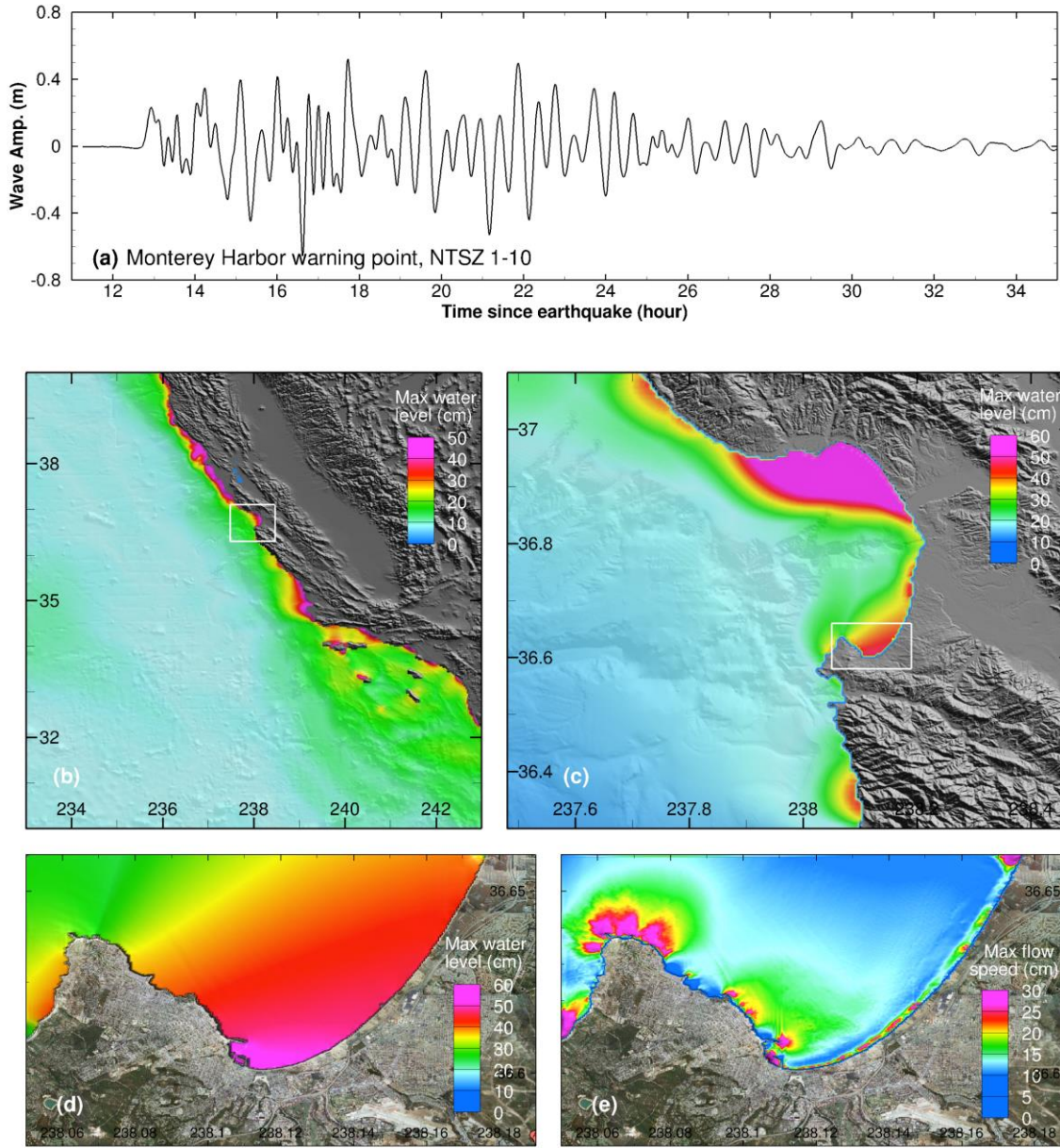
Figure 35 Model stability testing results at Monterey for synthetic mega tsunami scenario NTSZ 1-10. (a) Computed time series at the Monterey warning point; (b) Computed maximum wave amplitude in A grid of the forecast model; (c) Computed maximum current speed in B grid of the forecast model; (d) Computed maximum wave amplitude in C grid of the forecast model; (e) Computed current speed in C grid of the forecast model.
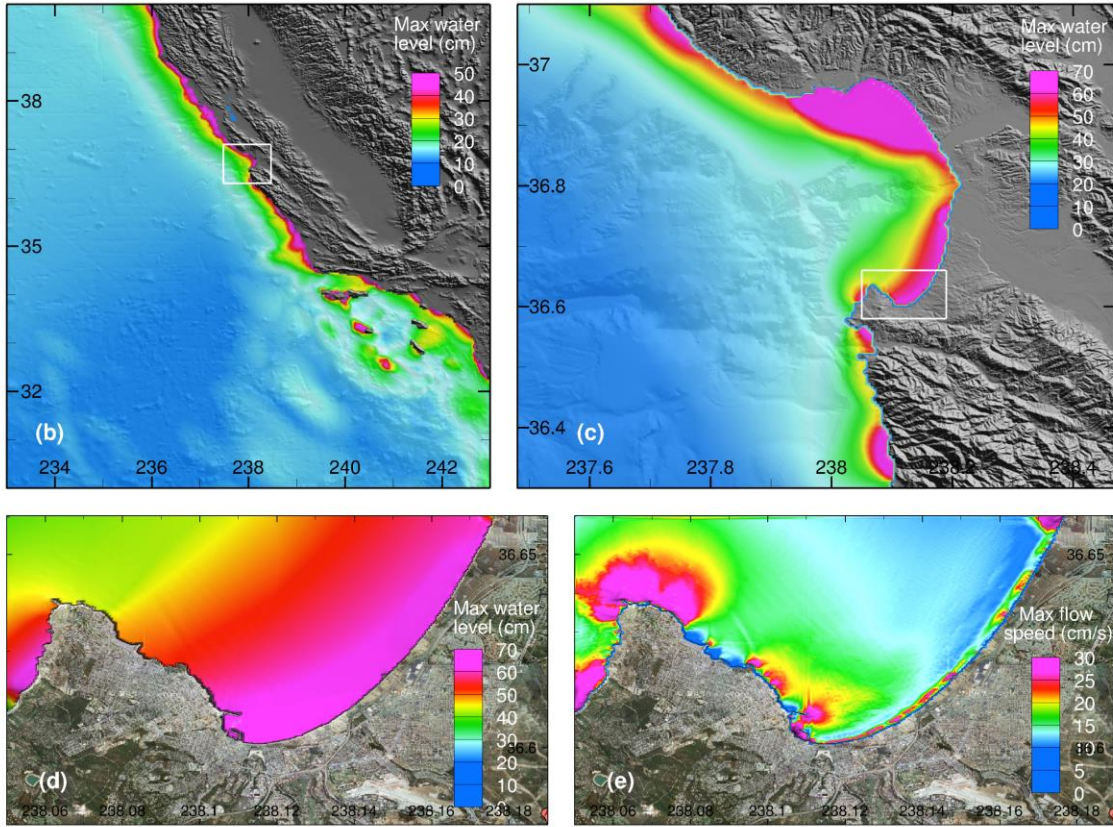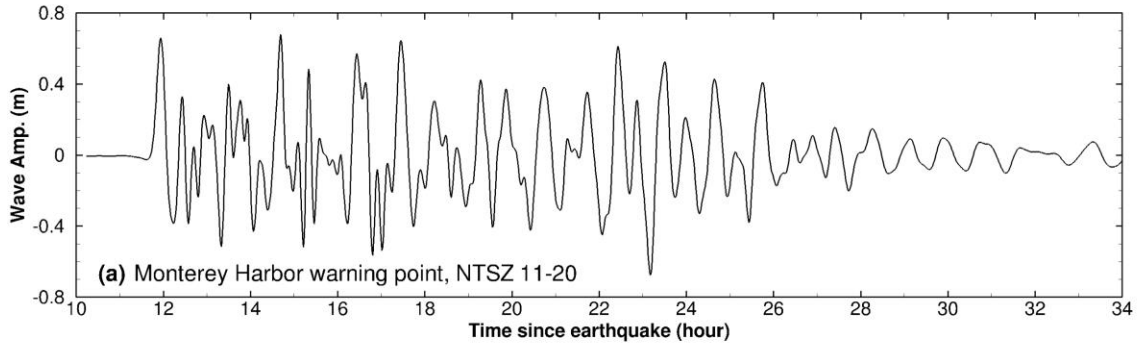
Figure 36 Model stability testing results at Monterey for synthetic mega tsunami scenario NTSZ 11-20. (a) Computed time series at the Monterey warning point; (b) Computed maximum wave amplitude in A grid of the forecast model; (c) Computed maximum current speed in B grid of the forecast model; (d) Computed maximum wave amplitude in C grid of the forecast model; (e) Computed current speed in C grid of the forecast model.
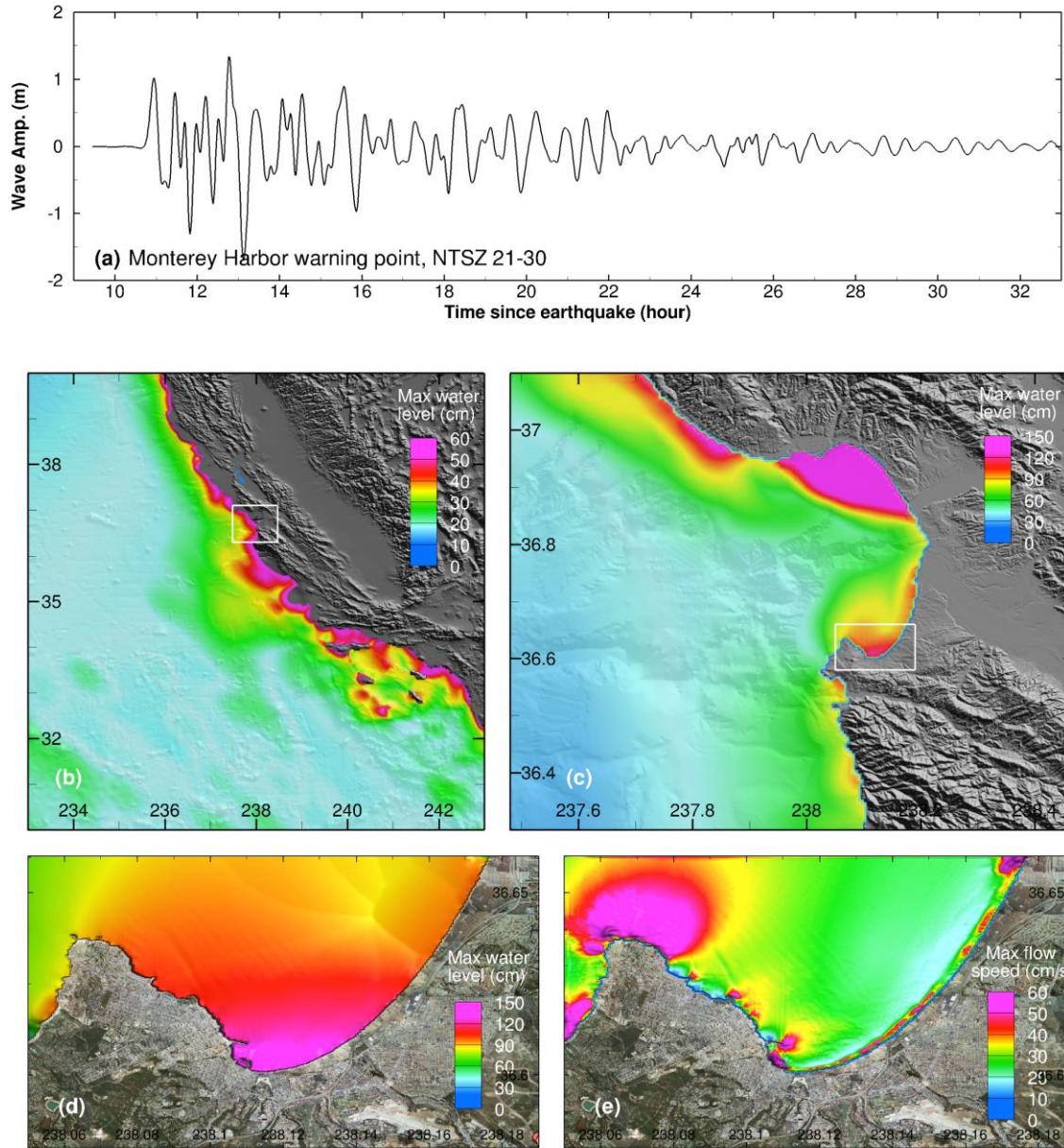
Figure 37 Model stability testing results at Monterey for synthetic mega tsunami scenario NTSZ 21-30. (a) Computed time series at the Monterey warning point; (b) Computed maximum wave amplitude in A grid of the forecast model; (c) Computed maximum current speed in B grid of the forecast model; (d) Computed maximum wave amplitude in C grid of the forecast model; (e) Computed current speed in C grid of the forecast model.
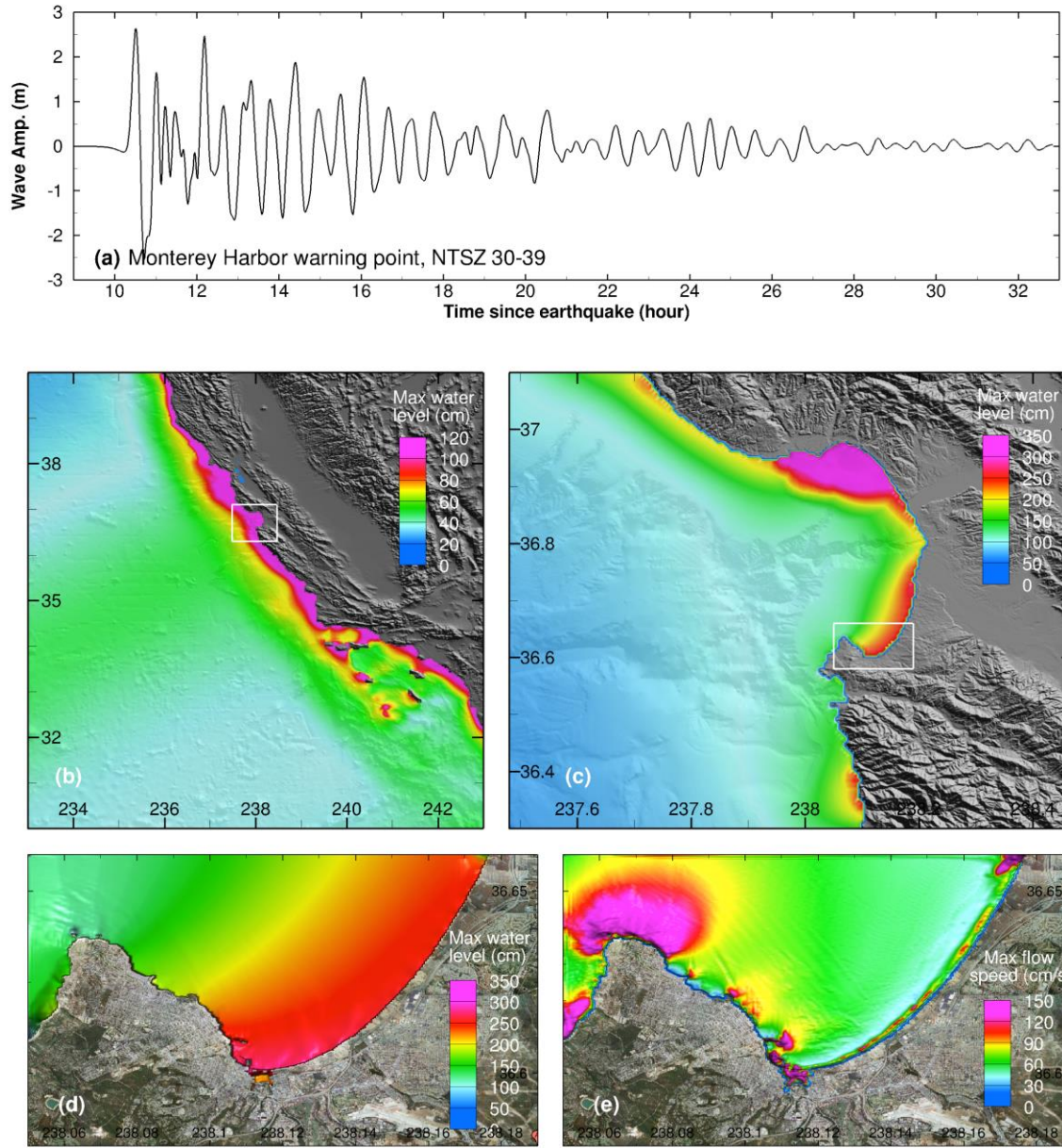
Figure 38 (a) Computed time series at the Monterey warning point; (b) Computed maximum wave amplitude in A grid of the forecast model; (c) Computed maximum current speed in B grid of the forecast model; (d) Computed maximum wave amplitude in C grid of the forecast model; (e) Computed current speed in C grid of the forecast model.
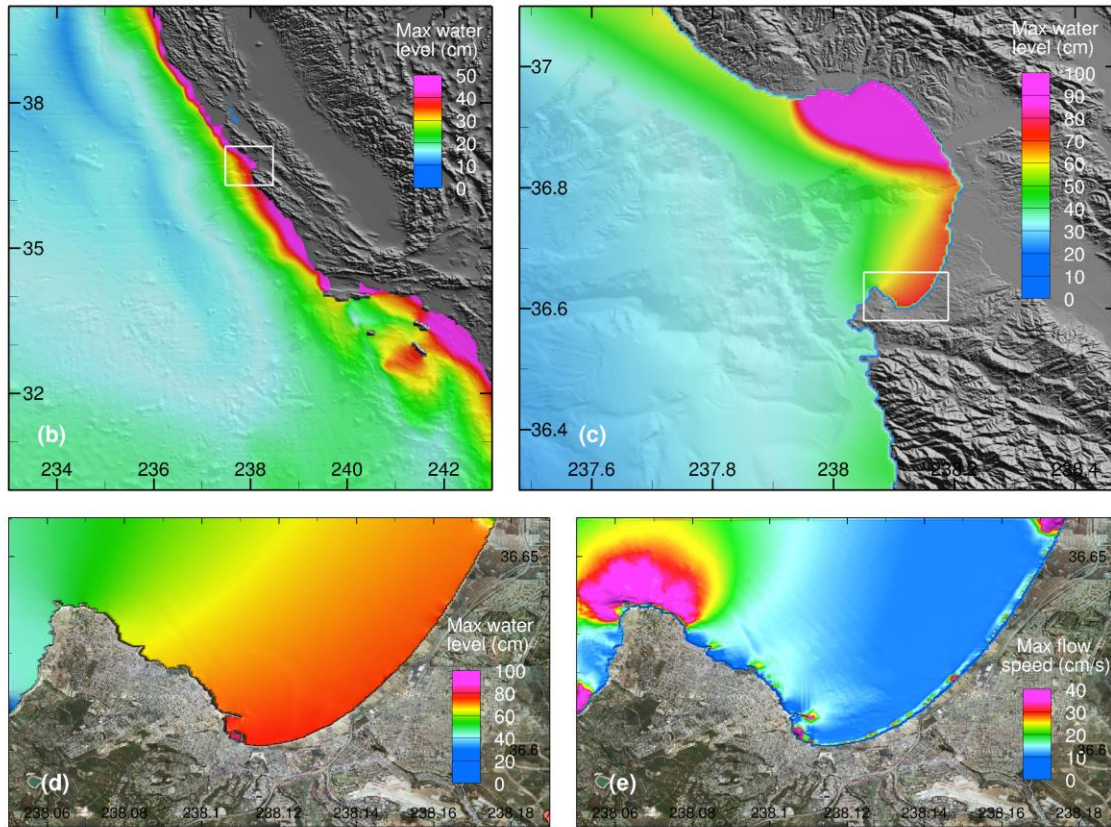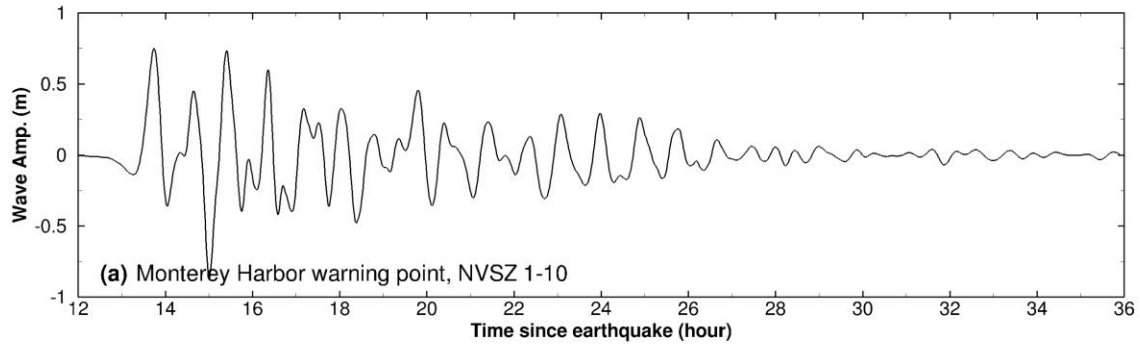
Figure 39 (a) Computed time series at the Monterey warning point; (b) Computed maximum wave amplitude in A grid of the forecast model; (c) Computed maximum current speed in B grid of the forecast model; (d) Computed maximum wave amplitude in C grid of the forecast model; (e) Computed current speed in C grid of the forecast model.
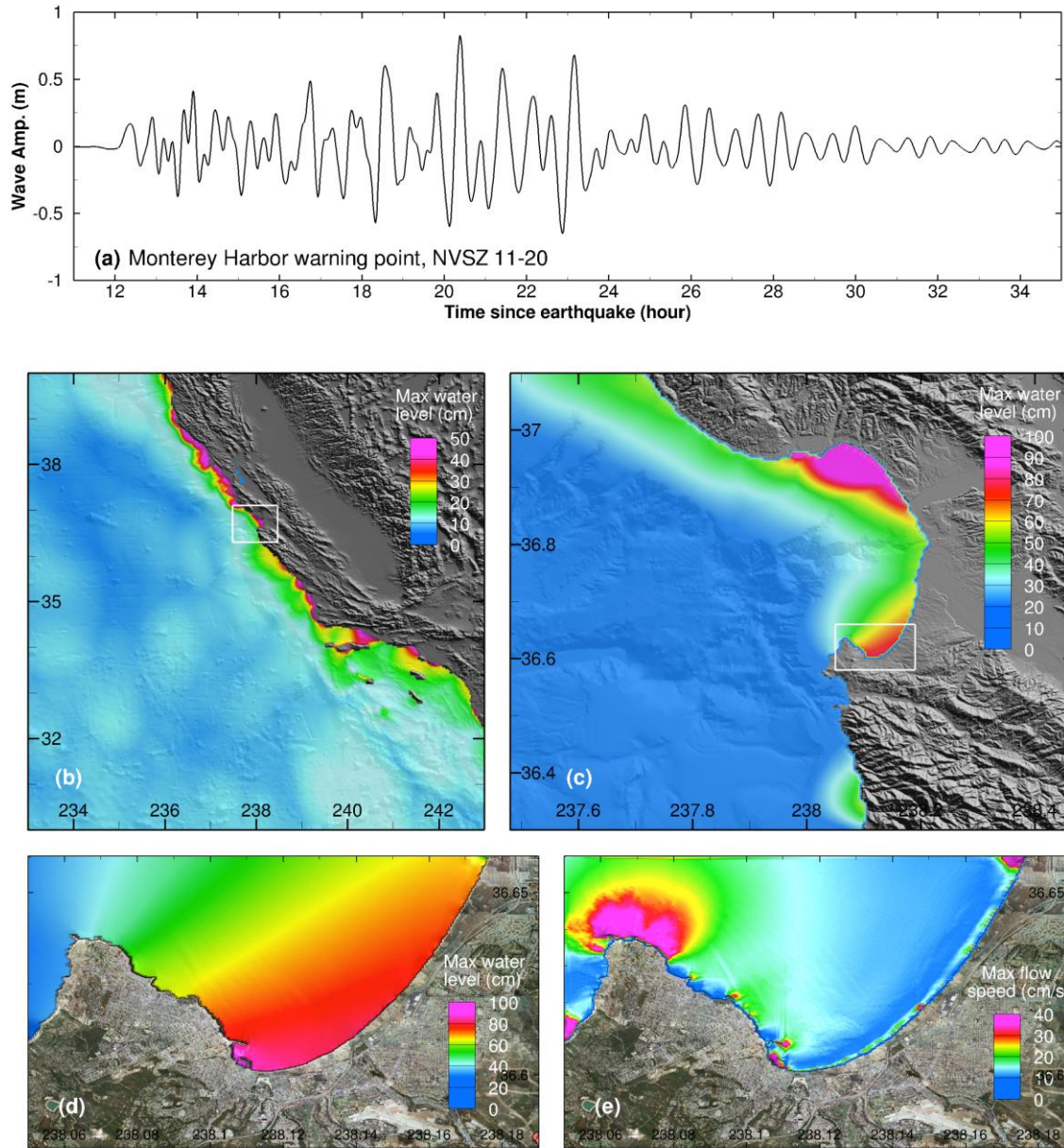
Figure 40 Model stability testing results at Monterey for synthetic mega tsunami scenario NVSZ 11-20. (a) Computed time series at the Monterey warning point; (b) Computed maximum wave amplitude in A grid of the forecast model; (c) Computed maximum current speed in B grid of the forecast model; (d) Computed maximum wave amplitude in C grid of the forecast model; (e) Computed current speed in C grid of the forecast model.
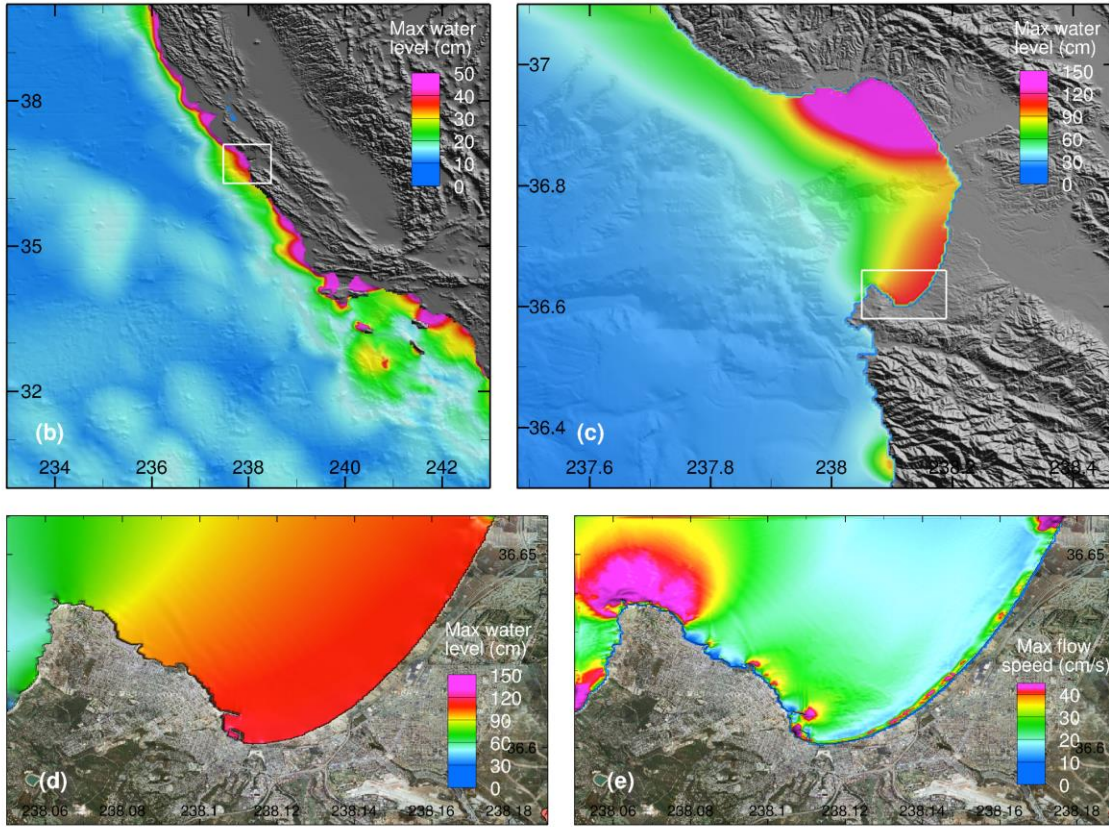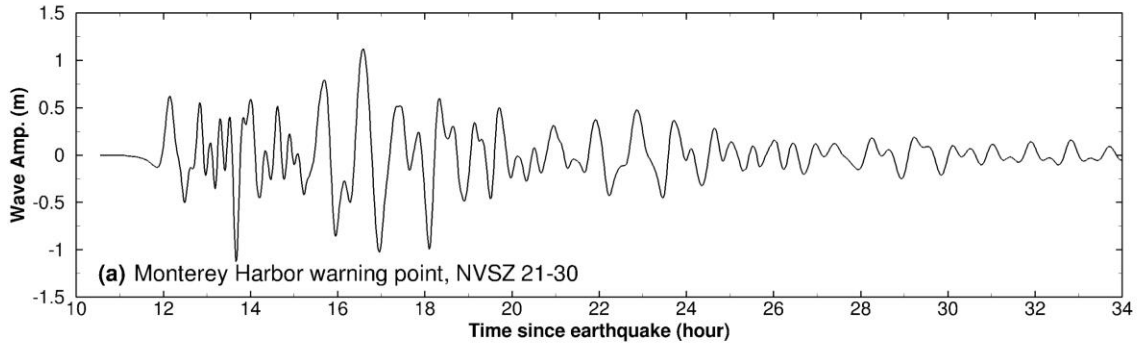
Figure 41 Model stability testing results at Monterey for synthetic mega tsunami scenario NVSZ 21-30. (a) Computed time series at the Monterey warning point; (b) Computed maximum wave amplitude in A grid of the forecast model; (c) Computed maximum current speed in B grid of the forecast model; (d) Computed maximum wave amplitude in C grid of the forecast model; (e) Computed current speed in C grid of the forecast model.
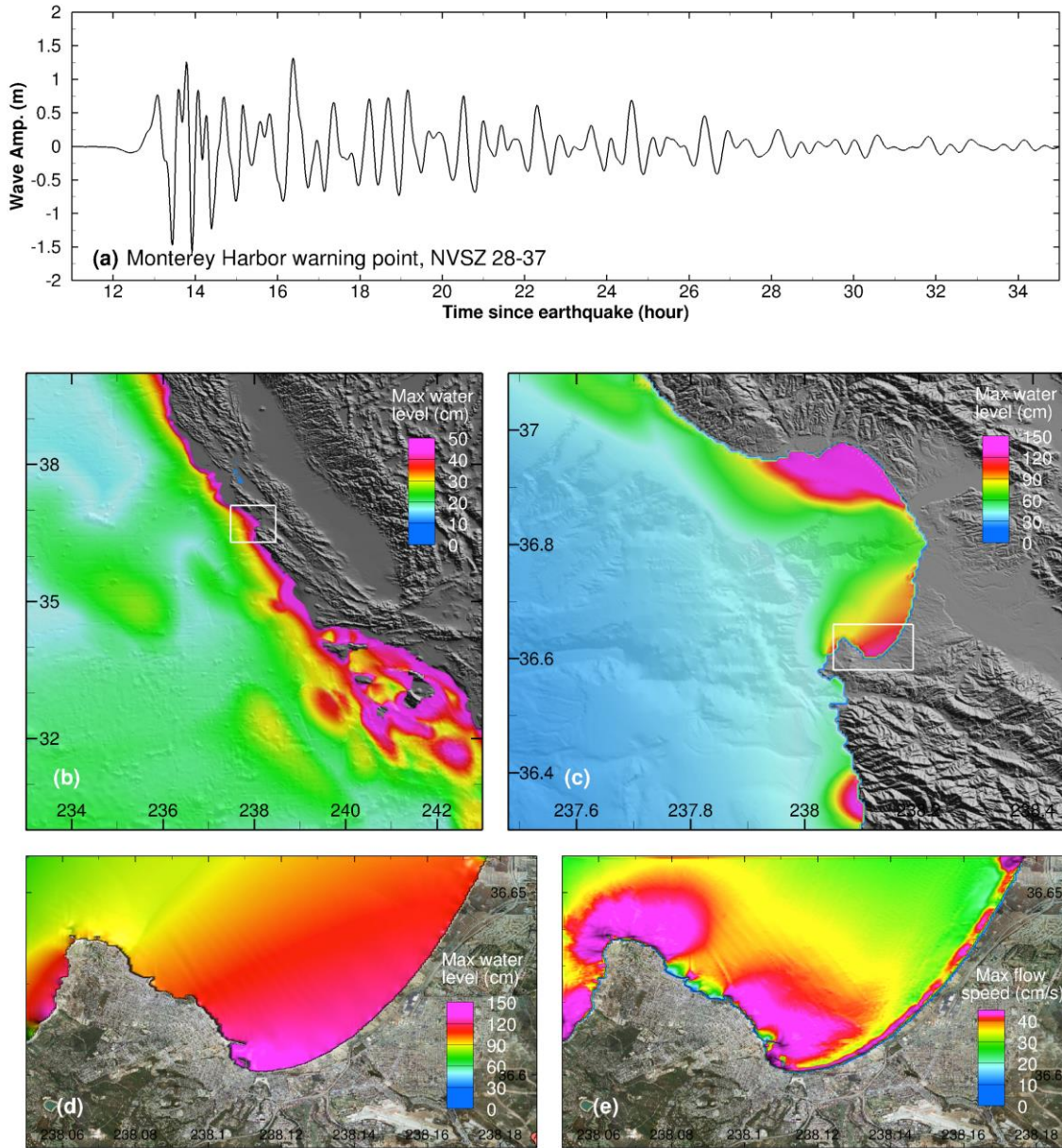
Figure 42 Model stability testing results at Monterey for synthetic mega tsunami scenario NVSZ 28-37. (a) Computed time series at the Monterey warning point; (b) Computed maximum wave amplitude in A grid of the forecast model; (c) Computed maximum current speed in B grid of the forecast model; (d) Computed maximum wave amplitude in C grid of the forecast model; (e) Computed current speed in C grid of the forecast model.
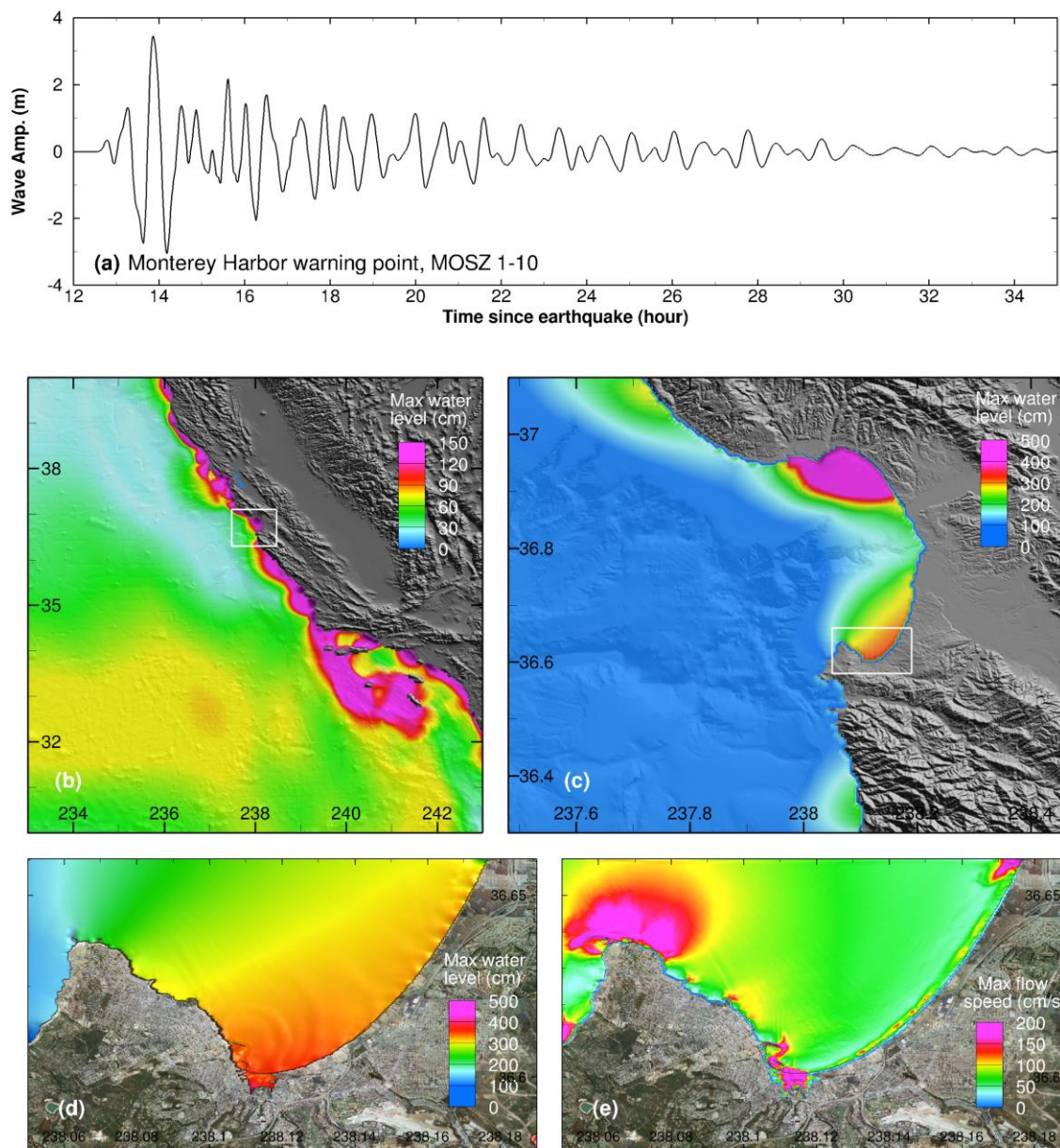
Figure 43 Model stability testing results at Monterey for synthetic mega tsunami scenario MOSZ 1-10. (a) Computed time series at the Monterey warning point; (b) Computed maximum wave amplitude in A grid of the forecast model; (c) Computed maximum current speed in B grid of the forecast model; (d) Computed maximum wave amplitude in C grid of the forecast model; (e) Computed current speed in C grid of the forecast model.
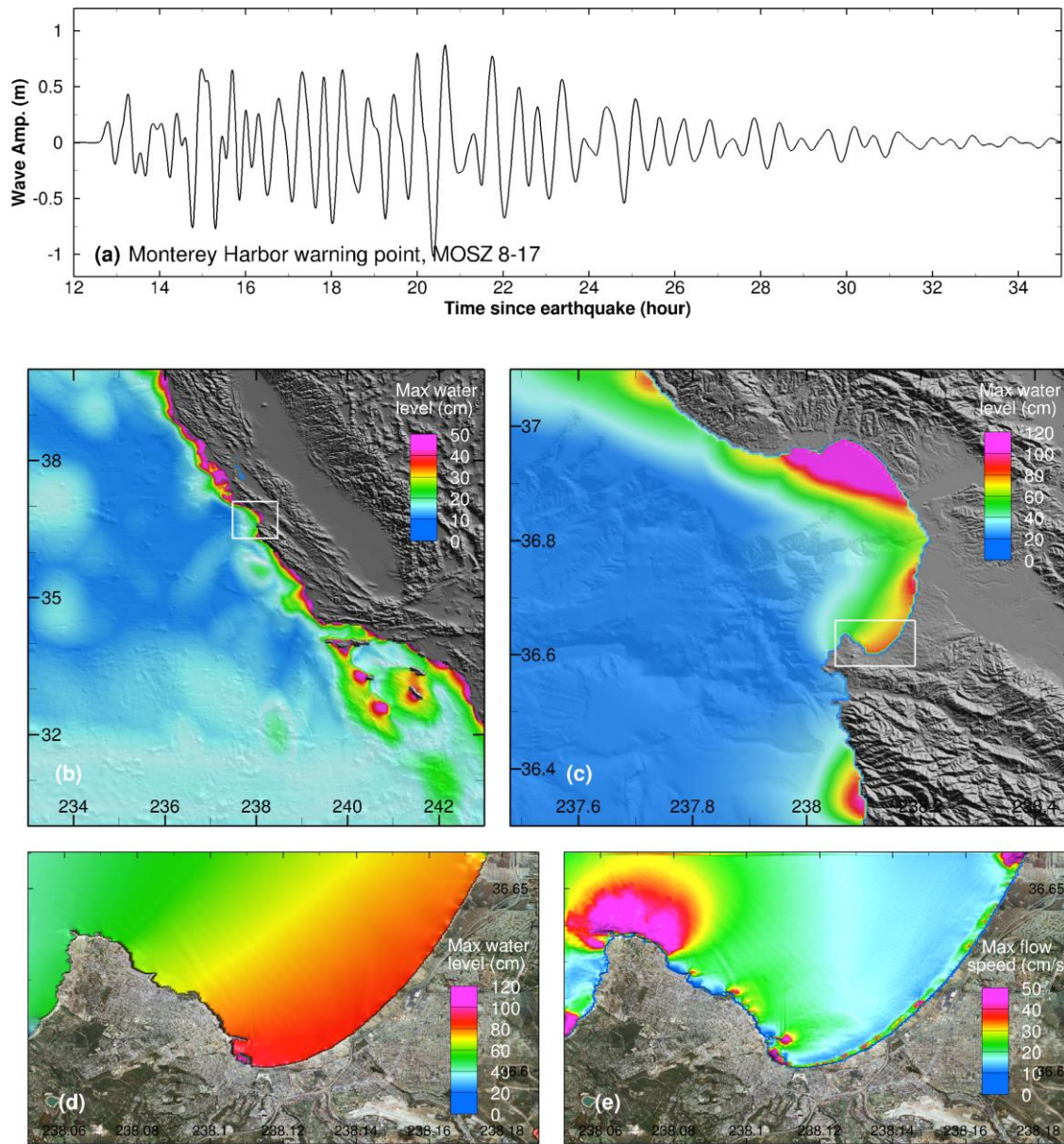
Figure 44 Model stability testing results at Monterey for synthetic mega tsunami scenario MOSZ 8-17. (a) Computed time series at the Monterey warning point; (b) Computed maximum wave amplitude in A grid of the forecast model; (c) Computed maximum current speed in B grid of the forecast model; (d) Computed maximum wave amplitude in C grid of the forecast model; (e) Computed current speed in C grid of the forecast model.
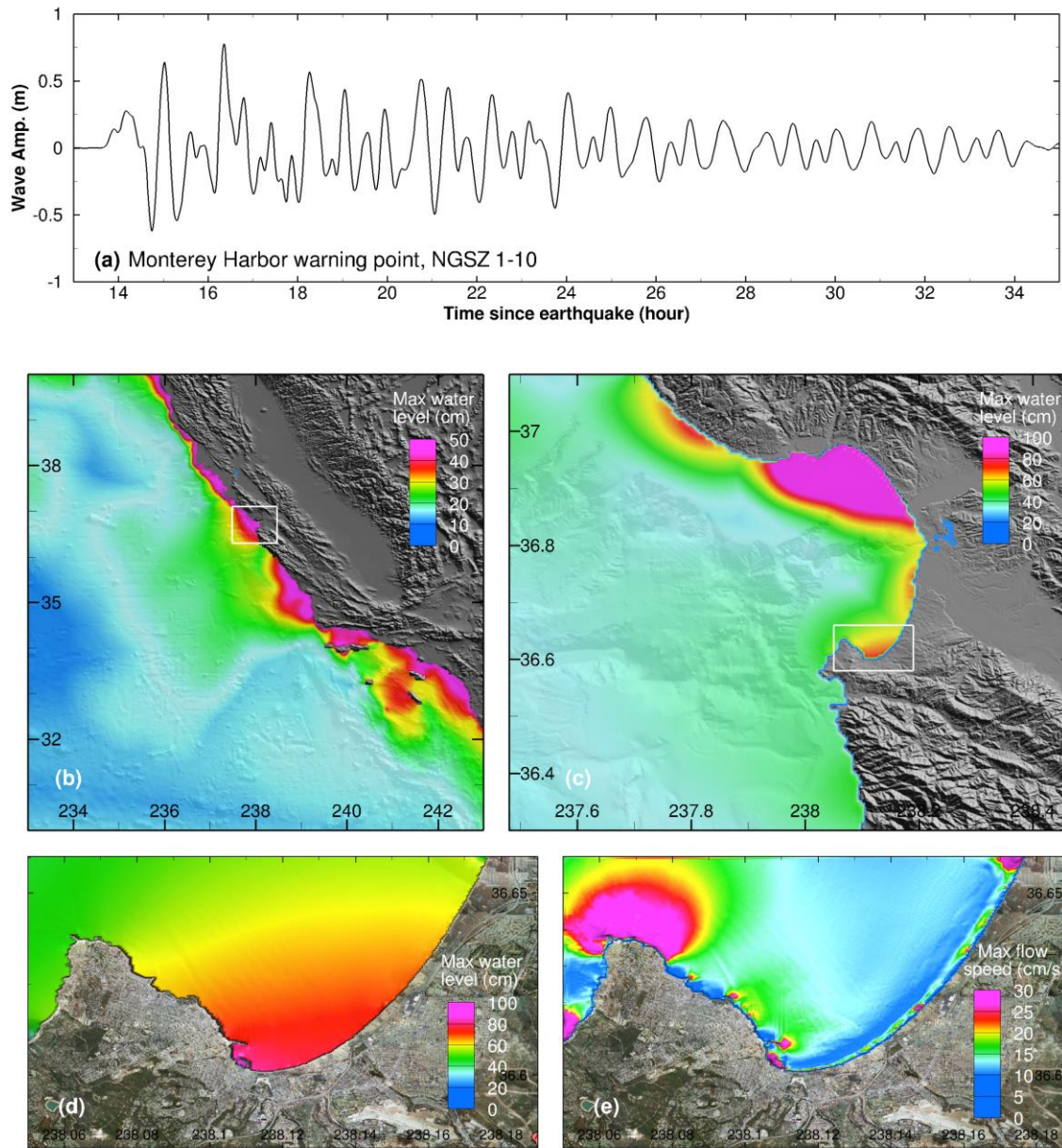
Figure 45 Model stability testing results at Monterey for synthetic mega tsunami scenario NGSZ 1-10. (a) Computed time series at the Monterey warning point; (b) Computed maximum wave amplitude in A grid of the forecast model; (c) Computed maximum current speed in B grid of the forecast model; (d) Computed maximum wave amplitude in C grid of the forecast model; (e) Computed current speed in C grid of the forecast model.
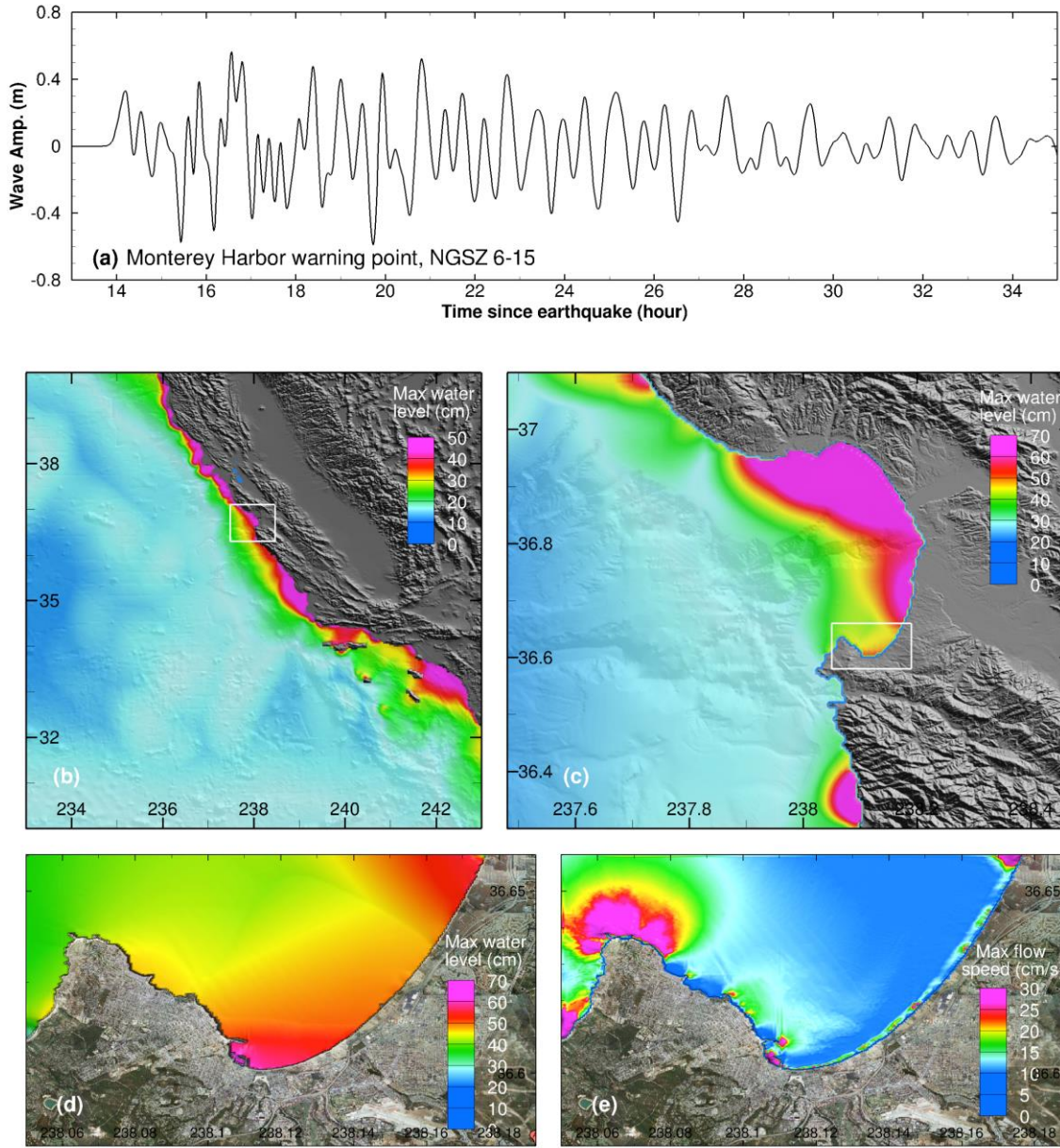
Figure 46 Model stability testing results at Monterey for synthetic mega tsunami scenario NGSZ 6-15. (a) Computed time series at the Monterey warning point; (b) Computed maximum wave amplitude in A grid of the forecast model; (c) Computed maximum current speed in B grid of the forecast model; (d) Computed maximum wave amplitude in C grid of the forecast model; (e) Computed current speed in C grid of the forecast model.
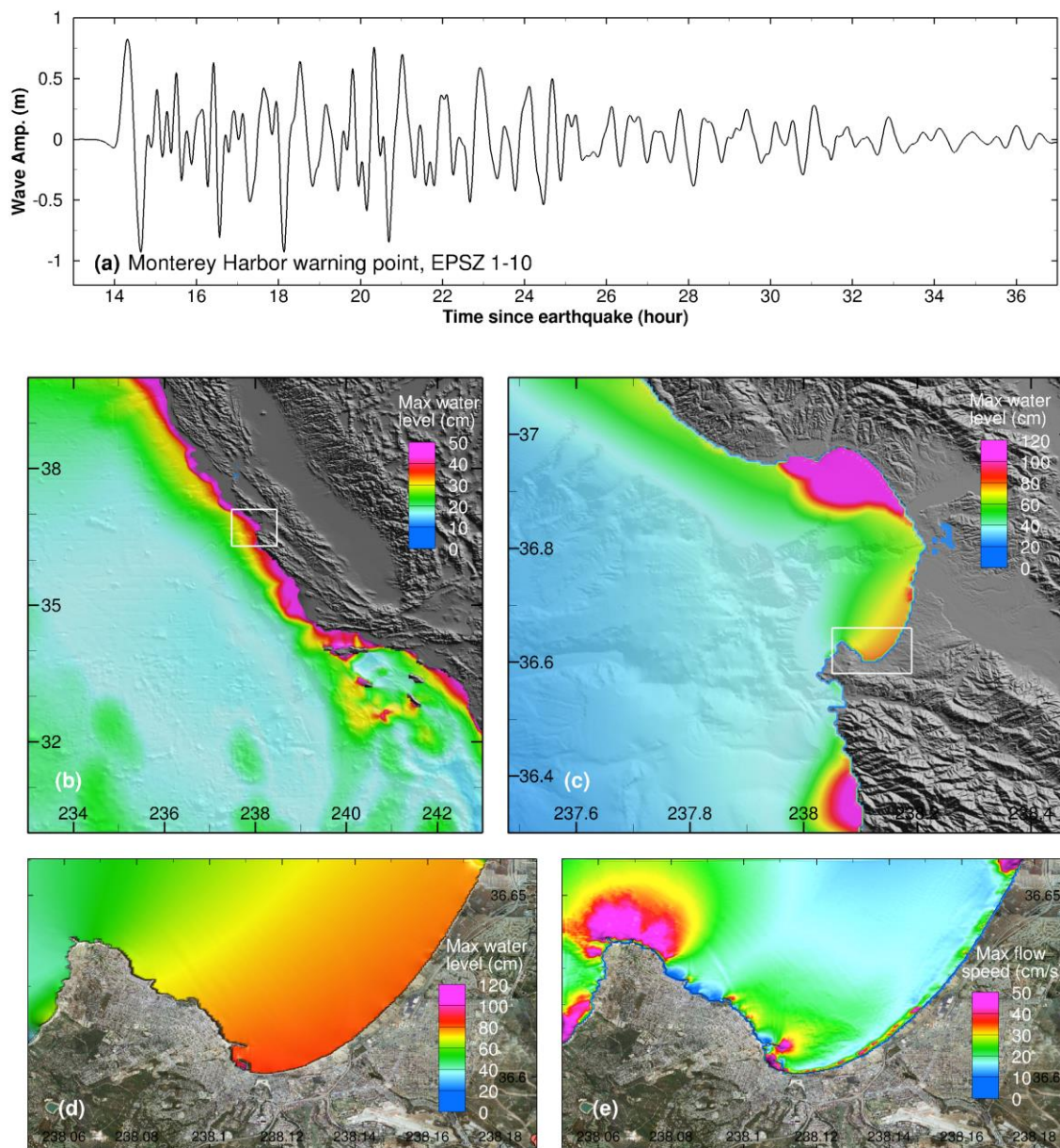
Figure 47 Model stability testing results at Monterey for synthetic mega tsunami scenario EPSZ 1-10. (a) Computed time series at the Monterey warning point; (b) Computed maximum wave amplitude in A grid of the forecast model; (c) Computed maximum current speed in B grid of the forecast model; (d) Computed maximum wave amplitude in C grid of the forecast model; (e) Computed current speed in C grid of the forecast model.
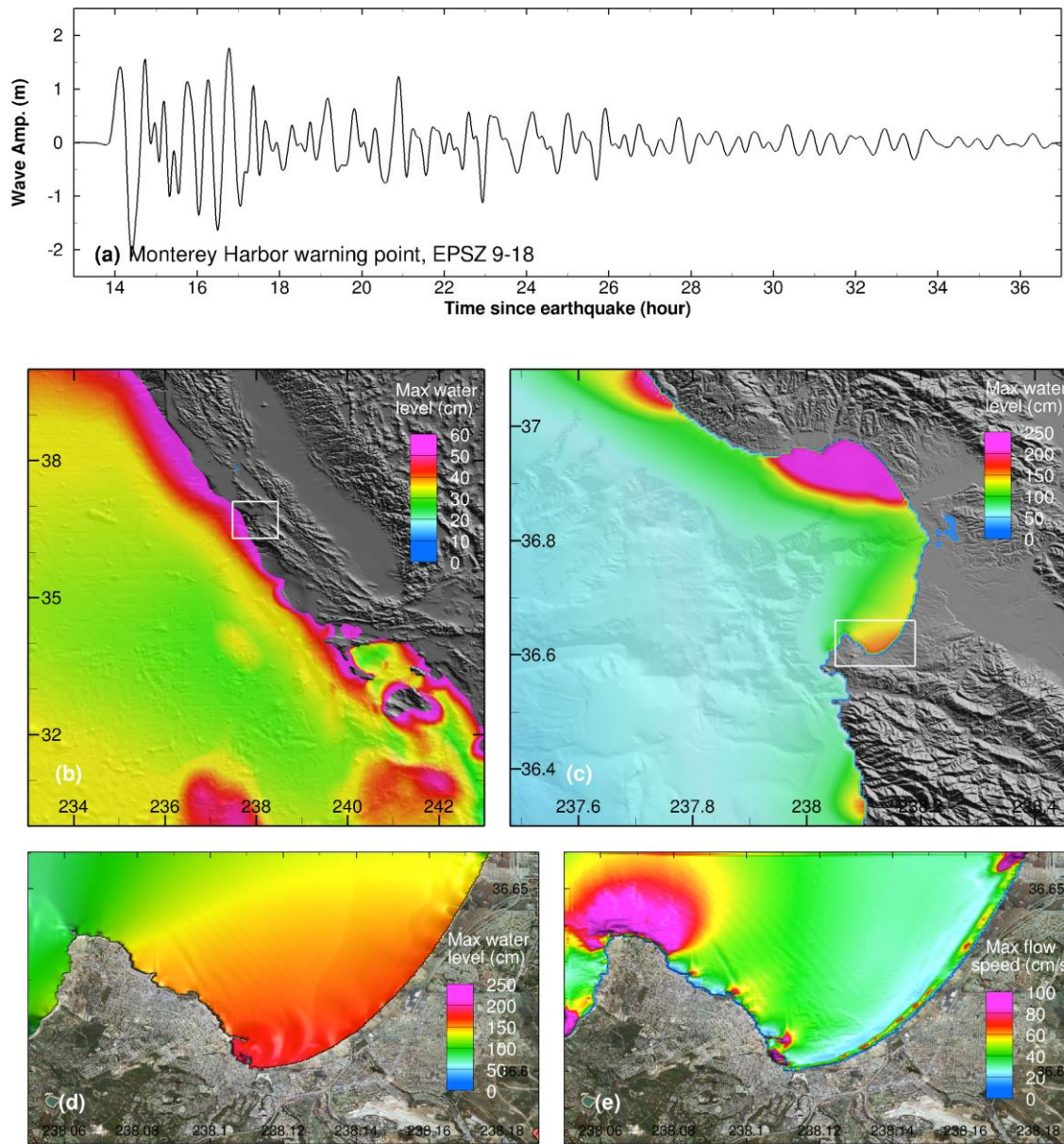
Figure 48 Model stability testing results at Monterey for synthetic mega tsunami scenario EPSZ 9-18. (a) Computed time series at the Monterey warning point; (b) Computed maximum wave amplitude in A grid of the forecast model; (c) Computed maximum current speed in B grid of the forecast model; (d) Computed maximum wave amplitude in C grid of the forecast model; (e) Computed current speed in C grid of the forecast model.
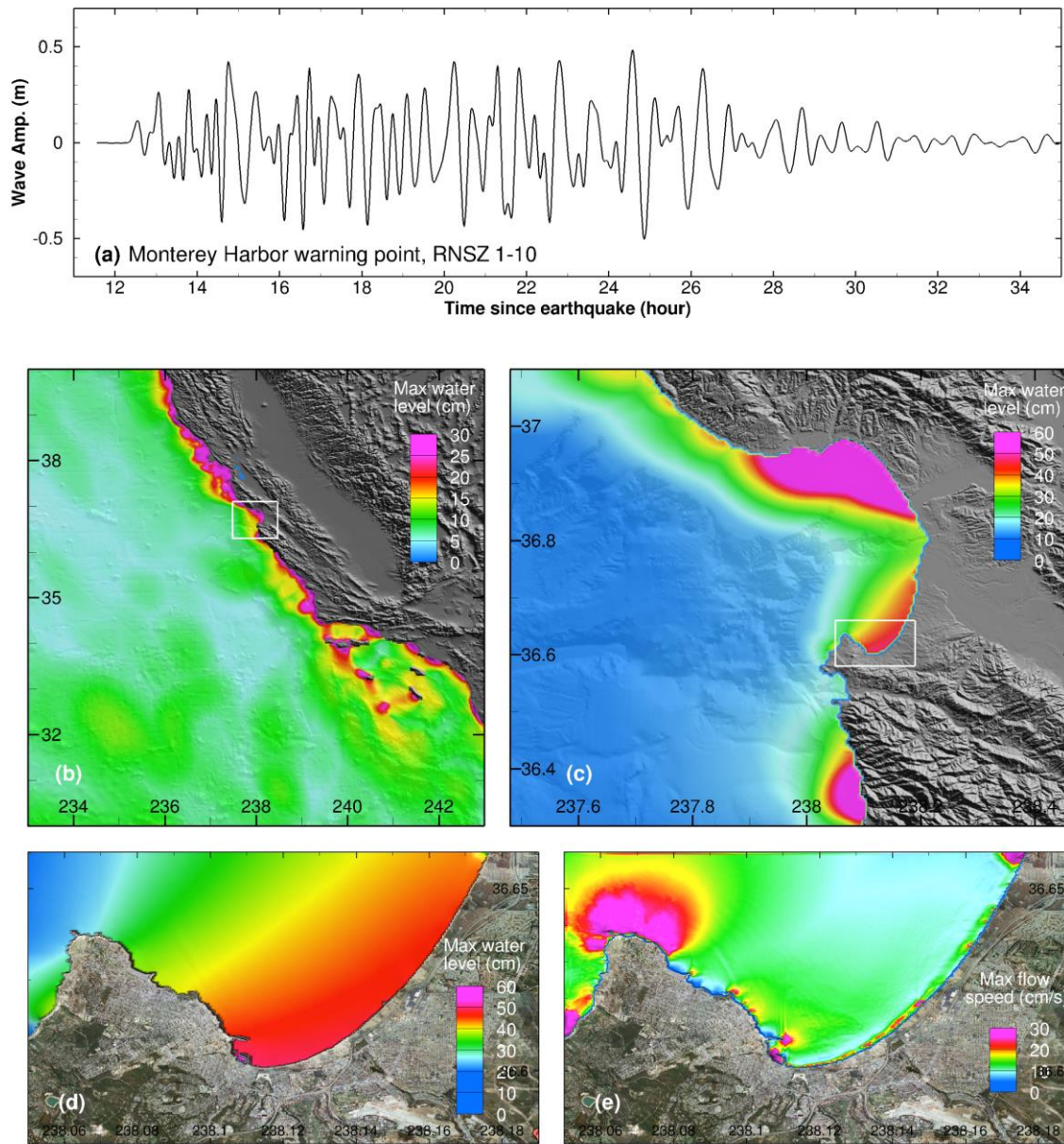
Figure 49 Model stability testing results at Monterey for synthetic mega tsunami scenario RNSZ 1-10. (a) Computed time series at the Monterey warning point; (b) Computed maximum wave amplitude in A grid of the forecast model; (c) Computed maximum current speed in B grid of the forecast model; (d) Computed maximum wave amplitude in C grid of the forecast model; (e) Computed current speed in C grid of the forecast model.
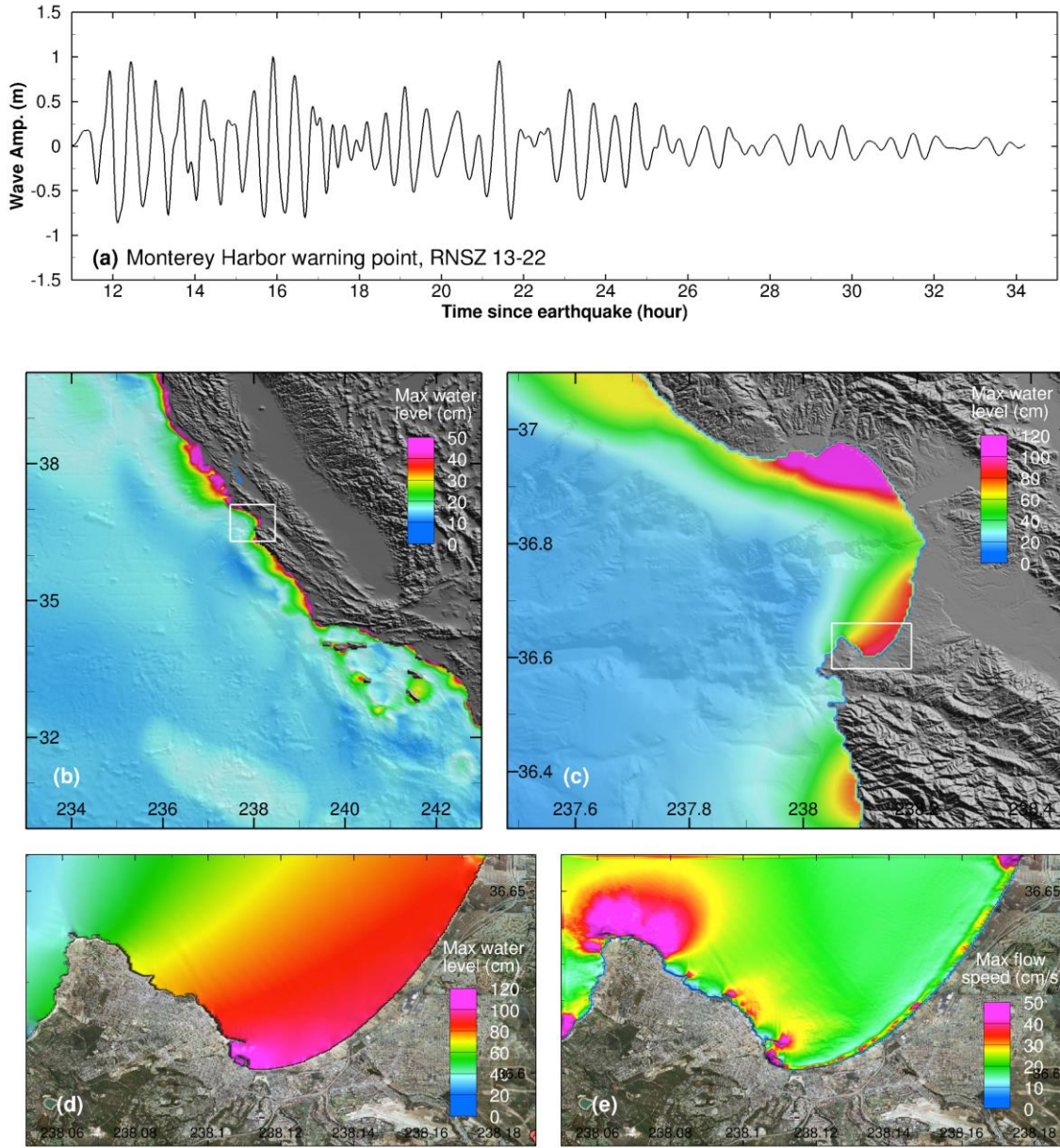
Figure 50 Model stability testing results at Monterey for synthetic mega tsunami scenario RNSZ 13-22. (a) Computed time series at the Monterey warning point; (b) Computed maximum wave amplitude in A grid of the forecast model; (c) Computed maximum current speed in B grid of the forecast model; (d) Computed maximum wave amplitude in C grid of the forecast model; (e) Computed current speed in C grid of the forecast model.
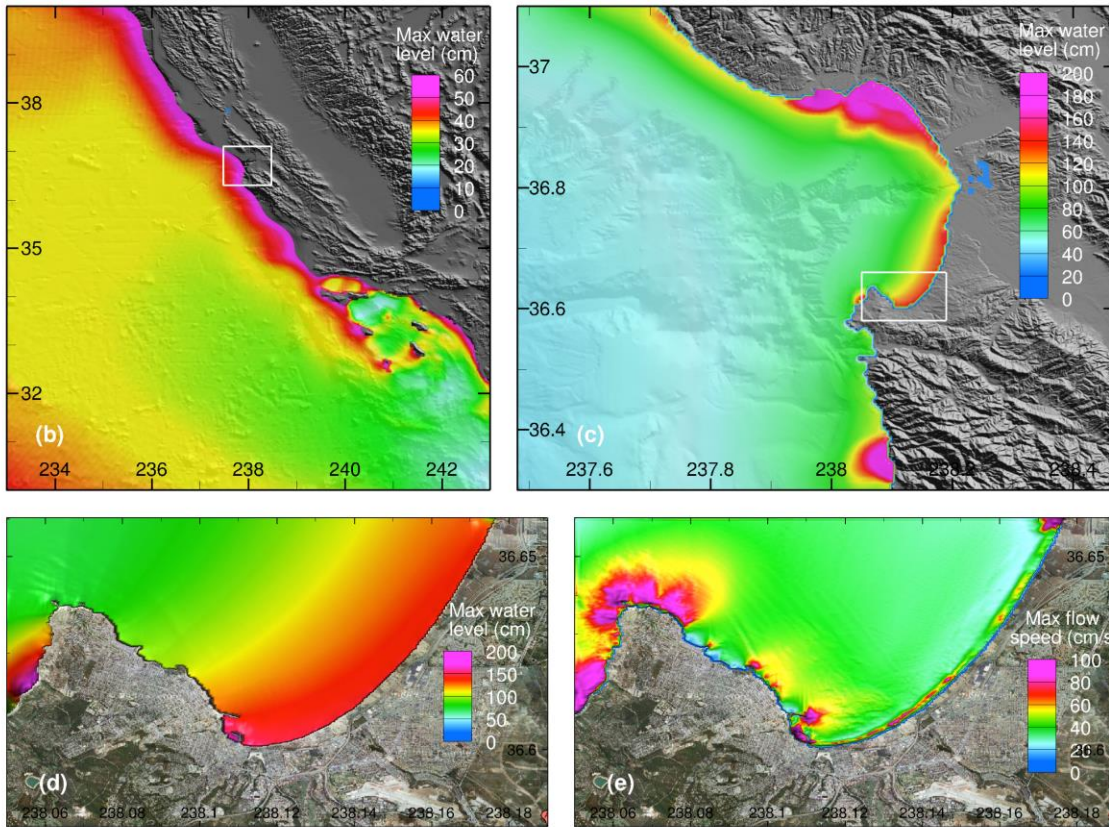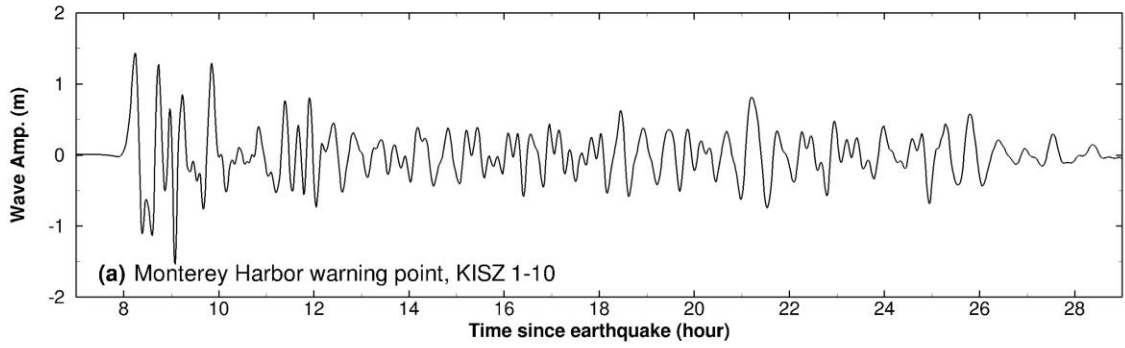
Figure 51 Model stability testing results at Monterey for synthetic mega tsunami scenario KISZ 1-10. (a) Computed time series at the Monterey warning point; (b) Computed maximum wave amplitude in A grid of the forecast model; (c) Computed maximum current speed in B grid of the forecast model; (d) Computed maximum wave amplitude in C grid of the forecast model; (e) Computed current speed in C grid of the forecast model.
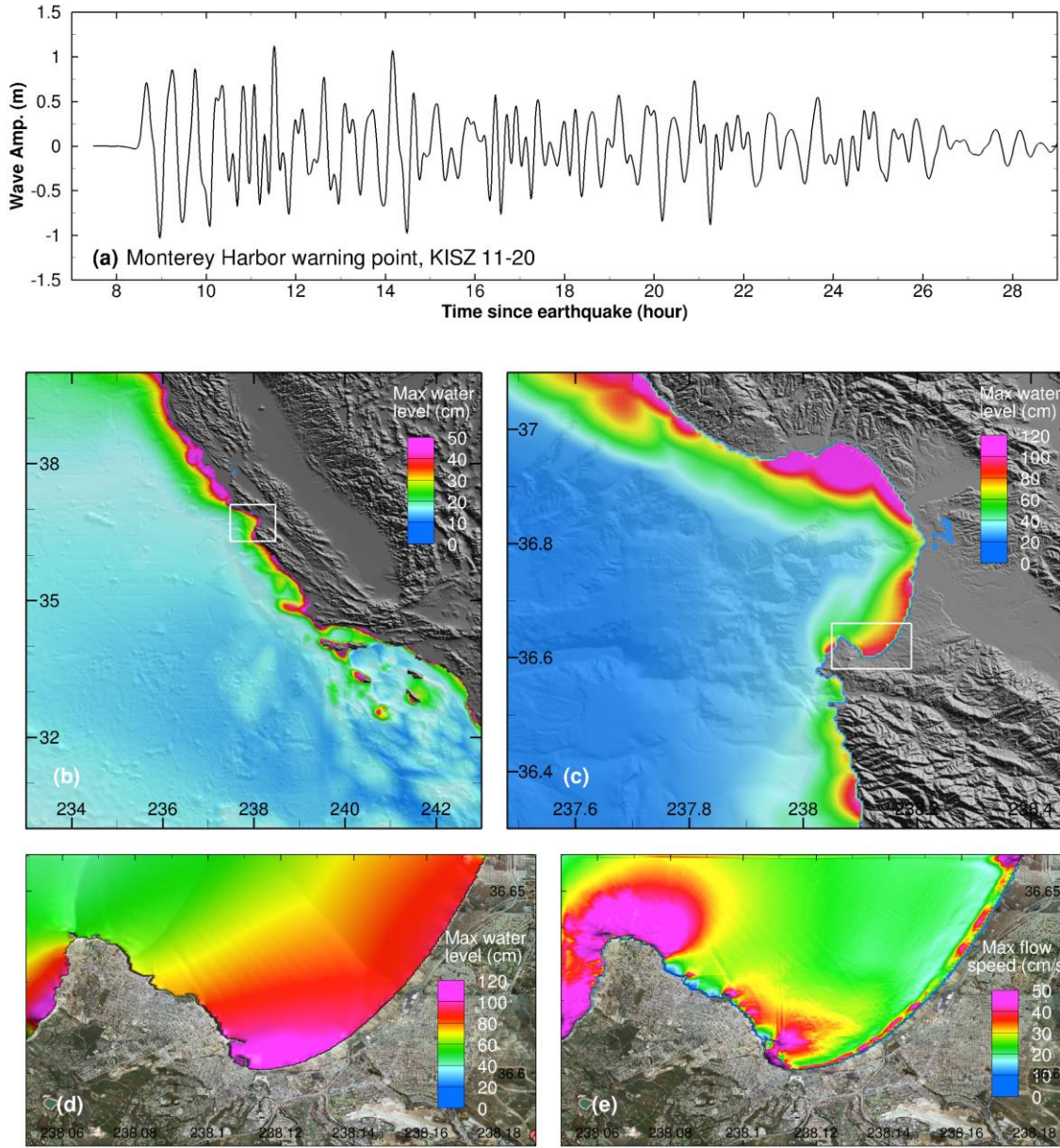
Figure 52 Model stability testing results at Monterey for synthetic mega tsunami scenario KISZ 11-20. (a) Computed time series at the Monterey warning point; (b) Computed maximum wave amplitude in A grid of the forecast model; (c) Computed maximum current speed in B grid of the forecast model; (d) Computed maximum wave amplitude in C grid of the forecast model; (e) Computed current speed in C grid of the forecast model.
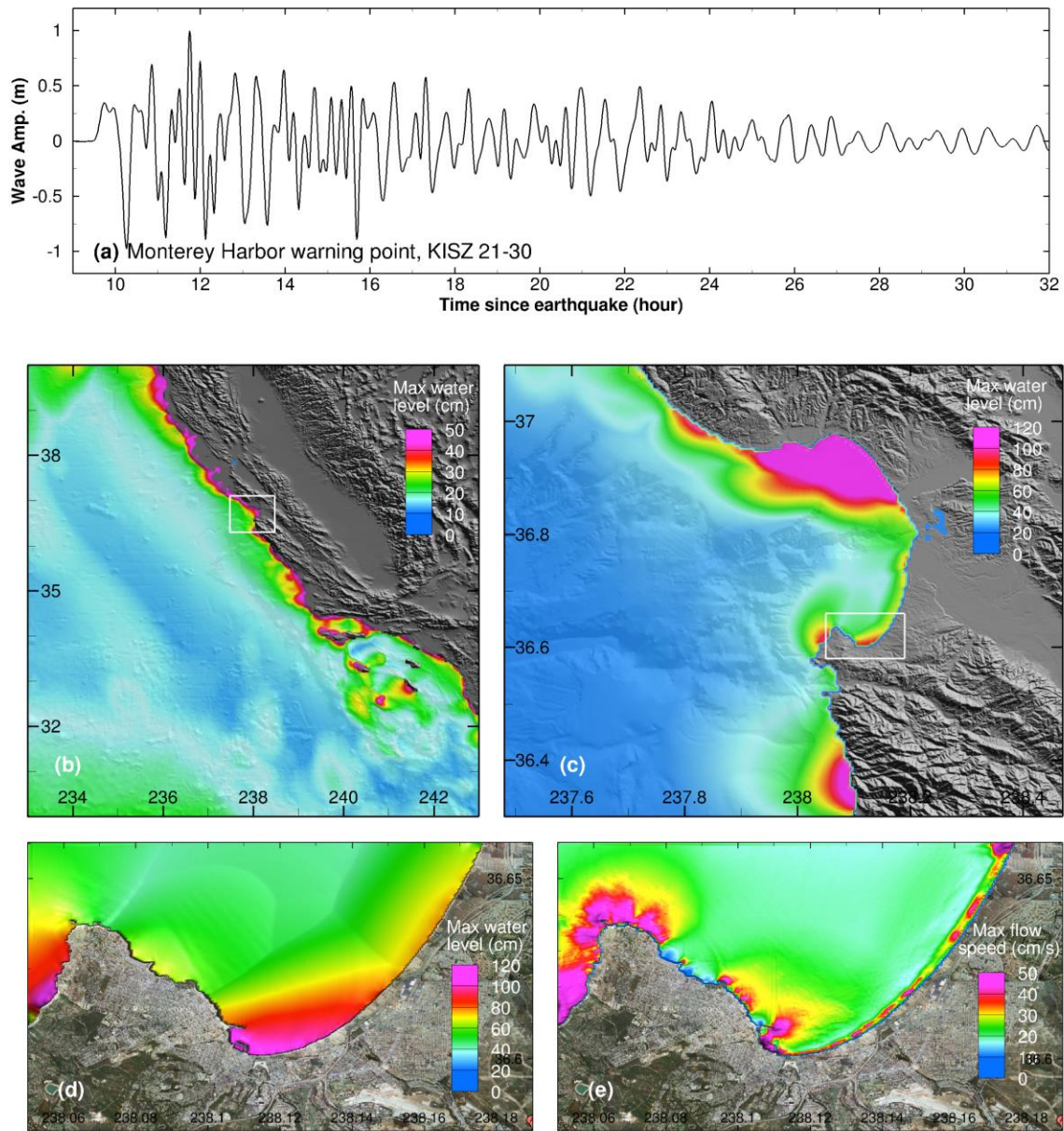
Figure 53 Model stability testing results at Monterey for synthetic mega tsunami scenario KISZ 21-30. (a) Computed time series at the Monterey warning point; (b) Computed maximum wave amplitude in A grid of the forecast model; (c) Computed maximum current speed in B grid of the forecast model; (d) Computed maximum wave amplitude in C grid of the forecast model; (e) Computed current speed in C grid of the forecast model.
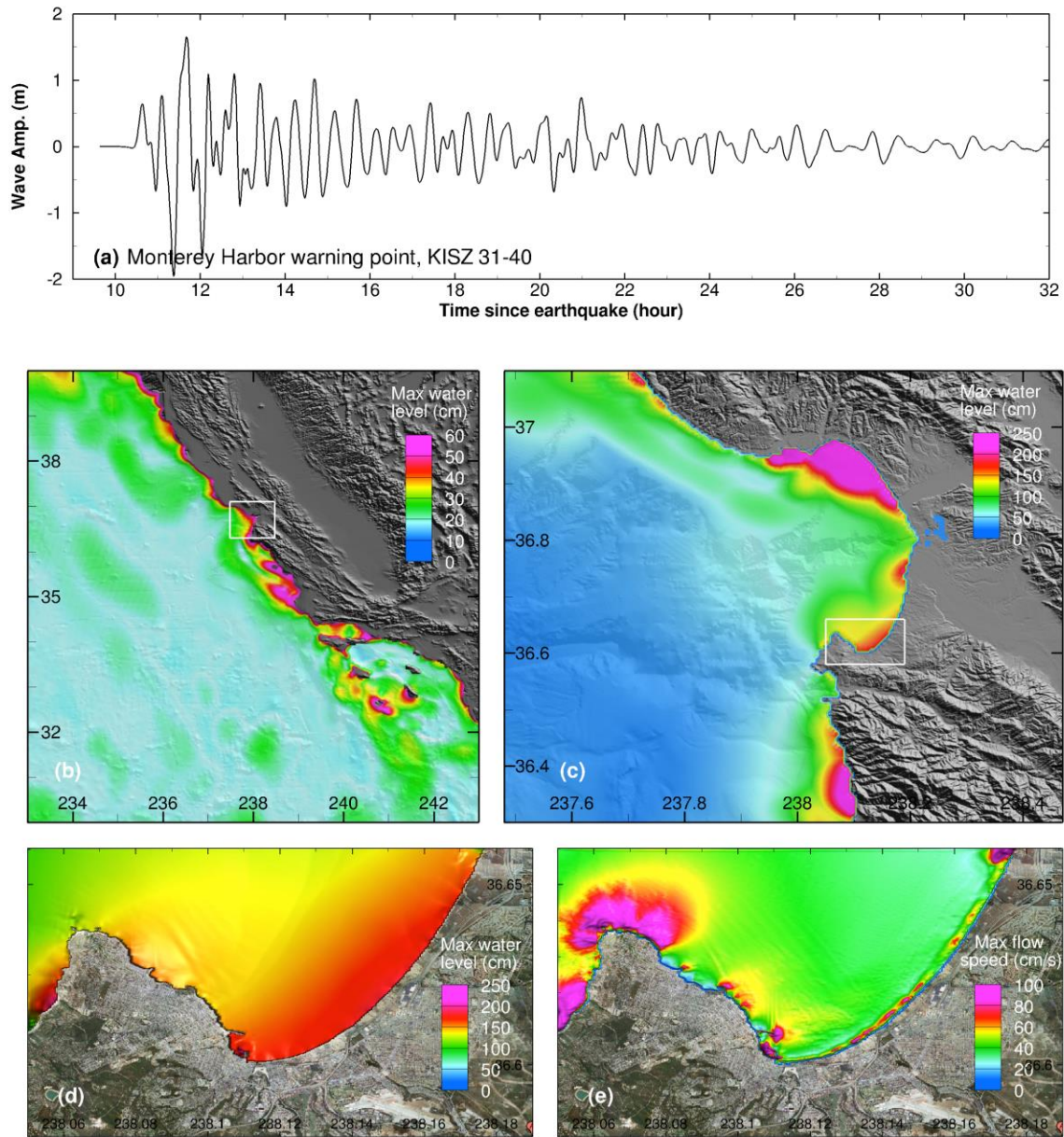
Figure 54 Model stability testing results at Monterey for synthetic mega tsunami scenario KISZ 31-40. (a) Computed time series at the Monterey warning point; (b) Computed maximum wave amplitude in A grid of the forecast model; (c) Computed maximum current speed in B grid of the forecast model; (d) Computed maximum wave amplitude in C grid of the forecast model; (e) Computed current speed in C grid of the forecast model.
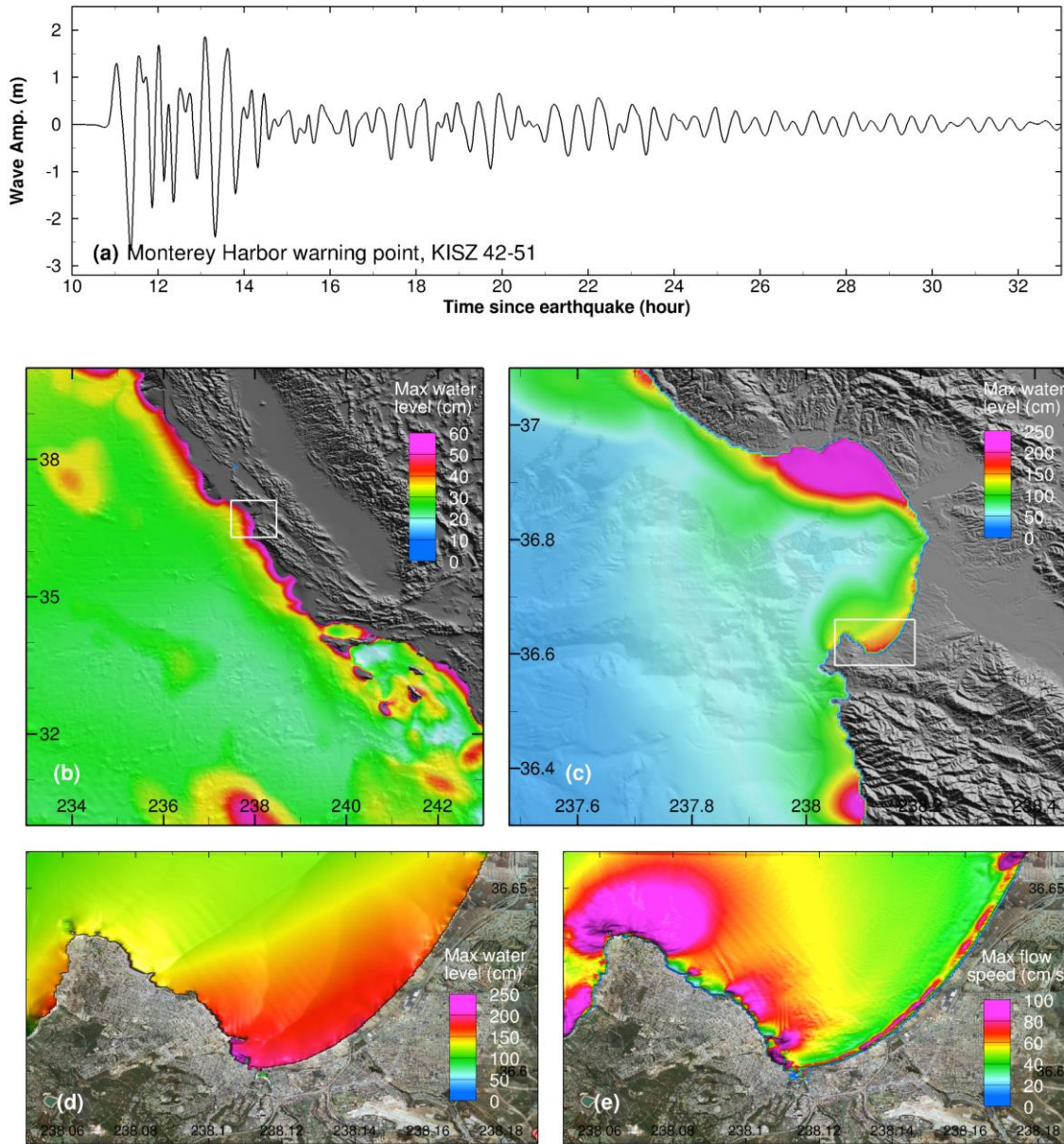
Figure 55 Model stability testing results at Monterey for synthetic mega tsunami scenario KISZ 42-51. (a) Computed time series at the Monterey warning point; (b) Computed maximum wave amplitude in A grid of the forecast model; (c) Computed maximum current speed in B grid of the forecast model; (d) Computed maximum wave amplitude in C grid of the forecast model; (e) Computed current speed in C grid of the forecast model.
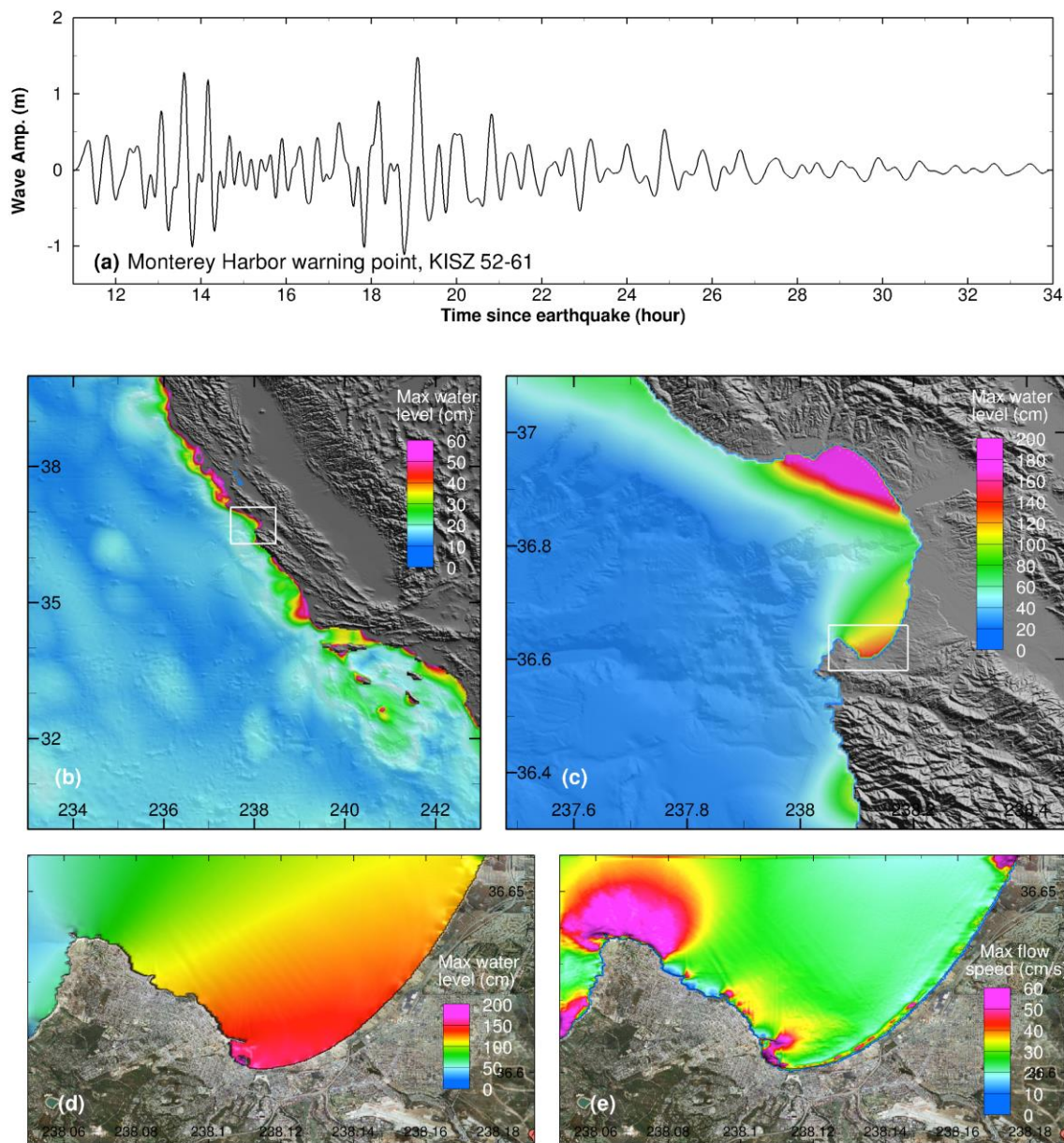
Figure 56 Model stability testing results at Monterey for synthetic mega tsunami scenario KISZ 52-61. (a) Computed time series at the Monterey warning point; (b) Computed maximum wave amplitude in A grid of the forecast model; (c) Computed maximum current speed in B grid of the forecast model; (d) Computed maximum wave amplitude in C grid of the forecast model; (e) Computed current speed in C grid of the forecast model.
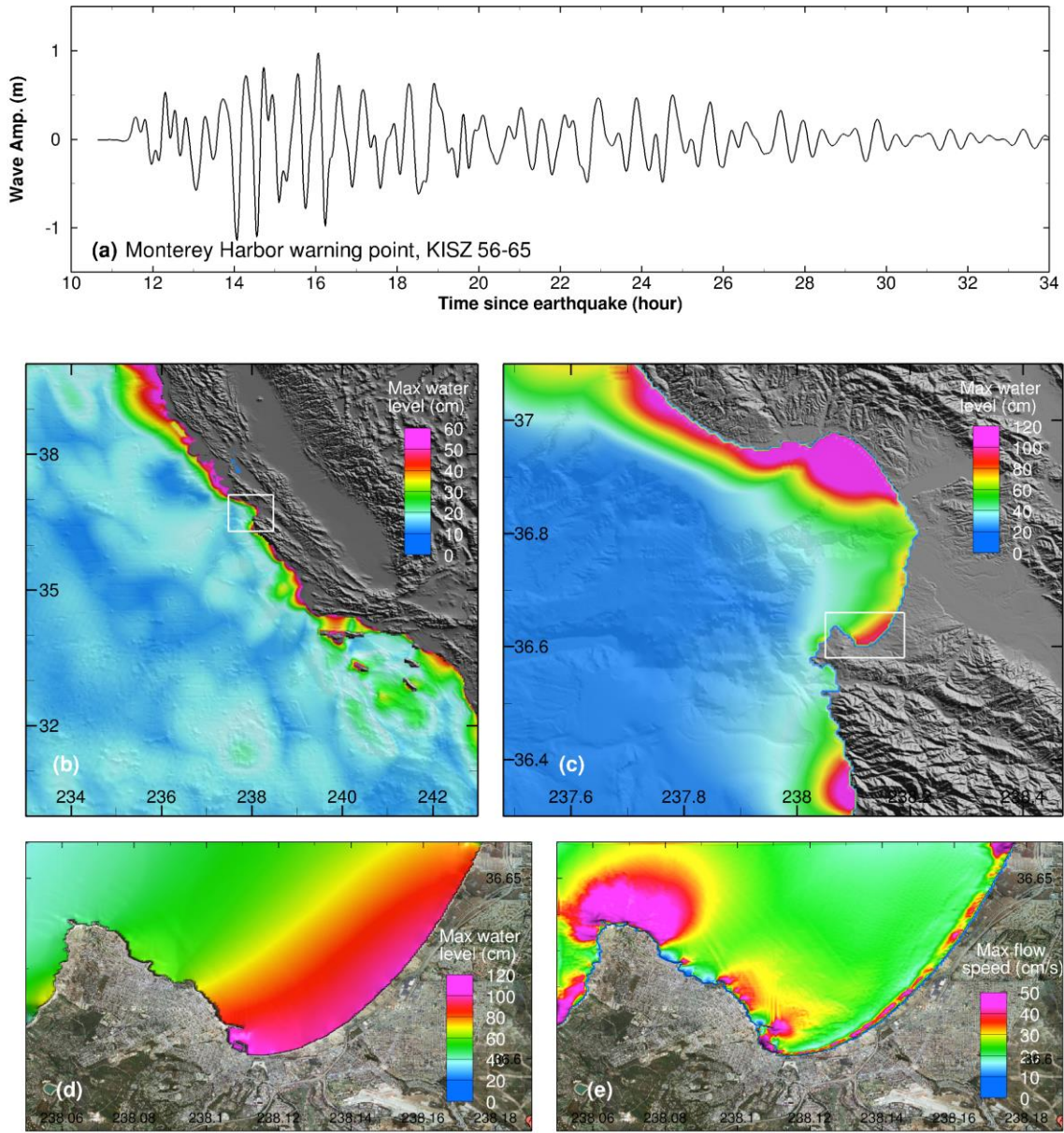
Figure 57 Model stability testing results at Monterey for synthetic mega tsunami scenario KISZ 56-65. (a) Computed time series at the Monterey warning point; (b) Computed maximum wave amplitude in A grid of the forecast model; (c) Computed maximum current speed in B grid of the forecast model; (d) Computed maximum wave amplitude in C grid of the forecast model; (e) Computed current speed in C grid of the forecast model.
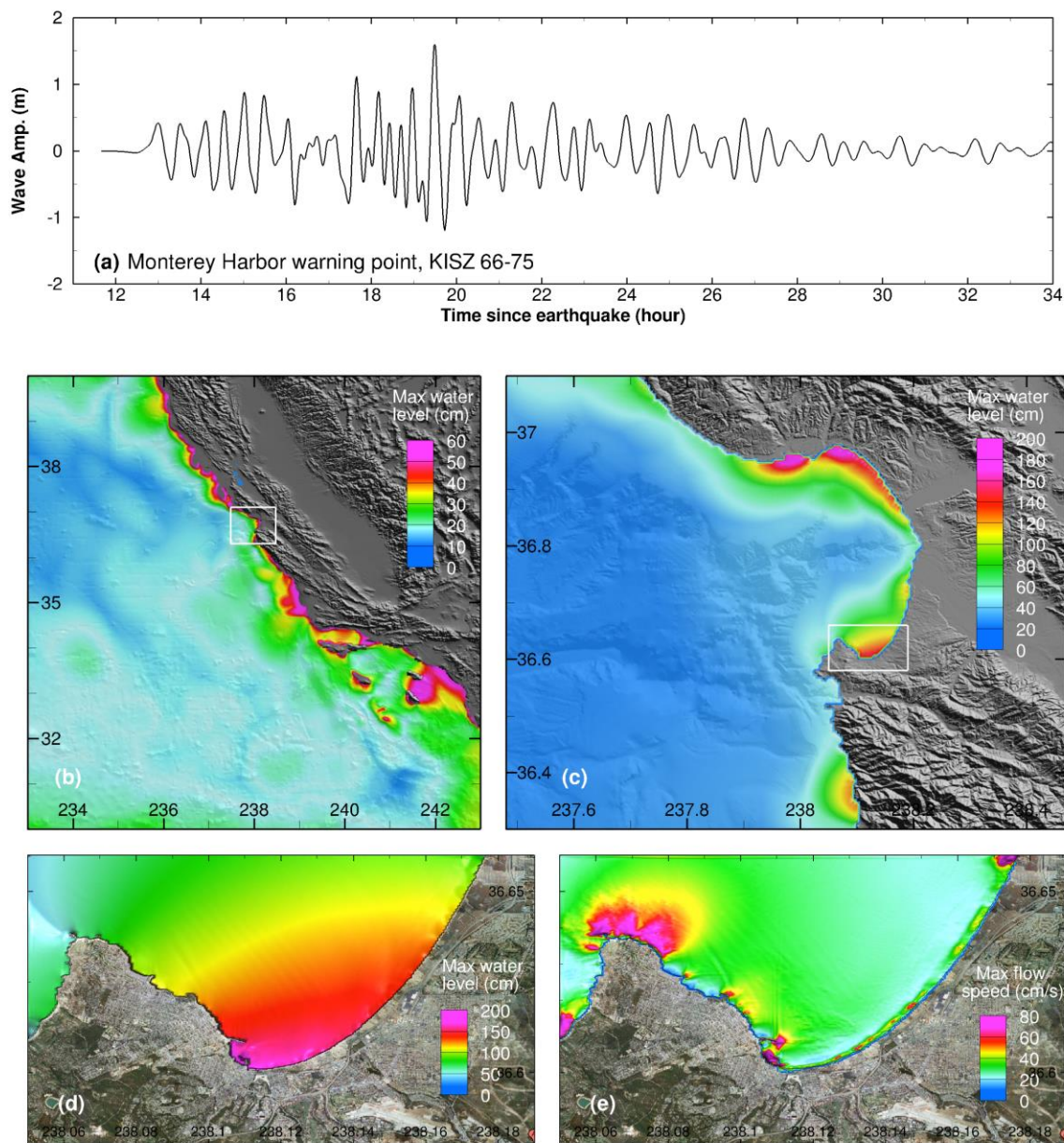
Figure 58 Model stability testing results at Monterey for synthetic mega tsunami scenario KISZ 66-75. (a) Computed time series at the Monterey warning point; (b) Computed maximum wave amplitude in A grid of the forecast model; (c) Computed maximum current speed in B grid of the forecast model; (d) Computed maximum wave amplitude in C grid of the forecast model; (e) Computed current speed in C grid of the forecast model.
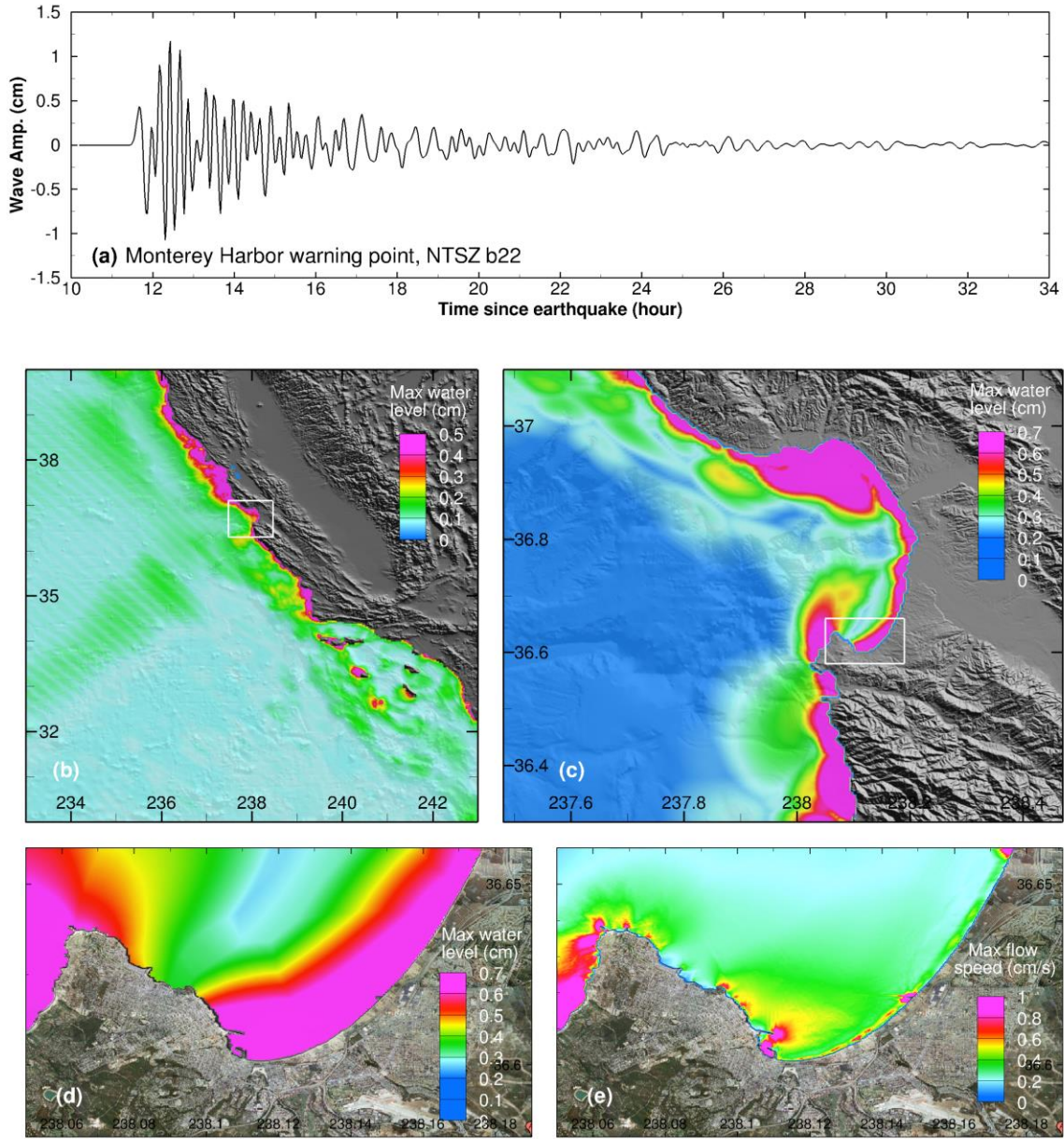
Figure 59 Model stability testing results at Monterey for synthetic tsunami scenario NTSZ b22. (a) Computed time series at the Monterey warning point; (b) Computed maximum wave amplitude in A grid of the forecast model; (c) Computed maximum current speed in B grid of the forecast model; (d) Computed maximum wave amplitude in C grid of the forecast model; (e) Computed current speed in C grid of the forecast model.
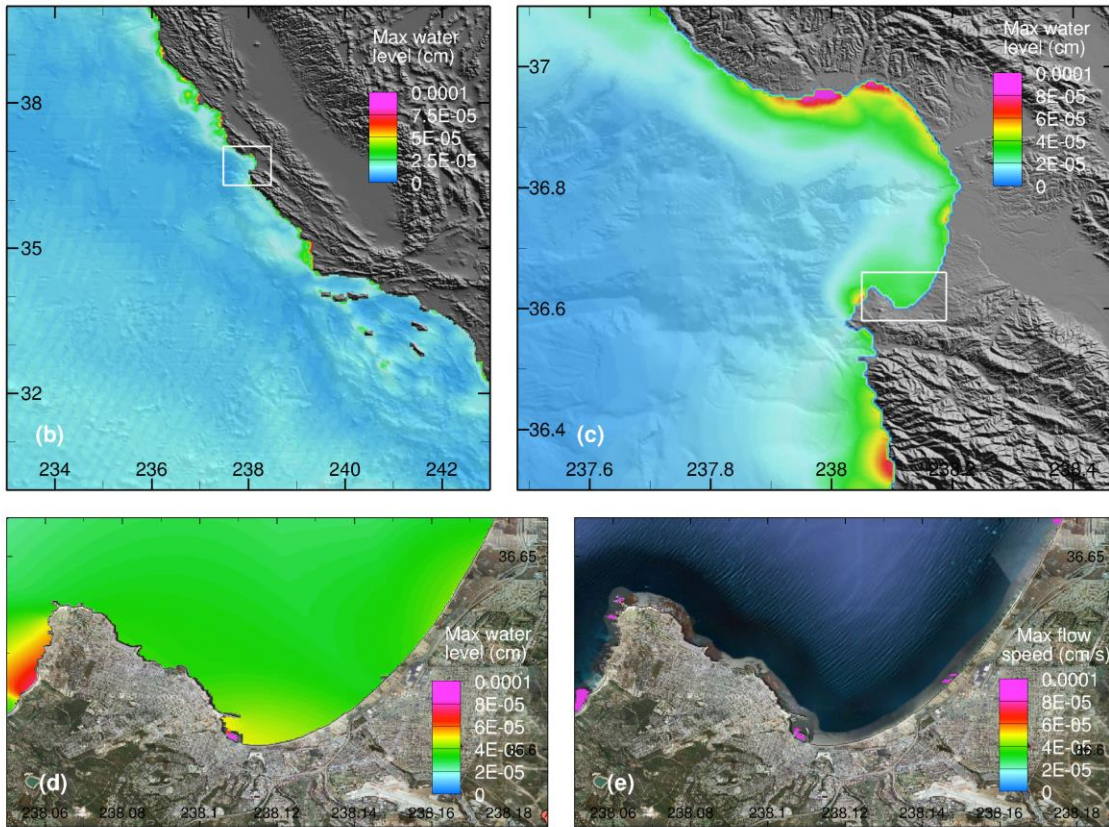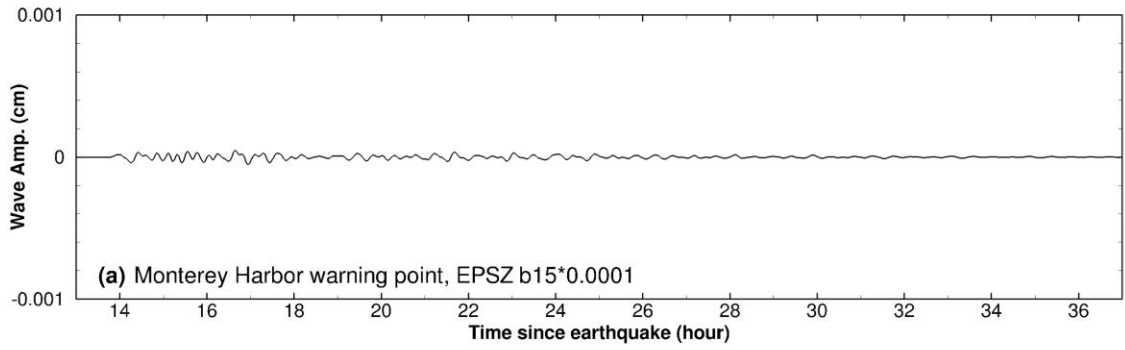
Figure 60 Model stability testing results at Monterey for synthetic micro tsunami scenario EPSZ b15. (a) Computed time series at the Monterey warning point; (b) Computed maximum wave amplitude in A grid of the forecast model; (c) Computed maximum current speed in B grid of the forecast model; (d) Computed maximum wave amplitude in C grid of the forecast model; (e) Computed current speed in C grid of the forecast model.

Tables:

Event	Date, Time (UTC), Epicenter	Mw	Earthquake source area	Max water elev. at Monterey, CA
1901 California	03 March 07:45:00 36.0ºN 120.5ºW	6.7	San Diego, California	observed
1946 Unimak	1 Apr. 12:28:56 53.32ºN 162.19ºW	8.1	Unimak Island, Alaska	0.91 m – 2.6 m at Monterey, 1.57 m at Pacific Grove.
1957 Alaska	9 Mar 14:22:31.9 51.292ºN, 175.629ºW	8.6	Alaska	0.6 m
1960 Chile	22 May 19:11:17 39.5ºS 74.5ºW	9.5	Valdivia, Chile	0.9 – 1.1 m
1964 Alaska	28 Mar. 03:36:14 61.04ºN, 147.73ºW	9.2	Prince William Sound, Alaska	Up to 2.6 m at Monterey, 1.4 m at Pacific Grove, and 4.5 m at Pebble Beach
1989 California	18 Oct. 00:04:15.2 37.036ºN, 121.883ºW	6.9	Loma Prieta, California	0.4 – 1.0 m
1992 California	25 Apr/ 18:06:4.2 40.368ºN, 124.316ºW	7.2	Humboldt County, California	0.03 m
1995 Chile	30 Jul. 05:11:23.6 23.34ºS, 70.294ºW	8.0	Antofagasta, Calama, and Mejillones, Chile	0.04 m
1995 Kuril	03 Dec. 18:01:8.9 44.63ºN, 149.3ºE	7.9	Kuril Islands	0.1 m
1996 Papua New Guinea	17 Feb. 05:59:30.5 0.891ºS, 136.953ºE	8.2	Papua New Guinea	0.05 m
1996 Andreanof	10 Jun. 04:03:35.4 51.564ºN, 177.632ºW	7.9	Andreanof Island, Alaska	observed
2001 Peru	23 Jun 20:33:14.1	8.4	Peru	0.08 m

	16.265ºS, 73.641ºW			
2003 Hokkaido	25 Sep 19:50:6.3 41.815ºN, 143.91ºE	8.3	Hokkaido, Japan	0.05 m
2004 Sumatra	26 Dec. 00:58:53.4 3.316ºN, 95.584ºE	9.1-9.3	Sumatra, Indonesia	0.1 m
2006 Kuril				
2007 Kuril				
2007 Peru	15 Aug. 23:40:57 13.354ºS, 76.509ºW	8.0	Central Peru	
2009 Samoa	29 Sep. 17:48:10.9 15.489ºS, 172.095ºW	8.0	Samoa Islands	0.15 m
2009 Vanuatu	7 Oct. 22:03:14.4 13.006ºS, 166.51ºE	7.6	Vanuatu Islands	0.05 m
2010 Chile	27 Feb. 06:34:11.5 36.122ºS, 72.898ºW	8.8	Maule, Chile	0.28 m
2011 Japan	11 Mar 05:46:24.1 38.297ºN 142.373ºE	9.0	Tohoku Island, Japan	0.7 m

Table 1. Historical tsunami events that have affected Monterey California.

Grid	Region	Reference Inundation Model (RIM)			Forecast Model		
		Coverage	Cell	Time	Coverage	Cell	Time
		Lat. [ºN]	Size	Step	Lat. [ºN]	Size	Step
		Lon. [ºW]	["]	[sec]	Lon. [ºW]	["]	[sec]
A	South Carolina	30-40	36	3.75	30-40	120	12.0
		127-117	(1001×1001)		127-117	(301×301)	
B	Monterey Bay	36.3 -37.1	3	0.25	36.3 -37.1	18	2.0
		122.52 –121.53	(1198×981)		122.52 – 121.53	(199×161)	
C	Monterey Harbor	33.58-36.71	1/3	0.25	36.58-36.66	2×1	2.0
		121.958-121.77	(2031×1405)		121.95-121.84	(253×289)	
Minimum amplitude of input offshore wave (m)		0.0001			0.0001		
Minimum offshore depth [m]		1			1		
Water depth for dry land [m]		0.1			0.1		
Friction coefficient (n^2)		0.0009			0.0009		
Let a and b runup		1			1		
Blowup limit (m)		300			300		
Input time step (sec)		0.25			1.0		
Input amount of steps		115200			43200		
Compute "A" arrays every n-th time step		15			12		
Compute "B" arrays every n-th time step		1			1		
Input number of steps between snapshots		120			36		
… Starting from		1			1		
… saving grid every n-th node		1			1		
CPU time for a 4-hour simulation (min)		1489			10.4		
Warning point coordinates		121.88667W, 36.605N					

Table 2. Model setup and input parameters of Monterey forecast model and reference model.

Event	Time (UTC)	Source Zone	Mw	Lat. (°)	Lon. (°)	Source
1946 Unimak	1946-04-01 12:28:56	ACSZ	[4]8.5	53.32N	163.19W	[4]7.5 × b23 + 19.7 × b24 + 3.7 × b25
1964 Alaska	1964-03-28 03:36:14	ACSZ	[2]9.2	61.10N	147.50W	[4]Tang *et al.* (2006)
1994 Kuril	1994-10-04 13:23:28.5	KISZ	[1]8.3	43.60N	147.63E	[4]9.0 × a20
1996 Andreanov	1996-06-10 04:04:03.4	ACSZ	[1]7.9	51.10N	177.410W	[3]2.40 × a15 + 0.80 × b16
2001 Peru	2001-06-23 20:34:23.3	CSSZ	[1]8.4	17.28S	72.71W	[5]5.70 × a15 + 2.90 × b16 + 1.98 × a16
2006 Tonga	2006-05-03 15:27:03.7	NTSZ	[1]8.0	20.39S	173.47W	[3]6.6 × b29
2006 Kuril	2006-11-15 11:15:08.0	KISZ	[1]8.3	46.71N	154.33E	[3]4 × a12 + 0.5 × b12 + 2 × a13 + 1.5 × b13
2007 Kuril	2007-01-13 04:23:48.1	KISZ	[1]8.1	46.17N	154.80E	[3]-3.64 × b13
2007 Peru	2007-08-15 23:41:57.9	CSSZ	[1]8.0	13.73S	77.04W	[5]4.3 × a9 + 4.1 × b9
2009 Samoa	2009-09-29 17:48:10	NTSZ	[2]8.1	15.509ºS	172.034ºW	[4]6.45 × b34 + 6.21 × c35;
2010 Chile	2010-02-27 06:43:14	CSSZ	[2]8.8	35.909ºS	72.733ºW	[3]17.24 × a88 + 11.86 × b88 + 20.78 × z88 + 18.39 × b89 + 8.82 × a90 + 16.75 × b90 + 7.05 × z90
2011 Japan	2011-03-11 05:46:24	KISZ	[2]9.1	38.297ºN	142.372ºE	[3]4.66 × b24 + 12.23 × b25 + 26.31 × a26 + 21.27 × b26 + 22.75 × a27 + 4.98 × b27

[1]Centroid Moment Tensor

[2]United States Geological Survey (USGS)

[3]Tsunami source was obtained in real time and applied to the forecast

[4]Tsunami source was obtained in hindcast study

[5]Tsunami source was obtained in real time based on older propagation database (Gica et al., 2008)

Table 3 Historical events used for model validation for Monterey, California, where ASCZ represents the Aleutian-Alaska-Cascadia subduction zone, KISZ the Kamchatka-Kuril-Japan-Izu-Mariana-Yap subduction zone, CSSZ the Central South America subduction zone, and NTSZ the New Zealand-Kermadec-Tonga subduction zone.

Scenario	Source Zone	Tsunami Source	Alpha (m)
ACSZ 1-10	Aleutian-Alaska-Cascadia	A1-A10, B1-B10	28.4
ACSZ 11-20	Aleutian-Alaska-Cascadia	A11-A20, B11-B20	28.4
ACSZ 21-30	Aleutian-Alaska-Cascadia	A21-A30, B21-B30	28.4
ACSZ 31-40	Aleutian-Alaska-Cascadia	A31-A40, B31-B40	28.4
ACSZ 41-50	Aleutian-Alaska-Cascadia	A41-A50, B41-B50	28.4
ACSZ 46-55	Aleutian-Alaska-Cascadia	A46-A55, B46-B55	28.4
ACSZ 56-65	Aleutian-Alaska-Cascadia	A56-A65, B56-B65	28.4
CSSZ 1-10	Central and South America	A1-A10, B1-B10	28.4
CSSZ 11-20	Central and South America	A11-A20, B11-B20	28.4
CSSZ 21-30	Central and South America	A21-A30, B21-B30	28.4
CSSZ 31-40	Central and South America	A31-A40, B31-B40	28.4
CSSZ 41-50	Central and South America	A41-A50, B41-B50	28.4
CSSZ 51-60	Central and South America	A51-A60, B51-B60	28.4
CSSZ 61-70	Central and South America	A61-A70, B61-B70	28.4
CSSZ 71-80	Central and South America	A71-A80, B71-B80	28.4
CSSZ 81-90	Central and South America	A81-A90, B81-B90	28.4
NTSZ 1-10	New Zealand-Kermadec-Tonga	A1-A10, B1-B10	28.4
NTSZ 11-20	New Zealand-Kermadec-Tonga	A11-20, B11-20	28.4
NTSZ 21-30	New Zealand-Kermadec-Tonga	A21-30, B21-30	28.4
NTSZ 30-39	New Zealand-Kermadec-Tonga	A30-39, B30-39	28.4
NVSZ 1-10	New-Britain-Solomons-Vanuatu	A1-A10, B1-B10	28.4
NVSZ 11-20	New-Britain-Solomons-Vanuatu	A11-A20, B11-B20	28.4
NVSZ 21-30	New-Britain-Solomons-Vanuatu	A21-A30, B21-B30	28.4
NVSZ 28-37	New-Britain-Solomons-Vanuatu	A28-A37, B28-37	28.4
MOSZ 1-10	Manus Ocean Convergence Boundary	A1-A10, B1-B10	28.4
MOSZ 8-17	Manus Ocean Convergence Boundary	A8-A17, B8-B17	28.4
NGSZ 1-10	New Guinea	A1-A10, B1-B10	28.4
NGSZ 6-15	New Guinea	A6-A15, B6-B15	28.4
EPSZ 1-10	East-Philippines	A1-A10, B1-B10	28.4

EPSZ 9-18	East-Philippines	A9-A18, B9-B18	28.4
RNSZ 1-10	Ryukyu-Kyushu-Nankai	A1-A10, B1-B10	28.4
RNSZ 13-22	Ryukyu-Kyushu-Nankai	A13-A22, B13-B22	28.4
KISZ 1-10	Kamchatka-Yap-Mariana-Izu-Bonin	A1-A10, B1-B10	28.4
KISZ 11-20	Kamchatka-Yap-Mariana-Izu-Bonin	A11-A20, B11-B20	28.4
KISZ 21-30	Kamchatka-Yap-Mariana-Izu-Bonin	A21-A30, B21-B30	28.4
KISZ 32-41	Kamchatka-Yap-Mariana-Izu-Bonin	A32-A41, B32-B41	28.4
KISZ 42-51	Kamchatka-Yap-Mariana-Izu-Bonin	A42-A51, B42-B51	28.4
KISZ 52-61	Kamchatka-Yap-Mariana-Izu-Bonin	A52-A61, B52-B61	28.4
KISZ 56-65	Kamchatka-Yap-Mariana-Izu-Bonin	A56-A65, B56-B65	28.4
KISZ 66-75	Kamchatka-Yap-Mariana-Izu-Bonin	A66-A75, B66-B75	28.4
NTSZ b22	New Zealand-Kermadec-Tonga	B22	1.0
EPSZ b15	East-Philippines	B15	0.0001

Table 4 Tsunami source of 51 synthetic scenarios used for stability testing, where ACSZ = Alaska-Aleutian-Canada source zone, CSSZ = Central and South America source zone; NTSZ = New Zealand-Kermadec-Tonga source zone; NVSZ = New Britain-Solomons-Vanuatu source zone; MOSZ = Manus OCB source zone; NGSZ = North New Guinea source zone; EPSZ = East Philippines source zone; RNSZ = Ryukyu-Kyushu-Nankai source zone; KISZ = Kamchatka-Kuril-Japan trench source zone.

Supplement: SIFT testing results

The Monterey forecast model was tested with NOAA's tsunami forecast system version 3.2. The Monterey forecast model was tested with four synthetic scenarios and one historical tsunami event. Test results from the forecast system and comparisons with the results obtained during the forecast model development are shown numerically in **Table S1** and graphically in **Figures S1 to S5**. The results show that the forecast model is stable and robust, with consistent and high quality results across geographically distributed tsunami sources and mega-event tsunami magnitudes. The model run time (wall clock time) was 22.77 minutes for 12 hours of simulation time, and 7.60 minutes for 4 hours. This run time is well within the 10 minute run time for 4 hours of simulation time and satisfies time efficiency requirements.

Four synthetic events were run on the Monterey forecast model. The modeled scenarios were stable for all cases tested, with no instabilities or ringing. Results show that the largest modeled height was 266.4 centimeters (cm) and originated in the New Zealand-Kermadec-Tonga (NTSZ 30-39) source. Amplitudes greater than 100 cm were computed for 3 of the 4 test sources. The smallest signal of 99.3 cm was computed at the Kamchatka-Yap-Mariana-Izu-Bonin (KISZ 21-30) source. Direct comparisons of output from the forecast tool with results of both the Tohoku 2011 historical event and available development synthetic events, demonstrated that the wave patterns were nearly identical in shape, pattern, and with very small difference in the amplitude. These differences are mainly attributed to update of the tsunami propagation database over the last years.

Source Zone	Tsunami Source	α [m]	SIFT Max (cm)	Development Max (cm)	SIFT Min (cm)	Development Min (cm)
Mega-tsunami scenarios						
KISZ	A21-A30, B21-B30	28.4	99.3	100.1	-99.9	-100.1
ACSZ	A56-A65, B56-B65	28.4	123.2	122.1	-77.7	-77.78
CSSZ	A81-A190, B81-B90	28.4	104.0	104.0	-94.6	-94.41
NTSZ	A30-39, B30-39	28.4	266.4	266.3	-265.5	-265.2
Historical events						
Tohoku 2011			72.3	72.3	-72.0	72.0

Table S1. Table of maximum and minimum amplitudes (cm) at the Monterey, California warning point for synthetic and historical events tested using SIFT 3.2 and obtained during development.
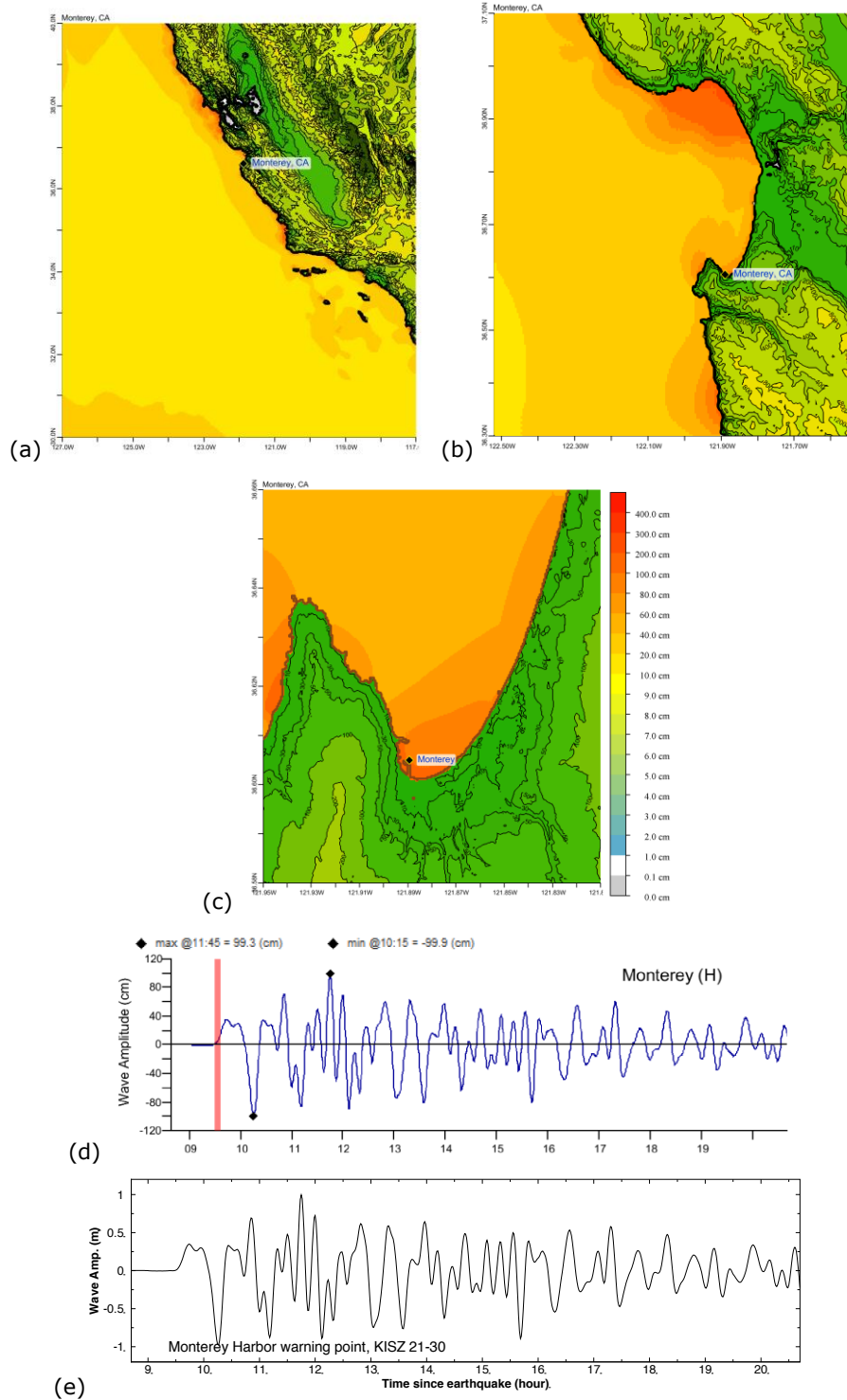
Figure S1. Max computed wave amplitude of (a) A grid; (b) B grid; (c) C grid of Monterey, California, for synthetic event KISZ 21-30; (d) SIFT Computed time series at Monterey tide gage for synthetic event KISZ 21-30: (e) Model computed time series shown in the forecast model report for synthetic event KISZ 21-30.
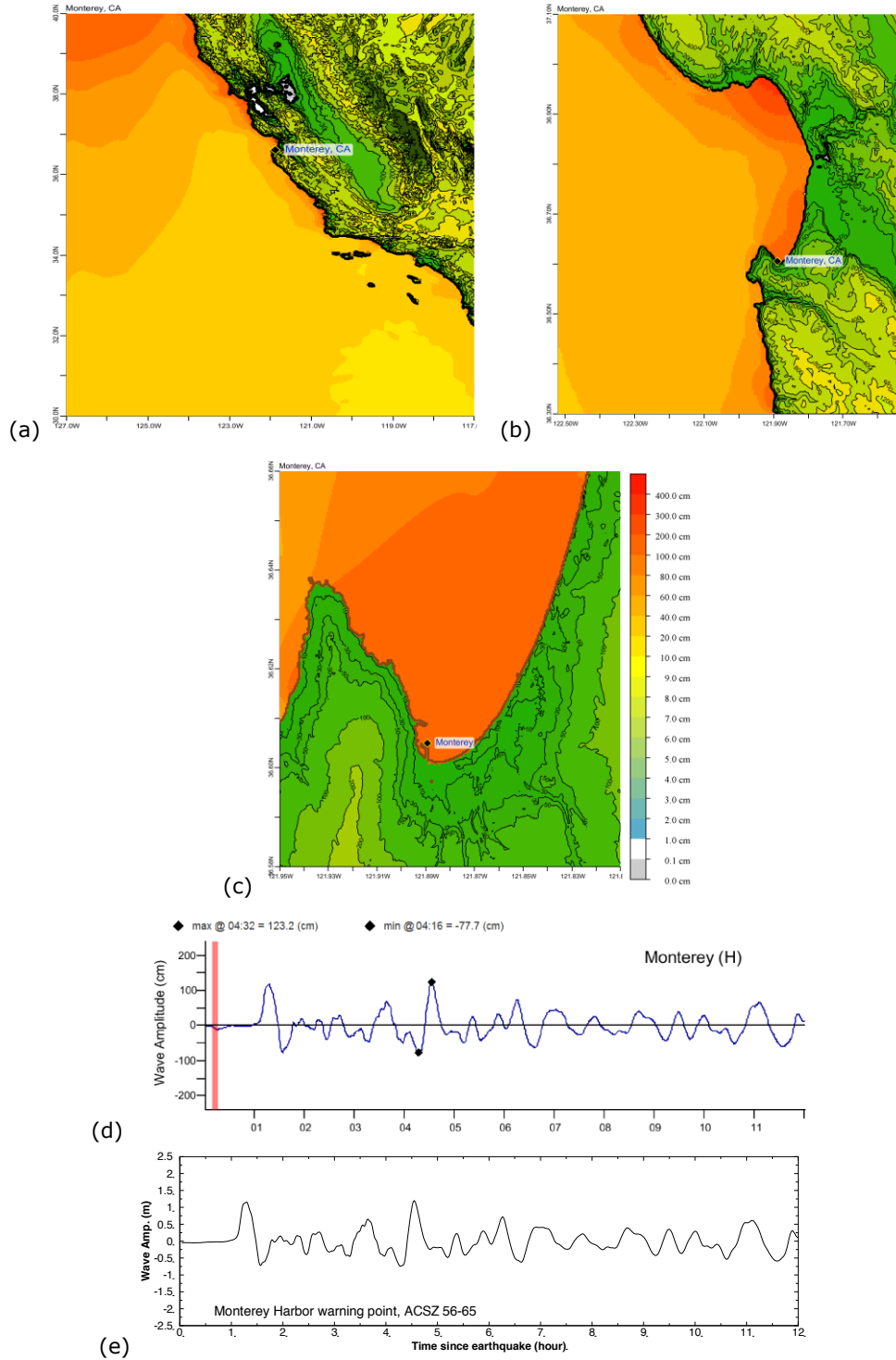
Figure S2. Max computed wave amplitude of (a) A grid; (b) B grid; (c) C grid of Monterey, California, for synthetic event ACSZ 56-65; (d) SIFT Computed time series at Monterey tide gage for synthetic event ACSZ 56-65: (e) Model computed time series shown in the forecast model report for synthetic event ACSZ 56-65.
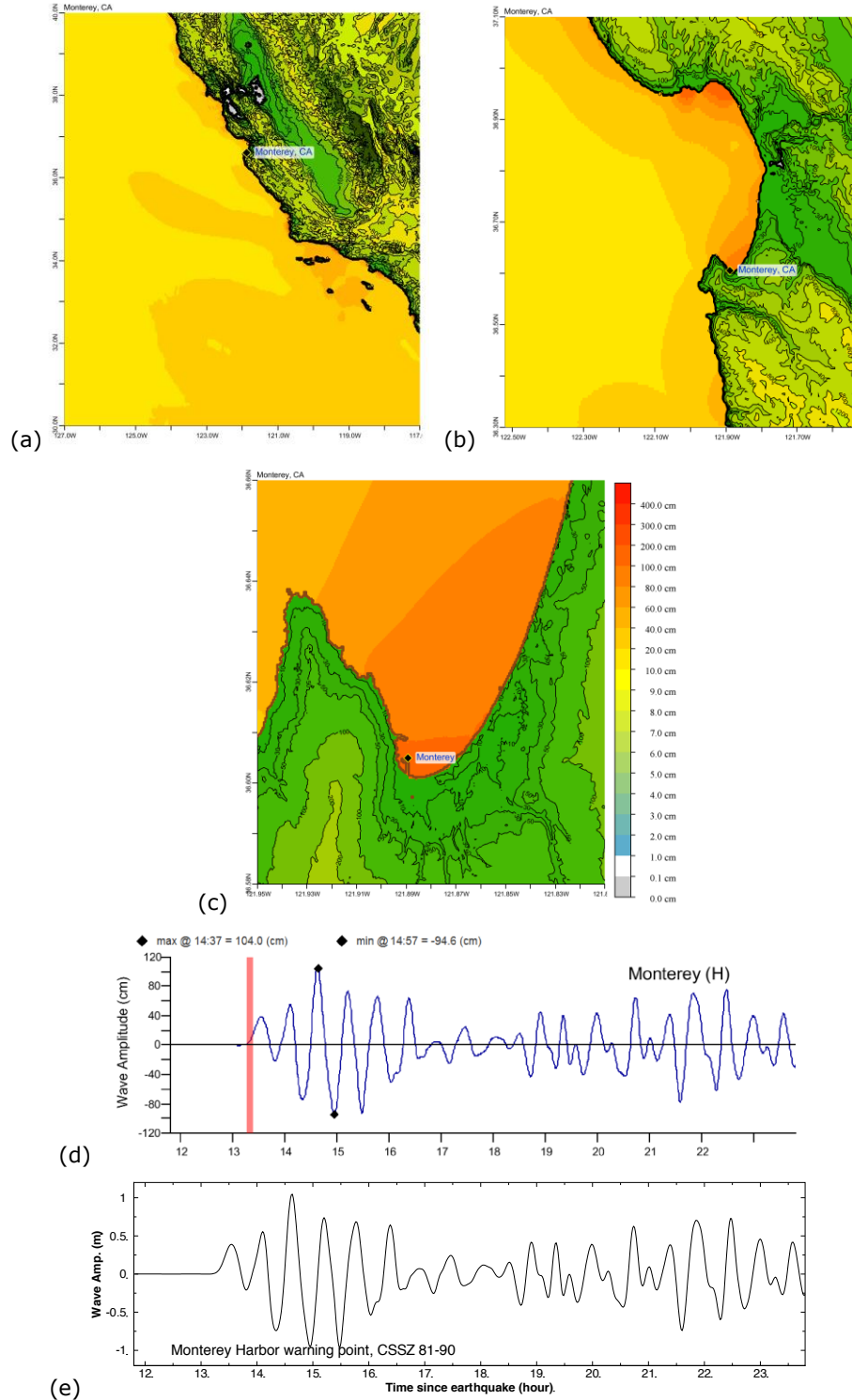
Figure S3. Max computed wave amplitude of (a) A grid; (b) B grid; (c) C grid of Monterey, California, for synthetic event CSSZ 81-90; (d) SIFT Computed time series at Monterey tide gage for synthetic event CSSZ 81-90: (e) Model computed time series shown in the forecast model report for synthetic event CSSZ 81-90.
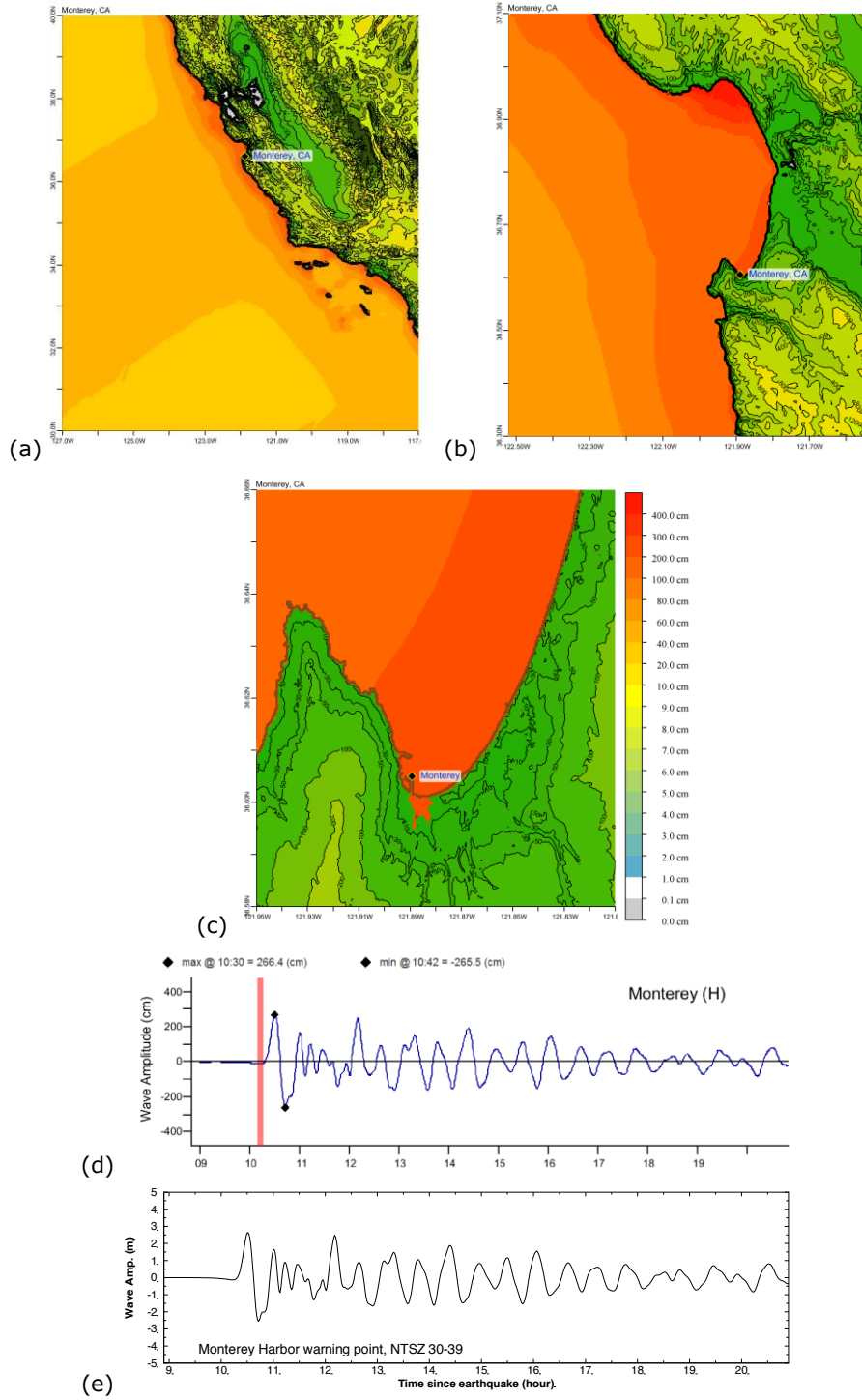
Figure S4. Max computed wave amplitude of (a) A grid; (b) B grid; (c) C grid of Monterey, California, for synthetic event NTSZ 30-39; (d) SIFT Computed time series at Monterey tide gage for synthetic event NTSZ 30-39: (e) Model computed time series shown in the forecast model report for synthetic event NTSZ 30-39.
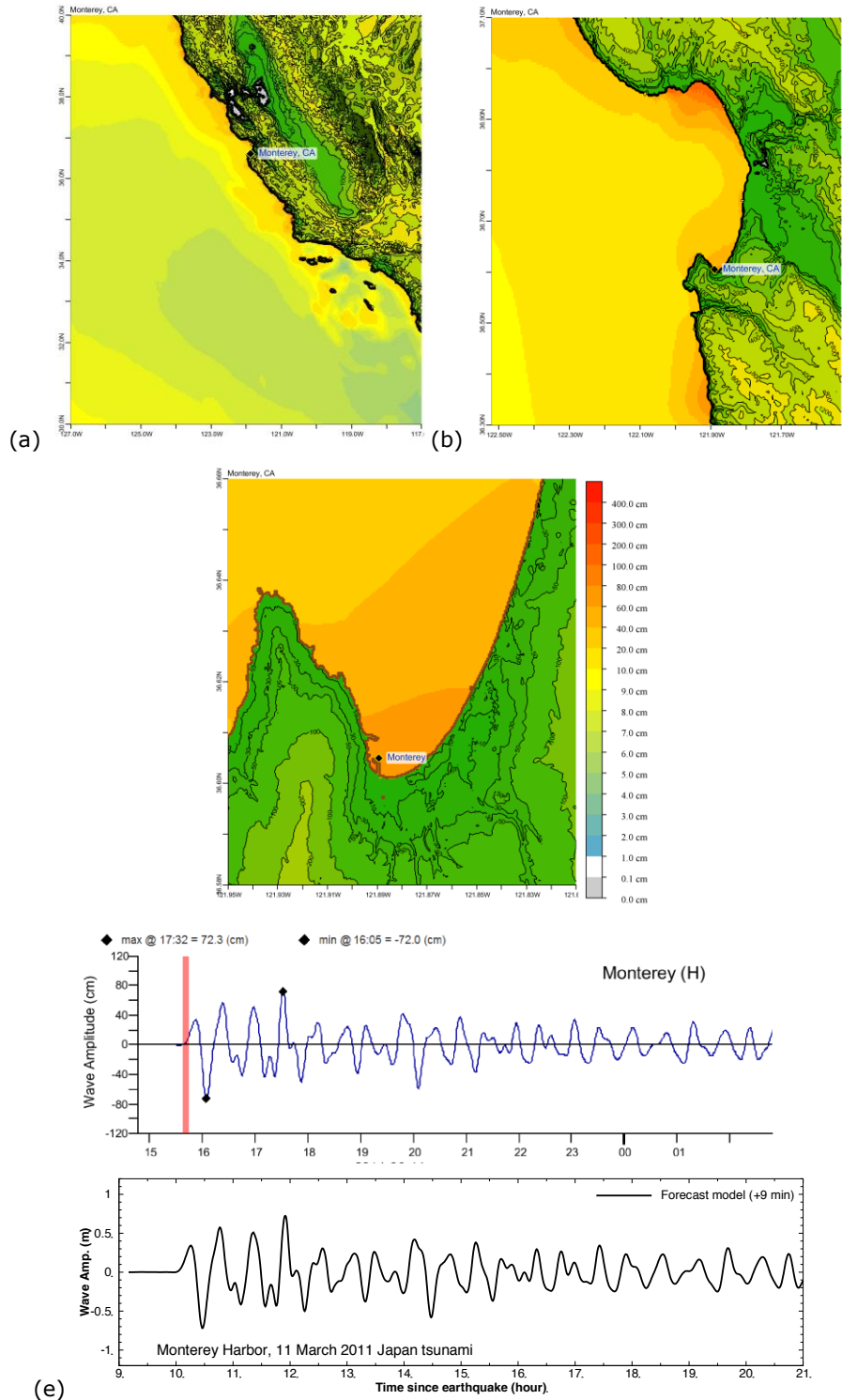
Figure S5. Max computed wave amplitude of (a) A grid; (b) B grid; (c) C grid of Monterey, California, for the 11 March 2011 Japan event; (d) SIFT Computed time series at Monterey tide gage for the 11 March 2011 Japan event: (e) Model computed time series shown in the forecast model report for the 11 March 2011 Japan event.

REFERENCES

Arcas, D.R., and B. Uslu (2010): A Tsunami Forecast Model for Crescent City, California. US Department of Commerce, NOAA OAR Special Report, PMEL Tsunami Forecast Series: Vol. 2, 112 pp.

Barberopoulou, A., J. C. Borrero, B. Uslu, M. R. Legg, and C. E. Synolakis (2011): A second generation of tsunami inundation maps for the state of California. *Pure and Appl. Geophys.*, *168*(11), 2133–2146.

Borrero, J.C., L. Dengler, B. Uslu, and C.E. Synolakis (2006): Numerical modeling of tsunami effects at marine oil terminals in San Francisco Bay. http://www.slc.ca.gov/division_pages/MFD/MOTEMS.html June 2006, Prepared for the California State Land Commission, Marine Facilities Division.

Bromirski, P.D., R.E. Flick, and D.R. Cayan (2002): Storminess variability along the California coast: 1858–2000. *J. Climate*, *16*, 982–993. Census (2000): http:/www.census.gov/population/www/cen2000/briefs/phc-t3/tables/tab03.txt. Accessed June 12, 2009.

Carignan, K.S., L.A. Taylor, B.W. Eakins, R.R. Warnken, R.J. Caldwell, D.Z. Friday, E. Lim, and P.R. Grothe (2010): Digital Elevation Models of Eureka, California: Procedures, Data Sources and Analysis, NOAA Technical Memorandum NESDIS NGDC-38, U.S. Dept. of Commerce, Boulder, CO, 41 pp.

Carignan, K.S., L.A. Taylor, B.W. Eakins, R.J. Caldwell, D.Z. Friday, P.R. Grothe, and E. Lim. (2010): Digital Elevation Models of Central California and San Francisco Bay: Procedures, Data Sources and Analysis. ngdc.noaa. gov/dem/report/download/1220.

Carver, G.A., A.S. Jayko, D.W. Valentine, and W.H. Li (1994): Coastal uplift associated with the 1992 Cape Mendocino earthquake, northern California. *Geology*, *22*(3), 195–198.

Census Bureau (2010): United States Census Bureau American FactFinder Community Facts. URL: factfinder2.census.gov/faces/nav/jsf/pages/community_facts.xhtml.

Dudley, W.C., and M. Lee (1998): *Tsunami!*, University of Hawai'i Press, Honolulu, Hawaii, 362 pp.

Dunbar, P. (2007): Increasing public awareness of natural hazards via the internet. *Nat. Hazards*, *42*(3) doi:10.1007/s11069-006-9072-3, 529–536.

Fine, I.V., A.B. Rabinovich, B.D. Bornhold, R.E. Thomson, and E.A. Kulikov (2005): The Grand Banks landslide-generated tsunami of November 18, 1929: Preliminary analysis and numerical modeling. *Mar. Geol.*, *215*(1), 45–57.

Friday, D.Z., L.A. Taylor, B.W. Eakins, R.R. Warnken, K.S. Carignan, R.J. Caldwell, E. Lim, and P.R. Medley (2009): Digital Elevation Model of Arena Cove, California: Procedures, Data Sources and Analysis. ngdc.noaa.gov/mgg/inundation/tsunami/data/arena_cove_ca/arena_cove_ca.pdf

Garfield, N., T. A. Rago, K. J. Schnebele, and C. A. Collins (1994), Evidence of a turbidity current in Monterey Submarine Canyon associated with the 1989 Loma Prieta earthquake, Cont. Shelf Res., 14, 673 – 686.

Gica, E., M. Spillane, V.V. Titov, C.D. Chamberlin, and J.C. Newman (2008): Development of the forecast propagation database for NOAA's Short-term Inundation Forecast for Tsunamis (SIFT). NOAA Tech. Memo. OAR PMEL-139, NTIS: PB2008-109391, 89 pp.

González, F.I., K. Satake, E.F. Boss, and H.O. Mofjeld (1995): Edge wave and non-trapped modes of the 25 April 1992 Cape Mendocino tsunami. *Pure and Appl. Geophys., 144*(3–4), 409–426, doi:10.1007/BF00874375.

Greene, H.G. and K.R. Hicks (1990). Ascension-Monterey canyon system: History and development. In: *Geology and Tectonics of the Central California Coastal Region, San Francisco to Monterey*, edited by R.E. Garrison, H.G. Greene, K.R. Hicks, G.E. Weber, and T.L. Wright. *American Association of Petroleum Geologists, Pacific Section, Volume and Guidebook*, **GB 67**: 229-250.

Greene, H.G., N.M. Maher and C.K. Paull (2002), Physiography of the Monterey Bay National Marine Sanctuary and implications about continental margin development, Marine Geology, 181, 55-82.

Greene, H.G. and S.N. Ward (2003), Mass movement features along the central California margin and their modeled consequences for tsunami generation, Submarine Mass Movements and Their Consequences, edited by Locat, L. and Mienert J., Kluwer Academic Publishers, Netherlands.

Haugan, J. (2005): Dog holes and wire chutes. *Maritime Life and Traditions, No. 29*, Winter.
Kanamori, H., and J.J. Cipar (1974): Focal process of the great Chilean earthquake, May 22, 1960. *Phys. Earth Planet. Inter., 9*, 128–136.

Kanamori, H., and J.J. Cipar (1974): Focal process of the great Chilean earthquake, May 22, 1960. Phys. Earth Planet. In., 9, 128{136.

Lander, J.F., P. Lockridge, and M. Kozuch (1993): Tsunamis affecting the West Coast of the United States, 1806–1992. NGDC Key to Geophysical Records Documentation No. 29, National Geophysical Data Center (NGDC), Boulder, CO, 242 pp.

López, A.M., and E.A. Okal (2006): A seismological reassessment of the source of the 1946 Aleutian "tsunami" earthquake. *Geophys. J. Int., 165*(3), 835–849, doi: 10.1111/j.1365-246x.2006.02899.x.

Kelly, A., L. Dengler, B. Uslu, A. Barberopoulou, S. Yim, and K.J. Bergen (2006), Recent tsunami highlights need for awareness of tsunami duration, *Eos Trans*. AGU, 87, 566-567.

Lander, J.F., and P.A. Lockridge (1989): United States tsunamis (including United States possessions): 1690–1988. US Department of Commerce, NOAA, NESDIS, and NGDC, Publication 41-2, 265 pp.

Loeffler, K., and J. Gesell, editors / cinematographers, (2010): Marin Tsunami: U.S. Geological Survey General Information Product 95 (video). URL: pubs. usgs.gov/gip/95/index.html.

López, A.M., and E.A. Okal (2006): A seismological reassessment of the source of the 1946 Aleutian "tsunami" earthquake. *Geophys*. *J*. *Int*., *165*(3), 835–849, doi:10.1111/j.1365-246x.2006.02899.x.

Marks, K.M., and Smith, W.H.F. (2006): An evaluation of publicly available global bathymetry grids. Marine Geophysical Researches, 27, 19-34.

Magoon, O.T. (1966): Structural damage by tsunamis. In *Specialty Conference on Coastal Engineering*, ASCE, Santa Barbara, CA.

Niemi, T.M., and N.T. Hall (1996): Historical changes in the tidal marsh of Tomales Bay and Olema Creek, Marin County, California. *J*. *Coastal Res*., *12*(1), 90–102.

O'Brien, M.P. (1946): Preliminary Report on Seismic Sea Waves from Aleutian Earthquake of April 1, 1946, Tech. Rep. HE 116207, Wave Project, Fluid Mechanics Lab., University of California, Berkeley.

Paros, J., E. Bernard, J. Delaney, C. Meinig, M. Spillane, P. Migliacio, L. Tang, W. Chadwick, T. Schaad, and S. Stalin (2011): Breakthrough underwater technology holds promise for improved local tsunami warnings. *Oceans '11 MTS/IEEE*, Kona, Hawaii, 19–22 September 2011.

PMSA (2003): Pacific Merchant Shipping Association. http://www.pmsaship.com/tradefiles/PMSAMaritimeDays.pps, accessed June 12, 2009.

Percival, D.B., D.W. Denbo, M.C. Eble, E. Gica, H.O. Mofjeld, M.C. Spillane, L. Tang, and V.V. Titov (2011): Extraction of tsunami source coefficients via inversion of DART® buoy data. *Nat*. *Hazards, 58*(1), doi:10.1007/s11069-010-9688-1, 567–590.

Ritter, J., and W. Dupre (1972): Maps showing areas of potential inundation by tsunamis in the San Francisco Bay Region, California. U.S. Geological Survey, Miscellaneous Field Studies, Map MF-480.

Schwing, F.B., Norton, J.G. and Pilskaln, C.H. (1990). Earthquake and bay: Response of Monterey Bay to the Loma Prieta Earthquake. *Eos, Transactions American Geophysical Union 71*. *doi: 10.1029/90EO00035*. *issn: 0096-3941*.

Smith, W. H. F. and D. T. Sandwell, (1997). Global Seafloor Topography from Satellite Altimetry and Ship Depth Soundings, Science 277: 1956-1962,

Spillane, M.C., E. Gica, V.V. Titov, and H.O. Mofjeld (2008): Tsunameter network design for the U.S. DART® arrays in the Pacific and Atlantic oceans. NOAA Tech. Memo. OAR PMEL-143, 165 pp.

Spillane, M.C.: A Tsunami Forecast Model for Arena Cove, California. US Department of Commerce, NOAA OAR Special Report, PMEL Tsunami Forecast Series, *in press*.

Tang, L., C. Chamberlin, E. Tolkova, M. Spillane, V.V. Titov, E.N. Bernard, and H.O. Mofjeld (2006): Assessment of potential tsunami impact for Pearl Harbor, Hawaii. NOAA Tech.Memo. OAR PMEL-131, NTIS: PB2007-100617, 36 pp.

Tang, L., V.V. Titov, and C.D. Chamberlin (2009): Development, testing, and applications of site-specific tsunami inundation models for real-time forecasting. *J. Geophys. Res., 114*, C12025, doi:10.1029/2009JC005476.

Tang, L., V.V. Titov, E. Bernard, Y. Wei, C. Chamberlin, J.C. Newman, H. Mofjeld, D. Arcas, M. Eble, C. Moore, B. Uslu, C. Pells, M.C. Spillane, L.M. Wright, and E. Gica (2012): Direct energy estimation of the 2011 Japan tsunami using deep-ocean pressure measurements. *J. Geophys. Res., 117*, C08008, doi:10.1029/2011JC007635.

Taylor, L.A., B.W. Eakins, K.S. Carignan, R.R. Warnken, T. Sazonova, and D.C. Schoolcraft (2008), Digital elevation model for Monterey, California: procedures, data sources and analysis, prepared for the Pacific Marine Environmental Laboratory (PMEL) NOAA Center for Tsunami Research by the NOAA National Geophysical Data Center, 33p.

Titov, V., and F.I. González (1997): Implementation and testing of the Method of Splitting Tsunami (MOST) model. NOAA Tech. Memo. ERL PMEL-112, NTIS: PB98-122773, NOAA/Pacific Marine Environmental Laboratory, Seattle, WA, 11 pp.

Titov, V.V., and C.E. Synolakis (1998): Numerical modeling of tidal wave runup. *J. Waterw. Port Coast. Ocean Eng., 124*(4), 157–171.

Titov, V.V., F.I. González, E.N. Bernard, M.C. Eble, H.O. Mofjeld, J.C. Newman, and A.J. Venturato (2005): Real-time tsunami forecasting: Challenges and solutions. *Nat. Hazards, 35*(1) Special Issue, U.S. National Tsunami Hazard Mitigation Program, 41–58.

Titov, V.V. (2009): Tsunami forecasting. In *The Sea*, Vol. 15, Chapter 12, Harvard University Press, Cambridge, MA, and London, England, 371–400.

Titov, V.V., C. Moore, D.J.M. Greenslade, C. Pattiaratchi, R. Badal, C.E. Synolakis, and U. Kânoğlu (2011): A new tool for inundation modeling: Community Modeling Interface for

Tsunamis (ComMIT). *Pure Appl. Geophys., 168*(11), 2121–2131, doi:10.1007/s00024-011-0292-4.

Tolkova, E., and W. Power (2011): Obtaining natural oscillatory modes of bays and harbors via Empirical Orthogonal Function analysis of tsunami wave fields. *Ocean Dynam., 61*(6), doi: 10.1007/s10236-011-0388-5, 731–751.

U.S. Census Bureau (2010): State and County Quickfacts: Eureka (city), California. Retrieved Sep. 22, 2015, from http://quickfacts.census.gov.

U.S. Census Bureau (2010b): State and County Quickfacts: Arcata (city), California. Retrieved Sep. 22, 2015, from http://quickfacts.census.gov.

U.S. Secretary of War (1914): Harbor of Refuge at Point Arena, or Elsewhere on the Pacific Coast, Between San Francisco and Humboldt Bay, California. Report to 63rd Congress, House of Representatives, Washington D.C., Document No. 1369, 39 pp.

Uslu, B., J.C. Borrero, L.A. Dengler, and C.E. Synolakis (2007), Tsunami inundation at Crescent City, California generated by earthquake along the Cascadia Subduction Zone, *Geophy. Res. Lett.*, 34, L20601, doi:10.1029/2007GL030188.

Uslu, B. (2008): Deterministic and probabilistic tsunami studies in California from near and farfield sources. Ph.D. thesis, University of Southern California, Los Angeles, CA.

Uslu, B., D. Arcas, V.V. Titov, and A.J. Venturato (2010): A Tsunami Forecast Model for San Francisco, California. US Department of Commerce, NOAA OAR Special Report, PMEL Tsunami Forecast Series: Vol. 3, 88 pp.

Ward, S.N. and S. Simon (2005), Tsunami thoughts, Canadian Society of Exploration Geophysicists Recorder, 30(10), 38-44.

Wei, Y., E. Bernard, L. Tang, R. Weiss, V. Titov, C. Moore, M. Spillane, M. Hopkins, and U. Kânoğlu (2008): Real-time experimental forecast of the Peruvian tsunami of August 2007 for U.S. coastlines. *Geophys. Res. Lett., 35*, L04609, doi:10.1029/2007GL032250.

Working Group on California Earthquake Probabilities (2003), Earthquake Probabilities in the San Francisco Bay Region: 2002 -2031, U.S. Geological Survey Open File Report 03-214, 235p.

Appendix A - Propagation Database: Pacific Ocean Unit Sources

Propagation source details reflect the database as of January 29, 2013 and there may have been updates in the earthquake source parameters after this date.
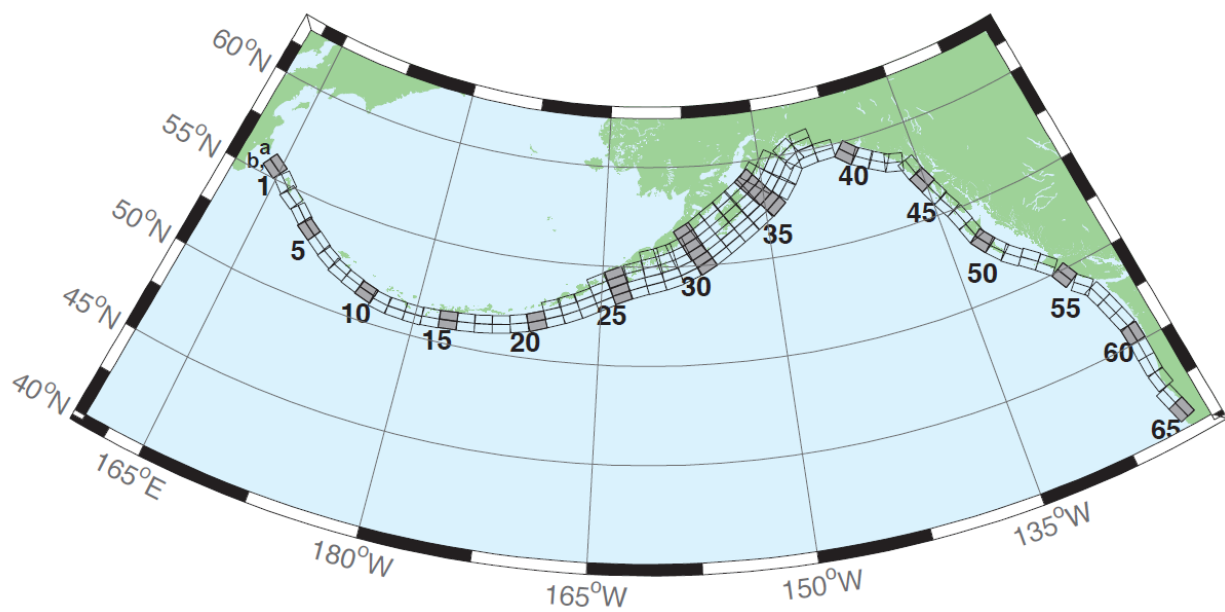
Figure A1. Aleutian-Alaska-Cascadia Subduction Zone unit sources

Table A1: Earthquake parameters for Aleutian-Alaska-Cascadia Subduction Zone unit sources.

Segment	Description	Longitude (°)	Latitude (°)	Strike (°)	Dip (°)	Depth (km)
acsz-01a	Aleutian-Alaska-Cascadia	164.7994	55.9606	17.00	299.00	19.61
acsz-01b	Aleutian-Alaska-Cascadia	164.4310	55.5849	17.00	299.00	5.00
acsz-02a	Aleutian-Alaska-Cascadia	166.3418	55.4016	17.00	310.17	19.61
acsz-02b	Aleutian-Alaska-Cascadia	165.8578	55.0734	17.00	310.17	5.00
acsz-03a	Aleutian-Alaska-Cascadia	167.2939	54.8919	23.36	300.22	24.82
acsz-03b	Aleutian-Alaska-Cascadia	166.9362	54.5356	23.36	300.22	5.00
acsz-04a	Aleutian-Alaska-Cascadia	168.7131	54.2852	38.51	310.21	25.33
acsz-04b	Aleutian-Alaska-Cascadia	168.3269	54.0168	24.00	310.21	5.00
acsz-05a	Aleutian-Alaska-Cascadia	169.7447	53.7808	37.02	302.77	23.54
acsz-05b	Aleutian-Alaska-Cascadia	169.4185	53.4793	21.77	302.77	5.00
acsz-06a	Aleutian-Alaska-Cascadia	171.0144	53.3054	35.31	303.16	22.92
acsz-06b	Aleutian-Alaska-Cascadia	170.6813	52.9986	21.00	303.16	5.00
acsz-07a	Aleutian-Alaska-Cascadia	172.1500	52.8528	35.56	298.16	20.16
acsz-07b	Aleutian-Alaska-Cascadia	171.8665	52.5307	17.65	298.16	5.00
acsz-08a	Aleutian-Alaska-Cascadia	173.2726	52.4579	37.92	290.75	20.35
acsz-08b	Aleutian-Alaska-Cascadia	173.0681	52.1266	17.88	290.75	5.00
acsz-09a	Aleutian-Alaska-Cascadia	174.5866	52.1434	39.09	289.03	21.05
acsz-09b	Aleutian-Alaska-Cascadia	174.4027	51.8138	18.73	289.03	5.00
acsz-10a	Aleutian-Alaska-Cascadia	175.8784	51.8526	40.51	286.07	20.87
acsz-10b	Aleutian-Alaska-Cascadia	175.7265	51.5245	18.51	286.07	5.00
acsz-11a	Aleutian-Alaska-Cascadia	177.1140	51.6488	15.00	280.00	17.94
acsz-11b	Aleutian-Alaska-Cascadia	176.9937	51.2215	15.00	280.00	5.00
acsz-12a	Aleutian-Alaska-Cascadia	178.4500	51.5690	15.00	273.00	17.94
acsz-12b	Aleutian-Alaska-Cascadia	178.4130	51.1200	15.00	273.00	5.00
acsz-13a	Aleutian-Alaska-Cascadia	179.8550	51.5340	15.00	271.00	17.94
acsz-13b	Aleutian-Alaska-Cascadia	179.8420	51.0850	15.00	271.00	5.00
acsz-14a	Aleutian-Alaska-Cascadia	181.2340	51.5780	15.00	267.00	17.94
acsz-14b	Aleutian-Alaska-Cascadia	181.2720	51.1290	15.00	267.00	5.00
acsz-15a	Aleutian-Alaska-Cascadia	182.6380	51.6470	15.00	265.00	17.94
acsz-15b	Aleutian-Alaska-Cascadia	182.7000	51.2000	15.00	265.00	5.00
acsz-16a	Aleutian-Alaska-Cascadia	184.0550	51.7250	15.00	264.00	17.94
acsz-16b	Aleutian-Alaska-Cascadia	184.1280	51.2780	15.00	264.00	5.00
acsz-17a	Aleutian-Alaska-Cascadia	185.4560	51.8170	15.00	262.00	17.94
acsz-17b	Aleutian-Alaska-Cascadia	185.5560	51.3720	15.00	262.00	5.00

Table A1: (continue)d

Segment	Description	Longitude (°)	Latitude (°)	Strike (°)	Dip (°)	Depth (km)
acsz-18a	Aleutian-Alaska-Cascadia	186.8680	51.9410	15.00	261.00	17.94
acsz-18b	Aleutian-Alaska-Cascadia	186.9810	51.4970	15.00	261.00	5.00
acsz-19a	Aleutian-Alaska-Cascadia	188.2430	52.1280	15.00	257.00	17.94
acsz-19b	Aleutian-Alaska-Cascadia	188.4060	51.6900	15.00	257.00	5.00
acsz-20a	Aleutian-Alaska-Cascadia	189.5810	52.3550	15.00	251.00	17.94
acsz-20b	Aleutian-Alaska-Cascadia	189.8180	51.9300	15.00	251.00	5.00
acsz-21a	Aleutian-Alaska-Cascadia	190.9570	52.6470	15.00	251.00	17.94
acsz-21b	Aleutian-Alaska-Cascadia	191.1960	52.2220	15.00	251.00	5.00
acsz-21z	Aleutian-Alaska-Cascadia	190.7399	53.0443	15.00	250.79	30.88
acsz-22a	Aleutian-Alaska-Cascadia	192.2940	52.9430	15.00	247.00	17.94
acsz-22b	Aleutian-Alaska-Cascadia	192.5820	52.5300	15.00	247.00	5.00
acsz-22z	Aleutian-Alaska-Cascadia	192.0074	53.3347	15.00	247.82	30.88
acsz-23a	Aleutian-Alaska-Cascadia	193.6270	53.3070	15.00	245.00	17.94
acsz-23b	Aleutian-Alaska-Cascadia	193.9410	52.9000	15.00	245.00	5.00
acsz-23z	Aleutian-Alaska-Cascadia	193.2991	53.6768	15.00	244.58	30.88
acsz-24a	Aleutian-Alaska-Cascadia	194.9740	53.6870	15.00	245.00	17.94
acsz-24b	Aleutian-Alaska-Cascadia	195.2910	53.2800	15.00	245.00	5.00
acsz-24y	Aleutian-Alaska-Cascadia	194.3645	54.4604	15.00	244.38	43.82
acsz-24z	Aleutian-Alaska-Cascadia	194.6793	54.0674	15.00	244.64	30.88
acsz-25a	Aleutian-Alaska-Cascadia	196.4340	54.0760	15.00	250.00	17.94
acsz-25b	Aleutian-Alaska-Cascadia	196.6930	53.6543	15.00	250.00	5.00
acsz-25y	Aleutian-Alaska-Cascadia	195.9009	54.8572	15.00	247.90	43.82
acsz-25z	Aleutian-Alaska-Cascadia	196.1761	54.4536	15.00	248.12	30.88
acsz-26a	Aleutian-Alaska-Cascadia	197.8970	54.3600	15.00	253.00	17.94
acsz-26b	Aleutian-Alaska-Cascadia	198.1200	53.9300	15.00	253.00	5.00
acsz-26y	Aleutian-Alaska-Cascadia	197.5498	55.1934	15.00	253.11	43.82
acsz-26z	Aleutian-Alaska-Cascadia	197.7620	54.7770	15.00	253.28	30.88
acsz-27a	Aleutian-Alaska-Cascadia	199.4340	54.5960	15.00	256.00	17.94
acsz-27b	Aleutian-Alaska-Cascadia	199.6200	54.1600	15.00	256.00	5.00
acsz-27x	Aleutian-Alaska-Cascadia	198.9736	55.8631	15.00	256.47	56.24
acsz-27y	Aleutian-Alaska-Cascadia	199.1454	55.4401	15.00	256.62	43.82
acsz-27z	Aleutian-Alaska-Cascadia	199.3135	55.0170	15.00	256.76	30.88
acsz-28a	Aleutian-Alaska-Cascadia	200.8820	54.8300	15.00	253.00	17.94
acsz-28b	Aleutian-Alaska-Cascadia	201.1080	54.4000	15.00	253.00	5.00

Table A1: (continued)

Segment	Description	Longitude (°)	Latitude (°)	Strike (°)	Dip (°)	Depth (km)
acsz-28x	Aleutian-Alaska-Cascadia	200.1929	56.0559	15.00	252.55	56.24
acsz-28y	Aleutian-Alaska-Cascadia	200.4167	55.6406	15.00	252.74	43.82
acsz-28z	Aleutian-Alaska-Cascadia	200.6360	55.2249	15.00	252.92	30.88
acsz-29a	Aleutian-Alaska-Cascadia	202.2610	55.1330	15.00	247.00	17.94
acsz-29b	Aleutian-Alaska-Cascadia	202.5650	54.7200	15.00	247.00	5.00
acsz-29x	Aleutian-Alaska-Cascadia	201.2606	56.2861	15.00	245.70	56.24
acsz-29y	Aleutian-Alaska-Cascadia	201.5733	55.8888	15.00	245.96	43.82
acsz-29z	Aleutian-Alaska-Cascadia	201.8797	55.4908	15.00	246.21	30.88
acsz-30a	Aleutian-Alaska-Cascadia	203.6040	55.5090	15.00	240.00	17.94
acsz-30b	Aleutian-Alaska-Cascadia	203.9970	55.1200	15.00	240.00	5.00
acsz-30w	Aleutian-Alaska-Cascadia	201.9901	56.9855	15.00	239.52	69.12
acsz-30x	Aleutian-Alaska-Cascadia	202.3851	56.6094	15.00	239.85	56.24
acsz-30y	Aleutian-Alaska-Cascadia	202.7724	56.2320	15.00	240.17	43.82
acsz-30z	Aleutian-Alaska-Cascadia	203.1521	55.8534	15.00	240.49	30.88
acsz-31a	Aleutian-Alaska-Cascadia	204.8950	55.9700	15.00	236.00	17.94
acsz-31b	Aleutian-Alaska-Cascadia	205.3400	55.5980	15.00	236.00	5.00
acsz-31w	Aleutian-Alaska-Cascadia	203.0825	57.3740	15.00	234.54	69.12
acsz-31x	Aleutian-Alaska-Cascadia	203.5408	57.0182	15.00	234.93	56.24
acsz-31y	Aleutian-Alaska-Cascadia	203.9904	56.6607	15.00	235.30	43.82
acsz-31z	Aleutian-Alaska-Cascadia	204.4315	56.3016	15.00	235.67	30.88
acsz-32a	Aleutian-Alaska-Cascadia	206.2080	56.4730	15.00	236.00	17.94
acsz-32b	Aleutian-Alaska-Cascadia	206.6580	56.1000	15.00	236.00	5.00
acsz-32w	Aleutian-Alaska-Cascadia	204.4129	57.8908	15.00	234.32	69.12
acsz-32x	Aleutian-Alaska-Cascadia	204.8802	57.5358	15.00	234.72	56.24
acsz-32y	Aleutian-Alaska-Cascadia	205.3385	57.1792	15.00	235.10	43.82
acsz-32z	Aleutian-Alaska-Cascadia	205.7880	56.8210	15.00	235.48	30.88
acsz-33a	Aleutian-Alaska-Cascadia	207.5370	56.9750	15.00	236.00	17.94
acsz-33b	Aleutian-Alaska-Cascadia	207.9930	56.6030	15.00	236.00	5.00
acsz-33w	Aleutian-Alaska-Cascadia	205.7126	58.3917	15.00	234.24	69.12
acsz-33x	Aleutian-Alaska-Cascadia	206.1873	58.0371	15.00	234.64	56.24
acsz-33y	Aleutian-Alaska-Cascadia	206.6527	57.6808	15.00	235.03	43.82
acsz-33z	Aleutian-Alaska-Cascadia	207.1091	57.3227	15.00	235.41	30.88
acsz-34a	Aleutian-Alaska-Cascadia	208.9371	57.5124	15.00	236.00	17.94
acsz-34b	Aleutian-Alaska-Cascadia	209.4000	57.1400	15.00	236.00	5.00

Table A1: (continued)

Segment	Description	Longitude (°)	Latitude (°)	Strike (°)	Dip (°)	Depth (km)
acsz-34w	Aleutian-Alaska-Cascadia	206.9772	58.8804	15.00	233.47	69.12
acsz-34x	Aleutian-Alaska-Cascadia	207.4677	58.5291	15.00	233.88	56.24
acsz-34y	Aleutian-Alaska-Cascadia	207.9485	58.1760	15.00	234.29	43.82
acsz-34z	Aleutian-Alaska-Cascadia	208.4198	57.8213	15.00	234.69	30.88
acsz-35a	Aleutian-Alaska-Cascadia	210.2597	58.0441	15.00	230.00	17.94
acsz-35b	Aleutian-Alaska-Cascadia	210.8000	57.7000	15.00	230.00	5.00
acsz-35w	Aleutian-Alaska-Cascadia	208.0204	59.3199	15.00	228.81	69.12
acsz-35x	Aleutian-Alaska-Cascadia	208.5715	58.9906	15.00	229.29	56.24
acsz-35y	Aleutian-Alaska-Cascadia	209.1122	58.6590	15.00	229.75	43.82
acsz-35z	Aleutian-Alaska-Cascadia	209.6425	58.3252	15.00	230.20	30.88
acsz-36a	Aleutian-Alaska-Cascadia	211.3249	58.6565	15.00	218.00	17.94
acsz-36b	Aleutian-Alaska-Cascadia	212.0000	58.3800	15.00	218.00	5.00
acsz-36w	Aleutian-Alaska-Cascadia	208.5003	59.5894	15.00	215.59	69.12
acsz-36x	Aleutian-Alaska-Cascadia	209.1909	59.3342	15.00	216.18	56.24
acsz-36y	Aleutian-Alaska-Cascadia	209.8711	59.0753	15.00	216.76	43.82
acsz-36z	Aleutian-Alaska-Cascadia	210.5412	58.8129	15.00	217.33	30.88
acsz-37a	Aleutian-Alaska-Cascadia	212.2505	59.2720	15.00	213.71	17.94
acsz-37b	Aleutian-Alaska-Cascadia	212.9519	59.0312	15.00	213.71	5.00
acsz-37x	Aleutian-Alaska-Cascadia	210.1726	60.0644	15.00	213.04	56.24
acsz-37y	Aleutian-Alaska-Cascadia	210.8955	59.8251	15.00	213.66	43.82
acsz-37z	Aleutian-Alaska-Cascadia	211.6079	59.5820	15.00	214.27	30.88
acsz-38a	Aleutian-Alaska-Cascadia	214.6555	60.1351	0.00	260.08	15.00
acsz-38b	Aleutian-Alaska-Cascadia	214.8088	59.6927	0.00	260.08	15.00
acsz-38y	Aleutian-Alaska-Cascadia	214.3737	60.9838	0.00	259.03	15.00
acsz-38z	Aleutian-Alaska-Cascadia	214.5362	60.5429	0.00	259.03	15.00
acsz-39a	Aleutian-Alaska-Cascadia	216.5607	60.2480	0.00	267.04	15.00
acsz-39b	Aleutian-Alaska-Cascadia	216.6068	59.7994	0.00	267.04	15.00
acsz-40a	Aleutian-Alaska-Cascadia	219.3069	59.7574	0.00	310.91	15.00
acsz-40b	Aleutian-Alaska-Cascadia	218.7288	59.4180	0.00	310.91	15.00
acsz-41a	Aleutian-Alaska-Cascadia	220.4832	59.3390	0.00	300.73	15.00
acsz-41b	Aleutian-Alaska-Cascadia	220.0382	58.9529	0.00	300.73	15.00
acsz-42a	Aleutian-Alaska-Cascadia	221.8835	58.9310	0.00	298.94	15.00
acsz-42b	Aleutian-Alaska-Cascadia	221.4671	58.5379	0.00	298.94	15.00
acsz-43a	Aleutian-Alaska-Cascadia	222.9711	58.6934	0.00	282.34	15.00

Table A1: (continued)

Segment	Description	Longitude (°)	Latitude (°)	Strike (°)	Dip (°)	Depth (km)
acsz-43b	Aleutian-Alaska-Cascadia	222.7887	58.2546	0.00	282.34	15.00
acsz-44a	Aleutian-Alaska-Cascadia	224.9379	57.9054	12.00	340.91	11.09
acsz-44b	Aleutian-Alaska-Cascadia	224.1596	57.7617	7.00	340.91	5.00
acsz-45a	Aleutian-Alaska-Cascadia	225.4994	57.1634	12.00	334.15	11.09
acsz-45b	Aleutian-Alaska-Cascadia	224.7740	56.9718	7.00	334.15	5.00
acsz-46a	Aleutian-Alaska-Cascadia	226.1459	56.3552	12.00	334.15	11.09
acsz-46b	Aleutian-Alaska-Cascadia	225.4358	56.1636	7.00	334.15	5.00
acsz-47a	Aleutian-Alaska-Cascadia	226.7731	55.5830	12.00	332.26	11.09
acsz-47b	Aleutian-Alaska-Cascadia	226.0887	55.3785	7.00	332.26	5.00
acsz-48a	Aleutian-Alaska-Cascadia	227.4799	54.6763	12.00	339.40	11.09
acsz-48b	Aleutian-Alaska-Cascadia	226.7713	54.5217	7.00	339.40	5.00
acsz-49a	Aleutian-Alaska-Cascadia	227.9482	53.8155	12.00	341.17	11.09
acsz-49b	Aleutian-Alaska-Cascadia	227.2462	53.6737	7.00	341.17	5.00
acsz-50a	Aleutian-Alaska-Cascadia	228.3970	53.2509	12.00	324.51	11.09
acsz-50b	Aleutian-Alaska-Cascadia	227.8027	52.9958	7.00	324.51	5.00
acsz-51a	Aleutian-Alaska-Cascadia	229.1844	52.6297	12.00	318.36	11.09
acsz-51b	Aleutian-Alaska-Cascadia	228.6470	52.3378	7.00	318.36	5.00
acsz-52a	Aleutian-Alaska-Cascadia	230.0306	52.0768	12.00	310.85	11.09
acsz-52b	Aleutian-Alaska-Cascadia	229.5665	51.7445	7.00	310.85	5.00
acsz-53a	Aleutian-Alaska-Cascadia	231.1735	51.5258	12.00	310.85	11.09
acsz-53b	Aleutian-Alaska-Cascadia	230.7150	51.1935	7.00	310.85	5.00
acsz-54a	Aleutian-Alaska-Cascadia	232.2453	50.8809	12.00	314.11	11.09
acsz-54b	Aleutian-Alaska-Cascadia	231.7639	50.5655	7.00	314.11	5.00
acsz-55a	Aleutian-Alaska-Cascadia	233.3066	49.9032	12.00	333.71	11.09
acsz-55b	Aleutian-Alaska-Cascadia	232.6975	49.7086	7.00	333.71	5.00
acsz-56a	Aleutian-Alaska-Cascadia	234.0588	49.1702	11.00	315.00	12.82
acsz-56b	Aleutian-Alaska-Cascadia	233.5849	48.8584	9.00	315.00	5.00
acsz-57a	Aleutian-Alaska-Cascadia	234.9041	48.2596	11.00	341.00	12.82
acsz-57b	Aleutian-Alaska-Cascadia	234.2797	48.1161	9.00	341.00	5.00
acsz-58a	Aleutian-Alaska-Cascadia	235.3021	47.3812	11.00	344.00	12.82
acsz-58b	Aleutian-Alaska-Cascadia	234.6776	47.2597	9.00	344.00	5.00
acsz-59a	Aleutian-Alaska-Cascadia	235.6432	46.5082	11.00	345.00	12.82
acsz-59b	Aleutian-Alaska-Cascadia	235.0257	46.3941	9.00	345.00	5.00
acsz-60a	Aleutian-Alaska-Cascadia	235.8640	45.5429	11.00	356.00	12.82

Table A1: (continued)

Segment	Description	Longitude (°)	Latitude (°)	Strike (°)	Dip (°)	Depth (km)
acsz-60b	Aleutian-Alaska-Cascadia	235.2363	45.5122	9.00	356.00	5.00
acsz-61a	Aleutian-Alaska-Cascadia	235.9106	44.6227	11.00	359.00	12.82
acsz-61b	Aleutian-Alaska-Cascadia	235.2913	44.6150	9.00	359.00	5.00
acsz-62a	Aleutian-Alaska-Cascadia	235.9229	43.7245	11.00	359.00	12.82
acsz-62b	Aleutian-Alaska-Cascadia	235.3130	43.7168	9.00	359.00	5.00
acsz-63a	Aleutian-Alaska-Cascadia	236.0220	42.9020	11.00	350.00	12.82
acsz-63b	Aleutian-Alaska-Cascadia	235.4300	42.8254	9.00	350.00	5.00
acsz-64a	Aleutian-Alaska-Cascadia	235.9638	41.9818	11.00	345.00	12.82
acsz-64b	Aleutian-Alaska-Cascadia	235.3919	41.8677	9.00	345.00	5.00
acsz-65a	Aleutian-Alaska-Cascadia	236.2643	41.1141	11.00	345.00	12.82
acsz-65b	Aleutian-Alaska-Cascadia	235.7000	41.0000	9.00	345.00	5.00
acsz-238a	Aleutian-Alaska-Cascadia	213.2878	59.8406	15.00	236.83	17.94
acsz-238y	Aleutian-Alaska-Cascadia	212.3424	60.5664	15.00	236.83	43.82
acsz-238z	Aleutian-Alaska-Cascadia	212.8119	60.2035	15.00	236.83	30.88
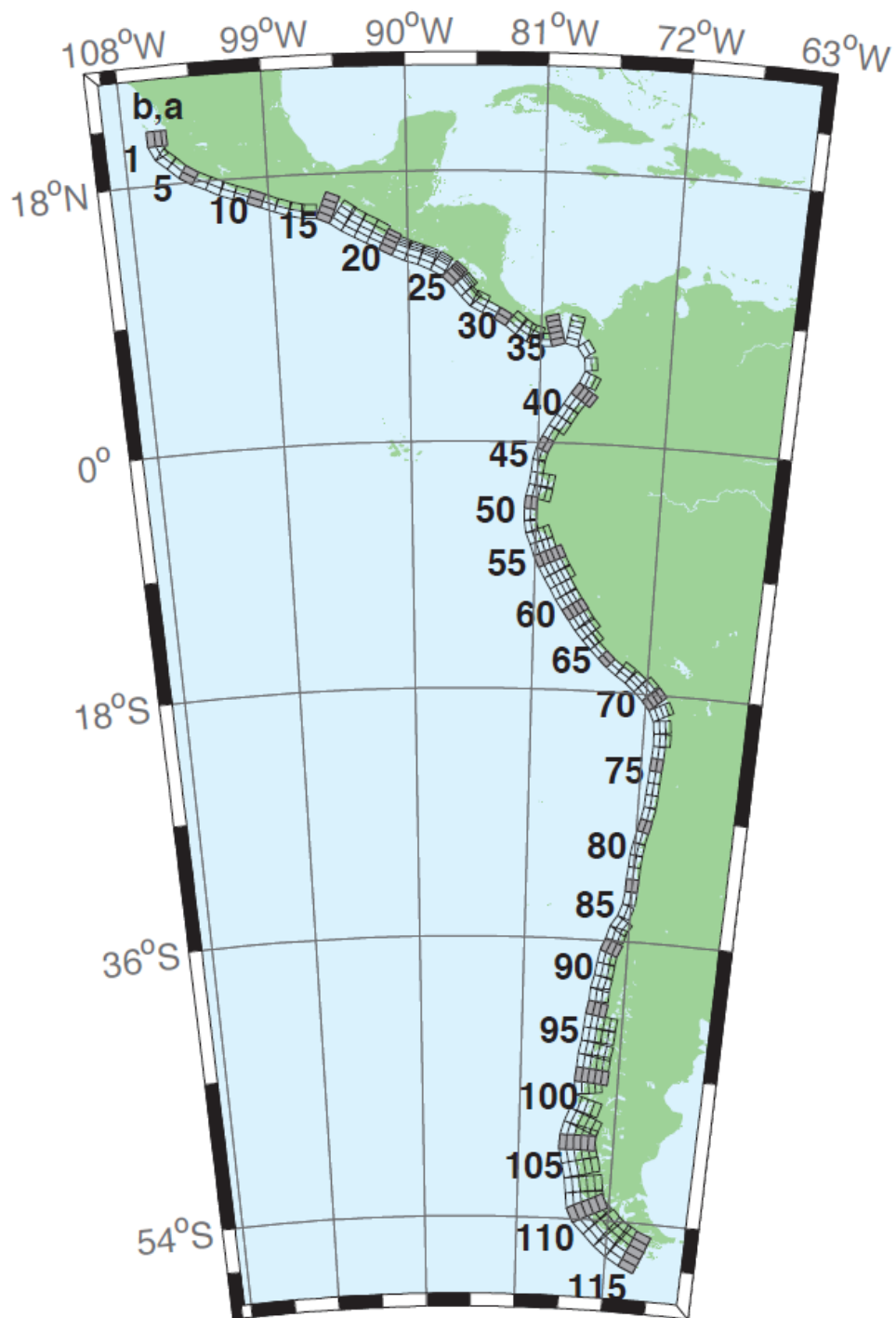
Figure A2. Central and South America Subduction Zone unit sources.

Table A2: Earthquake parameters for Central and South America Subduction Zone unit sources.

Segment	Description	Longitude (°)	Latitude (°)	Strike (°)	Dip (°)	Depth (km)
cssz-01a	Central and South America	254.4573	20.8170	19.00	358.97	15.40
cssz-01b	Central and South America	254.0035	20.8094	12.00	358.97	5.00
cssz-01z	Central and South America	254.7664	20.8222	50.00	358.97	31.67
cssz-02a	Central and South America	254.5765	20.2806	19.00	336.76	15.40
cssz-02b	Central and South America	254.1607	20.1130	12.00	336.76	5.00
cssz-03a	Central and South America	254.8789	19.8923	18.31	310.60	15.27
cssz-03b	Central and South America	254.5841	19.5685	11.85	310.60	5.00
cssz-04a	Central and South America	255.6167	19.2649	17.62	313.37	15.12
cssz-04b	Central and South America	255.3056	18.9537	11.68	313.37	5.00
cssz-05a	Central and South America	256.2240	18.8148	16.92	302.70	15.00
cssz-05b	Central and South America	255.9790	18.4532	11.54	302.70	5.00
cssz-06a	Central and South America	256.9425	18.4383	16.23	295.15	14.87
cssz-06b	Central and South America	256.7495	18.0479	11.38	295.15	5.00
cssz-07a	Central and South America	257.8137	18.0339	15.54	296.91	14.74
cssz-07b	Central and South America	257.6079	17.6480	11.23	296.91	5.00
cssz-08a	Central and South America	258.5779	17.7151	14.85	290.42	14.61
cssz-08b	Central and South America	258.4191	17.3082	11.08	290.42	5.00
cssz-09a	Central and South America	259.4578	17.4024	14.15	290.48	14.47
cssz-09b	Central and South America	259.2983	16.9944	10.92	290.48	5.00
cssz-10a	Central and South America	260.3385	17.0861	13.46	290.75	14.34
cssz-10b	Central and South America	260.1768	16.6776	10.77	290.75	5.00
cssz-11a	Central and South America	261.2255	16.7554	12.77	291.82	14.21
cssz-11b	Central and South America	261.0556	16.3487	10.62	291.82	5.00
cssz-12a	Central and South America	262.0561	16.4603	12.08	288.86	14.08
cssz-12b	Central and South America	261.9082	16.0447	10.46	288.86	5.00
cssz-13a	Central and South America	262.8638	16.2381	11.38	283.18	13.95
cssz-13b	Central and South America	262.7593	15.8094	10.31	283.18	5.00
cssz-14a	Central and South America	263.6066	16.1435	10.69	272.06	13.81
cssz-14b	Central and South America	263.5901	15.7024	10.15	272.06	5.00
cssz-15a	Central and South America	264.8259	15.8829	10.00	293.03	13.68
cssz-15b	Central and South America	264.6462	15.4758	10.00	293.03	5.00
cssz-15y	Central and South America	265.1865	16.6971	10.00	293.03	31.05
cssz-15z	Central and South America	265.0060	16.2900	10.00	293.03	22.36

Table A2: (continued)

Segment	Description	Longitude (°)	Latitude (°)	Strike (°)	Dip (°)	Depth (km)
cssz-16a	Central and South America	265.7928	15.3507	15.00	304.95	15.82
cssz-16b	Central and South America	265.5353	14.9951	12.50	304.95	5.00
cssz-16y	Central and South America	266.3092	16.0619	15.00	304.95	41.70
cssz-16z	Central and South America	266.0508	15.7063	15.00	304.95	28.76
cssz-17a	Central and South America	266.4947	14.9019	20.00	299.52	17.94
cssz-17b	Central and South America	266.2797	14.5346	15.00	299.52	5.00
cssz-17y	Central and South America	266.9259	15.6365	20.00	299.52	52.14
cssz-17z	Central and South America	266.7101	15.2692	20.00	299.52	35.04
cssz-18a	Central and South America	267.2827	14.4768	21.50	298.01	17.94
cssz-18b	Central and South America	267.0802	14.1078	15.00	298.01	5.00
cssz-18y	Central and South America	267.6888	15.2148	21.50	298.01	54.59
cssz-18z	Central and South America	267.4856	14.8458	21.50	298.01	36.27
cssz-19a	Central and South America	268.0919	14.0560	23.00	297.64	17.94
cssz-19b	Central and South America	267.8943	13.6897	15.00	297.64	5.00
cssz-19y	Central and South America	268.4880	14.7886	23.00	297.64	57.01
cssz-19z	Central and South America	268.2898	14.4223	23.00	297.64	37.48
cssz-20a	Central and South America	268.8929	13.6558	24.00	296.23	17.94
cssz-20b	Central and South America	268.7064	13.2877	15.00	296.23	5.00
cssz-20y	Central and South America	269.1796	14.2206	45.50	296.23	73.94
cssz-20z	Central and South America	269.0362	13.9382	45.50	296.23	38.28
cssz-21a	Central and South America	269.6797	13.3031	25.00	292.65	17.94
cssz-21b	Central and South America	269.5187	12.9274	15.00	292.65	5.00
cssz-21x	Central and South America	269.8797	13.7690	68.00	292.65	131.79
cssz-21y	Central and South America	269.8130	13.6137	68.00	292.65	85.43
cssz-21z	Central and South America	269.7463	13.4584	68.00	292.65	39.07
cssz-22a	Central and South America	270.4823	13.0079	25.00	288.59	17.94
cssz-22b	Central and South America	270.3492	12.6221	15.00	288.59	5.00
cssz-22x	Central and South America	270.6476	13.4864	68.00	288.59	131.79
cssz-22y	Central and South America	270.5925	13.3269	68.00	288.59	85.43
cssz-22z	Central and South America	270.5374	13.1674	68.00	288.59	39.07
cssz-23a	Central and South America	271.3961	12.6734	25.00	292.45	17.94
cssz-23b	Central and South America	271.2369	12.2972	15.00	292.45	5.00
cssz-23x	Central and South America	271.5938	13.1399	68.00	292.45	131.79

Table A2: (continued)

Segment	Description	Longitude (°)	Latitude (°)	Strike (°)	Dip (°)	Depth (km)
cssz-23y	Central and South America	271.5279	12.9844	68.00	292.45	85.43
cssz-23z	Central and South America	271.4620	12.8289	68.00	292.45	39.07
cssz-24a	Central and South America	272.3203	12.2251	25.00	300.23	17.94
cssz-24b	Central and South America	272.1107	11.8734	15.00	300.23	5.00
cssz-24x	Central and South America	272.5917	12.6799	67.00	300.23	131.12
cssz-24y	Central and South America	272.5012	12.5283	67.00	300.23	85.10
cssz-24z	Central and South America	272.4107	12.3767	67.00	300.23	39.07
cssz-25a	Central and South America	273.2075	11.5684	25.00	313.80	17.94
cssz-25b	Central and South America	272.9200	11.2746	15.00	313.80	5.00
cssz-25x	Central and South America	273.5950	11.9641	66.00	313.80	130.43
cssz-25y	Central and South America	273.4658	11.8322	66.00	313.80	84.75
cssz-25z	Central and South America	273.3366	11.7003	66.00	313.80	39.07
cssz-26a	Central and South America	273.8943	10.8402	25.00	320.42	17.94
cssz-26b	Central and South America	273.5750	10.5808	15.00	320.42	5.00
cssz-26x	Central and South America	274.3246	11.1894	66.00	320.42	130.43
cssz-26y	Central and South America	274.1811	11.0730	66.00	320.42	84.75
cssz-26z	Central and South America	274.0377	10.9566	66.00	320.42	39.07
cssz-27a	Central and South America	274.4569	10.2177	25.00	316.10	17.94
cssz-27b	Central and South America	274.1590	9.9354	15.00	316.10	5.00
cssz-27z	Central and South America	274.5907	10.3444	66.00	316.10	39.07
cssz-28a	Central and South America	274.9586	9.8695	22.00	297.10	14.54
cssz-28b	Central and South America	274.7661	9.4988	11.00	297.10	5.00
cssz-28z	Central and South America	275.1118	10.1643	42.50	297.10	33.27
cssz-29a	Central and South America	275.7686	9.4789	19.00	296.60	11.09
cssz-29b	Central and South America	275.5759	9.0992	7.00	296.60	5.00
cssz-30a	Central and South America	276.6346	8.9973	19.00	302.25	9.36
cssz-30b	Central and South America	276.4053	8.6381	5.00	302.25	5.00
cssz-31a	Central and South America	277.4554	8.4152	19.00	309.05	7.62
cssz-31b	Central and South America	277.1851	8.0854	3.00	309.05	5.00
cssz-31z	Central and South America	277.7260	8.7450	19.00	309.05	23.90
cssz-32a	Central and South America	278.1112	7.9425	18.67	302.97	8.49
cssz-32b	Central and South America	277.8775	7.5855	4.00	302.97	5.00
cssz-32z	Central and South America	278.3407	8.2927	21.67	302.97	24.49

Table A2: (continued)

Segment	Description	Longitude (°)	Latitude (°)	Strike (°)	Dip (°)	Depth (km)
cssz-33a	Central and South America	278.7082	7.6620	18.33	287.56	10.23
cssz-33b	Central and South America	278.5785	7.2555	6.00	287.56	5.00
cssz-33z	Central and South America	278.8328	8.0522	24.33	287.56	25.95
cssz-34a	Central and South America	279.3184	7.5592	18.00	269.48	17.94
cssz-34b	Central and South America	279.3223	7.1320	15.00	269.48	5.00
cssz-35a	Central and South America	280.0039	7.6543	17.67	255.90	14.54
cssz-35b	Central and South America	280.1090	7.2392	11.00	255.90	5.00
cssz-35x	Central and South America	279.7156	8.7898	29.67	255.90	79.22
cssz-35y	Central and South America	279.8118	8.4113	29.67	255.90	54.47
cssz-35z	Central and South America	279.9079	8.0328	29.67	255.90	29.72
cssz-36a	Central and South America	281.2882	7.6778	17.33	282.48	11.09
cssz-36b	Central and South America	281.1948	7.2592	7.00	282.48	5.00
cssz-36x	Central and South America	281.5368	8.7896	32.33	282.48	79.47
cssz-36y	Central and South America	281.4539	8.4190	32.33	282.48	52.73
cssz-36z	Central and South America	281.3710	8.0484	32.33	282.48	25.99
cssz-37a	Central and South America	282.5252	6.8289	17.00	326.91	10.23
cssz-37b	Central and South America	282.1629	6.5944	6.00	326.91	5.00
cssz-38a	Central and South America	282.9469	5.5973	17.00	355.37	10.23
cssz-38b	Central and South America	282.5167	5.5626	6.00	355.37	5.00
cssz-39a	Central and South America	282.7236	4.3108	17.00	24.13	10.23
cssz-39b	Central and South America	282.3305	4.4864	6.00	24.13	5.00
cssz-39z	Central and South America	283.0603	4.1604	35.00	24.13	24.85
cssz-40a	Central and South America	282.1940	3.3863	17.00	35.28	10.23
cssz-40b	Central and South America	281.8427	3.6344	6.00	35.28	5.00
cssz-40y	Central and South America	282.7956	2.9613	35.00	35.28	53.52
cssz-40z	Central and South America	282.4948	3.1738	35.00	35.28	24.85
cssz-41a	Central and South America	281.6890	2.6611	17.00	34.27	10.23
cssz-41b	Central and South America	281.3336	2.9030	6.00	34.27	5.00
cssz-41z	Central and South America	281.9933	2.4539	35.00	34.27	24.85
cssz-42a	Central and South America	281.2266	1.9444	17.00	31.29	10.23
cssz-42b	Central and South America	280.8593	2.1675	6.00	31.29	5.00
cssz-42z	Central and South America	281.5411	1.7533	35.00	31.29	24.85
cssz-43a	Central and South America	280.7297	1.1593	17.00	33.30	10.23

Table A2: (continued)

Segment	Description	Longitude (°)	Latitude (°)	Strike (°)	Dip (°)	Depth (km)
cssz-43b	Central and South America	280.3706	1.3951	6.00	33.30	5.00
cssz-43z	Central and South America	281.0373	0.9573	35.00	33.30	24.85
cssz-44a	Central and South America	280.3018	0.4491	17.00	28.80	10.23
cssz-44b	Central and South America	279.9254	0.6560	6.00	28.80	5.00
cssz-45a	Central and South America	279.9083	-0.3259	10.00	26.91	8.49
cssz-45b	Central and South America	279.5139	-0.1257	4.00	26.91	5.00
cssz-46a	Central and South America	279.6461	-0.9975	10.00	15.76	8.49
cssz-46b	Central and South America	279.2203	-0.8774	4.00	15.76	5.00
cssz-47a	Central and South America	279.4972	-1.7407	10.00	6.90	8.49
cssz-47b	Central and South America	279.0579	-1.6876	4.00	6.90	5.00
cssz-48a	Central and South America	279.3695	-2.6622	10.00	8.96	8.49
cssz-48b	Central and South America	278.9321	-2.5933	4.00	8.96	5.00
cssz-48y	Central and South America	280.2444	-2.8000	10.00	8.96	25.85
cssz-48z	Central and South America	279.8070	-2.7311	10.00	8.96	17.17
cssz-49a	Central and South America	279.1852	-3.6070	10.00	13.15	8.49
cssz-49b	Central and South America	278.7536	-3.5064	4.00	13.15	5.00
cssz-49y	Central and South America	280.0486	-3.8082	10.00	13.15	25.85
cssz-49z	Central and South America	279.6169	-3.7076	10.00	13.15	17.17
cssz-50a	Central and South America	279.0652	-4.3635	10.33	4.78	9.64
cssz-50b	Central and South America	278.6235	-4.3267	5.33	4.78	5.00
cssz-51a	Central and South America	279.0349	-5.1773	10.67	359.43	10.81
cssz-51b	Central and South America	278.5915	-5.1817	6.67	359.43	5.00
cssz-52a	Central and South America	279.1047	-5.9196	11.00	349.75	11.96
cssz-52b	Central and South America	278.6685	-5.9981	8.00	349.75	5.00
cssz-53a	Central and South America	279.3044	-6.6242	10.25	339.21	11.74
cssz-53b	Central and South America	278.8884	-6.7811	7.75	339.21	5.00
cssz-53y	Central and South America	280.1024	-6.3232	19.25	339.21	37.12
cssz-53z	Central and South America	279.7035	-6.4737	19.25	339.21	20.64
cssz-54a	Central and South America	279.6256	-7.4907	9.50	340.78	11.53
cssz-54b	Central and South America	279.2036	-7.6365	7.50	340.78	5.00
cssz-54y	Central and South America	280.4267	-7.2137	20.50	340.78	37.29
cssz-54z	Central and South America	280.0262	-7.3522	20.50	340.78	19.78
cssz-55a	Central and South America	279.9348	-8.2452	8.75	335.38	11.74

Table A2: (continued)

Segment	Description	Longitude (°)	Latitude (°)	Strike (°)	Dip (°)	Depth (km)
cssz-55b	Central and South America	279.5269	-8.4301	7.75	335.38	5.00
cssz-55x	Central and South America	281.0837	-7.7238	21.75	335.38	56.40
cssz-55y	Central and South America	280.7009	-7.8976	21.75	335.38	37.88
cssz-55z	Central and South America	280.3180	-8.0714	21.75	335.38	19.35
cssz-56a	Central and South America	280.3172	-8.9958	8.00	331.62	11.09
cssz-56b	Central and South America	279.9209	-9.2072	7.00	331.62	5.00
cssz-56x	Central and South America	281.4212	-8.4063	23.00	331.62	57.13
cssz-56y	Central and South America	281.0534	-8.6028	23.00	331.62	37.59
cssz-56z	Central and South America	280.6854	-8.7993	23.00	331.62	18.05
cssz-57a	Central and South America	280.7492	-9.7356	8.60	328.71	10.75
cssz-57b	Central and South America	280.3640	-9.9663	6.60	328.71	5.00
cssz-57x	Central and South America	281.8205	-9.0933	23.40	328.71	57.94
cssz-57y	Central and South America	281.4636	-9.3074	23.40	328.71	38.08
cssz-57z	Central and South America	281.1065	-9.5215	23.40	328.71	18.22
cssz-58a	Central and South America	281.2275	-10.5350	9.20	330.52	10.40
cssz-58b	Central and South America	280.8348	-10.7532	6.20	330.52	5.00
cssz-58y	Central and South America	281.9548	-10.1306	23.80	330.52	38.57
cssz-58z	Central and South America	281.5913	-10.3328	23.80	330.52	18.39
cssz-59a	Central and South America	281.6735	-11.2430	9.80	326.24	10.05
cssz-59b	Central and South America	281.2982	-11.4890	5.80	326.24	5.00
cssz-59y	Central and South America	282.3675	-10.7876	24.20	326.24	39.06
cssz-59z	Central and South America	282.0206	-11.0153	24.20	326.24	18.56
cssz-60a	Central and South America	282.1864	-11.9946	10.40	326.50	9.71
cssz-60b	Central and South America	281.8096	-12.2384	5.40	326.50	5.00
cssz-60y	Central and South America	282.8821	-11.5438	24.60	326.50	39.55
cssz-60z	Central and South America	282.5344	-11.7692	24.60	326.50	18.73
cssz-61a	Central and South America	282.6944	-12.7263	11.00	325.47	9.36
cssz-61b	Central and South America	282.3218	-12.9762	5.00	325.47	5.00
cssz-61y	Central and South America	283.3814	-12.2649	25.00	325.47	40.03
cssz-61z	Central and South America	283.0381	-12.4956	25.00	325.47	18.90
cssz-62a	Central and South America	283.1980	-13.3556	11.00	318.96	9.79
cssz-62b	Central and South America	282.8560	-13.6451	5.50	318.96	5.00
cssz-62y	Central and South America	283.8178	-12.8300	27.00	318.96	42.03

Table A2: (continued)

Segment	Description	Longitude (°)	Latitude (°)	Strike (°)	Dip (°)	Depth (km)
cssz-62z	Central and South America	283.5081	-13.0928	27.00	318.96	19.33
cssz-63a	Central and South America	283.8032	-14.0147	11.00	317.85	10.23
cssz-63b	Central and South America	283.4661	-14.3106	6.00	317.85	5.00
cssz-63z	Central and South America	284.1032	-13.7511	29.00	317.85	19.77
cssz-64a	Central and South America	284.4144	-14.6482	13.00	315.68	11.96
cssz-64b	Central and South America	284.0905	-14.9540	8.00	315.68	5.00
cssz-65a	Central and South America	285.0493	-15.2554	15.00	313.23	13.68
cssz-65b	Central and South America	284.7411	-15.5715	10.00	313.23	5.00
cssz-66a	Central and South America	285.6954	-15.7816	14.50	307.67	13.68
cssz-66b	Central and South America	285.4190	-16.1258	10.00	307.67	5.00
cssz-67a	Central and South America	286.4127	-16.2781	14.00	304.30	13.68
cssz-67b	Central and South America	286.1566	-16.6381	10.00	304.30	5.00
cssz-67z	Central and South America	286.6552	-15.9365	23.00	304.30	25.78
cssz-68a	Central and South America	287.2481	-16.9016	14.00	311.81	13.68
cssz-68b	Central and South America	286.9442	-17.2264	10.00	311.81	5.00
cssz-68z	Central and South America	287.5291	-16.6007	26.00	311.81	25.78
cssz-69a	Central and South America	287.9724	-17.5502	14.00	314.88	13.68
cssz-69b	Central and South America	287.6496	-17.8590	10.00	314.88	5.00
cssz-69y	Central and South America	288.5530	-16.9934	29.00	314.88	50.02
cssz-69z	Central and South America	288.2629	-17.2718	29.00	314.88	25.78
cssz-70a	Central and South America	288.6731	-18.2747	14.00	320.37	13.25
cssz-70b	Central and South America	288.3193	-18.5527	9.50	320.37	5.00
cssz-70y	Central and South America	289.3032	-17.7785	30.00	320.37	50.35
cssz-70z	Central and South America	288.9884	-18.0266	30.00	320.37	25.35
cssz-71a	Central and South America	289.3089	-19.1854	14.00	333.19	12.82
cssz-71b	Central and South America	288.8968	-19.3820	9.00	333.19	5.00
cssz-71y	Central and South America	290.0357	-18.8382	31.00	333.19	50.67
cssz-71z	Central and South America	289.6725	-19.0118	31.00	333.19	24.92
cssz-72a	Central and South America	289.6857	-20.3117	14.00	352.39	12.54
cssz-72b	Central and South America	289.2250	-20.3694	8.67	352.39	5.00
cssz-72z	Central and South America	290.0882	-20.2613	32.00	352.39	24.63
cssz-73a	Central and South America	289.7731	-21.3061	14.00	358.94	12.24
cssz-73b	Central and South America	289.3053	-21.3142	8.33	358.94	5.00

Table A2: (continued)

Segment	Description	Longitude (°)	Latitude (°)	Strike (°)	Dip (°)	Depth (km)
cssz-73z	Central and South America	290.1768	-21.2991	33.00	358.94	24.34
cssz-74a	Central and South America	289.7610	-22.2671	14.00	3.06	11.96
cssz-74b	Central and South America	289.2909	-22.2438	8.00	3.06	5.00
cssz-75a	Central and South America	289.6982	-23.1903	14.09	4.83	11.96
cssz-75b	Central and South America	289.2261	-23.1536	8.00	4.83	5.00
cssz-76a	Central and South America	289.6237	-24.0831	14.18	4.67	11.96
cssz-76b	Central and South America	289.1484	-24.0476	8.00	4.67	5.00
cssz-77a	Central and South America	289.5538	-24.9729	14.27	4.30	11.96
cssz-77b	Central and South America	289.0750	-24.9403	8.00	4.30	5.00
cssz-78a	Central and South America	289.4904	-25.8621	14.36	3.86	11.96
cssz-78b	Central and South America	289.0081	-25.8328	8.00	3.86	5.00
cssz-79a	Central and South America	289.3491	-26.8644	14.45	11.34	11.96
cssz-79b	Central and South America	288.8712	-26.7789	8.00	11.34	5.00
cssz-80a	Central and South America	289.1231	-27.7826	14.54	14.16	11.96
cssz-80b	Central and South America	288.6469	-27.6762	8.00	14.16	5.00
cssz-81a	Central and South America	288.8943	-28.6409	14.63	13.19	11.96
cssz-81b	Central and South America	288.4124	-28.5417	8.00	13.19	5.00
cssz-82a	Central and South America	288.7113	-29.4680	14.72	9.68	11.96
cssz-82b	Central and South America	288.2196	-29.3950	8.00	9.68	5.00
cssz-83a	Central and South America	288.5944	-30.2923	14.81	5.36	11.96
cssz-83b	Central and South America	288.0938	-30.2517	8.00	5.36	5.00
cssz-84a	Central and South America	288.5223	-31.1639	14.90	3.80	11.96
cssz-84b	Central and South America	288.0163	-31.1351	8.00	3.80	5.00
cssz-85a	Central and South America	288.4748	-32.0416	15.00	2.55	11.96
cssz-85b	Central and South America	287.9635	-32.0223	8.00	2.55	5.00
cssz-86a	Central and South America	288.3901	-33.0041	15.00	7.01	11.96
cssz-86b	Central and South America	287.8768	-32.9512	8.00	7.01	5.00
cssz-87a	Central and South America	288.1050	-34.0583	15.00	19.40	11.96
cssz-87b	Central and South America	287.6115	-33.9142	8.00	19.40	5.00
cssz-88a	Central and South America	287.5309	-35.0437	15.00	32.81	11.96
cssz-88b	Central and South America	287.0862	-34.8086	8.00	32.81	5.00
cssz-88z	Central and South America	287.9308	-35.2545	30.00	32.81	24.90
cssz-89a	Central and South America	287.2380	-35.5993	16.67	14.52	11.96

Table A2: (continued)

Segment	Description	Longitude (°)	Latitude (°)	Strike (°)	Dip (°)	Depth (km)
cssz-89b	Central and South America	286.7261	-35.4914	8.00	14.52	5.00
cssz-89z	Central and South America	287.7014	-35.6968	30.00	14.52	26.30
cssz-90a	Central and South America	286.8442	-36.5645	18.33	22.64	11.96
cssz-90b	Central and South America	286.3548	-36.4004	8.00	22.64	5.00
cssz-90z	Central and South America	287.2916	-36.7142	30.00	22.64	27.68
cssz-91a	Central and South America	286.5925	-37.2488	20.00	10.90	11.96
cssz-91b	Central and South America	286.0721	-37.1690	8.00	10.90	5.00
cssz-91z	Central and South America	287.0726	-37.3224	30.00	10.90	29.06
cssz-92a	Central and South America	286.4254	-38.0945	20.00	8.23	11.96
cssz-92b	Central and South America	285.8948	-38.0341	8.00	8.23	5.00
cssz-92z	Central and South America	286.9303	-38.1520	26.67	8.23	29.06
cssz-93a	Central and South America	286.2047	-39.0535	20.00	13.46	11.96
cssz-93b	Central and South America	285.6765	-38.9553	8.00	13.46	5.00
cssz-93z	Central and South America	286.7216	-39.1495	23.33	13.46	29.06
cssz-94a	Central and South America	286.0772	-39.7883	20.00	3.40	11.96
cssz-94b	Central and South America	285.5290	-39.7633	8.00	3.40	5.00
cssz-94z	Central and South America	286.6255	-39.8133	20.00	3.40	29.06
cssz-95a	Central and South America	285.9426	-40.7760	20.00	9.84	11.96
cssz-95b	Central and South America	285.3937	-40.7039	8.00	9.84	5.00
cssz-95z	Central and South America	286.4921	-40.8481	20.00	9.84	29.06
cssz-96a	Central and South America	285.7839	-41.6303	20.00	7.60	11.96
cssz-96b	Central and South America	285.2245	-41.5745	8.00	7.60	5.00
cssz-96x	Central and South America	287.4652	-41.7977	20.00	7.60	63.26
cssz-96y	Central and South America	286.9043	-41.7419	20.00	7.60	46.16
cssz-96z	Central and South America	286.3439	-41.6861	20.00	7.60	29.06
cssz-97a	Central and South America	285.6695	-42.4882	20.00	5.30	11.96
cssz-97b	Central and South America	285.0998	-42.4492	8.00	5.30	5.00
cssz-97x	Central and South America	287.3809	-42.6052	20.00	5.30	63.26
cssz-97y	Central and South America	286.8101	-42.5662	20.00	5.30	46.16
cssz-97z	Central and South America	286.2396	-42.5272	20.00	5.30	29.06
cssz-98a	Central and South America	285.5035	-43.4553	20.00	10.53	11.96
cssz-98b	Central and South America	284.9322	-43.3782	8.00	10.53	5.00
cssz-98x	Central and South America	287.2218	-43.6866	20.00	10.53	63.26

Table A2: (continued)

Segment	Description	Longitude (°)	Latitude (°)	Strike (°)	Dip (°)	Depth (km)
cssz-98y	Central and South America	286.6483	-43.6095	20.00	10.53	46.16
cssz-98z	Central and South America	286.0755	-43.5324	20.00	10.53	29.06
cssz-99a	Central and South America	285.3700	-44.2595	20.00	4.86	11.96
cssz-99b	Central and South America	284.7830	-44.2237	8.00	4.86	5.00
cssz-99x	Central and South America	287.1332	-44.3669	20.00	4.86	63.26
cssz-99y	Central and South America	286.5451	-44.3311	20.00	4.86	46.16
cssz-99z	Central and South America	285.9574	-44.2953	20.00	4.86	29.06
cssz-100a	Central and South America	285.2713	-45.1664	20.00	5.68	11.96
cssz-100b	Central and South America	284.6758	-45.1246	8.00	5.68	5.00
cssz-100x	Central and South America	287.0603	-45.2918	20.00	5.68	63.26
cssz-100y	Central and South America	286.4635	-45.2500	20.00	5.68	46.16
cssz-100z	Central and South America	285.8672	-45.2082	20.00	5.68	29.06
cssz-101a	Central and South America	285.3080	-45.8607	20.00	352.58	9.36
cssz-101b	Central and South America	284.7067	-45.9152	5.00	352.58	5.00
cssz-101y	Central and South America	286.5089	-45.7517	20.00	352.58	43.56
cssz-101z	Central and South America	285.9088	-45.8062	20.00	352.58	26.46
cssz-102a	Central and South America	285.2028	-47.1185	5.00	17.72	9.36
cssz-102b	Central and South America	284.5772	-46.9823	5.00	17.72	5.00
cssz-102y	Central and South America	286.4588	-47.3909	5.00	17.72	18.07
cssz-102z	Central and South America	285.8300	-47.2547	5.00	17.72	13.72
cssz-103a	Central and South America	284.7075	-48.0396	7.50	23.37	11.53
cssz-103b	Central and South America	284.0972	-47.8630	7.50	23.37	5.00
cssz-103x	Central and South America	286.5511	-48.5694	7.50	23.37	31.11
cssz-103y	Central and South America	285.9344	-48.3928	7.50	23.37	24.58
cssz-103z	Central and South America	285.3199	-48.2162	7.50	23.37	18.05
cssz-104a	Central and South America	284.3440	-48.7597	10.00	14.87	13.68
cssz-104b	Central and South America	283.6962	-48.6462	10.00	14.87	5.00
cssz-104x	Central and South America	286.2962	-49.1002	10.00	14.87	39.73
cssz-104y	Central and South America	285.6440	-48.9867	10.00	14.87	31.05
cssz-104z	Central and South America	284.9933	-48.8732	10.00	14.87	22.36
cssz-105a	Central and South America	284.2312	-49.4198	9.67	0.25	13.40
cssz-105b	Central and South America	283.5518	-49.4179	9.67	0.25	5.00
cssz-105x	Central and South America	286.2718	-49.4255	9.67	0.25	38.59

Table A2: (continued)

Segment	Description	Longitude (°)	Latitude (°)	Strike (°)	Dip (°)	Depth (km)
cssz-105y	Central and South America	285.5908	-49.4236	9.67	0.25	30.20
cssz-105z	Central and South America	284.9114	-49.4217	9.67	0.25	21.80
cssz-106a	Central and South America	284.3730	-50.1117	9.25	347.50	13.04
cssz-106b	Central and South America	283.6974	-50.2077	9.25	347.50	5.00
cssz-106x	Central and South America	286.3916	-49.8238	9.25	347.50	37.15
cssz-106y	Central and South America	285.7201	-49.9198	9.25	347.50	29.11
cssz-106z	Central and South America	285.0472	-50.0157	9.25	347.50	21.07
cssz-107a	Central and South America	284.7130	-50.9714	9.00	346.48	12.82
cssz-107b	Central and South America	284.0273	-51.0751	9.00	346.48	5.00
cssz-107x	Central and South America	286.7611	-50.6603	9.00	346.48	36.29
cssz-107y	Central and South America	286.0799	-50.7640	9.00	346.48	28.47
cssz-107z	Central and South America	285.3972	-50.8677	9.00	346.48	20.64
cssz-108a	Central and South America	285.0378	-51.9370	8.67	352.01	12.54
cssz-108b	Central and South America	284.3241	-51.9987	8.67	352.01	5.00
cssz-108x	Central and South America	287.1729	-51.7519	8.67	352.01	35.15
cssz-108y	Central and South America	286.4622	-51.8136	8.67	352.01	27.61
cssz-108z	Central and South America	285.7505	-51.8753	8.67	352.01	20.07
cssz-109a	Central and South America	285.2635	-52.8439	8.33	353.08	12.24
cssz-109b	Central and South America	284.5326	-52.8974	8.33	353.08	5.00
cssz-109x	Central and South America	287.4508	-52.6834	8.33	353.08	33.97
cssz-109y	Central and South America	286.7226	-52.7369	8.33	353.08	26.73
cssz-109z	Central and South America	285.9935	-52.7904	8.33	353.08	19.49
cssz-110a	Central and South America	285.5705	-53.4139	8.00	334.19	11.96
cssz-110b	Central and South America	284.8972	-53.6076	8.00	334.19	5.00
cssz-110x	Central and South America	287.5724	-52.8328	8.00	334.19	32.83
cssz-110y	Central and South America	286.9081	-53.0265	8.00	334.19	25.88
cssz-110z	Central and South America	286.2408	-53.2202	8.00	334.19	18.92
cssz-111a	Central and South America	286.1627	-53.8749	8.00	313.83	11.96
cssz-111b	Central and South America	285.6382	-54.1958	8.00	313.83	5.00
cssz-111x	Central and South America	287.7124	-52.9122	8.00	313.83	32.83
cssz-111y	Central and South America	287.1997	-53.2331	8.00	313.83	25.88
cssz-111z	Central and South America	286.6832	-53.5540	8.00	313.83	18.92
cssz-112a	Central and South America	287.3287	-54.5394	8.00	316.39	11.96

Table A2: (continued)

Segment	Description	Longitude (°)	Latitude (°)	Strike (°)	Dip (°)	Depth (km)
cssz-112b	Central and South America	286.7715	-54.8462	8.00	316.39	5.00
cssz-112x	Central and South America	288.9756	-53.6190	8.00	316.39	32.83
cssz-112y	Central and South America	288.4307	-53.9258	8.00	316.39	25.88
cssz-112z	Central and South America	287.8817	-54.2326	8.00	316.39	18.92
cssz-113a	Central and South America	288.3409	-55.0480	8.00	307.64	11.96
cssz-113b	Central and South America	287.8647	-55.4002	8.00	307.64	5.00
cssz-113x	Central and South America	289.7450	-53.9914	8.00	307.64	32.83
cssz-113y	Central and South America	289.2810	-54.3436	8.00	307.64	25.88
cssz-113z	Central and South America	288.8130	-54.6958	8.00	307.64	18.92
cssz-114a	Central and South America	289.5342	-55.5026	8.00	301.48	11.96
cssz-114b	Central and South America	289.1221	-55.8819	8.00	301.48	5.00
cssz-114x	Central and South America	290.7472	-54.3647	8.00	301.48	32.83
cssz-114y	Central and South America	290.3467	-54.7440	8.00	301.48	25.88
cssz-114z	Central and South America	289.9424	-55.1233	8.00	301.48	18.92
cssz-115a	Central and South America	290.7682	-55.8485	8.00	292.70	11.96
cssz-115b	Central and South America	290.4608	-56.2588	8.00	292.70	5.00
cssz-115x	Central and South America	291.6714	-54.6176	8.00	292.70	32.83
cssz-115y	Central and South America	291.3734	-55.0279	8.00	292.70	25.88
cssz-115z	Central and South America	291.0724	-55.4382	8.00	292.70	18.92
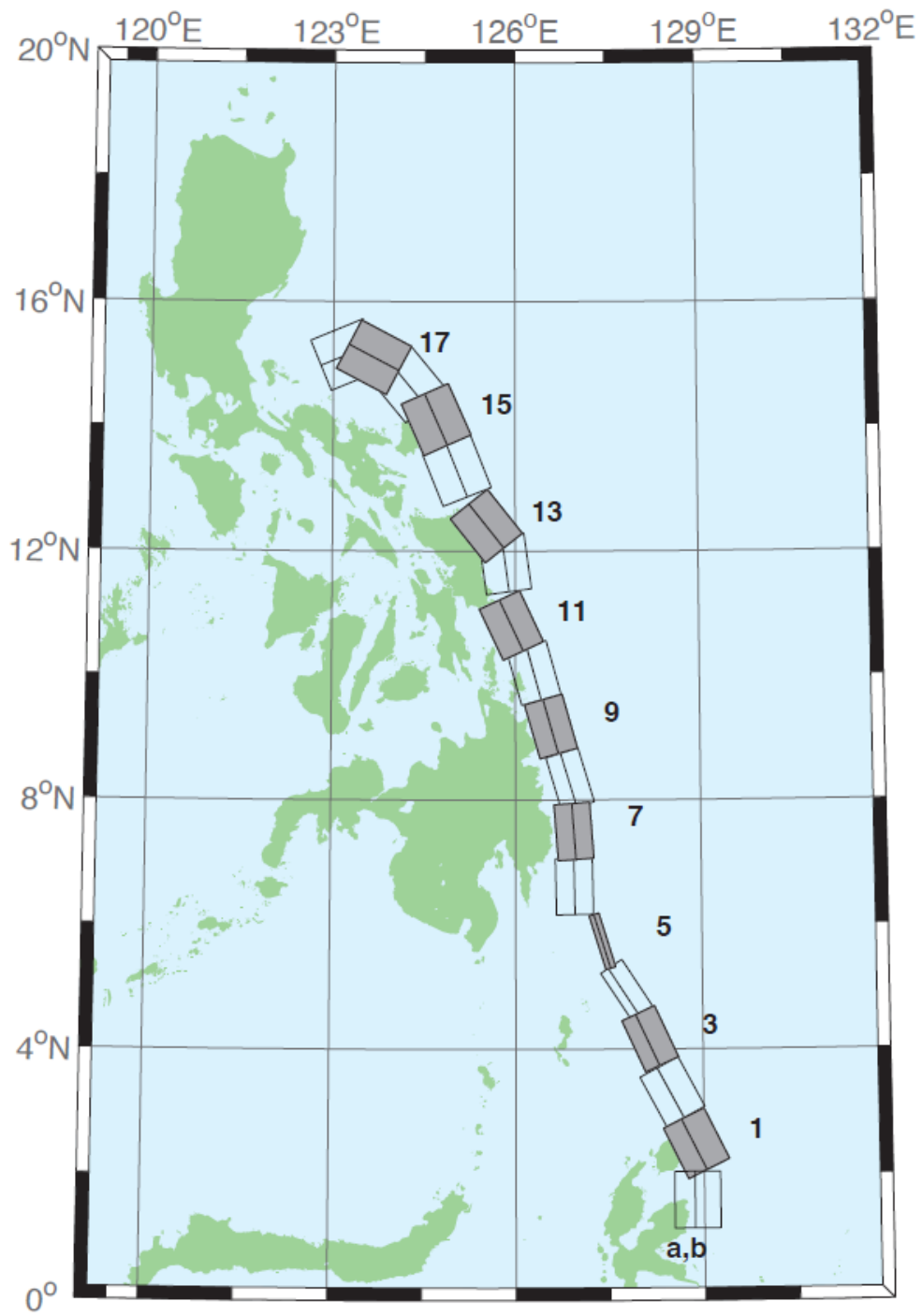
Figure A3. East Philippines Subduction Zone unit sources.

Table A3: Earthquake parameters for East Philippines Subduction Zone unit sources.

Segment	Description	Longitude (°)	Latitude (°)	Strike (°)	Dip (°)	Depth (km)
epsz-00a	East Philippines	128.5264	1.5930	44.00	180.00	26.92
epsz-00b	East Philippines	128.8496	1.5930	26.00	180.00	5.00
epsz-01a	East Philippines	128.5521	2.3289	44.20	153.61	27.62
epsz-01b	East Philippines	128.8408	2.4720	26.90	153.61	5.00
epsz-02a	East Philippines	128.1943	3.1508	45.90	151.93	32.44
epsz-02b	East Philippines	128.4706	3.2979	32.80	151.93	5.35
epsz-03a	East Philippines	127.8899	4.0428	57.30	155.22	40.22
epsz-03b	East Philippines	128.1108	4.1445	42.70	155.22	6.31
epsz-04a	East Philippines	127.6120	4.8371	71.40	146.84	48.25
epsz-04b	East Philippines	127.7324	4.9155	54.80	146.84	7.39
epsz-05a	East Philippines	127.3173	5.7040	79.90	162.87	57.40
epsz-05b	East Philippines	127.3930	5.7272	79.40	162.87	8.25
epsz-06a	East Philippines	126.6488	6.6027	48.60	178.89	45.09
epsz-06b	East Philippines	126.9478	6.6085	48.60	178.89	7.58
epsz-07a	East Philippines	126.6578	7.4711	50.70	175.76	45.52
epsz-07b	East Philippines	126.9439	7.4921	50.70	175.76	6.83
epsz-08a	East Philippines	126.6227	8.2456	56.70	163.31	45.60
epsz-08b	East Philippines	126.8614	8.3164	48.90	163.31	7.92
epsz-09a	East Philippines	126.2751	9.0961	47.00	164.09	43.59
epsz-09b	East Philippines	126.5735	9.1801	44.90	164.09	8.30
epsz-10a	East Philippines	125.9798	9.9559	43.10	164.46	42.25
epsz-10b	East Philippines	126.3007	10.0438	43.10	164.46	8.09
epsz-11a	East Philippines	125.6079	10.6557	37.80	154.97	38.29
epsz-11b	East Philippines	125.9353	10.8059	37.80	154.97	7.64
epsz-12a	East Philippines	125.4697	11.7452	36.00	172.14	37.01
epsz-12b	East Philippines	125.8374	11.7949	36.00	172.14	7.62
epsz-13a	East Philippines	125.2238	12.1670	32.40	141.53	33.87
epsz-13b	East Philippines	125.5278	12.4029	32.40	141.53	7.08
epsz-14a	East Philippines	124.6476	13.1365	23.00	158.23	25.92
epsz-14b	East Philippines	125.0421	13.2898	23.00	158.23	6.38
epsz-15a	East Philippines	124.3107	13.9453	24.10	156.12	26.51
epsz-15b	East Philippines	124.6973	14.1113	24.10	156.12	6.09
epsz-16a	East Philippines	123.8998	14.4025	19.50	140.32	21.69

Table A3: (continued)

Segment	Description	Longitude (°)	Latitude (°)	Strike (°)	Dip (°)	Depth (km)
epsz-16b	East Philippines	124.2366	14.6728	19.50	140.32	5.00
epsz-17a	East Philippines	123.4604	14.7222	15.30	117.58	18.19
epsz-17b	East Philippines	123.6682	15.1062	15.30	117.58	5.00
epsz-18a	East Philippines	123.3946	14.7462	15.00	67.40	17.94
epsz-18b	East Philippines	123.2219	15.1467	15.00	67.40	5.00
epsz-19a	East Philippines	121.3638	15.7400	15.00	189.63	17.94
epsz-19b	East Philippines	121.8082	15.6674	15.00	189.63	5.00
epsz-20a	East Philippines	121.6833	16.7930	15.00	203.26	17.94
epsz-20b	East Philippines	122.0994	16.6216	15.00	203.26	5.00
epsz-21a	East Philippines	121.8279	17.3742	15.00	184.19	17.94
epsz-21b	East Philippines	122.2814	17.3425	15.00	184.19	5.00
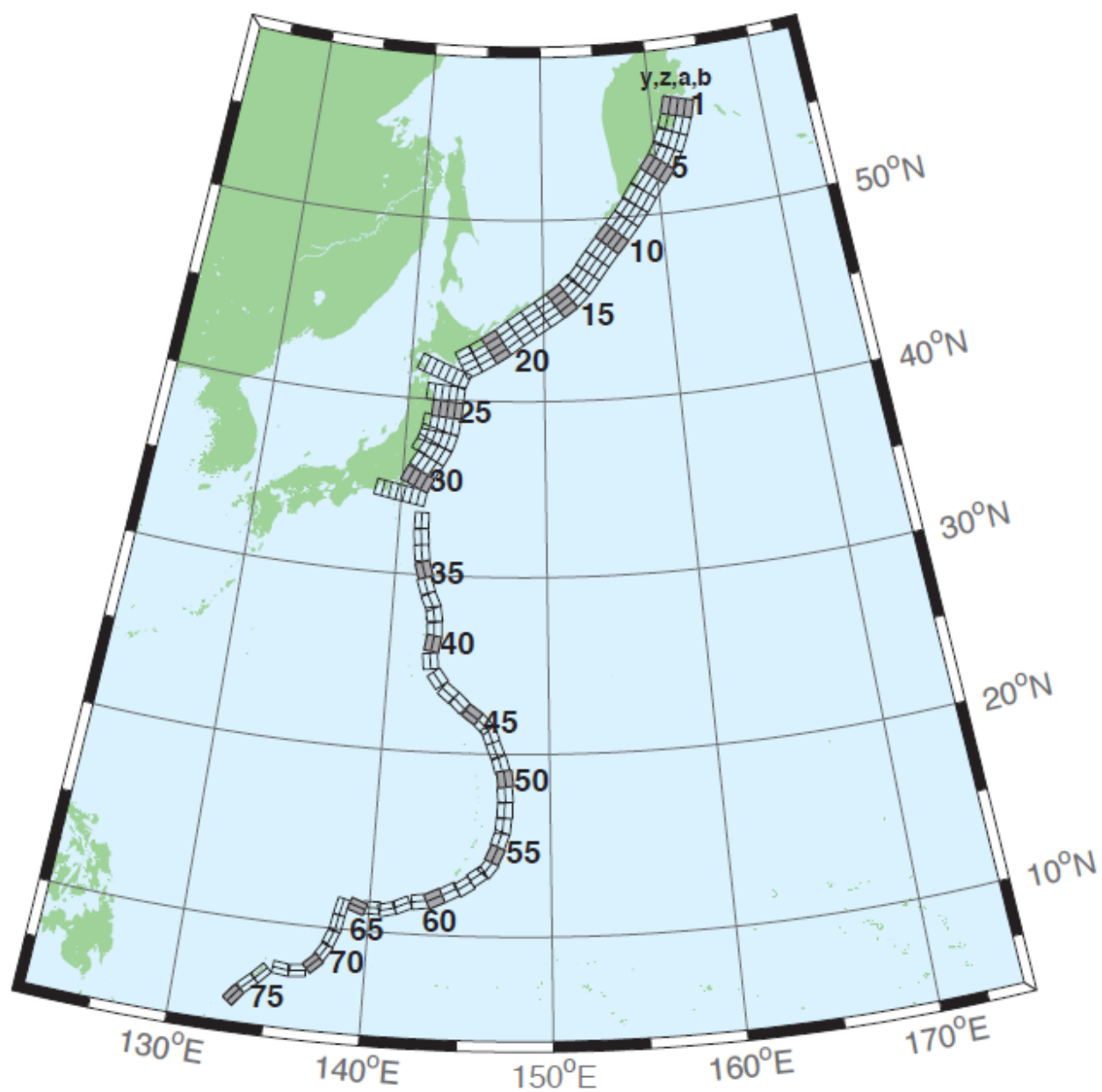
Figure A4. Kamchatka-Kuril-Japan-Izu-Mariana-Yap Subduction Zone unit sources.

Table A4: Earthquake parameters for Kamchatka-Kuril-Japan-Izu-Mariana-Yap Subduction Zone unit sources.

Segment	Description	Longitude (°)	Latitude (°)	Strike (°)	Dip (°)	Depth (km)
kisz-00a	Kamchatka-Kuril-Japan-Izu-Mariana-Yap	162.8200	56.3667	29.00	194.41	26.13
kisz-00b	Kamchatka-Kuril-Japan-Izu-Mariana-Yap	163.5057	56.2677	25.00	195.00	5.00
kisz-00z	Kamchatka-Kuril-Japan-Izu-Mariana-Yap	162.1309	56.4618	29.00	193.84	50.37
kisz-01a	Kamchatka-Kuril-Japan-Izu-Mariana-Yap	162.4318	55.5017	29.00	195.00	26.13
kisz-01b	Kamchatka-Kuril-Japan-Izu-Mariana-Yap	163.1000	55.4000	25.00	195.00	5.00
kisz-01y	Kamchatka-Kuril-Japan-Izu-Mariana-Yap	161.0884	55.7050	29.00	195.00	74.61
kisz-01z	Kamchatka-Kuril-Japan-Izu-Mariana-Yap	161.7610	55.6033	29.00	195.00	50.37
kisz-02a	Kamchatka-Kuril-Japan-Izu-Mariana-Yap	161.9883	54.6784	29.00	200.00	26.13
kisz-02b	Kamchatka-Kuril-Japan-Izu-Mariana-Yap	162.6247	54.5440	25.00	200.00	5.00
kisz-02y	Kamchatka-Kuril-Japan-Izu-Mariana-Yap	160.7072	54.9471	29.00	200.00	74.61
kisz-02z	Kamchatka-Kuril-Japan-Izu-Mariana-Yap	161.3488	54.8127	29.00	200.00	50.37
kisz-03a	Kamchatka-Kuril-Japan-Izu-Mariana-Yap	161.4385	53.8714	29.00	204.00	26.13
kisz-03b	Kamchatka-Kuril-Japan-Izu-Mariana-Yap	162.0449	53.7116	25.00	204.00	5.00
kisz-03y	Kamchatka-Kuril-Japan-Izu-Mariana-Yap	160.2164	54.1910	29.00	204.00	74.61
kisz-03z	Kamchatka-Kuril-Japan-Izu-Mariana-Yap	160.8286	54.0312	29.00	204.00	50.37
kisz-04a	Kamchatka-Kuril-Japan-Izu-Mariana-Yap	160.7926	53.1087	29.00	210.00	26.13
kisz-04b	Kamchatka-Kuril-Japan-Izu-Mariana-Yap	161.3568	52.9123	25.00	210.00	5.00

Segment	Description	Longitude (°)	Latitude (°)	Strike (°)	Dip (°)	Depth (km)
kisz-04y	Kamchatka-Kuril-Japan-Izu-Mariana-Yap	159.6539	53.5015	29.00	210.00	74.61
kisz-04z	Kamchatka-Kuril-Japan-Izu-Mariana-Yap	160.2246	53.3051	29.00	210.00	50.37
kisz-05a	Kamchatka-Kuril-Japan-Izu-Mariana-Yap	160.0211	52.4113	29.00	218.00	26.13
kisz-05b	Kamchatka-Kuril-Japan-Izu-Mariana-Yap	160.5258	52.1694	25.00	218.00	5.00
kisz-05y	Kamchatka-Kuril-Japan-Izu-Mariana-Yap	159.0005	52.8950	29.00	218.00	74.61
kisz-05z	Kamchatka-Kuril-Japan-Izu-Mariana-Yap	159.5122	52.6531	29.00	218.00	50.37
kisz-06a	Kamchatka-Kuril-Japan-Izu-Mariana-Yap	159.1272	51.7034	29.00	218.00	26.13
kisz-06b	Kamchatka-Kuril-Japan-Izu-Mariana-Yap	159.6241	51.4615	25.00	218.00	5.00
kisz-06y	Kamchatka-Kuril-Japan-Izu-Mariana-Yap	158.1228	52.1871	29.00	218.00	74.61
kisz-06z	Kamchatka-Kuril-Japan-Izu-Mariana-Yap	158.6263	51.9452	29.00	218.00	50.37
kisz-07a	Kamchatka-Kuril-Japan-Izu-Mariana-Yap	158.2625	50.9549	29.00	214.00	26.13
kisz-07b	Kamchatka-Kuril-Japan-Izu-Mariana-Yap	158.7771	50.7352	25.00	214.00	5.00
kisz-07y	Kamchatka-Kuril-Japan-Izu-Mariana-Yap	157.2236	51.3942	29.00	214.00	74.61
kisz-07z	Kamchatka-Kuril-Japan-Izu-Mariana-Yap	157.7443	51.1745	29.00	214.00	50.37
kisz-08a	Kamchatka-Kuril-Japan-Izu-Mariana-Yap	157.4712	50.2459	31.00	218.00	27.70
kisz-08b	Kamchatka-Kuril-Japan-Izu-Mariana-Yap	157.9433	50.0089	27.00	218.00	5.00
kisz-08y	Kamchatka-Kuril-Japan-Izu-Mariana-Yap	156.5176	50.7199	31.00	218.00	79.20

Table A4: (continued)

Segment	Description	Longitude (°)	Latitude (°)	Strike (°)	Dip (°)	Depth (km)
kisz-08z	Kamchatka-Kuril-Japan-Izu-Mariana-Yap	156.9956	50.4829	31.00	218.00	53.45
kisz-09a	Kamchatka-Kuril-Japan-Izu-Mariana-Yap	156.6114	49.5584	31.00	220.00	27.70
kisz-09b	Kamchatka-Kuril-Japan-Izu-Mariana-Yap	157.0638	49.3109	27.00	220.00	5.00
kisz-09y	Kamchatka-Kuril-Japan-Izu-Mariana-Yap	155.6974	50.0533	31.00	220.00	79.20
kisz-09z	Kamchatka-Kuril-Japan-Izu-Mariana-Yap	156.1556	49.8058	31.00	220.00	53.45
kisz-10a	Kamchatka-Kuril-Japan-Izu-Mariana-Yap	155.7294	48.8804	31.00	221.00	27.70
kisz-10b	Kamchatka-Kuril-Japan-Izu-Mariana-Yap	156.1690	48.6278	27.00	221.00	5.00
kisz-10y	Kamchatka-Kuril-Japan-Izu-Mariana-Yap	154.8413	49.3856	31.00	221.00	79.20
kisz-10z	Kamchatka-Kuril-Japan-Izu-Mariana-Yap	155.2865	49.1330	31.00	221.00	53.45
kisz-11a	Kamchatka-Kuril-Japan-Izu-Mariana-Yap	154.8489	48.1821	31.00	219.00	27.70
kisz-11b	Kamchatka-Kuril-Japan-Izu-Mariana-Yap	155.2955	47.9398	27.00	219.00	5.00
kisz-11c	Kamchatka-Kuril-Japan-Izu-Mariana-Yap	156.0358	47.5375	57.89	39.00	4.60
kisz-11y	Kamchatka-Kuril-Japan-Izu-Mariana-Yap	153.9472	48.6667	31.00	219.00	79.20
kisz-11z	Kamchatka-Kuril-Japan-Izu-Mariana-Yap	154.3991	48.4244	31.00	219.00	53.45
kisz-12a	Kamchatka-Kuril-Japan-Izu-Mariana-Yap	153.9994	47.4729	31.00	217.00	27.70
kisz-12b	Kamchatka-Kuril-Japan-Izu-Mariana-Yap	154.4701	47.2320	27.00	217.00	5.00
kisz-12c	Kamchatka-Kuril-Japan-Izu-Mariana-Yap	155.2207	46.8473	57.89	37.00	4.60

Table A4: (continued)

Segment	Description	Longitude (°)	Latitude (°)	Strike (°)	Dip (°)	Depth (km)
kisz-12y	Kamchatka-Kuril-Japan-Izu-Mariana-Yap	153.0856	47.9363	31.00	217.00	79.20
kisz-12z	Kamchatka-Kuril-Japan-Izu-Mariana-Yap	153.5435	47.7046	31.00	217.00	53.45
kisz-13a	Kamchatka-Kuril-Japan-Izu-Mariana-Yap	153.2239	46.7564	31.00	218.00	27.70
kisz-13b	Kamchatka-Kuril-Japan-Izu-Mariana-Yap	153.6648	46.5194	27.00	218.00	5.00
kisz-13c	Kamchatka-Kuril-Japan-Izu-Mariana-Yap	154.3957	46.1258	57.89	38.00	4.60
kisz-13y	Kamchatka-Kuril-Japan-Izu-Mariana-Yap	152.3343	47.2304	31.00	218.00	79.20
kisz-13z	Kamchatka-Kuril-Japan-Izu-Mariana-Yap	152.7801	46.9934	31.00	218.00	53.45
kisz-14a	Kamchatka-Kuril-Japan-Izu-Mariana-Yap	152.3657	46.1515	23.00	225.00	24.54
kisz-14b	Kamchatka-Kuril-Japan-Izu-Mariana-Yap	152.7855	45.8591	23.00	225.00	5.00
kisz-14c	Kamchatka-Kuril-Japan-Izu-Mariana-Yap	153.4468	45.3976	57.89	45.00	4.60
kisz-14y	Kamchatka-Kuril-Japan-Izu-Mariana-Yap	151.5172	46.7362	23.00	225.00	63.62
kisz-14z	Kamchatka-Kuril-Japan-Izu-Mariana-Yap	151.9426	46.4438	23.00	225.00	44.08
kisz-15a	Kamchatka-Kuril-Japan-Izu-Mariana-Yap	151.4663	45.5963	25.00	233.00	23.73
kisz-15b	Kamchatka-Kuril-Japan-Izu-Mariana-Yap	151.8144	45.2712	22.00	233.00	5.00
kisz-15y	Kamchatka-Kuril-Japan-Izu-Mariana-Yap	150.7619	46.2465	25.00	233.00	65.99
kisz-15z	Kamchatka-Kuril-Japan-Izu-Mariana-Yap	151.1151	45.9214	25.00	233.00	44.86
kisz-16a	Kamchatka-Kuril-Japan-Izu-Mariana-Yap	150.4572	45.0977	25.00	237.00	23.73

Table A4: (continued)

Segment	Description	Longitude (°)	Latitude (°)	Strike (°)	Dip (°)	Depth (km)
kisz-16b	Kamchatka-Kuril-Japan-Izu-Mariana-Yap	150.7694	44.7563	22.00	237.00	5.00
kisz-16y	Kamchatka-Kuril-Japan-Izu-Mariana-Yap	149.8253	45.7804	25.00	237.00	65.99
kisz-16z	Kamchatka-Kuril-Japan-Izu-Mariana-Yap	150.1422	45.4390	25.00	237.00	44.86
kisz-17a	Kamchatka-Kuril-Japan-Izu-Mariana-Yap	149.3989	44.6084	25.00	237.00	23.73
kisz-17b	Kamchatka-Kuril-Japan-Izu-Mariana-Yap	149.7085	44.2670	22.00	237.00	5.00
kisz-17y	Kamchatka-Kuril-Japan-Izu-Mariana-Yap	148.7723	45.2912	25.00	237.00	65.99
kisz-17z	Kamchatka-Kuril-Japan-Izu-Mariana-Yap	149.0865	44.9498	25.00	237.00	44.86
kisz-18a	Kamchatka-Kuril-Japan-Izu-Mariana-Yap	148.3454	44.0982	25.00	235.00	23.73
kisz-18b	Kamchatka-Kuril-Japan-Izu-Mariana-Yap	148.6687	43.7647	22.00	235.00	5.00
kisz-18y	Kamchatka-Kuril-Japan-Izu-Mariana-Yap	147.6915	44.7651	25.00	235.00	65.99
kisz-18z	Kamchatka-Kuril-Japan-Izu-Mariana-Yap	148.0194	44.4316	25.00	235.00	44.86
kisz-19a	Kamchatka-Kuril-Japan-Izu-Mariana-Yap	147.3262	43.5619	25.00	233.00	23.73
kisz-19b	Kamchatka-Kuril-Japan-Izu-Mariana-Yap	147.6625	43.2368	22.00	233.00	5.00
kisz-19y	Kamchatka-Kuril-Japan-Izu-Mariana-Yap	146.6463	44.2121	25.00	233.00	65.99
kisz-19z	Kamchatka-Kuril-Japan-Izu-Mariana-Yap	146.9872	43.8870	25.00	233.00	44.86
kisz-20a	Kamchatka-Kuril-Japan-Izu-Mariana-Yap	146.3513	43.0633	25.00	237.00	23.73
kisz-20b	Kamchatka-Kuril-Japan-Izu-Mariana-Yap	146.6531	42.7219	22.00	237.00	5.00

Table A4: (continued)

Segment	Description	Longitude (°)	Latitude (°)	Strike (°)	Dip (°)	Depth (km)
kisz-20y	Kamchatka-Kuril-Japan-Izu-Mariana-Yap	145.7410	43.7461	25.00	237.00	65.99
kisz-20z	Kamchatka-Kuril-Japan-Izu-Mariana-Yap	146.0470	43.4047	25.00	237.00	44.86
kisz-21a	Kamchatka-Kuril-Japan-Izu-Mariana-Yap	145.3331	42.5948	25.00	239.00	23.73
kisz-21b	Kamchatka-Kuril-Japan-Izu-Mariana-Yap	145.6163	42.2459	22.00	239.00	5.00
kisz-21y	Kamchatka-Kuril-Japan-Izu-Mariana-Yap	144.7603	43.2927	25.00	239.00	65.99
kisz-21z	Kamchatka-Kuril-Japan-Izu-Mariana-Yap	145.0475	42.9438	25.00	239.00	44.86
kisz-22a	Kamchatka-Kuril-Japan-Izu-Mariana-Yap	144.3041	42.1631	25.00	242.00	23.73
kisz-22b	Kamchatka-Kuril-Japan-Izu-Mariana-Yap	144.5605	41.8037	22.00	242.00	5.00
kisz-22y	Kamchatka-Kuril-Japan-Izu-Mariana-Yap	143.7854	42.8819	25.00	242.00	65.99
kisz-22z	Kamchatka-Kuril-Japan-Izu-Mariana-Yap	144.0455	42.5225	25.00	242.00	44.86
kisz-23a	Kamchatka-Kuril-Japan-Izu-Mariana-Yap	143.2863	41.3335	21.00	202.00	21.28
kisz-23b	Kamchatka-Kuril-Japan-Izu-Mariana-Yap	143.8028	41.1764	19.00	202.00	5.00
kisz-23v	Kamchatka-Kuril-Japan-Izu-Mariana-Yap	140.6816	42.1189	21.00	202.00	110.87
kisz-23w	Kamchatka-Kuril-Japan-Izu-Mariana-Yap	141.2050	41.9618	21.00	202.00	92.95
kisz-23x	Kamchatka-Kuril-Japan-Izu-Mariana-Yap	141.7273	41.8047	21.00	202.00	75.04
kisz-23y	Kamchatka-Kuril-Japan-Izu-Mariana-Yap	142.2482	41.6476	21.00	202.00	57.12
kisz-23z	Kamchatka-Kuril-Japan-Izu-Mariana-Yap	142.7679	41.4905	21.00	202.00	39.20

Table A4: (continued)

Segment	Description	Longitude (°)	Latitude (°)	Strike (°)	Dip (°)	Depth (km)
kisz-24a	Kamchatka-Kuril-Japan-Izu-Mariana-Yap	142.9795	40.3490	21.00	185.00	21.28
kisz-24b	Kamchatka-Kuril-Japan-Izu-Mariana-Yap	143.5273	40.3125	19.00	185.00	5.00
kisz-24x	Kamchatka-Kuril-Japan-Izu-Mariana-Yap	141.3339	40.4587	21.00	185.00	75.04
kisz-24y	Kamchatka-Kuril-Japan-Izu-Mariana-Yap	141.8827	40.4221	21.00	185.00	57.12
kisz-24z	Kamchatka-Kuril-Japan-Izu-Mariana-Yap	142.4312	40.3856	21.00	185.00	39.20
kisz-25a	Kamchatka-Kuril-Japan-Izu-Mariana-Yap	142.8839	39.4541	21.00	185.00	21.28
kisz-25b	Kamchatka-Kuril-Japan-Izu-Mariana-Yap	143.4246	39.4176	19.00	185.00	5.00
kisz-25y	Kamchatka-Kuril-Japan-Izu-Mariana-Yap	141.8012	39.5272	21.00	185.00	57.12
kisz-25z	Kamchatka-Kuril-Japan-Izu-Mariana-Yap	142.3426	39.4907	21.00	185.00	39.20
kisz-26a	Kamchatka-Kuril-Japan-Izu-Mariana-Yap	142.7622	38.5837	21.00	188.00	21.28
kisz-26b	Kamchatka-Kuril-Japan-Izu-Mariana-Yap	143.2930	38.5254	19.00	188.00	5.00
kisz-26x	Kamchatka-Kuril-Japan-Izu-Mariana-Yap	141.1667	38.7588	21.00	188.00	75.04
kisz-26y	Kamchatka-Kuril-Japan-Izu-Mariana-Yap	141.6990	38.7004	21.00	188.00	57.12
kisz-26z	Kamchatka-Kuril-Japan-Izu-Mariana-Yap	142.2308	38.6421	21.00	188.00	39.20
kisz-27a	Kamchatka-Kuril-Japan-Izu-Mariana-Yap	142.5320	37.7830	21.00	198.00	21.28
kisz-27b	Kamchatka-Kuril-Japan-Izu-Mariana-Yap	143.0357	37.6534	19.00	198.00	5.00
kisz-27x	Kamchatka-Kuril-Japan-Izu-Mariana-Yap	141.0142	38.1717	21.00	198.00	75.04

Table A4: (continued)

Segment	Description	Longitude (°)	Latitude (°)	Strike (°)	Dip (°)	Depth (km)
kisz-27y	Kamchatka-Kuril-Japan-Izu-Mariana-Yap	141.5210	38.0421	21.00	198.00	57.12
kisz-27z	Kamchatka-Kuril-Japan-Izu-Mariana-Yap	142.0269	37.9126	21.00	198.00	39.20
kisz-28a	Kamchatka-Kuril-Japan-Izu-Mariana-Yap	142.1315	37.0265	21.00	208.00	21.28
kisz-28b	Kamchatka-Kuril-Japan-Izu-Mariana-Yap	142.5941	36.8297	19.00	208.00	5.00
kisz-28x	Kamchatka-Kuril-Japan-Izu-Mariana-Yap	140.7348	37.6171	21.00	208.00	75.04
kisz-28y	Kamchatka-Kuril-Japan-Izu-Mariana-Yap	141.2016	37.4202	21.00	208.00	57.12
kisz-28z	Kamchatka-Kuril-Japan-Izu-Mariana-Yap	141.6671	37.2234	21.00	208.00	39.20
kisz-29a	Kamchatka-Kuril-Japan-Izu-Mariana-Yap	141.5970	36.2640	21.00	211.00	21.28
kisz-29b	Kamchatka-Kuril-Japan-Izu-Mariana-Yap	142.0416	36.0481	19.00	211.00	5.00
kisz-29y	Kamchatka-Kuril-Japan-Izu-Mariana-Yap	140.7029	36.6960	21.00	211.00	57.12
kisz-29z	Kamchatka-Kuril-Japan-Izu-Mariana-Yap	141.1506	36.4800	21.00	211.00	39.20
kisz-30a	Kamchatka-Kuril-Japan-Izu-Mariana-Yap	141.0553	35.4332	21.00	205.00	21.28
kisz-30b	Kamchatka-Kuril-Japan-Izu-Mariana-Yap	141.5207	35.2560	19.00	205.00	5.00
kisz-30y	Kamchatka-Kuril-Japan-Izu-Mariana-Yap	140.1204	35.7876	21.00	205.00	57.12
kisz-30z	Kamchatka-Kuril-Japan-Izu-Mariana-Yap	140.5883	35.6104	21.00	205.00	39.20
kisz-31a	Kamchatka-Kuril-Japan-Izu-Mariana-Yap	140.6956	34.4789	22.00	190.00	22.10
kisz-31b	Kamchatka-Kuril-Japan-Izu-Mariana-Yap	141.1927	34.4066	20.00	190.00	5.00

Table A4: (continued)

Segment	Description	Longitude (°)	Latitude (°)	Strike (°)	Dip (°)	Depth (km)
kisz-31v	Kamchatka-Kuril-Japan-Izu-Mariana-Yap	138.2025	34.8405	22.00	190.00	115.75
kisz-31w	Kamchatka-Kuril-Japan-Izu-Mariana-Yap	138.7021	34.7682	22.00	190.00	97.02
kisz-31x	Kamchatka-Kuril-Japan-Izu-Mariana-Yap	139.2012	34.6958	22.00	190.00	78.29
kisz-31y	Kamchatka-Kuril-Japan-Izu-Mariana-Yap	139.6997	34.6235	22.00	190.00	59.56
kisz-31z	Kamchatka-Kuril-Japan-Izu-Mariana-Yap	140.1979	34.5512	22.00	190.00	40.83
kisz-32a	Kamchatka-Kuril-Japan-Izu-Mariana-Yap	141.0551	33.0921	32.00	180.00	23.48
kisz-32b	Kamchatka-Kuril-Japan-Izu-Mariana-Yap	141.5098	33.0921	21.69	180.00	5.00
kisz-33a	Kamchatka-Kuril-Japan-Izu-Mariana-Yap	141.0924	32.1047	27.65	173.85	20.67
kisz-33b	Kamchatka-Kuril-Japan-Izu-Mariana-Yap	141.5596	32.1473	18.27	173.85	5.00
kisz-34a	Kamchatka-Kuril-Japan-Izu-Mariana-Yap	141.1869	31.1851	25.00	172.14	18.26
kisz-34b	Kamchatka-Kuril-Japan-Izu-Mariana-Yap	141.6585	31.2408	15.38	172.14	5.00
kisz-35a	Kamchatka-Kuril-Japan-Izu-Mariana-Yap	141.4154	30.1707	25.00	162.98	17.12
kisz-35b	Kamchatka-Kuril-Japan-Izu-Mariana-Yap	141.8662	30.2899	14.03	162.98	5.00
kisz-36a	Kamchatka-Kuril-Japan-Izu-Mariana-Yap	141.6261	29.2740	25.73	161.68	18.71
kisz-36b	Kamchatka-Kuril-Japan-Izu-Mariana-Yap	142.0670	29.4012	15.91	161.68	5.00
kisz-37a	Kamchatka-Kuril-Japan-Izu-Mariana-Yap	142.0120	28.3322	20.00	154.72	14.54
kisz-37b	Kamchatka-Kuril-Japan-Izu-Mariana-Yap	142.4463	28.5124	11.00	154.72	5.00

Table A4: (continued)

Segment	Description	Longitude (°)	Latitude (°)	Strike (°)	Dip (°)	Depth (km)
kisz-38a	Kamchatka-Kuril-Japan-Izu-Mariana-Yap	142.2254	27.6946	20.00	170.27	14.54
kisz-38b	Kamchatka-Kuril-Japan-Izu-Mariana-Yap	142.6955	27.7659	11.00	170.27	5.00
kisz-39a	Kamchatka-Kuril-Japan-Izu-Mariana-Yap	142.3085	26.9127	24.23	177.23	17.42
kisz-39b	Kamchatka-Kuril-Japan-Izu-Mariana-Yap	142.7674	26.9325	14.38	177.23	5.00
kisz-40a	Kamchatka-Kuril-Japan-Izu-Mariana-Yap	142.2673	26.1923	26.49	189.44	22.26
kisz-40b	Kamchatka-Kuril-Japan-Izu-Mariana-Yap	142.7090	26.1264	20.20	189.44	5.00
kisz-41a	Kamchatka-Kuril-Japan-Izu-Mariana-Yap	142.1595	25.0729	22.07	173.72	19.08
kisz-41b	Kamchatka-Kuril-Japan-Izu-Mariana-Yap	142.6165	25.1184	16.36	173.72	5.00
kisz-42a	Kamchatka-Kuril-Japan-Izu-Mariana-Yap	142.7641	23.8947	21.54	143.50	18.40
kisz-42b	Kamchatka-Kuril-Japan-Izu-Mariana-Yap	143.1321	24.1432	15.54	143.50	5.00
kisz-43a	Kamchatka-Kuril-Japan-Izu-Mariana-Yap	143.5281	23.0423	23.02	129.21	18.77
kisz-43b	Kamchatka-Kuril-Japan-Izu-Mariana-Yap	143.8128	23.3626	15.99	129.21	5.00
kisz-44a	Kamchatka-Kuril-Japan-Izu-Mariana-Yap	144.2230	22.5240	28.24	134.63	18.56
kisz-44b	Kamchatka-Kuril-Japan-Izu-Mariana-Yap	144.5246	22.8056	15.74	134.63	5.00
kisz-45a	Kamchatka-Kuril-Japan-Izu-Mariana-Yap	145.0895	21.8866	36.73	125.83	22.79
kisz-45b	Kamchatka-Kuril-Japan-Izu-Mariana-Yap	145.3171	22.1785	20.84	125.83	5.00
kisz-46a	Kamchatka-Kuril-Japan-Izu-Mariana-Yap	145.6972	21.3783	30.75	135.90	20.63

Table A4: (continued)

Segment	Description	Longitude (°)	Latitude (°)	Strike (°)	Dip (°)	Depth (km)
kisz-46b	Kamchatka-Kuril-Japan-Izu-Mariana-Yap	145.9954	21.6469	18.22	135.90	5.00
kisz-47a	Kamchatka-Kuril-Japan-Izu-Mariana-Yap	146.0406	20.9341	29.87	160.07	19.62
kisz-47b	Kamchatka-Kuril-Japan-Izu-Mariana-Yap	146.4330	21.0669	17.00	160.07	5.00
kisz-48a	Kamchatka-Kuril-Japan-Izu-Mariana-Yap	146.3836	20.0690	32.75	157.96	19.68
kisz-48b	Kamchatka-Kuril-Japan-Izu-Mariana-Yap	146.7567	20.2108	17.07	157.96	5.00
kisz-49a	Kamchatka-Kuril-Japan-Izu-Mariana-Yap	146.6689	19.3123	25.07	164.48	21.41
kisz-49b	Kamchatka-Kuril-Japan-Izu-Mariana-Yap	147.0846	19.4212	19.16	164.48	5.00
kisz-50a	Kamchatka-Kuril-Japan-Izu-Mariana-Yap	146.9297	18.5663	22.00	172.07	22.10
kisz-50b	Kamchatka-Kuril-Japan-Izu-Mariana-Yap	147.3650	18.6238	20.00	172.07	5.00
kisz-51a	Kamchatka-Kuril-Japan-Izu-Mariana-Yap	146.9495	17.7148	22.06	175.11	22.04
kisz-51b	Kamchatka-Kuril-Japan-Izu-Mariana-Yap	147.3850	17.7503	19.93	175.11	5.00
kisz-52a	Kamchatka-Kuril-Japan-Izu-Mariana-Yap	146.9447	16.8869	25.51	180.00	18.61
kisz-52b	Kamchatka-Kuril-Japan-Izu-Mariana-Yap	147.3683	16.8869	15.79	180.00	5.00
kisz-53a	Kamchatka-Kuril-Japan-Izu-Mariana-Yap	146.8626	16.0669	27.39	185.18	18.41
kisz-53b	Kamchatka-Kuril-Japan-Izu-Mariana-Yap	147.2758	16.0309	15.56	185.18	5.00
kisz-54a	Kamchatka-Kuril-Japan-Izu-Mariana-Yap	146.7068	15.3883	28.12	199.05	20.91
kisz-54b	Kamchatka-Kuril-Japan-Izu-Mariana-Yap	147.0949	15.2590	18.56	199.05	5.00

Table A4: (continued)

Segment	Description	Longitude (°)	Latitude (°)	Strike (°)	Dip (°)	Depth (km)
kisz-55a	Kamchatka-Kuril-Japan-Izu-Mariana-Yap	146.4717	14.6025	29.60	204.35	26.27
kisz-55b	Kamchatka-Kuril-Japan-Izu-Mariana-Yap	146.8391	14.4415	25.18	204.35	5.00
kisz-56a	Kamchatka-Kuril-Japan-Izu-Mariana-Yap	146.1678	13.9485	32.04	217.45	26.79
kisz-56b	Kamchatka-Kuril-Japan-Izu-Mariana-Yap	146.4789	13.7170	25.84	217.45	5.00
kisz-57a	Kamchatka-Kuril-Japan-Izu-Mariana-Yap	145.6515	13.5576	37.00	235.81	24.54
kisz-57b	Kamchatka-Kuril-Japan-Izu-Mariana-Yap	145.8586	13.2609	23.00	235.81	5.00
kisz-58a	Kamchatka-Kuril-Japan-Izu-Mariana-Yap	144.9648	12.9990	37.72	237.80	24.54
kisz-58b	Kamchatka-Kuril-Japan-Izu-Mariana-Yap	145.1589	12.6984	23.00	237.80	5.00
kisz-59a	Kamchatka-Kuril-Japan-Izu-Mariana-Yap	144.1799	12.6914	34.33	242.87	22.31
kisz-59b	Kamchatka-Kuril-Japan-Izu-Mariana-Yap	144.3531	12.3613	20.25	242.87	5.00
kisz-60a	Kamchatka-Kuril-Japan-Izu-Mariana-Yap	143.3687	12.3280	30.90	244.95	20.62
kisz-60b	Kamchatka-Kuril-Japan-Izu-Mariana-Yap	143.5355	11.9788	18.20	244.95	5.00
kisz-61a	Kamchatka-Kuril-Japan-Izu-Mariana-Yap	142.7051	12.1507	35.41	261.84	25.51
kisz-61b	Kamchatka-Kuril-Japan-Izu-Mariana-Yap	142.7582	11.7883	24.22	261.84	5.00
kisz-62a	Kamchatka-Kuril-Japan-Izu-Mariana-Yap	141.6301	11.8447	39.86	245.69	34.35
kisz-62b	Kamchatka-Kuril-Japan-Izu-Mariana-Yap	141.7750	11.5305	35.94	245.69	5.00
kisz-63a	Kamchatka-Kuril-Japan-Izu-Mariana-Yap	140.8923	11.5740	42.00	256.20	38.46

Table A4: (continued)

Segment	Description	Longitude (°)	Latitude (°)	Strike (°)	Dip (°)	Depth (km)
kisz-63b	Kamchatka-Kuril-Japan-Izu-Mariana-Yap	140.9735	11.2498	42.00	256.20	5.00
kisz-64a	Kamchatka-Kuril-Japan-Izu-Mariana-Yap	140.1387	11.6028	42.48	269.61	38.77
kisz-64b	Kamchatka-Kuril-Japan-Izu-Mariana-Yap	140.1410	11.2716	42.48	269.61	5.00
kisz-65a	Kamchatka-Kuril-Japan-Izu-Mariana-Yap	139.4595	11.5883	44.16	288.71	39.83
kisz-65b	Kamchatka-Kuril-Japan-Izu-Mariana-Yap	139.3541	11.2831	44.16	288.71	5.00
kisz-66a	Kamchatka-Kuril-Japan-Izu-Mariana-Yap	138.1823	11.2648	45.00	193.08	40.36
kisz-66b	Kamchatka-Kuril-Japan-Izu-Mariana-Yap	138.4977	11.1929	45.00	193.08	5.00
kisz-67a	Kamchatka-Kuril-Japan-Izu-Mariana-Yap	137.9923	10.3398	45.00	189.83	40.36
kisz-67b	Kamchatka-Kuril-Japan-Izu-Mariana-Yap	138.3104	10.2856	45.00	189.83	5.00
kisz-68a	Kamchatka-Kuril-Japan-Izu-Mariana-Yap	137.7607	9.6136	45.00	201.68	40.36
kisz-68b	Kamchatka-Kuril-Japan-Izu-Mariana-Yap	138.0599	9.4963	45.00	201.68	5.00
kisz-69a	Kamchatka-Kuril-Japan-Izu-Mariana-Yap	137.4537	8.8996	45.00	213.54	40.36
kisz-69b	Kamchatka-Kuril-Japan-Izu-Mariana-Yap	137.7215	8.7241	45.00	213.54	5.00
kisz-70a	Kamchatka-Kuril-Japan-Izu-Mariana-Yap	137.0191	8.2872	45.00	226.47	40.36
kisz-70b	Kamchatka-Kuril-Japan-Izu-Mariana-Yap	137.2400	8.0569	45.00	226.47	5.00
kisz-71a	Kamchatka-Kuril-Japan-Izu-Mariana-Yap	136.3863	7.9078	45.00	263.92	40.36
kisz-71b	Kamchatka-Kuril-Japan-Izu-Mariana-Yap	136.4202	7.5920	45.00	263.92	5.00
kisz-72a	Kamchatka-Kuril-Japan-Izu-Mariana-Yap	135.6310	7.9130	45.00	276.87	40.36

Table A4: (continued)

Segment	Description	Longitude (°)	Latitude (°)	Strike (°)	Dip (°)	Depth (km)
kisz-72b	Kamchatka-Kuril-Japan-Izu-Mariana-Yap	135.5926	7.5977	45.00	276.87	5.00
kisz-73a	Kamchatka-Kuril-Japan-Izu-Mariana-Yap	134.3296	7.4541	45.00	223.98	40.36
kisz-73b	Kamchatka-Kuril-Japan-Izu-Mariana-Yap	134.5600	7.2335	45.00	223.98	5.00
kisz-74a	Kamchatka-Kuril-Japan-Izu-Mariana-Yap	133.7125	6.8621	45.00	228.06	40.36
kisz-74b	Kamchatka-Kuril-Japan-Izu-Mariana-Yap	133.9263	6.6258	45.00	228.06	5.00
kisz-75a	Kamchatka-Kuril-Japan-Izu-Mariana-Yap	133.0224	6.1221	45.00	217.68	40.36
kisz-75b	Kamchatka-Kuril-Japan-Izu-Mariana-Yap	133.2751	5.9280	45.00	217.68	5.00
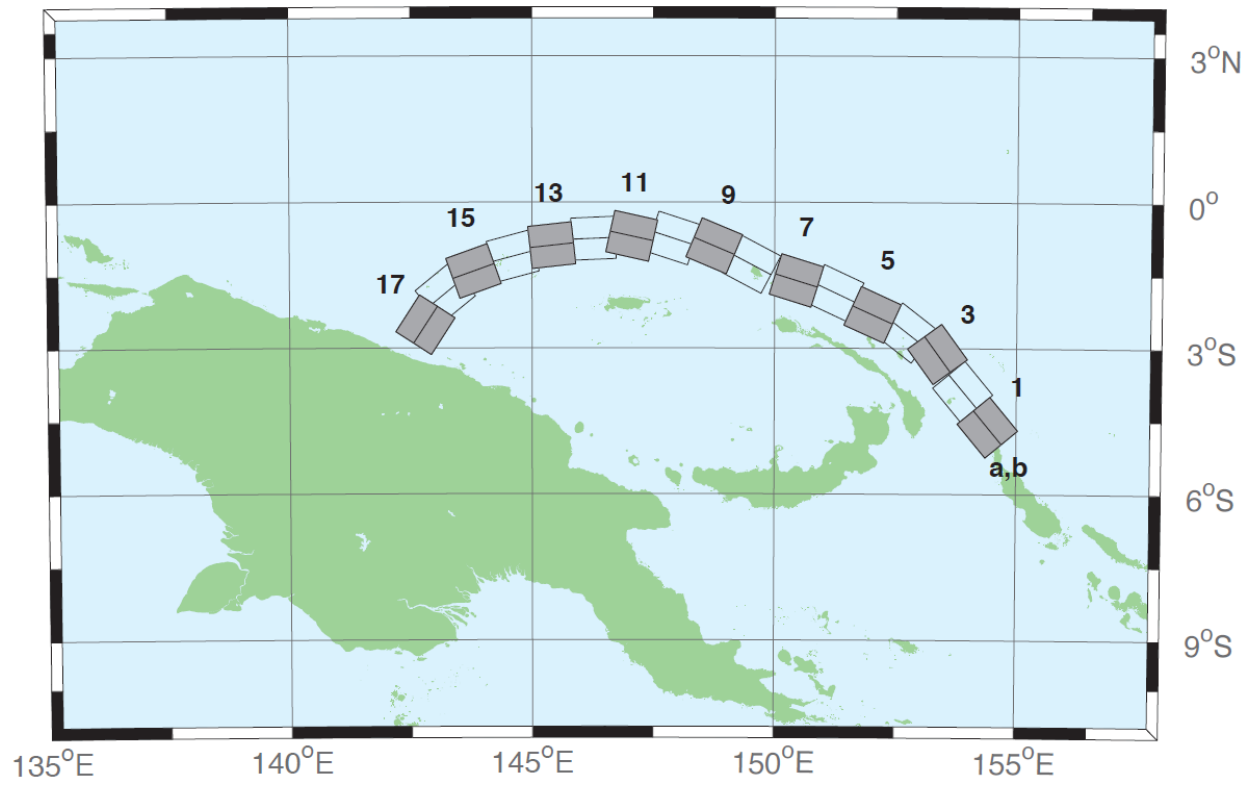
Figure A5. Manus Oceanic Convergent Boundary Subduction Zone unit sources.

Table A5: Earthquake parameters for Manus Oceanic Convergent Boundary Subduction Zone unit sources.

Segment	Description	Longitude (°)	Latitude (°)	Strike (°)	Dip (°)	Depth (km)
mosz-01a	Manus	154.0737	-4.8960	15.00	140.23	15.88
mosz-01b	Manus	154.4082	-4.6185	15.00	140.23	2.94
mosz-02a	Manus	153.5589	-4.1575	15.00	140.23	15.91
mosz-02b	Manus	153.8931	-3.8800	15.00	140.23	2.97
mosz-03a	Manus	153.0151	-3.3716	15.00	143.91	16.64
mosz-03b	Manus	153.3662	-3.1160	15.00	143.91	3.70
mosz-04a	Manus	152.4667	-3.0241	15.00	127.66	17.32
mosz-04b	Manus	152.7321	-2.6806	15.00	127.66	4.38
mosz-05a	Manus	151.8447	-2.7066	15.00	114.32	17.57
mosz-05b	Manus	152.0235	-2.3112	15.00	114.32	4.63
mosz-06a	Manus	151.0679	-2.2550	15.00	114.99	17.66
mosz-06b	Manus	151.2513	-1.8618	15.00	114.99	4.72
mosz-07a	Manus	150.3210	-2.0236	15.00	107.20	17.73
mosz-07b	Manus	150.4493	-1.6092	15.00	107.20	4.79
mosz-08a	Manus	149.3226	-1.6666	15.00	117.82	17.83
mosz-08b	Manus	149.5251	-1.2829	15.00	117.82	4.89
mosz-09a	Manus	148.5865	-1.3017	15.00	112.71	17.84
mosz-09b	Manus	148.7540	-0.9015	15.00	112.71	4.90
mosz-10a	Manus	147.7760	-1.1560	15.00	108.01	17.78
mosz-10b	Manus	147.9102	-0.7434	15.00	108.01	4.84
mosz-11a	Manus	146.9596	-1.1226	15.00	102.45	17.54
mosz-11b	Manus	147.0531	-0.6990	15.00	102.45	4.60
mosz-12a	Manus	146.2858	-1.1820	15.00	87.48	17.29
mosz-12b	Manus	146.2667	-0.7486	15.00	87.48	4.35
mosz-13a	Manus	145.4540	-1.3214	15.00	83.75	17.34
mosz-13b	Manus	145.4068	-0.8901	15.00	83.75	4.40
mosz-14a	Manus	144.7151	-1.5346	15.00	75.09	17.21
mosz-14b	Manus	144.6035	-1.1154	15.00	75.09	4.27
mosz-15a	Manus	143.9394	-1.8278	15.00	70.43	16.52

Table A5: continued

Segment	Description	Longitude (°)	Latitude (°)	Strike (°)	Dip (°)	Depth (km)
mosz-15b	Manus	143.7940	-1.4190	15.00	70.43	3.58
mosz-16a	Manus	143.4850	-2.2118	15.00	50.79	15.86
mosz-16b	Manus	143.2106	-1.8756	15.00	50.79	2.92
mosz-17a	Manus	143.1655	-2.7580	15.00	33.00	16.64
mosz-17b	Manus	142.8013	-2.5217	15.00	33.00	3.70
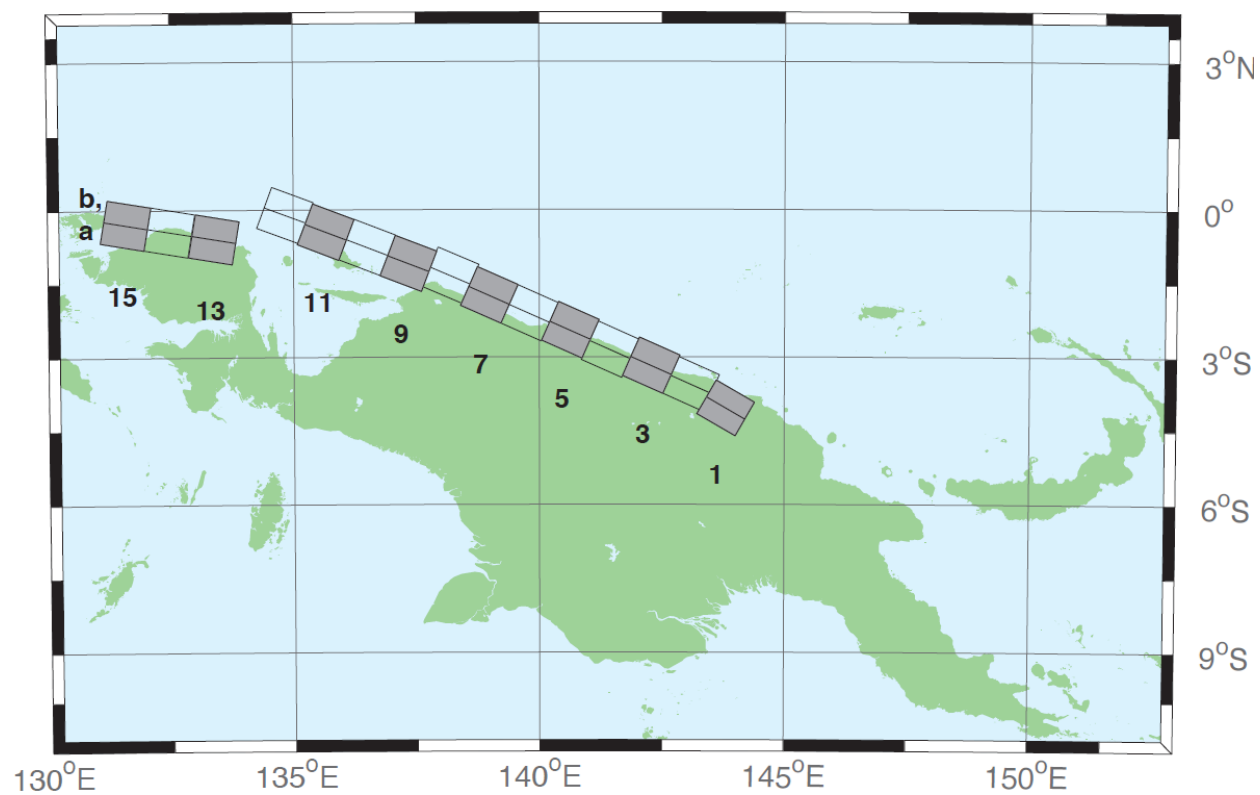
Figure A6. New Guinea Subduction Zone unit sources.

Table A6. Earthquake parameters for Manus Oceanic Convergent Boundary Subduction Zone unit sources.

Segment	Description	Longitude (°)	Latitude (°)	Strike (°)	Dip (°)	Depth (km)
ngsz-01a	New Guinea	143.6063	-4.3804	29.00	120.00	25.64
ngsz-01b	New Guinea	143.8032	-4.0402	29.00	120.00	1.40
ngsz-02a	New Guinea	142.9310	-3.9263	27.63	114.00	20.10
ngsz-02b	New Guinea	143.0932	-3.5628	21.72	114.00	1.60
ngsz-03a	New Guinea	142.1076	-3.5632	20.06	114.00	18.73
ngsz-03b	New Guinea	142.2795	-3.1778	15.94	114.00	5.00
ngsz-04a	New Guinea	141.2681	-3.2376	21.00	114.00	17.76
ngsz-04b	New Guinea	141.4389	-2.8545	14.79	114.00	5.00
ngsz-05a	New Guinea	140.4592	-2.8429	21.26	114.00	16.14
ngsz-05b	New Guinea	140.6296	-2.4605	12.87	114.00	5.00
ngsz-06a	New Guinea	139.6288	-2.4960	22.72	114.00	15.40
ngsz-06b	New Guinea	139.7974	-2.1175	12.00	114.00	5.00
ngsz-07a	New Guinea	138.8074	-2.1312	21.39	114.00	15.40
ngsz-07b	New Guinea	138.9776	-1.7491	12.00	114.00	5.00
ngsz-08a	New Guinea	138.0185	-1.7353	18.79	113.09	15.14
ngsz-08b	New Guinea	138.1853	-1.3441	11.70	113.09	5.00
ngsz-09a	New Guinea	137.1805	-1.5037	15.24	111.00	13.23
ngsz-09b	New Guinea	137.3358	-1.0991	9.47	111.00	5.00
ngsz-10a	New Guinea	136.3418	-1.1774	13.51	111.00	11.09
ngsz-10b	New Guinea	136.4983	-0.7697	7.00	111.00	5.00
ngsz-11a	New Guinea	135.4984	-0.8641	11.38	111.00	12.49
ngsz-11b	New Guinea	135.6562	-0.4530	8.62	111.00	5.00
ngsz-12a	New Guinea	134.6759	-0.5216	10.00	110.48	13.68
ngsz-12b	New Guinea	134.8307	-0.1072	10.00	110.48	5.00
ngsz-13a	New Guinea	133.3065	-1.0298	10.00	99.50	13.68
ngsz-13b	New Guinea	133.3795	-0.5935	10.00	99.50	5.00
ngsz-14a	New Guinea	132.4048	-0.8816	10.00	99.50	13.68
ngsz-14b	New Guinea	132.4778	-0.4453	10.00	99.50	5.00
ngsz-15a	New Guinea	131.5141	-0.7353	10.00	99.50	13.68
ngsz-15b	New Guinea	131.5871	-0.2990	10.00	99.50	5.00
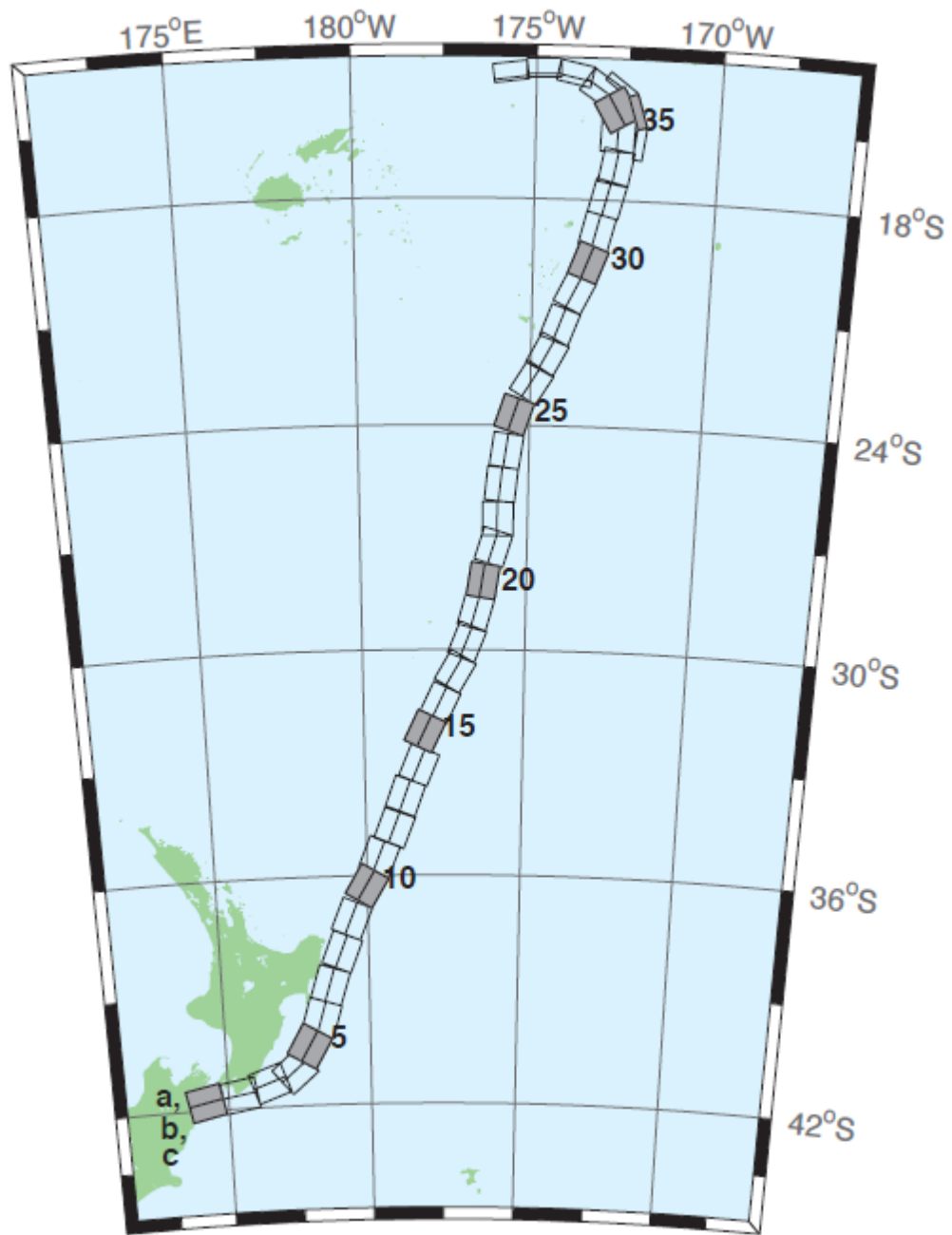
Figure A7. New Zealand-Kermadec-Tonga Subduction Zone unit sources.

Table A7. Earthquake parameters for New Zealand-Kermadec-Tonga Subduction Zone unit sources.

Segment	Description	Longitude (°)	Latitude (°)	Strike (°)	Dip (°)	Depth (km)
ntsz-01a	New Zealand-Tonga	174.0985	-41.3951	24.00	258.57	25.34
ntsz-01b	New Zealand-Tonga	174.2076	-41.7973	24.00	258.57	5.00
ntsz-02a	New Zealand-Tonga	175.3289	-41.2592	29.38	260.63	23.17
ntsz-02b	New Zealand-Tonga	175.4142	-41.6454	21.31	260.63	5.00
ntsz-03a	New Zealand-Tonga	176.2855	-40.9950	29.54	250.65	21.74
ntsz-03b	New Zealand-Tonga	176.4580	-41.3637	19.56	250.65	5.00
ntsz-04a	New Zealand-Tonga	177.0023	-40.7679	24.43	229.42	18.87
ntsz-04b	New Zealand-Tonga	177.3552	-41.0785	16.10	229.42	5.00
ntsz-05a	New Zealand-Tonga	177.4114	-40.2396	18.80	210.04	19.29
ntsz-05b	New Zealand-Tonga	177.8951	-40.4525	16.61	210.04	5.00
ntsz-06a	New Zealand-Tonga	177.8036	-39.6085	18.17	196.68	15.80
ntsz-06b	New Zealand-Tonga	178.3352	-39.7310	12.48	196.68	5.00
ntsz-07a	New Zealand-Tonga	178.1676	-38.7480	28.10	197.03	17.85
ntsz-07b	New Zealand-Tonga	178.6541	-38.8640	14.89	197.03	5.00
ntsz-08a	New Zealand-Tonga	178.6263	-37.8501	31.47	201.41	18.78
ntsz-08b	New Zealand-Tonga	179.0788	-37.9899	16.00	201.41	5.00
ntsz-09a	New Zealand-Tonga	178.9833	-36.9770	29.58	202.19	20.02
ntsz-09b	New Zealand-Tonga	179.4369	-37.1245	17.48	202.19	5.00
ntsz-10a	New Zealand-Tonga	179.5534	-36.0655	32.10	210.62	20.72
ntsz-10b	New Zealand-Tonga	179.9595	-36.2593	18.32	210.62	5.00
ntsz-11a	New Zealand-Tonga	179.9267	-35.3538	25.00	201.65	16.09
ntsz-11b	New Zealand-Tonga	180.3915	-35.5040	12.81	201.65	5.00
ntsz-12a	New Zealand-Tonga	180.4433	-34.5759	25.00	201.18	15.46
ntsz-12b	New Zealand-Tonga	180.9051	-34.7230	12.08	201.18	5.00
ntsz-13a	New Zealand-Tonga	180.7990	-33.7707	25.87	199.75	19.06
ntsz-13b	New Zealand-Tonga	181.2573	-33.9073	16.33	199.75	5.00
ntsz-14a	New Zealand-Tonga	181.2828	-32.9288	31.28	202.41	22.73

Table A7: (continued)

Segment	Description	Longitude (°)	Latitude (°)	Strike (°)	Dip (°)	Depth (km)
ntsz-14b	New Zealand-Tonga	181.7063	-33.0751	20.77	202.41	5.00
ntsz-15a	New Zealand-Tonga	181.4918	-32.0035	32.33	205.43	22.64
ntsz-15b	New Zealand-Tonga	181.8967	-32.1665	20.66	205.43	5.00
ntsz-16a	New Zealand-Tonga	181.9781	-31.2535	34.29	205.48	23.59
ntsz-16b	New Zealand-Tonga	182.3706	-31.4131	21.83	205.48	5.00
ntsz-17a	New Zealand-Tonga	182.4819	-30.3859	37.60	210.31	25.58
ntsz-17b	New Zealand-Tonga	182.8387	-30.5655	24.30	210.31	5.00
ntsz-18a	New Zealand-Tonga	182.8176	-29.6545	37.65	201.63	26.13
ntsz-18b	New Zealand-Tonga	183.1985	-29.7856	25.00	201.63	5.00
ntsz-19a	New Zealand-Tonga	183.0622	-28.8739	34.41	195.70	26.13
ntsz-19b	New Zealand-Tonga	183.4700	-28.9742	25.00	195.70	5.00
ntsz-20a	New Zealand-Tonga	183.2724	-28.0967	38.00	188.80	26.13
ntsz-20b	New Zealand-Tonga	183.6691	-28.1508	25.00	188.80	5.00
ntsz-21a	New Zealand-Tonga	183.5747	-27.1402	32.29	197.10	24.83
ntsz-21b	New Zealand-Tonga	183.9829	-27.2518	23.37	197.10	5.00
ntsz-22a	New Zealand-Tonga	183.6608	-26.4975	29.56	180.00	18.63
ntsz-22b	New Zealand-Tonga	184.0974	-26.4975	15.82	180.00	5.00
ntsz-23a	New Zealand-Tonga	183.7599	-25.5371	32.42	185.77	20.56
ntsz-23b	New Zealand-Tonga	184.1781	-25.5752	18.13	185.77	5.00
ntsz-24a	New Zealand-Tonga	183.9139	-24.6201	33.31	188.17	23.73
ntsz-24b	New Zealand-Tonga	184.3228	-24.6734	22.00	188.17	5.00
ntsz-25a	New Zealand-Tonga	184.1266	-23.5922	29.34	198.48	19.64
ntsz-25b	New Zealand-Tonga	184.5322	-23.7163	17.03	198.48	5.00
ntsz-26a	New Zealand-Tonga	184.6613	-22.6460	30.26	211.67	19.43
ntsz-26b	New Zealand-Tonga	185.0196	-22.8497	16.78	211.67	5.00
ntsz-27a	New Zealand-Tonga	185.0879	-21.9139	31.73	207.93	20.67
ntsz-27b	New Zealand-Tonga	185.4522	-22.0928	18.27	207.93	5.00
ntsz-28a	New Zealand-Tonga	185.4037	-21.1758	32.44	200.48	21.76
ntsz-28b	New Zealand-Tonga	185.7849	-21.3084	19.58	200.48	5.00
ntsz-29a	New Zealand-Tonga	185.8087	-20.2629	32.47	206.37	20.40
ntsz-29b	New Zealand-Tonga	186.1710	-20.4312	17.94	206.37	5.00
ntsz-30a	New Zealand-Tonga	186.1499	-19.5087	32.98	200.91	22.46

Table A7: (continued)

Segment	Description	Longitude (°)	Latitude (°)	Strike (°)	Dip (°)	Depth (km)
ntsz-30b	New Zealand-Tonga	186.5236	-19.6432	20.44	200.91	5.00
ntsz-31a	New Zealand-Tonga	186.3538	-18.7332	34.41	193.88	21.19
ntsz-31b	New Zealand-Tonga	186.7339	-18.8221	18.89	193.88	5.00
ntsz-32a	New Zealand-Tonga	186.5949	-17.8587	30.00	194.12	19.12
ntsz-32b	New Zealand-Tonga	186.9914	-17.9536	16.40	194.12	5.00
ntsz-33a	New Zealand-Tonga	186.8172	-17.0581	33.15	190.04	23.34
ntsz-33b	New Zealand-Tonga	187.2047	-17.1237	21.52	190.04	5.00
ntsz-34a	New Zealand-Tonga	186.7814	-16.2598	15.00	182.13	13.41
ntsz-34b	New Zealand-Tonga	187.2330	-16.2759	9.68	182.13	5.00
ntsz-34c*	New Zealand-Tonga	187.9697	-16.4956	57.06	7.62	6.57
ntsz-35a	New Zealand-Tonga	186.8000	-15.8563	15.00	149.85	12.17
ntsz-35b	New Zealand-Tonga	187.1896	-15.6384	8.24	149.85	5.00
ntsz-35c*	New Zealand-Tonga	187.8775	-15.6325	57.06	342.45	6.57
ntsz-36a	New Zealand-Tonga	186.5406	-15.3862	40.44	123.91	36.72
ntsz-36b	New Zealand-Tonga	186.7381	-15.1025	39.38	123.91	5.00
ntsz-36c*	New Zealand-Tonga	187.3791	-14.9234	57.06	307.04	6.57
ntsz-37a	New Zealand-Tonga	185.9883	-14.9861	68.94	101.95	30.99
ntsz-37b	New Zealand-Tonga	186.0229	-14.8282	31.32	101.95	5.00
ntsz-38a	New Zealand-Tonga	185.2067	-14.8259	80.00	88.40	26.13
ntsz-38b	New Zealand-Tonga	185.2044	-14.7479	25.00	88.40	5.00
ntsz-39a	New Zealand-Tonga	184.3412	-14.9409	80.00	82.55	26.13
ntsz-39b	New Zealand-Tonga	184.3307	-14.8636	25.00	82.55	5.00

*Rake angle is -90°
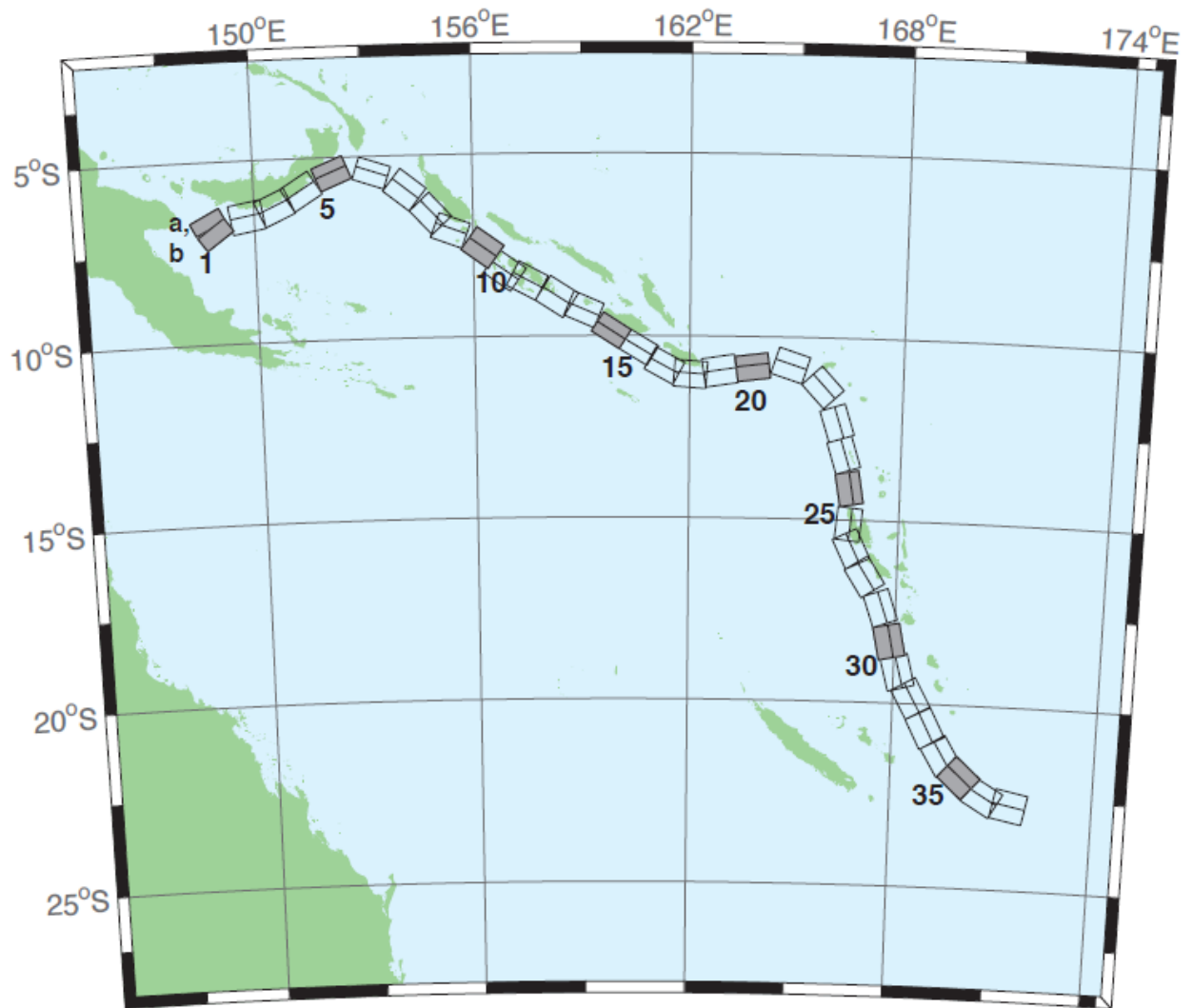
Figure A8. New Britain-Solomons-Vanuatu Zone unit sources.

Table A8. Earthquake parameters for New Zealand-Kermadec-Tonga Subduction Zone unit sources.

Segment	Description	Longitude (°)	Latitude (°)	Strike (°)	Dip (°)	Depth (km)
nvsz-01a	New Britain-Vanuatu	148.6217	-6.4616	32.34	243.15	15.69
nvsz-01b	New Britain-Vanuatu	148.7943	-6.8002	12.34	234.15	5.00
nvsz-02a	New Britain-Vanuatu	149.7218	-6.1459	35.10	260.06	16.36
nvsz-02b	New Britain-Vanuatu	149.7856	-6.5079	13.13	260.06	5.00
nvsz-03a	New Britain-Vanuatu	150.4075	-5.9659	42.35	245.69	18.59
nvsz-03b	New Britain-Vanuatu	150.5450	-6.2684	15.77	245.69	5.00
nvsz-04a	New Britain-Vanuatu	151.1095	-5.5820	42.41	238.22	23.63
nvsz-04b	New Britain-Vanuatu	151.2851	-5.8639	21.88	238.22	5.00
nvsz-05a	New Britain-Vanuatu	152.0205	-5.1305	49.22	247.73	32.39
nvsz-05b	New Britain-Vanuatu	152.1322	-5.4020	33.22	247.73	5.00
nvsz-06a	New Britain-Vanuatu	153.3450	-5.1558	53.53	288.58	33.59
nvsz-06b	New Britain-Vanuatu	153.2595	-5.4089	34.87	288.58	5.00
nvsz-07a	New Britain-Vanuatu	154.3814	-5.6308	39.72	308.27	19.18
nvsz-07b	New Britain-Vanuatu	154.1658	-5.9017	16.48	308.27	5.00
nvsz-08a	New Britain-Vanuatu	155.1097	-6.3511	45.33	317.22	22.92
nvsz-08b	New Britain-Vanuatu	154.8764	-6.5656	21.00	317.22	5.00
nvsz-09a	New Britain-Vanuatu	155.5027	-6.7430	48.75	290.51	22.92
nvsz-09b	New Britain-Vanuatu	155.3981	-7.0204	21.00	290.51	5.00
nvsz-10a	New Britain-Vanuatu	156.4742	-7.2515	36.88	305.85	27.62
nvsz-10b	New Britain-Vanuatu	156.2619	-7.5427	26.90	305.85	5.00
nvsz-11a	New Britain-Vanuatu	157.0830	-7.8830	32.97	305.36	29.72
nvsz-11b	New Britain-Vanuatu	156.8627	-8.1903	29.63	305.36	5.00
nvsz-12a	New Britain-Vanuatu	157.6537	-8.1483	37.53	297.94	28.57
nvsz-12b	New Britain-Vanuatu	157.4850	-8.4630	28.13	297.94	5.00
nvsz-13a	New Britain-Vanuatu	158.5089	-8.5953	33.62	302.73	23.02
nvsz-13b	New Britain-Vanuatu	158.3042	-8.9099	21.12	302.73	5.00
nvsz-14a	New Britain-Vanuatu	159.1872	-8.9516	38.44	293.32	34.06
nvsz-14b	New Britain-Vanuatu	159.0461	-9.2747	35.54	293.32	5.00
nvsz-15a	New Britain-Vanuatu	159.9736	-9.5993	46.69	302.76	41.38
nvsz-15b	New Britain-Vanuatu	159.8044	-9.8584	46.69	302.76	5.00
nvsz-16a	New Britain-Vanuatu	160.7343	-10.0574	46.05	300.99	41.00
nvsz-16b	New Britain-Vanuatu	160.5712	-10.3246	46.05	300.99	5.00
nvsz-17a	New Britain-Vanuatu	161.4562	-10.5241	40.12	298.37	37.22
nvsz-17b	New Britain-Vanuatu	161.2900	-10.8263	40.12	298.37	5.00

Table A8: (continued)

Segment	Description	Longitude (°)	Latitude (°)	Strike (°)	Dip (°)	Depth (km)
nvsz-18a	New Britain-Vanuatu	162.0467	-10.6823	40.33	274.07	29.03
nvsz-18b	New Britain-Vanuatu	162.0219	-11.0238	28.72	274.07	5.00
nvsz-19a	New Britain-Vanuatu	162.7818	-10.5645	34.25	261.27	24.14
nvsz-19b	New Britain-Vanuatu	162.8392	-10.9315	22.51	261.27	5.00
nvsz-20a	New Britain-Vanuatu	163.7222	-10.5014	50.35	262.93	26.30
nvsz-20b	New Britain-Vanuatu	163.7581	-10.7858	25.22	262.93	5.00
nvsz-21a	New Britain-Vanuatu	164.9445	-10.4183	40.31	287.89	23.30
nvsz-21b	New Britain-Vanuatu	164.8374	-10.7442	21.47	287.89	5.00
nvsz-22a	New Britain-Vanuatu	166.0261	-11.1069	42.39	317.08	20.78
nvsz-22b	New Britain-Vanuatu	165.7783	-11.3328	18.40	317.08	5.00
nvsz-23a	New Britain-Vanuatu	166.5179	-12.2260	47.95	342.37	22.43
nvsz-23b	New Britain-Vanuatu	166.2244	-12.3171	20.40	342.37	5.00
nvsz-24a	New Britain-Vanuatu	166.7236	-13.1065	47.13	342.6	28.52
nvsz-24b	New Britain-Vanuatu	166.4241	-13.1979	28.06	342.6	5.00
nvsz-25a	New Britain-Vanuatu	166.8914	-14.0785	54.10	350.28	31.16
nvsz-25b	New Britain-Vanuatu	166.6237	-14.1230	31.55	350.28	5.00
nvsz-26a	New Britain-Vanuatu	166.9200	-15.1450	50.46	365.62	29.05
nvsz-26b	New Britain-Vanuatu	166.6252	-15.1170	28.75	365.62	5.00
nvsz-27a	New Britain-Vanuatu	167.0053	-15.6308	44.74	334.23	25.46
nvsz-27b	New Britain-Vanuatu	166.7068	-15.7695	24.15	334.23	5.00
nvsz-28a	New Britain-Vanuatu	167.4074	-16.3455	41.53	327.46	22.44
nvsz-28b	New Britain-Vanuatu	167.1117	-16.5264	20.42	327.46	5.00
nvsz-29a	New Britain-Vanuatu	167.9145	-17.2807	49.10	341.16	24.12
nvsz-29b	New Britain-Vanuatu	167.6229	-17.3757	22.48	341.16	5.00
nvsz-30a	New Britain-Vanuatu	168.2220	-18.2353	44.19	348.58	23.99
nvsz-30b	New Britain-Vanuatu	167.8895	-18.2991	22.32	348.58	5.00
nvsz-31a	New Britain-Vanuatu	168.5022	-19.0510	42.20	345.59	22.26
nvsz-31b	New Britain-Vanuatu	168.1611	-19.1338	20.20	345.59	5.00
nvsz-32a	New Britain-Vanuatu	168.8775	-19.6724	42.03	331.06	21.68
nvsz-32b	New Britain-Vanuatu	168.5671	-19.8338	19.49	331.06	5.00
nvsz-33a	New Britain-Vanuatu	169.3422	-20.4892	40.25	332.91	22.40
nvsz-33b	New Britain-Vanuatu	169.0161	-20.6453	20.37	332.91	5.00
nvsz-34a	New Britain-Vanuatu	169.8304	-21.2121	39.00	329.15	22.73

Table A8. (continued)

Segment	Description	Longitude (°)	Latitude (°)	Strike (°)	Dip (°)	Depth (km)
nvsz-34b	New Britain-Vanuatu	169.5086	-21.3911	20.77	329.15	5.00
nvsz-35a	New Britain-Vanuatu	170.3119	-21.6945	39.00	311.89	22.13
nvsz-35b	New Britain-Vanuatu	170.0606	-21.9543	20.03	311.89	5.00
nvsz-36a	New Britain-Vanuatu	170.9487	-22.1585	39.42	300.43	23.50
nvsz-36b	New Britain-Vanuatu	170.7585	-22.4577	21.71	300.43	5.00
nvsz-37a	New Britain-Vanuatu	171.6335	-22.3087	30.00	281.26	22.10
nvsz-37b	New Britain-Vanuatu	171.5512	-22.6902	20.00	281.26	5.00
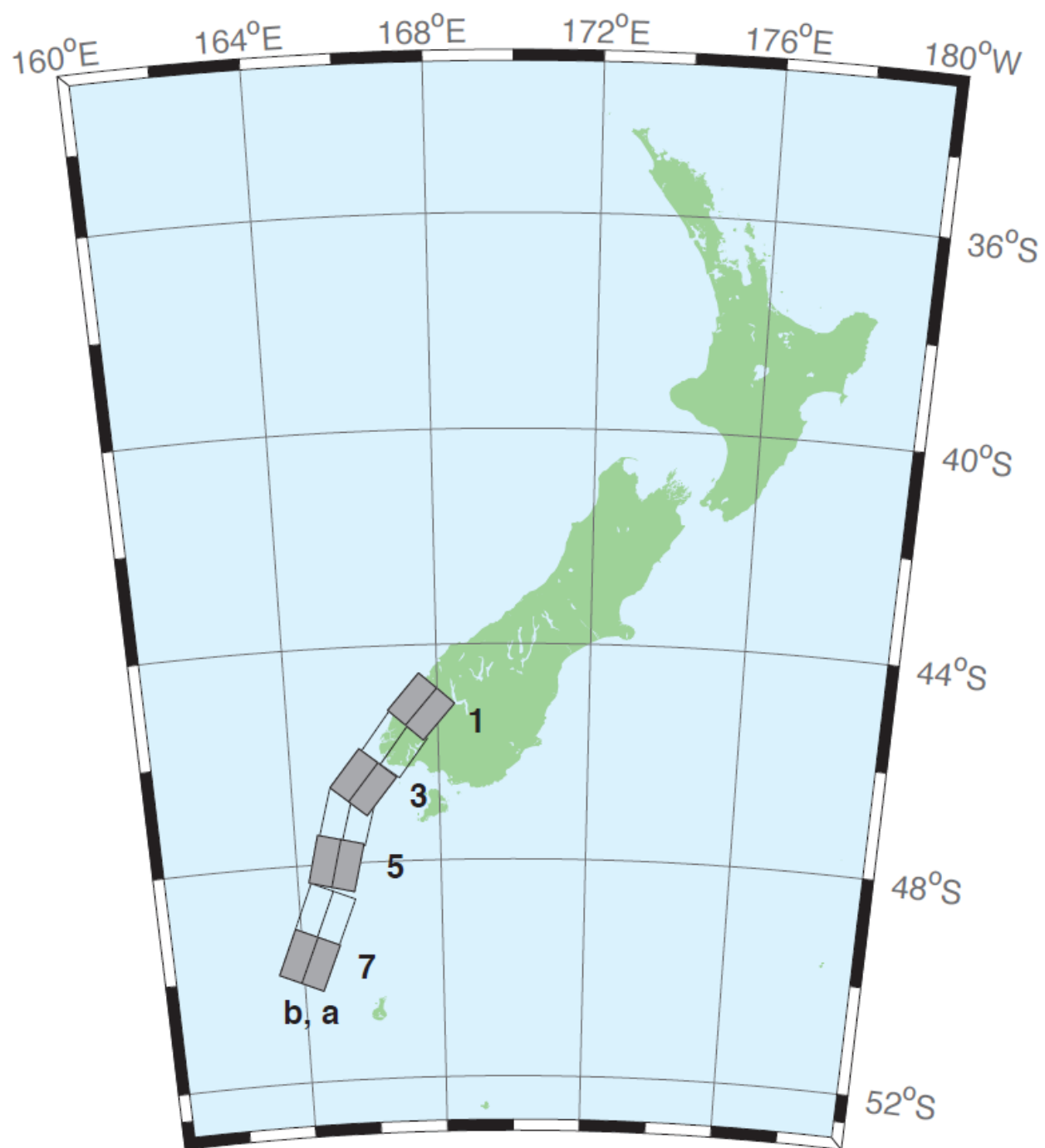
Figure A9. New Zealand-Puyseger Zone unit sources.

Table A9. Earthquake parameters for New Zealand-Puyseger Subduction Zone unit sources.

Segment	Description	Longitude (°)	Latitude (°)	Strike (°)	Dip (°)	Depth (km)
nzsz-01a	New Zealand-Puyseger	168.0294	-45.4368	15.00	41.50	17.94
nzsz-01b	New Zealand-Puyseger	167.5675	-45.1493	15.00	41.50	5.00
nzsz-02a	New Zealand-Puyseger	167.3256	-46.0984	15.00	37.14	17.94
nzsz-02b	New Zealand-Puyseger	166.8280	-45.8365	15.00	37.14	5.00
nzsz-03a	New Zealand-Puyseger	166.4351	-46.7897	15.00	39.53	17.94
nzsz-03b	New Zealand-Puyseger	165.9476	-46.5136	15.00	39.53	5.00
nzsz-04a	New Zealand-Puyseger	166.0968	-47.2583	15.00	15.38	17.94
nzsz-04b	New Zealand-Puyseger	165.4810	-47.1432	15.00	15.38	5.00
nzsz-05a	New Zealand-Puyseger	165.7270	-48.0951	15.00	13.94	17.94
nzsz-05b	New Zealand-Puyseger	165.0971	-47.9906	15.00	13.94	5.00
nzsz-06a	New Zealand-Puyseger	165.3168	-49.0829	15.00	22.71	17.94
nzsz-06b	New Zealand-Puyseger	164.7067	-48.9154	15.00	22.71	5.00
nzsz-07a	New Zealand-Puyseger	164.8017	-49.9193	15.00	23.25	17.94
nzsz-07b	New Zealand-Puyseger	164.1836	-49.7480	15.00	23.25	5.00
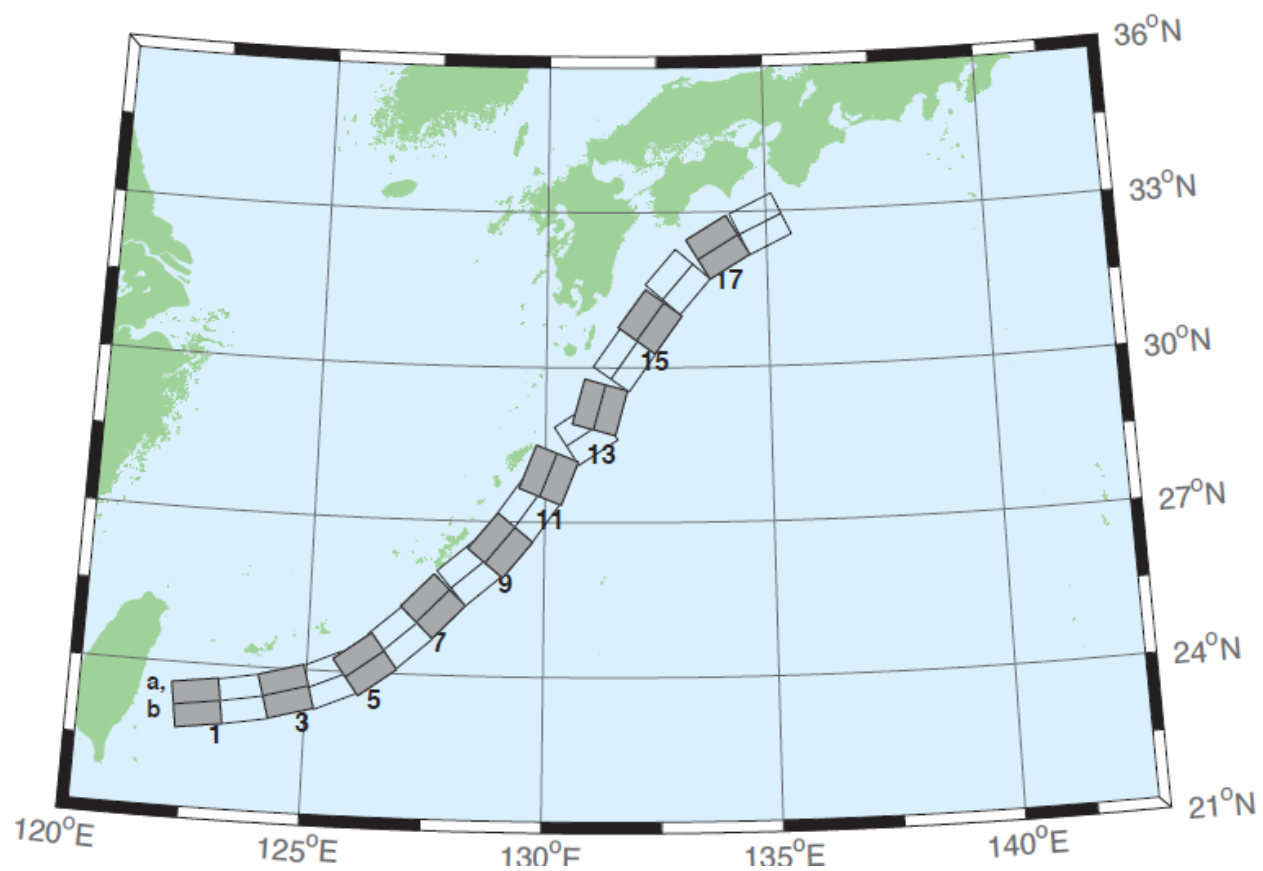
Figure A10. Ryukyu-Kyushu-Nankai Zone unit sources.

Table A10. Earthquake parameters for New Zealand-Puyseger Subduction Zone unit sources.

Segment	Description	Longitude (°)	Latitude (°)	Strike (°)	Dip (°)	Depth (km)
rnsz-01a	Ryukyu-Nankai	122.6672	23.6696	14.00	262.00	11.88
rnsz-01b	Ryukyu-Nankai	122.7332	23.2380	10.00	262.00	3.20
rnsz-02a	Ryukyu-Nankai	123.5939	23.7929	18.11	259.95	12.28
rnsz-02b	Ryukyu-Nankai	123.6751	23.3725	10.00	259.95	3.60
rnsz-03a	Ryukyu-Nankai	124.4604	23.9777	19.27	254.63	14.65
rnsz-03b	Ryukyu-Nankai	124.5830	23.5689	12.18	254.63	4.10
rnsz-04a	Ryukyu-Nankai	125.2720	24.2102	18.00	246.75	20.38
rnsz-04b	Ryukyu-Nankai	125.4563	23.8177	16.00	246.75	6.60
rnsz-05a	Ryukyu-Nankai	125.9465	24.5085	18.00	233.64	20.21
rnsz-05b	Ryukyu-Nankai	126.2241	24.1645	16.00	233.64	6.43
rnsz-06a	Ryukyu-Nankai	126.6349	25.0402	17.16	228.73	19.55
rnsz-06b	Ryukyu-Nankai	126.9465	24.7176	15.16	228.73	6.47
rnsz-07a	Ryukyu-Nankai	127.2867	25.6343	15.85	224.04	17.98
rnsz-07b	Ryukyu-Nankai	127.6303	25.3339	13.56	224.04	6.26
rnsz-08a	Ryukyu-Nankai	128.0725	26.3146	14.55	229.69	14.31
rnsz-08b	Ryukyu-Nankai	128.3854	25.9831	9.64	229.69	5.94
rnsz-09a	Ryukyu-Nankai	128.6642	26.8177	15.40	219.24	12.62
rnsz-09b	Ryukyu-Nankai	129.0391	26.5438	8.00	219.24	5.66
rnsz-10a	Ryukyu-Nankai	129.2286	27.4879	17.00	215.21	12.55
rnsz-10b	Ryukyu-Nankai	129.6233	27.2402	8.16	215.21	5.45
rnsz-11a	Ryukyu-Nankai	129.6169	28.0741	17.00	201.30	12.91
rnsz-11b	Ryukyu-Nankai	130.0698	27.9181	8.80	201.30	5.26
rnsz-12a	Ryukyu-Nankai	130.6175	29.0900	16.42	236.69	13.05
rnsz-12b	Ryukyu-Nankai	130.8873	28.7299	9.57	236.69	4.74
rnsz-13a	Ryukyu-Nankai	130.7223	29.3465	20.25	195.18	15.89
rnsz-13b	Ryukyu-Nankai	131.1884	29.2362	12.98	195.18	4.66
rnsz-14a	Ryukyu-Nankai	131.3467	30.3899	22.16	215.11	19.73
rnsz-14b	Ryukyu-Nankai	131.7402	30.1507	17.48	215.11	4.71
rnsz-15a	Ryukyu-Nankai	131.9149	31.1450	15.11	216.04	16.12
rnsz-15b	Ryukyu-Nankai	132.3235	30.8899	13.46	216.04	4.48
rnsz-16a	Ryukyu-Nankai	132.5628	31.9468	10.81	220.90	10.88
rnsz-16b	Ryukyu-Nankai	132.9546	31.6579	7.19	220.90	4.62

Table A10: (continued)

Segment	Description	Longitude (°)	Latitude (°)	Strike (°)	Dip (°)	Depth (km)
rnsz-17a	Ryukyu-Nankai	133.6125	32.6956	10.14	238.96	12.01
rnsz-17b	Ryukyu-Nankai	133.8823	32.3168	8.41	238.96	4.70
rnsz-18a	Ryukyu-Nankai	134.6416	33.1488	10.99	244.70	14.21
rnsz-18b	Ryukyu-Nankai	134.8656	32.7502	10.97	244.47	4.70
rnsz-19a	Ryukyu-Nankai	135.6450	33.5008	14.49	246.46	14.72
rnsz-19b	Ryukyu-Nankai	135.8523	33.1021	11.87	246.46	4.44
rnsz-20a	Ryukyu-Nankai	136.5962	33.8506	15.00	244.77	14.38
rnsz-20b	Ryukyu-Nankai	136.8179	33.4581	12.00	244.77	3.98
rnsz-21a	Ryukyu-Nankai	137.2252	34.3094	15.00	231.90	15.40
rnsz-21b	Ryukyu-Nankai	137.5480	33.9680	12.00	231.90	5.00
rnsz-22a	Ryukyu-Nankai	137.4161	34.5249	15.00	192.27	15.40
rnsz-22b	Ryukyu-Nankai	137.9301	34.4327	12.00	192.27	5.00

Appendix B: Glossary

Alpha(s) or 'α' or Same as **scaling factors**.

Arrival time The time when the first tsunami wave is observed at a particular location, typically given in local and/or universal time, but also commonly noted in minutes or hours relative to the time of the earthquake.

Bathymetry The measurement of water depth of an undisturbed body of water.

Cascadia Subduction Zone Fault that extends from Cape Mendocino in Northern California northward to mid-Vancouver Island, Canada. The fault marks the convergence boundary where the Juan de Fuca tectonic plate is being subducted under the margin of the North America plate.

Current speed The scalar rate of water motion measured as distance/time.

Current velocity Movement of water expressed as a vector quantity. Velocity is the distance of movement per time coupled with direction of motion.

Deep-ocean Assessment and Reporting of Tsunamis (DART®) Tsunami detection and transmission system that measures the pressure of an overlying column of water and detects the passage of a tsunami.

Digital Elevation Model (DEM) A digital representation of bathymetry or topography based on regional survey data or satellite imagery. Data are arrays of regularly spaced elevations referenced to a map projection of the geographic coordinate system.

Epicenter The point on the surface of the earth that is directly above the focus of an earthquake.

Far-field Region outside of the source of a tsunami where no direct observations of the tsunami-generating event are evident, except for the tsunami waves themselves.

Focus The point beneath the surface of the earth where a rupture or energy release occurs due to a buildup of stress or the movement of Earth's tectonic plates relative to one another.

Inundation The horizontal inland extent of land that a tsunami penetrates, generally measured perpendicularly to a shoreline.

Marigram Tide gauge recording of wave level as a function of time at a particular location. The instrument used for recording is termed a marigraph.

Method of Splitting Tsunami (MOST) A suite of numerical simulation codes used to provide estimates of the three processes of tsunami evolution: tsunami generation, propagation, and inundation.

Moment magnitude (Mw) The magnitude of an earthquake on a logarithmic scale in terms of the energy released. Moment magnitude is based on the size and characteristics of a fault rupture as determined from long-period seismic waves.

Near–field Region of primary tsunami impact near the source of a tsunami. The near-field is defined as the region where non-tsunami effects of the tsunami-generating event have been observed, such as earth shaking from the earthquake, visible or measured ground deformation, or other direct (non-tsunami) evidences of the source of the tsunami wave.

Propagation database A basin-wide database of precomputed water elevations and flow velocities at uniformly spaced grid points throughout the world oceans. Values are computed from tsunamis generated by earthquakes with a fault rupture at any one of discrete 100×50 km unit sources along worldwide subduction zones.

Reference point or Warning point A selected grid point where the simulated tsunami signal is compared with observations or with a numerical solution obtained on a higher resolution grid.

Runup Vertical difference between the elevation of tsunami inundation and the sea level at the time of a tsunami. Runup is the elevation of the highest point of land inundated by a tsunami as measured relative to a stated datum, such as mean sea level.

Scaling factors Multiplicative coefficients applied to each unit source in a linear combination of unit sources representing a propagation solution for a specific tsunami event. The scaling factors can also be interpreted as the slip amount associated with each unit source.

Short-term Inundation Forecasting for Tsunamis (SIFT) A tsunami forecast system that integrates tsunami observations in deep ocean with numerical models to provide an estimate of tsunami wave arrival and amplitude at specific coastal locations while a tsunami propagates across an ocean basin.

Subduction zone A submarine region of the earth's crust at which two or more tectonic plates converge to cause one plate to sink under another, overriding plate. Subduction zones are regions of high seismic activity.

Synthetic event Hypothetical events based on computer simulations or theory of possible or even likely future scenarios.

Tele-tsunami or **distant tsunami** or **far-field tsunami** Most commonly, a tsunami originating from a source greater than 1000 km away from a particular location. In some contexts, a tele-tsunami is one that propagates through deep ocean before reaching a particular location without regard to distance separation.

Tidal wave Term frequently used incorrectly as a synonym for tsunami. A tsunami is unrelated to the predictable periodic rise and fall of sea level due to the gravitational attractions of the moon and sun; see **Tide**, below.

Tide The predictable rise and fall of a body of water (ocean, sea, bay, etc.) due to the gravitational attractions of the moon and sun.

Tide gauge An instrument for measuring the rise and fall of a column of water over time at a particular location.

Travel time The time it takes for a tsunami to travel from the generating source to a particular location.

Tsunameter An oceanographic instrument used to detect and measure tsunamis in the deep ocean. Tsunami measurements are typically transmitted acoustically to a surface buoy that in turn relays them in real time to ground stations via satellite.

Tsunami A Japanese term that literally translates to "harbor wave." Tsunamis are a series of long-period shallow water waves that are generated by the sudden displacement of water due to subsea disturbances such as earthquakes, submarine landslides, or volcanic eruptions. Less commonly, meteoric impact to the ocean or meteorological forcing can generate a tsunami.

Tsunami hazard assessment A systematic investigation of seismically active regions of the world oceans to determine their potential tsunami impact at a particular location. Numerical models are typically used to characterize tsunami generation, propagation, and inundation, and to quantify the risk posed to a particular community from tsunamis generated in each source region investigated.

Tsunami propagation The directional movement of a tsunami wave outward from the source of generation. The speed at which a tsunami propagates depends on the depth of the water column in which the wave is traveling. Tsunamis travel at a speed of 700 km/hr (450 mi/hr) over the average depth of 4000 m in the open deep Pacific Ocean.

Tsunami source Location of tsunami origin, most typically an underwater earthquake epicenter. Tsunamis are also generated by submarine landslides, underwater volcanic eruptions, or, less commonly, by meteoric impact of the ocean.

Wall-clock time The time that passes on a common clock or watch between the start and end of a model run, as distinguished from the time needed by a CPU or computer processor to complete the run, typically less than wallclock time.

Wave amplitude The maximum vertical rise or drop of a column of water as measured from wave crest (peak) or trough to a defined mean water level state.

Wave crest or peak The highest part of a wave or maximum rise above a defined mean water level state, such as mean lower low water.

Wave height The vertical difference between the highest part of a specific wave (crest) and its corresponding lowest point (trough).

Wavelength The horizontal distance between two successive wave crests or troughs.

Wave period The length of time between the passage of two successive wave crests or troughs as measured at a fixed location.

Wave trough The lowest part of a wave or the maximum drop below a defined mean water level state, such as mean lower low water.